Cyclic Behavior, Development, and Characteristics of a Ductile Hybrid Fiber Reinforced Polymer (DHFRP) for Reinforced Concrete Members

A Thesis

Submitted to the Faculty

of

Drexel University

by

Francis Patrick Hampton

in partial fulfillment of the

requirements for the degree

of

Doctor of Philosophy

May 2004

DEDICATIONS

This work would not be possible without the unfailing support and love of my parents, John and Marlene Hampton.

I would especially like to thank my father John for his assistance and guidance throughout my engineering education. His knowledge, insight, and experience in civil and structural engineering has been invaluable, and for this, I will always be eternally grateful.

Finally, I wish to thank almighty God for His support and guidance during my education and life, without which this work would have no meaning.

ACKNOWLEDGEMENTS

I would like to thank my advisor, Dr. Harry Harris, for his guidance, support, and patience throughout my study at Drexel University. His expertise in modeling, testing, and mechanics has molded my academic interests. I would like to thank my co-advisor, Dr. Frank K. Ko of the Department of Materials Engineering for his support, encouragement, and assistance and his introduction into the world of composites and materials manufacturing.

I would like to thank my committee, Dr. Elgaaly, Dr. Wartman, and Dr. Tan for their academic and scholarly guidance.

I would like to offer special thanks to the Department of Civil Engineering for financial support and guidance, especially Dr. Haas, Dr. Martin, Dr. Weggel and Dr. Hsuan. I would like to thank Mr. Mark Sheible of the machine shop and the staff for their effort in making test fixtures; Mr. Greg Hilley of Civil Engineering for assisting me in testing; Mr. David von Rohr of Materials Engineering for use of the microscopy equipment; and Mr. John McKelvie for assisting me at the Fibrous Materials Research Center.

I would like to thank Hoa Lam, graduate student in Materials Engineering, for her help with the DHFRP project, and her many discussions on the production and mechanics of DHFRP. Her expertise in the area of composites manufacturing has added so much to this project and in my knowledge of braiding, to this I am forever grateful.

Finally, I would like to thank my family and friends for supporting me and tolerating me during my academic endeavors. To this, I am eternally grateful.

TABLE OF CONTENTS

LIST OF TABLES

LIST OF FIGURES

ABSTRACT

Cyclic Behavior, Development, and Characteristics of a Ductile Hybrid Fiber Reinforced Polymer (DHFRP) for Reinforced Concrete Members
Frank Patrick Hampton
Harry G. Harris, Ph.D.
Frank K. Ko, Ph.D.

Reinforced concrete (R/C) structures especially pavements and bridge decks that constitute vital elements of the infrastructure of all industrialized societies are deteriorating prematurely. Structural repair and upgrading of these structural elements have become a more economical option for constructed facilities especially in the United States and Canada.

One method of retrofitting concrete structures is the use of advanced materials. Fiber reinforced polymer (FRP) composite materials typically are in the form of fabric sheets or reinforcing bars. While the strength and stiffness of the FRP is high, composites are inherently brittle, with limited or no ductility. Conventional FRP systems cannot currently meet ductility demand, and therefore, may fail in a catastrophic failure mode.

The primary goal of this research was to develop an improved prototype 10-mm diameter DHFRP bar. The behavior of the bar under full load reversals to failure was investigated. However, this bar first needed to be designed and manufactured in the Fibrous Materials Research at Drexel University. Material properties were determined through testing to categorize the strength properties of the DHFRP. Similitude was used to demonstrate the scaling of properties from the original model bars. The four most important properties of the DHFRP bars are sufficient strength and stiffness, significant

ductility for plasticity to develop in the R/C section, and sufficient bond strength for the R/C section to develop its full strength.

Once these properties were determined the behavior of reinforced concrete members was investigated. This included the testing of prototype-size beams under monotonic loading and model and prototype beam-columns under reverse cyclic loading. These tests confirmed the large ductility exhibited by the DHFRP. Also the energy absorption capacity of the bar was demonstrated by the hysteretic behavior of the beam-columns. Displacement ductility factors in the range of 3-6 were achieved for all concrete elements tested.

To study the long-term behavior of DHFRP, the creep-rupture strength of 5-mm bars was tested. This was conducted first on individual bar specimens and is important in the life-cycle design and performance of DHFRP reinforced concrete.

CHAPTER 1. INTRODUCTION

Reinforced concrete (R/C) structures especially pavements and bridge decks that constitute vital elements of the infrastructure of all industrialized societies are deteriorating prematurely. Structural repair and upgrading of these structural elements have become a more economical option for constructed facilities especially in the United States and Canada.

Much of the U.S. highway system has been deteriorating prematurely due to corrosion of steel reinforcement. In 2001, according to the Federal Highway Administration (FHWA), total disbursements for highways are going to be approximately $126.2 billion, an increase of almost 17 percent over 1998 (FHWA (2001)). The Transportation Equity Act for the Twenty-first Century (TEA-21) provided a significant increase in Federal funds for capital programs. Capital expenditures are expected to rise to $64.8 billion in 2001, accounting for over 51 percent of total highway expenditures (FHWA (2001)). This is an increase of $23.5 billion or almost 24 percent compared to 1998 (FHWA (2001)). Highway maintenance will account for $31 billion. The National Highway System (NHS) includes 114,000 bridges. Approximately 30.8 percent of the deck area on these bridges is either structurally deficient or obsolete. Of the approximately 472,000 non-NHS bridges identified in the National Bridge Inventory (NBI), 32.6 percent of the deck area is considered to be deficient (FHWA (2001)). These bridges are classified as structurally deficient primarily because of corrosion of steel reinforcement. For fiscal year 2002, the Federal Highway Administration (FHWA) plans to spend $4.4 billion for the Highway Bridge Replacement and Rehabilitation Program and over $5 billion in Interstate Maintenance (IM) Funds and $6 billion in NHS funds for

pavement rehabilitation. The American Society of Civil Engineers recently gave a grade of D+ for the Report Card on America's Infrastructure.

Epoxy-coated reinforcing steel (ECRS) has been used as the primary means of corrosion protection during the past two decades. Many states now specify ECRS as the preferred protective system to reduce corrosion-induced deterioration in concrete bridge decks. However, severe corrosion was reported in ECRS (Keeslar and Powers, 1988). This extensive premature corrosion of ECRS had prompted the Transportation Research Board to conduct an investigation on ECRS performance in concrete. They concluded in Report 370 (Clear et al., 1995) that ECRS could not be relied on to provide long-term (50-plus years) corrosion protection to concrete transportation structures.

One method of retrofitting concrete structures is the use of advanced materials. These fiber reinforced polymer (FRP) composite materials typically are in the form of fabric sheets or reinforcing bars. Possible applications for FRPs are in two broad categories, corrosive applications and electromagnetic applications. Various applications are given in Table 1.1. Benefits of FRPs include their imperviousness to chloride ion and chemical attack, tensile strength greater than steel, weight up to ¼ that of steel reinforcement, and non-conductivity. It is also transparent to magnetic fields and radio frequencies. While the strength and stiffness of the FRP is high, composites are inherently brittle, with limited or no ductility. This gives no warning of failure and design must be made on providing sufficient strength that no possibility of failure can occur, otherwise, a catastrophic failure can result. For conventional design of reinforced concrete (R/C) structures, the ductility of the reinforcing steel is a necessary condition for the member to behave properly and fail in a ductile mode. This is especially important in

regions of moderate to high seismicity where the ductility demand is greater and needed for the proper response of the structure. In seismic design of R/C structures, the ability of a structure to survive a seismic event relies on the ability of the reinforcement to undergo large inelastic strains. During these seismic events, the reinforcing steel needs to be capable of absorbing the energy induced by the ground motion. Conventional FRP systems cannot currently meet this demand with a resulting catastrophic failure.

Table 1.1: Applications for FRP Bars.

Corrosive Applications			**Electromagnetic Applications**
Concrete Exposed to De-Icing Salts	Concrete Exposed to Marine Salts	Other	
-Bridge decks	*-Seawalls*	*-Concrete used in chemical plants and containers*	*-MRI rooms in hospitals*
-Median barriers	*-Structures near waterfronts*	*-Pipeline and chemical distribution facilities*	*-Airport radio and compass calibration pads*
-Approach slabs	*-Aquaculture operations*	*-Brine tanks*	*-Electrical high voltage transformer vaults*
-Parking structures	*-Artificial reefs and break waters*	*-Swimming pools*	*-Concrete near high voltage cables and substations*
-Railroad crossings	*-Floating marine docks*	*-Mining applications-rock nails*	
-Salt storage facilities			

A ductile hybrid FRP reinforcement was developed at Drexel University in the form of a ductile hybrid bar (DHFRP) which simulated the stress-strain characteristics of conventional steel reinforcement (Somboonsong, 1997). These bars were manufactured in model sizes of 3-mm and 5-mm diameters. Testing of these bars demonstrated significant ductility with a bilinear stress-strain behavior with a definite yield and an ultimate stress higher than yield. The bond strength was lower than steel and needed to be improved to a level closer to that of the steel reinforcing bond strength. Tests on beams reinforced with 5-mm bars were loaded both monotonically and cyclically and showed significant ductility with displacement ductility factors of between 3 and 5 (Huesgen, 1998). Also, preliminary tests on beams subjected to increasing cycles of reverse cyclic loading (Harris et al., 2000) have shown ductility and significant energy absorption capacity with a stable hysteretic behavior.

The primary goal of this research was to develop an improved prototype second-generation DHFRP bar in sizes of approximately 10-mm diameter which is the equivalent to a conventional Number 3 steel bar. The behavior of the bar under full load reversals up to failure was investigated. However, this bar first needed to be designed and manufactured in the Fibrous Materials Research Center in the Materials Engineering Department at Drexel University. Material properties were determined through testing in order to categorize the strength properties of the DHFRP. Similitude was used to demonstrate the scaling of properties from the original model bars. The four most important properties of the DHFRP bars are sufficient strength and stiffness, significant ductility for plasticity to develop in the R/C section, and sufficient bond strength for the

R/C section to develop its full strength. Improvement of all four of these properties together is necessary; otherwise the DHFRP will be inferior to conventional steel rebar.

Once these properties were determined the behavior of reinforced concrete members was investigated. This included the testing of prototype-size beams under monotonic loading and model and prototype beam-columns under reverse cyclic loading. These tests confirmed the large ductility exhibited by the DHFRP. Also the energy absorption capacity of the bar was demonstrated by the hysteretic behavior of the beam-columns. Displacement ductility factors in the range of 3-6 are needed for the plastic strength of the member to be reached. This is essential in regions of moderate to high seismicity where R/C members are designed based on ductility demand.

To study the long-term behavior of DHFRP, the creep-rupture strength of 5-mm bars was tested. This was conducted on individual bar specimens and is important in the life-cycle design and performance of DHFRP reinforced concrete.

CHAPTER 2. LITERATURE REVIEW

Fiber Reinforced Polymer (FRP) is being used increasingly more often in reinforced concrete structures for repair and retrofit. This chapter reviews current research in the area of FRP design, manufacturing, and applications. Current work on the application of FRPs in concrete structures was reviewed; particularly the cyclic and flexural behavior of concrete elements reinforced with FRP. Next, material modeling and processing of FRP were reviewed. The material properties of FRP were divided into two areas: static properties including tensile and bond behavior and long-term properties including fatigue strength, creep-rupture and relaxation, and durability and environmental effects. The current life-cycle cost analyses were reviewed for bridge systems that could utilize DHFRP and FRP materials as a retrofit alternative. Finally, current United States standards and codes related to FRP materials were reviewed.

2.1 Cyclic Behavior of Concrete Elements Reinforced with Steel and FRP

Since very limited work has been done on cyclic behavior of R/C elements reinforced with FRP bars, work using steel reinforcing was also reviewed. This is appropriate since the design philosophy of the DHFRP bar is to have a behavior similar to steel, which is different from currently used FRPs.

Lim and McLean (1991) gave results of an experimental investigation of the seismic performance of bridge columns incorporating moment-reducing hinge details. Tests were conducted on 1/20-scale models and 1/5-scale prototype reinforced concrete columns subjected to constant axial load and cycled inelastic lateral displacements. Variables that were studied included the column aspect ratio (*H/D*), the hinge detail, the

axial load effect, the number of cycles to failure, the low-cycle fatigue behavior, the plastic hinge length, and the longitudinal and transverse reinforcing ratios.

Nine 1/5-scale and approximately 50 1/20-scale specimens were tested. The model test setup is shown in Figure 2.1 and the prototype test setup is given in Figure 2.2. The loading histories for the 1/20-scale and 1/5-scale specimens were similar but not identical. The typical loading sequence for the 1/20-scale tests was two cycles at displacement ductility factors (i.e., multiple values of Δ_y) of μ = 1, 2, 3, 4, 5, 6, 8, and 10. The loading sequences for the 1/5-scale tests was two cycles at displacement ductility factors of μ = 1, 2, 4, 6, 8, 10, and 12, as shown in Figure 2.3.

The energy dissipated during a complete displacement cycle is the shaded area of the parallelogram *BCDE*, Figure 2.4. For a particular displacement level, μ, the ideal plastic energy dissipated, E_p, is given as

$$E_P = 4(\mu - 1)V\Delta_y \qquad 2\text{-}1$$

where μ is the displacement ductility factor, V is the maximum shear force attained at that given displacement factor, and Δ_y is the prescribed yield displacement. The rates of stiffness deterioration with force-reversal regions were higher for the 1/20-scale specimens as a result of weaker bond between model reinforcement and mortar. Also fatigue resistance was lower in the 1/20-scale specimens due to lower ultimate strain capacity in the 1/20-scale reinforcement. Greater strength degradation was observed in the columns with higher aspect ratios.

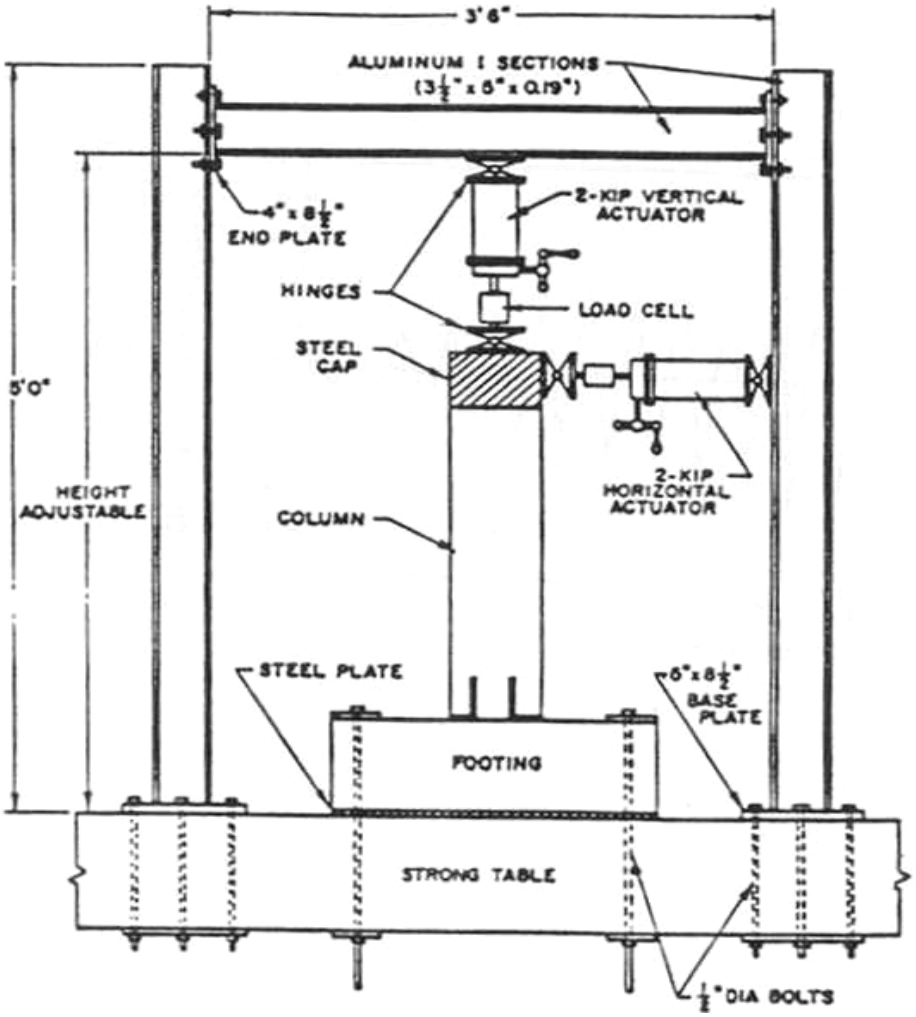

Figure 2.1: Model Column Test Setup By Kim (1990).

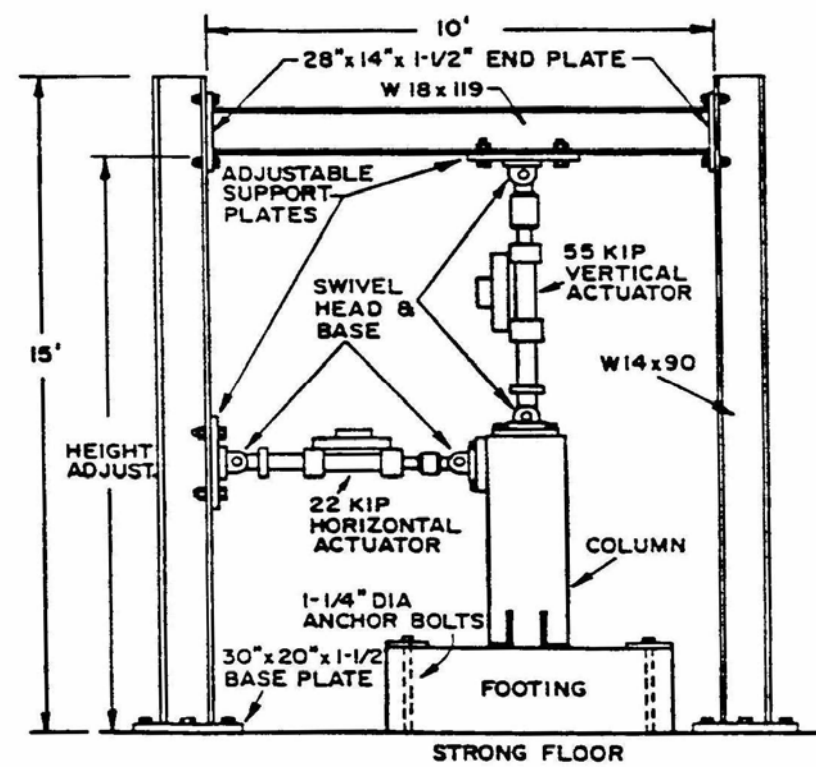

Figure 2.2: Prototype Column Test Setup By Kim (1990).

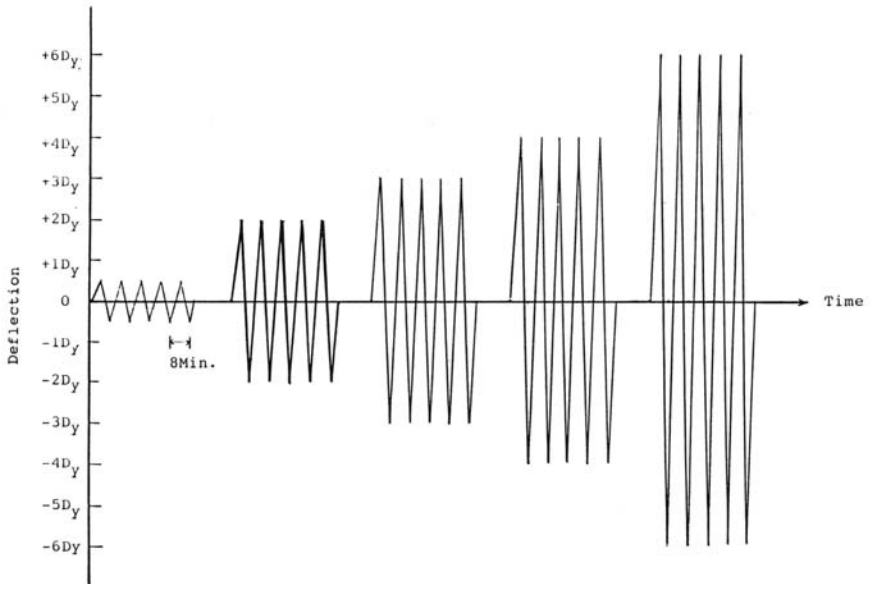

Figure 2.3: Cyclic Loading History Used By Kim (1990).

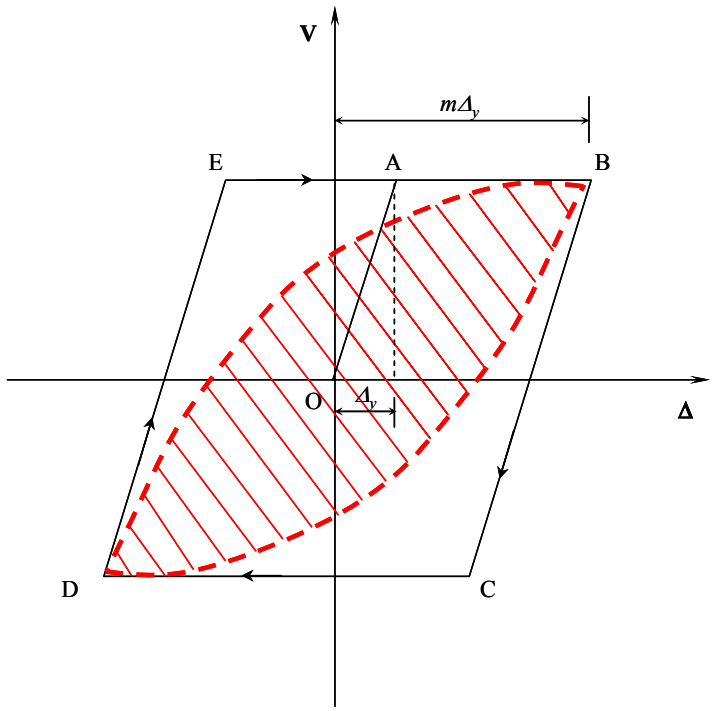

Figure 2.4: Theoretical Hysteretic Energy Dissipation Model (Kim, 1990).

Esmaeily and Xiao (2004) studied the effects of variable axial load on the seismic behavior of bridge piers. Six large-scale (1/4 to 1/3-scale) columns were tested. The experimental parameters were axial load levels and both lateral and axial loading patterns. The axial loading patterns included both constant and variable loading, either proportional or non-proportional to the lateral forces. Experimental evidence showed that the magnitude and loading pattern of axial force had a significant effect on the seismic response of the columns. The effects of the variable axial load were seen in the column failure patterns, hysteresis loops, and load-carrying capacities, and these were compared with constant axial force specimens. The research also concluded that the plastic hinge models need to be modified to account for the effects of variable axial load.

Moment-curvature at different heights of the column was evaluated by using two vertically-placed LVDTs at the same cross section. The average curvature of a segment of the column was obtained using the local longitudinal deformations measured by a pair of linear potentiometers installed on the opposite sides of the segment. The average curvature was expressed as

$$\varphi_{ave} = \frac{(\delta_1 - \delta_2)}{D'l} \qquad 2\text{-}2$$

where ϕ_{ave} is the average curvature over the specified length l of the segment, δ_1 and δ_2 are the measured longitudinal deformations on the two opposite sides of the segment, and D' is the distance between the tips of the two linear potentiometers. The setup is shown in Figure 2.5.

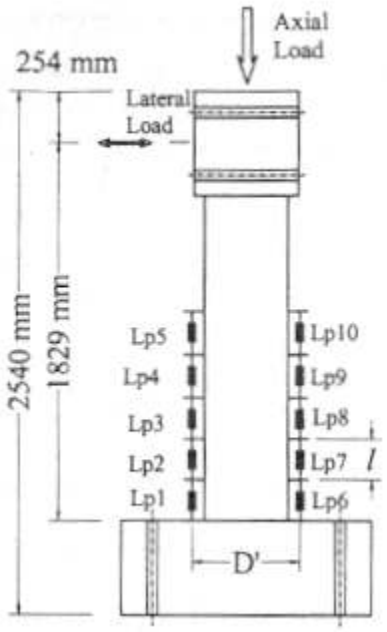

Figure 2.5: Location of Linear Potentiometers for Experiments by Esmaeily and Xiao (2004).

Jaradat et al. (1998) investigated the flexural and shear performance of older steel-reinforced columns for purposes of seismic assessment and retrofit design. Experimental results of tests on eight reduced-scale columns with a size scaling factor of 3.6 that incorporated deficiencies present in older bridge columns were presented. The test setup for the model columns are shown in Figure 2.6. The columns were 10 inches in diameter and clear heights from 40 to 70 inches. The columns were fixed against rotation at both the top and the bottom to enable shear transfer. Test variables included the column aspect ratio, longitudinal reinforcing ratio, lap splice length, and retrofitting detail. Displacements of the specimens were measured at the center of the cap beam using an LVDT. The axial load level of 19.0 kips corresponding to $0.05f'_cA_g$ (short columns). The actual axial load resisted by the column varied depending on the applied later load due to framing action. The determination of Δ_y and the loading sequence were similar to the procedures developed by Priestley and Park (1987). Three cycles at each displacement level were imposed at displacement ductility levels of ±1, ±2, ±3, ±4, ±5, and ±6 unless there was premature failure. The specimen performance was evaluated on the basis of moment capacity, shear strength, displacement ductility, strength degradation, and hysteretic behavior. Poor cyclic behavior resulted in the plastic hinge region due to poor confinement and lap splices, leading to rapid flexural strength degradation. However, axial load and shear were still transmitted into the footing. Specimens with larger span-to-depth ratios dissipated more energy and experienced less pinching in the hysteresis curves.

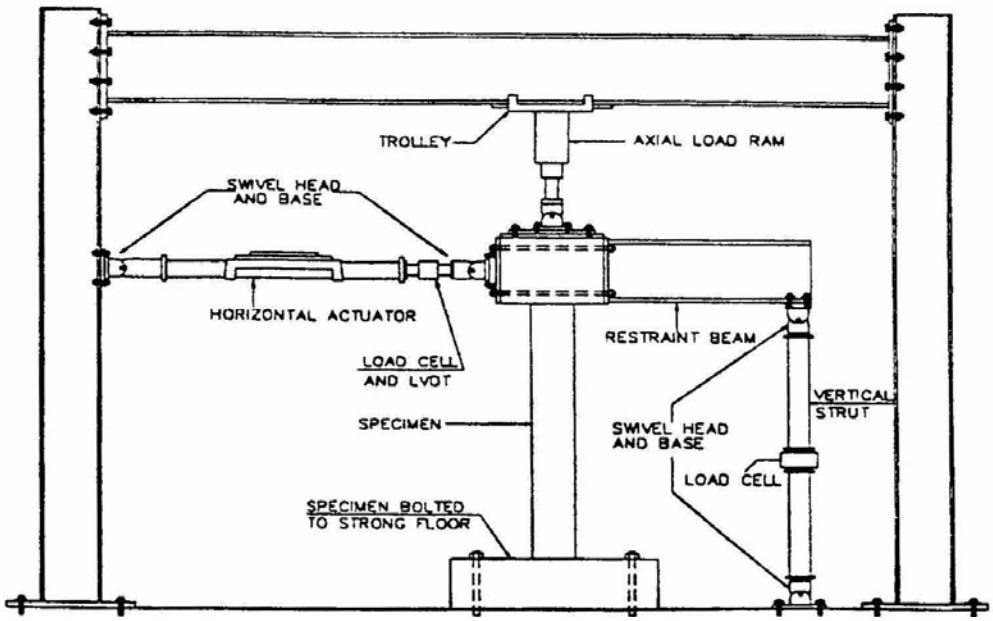

Figure 2.6: Cyclic Testing Setup Used By Jaradat et al. (1998).

In the second part of a two-part paper by Jaradat et al. (1999), observed experimental results from a series of column tests were evaluated and compared to various predictive models of column shear and flexural behavior. Current design approaches included the ACI/AASHTO shear design equations, UC at San Diego proposed model, UC Berkeley proposed model, the Caltrans model, and the Priestly and Seible flexural strength model. The Priestley and Seible flexural strength model closely predicted the moment capacity, onset point and rate of degradation, and the eventual residual moment strength at large displacements for the column plastic-hinge region with poor confinement and lap splices. The ACI/AASHTO, Caltrans, and UCB shear strength models were conservative in predicting column shear strength. The influence of

displacement ductility, aspect ratio, axial load ratio, and transverse steel ratio on shear strength was best represented by the UCSD model.

Sheikh and Yau (2002) tested twelve 356-mm (14.02 in) diameter and 1473-mm (58 in) long columns subjected to constant axial and reversed cyclic lateral loadings. Figure 2.7 shows the specimen details including geometry and reinforcement details. The test setup is shown in Figure 2.8. Each specimen had a total of 18 strain gages installed on the longitudinal reinforcement. The concrete core deformations were measured using 18 LVDTs with 10 on one side and 8 on the other side. Transverse displacements were measured at six different locations along its length using LVDTs. Displacement control of loading was used to apply a predetermined displacement history. The loading sequence is shown in Figure 2.9. The testing apparatus was specially designed to allow in-plane rotation of test specimens. The lateral load sequence consisted of one cycle to a displacement of $0.74\Delta_I$ followed by two cycles each to Δ_I, $2\,\Delta_I$, $3\,\Delta_I$, … and so on. Deflection Δ_I was defined as the lateral deflection corresponding to the maximum lateral load along a line that represented the initial stiffness of the specimen.

The specimens were divided into three groups. The first group consisted of four columns that were conventionally reinforced with longitudinal and spiral steel reinforcement; the second group contained six columns that were strengthened with CFRP or GFRP before testing; the last group included two columns that were damaged, repaired with FRP under axial load, and then tested to failure. The variables investigated included axial load level, spacing of spirals, thickness, and type of FRP. The use of FRP significantly improved the column performance, resulting in large increases in ductility, energy dissipation capacity, and strength. For a column subjected to an axial load equal

to $0.27P_0$ (approximately equal to a balanced load), one layer of CFRP or GFRP increased the energy dissipation capacity by a factor of more than 100. The column ductility deteriorated as the level of axial load increased. The amount of FRP needed to improve column behavior depended on the level of axial load. A failed specimen is shown in Figure 2.10. This shows the failed plastic hinge region at the base of the column.

Ductility in elasto-plastic structures is easily defined. In R/C members lacking such characteristics, there is no universal definition for ductility. Figure 2.11 describes various ductility parameters used for steel-reinforced concrete members. These included curvature ductility factor μ_ϕ, cumulative ductility ratio N_ϕ, and energy damage indicator E. L_f is the length of the most damaged region measured from the test and h is defined as the depth of the column section.

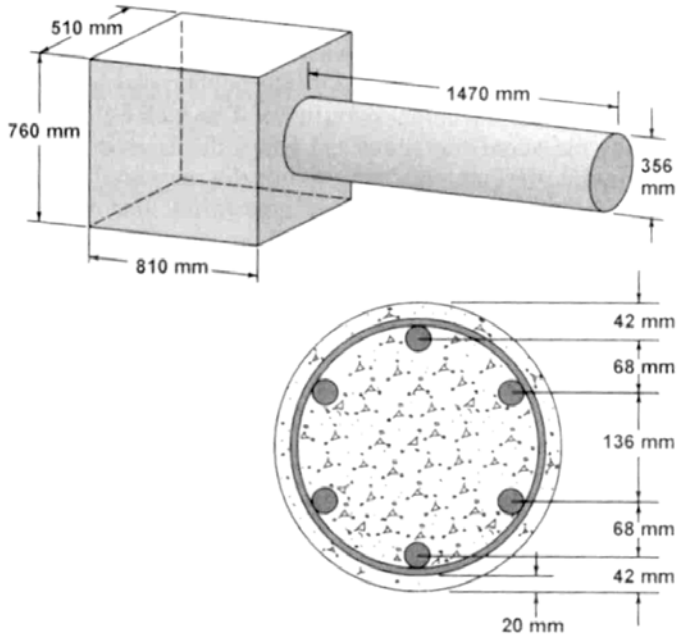

Figure 2.7: Column Specimen and Dimensions (Sheikh and Yau, 2002).

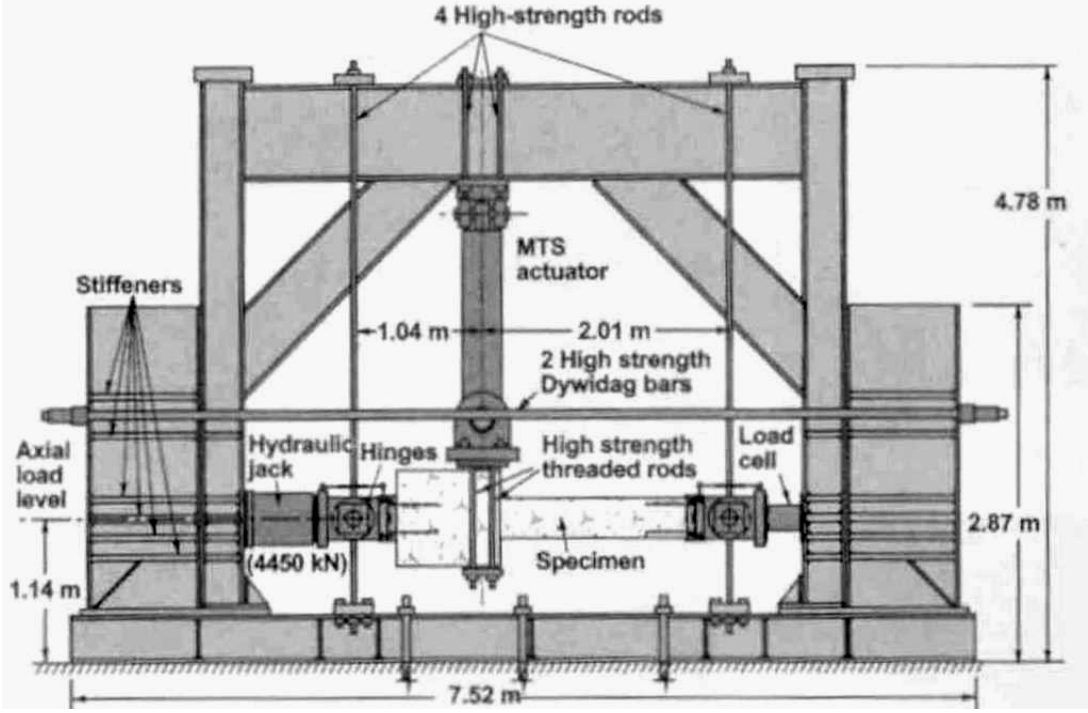

Figure 2.8: Test Setup Used by Sheikh and Yau (2002).

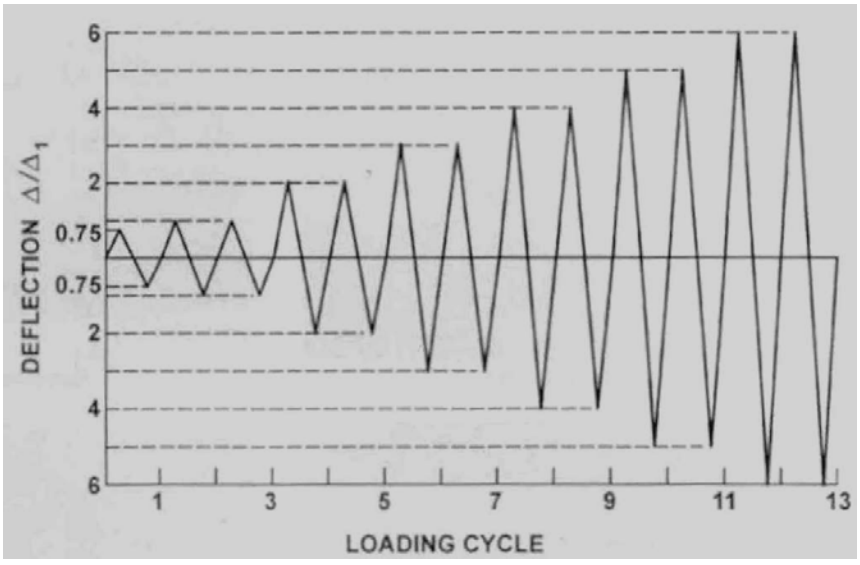

Figure 2.9: Loading Sequence Used by Sheikh and Yau (2002).

Figure 2.10: Plastic Hinge Region of Failed Column Specimen Tested by Sheikh and Yau (2002).

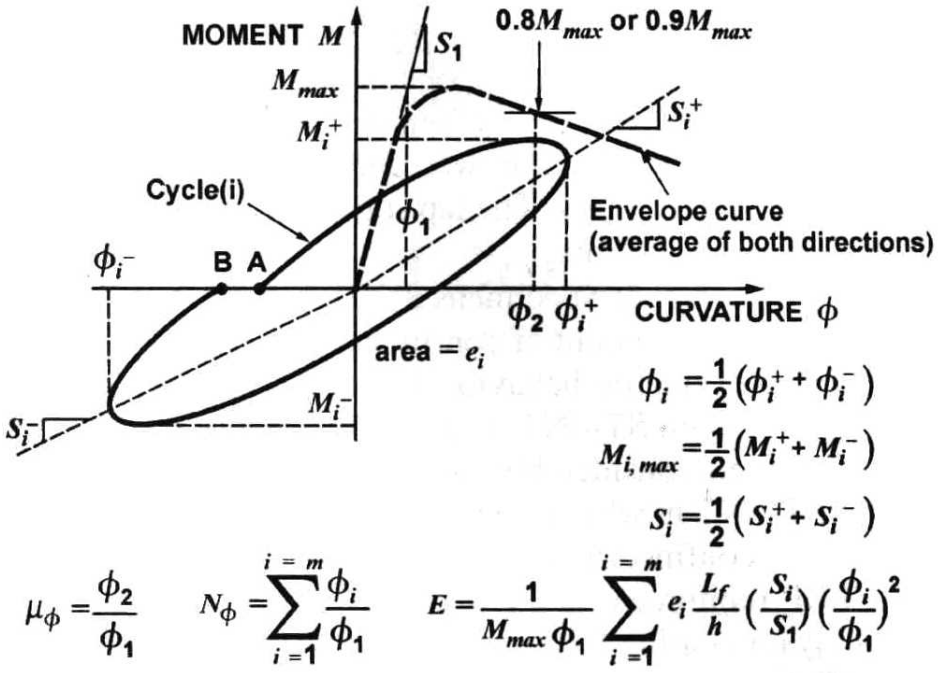

Figure 2.11: Definition of Ductility Parameters Used by Sheikh and Yau (2002).

Bedell and Abrams (1983) investigated exterior base story columns in which the applied vertical load was expected to vary with the horizontal load when the structure was subjected to strong ground motions. The ratio of axial to shear force was 4:1. This was used to produce a gravity stress equal to that in a full-scale multistory building.

Two large-scale specimens were tested. The test variable was the amount of dead load applied to each specimen. The specimens were ½ -scale models of first story external columns. Each specimen was reinforced with four #6 bars. Four parameters of response were measured for each specimen: applied load, displacement at the top of the column, rotation at the base of the column and strains in the reinforcement. The LVDT was measured independent of the system at the same elevation as the lateral load. Since considerable damage was expected at the bottom of the column, the base rotation was measured at a distance equal to the effective depth of the column above the base. LVDTs were mounted with swivel connections on the outside edge of each side of the footing. An average value for the base rotation could be calculated by adding the displacements and dividing by the distance between them. Mechanical dial gages were mounted in addition to the LVDTs to check the electronic measurements. Strains on the reinforcing bars were measured at twelve locations.

Each specimen was loaded in accordance with the displacement measured at the top of the column. This parameter could be non-dimensionalized as a percent of the height. Loading in the first half cycle consisted of a constantly decreasing axial compression combined with the lateral load. The behavior of the column was investigated solely in terms of the moment-curvature relationship for the base of the column. Approximately 65% of the deflection at the top of the column was attributed to

rotation at the base. Comparing load-deflection and load-rotation curves suggested that all nonlinear behavior occurred in the base region.

Saatcioglu and Razvi (2002) developed a displacement-based design procedure for confinement of earthquake-resistant concrete columns. The amount, grade, spacing, and arrangement of transverse reinforcement; concrete strength and cover thickness; and the level of axial compression and drift ratio were considered as parameters of confinement. Both normal and high-strength concrete columns with circular and square cross sections were considered. Static inelastic pushover analyses were conducted.

Palermo and Vecchio (2004) developed general constitutive models for R/C subjected to reverse cyclic loading using two-dimensional nonlinear finite element analyses based on the smeared rotating crack assumption. Verification was provided through analyses of slender walls which are controlled by flexure and squat walls, which are controlled by shear. Behavioral aspects such as ultimate strength, ductility, energy dissipation, and failure mechanisms were well simulated.

Currently, a significant amount of research on columns is FRP wrapping or confinement of concrete columns with fabrics for increased strength and ductility. Even though this is not directly related to the DHFRP research, a few cases are mentioned since this is such a large area of application for FRPs.

Harajli and Rteil (2004) investigated the seismic performance of R/C columns designed for gravity load and confined externally with carbon fiber-reinforced polymer (CFRP) flexible sheets. The main parameters included the reinforcement ratio in the columns and the area of CFRP sheets. To simulate gravity load design, the column reinforcement in all specimens was spliced at the column base. All specimens

experienced significant slip of the column reinforcement and widening of one single crack located at the column-stub interface. Most of the column drift was attributed to the fixed-end column base rotation. By confining the columns with the CFRP sheets, the bond failure was reduced, and the energy absorption and dissipation capabilities were increased, thereby increasing seismic performance of the columns.

Mirmiran et al. (1998) studied the effect of using an FRP tube as the sole reinforcement of a concrete column. The tube acted as formwork, protective jacket, confinement, shear and flexural reinforcement. Longitudinal transverse stiffening ribs in the tube acted as shear connectors.

Monti et al. (2001) investigated the use of FRP jackets of upgrading circular bridge piers. A procedure was proposed that aims at designing the optimal thickness of the FRP jacket, for the purpose of enhancing the ductility of existing RC bridge piers having circular cross sections. The design procedure stems from the definition of an upgrading index, given as the ratio of the target to availability ductility at the pier base section, to be attained through FRP jacketing. The developed equation allowed the design of the optimal thickness of FRP jackets in terms of the desired upgrading index and mechanical characteristics of the selected composite material. Additional work done in Canada on rehabilitation of columns with FRP sheets and wraps was documented in Green (2000). Harmon et al. (2002) developed a series of material and structural models for predicting the behavior of circular confined concrete columns subjected to constant axial load, cyclic shear, and flexure. Experimental verification was described in Gould and Harmon (2002) from tests of cantilever concrete columns confined with FRP (i.e., wrapped columns).

Sakino and Sun (2000) investigated the improvement of column strength and ductility by the use of steel jacketing.

Monti and Spacone (1998) developed a new R/C finite element that explicitly accounted for the slip between the reinforcing bars and the surrounding concrete. The steel fiber strains were computed as the sum of two contributions, the rebar deformation and the anchorage slip. The model was applicable to both monotonic and cyclic loadings. The model illustrated the bar's reduced initial stiffness, bond degradation, and anchorage loss for insufficient anchorage length. The model was then compared with experimental data on a circular column subjected to cyclic loading. The original fiber model with perfect bond overestimated the hysteretic energy dissipated during loading cycles.

2.2 Flexural Behavior of Beams Reinforced with Internal FRP

The strengthening of cantilever and continuous beams using a triaxially braided ductile fabric was investigated by Grace et al. (2004). Two series of beams were experimentally tested: the first series included beams with one overhanging cantilever strengthened in flexure and loaded with one concentrated load at the end of the cantilever, and the second series included continuous beams with two spans strengthened in flexure along their positive and negative moment regions and loaded with a concentrated load at the middle of each span. All beams were symmetrically reinforced with two No. 5 (16-mm diameter) bars at the top and the bottom. To avoid shear failure, the beams were over-reinforced for shear with No. 4 closed stirrups spaced at 102 mm (4.0 in). The behavior of the beams strengthened with the triaxial fabric was compared with beams strengthened with a commercially available carbon fiber sheet. The responses of the beams were examined in terms of deflections, strains, and failure modes.

The beams strengthened with the new fabric showed greater ductility than those strengthened with the carbon fiber sheet. The new fabric allowed the formation of plastic hinges that enabled the redistribution of the moment between the positive and negative moment zones of the continuous beam.

The stress redistribution in cyclically loaded R/C beams was investigated by Heffernan et al. (2004). A predictive fatigue model was developed using the concept of stress redistributions in an R/C beam when loaded cyclically. The cyclic properties of the constituent materials were combined with a strain-life approach to metal fatigue prediction to calculate the fatigue life of R/C beams. The theoretical results were compared with previously reported experimental data. The cyclic stress redistribution and strain-life approach to fatigue calculations appeared appropriate for calculating the residual fatigue life of R/C members considered for rehabilitation.

Burgueño et al. (2004) investigated analytically and experimentally the flexural behavior of a hybrid FRP-concrete beam- slab bridge component. The beam element consisted of a carbon/ epoxy cylindrical shell filled with concrete where the FRP shell served as both the formwork and the reinforcement. A conventional R/C slab connected the FRP beam through steel dowels anchored in the FRP beam concrete core. The beam-slab system was tested using a full-scale four-point bending flexural test. Section analysis procedures and approximate flexural response formulae were developed and correlated with experimental results. The overall investigation demonstrated that the hybrid FRP-concrete system is viable for beam-and-slab bridges.

The flexural behavior of beams reinforced with deformed GFRP bars was investigated by Masmoudi et al. (1998). The deformed bars used were 14.9-mm in

diameter and had a linear stress-strain behavior to failure. Four series of R/C beams were tested. The beams were 200-mm (7.8") wide, 300-mm (11.8") high and 3300-mm (130") long. The beams were tested in four-point loading. Results showed that the average crack spacing in beams reinforced with FRP was similar to steel beams at low load levels (0.25 M_u). However, at moderate and high load levels (0.65 M_u), the spacing was greater than that of beams reinforced with steel bars. The maximum observed crack width in beams reinforced with FRP was three to five times that of identical beams reinforced with steel bars. The deformability-based approach developed by Jaeger et al. (1995) was used to evaluate the ductility of FRP beams. Using this approach, at 90% of the ultimate capacity, the deformability factor was around 6.4 for the FRP beams.

Sanhdars and Oehlers (2000) overcame the brittle failure common to beams reinforced with FRP materials by placing FRP bars in the compression zone of the beam. Four beams, 5.0 m long and 200-mm wide by 300-mm high were tested; 1 without compression FRP reinforcement and two with compression FRP reinforcement. Results showed that the pseudo-ductile behavior was a result of the fact that the compression FRP bars took over from the crushed concrete, allowing ductility in the beams until the compression bars fracture.

Aiello and Ombres (2000) investigated the deformability of concrete flexural members reinforced with FRP rebars. Aramid FRP reinforced beams were tested. A general procedure that considered different cracking configurations that was derived from a cracking analysis based on slip and bond stresses was used to evaluate the deformability of FRP R/C members. A block model was used where deformability of flexural R/C members was evaluated referring to the member block between two consecutive cracks.

Local slippage between the reinforcement and concrete was assumed. The solution of a system of differential equations from the constitutive equations and local bond-slip law allowed the evaluation of the state of strain and stress at every cross section of the block, and the subsequent moment-curvature.

Zou et al. (2000) reviewed the ductility and deformability indices for concrete beams reinforced or prestressed with steel or FRP tendons. The authors then proposed a new definition of a deformability index for prestressed concrete beams. The new factor was defined as an overall factor that combined a deflection factor and a strength factor. The deflection factor was the ratio of the deflection at failure to the deflection at first cracking, while the strength factor was the ratio of the ultimate moment (or load) to the cracking moment (or load). Two sets of simply supported beams were tested. The results showed that the conventional ductility index for concrete beams with steel reinforcement was not suitable for beams with FRP reinforcement without a definite yield point. Other researchers who have proposed new equations to quantify the ductility of concrete beams prestressed by FRP and steel so that a comparison can be made between them are Naaman and Jeong (1995), Abdelrahman et al. (1995), and Mufti et al. (1997).

Theriault and Benmokrane (1998) tested 12 beams reinforced with 12.3-mm diameter C-Bar (GFRP) rods manufactured by Marshall Industries Composites. These bars were linear elastic up to failure. The beams were designed to fail by crushing of the concrete. This was accomplished by using a reinforcement ratio greater than ρ_b. The beams were tested in four-point bending, with the load applied in step increments of 20 kN. As the concrete strength and reinforcement ratio increased, the ultimate moment

capacity of the tested beams increased, but this increase was limited by the concrete compressive failure strain of over-reinforced beams.

The interpretation of ductility of FRP-reinforced beams on the basis of conventional definitions is misleading due to the linear stress-strain behavior of FRP bars. At loading, FRP shows significant deformation, and since only 20-30% of the FRP strength is recommended for design, energy dissipation is possible through elastic deformation. Therefore, a new way to compare the safety of both FRP and steel rebar was introduced. The new definition, called the *J*-factor takes into account the increase of moment as well as the increase in curvature or deflection. The *J*-factor is defined as

$$J\ factor = strength\ factor\ x\ Deformability\ factor\ (curvature\ or\ deflection) \tag{2-3}$$

where

$$Strength\ factor = \frac{Moment\ at\ ultimate}{Moment\ at\ concrete\ compressive\ strain\ of\ 0.001} \tag{2-4}$$

$$Curvature\ factor = \frac{Curvature\ at\ ultimate}{Curvature\ at\ concrete\ compressive\ strain\ of\ 0.001} \tag{2-5}$$

$$Deflection\ factor = \frac{Deflection\ at\ ultimate}{Deflection\ at\ concrete\ compressive\ strain\ of\ 0.001} \tag{2-6}$$

Grace et al. (1998) studied the behavior of simply and continuously supported beams reinforced with FRP materials. Seven simple rectangular beams were tested and

had reinforcing bars and stirrups made of steel, carbon or glass FRP. It was concluded that the use of GFRP stirrups increased shear deformation, resulting in an overall increase in deflections. Also, GFRP stirrups changed the failure mode from flexure to shear or flexure-shear, depending on the type of longitudinal bars (steel or FRP). The various FRP arrangements had the same load capacity as steel reinforcements; however, the failure modes and ductility differed.

Two methods for determining the ductility were evaluated: a deformation based method proposed by Jaeger et al. (1995) and an energy based method. The first method demonstrated that for beams which failed by tensile rupture with small percentages of tensile reinforcement had larger deformability factors than beams failing in compression. This is a shortcoming of this method. The energy method defined ductility as the ratio of the inelastic to total energies. However for linear elastic FRPs, it is difficult to determine which energy is elastic and which is inelastic. Therefore, a modified energy method to calculate ductility was developed by the authors, where the failure mode was considered in addition to the modulus and failure strength of the FRP, the type of reinforcing bars, and the concrete softening at compressive flexural failure. The beams were then classified by the energy ratio as either ductile (ratio > 75%), semi-ductile (70% < ratio <74%) or brittle (ratio < 69%).

Al-Salloum et al. (2000) investigated the suitability of using the currently practiced ACI-318 model to predict the deflection at service load for beams reinforced by GFRP bars. Also, the researchers used several modified models to predict the deflection for those beams. Also, they developed a simple model to predict the deflection at service load for beams reinforced with FRP bars. These models were compared with the

experimental results of fifteen beams that were simply supported and subjected to two point loading. These values were then compared with the modified models and the ACI model. The results of the study revealed that due to the low modulus of elasticity of GFRP bars (E_{GFRP} / E_{steel} ≈ 0.25), deflection criterion may control the design of intermediate and long beams reinforced with GFRP bars. Since the ACI code was developed for steel reinforcement, the actual deflections are highly underestimated. Also, based on experimental results, a simple empirical model was suggested to predict the actual service load deflection.

LeTegola (1998) studied the use of FRP bars with higher strength values and lower moduli than steel at the serviceability limit state (SLS) and the ultimate limit state (ULS), since the design of structures with FRP will be influenced almost exclusively at the SLS. Various statistical distributions of actions for the verification at the SLS and ULS were evaluated. LeTegola performed a numerical application on a beam reinforced with FRP or steel, and results showed a dominance of the SLS and how its compliance ensured with ample margins the verification of the ULS.

Letsch (2001) investigated the use of polymer concrete reinforced with GFRP and steel reinforcement. Both plain and polyester concrete were used. Bending tests with beams reinforced with either one or two 8-mm square GFRP bars or one or two 8-mm diameter steel bars were tested. The same ultimate loads were obtained from both beams. Beams reinforced either with one GFRP bar or one deformed steel bar had the same flexural strength, however, the GFRP reinforced beam failed in a brittle manner. Also, the deflection of the GFRP reinforced beams was twice that of the steel reinforced beams

while the modulus of elasticity of the GFRP beam was 46000 MPa, only 22% of the steel beams.

The behavior of R/C beam sections reinforced with conventional steel bars and steel fibers and subjected to flexural cyclic loading beyond the yield point was investigated by means of a mechanical model by Spadea and Bencardino (1997). The stress-strain relationships for the concrete, steel fiber, and the steel bars were assumed to be piecewise linear. These constitutive laws were first used to obtain the primary moment-curvature relationship for monotonic loading to failure. From this curve, the successive stiffness degradation was created as a function of stress and strain levels reached in the section at each load cycle. Strain hardening of steel and the combined effect of confinement by the stirrups and metal fibers were taken into account. The model was compared to experimental results with first, steel bars only, and then with bars and fibers.

Ibell and Burgoyne (1999) studied the use of FRP versus steel for shear reinforcement. Pushoff tests were presented for the shear capacity of concrete reinforced with FRPs and compared these results with specimens containing steel stirrups. It was shown that while plasticity theory may be used in the steel-reinforced situation, other analysis techniques were required for FRP-reinforced specimens. This was because the brittle nature of the new materials made them susceptible to localized stress concentrations. GFRP-reinforced specimens failed in a brittle manner. However, debonding of the GFRP stirrups was an important observation. This debonding allowed substantial deformation of the structure to occur prior to delamination of the GFRP. AFRP helically-reinforced specimens failed in a very brittle manner. Failure was due to

snapping of the AFRP at relatively low loads. An upper-bound plasticity approach was shown to adequately model the behavior of the steel-reinforced specimens. Conversely, it was suggested that plasticity theory should not be applied to the FRP-reinforced specimens where the constituent reinforcing materials exhibit no plastic energy dissipation during stretching to failure.

Eddie et al. (2001) investigated the use of GFRP dowel bars as a possible maintenance-free alternative that will potentially reduce the overall life-cycle cost of pavements. The performance of FRP dowel bars under static and cyclic loads was studied. GFRP dowels with a 38 mm diameter were used. The test variables included two different base support levels and two GFRP dowel types in addition to standard epoxy-coated rebar. The lower flexural stiffness modulus of GFRP compared to the stiffness modulus of steel and the larger dowel diameter were both advantageous in this type of application because of the reduced bearing stresses on the concrete surrounding the dowel. Bearing stresses were one of the major causes of joint failure.

Bonacci and Maalej (2001) studied the performance of conventionally reinforced concrete (R/C) beams strengthened in flexure with externally bonded fiber-reinforced polymers (EB-FRP) by compiling and analyzing an experimental database. Failure by debonding of FRP was prevalent among specimens in the database. One-third of the specimens with external reinforcement added showed strength increases of 50% or more in combination with considerable deflection capacity. The procedures followed were most representative of member strengthening rather than repair. All but five of the specimens in the database were repaired in an unloaded condition. Consideration of damage to existing conventional reinforcement or sustained stress in the compression

zone would lead to considerably different trends in failure mode, strength, and deformability. Fanning and Kelly (2001) studied the response of RC beams strengthened with CRFP Plates and Nguyen et al. (2001) studied the brittle failure and bond development length of CFRP-concrete beams.

Yost et al. (2001) evaluated the shear strength of intermediate length ($2.5 < a/d < 6$) simply supported concrete beams subjected to four-point monotonic loading and reinforced with deformed GFRP bars. Six different over-reinforced designs were used. All samples failed in diagonal tension, and theoretical results were compared. Both the traditional design method for steel (ACI 318-99) and the ACI 440 code for design with FRP materials were used. The shear capacity was significantly overestimated using ACI 318-99.

Yost et al. (2001) studied the flexural performance of simply supported concrete beams reinforced with a 2D FRP grid. With respect to ACI 318-95, flexural capacity was accurately predicted, but shear strength was not.

2.3 Material Processing and Modeling

In this literature review, material modeling included the modeling of general textile systems including braided structures. These models were based on textile mechanics and the concept of the structural hierarchy of textile systems (Ko, 1987). In composite material manufacturing and processing, many processes exist in developing various materials. Only current research in the pultrusion process was reviewed. This is the most used manufacturing technique for FRP rebars.

2.3.1 Material Modeling

Lomov et al. (2001) developed an integrated modeling and design tool for textile composites taking advantage of the hierarchical principle of textile composites. The researchers followed the hierarchy of structure and models of a textile composite, namely, fiber, yarn, textile, preform, and composite. The model of the textile geometry served as a basis for meso-mechanical and permeability models for composites. These provided simulation tools for analysis of composites processing and properties. The model used manufacturer's fabric and yarn data obtained from textile testing, as a starting point for modeling a composite material. This gave *a priori* predictions of mechanical properties of composites, allowing for the possibilities of geometry peculiarities such as complex crimp and porosity pattern and yarn mechanical behavior such as compression. A user-friendly software application, *WiseTex* allowed for manipulation of fabric and yarn data utilizing a graphical user interface. Experimental results on two glass fabrics produced in an autoclave were compared and showed good correlation between theoretical and experimental results.

Crookston et al. (2001) described an approach to composite modeling which incorporated drape modeling to determine deformation of the reinforcement due to preform manufacturing. Also, an element-wise property prediction for subsequent macroscopic (component) mechanical performance prediction was described. A modular method was employed such that various mechanical property models could be incorporated as appropriate. The intention of the authors was to develop a generic approach to mechanical analysis of components by means of a mesoscopic model for mechanical properties at element level. An intermediate stiffness model must be provided by finite element (FE) analysis of solid models for a general textile composite

unit cell, incorporating changes in properties due to shear deformation during preform manufacturing.

2.3.2 Material Processing

Karbhari (2000) reviewed recent applications of FRP composites with an emphasis on material selection and manufacturing processes. Differentiation was made between three commonly used terms: repair, strengthening, and retrofit. In repairing a structure, the composite is used to fix a structural deficiency to restore the component to its original performance level. Strengthening is specific to cases where the addition of the composite enhances the existing designed performance level, for example, increasing the load rating of a bridge deck. Retrofit is used specifically as related to seismic upgrade of structures or components. Processes most commonly used for civil applications include wet lay-up, pultrusion, and resin infusion.

Work on the optimization of die heating for pultrusion processes was conducted by Li et al. (2001). An optimization algorithm for die heating for the pultrusion process was developed and validated. A mathematical relationship between die-heater temperatures and the uniformity of the degree of cure across the cross-section of a pultruded part was established. The application of the procedure was demonstrated by simulating pultrusion of a CFRP C-section using a die with six heaters. The influences of the element aspect ratio and different initial heater conditions were studied. For the case study on the pultrusion of an uneven C-section, an improvement of 75% was observed in the uniformity of the degree of cure.

During the pultrusion process, the temperature and cure profiles are initially transient, and approach a quasi-steady state. The evolution of temperature and cure

profiles during this transient period determines if a stable pultrusion process can be established and also has a significant impact on the production efficiency. Liu and Paton (2001) developed a numerical procedure to investigate the evolution of temperature and cure profiles during the start-up period for the pultrusion of a carbon-vinyl ester composite I beam. The quasi-steady temperature and cure profiles for a pultrusion process were determined by the processing parameters, including the pulling speed and the heater control temperature. Increasing the pulling speed or decreasing the heating temperature tended to shift the quasi-steady profiles towards the die exit.

Karbhari (2001) reviewed material considerations for the use of FRP composites for the seismic retrofit of columns and piers, the flexural strengthening of beams and slabs. Composite jacketing techniques and processing and material systems were reviewed.

Ohnstad and Kachlakev (2001) developed a hollow composite rebar that used a modified pultrusion process. A carbon fiber-based bulk molding compound was continuously over-molded and joined to a hollow E-glass pultruded tube. This process produced a carbon reinforced resin coating or envelopment which formed the deformation pattern on the exterior surface of the rebar and also shielded the rebar load carrying uni-directional glass filaments from the alkaline environment of concrete. Changing the size of the inner mandrel diameter used for the bar varied the size of the rebar.

2.4 Static Material Properties

The static material properties reviewed included standard material tests obtained in the short-term behavior of FRPs. For FRP bars and rods, these included the axial

tensile strength and behavior and bond strength. The review of tensile testing also included various ways of gripping FRP bars to obtain the tensile properties, since this was a difficult task for larger diameter bars with high ultimate load levels.

2.4.1 Tensile Behavior

Vermeeren and Tsang (2001) investigated the distribution of stresses on a rod inside a resin-wedge anchoring system using the finite element method (FEM). These rods were used as prestressing cables in the Dintelhaven Bridge, the Netherlands. The influence of various design parameters and modifications of the anchorage system for anchorage design optimization was investigated. Tests were conducted on single rods and cables consisting of 91 and 214 rods. It was found that the peak stresses occurred for both the lateral compressive stress and the shear stress between the rod and the wedge, and the peaks were located where the rod entered the wedge. From the literature, it was concluded that the efficiency of an anchorage system was lower when a steel wedge was used as opposed to a resin wedge. The steel wedge induced higher lateral compressive peak stresses on the rod. However, the FE results in this study concluded that the lateral compressive stresses on the rod were lower for the steel wedge compared to the resin wedge.

Design aspects for concrete members pretensioned with Arapree (Aramid Prestressing Element) were investigated by Gerritse (2000). The tensile strength of the fibers in the Arapree elements was 3000 MPa, while the modulus of elasticity ranged between 70 and 130 GPa, depending on whether the bar was low, intermediate, or high modulus (LM, IM, HM). These stress values were based on the bar specific area. The ultimate strain of the HM was 2.4%.

DeLorenzis and Nanni (2001) conducted tensile and bond tests on commercially available carbon FRP deformed rods for application as near surface mounted (NSM) reinforcement. Three full-size beams, one control beam and two beams strengthened in shear with NSM FRP rods were tested. Two bond failure modes were observed: splitting of the epoxy cover and cracking of the concrete surrounding the groove, depending on the groove size.

An exploratory study by Castro and Carino (1998) was performed to support the development of standard test methods for FRP bars used as concrete reinforcement. The objectives were to develop a system to permit tensile loading of the bars in a universal test machine; to evaluate the influence of the free-length-to-bar-diameter ratio on the measured tensile strength; and to explore the potential of measuring the elastic modulus using available nondestructive test methods.

A successful system was developed for applying tensile load. The ends of a bar were embedded in steel tubes using a high-strength gypsum cement mortar. The bars were loaded by gripping the tubes in the conventional wedge friction grips of a universal machine. There was no statistically significant influence of the free-length-to-diameter ratio for ratios varying between 40 and 70.

The dynamic Young's modulus of elasticity based on the measured time for an ultrasonic pulse to travel a known distance is

$$E_{upv} = \frac{\rho}{k}\left(\frac{D}{\Delta t}\right)^2 \qquad 2\text{-}7$$

where D = the distance between transducers, Δt = the measured travel time, ρ = density, ν = Poisson's ratio of the FRP. The dynamic modulus of elasticity was determined using two stress-wave propagation methods: ultrasonic pulse velocity (ASTM C 597) and

resonant frequency (ASTM C 215). The dynamic values compared well with static values obtained from the tensile stress-strain curves.

2.4.2 Bond Behavior

Soong et al. (2001) studied the bond between concrete and a polymer composite tendon using a single fiber pull-out test. Two types of bond strength, intrinsic interfacial bond strength and apparent interfacial bond strength were defined and measured. The influence of surface deformations and roughness were investigated to delineate the contributions of chemical, bonding, bearing and frictional resistances to the bond strength. The composite tendons were pultruded rods of GFRP with a diameter of 12.7-mm and a tensile modulus of 40 GPa (ISOROD), smooth (S) and sand-coated (SC) purchased from Pultrall Inc. Also, tendons with lugs (C-Bar) with a diameter of 12.7-mm and a modulus of 42 GPa were purchased from Marshall Industries. The number of lugs in the C-Bar was 12 per 88.9 mm. These lugs were helically wound fiber strands over the pultruded rod. The test setup is shown in Figure 2-12. 6" x 12" concrete cylinders were used to embed the bars into concrete. PVC tubes were used at both ends to prevent any edge effects. The length of this tube at the free end was varied to accommodate various tendon embedment lengths. A steel tube was bonded to the load-end of the tendon using a room temperature curing epoxy.

The bearing and frictional resistance caused by the lugs and surface roughness, respectively, influenced significantly the apparent interfacial bond strength and marginally the intrinsic interfacial bond strength. The bar deformation pattern is shown in Figure 2.13. This confirmed that the intrinsic interfacial bond strength was mainly a measure of the chemical bonding between the concrete and the tendon. A low value of

the intrinsic bond strength indicated that the contribution by chemical bonding to the total bond resistance was minimal. It also showed that the apparent interfacial bond strength was the sum of the intrinsic interfacial bond strength, bearing resistance, and frictional stress, where the bearing resistance was more significant than the frictional resistance.

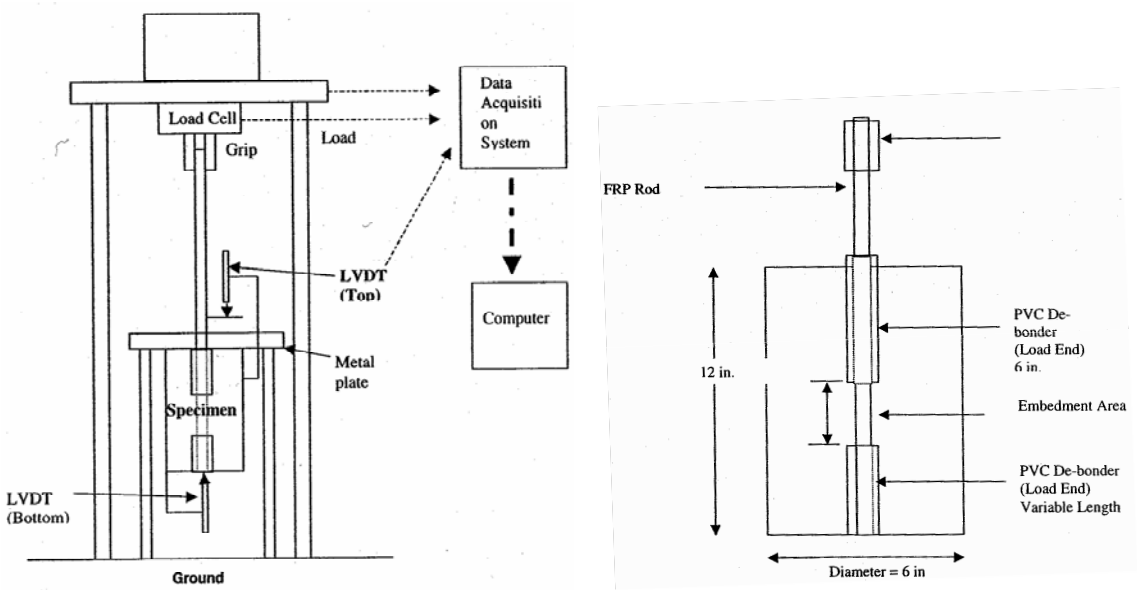

Figure 2.12: Bond Test Setup and Detail Conducted By Soong et al. (2001).

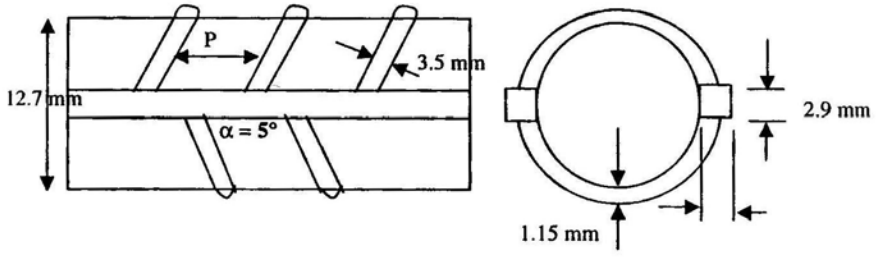

Figure 2.13: Deformation Pattern on FRP Bar Used By Soong et al. (2001).

The performance of bond of FRP reinforcement in concrete was studied by Tamuzs et al. (2001). For the estimation of the local bond slip law between the bar and the concrete, pull-out tests with centric placement of the bar surrounded by massive confining concrete was used. The test setup is shown in Figure 2.14. The bond length should be such that the bond stresses are evenly distributed in all loading stages. In most cases, the length should be between 3 and 5 bar diameters. The bond stress slip relation was compared for various bars and is shown in Figure 2.15. The bond lengths were 45-50 mm (1.77 in – 1.96 in).

For increasing load, the GFRP bar had in comparison with the other bars a considerable slip with ductile behavior. The GFRP bar reached its ultimate bond strength at a slip of 4-mm and had the bond strength level of the CFCC strand. The C-Bar had the same bond stress-slip relation as the steel rebar with full concrete confinement. However, the steel rebar had higher relative rib areas (0.13) than the C-Bar (0.08). Finally, as the concrete cover cracked along the FRP bars, the slip increased and the C-Bars split off the concrete cover due to glossy bar surface giving high lateral bond forces. The GFRP bars (Hughes Brothers) had lower bond resistance, but did not split off the concrete cover as easily due to a sanded and wavy bar surface giving low lateral bond forces.

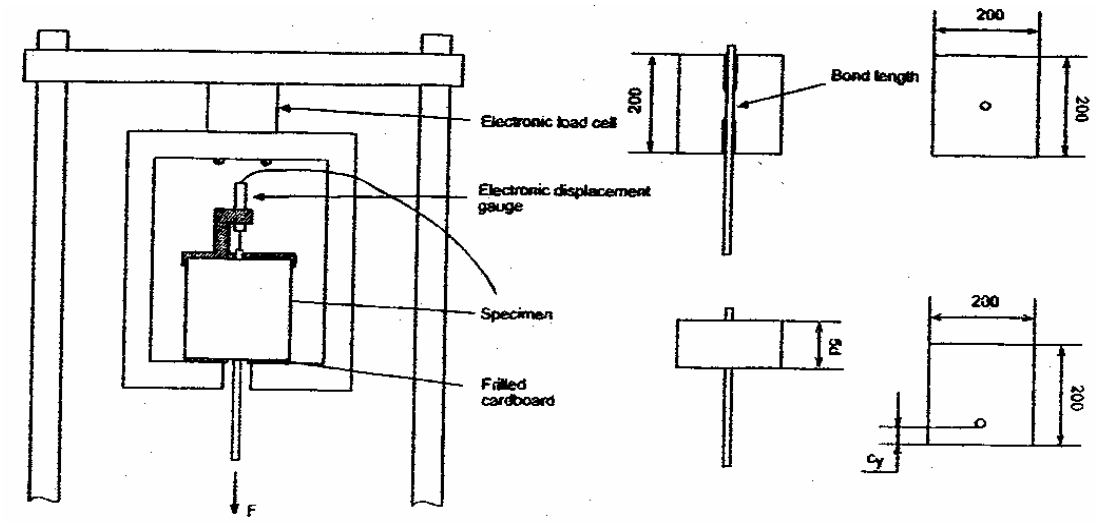

Figure 2.14: Pullout Test Setup By Tamuzs et al. (2001).

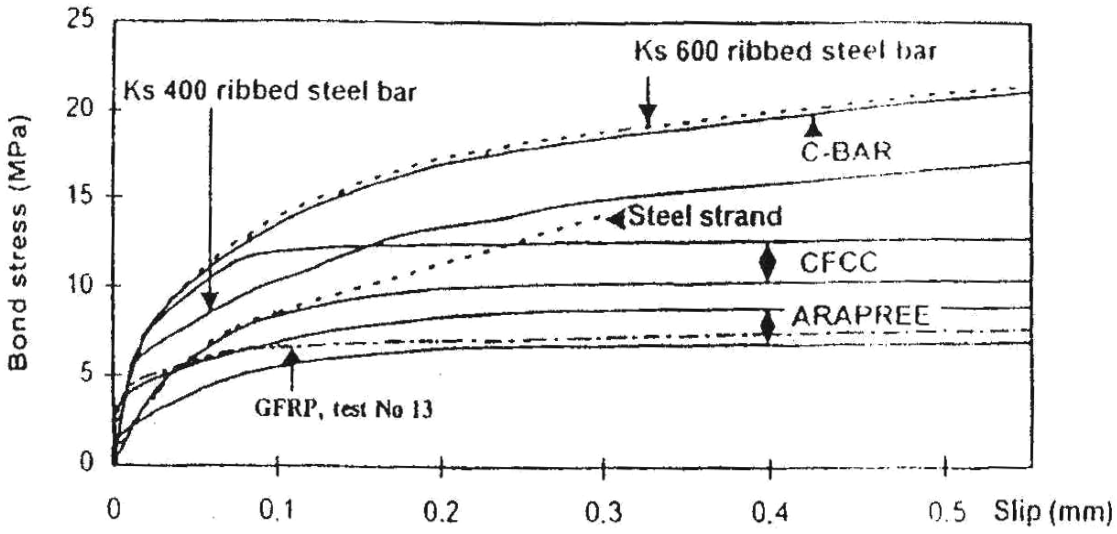

Figure 2.15: Results From FRP Tests Reported By Tamuzs, (2001).

Larralde et al. (1998) presented the bond strength test results of GFRP, AFRP, and steel rebars. The test setup used for pullout tests is shown in Figure 2.16. The tests

were conducted using single bars, embedment lengths of 2 in. (50 mm) to 10 in. (250 mm) and concrete compressive strengths from 3900 psi (7 MPa) to 5900 psi (41 MPa). The bar diameters were between 0.25 in (6.35-mm) and 3/8 in (9.53-mm). The specimens were tested at an age of 7 days of accelerated curing. The pullout tests consisted of pulling a single bar embedded in concrete cylinders of 6 in. in diameter by 12 in. in length. The bar was placed symmetrically and partially covered with a plastic sleeve to achieve the desired embedded length. LVDTs were used to measure the amount of deformation and slip in the bar both at the loaded- end and free-end of the bar. The pullout force was applied at a constant rate of displacement of 0.1 in/min.

There was a significant difference in the nominal bond strength values for the different types of bars tested. The AFRP bars, which had a relatively straight surface with only a sandpaper-like texture had the lowest bond strength. The GFRP bars exhibited only a slight increase in the bond strength in spite of the indentations produced by fiber wrapping around the bars.

The values of K_1, to be used in the basic equation to calculate the required development length are similar to those reported previously by other investigators; however, the values obtained in this project are slightly greater, which indicates a longer required development length.

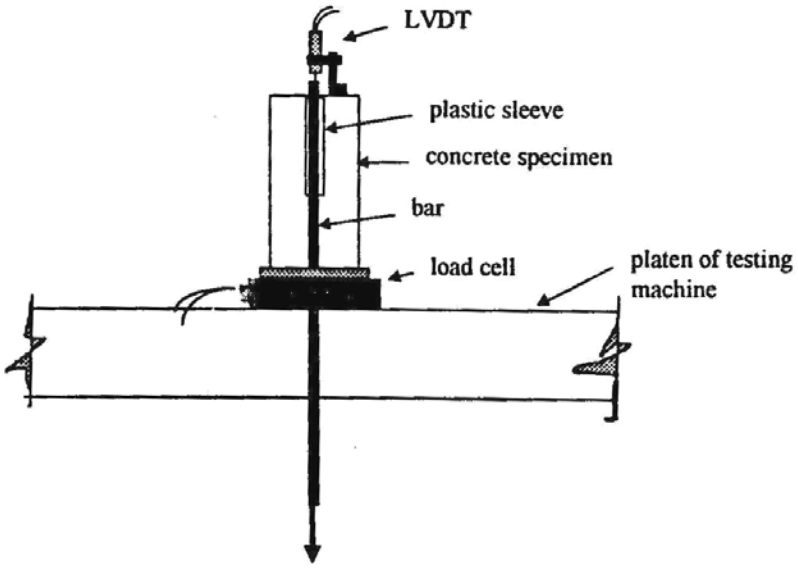

Figure 2.16: Bond Test Setup As Used By Larralde et al. (1998).

Taly and GangaRao (2001) conducted a study on the variables affecting both FRP bars and steel rebar. The bond characteristics of FRP bars depend on the following variables: size, shape, surface configuration (e.g., ribs) and surface roughness, position of the bars in the concrete element, confinement pressure, compressive strength of the concrete, embedment length, environmental conditions, temperature change, moisture absorption, mechanical interlock of bars against the concrete, chemical adhesion, and hydrostatic pressure against the FRP bars due to shrinkage of hardened concrete.

Freimanis et al. (1998) investigated commercially available FRP rods with variations in depth and pitch of indented helical wrappings to determine the effect of rod geometry on concrete bond and strength.

The specimens were 1-m-long rods cast in the horizontal direction and were fitted with elastomeric tubing to control the embedment length in the cube of concrete. The

concrete block was properly sized to prevent splitting. The tests were performed on a Tinius-Olsen test machine; the specimens were placed on the upper, stationary cross-head of the machine with the rod pointing downward through the lower, movable cross head. A thin layer of plaster was placed between the concrete block and the upper cross head to fill in any irregularities of the block which might cause it to sit unevenly. The bottom cross head was lowered at a constant rate of 1.25 mm/ min (.05 in/ min).

Maximum bond stress increased with increasing indent depth, but did not display any particular dependence on indent pitch. Loaded-end slip at the onset of free-end slip increased with increasing embedment length and decreasing rod diameter and was relatively constant for rods with similar embedment length to diameter ratios.

Tighiouart et al. (1998) experimentally investigated the bond strength of FRP rebars and compared the results to steel rebars. A total of 64 concrete beams reinforced with two types of FRP bars were tested. Four nominal diameters, 12.7, 15.9, 19.1, and 25.4 mm and three embedment lengths, six, 10, and 16 times the bar diameter were used. Also, three concrete depths of 200, 600, and 1000-mm were investigated in the 18 pullout specimens. The bond strength of the GFRP bars was lower than the steel bars, and the bond strength varied from 5.1 MPa to 12.3 MPa (740 to 1784 psi) depending on the bar diameter and the embedment length. Results showed that for GFRP bars, the adhesion and the friction controlled the bond strength, not mechanical interlock. The average maximum bond strength decreased as the diameter of the bar increased. The K value for GFRP rebars was 0.064.

Monti and Spacone (2000) developed a new R/C beam finite element that explicitly accounted for the slip between the reinforcing bars and the surrounding

concrete. The element formulation combined the fiber-section model with the finite-element model of a reinforcing bar with continuous slip. The model applies to any cross-sectional shape and for both monotonic and cyclic loads. Comparison with an experimental test on a circular column showed good agreement with the model, whereas the original fiber model with perfect bond overestimated the hysteretic energy dissipated during the loading cycles.

Hoa and Xie (2001) examined the interface between FRP rods and concrete. Tests were conducted on concrete samples with steel, and two types of FRP bars. Type one was 3/8" (9.53-mm) diameter GFRP rods by Hughes Brothers with helical ribs wound over the rod. Observations revealed that the main mechanism responsible for the shear transfer between the two materials was mechanical friction and mechanical interlock. For the FRP rods, friction was enhanced by the addition of sand particles and mechanical interlock was provided by helical ribs wound onto the bar.

A new rebar design was proposed to improve the mechanical interlock. The design consisted of regular rod which had lobes along the rod that give the rod a wavy configuration. The rebar is called HOAREBAR. The reinforcement was continuously integrated with the main part of the bar. Preliminary tests showed increased shear transfer and higher bond strength.

Aiello and Ombres (2000) developed a deformability model for R/C flexural members reinforced with FRP bars. In the block model, the bond-slip relationship that described the effective interaction between the FRP bars and the concrete matrix was developed. Results of experimental studies on bond of FRPs (Nanni et al, 1995, Cosenza et al., 1997, and Benmokrane et al., 1998) showed that the bond behavior was affected by

both fiber types and surface treatment of rebars. Also, the compression strength of the concrete and the confinement pressure at the FRP-concrete interface influenced bond behavior. Cosenza et al. (1997) proposed the following non-linear bond-slip relationship for FRP:

$$\frac{\tau}{\tau_1} = \left(\frac{s}{s_1}\right)^{\alpha} \qquad \text{if } s \le s_1 \qquad \text{2-8}$$

$$\frac{\tau}{\tau_1} = 1 - p\left(\frac{s}{s_1} - 1\right) \qquad \text{if } s_1 \le s \le s_3;\ \tau = \tau_3;\ \tau = \tau_3 \text{ if } s \ge s_3 \qquad \text{2-9}$$

where τ_1 and s_1 = peak bond stress and slip at the peak bond stress, respectively; α and p = experimental parameters, and τ_3 = value of τ due to the development of friction.

Additional theoretical study on the bond of FRP bars to concrete was conducted by Pecce et al. (2001) and Focacci et al. (2000). Experimental experiments on pull-out specimens were also conducted by Tepfers et al. (1998) and Larralde and Silva-Rodriguez (1993).

2.4.2.1 Bond Strength of FRPs Under Cyclic Loading

Katz (2000) studied the bond mechanism of FRP rebars to concrete to evaluate the effect of cyclic loading. Five different types of 12-mm and 12.7-mm rebars were tested; some had a helical fiber wrap, some were sand coated, and some smooth without any surface treated. The test setup is shown in Figure 2.17. The FRP rods were embedded in concrete blocks and were subjected to up to 4,500,000 cycles at 3 Hz at service stress level. The loading was accompanied by immersion in water at 60°C and 20°C to accelerate deterioration of the bars. Pullout behavior of the rods was then

determined at the end of the loading period. Results indicated a reduction in bond strength after loading. Three failure mechanisms were identified: 1) abrasion of the surface of the rod, 2) delamination of the outer layer of resin at the surface of the rod, and 3) abrasion of cement particles entrapped between the rod and the concrete, which is the main source of bond for smooth FRP bars. The first mechanism resulted in a bond strength reduction of 20-30% while the second and third failure modes resulted in a bond strength reduction of up to 60% and 70%, respectively. Finally, it was observed that helical wrapping of FRP rods reduced the resistance to cyclic loading by 20-30%.

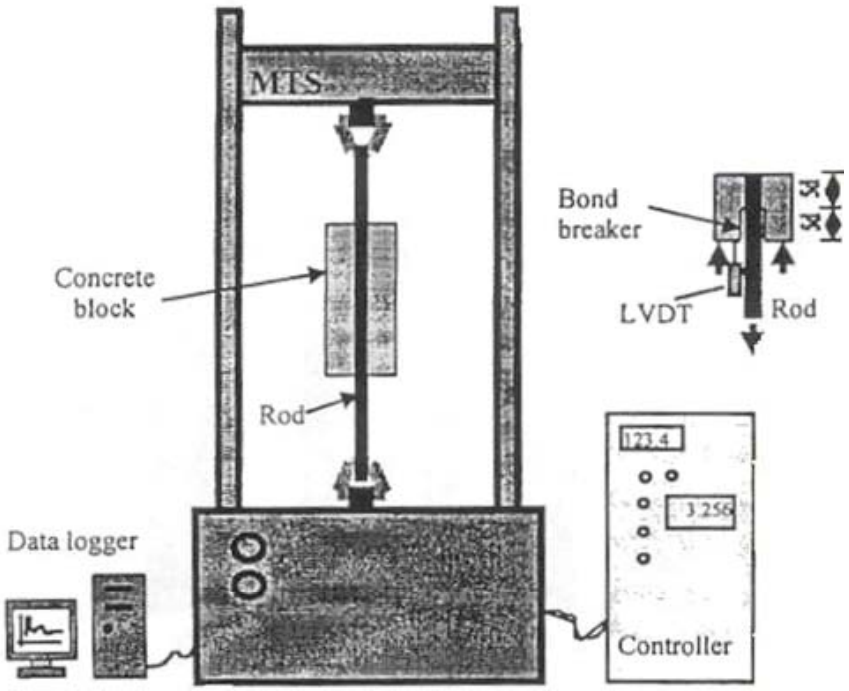

Figure 2.17: Cyclic Bond Test Setup Used by Katz (2000).

Ayoub and Fillippou (1999) studied the stress transfer mechanism between reinforcing steel and surrounding concrete through bond and the resulting slip and its effect on the hysteretic behavior of R/C structures. Early models of the stress transfer problem were based on a displacement formulation while recent models have used a flexibility formulation which has greater accuracy and stability under large inelastic strains. An evaluation of existing anchored reinforcing bar models was conducted, and a new model was developed based on a two-field mixed formulation. In this model, independent interpolation functions were used for relative slip and the reinforcing steel forces.

2.5 Long-Term Behavior of FRPs

Since FRPs are designed based on a life-cycle cost and analysis, the long-term behavior is vital for the proper design of structures with FRPs. These properties include the fatigue strength (high-cycle loading), creep and creep-rupture strength, and relaxation.

2.5.1 Fatigue Strength

Khatibi and Mai (2001) conducted an experimental study to examine the influence of cyclic loading on interfacial properties of glass fiber/ epoxy resin composites. Two material systems having the same fibers and epoxy were used, but with different fiber sizing (treatment). The commercial sizing was removed from the fibers by keeping them in Acetone for 72 hours. Unidirectional specimens of 70 x 10 x 0.4 mm (2.76 x 0.39 x 0.016 in) with various fiber volume fractions, manufactured using compression molding, were tested under a three-point-bending configuration. Dynamic

mechanical analysis (DMA) was used in this study to detect the existence of different interfaces in these materials. The fiber/ matrix interfacial degradation was then characterized under cyclic loading. Under cyclic fatigue loading, the fibers with surface treatment exhibited less interfacial degradation compared to the untreated (i.e., unsized) fibers.

Tang et al. (2000) developed a fatigue model based on cumulative damage for fiber-reinforced polymeric composites. This model incorporated applied maximum stress, stress amplitude, loading frequency, residual tensile modulus, and material constants as parameters. The model was verified with experimental fatigue data on a glass fiber/ vinyl ester composite. Three environmental conditions, air, freshwater and seawater were used in this study. The specimens were subjected to tension-tension stress at four levels of applied maximum tensile stress in each of two frequencies. The results showed that the loss of residual tensile strength and modulus in saltwater was approximately the same as for freshwater, but the fatigue life in these aqueous environments was shorter than that in air. The composite lost about 25 and 30 % of its tensile strength in freshwater and saltwater and 15% and 11% of its tensile modulus, respectively.

A newly developed specimen for testing FRP bars under cyclic loading was proposed by Adimi et al. (2000). In this setup, the FRP rod was completely encased in concrete. The specimen was formed of three blocks. The end blocks served as anchors for the rod, and the central block provided the concrete environment to the part of the rod where failure was expected to occur. Tests on 7.8-mm diameter (0.31 in) CFRP Leadline rods (Mitsubishi Kasei Corporation) were conducted. Tension-tension sinusoidal cyclic

loading at a frequency of 4 Hz was applied. At higher frequencies, heat generation during cycling became significant (at 6 Hz, the temperature differential was as high as 15° C). The ratio of minimum-to-maximum stress in the rod was 0.1 for all tests. For a desirable fatigue life of 4000000 cycles, the maximum stress should not exceed 1,000 MPa or 35% of its tensile strength.

Katz (1998) studied the fatigue behavior of helically-wrapped GFRP rods. When the bars were subjected to cyclic loading, extensive damage was caused to the longitudinal fibers by lateral load imposed by the helical fiber, which may lead to a premature failure of the rod. The longitudinal fibers in the region underneath the helical fiber fractured, locally to a depth of 1-2 mm, by local shear or bending, while the other fibers in the core failed under direct tension. This was also verified by microscopic evaluations.

To compare the testing parameters for testing steel rebar, Zheng and Abel (1999) studied the fatigue performance of 400 MPa-grade reinforcing steel by the TEMPCORE process. A sinusoidal constant axial-stress amplitude with $R = 0$ was applied at a frequency of 6 Hz. The fatigue limits of the tested bars with diameters of 12-mm to 36-mm were as high as 40% of the measured tensile strength and in some cases reached 60%.

2.5.2 Durability, Creep-Rupture and Relaxation, and Environmental Effects

Kootsookos et al. (2001) investigated the long-term seawater durability of glass/ polyester, carbon/ polyester, glass/ vinyl ester, and carbon/ vinyl ester composites that are used in marine structures. Since the composites were identical in processing and dimensions, the effects of fiber types and resins were determined. Glass and carbon

panels were immersed in a bath of seawater with a salinity content of about 2.9%. The panels were withdrawn from the bath at regular intervals to measure the weight change to determine the rate of moisture uptake. When immersed in seawater at 30° C, the carbon composites displayed better durability than the glass composites. Weight change measurements showed that the amount of moisture absorbed by the carbon systems was lowered compared with the glass systems. The flexural properties (stiffness and strength) of the glass composites declined slowly when immersed for long periods in seawater. Water absorption also appeared to affect the stability of mode I delamination cracks in the glass/ polyester composite.

Zhang and Karbhari (2000) investigated the effects of water and alkaline solution exposure on irreversible damage in glass/ vinylester composites. The specimens were wet and re-dried and characterized by tensile tests and optical microscopy for irreversible degradation. The results indicated that the irreversible damage was induced over time by both chemical and physical aging at different levels and failure mechanisms.

Saadatmanesh et al. (1999) studied high strength, corrosion-resistant FRP tendons that could replace steel tendons in prestressed or post-tensioned concrete structures. Behavior of AFRP tendons was examined. Test results of relaxation, creep, and fatigue behavior of 10-mm diameter tendons under simulated field conditions were presented. Fatigue specimens were tested at minimum stress levels between 30 and 50% of the ultimate tensile strength. Results showed that AFRP tendons exhibited good fatigue characteristics for stress ranges of 58 and 116 MPa (8.4 and 16.8 ksi), and for minimum tensile stress of up to 50% of the ultimate tensile stress. Fatigue life was reduced with

increasing stress range and minimum tensile stress. Creep specimens exhibited good creep behavior at sustained dead loads corresponding to 40% of the ultimate strength.

Saadatmanesh et al. (1999) investigated the long-term behavior of FRPs. The relaxation, creep, and tension-tension fatigue test results of two CFRP tendons, namely, Leadline PC-D8 8-mm diameter and 1x 7.5-mm diameter carbon fiber composite cable (CFCC) were presented. Three different stress ranges and seven minimum stress levels were used n the fatigue tests. The effects of repeated loading on the modulus of elasticity, Poisson's ratio, and the tensile strength were investigated. Both Leadline and CFCC exhibited good fatigue strength for stress range of 100 and 107 MPa (14.5 and 15.5 ksi), respectively. Both products exhibited good creep behavior with limited creep strains at a sustained load of approximately 40% of their ultimate tensile strength for the 3000 hour duration of the test. The extrapolated losses in tensile force due to relaxation were limited to 10 % over a 50-year time period.

Sen et al. (1999) studied the durability of aramid FRPs (AFRPs). The results were to assess the likely effect of diurnal/ seasonal temperature change on the durability of AFRPs. Twelve pretensioned, precracked AFRP beams were placed outdoors in two saltwater tanks. The beams were exposed to wet/ dry cycles and hot/ cold cycles. The results showed that the exposure led to visible cracking and a rapid deterioration in bond. Exposed specimens experienced a 13.6% loss in strength within 6500 hr (9 months), and accompanying strength reductions ranged from 43 to 55 % in specimens exposed to more than 21 months (15 500 hrs.). Loss of ultimate load capacity was primarily the result of bond deterioration between the AFRP and concrete. The failure mode of the exposed specimens changed from flexure-dominated modes in control specimens to ones

dominated by bond with 6500 hr. In the flexure dominated modes, failure was due to rupture of the AFRP rods. In contrast, in the bond dominated modes, there was no rupture of the AFRP rod but its separation from concrete. This provides persuasive evidence of the unsuitability of AFRP as a pretensioning element for piles driven in tidal waters.

Hamidah et al. (2001) studied the absorption characteristics of aramid prestressing rods with epoxy matrix in terms of weight gain or loss by immersing the rods in water, alkaline, and acid solutions for more than one year. Eight millimeter diameter rods were used in the study. The AFRP rods immersed in water showed only marginal weight gain; however, the weight of the rods immersed in alkaline or acid solution increased significantly. SEM scans showed the penetration zone at the cross section of the rods when immersed in three different solutions. The water caused bar swelling, which was primarily the filling of voids in the composite. As the matrix swelled, cracks occurred due to this expansion. The alkaline solution caused a weight decrease as SEM showed that the alkaline solution dissolved the outside layer of matrix, thereby exposing the fiber. However, the penetration was not deep, as in the bar in water.

Material testing on Arapree prestressing bars by Gerritse (2000) indicated that the stress-rupture and strength retention was fixed at 0.55 f_u, the ultimate strength of the bar.

2.6 Cost Analysis of Bridge Rehabilitation and FRP Systems

Ehlen (1999) examined the life-cycle cost-effectiveness of three FRP bridge decks, using a life-cycle cost method specifically tailored for comparing new materials with conventional ones. This method included a cost classification scheme for using all project related costs and comparing the cost advantages and disadvantages of different

materials. It was realized that in regions of low traffic, none of the FRP decks had sufficient user costs savings to overcome the relatively large initial FRP costs of their construction.

The corrosion of highway bridges in the United States and the economic impact was studied by Yunovich and Thompson (2003). There are approximately 600,000 bridges in the United States, according to the National Bridge Inventory Database, of which half were built between 1950 and 1994. Shown in Table 2.1 is the number of bridges which are defined as structurally deficient (i.e., a bridge that can no longer sustain the loads for which it was designed) for the past eight years. Table 2.2 specifically shows structurally conventionally reinforced and prestressed concrete deficient bridges. The estimated total service life for many of these bridges is shown in Table 2.3. Many of the R/C bridges have reached or are approaching the end of their design service life. These bridges need significant retrofitting or complete replacement.

An FHWA report on corrosion protection of concrete bridges estimated that the total cost to eliminate the backlog of deficient bridges was between $78 billion and $112 billion, depending on the time required to carry out the tasks (Virmani, and Clemena, 1998). Also, the average annual maintenance cost of deficient bridges through the year 2011 was estimated at $5.2 billion. Therefore, significant measures must be taken to eliminate and prevent the corrosion of R/C highway bridges. Shown in Table 2.4 are the unit costs for bridge replacement from the National Bridge Inventory data. This gives an average cost of replacement in terms of dollars per square meter of bridge. The overall area of structurally deficient R/C bridges is 34.2 million m^2 (Yunovich and Thompson,

2003). Using the average unit cost ($ 858 / m^2 [$80/ ft^2]), the total cost of replacing the structurally deficient bridges was estimated to be $29.3 billion.

The annual direct cost of corrosion for highway bridges was estimated to be between $6.43 billion and $10.15 billion: $3.79 billion to replace structurally deficient bridges over the next 10 years; $1.07 billion to $2.93 billion for maintenance and cost of capital for concrete decks; and $1.07 billion to $2.93 billion for maintenance and cost of capital for concrete substructures and superstructures (minus decking), (Yunovich and Thompson, 2003). This gave an average annual cost of $8.29 billion.

Life-cycle analysis (www.corrosioncost.com, 2003) estimated the indirect costs to the user due to traffic delays and lost productivity to be more than 10 times the direction cost of corrosion.

Table 2.1: National Bridge Inventory Data - Structurally Deficient Bridges (Yunovich and Thompson, 2003).

	1992	1993	1994	1995	1996	1997	1998	1999
Bridges in inventory	572633	574191	576472	577919	582043	583207	583414	585947
Number deficient	118757	111543	107512	103686	101544	98521	93119	88184
Percent deficient	20.7	19.4	18.6	17.9	17.4	16.9	16.0	15.0

Table 2.2: Structurally Deficient Bridges Based on Material of Construction, 1998 (Yunovich and Thompson, 2003).

	Conventional reinf. concrete	Prestressed concrete	Other	Total
Bridges in inventory	235 151	107 666	240 597	583 414
Structurally deficient	21 164	3230	68 725	93 119
Percent deficient	9	3	29	16

Table 2.3: Estimated Service Life for Concrete Bridges with Different Construction Methods (Yunovich and Thompson, 2003).

Material of construction	Average estimate, years
Conventional reinf. Concrete	72
Prestressed concrete	73

Table 2.4: Highway Bridge Replacement and Rehabilitation Program Unit Costs (Yunovich and Thompson, 2003).

	1995	1996	1997	1998	1999
Unit costs, $\$/m^2$	$ 768	$ 771	$ 836	$ 855	$ 858

2.7 Standards and Codes

Various prestandards, standards and codes have been developed in the United States for the design and use of FRP for concrete structures. Also, work is currently

being conducted on the manufacturing standards for pultruded products used for civil infrastructure applications, including rods that are used are reinforcing.

2.7.1 ACI Report 440.R1-01

This document provides recommendations for the design and construction of FRP reinforced concrete structures. It only addresses non-prestressed FRP reinforcement. It states that "FRP materials do not exhibit yielding; rather, they are elastic until failure. Design procedures should account for lack of ductility in concrete reinforced with FRP bars". The design philosophy of ACI Report 440.R1-01 is that when loaded in tension, FRP bars do not exhibit any plastic behavior (yielding) before rupture. If the FRP ruptures, failure of the member is sudden and catastrophic. The other failure mode is the concrete crushing failure mode, which is also a brittle mode. In any case, the member would not exhibit ductility as is commonly observed for under-reinforced concrete beams reinforced with steel rebars.

For FRP, both failure modes (FRP rupture and concrete crushing) are acceptable in governing the design of flexural members reinforced with FRP bars provided that strength and serviceability criteria are met. To compensate for the lack of ductility, the member should possess higher reserve strength. The suggested margin of safety against failure, therefore, is higher than that used in traditional steel-reinforced concrete design.

Section 8.1.2 states that the tensile behavior of the FRP reinforcement is linear elastic until failure. Also, Section 8.2.5.2 states that the failure mechanism of FRP reinforced flexural members should not be based on the formation of plastic hinges, because FRP materials demonstrate a linear-elastic behavior up to failure. Therefore,

moment redistribution in continuous beams or other statically determinate structures should not be considered for FRP reinforced concrete.

The failure capacity of an FRP reinforced flexural member is dependent on the failure mode, either concrete crushing or FRP rupture. The failure mode is determined by comparing the FRP reinforcement ratio to the balanced reinforcement ratio (i.e., where concrete crushing and FRP rupture occur simultaneously). The design tensile strength is used since the FRP does not yield. The FRP reinforcement ratio and the balanced ratio is given as

$$\rho_f = \frac{A_f}{bd} \qquad \text{and} \qquad \rho_{fb} = 0.85\beta_1 \frac{f_c'}{f_{fu}} \frac{E_f \varepsilon_{cu}}{E_f \varepsilon_{cu} + f_{fu}} \qquad \text{2-10 a, b}$$

If $\rho_f < \rho_{fb}$, the FRP rupture failure mode governs, otherwise concrete crushing occurs. Values for the balanced reinforcement ratio are shown in Table 2.5. For FRP, ρ_{fb} can be lower than the minimum reinforcement ratio for steel (ρ_{min} = 0.0035 for Grade 60 steel).

Table 2.5: Values for the Balanced Reinforcement Ratio for a Rectangular Section with f'_c = 5000 psi (34.5 MPa).

Bar Type	Tensile strength, f_y or f_{fu}, ksi (MPa)	Modulus of elasticity, ksi (GPa)	ρ_b or ρ_{fb}
Steel	60 (414)	29,000 (200)	0.0335
GFRP	80 (552)	6000 (41.4)	0.0078
AFRP	170 (1172)	12,000 (82.7)	0.0035
CFRP	300 (2070)	22,000 (152)	0.0020

The design tensile strength of the FRP bar, f_{fu}, is given as

$$f_{fu} = C_E f_{fu}^* \qquad \text{2-11}$$

where C_E is the environmental reduction factor for various fiber types and exposure conditions given in Table 2.6 and f^*_{fu} is the guaranteed tensile strength of an FRP bar defined as the mean tensile strength of test specimens minus three times the standard deviation.

When $\rho_f > \rho_{fb}$ (concrete crushing failure), the stress distribution in the concrete can be approximated with the ACI rectangular stress block. The nominal flexural capacity is

$$M_n = A_f f_f \left(d - a/2\right) \qquad 2\text{-}12$$

where

$$a = \frac{A_f f_f}{0.85 f_c^{'} b} \quad \text{and} \quad f_f = \left(\sqrt{\frac{\left(E_f \varepsilon_{cu}\right)^2}{4} + \frac{0.85 \beta_1 f_c^{'}}{\rho_f} E_f \varepsilon_{cu}} - 0.5 E_f \varepsilon_{cu} \right) \le f_{fu} \qquad 2\text{-}13 \text{ a, b}$$

Alternatively, the nominal flexural capacity can be expressed in terms of the FRP reinforcement ratio as

$$M_n = \rho_f f_f \left(1 - 0.59 \frac{\rho_f f_f}{f_c^{'}}\right) b d^2 \qquad 2\text{-}14$$

When $\rho_f < \rho_{fb}$, the failure of the member is initiated by FRP bar rupture and the ACI stress block can not be used since the maximum concrete strain of 0.003 may not be attained. The modified nominal moment capacity is given as

$$M_n = 0.8 A_f f_{fu} \left(d - \frac{\beta_1 c_b}{2}\right) \qquad 2\text{-}15$$

where

$$c_b = \left(\frac{\varepsilon_{cu}}{\varepsilon_{cu} + \varepsilon_{fu}} \right) d \qquad 2\text{-}16$$

Table 2.6: Environmental Reduction Factor for Various Fibers and Exposure Conditions.

Exposure condition	Fiber type	Environmental reduction factor, CE
Concrete not exposed to earth and weather	Carbon	1.0
	Glass	0.8
	Aramid	0.9
Concrete exposed to earth and weather	Carbon	0.9
	Glass	0.7
	Aramid	0.8

Since FRP members do not exhibit ductile behavior, conservative values of the strength reduction factors were adopted to provide higher reserve strength in the member. Shown in Figure 2.18 is the strength reduction factor ϕ as a function of the reinforcement ratio ρ_f.

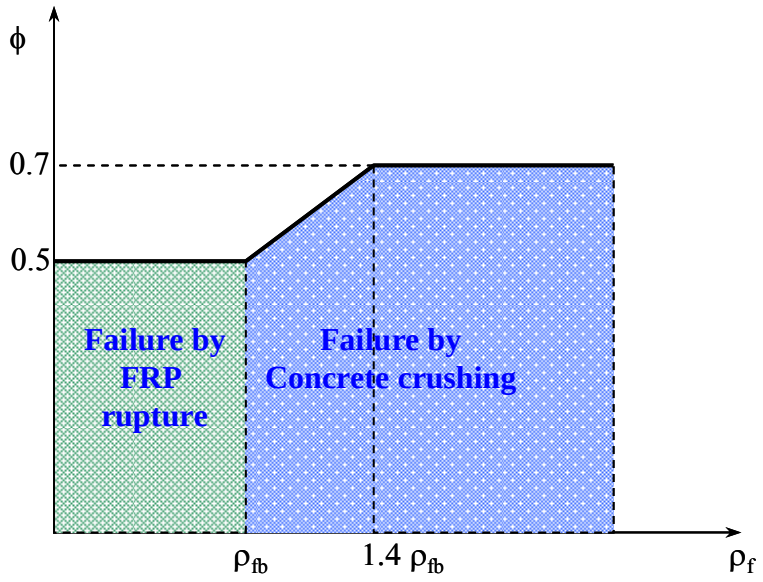

Figure 2.18: Strength Reduction Factor as a Function of the Reinforcement Ratio.

2.7.2 ACI 408.3-01/ 408.3R-01: Splice and Development Length of High Relative Rib Area Reinforcing Bars in Tension (408.3-01) and Commentary (408.3R-01)

This standard, as reported by ACI Committee 408, was created to help designers take advantage of the improved bond characteristics of high relative rib area deformed reinforcement. Increasing rib height, decreasing rib spacing, or employing a combination of the two can produce this reinforcement. This standard was intended to be a more efficient means of providing a development and splice length expressions for the high relative rib area bars than altering the current ACI 318-02 Chapter 12 provisions to accommodate bars that are not yet in commercial production.

2.7.3 ASCE Prestandard Document for Pultruded Shapes

Mosallam (2000) summarized the activities and content of the Phase I American Society of Civil Engineers(ASCE) / Pultrusion Industry Council (PIC) of the Society of Plastic Industry (ASCE/ PIC) Prestandard Document that covered standards for structural design, fabrication, and erection of pultruded FRP structural shapes, plates, and rods. First a database was developed that divided information into seven categories representing key subjects in FRP composites structural design. These categories included a) material properties, b) environmental durability, c) time effects including creep and creep-rupture and cyclic fatigue, and d) member performance. The contemporary Load and Resistance Factor Design (LRFD) protocol was used as a guide for establishing the prestandard outline.

CHAPTER 3. THEORY OF MODELING AND SIMILTUDE

3.1 Background

A structural model is any physical representation of a structure or portion of a structure constructed at reduced scale and which laws of similitude must be employed to interpret test results (Harris and Sabnis, 1999). The advantages of models include cost reduction, both in fabrication and material, reduced demands of loading equipment and disposal costs. Factors affecting the accuracy of model accuracy include model material properties, fabrication accuracy, loading techniques, measurement results, and interpretation of results. The geometric scale of a model affects the fabrication and loading requirements. For example, small models require light loads but are more difficult to fabricate; larger models are easier to build but require much larger loads.

There are five main types of model classifications including, elastic, indirect, direct, strength, and instructional models. Only the direct model was used in this research. The direct model is geometrically similar to the prototype in all respects and the loads are applied in the same manner as the prototype.

The strength model is an ultimate strength direct model. This model is made of materials similar to the prototype materials, and it predicts the prototype behavior for all loads up to failure. The materials satisfy similitude conditions for the prototype materials. The similitude conditions are explained later.

There are two general characteristics in dimensional analysis: qualitative and quantitative. Qualitative allows physical phenomena to be expressed in certain fundamental measures, for example, length, force, time, and temperature. Quantitative has a number and a standard of comparison (i.e., unit). For an equation to be in a

dimensionally homogeneous form, the governing equation must be valid regardless of the choice of dimensional units in which physical variables are measured.

3.2 Buckingham's Pi Theorem

The Buckingham's Pi Theorem is the method used for dimensional analysis. It states that any dimensionally homogeneous equation involving certain physical quantities can be reduced to an equivalent equation involving a complete set of dimension products. For example, an equation of the form

$$F(X_1, X_2, ..., X_n) = 0 \qquad 3\text{-}1$$

can be expressed as

$$G(\pi_1, \pi_2, ..., \pi_m) = 0 \qquad 3\text{-}2$$

where the π terms are dimensionless products of the n physical variables, X_1 through X_n, and a complete set of dimensionless products are

$$m = n - r \qquad 3\text{-}3$$

where r is the number of fundamental dimensions involved in the physical variables. The terms of the complete set, m, are independent products formed from the physical variables X_1 through X_n. In terms of definitions, Equation 3-3 can be written as

$$products = number\ of\ physical\ variables - number\ of\ fundamental\ measures \qquad 3\text{-}4$$

The dimensional analysis is to combine the physical variables into groupings of π terms, and a subsequent reduction in the unknown quantities. Two conditions must be

satisfied for proper dimensional analysis. First, all variables must be included, and second, the *m* terms must be independent. The process for dimensional analysis is:

1. Choose the *r* variables that embrace the *r* dimensions (fundamental measures) required in expressing all variables of the problem and that are dimensionally independent (DI). For example, for a problem involving force, length, and temperature (*F, L, T*), *r* = 3 since there are three fundamental measures. Therefore, the three *r* terms collectively must include *F, L*, and *T*, but no two variables can have the same dimensions. Also, dimensionless variables cannot be included in the *r* group; for example, strain, ε, Poisson's ratio, ν, and angular measurements.
2. Form *m* π-terms by taking the remaining (*n*-*r*) variables and grouping them with *r* variables to get all groups dimensionless. The *r* variables will appear more than once in the π terms, but the $m = n - r$ variables appear only once.

The application of dimensional analysis is the development of scale factors relating physical quantities in the model to the prototype. A complete set of dimensionless products of the form

$$\pi_1 = \phi\left(\pi_2, \pi_3, ..., \pi_n\right) \tag{3-5}$$

can be written for both the model and the prototype. Forming a quotient from both equations (model and prototype) yields

$$\frac{\pi_{1P}}{\pi_{1m}} = \frac{\phi\left(\pi_{2P}, \pi_{3P}, ..., \pi_{nP}\right)}{\phi\left(\pi_{2m}, \pi_{3m}, ..., \pi_{nm}\right)} \tag{3-6}$$

Complete similarity is defined as a condition where all dimensionless products are the same in both the model and prototype. When complete similarity is maintained,

$$\left.\begin{array}{l}\pi_{2m}=\pi_{2P}\\ \pi_{3m}=\pi_{3P}\\ \vdots\ =\ \vdots\\ \pi_{nm}=\pi_{nP}\end{array}\right\}\ \text{design and operating conditions} \qquad 3\text{-}7$$

and therefore,

$$\frac{\pi_{1P}}{\pi_{1m}}=\frac{\phi\left(\pi_{2P},\pi_{3P},...,\pi_{nP}\right)}{\phi\left(\pi_{2m},\pi_{3m},...,\pi_{nm}\right)}=1 \quad \text{or} \quad \pi_{1P}=\pi_{1m} \qquad 3\text{-}8\text{ a, b}$$

Equation 3-8b is the prediction equation of the dependent variable of the problem.

To solve for the scale factors, similitude relations are derived by equating $\pi_m = \pi_p$ for each of the π terms derived. The scale factor is solved for the quantity *i* as

$$s_i=\frac{i_P}{i_m} \qquad 3\text{-}9$$

For a true model, model and prototype strains must be identical, that is $s_{\varepsilon m} = s_{\varepsilon p}$. This condition is automatically satisfied when the same material is used in both the model and the prototype.

An example of the formation of π terms and corresponding scale factors is the case of a simply supported beam and subjected to transverse four-point loading as shown in Figure 3.1. The beam is of length *l*, width *w* and height *h*. The model and prototype materials both have a modulus *E*, and a Poisson's ratio *v*, which are not necessarily the same. In this example, the design conditions and the prediction equation for the deflection at any point are developed from the model to the prototype. The calculation details are given in Appendix A. The results are as follows. The prediction equation is

$$\pi_{1P}=\pi_{1m}\Rightarrow\frac{\delta_P}{l_P}=\frac{\delta_m}{l_m}\Rightarrow\delta_P=\frac{l_P}{l_m}\delta_m=s_l\delta_m \qquad 3\text{-}10$$

and the design equation for load is

$$\pi_{2P} = \pi_{2m} \Rightarrow \frac{P_P}{E_P l_P^2} = \frac{P_m}{E_m l_m^2} \Rightarrow P_P = s_E s_l^2 P_m \qquad 3\text{-}11$$

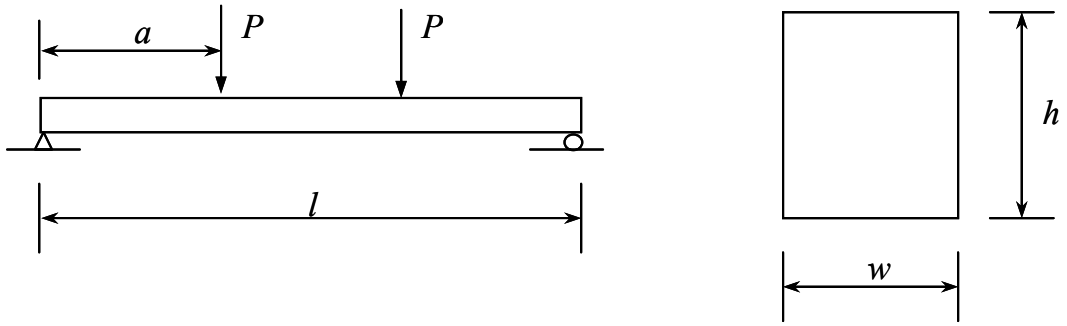

Figure 3.1: Dimensional Analysis for Simply-Supported Beam Under Four-Point Loading.

3.3 Applications and Similitude Terms

The application of dimensional analysis is to relate results from structural models to prototype-size structures. The applications of this for the DHFRP bar include the scaling of material properties from model sizes to prototype sizes, the scaling of flexural concrete member test results, and the scaling of concrete column members subjected to reverse cyclic loading. Shown in Table 3.1 are similitude requirements for static elastic modeling used in the current research. This is applicable for modeling certain material properties of DHFRP bars including tensile, creep, and fatigue strengths. The independent scale factors chosen were the modulus of elasticity E and length l. All remaining scale factors are either unity or functions of s_E and s_l. The loadings of the model are scaled by the factors given in Table 3.1, the model stresses are s_E times as

small as those in the prototype, and the model strains are identical to prototype strains. For example, a concentrated load is reduced from the prototype load by the factor $S_E S_l^2$ which is a significant load reduction.

Table 3.1: Similitude Requirements for Static Elastic Models.

Quantities	Dimensions	Scale Factor
Material properties		
Stress	FL^{-2}	S_E
Modulus of elasticity	FL^{-2}	S_E
Poisson's ratio	—	*1*
Strain	—	*1*
Geometry		
Linear dimension	L	S_l
Linear displacement	L	S_l
Area	L^2	S_l^2
Moment of Inertia	L^4	S_l^4
Loading		
Concentrated Load, Q or V	F	$S_E S_l^2$
Uniform load, w	FL^{-1}	$S_E S_l$
Moment, M	FL	$S_E S_l^3$

The modeling of the complete inelastic behavior of reinforced concrete models is more difficult, including the failure mode, capacity, and bond behavior. Attention must be made to correctly model both the concrete compressive and tensile strength properties, and the surface conditions (e.g., deformations, roughness) of the reinforcing bars must be carefully replicated at model scale. The requirement that the failure criteria for model concrete subjected to multi-axial stresses should be identical with that of the prototype concrete is usually relaxed. The two requirements are:

1. Stress-strain curves must be geometrically similar in model and prototype concrete for both uniaxial tension and compression
2. $\varepsilon_m = \varepsilon_p$ at failure under uniaxial tension and compression

The similitude requirements for reinforced concrete models are given in Table 3.2. These were used comparing model and prototype beam and column results. The independent scale factors are s_σ and s_l, the stress and the length; therefore, $s_\sigma = s_E = 1$.

Table 3.2: Scale Factors Used for Reinforced Concrete Models.

Quantities	Dimensions	Scale Factor
Material properties		
Concrete stress, σ_c	FL^{-2}	$S_\sigma = (1^*)$
Concrete strain, ε_c	—	1
Modulus of concrete, E_c	FL^{-2}	$S_\sigma = (1)$
Poisson's ratio	—	1
Reinforcing stress, σ_r	FL^{-2}	$S_\sigma = (1)$
Reinforcing strain, ε_r	—	1
Modulus of reinf., E_r	FL^{-2}	$S_\sigma = (1)$
Bond stress, u	FL^{-2}	$S_\sigma = (1)$
Geometry		
Linear dimension, l	L	S_l
Linear displacement, δ	L	S_l
Area of reinf., A_r	L^2	S_l^2
Loading		
Concentrated Load, Q or V	F	$S_\sigma S_l^2 = (S_l^2)$
Uniform load, w	FL^{-1}	$S_\sigma S_l = (S_l)$
Moment, M	FL	$S_\sigma S_l^3 = (S_l^3)$
* these values in parentheses are the values for practical true models		

CHAPTER 4. PROTOTYPE MATERIAL PROCESSING AND MANUFACTURING BY BRAIDTRUSION

4.1 Background

One component of the research was to develop a DHFRP bar that could be used at the prototype level. This included the development of a manufacturing process that would result in a bar with good material properties. Initially, the same process used to manufacture the model 3-mm and 5-mm DHFRP bars (Somboonsong, 1997) was used to manufacture the prototype 10-mm diameter DHFRP bars. However, it became evident that this process was not providing sufficient quality results for the larger bars, and therefore, modifications from the original manufacturing process for smaller diameter bars were made.

Many of the current commercially available products used are manufactured using the traditional pultrusion process for composites (see Chapter 2 for a review of current products and practices). These are bars that have constant cross section when manufactured. As discussed in Chapter 2, some products have surface treatments or filament windings added to the bar to increase bond strength, but the bars initially are of constant cross section when pultruded.

A review of the literature of current FRP systems being used for R/C structures indicates that most commercially produced FRP bars are linear-elastic to failure, with limited ductility and ultimate strain. Therefore, an R/C element reinforced solely with linear-elastic FRP must be over-designed to prevent the ultimate strength of the material from being reached, and therefore, preventing brittle (i.e., catastrophic) failure. Also, for areas of moderate to high seismicity where structures experience

reverse cyclic loading and earthquake loading, plastic response of the reinforcement is necessary for proper response of R/C structures. Current FRPs do not have this inelastic behavior.

In comparison to this, the 3-mm and 5- mm diameter model DHFRP bars already developed at Drexel University (Somboonsong, 1997) were FRP bars with a bilinear stress-strain response. This was due in part to the use of a hybrid composite structure. A hybrid composite uses multiple material systems (two or more) with different properties. The combinations of these individual and unique properties enabled a composite material to be developed with new and tailorable properties that would not exist otherwise. Also, the architecture of the bar itself, being a braided structure, produced geometric nonlinearity which resulted in a pseudo-ductile stress-strain curve. Shown in Figure 4.1 is the stress strain behavior of various FRP bars, steel bars, and the DHFRP bar. Figure 4.2 shows the stiffness of various FRP, steel, and DHFRP bars. Observations need to be made based on stiffness, strength, and ductility. The DHFRP bar exhibits significant ductility and stiffness for a FRP bar. A definite yield point exists followed by a yield plateau and a strain-hardening region to failure. The failure mechanism is discussed in Chapter 5.

The objective was to manufacture a 10-mm diameter DHFRP bar, comparable to a commercially available Number 3 steel rebar, with both sufficient stiffness and superior ductility compared with presently manufactured FRP bars. Previous preliminary manufacturing techniques for 10-mm DHFRP bars demonstrated bars with adequate stiffness but insufficient ductility. Also, preliminary testing for bond strength showed satisfactory bond strength but with improvement needed. The new

bar must have increased ductility for proper applications in R/C structures, especially for earthquake (EQ) applications. Also, while meeting this ductility demand, sufficient stiffness must still be maintained, which is an issue for many currently used FRP systems. This is a challenge since theoretically, higher stiffness usually results in reduced ductility and vice versa. This challenge, however, should be obtainable with the DHFRP through proper design, as discussed in Chapter 5.

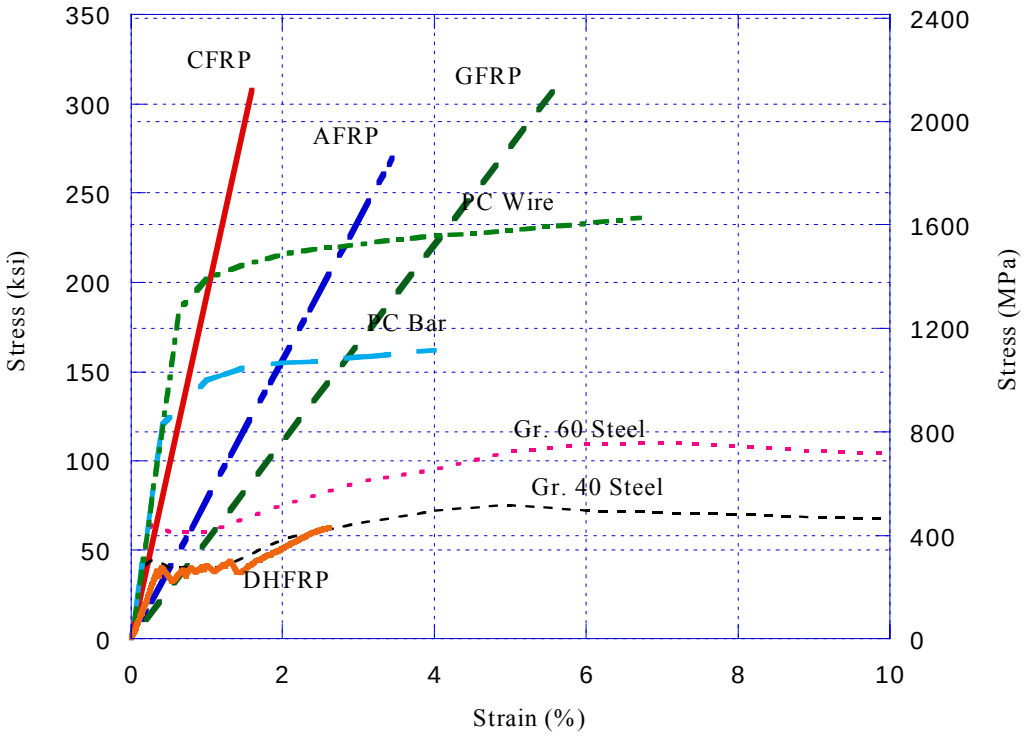

Figure 4.1: Ductility Comparison of Various Reinforcements.

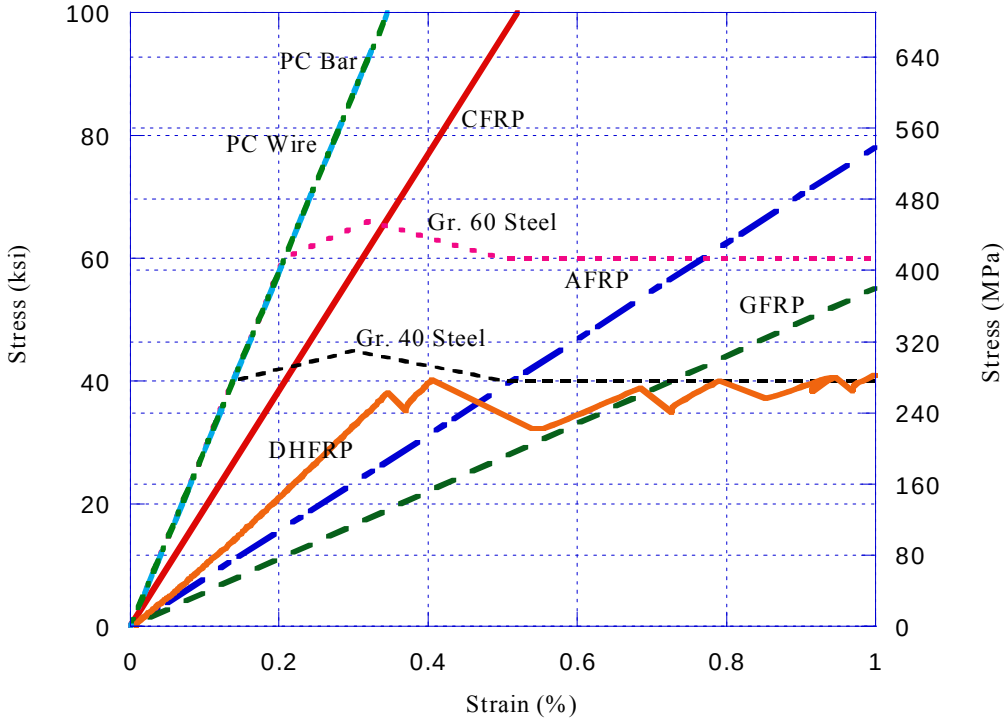

Figure 4.2: Stiffness Comparison of Various Reinforcements.

4.1.1 Design Philosophy of DHFRP Bars

A brief description of the DHRP bar design is presented in this section. A more detailed description of the design of the DHFRP bar is given in Chapter 5 which discusses material modeling of the bar behavior and microscopic analysis.

The DHFRP bar is a 2-dimensional braided structure with an elastic core (Ko, 1987). The DHFRP bar is designed based on the hierarchy of textile composites (Ko et al., 1989). This is illustrated in Figure 4.3. Four separate levels of hierarchy or order can be isolated which include the fiber level, the yarn or twist level, the crimp or weave level, and the composite or braid level. The translation efficiency of each level

must be accounted for in order to get the full behavior of the composite. The translation efficiency is the translation of various properties from one level to the other, beginning at the molecular level. These properties can include strength, stiffness, and strain characteristics. More detail of the theory governing the translation efficiency is discussed in Chapter 5.

The DHFRP bar is a hybrid composite consisting of two or more fibrous materials. Figure 4.4 is a schematic of the design philosophy of the bar. The top figure shows the yarns that the 10-mm bar is comprised of; this includes braiding yarns, rib yarns, and core yarns. These are held together by a thermoset resin. The number of yarns given is for the 10-mm bar design. The bottom figure shows a cross-section along the length of the bar at the indicated point. The cross section has some variation along the length of the bar, which is discussed in the next section.

The DHFRP has two unique features. The first is developed on material considerations and the second is based on architectural or geometric considerations. First, being a hybrid composite system, DHFRP bar has multiple fibrous material systems. Typically, different materials for the core and the braided sleeve are chosen. For the current design, the core yarns are unidirectional and the material chosen has a high modulus to give the DHFRP bar high initial stiffness. Various carbon fibers could be used for the elastic core, which provide high initial stiffness with low elongations. The braided sleeve material is chosen to provide ductility to the DHFRP bar. Therefore, a material such as Kevlar that has relatively large elongations could be used. This combination of material systems enables a bar to possess a pseudo-ductile

behavior due to the combination of various stiffness and elongation behaviors. This can be modified to provide bars with a spectrum of material properties.

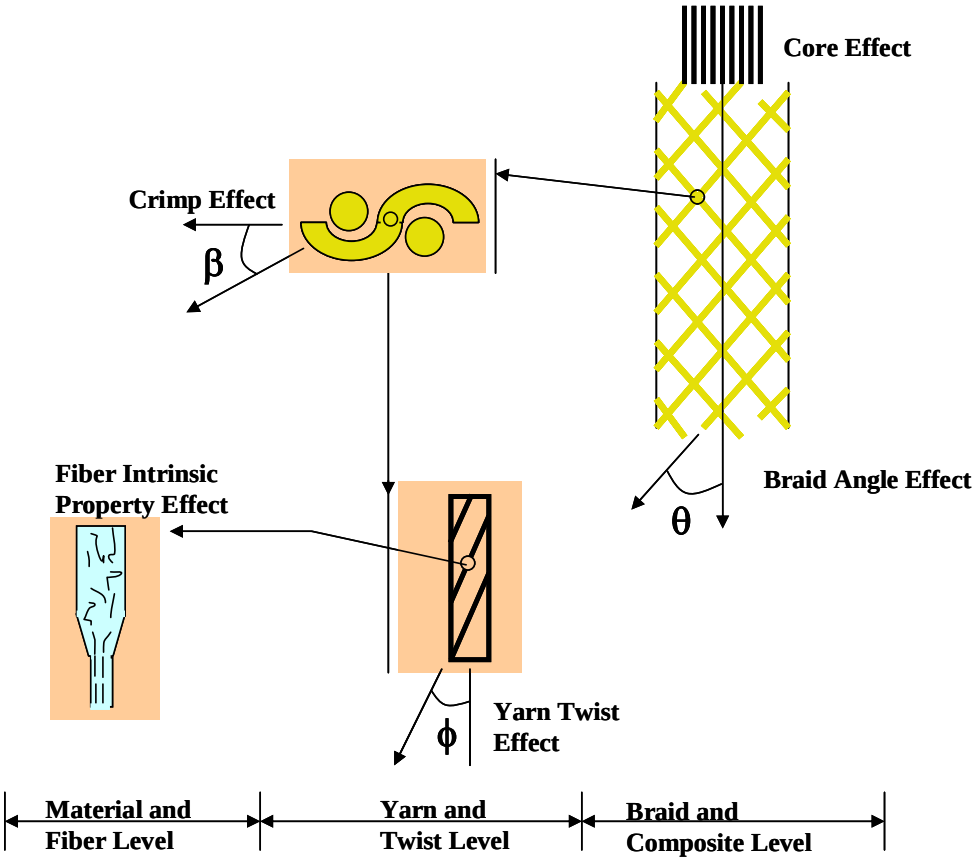

Figure 4.3: Structural Hierarchy of Textile Composites.

The architectural or geometrical feature of the bar results from the bar being a braided composite structure. The braided composite bar allows the bar to be a fully-integrated structure. Unique properties can be tailored by using the architecture of the braid. The ductility of the bar is very dependent on the braid profile or angle. The

strength is also dependent, but to a lesser extent. Again, a broad spectrum of material properties can be developed by varying the braid profile. Also, by varying the bundle size of the yarn, deformations similar to conventional steel bar can be integrated into the bar structure.

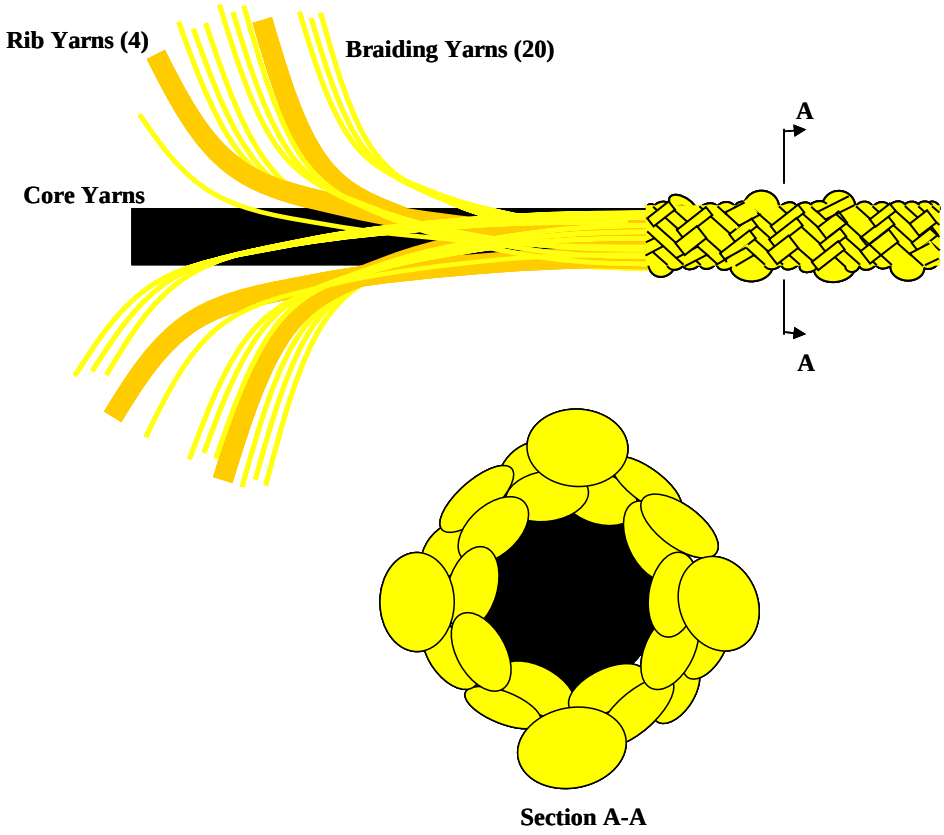

Figure 4.4: Design Philosophy of the DHFRP Bar.

By using the intrinsic material and geometric properties of the bar (i.e., hybrid and braided composite), a pseudo-ductile composite bar was developed. Also, by

varying these parameters, a wide spectrum of bars can be made with various material properties.

4.2 Manufacturing Program

Previous manufacturing techniques for 3-mm, 5-mm and 10-mm DHFRP bars demonstrated bars with sufficient stiffness but insufficient ductility and bond strength. As will be shown in Chapter 5, the earlier manufactured bar microstructure had dry fiber and voids due to poor wetting. This was most evident in the 10-mm diameter bars. This caused premature failure since the stress transfer capability was reduced due to dry fiber and voids. The new bar must have increased ductility for proper applications in R/C structures. Also, the bond strength must be increased by means of the deformation pattern and rib yarn parameters such as the rib height, spacing, and braiding angle (Chapter 6).

Many commercially available FRP bars are made using the pultrusion process. This process is described below. In traditional pultrusion, fibrous composites are prismatic with a constant cross section. Also, many of the fibers are oriented in the zero or unidirectional axial orientation. Shown in Figure 4.5 are some of the current commercially used FRP bars for concrete reinforcement. Also, many pultruded shapes are formed as shown in Figure 4.6, for both R/C and non R/C applications. Both solid and hollow sections can be formed, depending on the application.

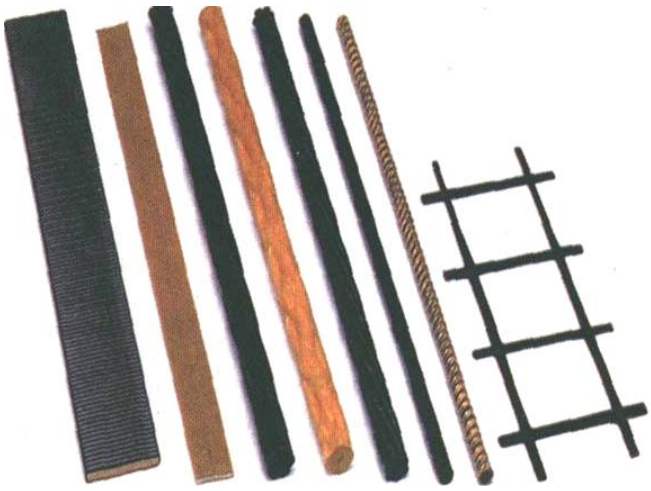

Figure 4.5: Various Commercially Available FRP Products for R/C Structures (Hughes Brothers, 2003).

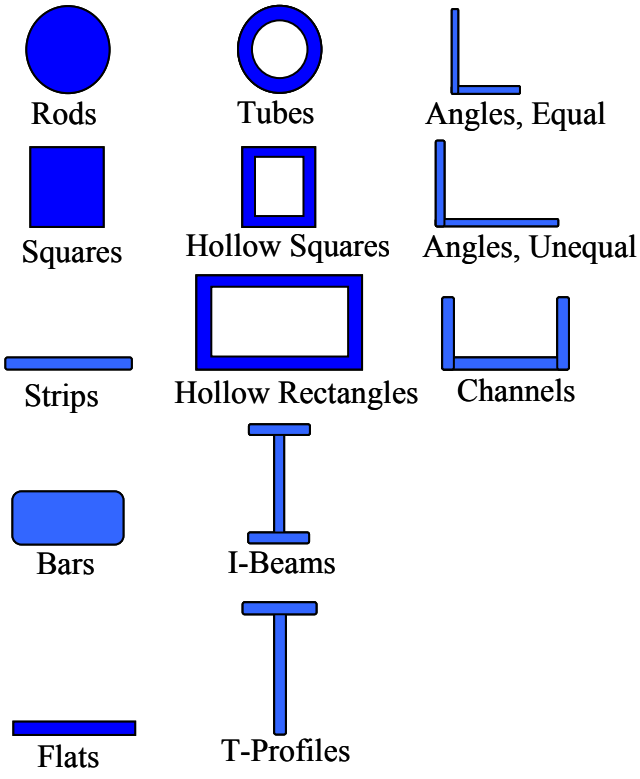

Figure 4.6: Various Pultruded Structural Shapes.

DHFRP was manufactured using a process called ‘braidtrusion’. Combining braiding with the pultrusion process, the term ‘braidtrusion’ was coined by Dr. Frank Ko of Drexel University. The bar is a hybrid composite (Figure 4.4) comprised of a unidirectional core for high initial stiffness (e.g., carbon) and a braided sleeve for ductility (e.g., Kevlar 29 or Kevlar 49). In the braidtrusion process, there are four major zones in the manufacturing process. These are the take-up zone, the impregnation zone, the braiding zone, and the curing zone. The manufacturing process from start to finish is described below.

A schematic setup of both a typical braiding process and the pultrusion processes are shown in Figure 4.7. Figure 4.8 shows the braidtrusion process and Figure 4.9 provides a flowchart summarizing the tasks for developing and manufacturing the composite DHFRP rebars. This process is discussed in more detail below.

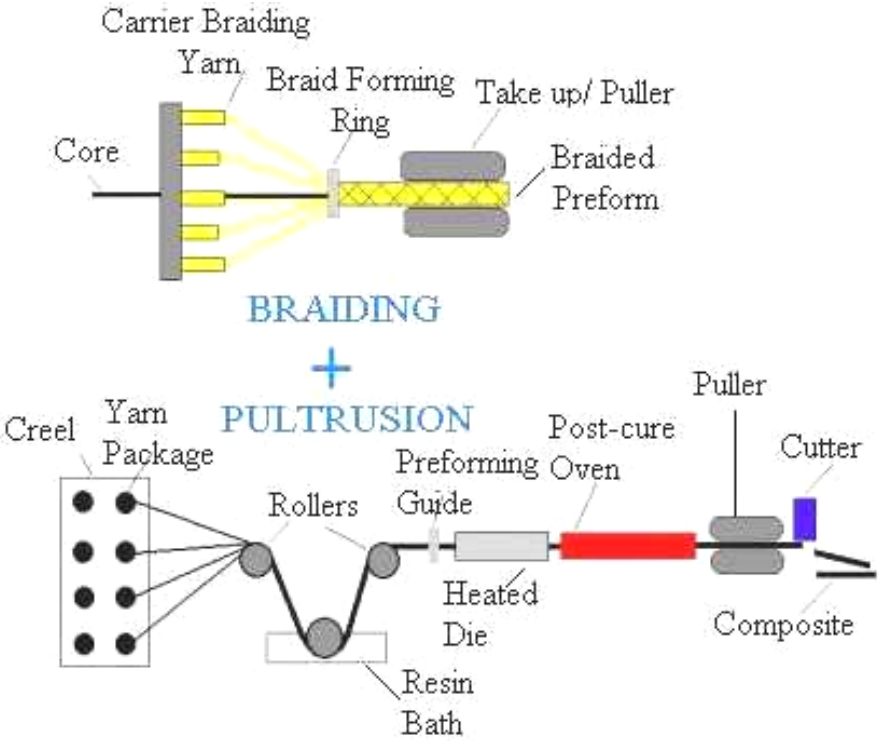

Figure 4.7: Braiding and Pultrusion Processes.

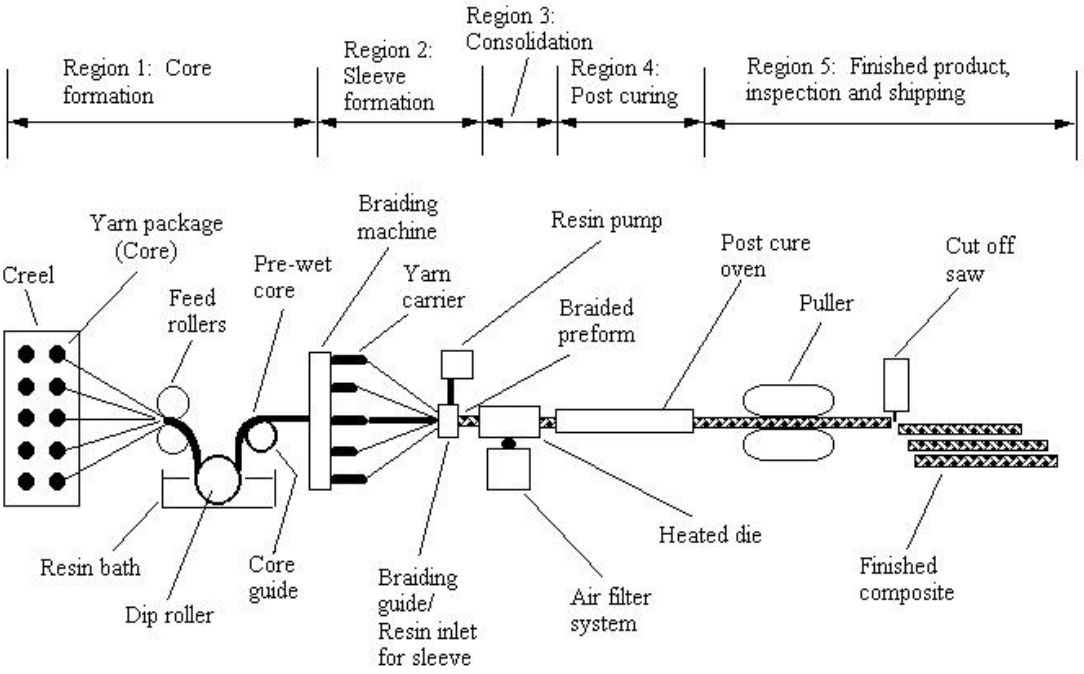

Figure 4.8: Schematic of the Braidtrusion Process.

Three possible fibrous material systems used for 10-mm DHFRP bars are listed in Table 4-1. The theoretical strength and stress-strain properties of these systems are computed and compared in Chapter 5. Shown in Table 4-2 is the number of yarns (or ends) that are needed for a 10-mm bar using the various material systems and shown in Table 4-3 is the material properties of these various yarns.

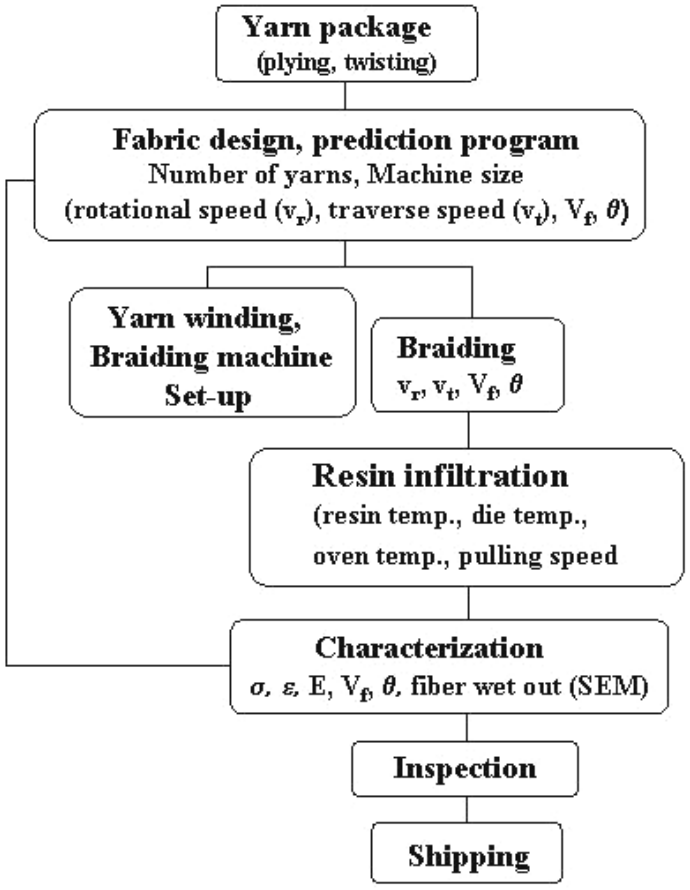

Figure 4.9: Integrated Design for Manufacturing of Composite Rebars.

Table 4.1: Possible Fibrous Material Systems for 10-mm Diameter DHFRP Bars.

Possible Rebar Type	Sleeve Material	Core Material
DHFRP #1	Kevlar 49	P55S-4K
DHFRP #2	Kevlar 29	IM7-12K
DHFRP #3	Kevlar 49	IM7-12K

Table 4.2: Fiber Materials for 10-mm Diameter Braided Rebar.

		No. of ends/carrier (ends)			**Number of Carriers (carrier)**			**Braid Angle**
Material	**Denier/end**	**Core**	**Sleeve**	**Rib**	**Core**	**Sleeve**	**Rib**	**(deg.)**
Kevlar 29	1500	0	4	40	0	20	4	45
IM7-12K	4014	43	0	0	43	0	0	0
Kevlar 49 sleeve	2840	0	2	0	0	20	0	45
Kevlar 49 rib	8520	0	0	7	0	0	4	45
P55S-4K	6429	120	0	0	120	0	0	0
1 Denier = 1 gram/ 9000 m of material								

Table 4.3: Properties of Fibers and Resin.

Properties	**Kevlar 29 (1500 Denier)**	**Kevlar 49 (1400 Denier)**	**IM7-12K**	**P55S-4K**	**Resin***
Density (g/cc)	1.44	1.45	1.78	2.0	1.16
Ult. Ten. Str., ksi, (MPa)	400305 (2760.0)	400305 (2760.0)	746750 (5148.7)	249400 (1719.6)	9200 (63.4)
Elast. Mod., ksi (GPa)	8992 (62.0)	17840 (123.0)	40030 (276.0)	55000 (379.2)	450 (3.1) (yield)
Elong. at break (%)	3.7	1.9	1.9	0.5	11.3
Manufacturer	DuPont	DuPont	Hexcel	Amoco	Shell
*** Resin System: Epon 9500/Epi-Cure Curing Agent 9550**					

4.2.1 Yarn Preparation

Since the DHFRP bars were made in the Fibrous Materials Research Center at Drexel University, all aspects of manufacturing were performed. This included the winding of the yarn which comprised the DHFRP bars. The yarn preparation was a critical process in the manufacturing of larger diameter bars. The ease of manufacturing and the quality of the braided bar were directly related to the quality of the yarn winding.

The fiber materials were received in the form of a large spool of single-end yarn. Since the number of spools supplied was not enough, the yarn had to be wound into multiple single-end tubes and then rewound into the desired number of ends per tube. Multiple winding steps were carried out to transfer the fiber into smaller tubes suitable for braiding carriers and to obtain multiple ends per tube. Winding was done on a Leesona tube winder with a six-inch traverse cam as shown in Figure 4.10.

A detailed explanation of the yarn winding procedure is provided in Appendix B. In the development of prototype-size 10-mm diameter DHFRP bars, the yarn winding process was the most critical parameter from a quality control viewpoint. Improper yarn tension resulted from poor winding. This was critical during manufacturing since improper yarn tension resulted in yarn jamming on the braiding carriers. This caused a complete shutdown of the braidtrusion process until the jam was fixed.

After yarn winding, the yarn plying schedule and specific winding procedures are described. These procedures are specifically described for the larger denier Kevlar 49 yarns (2840 and 8520); however, this same procedure would be used for any type of yarn plying, depending on the application.

Figure 4.11 illustrates the yarn plying schedule for both braiding and rib yarns. The 2840 denier yarns used to make general braiding yarns were first wound onto one-ply tubes. Then two 1-ply tubes were plied together to make a 5680 denier braiding yarn. The 8520 yarns used wound onto 1-ply tubes. Then three 1-ply tubes were combined to make a 3-ply yarn and four 1-ply tubes were combined to make a 4-ply yarn. Finally, the 3-ply yarn and the 4-ply yarn were combined to make a 7-ply rib yarn with a denier of 59640.

Figure 4.10: Leesona Yarn Winder with 6" Traverse Cam.

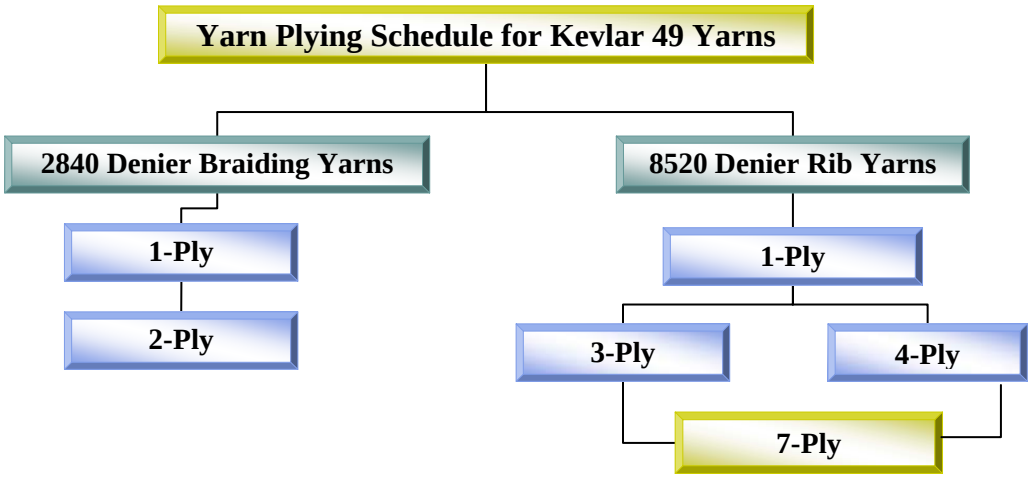

Figure 4.11: Plying Schedule for Kevlar 49 Braiding and Rib Yarns.

Table 4.4 illustrates the schedule for winding yarns. The following schedule is based on the research experience of yarn winding. Column three is the ply number for each type of yarn. Column four gives the number of strokes of each yarn. The number of strokes was defined as one complete movement or cycle up and back the traverse cam. This was defined so all yarns would be wound to the same length. This was part of the improvement process whereby yarn waste was minimized. Column five gives the number of movements of the spring-buttoned arm on the winding machine. Two lengths of bar were made, 12.5 foot and two 10.5 foot lengths. In Table 4.4, *-1 entries refer to the amount of rib yarn to make two 10.5 foot lengths and *-2 entries refer to the amount of rib yarn to make one 12.5 foot bar. Shown in Figure 4.12 is a properly wound bobbin of Kevlar yarn used for general braiding yarns.

Table 4.4: Yarn Winding Schedule.

Yarn	Denier	Number of Plies	Number of Strokes	Movements of Arm
Kevlar 49	2860	1	200	200s/10s/m=**10m**
		2	100	100s/10s/m=**10m**
Kevlar 49	8210	1	100	100s/10s/m=**10m**
		3-1	18	4m of 3s each + 1m of 6s =18s
		4-1	18	4m of 3s each + 1m of 6s =18s
		7-1	18	Same procedure as above
		3-2	12	12s/3s/m=**4m**
		4-2	12	12s/3s/m=**4m**
		7-2	12	Same procedure as above

Figure 4.12: Kevlar Yarn Wound on Paper Tubes; Note That Yarn is Stepped-Up on the Ends.

In addition to the braiding yarns, the unidirectional carbon used for the core was also wound onto individual bobbins and placed on a creel. This allowed for a continuous supply of carbon. The Kevlar tubes (sleeve and rib yarns) were then loaded onto the braiding machine. The bar manufacturing procedure is described in the next sections.

4.3 New Preform Design

The design and configuration of rebar is related to the three most important parameters: high initial stiffness, high ductility, and good bond strength. Therefore, by a judicious choice of materials, the hybridization of fibers will result in a bilinear stress-strain with sufficient initial stiffness and ultimate strain. Equally as important is the bond strength of the bar with concrete. The bond strength is directly related to the deformation (rib) pattern and rib height and spacing.

Results from Scanning Electron Microscopy (SEM) observations (Chapter 5) and mechanical testing (Chapter 6) indicated that the originally designed 10-mm DHFRP rebar had some deficiencies that compromised the full utilization of DHFRP bars. First, the original preform design had a non-symmetric deformation or interlacing pattern on the surface. The spacing or distance between interlaces was approximately two inches apart, and therefore, did not meet the ASTM A615 requirement of a maximum of 0.3 inches between crossings for a bar of this diameter. Second, there was a noticeable difference in stiffness due to an asymmetric rib pattern. As shown in Figure 4.13, two rib yarns produced an interlace along two edges of the bar and the crossing never existed directly opposite at a given cross section. Only one criss-cross is possible at a given cross section along the length of the bar leading to a

lower bending stiffness along the less reinforced edges (edges with absence of rib yarn crossings). This caused the bar to have two different moments of inertia, depending on whether the bar was subjected to strong or weak axis bending. In addition, a non-uniform rib pattern resulted in higher pressure at rib yarn intersections, thereby producing areas of densely packed fibers and a separation of the core-sleeve interface. This is evident from SEM scans shown in Chapter 5. Areas without rib yarn crossings appeared to have higher void content around the core-sleeve interface. Rib yarns crossing also caused distortion in core shape as predicted in Figure 4.13. Again this was verified by SEM observations (Chapter 5). The asymmetry in rib pattern and core distortion needed to be corrected in order to obtain uniform bending rigidity along all edges of the bar. At the same time, sufficient surface roughness or surface deformation was provided to ensure adequate bonding to concrete, in accordance with ASTM A615.

Therefore, a new trial bar was produced using Kevlar 29 (1,500 denier) as sleeve and rib yarns, and IM7-12K carbon as the core. These materials were chosen due to their easy availability at FRMC. Comparison between the original bar materials and the trial materials were listed in Tables 4.1 through 4.3. Two more rib yarns were added to the bar to first correct the symmetry problem and also reduce the spacing between criss-crosses. Figure 4.14 shows the symmetric rib pattern around the circumference and along the length of the bar when two additional rib yarns are introduced. From Figure 4.14, a smaller *d*-spacing provided more surface area and surface roughness for bonding to concrete. The effect on the bond strength and deformation pattern is explained in Chapter 6. Shown in Figure 4.15 is the original

preform cross section with only two rib yarns and Figure 4.16 shows the new symmetric preform with the use of four rib yarns.

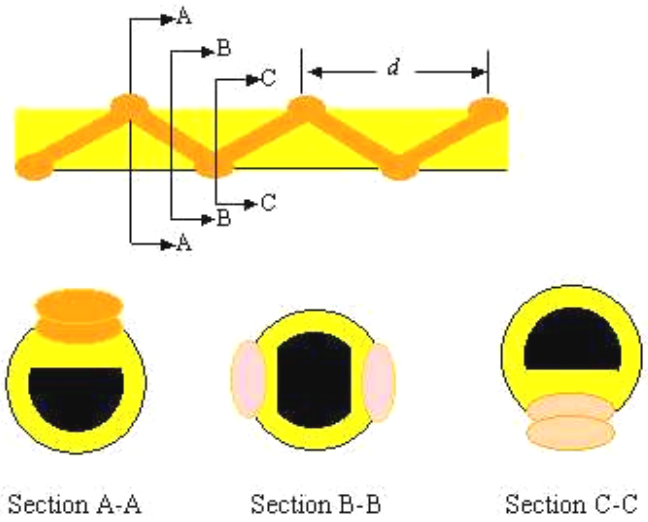

Figure 4.13: Originally Designed Composite Rebar with 2 Rib Yarns Showing Non-symmetric Rib Pattern.

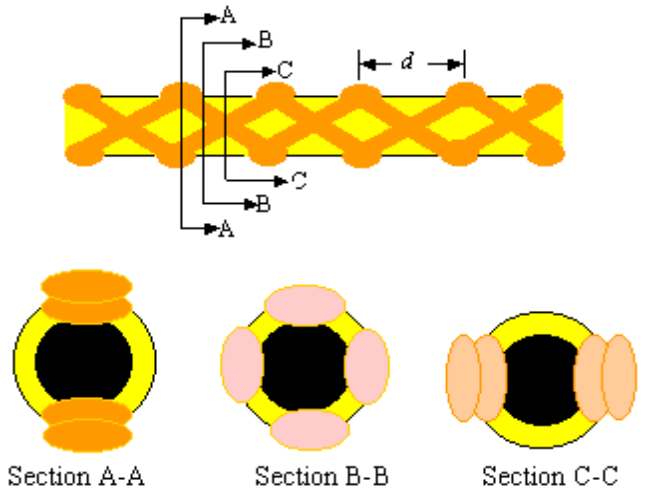

Figure 4.14: Modified Rebar Showing Uniform Rib Pattern and Smaller Spacing *d* Between Criss-Crosses.

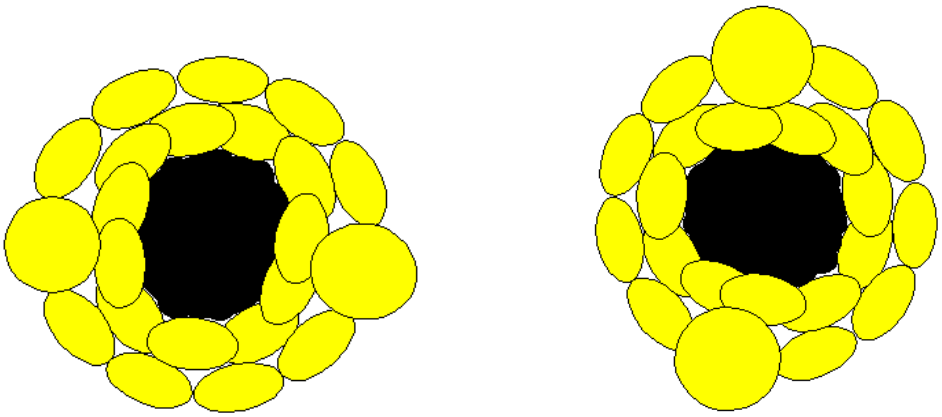

Figure 4.15: Original Preform Design Showing the Use of Two Rib Yarns with Core Distortion.

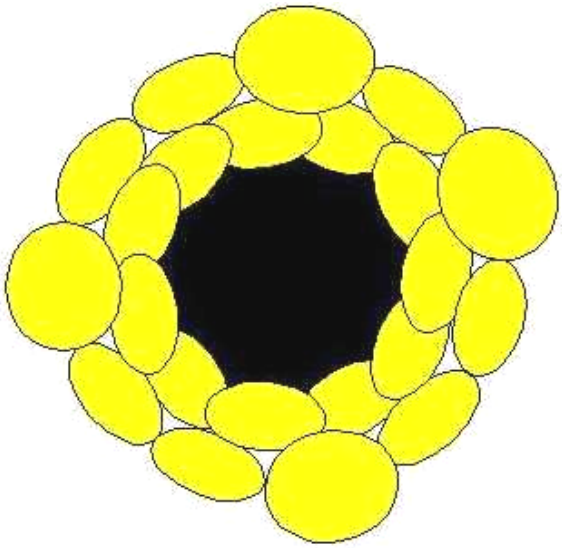

Figure 4.16: Modified Preform Using Four Rib Yarns Illustrating Symmetry and No Core Distortion.

4.4 Rebar Manufacturing

The manufacturing of the DHFRP bars of any size was performed using the braidtrusion process at Drexel University. This process was modified several times throughout the course of research. Later results in Chapter 5 of the microscopic structure of the bar indicated that the current production method was the most improved condition, especially for prototype-size bars. Two main methods of manufacturing DHFRP bar are discussed: one using more tradition braidtrusion methods and the other using a new modified braidtrusion method. One case study using the traditional method and two case studies using the modified method of production are then discussed.

4.4.1 Traditional Braidtrusion Process

The traditional braidtrusion process was illustrated in Figure 4.8. This combined the various zones of the traditional pultrusion process and introduced 2-D braiding into the process. As shown in Figure 4.8, five distinct regions or zones exist in traditional braidtrusion and include the core formation region, the sleeve formation region (where both of these regions are combined to become the take-up zone), the consolidation region, the post-cure region, and the finish product/ product inspection region.

The take-up zone provided the yarns to create the preform and included both the core formation region and the sleeve formation region. This included the unidirectional carbon yarns as well as the Kevlar yarns for braiding. The impregnation zone was where the resin was applied to either the dry yarns or the preform. The earlier braidtrusion method (Somboonsong, 1997) was modified by

placing a resin bath before the braid point to saturate the core yarns. Therefore, the impregnation zone was placed in the middle of the take-up zone, between the core yarns and braiding yarns take-up locations.

In the core formation region, core yarns required sufficient tension and alignment in order to prevent yarns from crossing each other. Crossing of yarns can be detrimental since fiber damage leads to jamming in both the braiding and die regions. In addition, misalignment of yarns reduces composite strength since not all of the yarns are unidirectional. Core yarns were mounted on a creel located behind the braiding machine and tension was applied by means of friction as the yarns were wrapped around polyethylene tubes and pulled. A series of plastic guides and rollers were utilized to align and arrange the fiber into a thin sheet. The sheet was then passed under a dip roller located in the resin bath. As the core yarn passed through the resin bath excess resin was picked up and carried through the braiding process. A picture of the creel and resin bath is shown in Figure 4.17. No additional resin was added at the braiding point since the pressure asserted by the braided sleeve was sufficient enough to force the resin outward to wet both the braiding and thick rib yarns.

The next process in braidtrusion was the sleeve formation region. In the braiding process, yarn tension was very critical, both during winding (as described in Section 4.2.1 and Appendix B) and braiding. Over-tensioning resulted in yarn damage can lead to entanglement of the yarns near the braiding point (Ko et al., 1989). Insufficient tension did not provide adequate pressure required to force the resin through the braiding yarn, and therefore, the fabric did not conform. Yarn tension on the braiding carrier was controlled by a tension spring. Tension springs for carriers

are specified by color and wire diameter. Blue springs with 0.20" wire diameter were used for both braiding and rib yarns. Half the rib yarns were arranged so that they traveled in a clockwise direction and the other half traveled in the counter-clockwise direction. When the two opposite yarns met on the circumference of the braid it formed a criss-cross (Figures 4.4 and 4.14). The braiding machine used in this process was a maypole-type circular braider manufactured by Wardwell Braiding Machine Company. It was a 24-carrier machine with 12 locations for axial (0°) yarns.

The consolidation region in traditional pultrusion consists of a heated die that shapes the pultruded part under heat and pressure. Also, a post-cure oven may be provided for additional increase in thermal properties of the composite. In the consolidation zone, the wet preform entered a heated die at 150° C (Shell, 1995) where partial curing occurred. The braiding and curing regions are shown in Figure 4.18. Due to the reduction in diameter as the preform entered the die, excess resin once again was removed. At the die exit the composite was still tacky and did not have sufficient strength to survive the clamping force from the caterpillar take-up. Therefore a post- curing oven was placed in front of the puller (Figure 4.19), in a tube-type oven at 120° C. This is the fourth region of braidtrusion. Each run allowed a continuous bar of approximately 16 feet to be produced. This length was close to the limit of the size of the rib yarn tubes that were able to be placed on the braiding machine and the length of the braidtrusion machine. Rib yarns any larger than this would not fit onto the carriers of the braider.

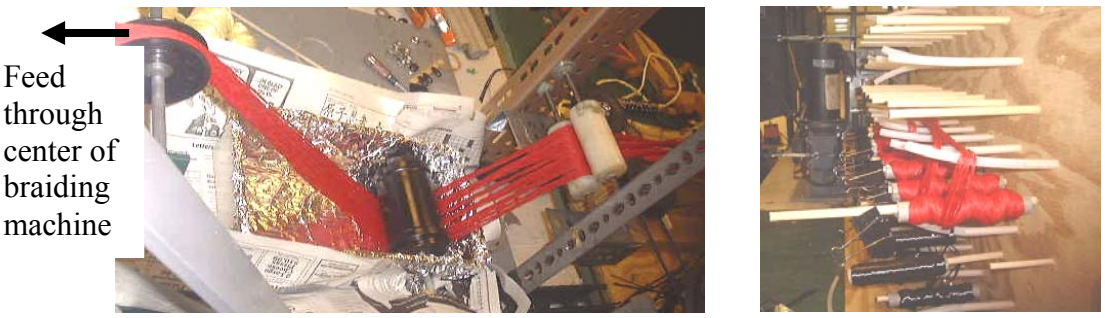

Figure 4.17: Creel-Resin Bath Assembly.

Figure 4.18: Setup of 24-Carrier Vertical Braider Machine with Heated Die.

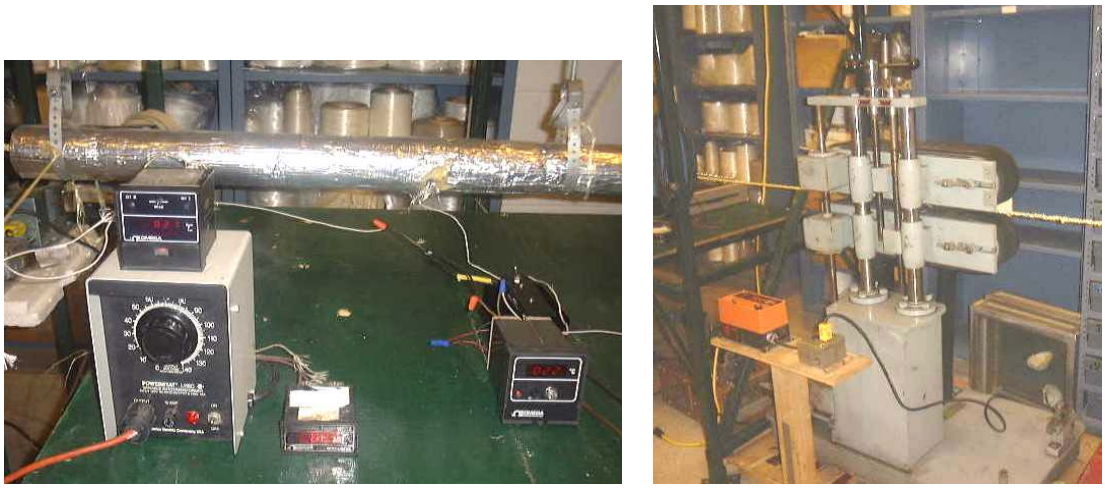

Figure 4.19: Post-Cure Oven and Caterpillar Assembly.

The resin system used in manufacturing the rebar was the Shell Chemical Epon Resin 9500/Epi-Cure 9550 curing agent system. This resin system was designed specifically for pultrusion and was recommended by the manufacturer for this application. The manufacturer recommended mixing ratio for this resin system is tabulated in Table 4.5. Two batches of the resin mixture were needed for each run of 16 feet bar. The resin was poured into an aluminum container and weighed. At room temperature the resin viscosity is relatively thick, in the range of 900 centipoises. If the resin was kept at room temperature, introduction of air bubbles during mixing could not be avoided, and these entrapped air pockets would reside in the finished composite. In an effort of reducing air bubbles and improving fiber wet out, the resin was placed in a 150° F oven for 30 minutes prior to mixing. The resulting decrease in resin viscosity significantly reduced the amount of air bubbles during mixing. The 10-mm bar made using traditional braidtrusion with a die is shown in Figure 4.20. Note the absence of a rib or deformation pattern on the bar surface.

Figure 4.20: 10-mm Bar Made with Fully-Heated Die by Traditional Pultrusion.

Shell Chemical recommended processing conditions for this resin system; however, these conditions could not be adopted because manufacturing of the DHFRP rebar by braidtrusion was not as simple as pultruding a constant cross sectional profile. Pultrusion was designed for producing constant cross sections, and therefore, the composite is expected to be completely cured and conformed to the shape of the die as it exits. Since the DHFRP bar was designed to have a non-uniform profile due to the rib yarns, modifications were made to the curing profile for the Epon 9500 resin system. These and other modifications related to the curing profile are described in the next section.

Table 4.5: Manufacturer Recommended Mixing Ratio for Epon Resin 9500/Epi-Cure 9550 Curing Agent.

Material	**Ratio (pbw)**	**Batch Mix (g)**
Resin (Epon Resin 9500)	100	250
Hardener (Epon Epi-Cure 9550)	33	82.5
Internal mold release (INT-1846N)	0.5%	1.66
Note: Two batches are needed per run.		

4.4.2 Modified Manufacturing Process Using IM-7 Carbon Core

The manufacturing process for the DHFRP needed to be improved to get a material with excellent mechanical properties. Therefore, different processing techniques were experimented with to find an improved manufacturing process for prototype-size bars. During the improvement process, the fiber materials, IM7-12K and Kevlar 29, were initially selected because they were readily available in small tubes and so that the more expensive P-55S carbon was not wasted. They were chosen as trial materials for establishing the processing parameters. The amount of fibers used was equivalent to the original P-55S 4K and Kevlar 49 system based on linear density (i.e., denier). The distribution of Kevlar 29 sleeve/rib and IM7-12K core were listed in Table 4.2 and mechanical properties of individual components were provided in Table 4.3. Behavior predictions and microscopy results were obtained and are presented in Chapter 5 while mechanical behavior results are presented in Chapter 6.

The creel to dispense the core yarns (Figure 4.17) was used for the IM7-12K yarns. The critical bending radius of a yarn, defined as the smallest radius a fiber can be bent around before fiber failure, is given by

$$R_c = \frac{D}{2}\left(\frac{E}{\sigma} - 1\right) \qquad 4\text{-}1$$

where R_c = critical bending radius (curvature)

D = fiber diameter

σ = fiber strength

E = fiber stiffness

The critical diameter of IM7-12K is less than the diameter of a standard paper tube, and therefore, the IM-7 was wound onto paper tubes. This allowed the creel (shown in Fig. 4.17) to be used. A conclusion about the processability of certain yarns can be made. High modulus fiber, such as P-55S, can slow down the processing speed due to the fragile nature of the material; however, lower modulus fiber, such as IM-7, has much more desirable processing properties. The critical bending diameter is a measure of brittleness or fragileness of a fiber.

Unlike traditional pultrusion where fibers are unidirectionally oriented along the bar axis, the braidtrusion process allows oriented fibers to be incorporated in the design of the net shape. In the case of the DHFRP rebar, the net shape does not have a constant cross section since it varies both circumferentially and along the length due to the rib pattern. Traditionally, a non-constant cross-sectional profile cannot be fabricated by pultrusion. Therefore for the DHFRP, if the recommended processing temperature was used (Shell Chemical, 1995), there would be no rib pattern on the surface (Fig. 4.20), because the pressure inside the die would collapse and consolidate the ribs before the bar could exit the die. In order to preserve the rib pattern, a new processing condition was developed such that the composite was partially cured at the die exit. This allowed the preform to slightly expand radially after exiting the die. In this case the die was not utilized as a shape former or a curing device, but rather its function was more like a hot squeegee. Figure 4.21 shows the 10-mm bar made with a die heated below the recommended curing temperature. Note the existence of some deformation pattern on the bar surface which was absent in the bar made with a fully-heated die (Fig. 4.20).

Figure 4.21: DHFRP Bar Made with Partially-Heated Die.

From SEM analysis and observations of the surface deformation conditions of bars made with a fully-heated and partially-heated die (Chapter 5), there were indications that the die could possibly be omitted in the braidtrusion of rebar. This parametric study was done using the IM-7 and the Kevlar 29 materials. Therefore, after the sleeve formation region (Fig. 4.8), the consolidation region was eliminated. This included the elimination of the heated die. Also, from visual analyses (Chapter 5), the post-cure oven was also eliminated. This braidtrusion process, named dieless braidtrusion, is shown in Figure 4.22. After the braiding point, the bar was pulled under tension by the belt puller and allowed to cure at room temperature for approximately 24 hours before cut. Since the preform was wet, it could not pass under the belt puller. SEM observations of the bars made without the die (Chapter 5) showed good microstructure results. Shown in Figure 4.23 is the bar made without the die or post-cure oven. Also shown in Table 4.6 are the processing parameters for the various 10-mm rebars made, both with and without a die (Lam, 2001).

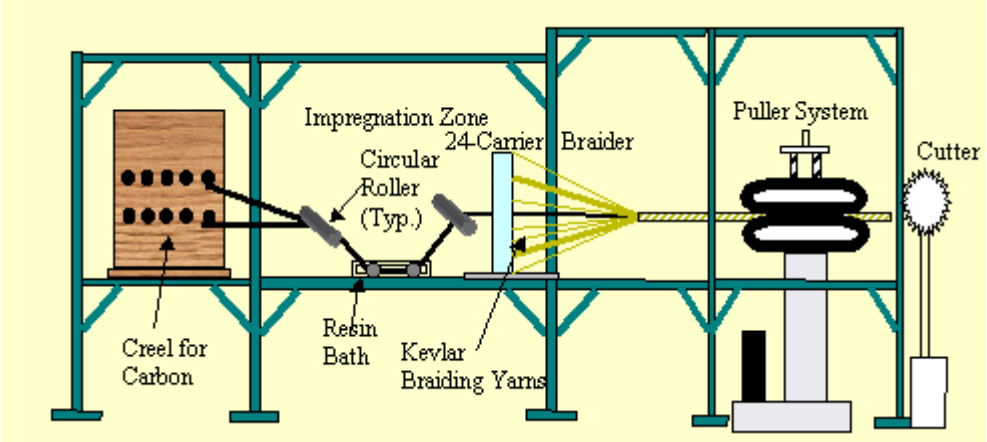

Figure 4.22: Dieless Braidtrusion Process.

Figure 4.23: DHFRP Bar Made Using Dieless Braidtrusion Process.

Table 4.6: Processing Parameters for 10-mm Diameter Rebars (Lam, 2001).

Design	**Braiding or Rotational Speed (carrier RPM)**	**Pull Speed (in/min)**	**Resin Temp. (^{0}C)**	**Die Temp. (^{0}C)**	**Oven Temp. (^{0}C)**	**Post Cure Temp. * (^{0}C)**	**Post Cure Time * (hrs)**
2 Rib Yarns	8.0	9.6	55	150	150	55	5
4 Rib Yarns	8.0	10.0	55	No Die	No Oven	55	5
*** These are post-cure specifications for an oven once the bar is cut to length; these are necessary for the bar to gain full strength.**							

4.4.3 Modified Manufacturing Process Using P-55S Carbon Core

Once the braidtrusion process was improved using trial materials (Kevlar 29 and IM7-12K), the original materials were used (P-55S and Kevlar 49). From SEM analysis, the dieless pultrusion process described above was used to make this prototype bar. Again, several minor modifications were made due to the selected materials.

P-55S 4K carbon is much more brittle than IM7-12K carbon, where the critical bending diameter of P-55S carbon is much smaller than IM7 carbon. For the first several bar runs, the P-55S carbon was wound onto the 5 ¾" (146.1 mm) paper tubes using a mechanical winder and placed on the creel, similar to the procedure used for IM7 carbon. 30 ends of the 4K P-55S were needed for the core. However, when using the creel for P-55S, there was extensive fiber damage during manufacturing. The resin became black (usually it was yellowish-clear) indicating broken fibers interspersed in the resin bath. Also, tension tests on these bars had less strength and stiffness. The paper tubes could not be used for fibers this brittle, and therefore, another creel system for dispensing the P-55S or any other brittle fiber needed to be developed.

A new process was developed for the dispensing of the P-55S 4K carbon core yarns. Since the mechanical winder could not be used, the P-55S 4K had to be cut to a certain length and wound manually. Shown in Figure 4.24 is the yarn preparation for the P-55S 4K. Since P-55S is very brittle and can be damaged if it touches rough surfaces, the yarn was placed on a smooth plastic material to prevent it from touching the floor. The one end of the yarn was attached to a tape strip, and 30 single ends were placed next to each other. The tape allowed the yarn to be kept under tension

while winding. The yarn length was 28 feet (8.53 m) (enough for two 12.5 foot bar runs, with extra length for waste). Shown in Figure 4.25 are the 30-P-55S plied core yarns being wound onto a 3.5" (88.9 mm) diameter creel. This creel had a large enough diameter to prevent fiber damage.

Shown in Figures 4.26 and 4.27 is the creel used for brittle yarns used for the core and the resin bath with rollers. The Unistrut frame used in the production line was modified for this creel.

Shown in Figure 4.28 is the resin bath that was used for all production runs. This system was still sufficient even for the more brittle P-55S yarns. Figure 4.29 illustrates the braiding and pulling of a piece of bar during production utilizing dieless braidtrusion. Figure 4.30 shows the bar curing at room temperature after the manufacturing. Since the bar cured at room temperature for 24 hours, it was critical to keep the bar under sufficient tension to prevent sagging. Sufficiently high tension was maintained using the puller. Also, after manufacturing, the bar was tied by small denier Kevlar yarn to the Unistrut frame in several locations to prevent sagging of the bar, keeping the bar straight and uniform.

Figure 4.24: Yarn Preparation of P-55S 4K Carbon Yarn for the Core.

Figure 4.25: Winding of the Plied Carbon Yarn onto the 3.5" Diameter Creel.

Figure 4.26: Modified Carbon Creel for Brittle Core Yarns.

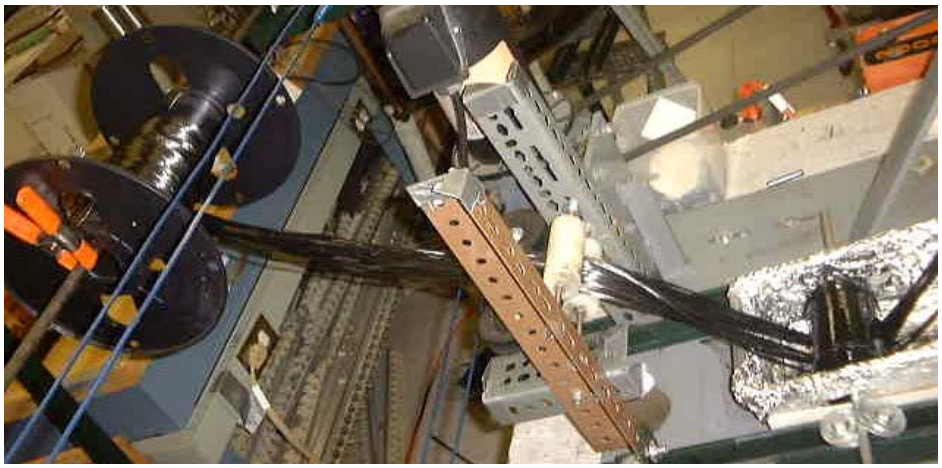

Figure 4.27: Modified Creel and Resin Bath for Braidtrusion with Brittle Core Yarns.

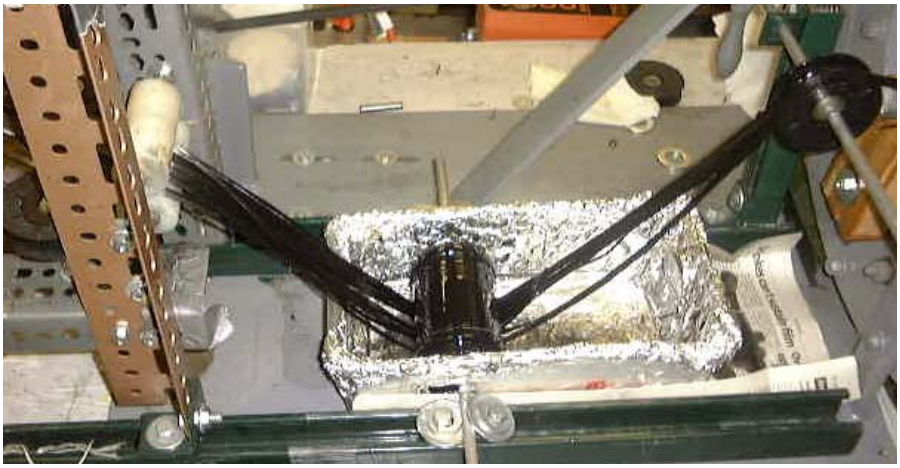

Figure 4.28: Resin Bath Used in Braidtrusion Process.

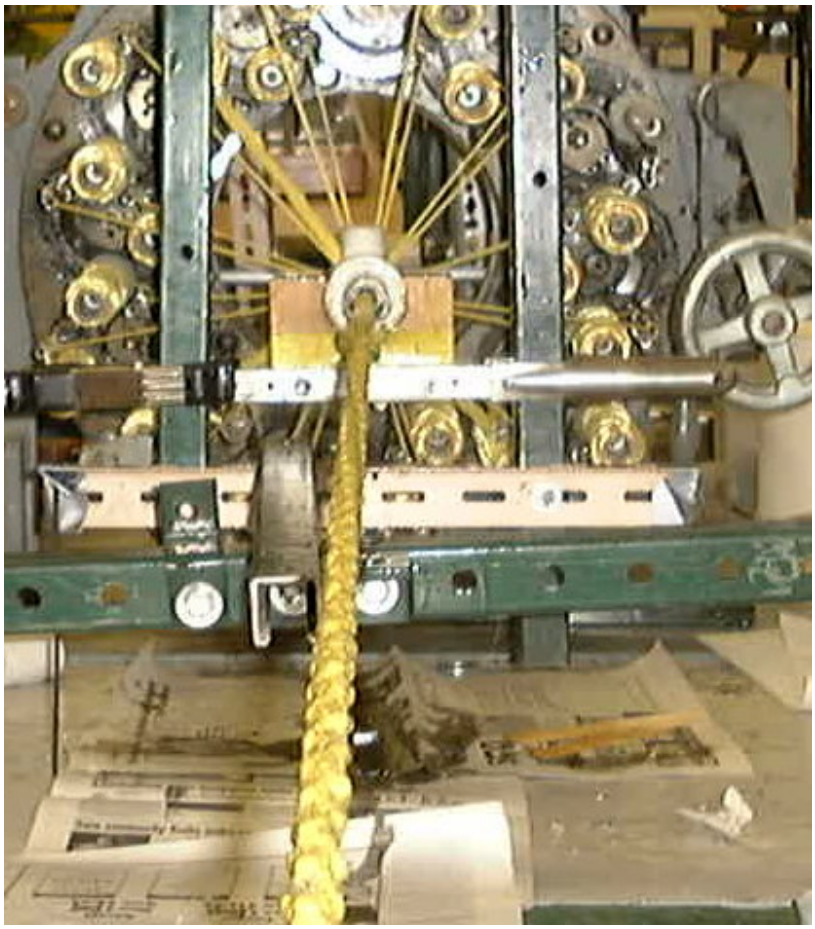

Figure 4.29: Braiding and Pulling of Prototype DHFRP Bar During the Manufacturing Process.

Figure 4.30: Prototype DHFRP Bar During the Manufacturing Process.

CHAPTER 5. MATERIAL PROPERTY AND MICROSTRUCTURE CHARACTERIZATION

Before the DHFRP bars could be used as reinforcement in concrete elements, the material and mechanical properties of the bars needed to be quantified. Both short-term and long-term characterizations were studied. First, the theoretical development and subsequent experimental verification of the uniaxial tensile strength of the material were investigated, thereby defining the modulus of elasticity, the yield and ultimate strengths and strains. Next, the microstructure of the bar was studied to define the internal structure of the bar and also the interfacial behavior. This included the interfaces between the sleeve and core yarns, the interface between the rib and braiding yarns, and the interface between the yarns and resin. This was a quality control verification of the manufacturing process of braidtrusion. From the microstructure analysis and the stress strain behavior, the failure mechanism was explained. Next, the bond strength of the DHFRP bar with concrete was investigated and the surface deformation pattern and parameters were studied. The last short-term test to be studied was the bending capacity of the bar which is a serviceability issue, especially for long lengths of bar.

Once the short-term behavior was quantified, the long-term behavior of DHFRP bars was investigated. The creep and stress-rupture was defined for the long-term behavior of materials. This test was critical for long-term life-cycle prediction using DHFRP, especially for highway bridge decks.

5.1 Fiber Architecture Design Model (FADM)

A computer model was developed to obtain the general stress-strain properties of DHFRP bars. The model was valid for any material system, geometry, and bar architecture. The theoretical development of the FADM is presented followed by results for various material systems and braiding architectures.

5.1.1 Background

The structure of the DHFRP bar is comprised of both geometric and material hybrid systems. The geometric hybridization includes the braided structure with an elastic core that follows a hierarchical design methodology (Ko, 1987). The design concept of the bar is shown in Figure 5.1. This figure illustrates the use of a braided structure of both braiding yarns and rib yarns. The rib yarns were specifically utilized so the DHFRP bar had a non-uniform profile for bonding purposes; however, this was not necessary for the operation of the FADM. A bar with only braiding yarns (i.e., a constant cross section bar) could also be designed. The core yarns were placed within the braided sleeve structure and acted as a mandrel that the sleeve could be braided around. The core yarns were unidirectional for the DHFRP bar, but the core yarns could be oriented using the FADM.

The material hybridization develops from the use of the different materials for the core and the braided sleeve. The concept of the DHFRP bar was to design a material that had a stress-strain behavior similar to conventional steel reinforcing. This meant that the bar should have high initial stiffness ($E \approx 30\ 000$ ksi), a definite yield point (f_y = 40–60 ksi), and a significant post-elastic stress-strain region. Therefore, materials were chosen that could develop these properties. By using both

forms of hybridization, a material with a controlled bilinear stress-strain behavior was developed.

The impetus of this model was to develop a generalized design module that would enable a material designer to design a braided hybrid bar of any size, architecture, geometry, or material system. The bar could either be a braided bar with constant cross section, a non-uniform cross section with rib yarns incorporated, or a bar with or without an elastic core, depending on the need of the designer. Also, various design concepts using multiple yarn systems could be developed. The experimental results of the DHFRP bars (Chapter 6) were used to verify the validity of the FADM.

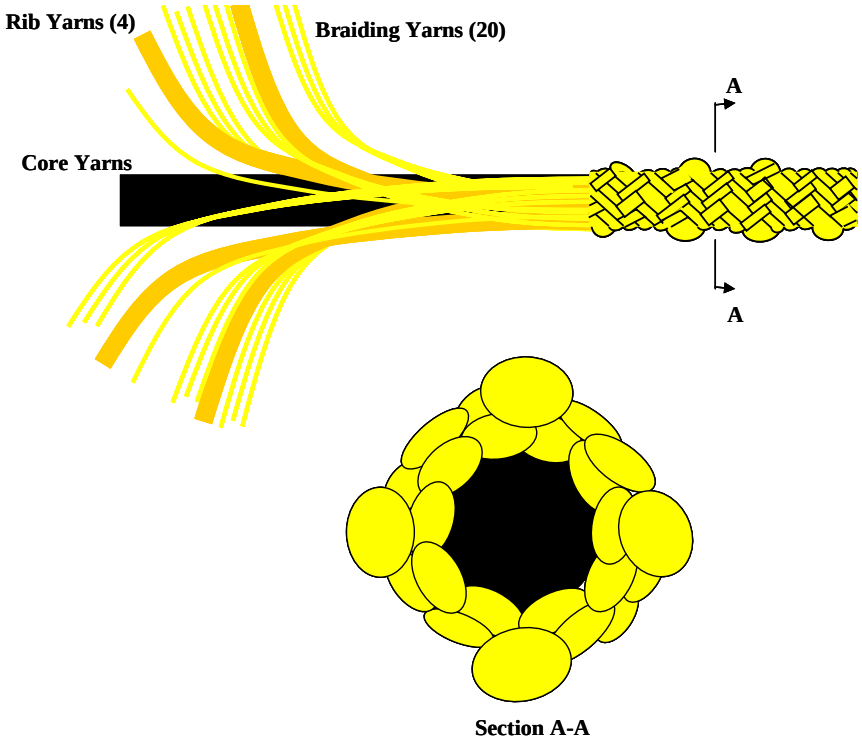

Figure 5.1: Design Concept of Braided Hybrid Bars (Fig.4.4 Repeated).

5.1.2 Theoretical Development

From a material design viewpoint, given a database of fibrous yarn materials commercially available, the behavior of the DHFRP bar of any size and material composition can be predicted. The development of the FADM was to design a hybrid composite bar of two materials, one for the braided sleeve and one for the elastic core. The only requirements necessary for the FADM to work are that a resin system and various fibrous materials be defined. The resin system can be any system suitable for the pultrusion process. Several systems defined by Shell Chemical were well-suited for pultrusion. The fibrous materials used can be any linearly elastic fibers. The model divides the yarns into three categories: general braiding yarns, rib yarns, and core yarns. Therefore, a bar of three different fiber types can be designed. The specific design for the DHFRP bars was to utilize the material and geometric hybridizations in the following manner.

The requirement for the DHFRP bar was that a composite bar be developed that had the stress strain characteristics similar to steel with high initial stiffness, a definite yield point and high elongation to failure. Also, sufficient bonding to concrete was necessary, and therefore, the deformation profile was considered when developing the FADM.

The design concept was that a unidirectional elastic core could be used to provide the initial portion of the stress-strain curve with high initial stiffness, provided that a stiffer material was used for the core than the sleeve. Since the core yarns were oriented in the zero direction (longitudinal axis direction), the maximum strength of the core yarns was utilized. Any other off-axis orientation of the yarn would result in a strength reduction. A material that can be used is carbon fiber that has a high

stiffness. The carbon fiber also has low elongation compared with the materials used for the sleeve. Therefore, when the ultimate strain of the carbon core is reached, assuming complete fiber wetting, the carbon core fractures and the load is picked up by the sleeve structure. This fracture is considered the yield point of the bar. The stress and strain at this fracture is defined as the yield stress, σ_y and yield strain, ε_y of the DHFRP bar. Examples of materials used in the experimental study included P55S 4-K carbon from Amoco and Hexcel IM-7 12-K carbon fibers. Other possible core materials include T-300, coal tar pitch-based carbon fiber DIALEAD® (Mitsubishi, 2000) and low cost, high stiffness pan-based carbon systems.

The braiding yarns are necessary for high elongation to bar rupture since the sleeve material is most significant for the post-yielding portion of the stress-strain curve. Therefore, a high elongation fiber such as aramid fibers was used. Examples used included Kevlar 29 and Kevlar 49, depending on the amount of elongation that is needed for a specific application. The rib yarns were made of the same material as the braiding yarns (in this study, either Kevlar 29 or Kevlar 49). The main function of the ribs was to improve the bonding of the bar to concrete by having an integrated system. Many bars have deformation patterns that are wrapped around the bar surface after pultrusion, and therefore, are not integrated into the bar structure. The DHFRP integrated rib system, where the rib deformations are part of the bar structure, allows for mechanical interlock to occur between the reinforcing bar and the surrounding concrete, thereby developing high bond stresses.

The design used for the FADM was the concept of the structural hierarchy of fibrous systems. This concept is demonstrated in Figure 5.2. In this figure, the

various structural levels of a braided textile composite are illustrated. Since the final composite bar was made of two types of yarns and resin, the actual structure of the bar was quite complex. Also, since the yarns consist of many fibers, the translation efficiency defined as the property transfer (e.g., strength, stiffness, elongation) from the level of the fiber to the level of the final composite must be defined to get the actual strength of the braided composite bar.

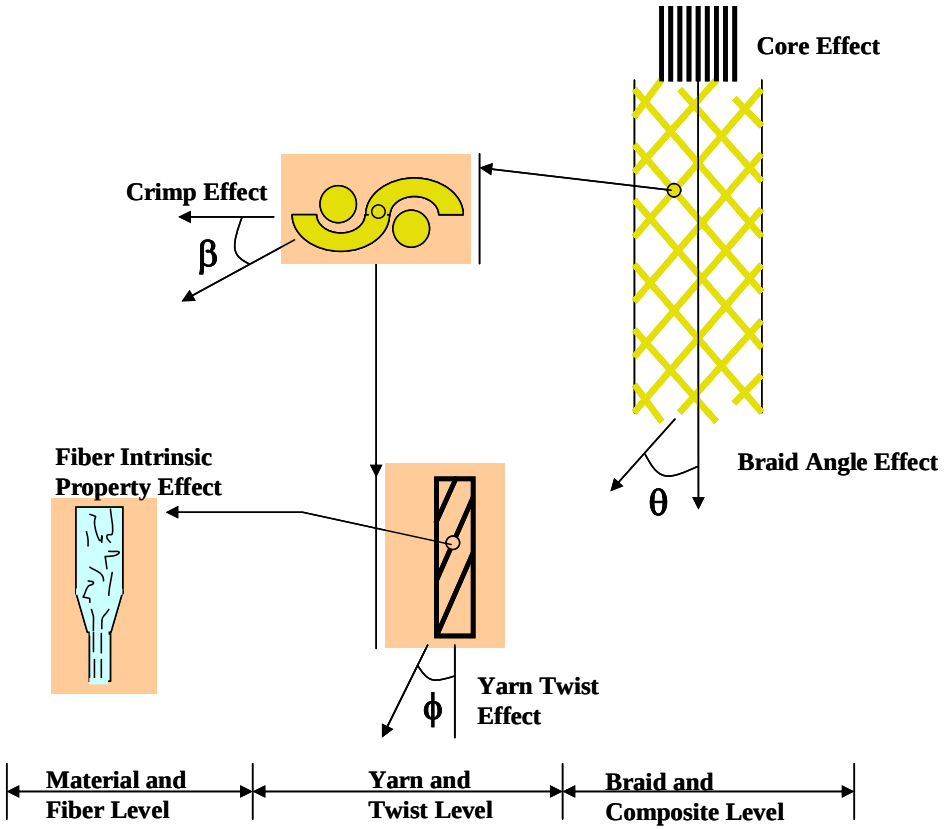

Figure 5.2: Textile Structural Hierarchy (Figure 4.3 Repeated).

Four separate levels of translation efficiency are illustrated in Fig. 5.2 that comprise the structural hierarchy of fibrous assemblies. These include the fiber level, the yarn level, the weave level, and the braid level.

At the fiber level, the intrinsic properties of the fibers including the orientation of the bonds and the molecular structure are the two most important parameters. The bulk polymer is strengthened during the spinning process which produces continuous fibers. During this process, the polymer chains are aligned and oriented along the axis of the fibers. Molecular chains with high crystallinity result in fibers with high mechanical properties. Individual tests on fibers must be conducted in order to obtain the mechanical properties of each fiber.

Continuous strands of fiber are then combined together to form a fiber bundle called a yarn. Each individual yarn consists of a number of fibers, defined as a multifilament yarn, where the fiber properties must translate into the yarn with the specified yarn geometry. The yarn geometry is defined based on the yarn processing method.

Yarn systems based on the linear density of the fibers are based on a unit of mass per unit length. The unit of measurement of the size of a yarn is defined either by the denier or tex, where the denier is defined as

$$1\ denier = {}^{1\,gm}\!/_{9000\,m} \tag{5-1}$$

At the yarn level, the yarn twist effects must be accounted for. The carbon fiber used was a PAN-based fiber with no twist on the fibers. However, the braiding yarns

(Kevlar for the sleeve design) do have a small amount of twist inherent in the yarns. Also, additional twist might be added during the winding process when producing larger yarn bundles, especially for the rib yarns. The yarn level is important from a design viewpoint since most available databases on fibrous material properties are yarn properties, not individual fiber properties. Fiber and yarn packing in combination with twist helix angle are the governing parameters at this level. The relationships between fiber and yarn mechanical properties given by Hearle (1969a, b) are

$$E_y = E_f \cos^2 \phi \tag{5-2}$$

$$\sigma_y = \sigma_f \cos^2 \phi \tag{5-3}$$

$$\varepsilon_y = \varepsilon_f \Big/ \cos^2 \phi \tag{5-4}$$

where

E_y, E_f = yarn and fiber tensile modulus, respectively

σ_y, σ_f = yarn and fiber tensile strength, respectively

ϕ = twist angle or twist helix

The crimp geometry refers to a woven fabric. The crimp refers to the additional source of elongation due to the interlacing of one set of yarns over the other (i.e., the yarns are bent one over the other). The crimp can increase both the strain (elongation) and the fiber volume fraction. This effect is described by the crimp angle, β, which occurs at the yarn intersections. A crimp model of a unit cell and governing equations developed by Pierce (1945) define the crimp of a fabric. The crimp is defined as the additional length of yarn required for producing a specified length of fabric (Lam,

2001). The Pierce geometric model for a plain weave fabric (a one-up-one-down weave construction) was shown in Lam, 2001. The assumptions of the model were: the yarn was flexible ($EI = 0$); the yarn had a circular cross section; the yarn possessed uniform properties; and a unit cell representing the fabric consisted of a straight yarn and a circular portion. Pierce developed seven equations with 11 geometric parameters, where four parameters must be determined experimentally to solve for the remaining seven unknowns. The model allows the estimation of the exact yarn length within specified fabric dimensions. The seven equations are

1. Crimp

$$C_w = \frac{\left(L_w - P_f\right)}{P_f} = \frac{L_w}{P_f} - 1$$
$$C_f = \frac{L_w}{P_f} - 1 \qquad \text{5-5a, b}$$

where L = modular length

P = yarn spacing

Subscripts w and f are the warp (0°) and fill (90°) directions

2. Diameter

$$D = h_w + h_f = d_w + d_f \qquad \text{5-6}$$

where h = fabric thickness

d = yarn thickness

3. Texture

$$P_f = \left[L_w - 2\left(\frac{D}{2}\right)\beta_w \right] + 2\left[\left(\frac{D}{2}\right)\sin\beta_w\right]$$
$$= \left(L_w - D\beta_w\right)\cos\beta_w + D\sin\beta_w \qquad \text{5-7a, b}$$
$$P_w = \left(L_f - D\beta_f\right)\cos\beta_f + D\sin\beta_f$$

where β = crimp angle (yarn inclination angle)

P = spacing = 1/ (yarns per inch per direction) –warp and fill

Warp— ends/ inch

Fill—picks/ inch

4. Fabric Thickness

$$h_w = (L_w - D\beta_w)\sin\beta_w + D[1-\cos\beta_w]$$
$$h_f = (L_f - D\beta_f)\sin\beta_f + D[1-\cos\beta_f] \qquad \text{5-8a, b}$$

The above equations are valid for any woven or braided fabric having similar or dissimilar warp and fill yarns. For fabrics where the same yarn was used in both directions, as in the DHFRP bar, the above seven equations were reduced to four equations since $h_w = h_f$, $d_w = d_f$, $\beta_w = \beta_f$, $L_w = L_f$, $P_w = P_f$, and $C_w = C_f$. The four equations reduced to

$$C = \left(L/P\right) - 1$$
$$P = (L - D\beta)\cos\beta + D\sin\beta$$
$$H = (L - D\beta)\sin\beta + D[L - \cos\beta] \qquad \text{5-9a, b, c, d}$$
$$D = 2h = 2d$$

where β and L can be determined from the geometry of the unit cell

$$\beta = 2\arctan\left[\frac{P \pm \sqrt{P^2 - 3d^2}}{3d}\right]$$
$$L = d\,\frac{\left\{-1 + 4\sin\left(2\arctan\left[\beta\right]^2\right) + 2\cos\left(2\arctan\ \beta\right)\right\}}{\sin\left(2\arctan\ \beta\right)} \qquad \text{5-10a, b}$$

L is the modular length of warp yarn (0°, machine direction) between the center of two fill yarns (90° perpendicular to machine direction), P is the spacing between fill yarns

center (the inverse of the number of yarns per unit length (i.e., yarns/in or yarns/ cm), D is the sum of warp and fill yarn diameters, h is the maximum displacement of the thread axis normal to the plane of the fabric, and H is the fabric thickness.

The braid level is the fabric level of the bar. The braid angle, θ, is the geometric parameter at this level. Due to the braid angle, the composite strength, stiffness and final elongation are affected due to the orientation of the fibers. For a given fiber orientation, fiber volume fraction, yarn properties, and fabric dimensions, the amount of yarns to be used can be determined. The specific area of the yarn, A_{sp}, is defined as the area of the yarns, based on the denier of the yarn (Ko et al., 1989). The expressions are

For oriented braiding yarn:

$$A_{sp}(\theta) = \frac{D}{\left(9\times10^{5}\right)\rho\cos\theta} \quad (\text{cm}^2)$$

$$A_{sp}(\theta) = \frac{D}{\left(5.8\times10^{6}\right)\rho\cos\theta} \quad (\text{in}^2) \qquad \text{5-11a, b}$$

For axial (0°) yarn (core or lay-in):

$$A_{sp}(\theta) = \frac{D}{\left(9\times10^{5}\right)\rho} \quad (\text{cm}^2)$$

$$A_{sp}(\theta) = \frac{D}{\left(5.8\times10^{6}\right)\rho} \quad (\text{in}^2) \qquad \text{5-12a, b}$$

where ρ = yarn density in grams/ cm^3

θ = braid angle in degrees

D = denier, yarn linear density (g/ 9000 m)

The total fiber area in the cross-section of the braid A_f, and the cross-sectional area of the braid, A_b are defined as

$$A_f = {N_y A_{sp}}/{\cos\theta} \tag{5-13}$$

$$A_b = \frac{\pi}{4}\left[D^2 - \left(D - 2T_b\right)^2\right] \tag{5-14}$$

where N_y = the number of yarns in the braid, D = outer diameter of the braided fabric, and T_b = wall thickness of the braid. If more than one yarn is used per carrier, then

$$N_y = nN_c \tag{5-15}$$

Where n is the number of ends per carrier and N_c is the number of carriers in the machine. Equation 5-13 is defined for braids with one hundred percent braiding yarns. If the braid contains core yarns, Equation 5-13 becomes

$$A_f = \left[\frac{N_y(\theta)A_{sp}(\theta)}{\cos\theta} + N_y(0°)A_{sp}(0°)\right] = A_b + A_{core} \tag{5-16}$$

The maximum stiffness and load carrying capacity are achieved when the fibers are oriented along the longitudinal axis of the braid (0°). Reduced strength but increased strain capacity results when the yarns are oriented off axis (±10° < θ < ±80°). The governing equations for the translation of properties from yarn to fabric are

$$E_F = E_y \cos^4\phi \tag{5-17}$$

$$\sigma_F = \sigma_y \cos^2\phi \tag{5-18}$$

$$\varepsilon_F = \frac{\varepsilon_y}{\cos^2\phi} \tag{5-19}$$

where E is the modulus of elasticity, σ is the strength, and ε is the strain; the subscripts F and y designate the fabric and yarn, respectively.

The total force in the braided fabric related to the weave construction (crimp) is given as

$$P_b = P_\phi \cos\theta$$
$$P_\phi = P_y N \cos\beta \qquad \text{5-20a, b}$$

where P_ϕ is the total force on the yarns undergoing crimp, N is the number of yarns in the weave level, and β is the crimp angle. P_y is the load parallel to the yarn axis and is defined by

$$P_y = \frac{\pi R^2 E_f \varepsilon_y}{\upsilon_y \cos^2 \alpha} \qquad \text{5-21}$$

where v_y is the yarn specific volume in gram/ cm^3

$$\upsilon_y = \frac{\tan^2 \alpha}{4\pi\left(D_n / 9\right) T^2} \qquad \text{5-22}$$

where R_y = yarn radius, D_n = yarn denier, E_f = fiber modulus, ε_y = yarn strain, α = twist angle, and T = yarn twist (turns/ unit length, turns/ cm).

Combining the above effects for a dry fabric and using the rule of mixtures, a prediction of the stress-strain behavior for braided composite structures was obtained. The rules of mixtures in terms of strength and modulus are

$$E_c = E_m V_m + E_f V_f$$
$$\sigma_c = \sigma_m V_m + \sigma_f V_f \qquad \text{5-23a, b}$$

where the subscripts *c*, *m*, and *f* specify properties of the composite, matrix, and fibers, respectively, and *V* is the volume fraction of each component. The fiber volume fractions for the fibers and matrix are given as

V_f = (vol. of fiber in composite)/V_c

V_m = vol. of matrix in composite)/V_c

$V_f + V_m = 1$

Equations 5-23*a* and *b* do not take into account the effects of fiber orientation. For braided composites, the values of E_f, σ_f, and V_f should first be calculated taking into account the effect of fiber orientation, and then applied to the rule of mixture in the final step. Shown in Figure 5-3 is a flowchart for the FADM program. The MATLAB program is listed in Appendix E.

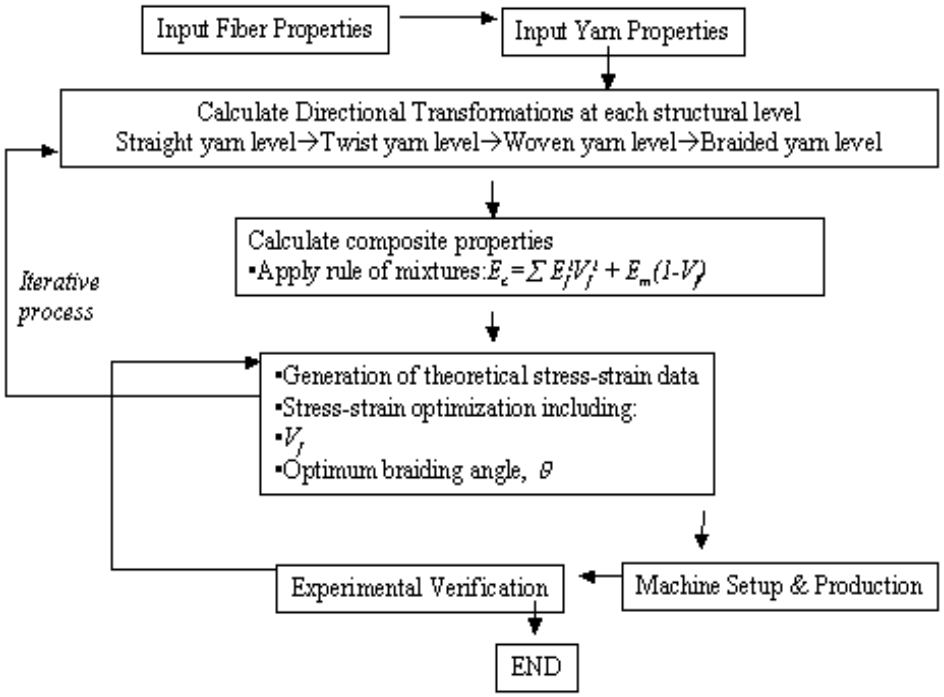

Figure 5.3: Hierarchical Textile Composite Design Logic Flow.

5.1.3 Results

The design stress-strain curves for several material systems are shown in Figures 5.4 through 5.10. Figure 5.4 shows the Kevlar 49/ P-55S 4K system with four rib yarns. The other systems used were Kevlar 29/ P-55S (Figure 5.5) and Kevlar 29/ IM-7 carbon (Figure 5.6). Shown in Figure 5.7 are the predicted tensile properties of all three systems shown together.

Figure 5.8 shows the effects of varying the braid angle on the tensile properties. The Kevlar 49/ P-55S material system was used to illustrate this effect. Braid angles were varied between 15 and 45 degrees with 10 degree increments. Shown in Figure 5.9 is the variation in braiding angle for the Kevlar 29/ P-55S material system and in Figure 5.10 is the braid angle effect for the Kevlar 29/ IM7-12K material system.

Given in Tables 5.1 through 5.3 are the predicted strength properties of several bars. First, the system using Kevlar 29 and IM7-12K carbon is compared using two rib yarns (unsymmetrical pattern) and four rib yarns (symmetric pattern). These tables illustrate the effects of using the two-rib and four-rib preforms. In Table 5.3, the Kevlar 49/ P-55S system properties are tabulated.

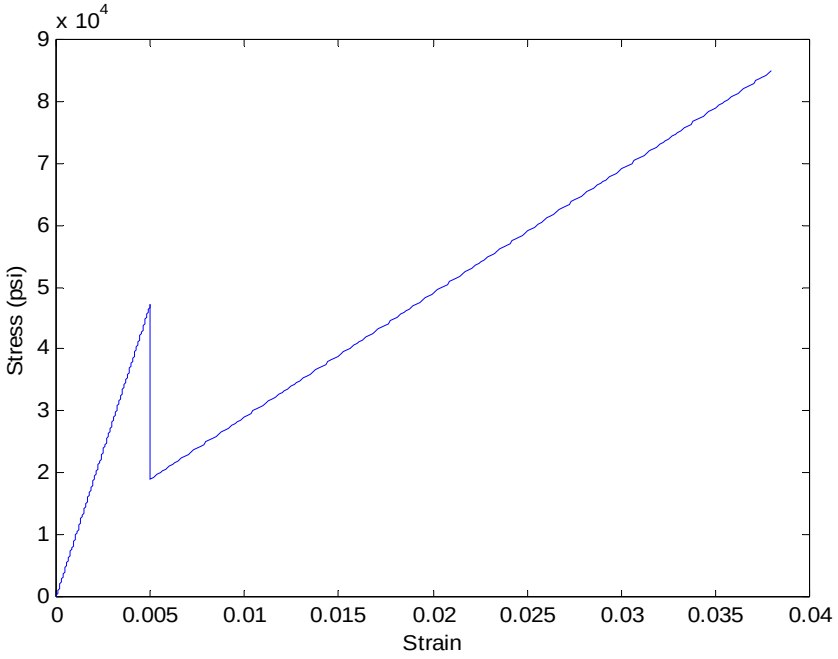

Figure 5.4: Stress-Strain Behavior from FADM for Kevlar 49 / P-55S 10-mm Bar, 4K Ribs.

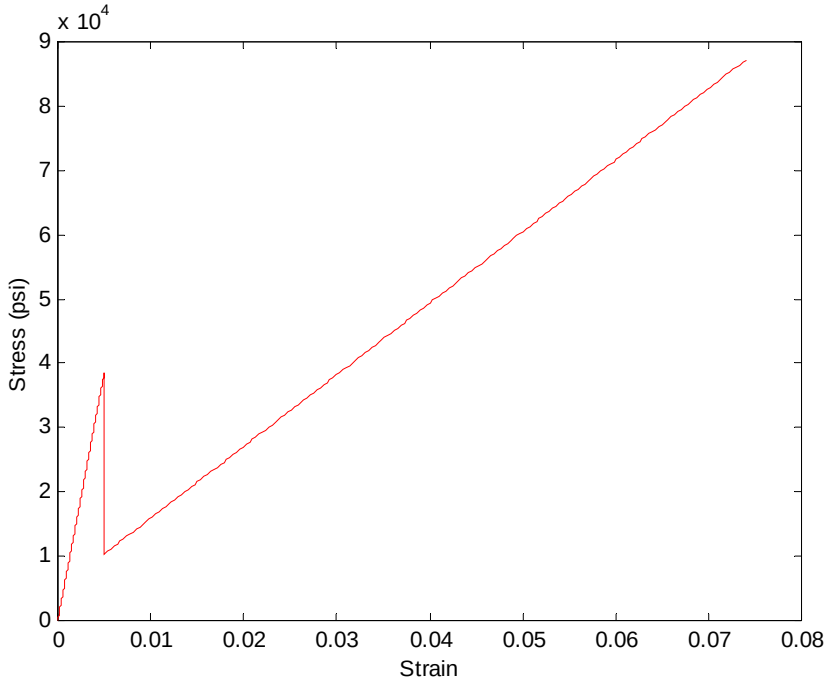

Figure 5.5: Stress-Strain Behavior from FADM for Kevlar 29 / P-55S 10-mm Bar, 4 Ribs.

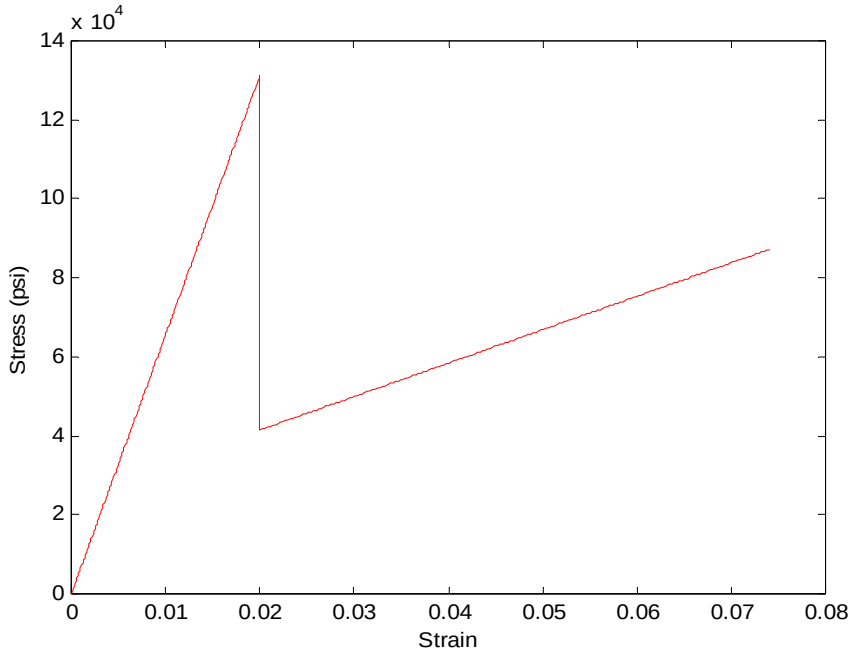

Figure 5.6: Stress-Strain Behavior from FADM for Kevlar 29 / IM-7- 12K 10-mm Bar, 4 Ribs.

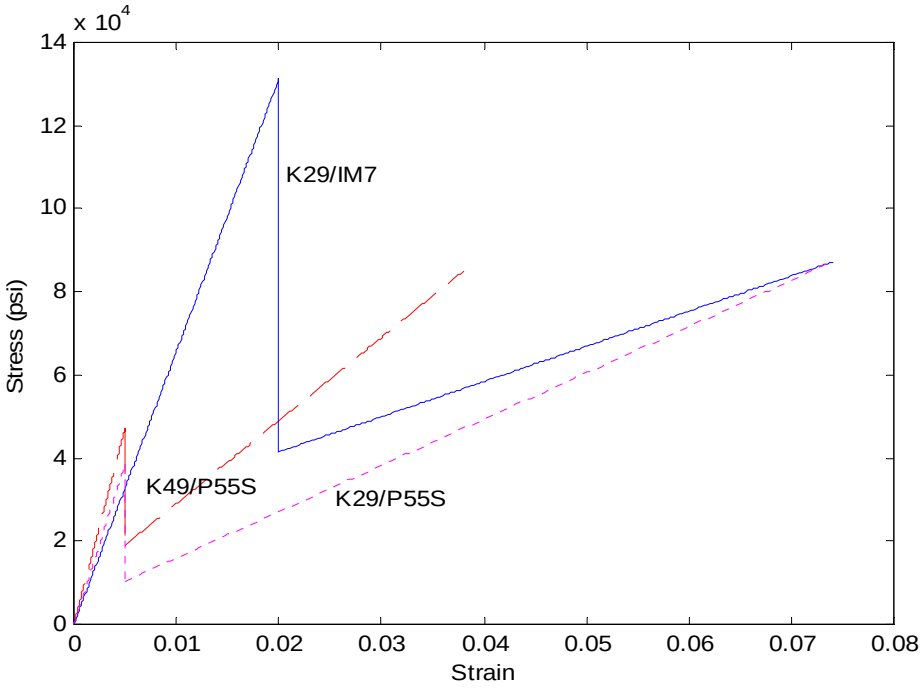

Figure 5.7: Stress-Strain Behavior of Various Combinations of Kevlar and Carbon Yarn Systems.

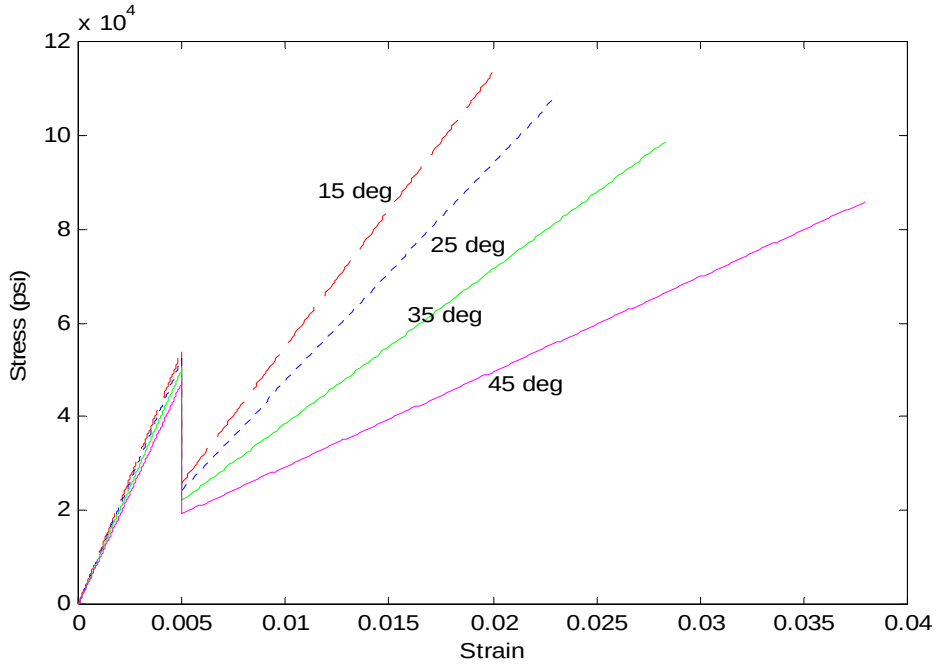

Figure 5.8: Variation in Braiding Angles for Kevlar 49/ P-55S 4-K Carbon, 10-mm Bars.

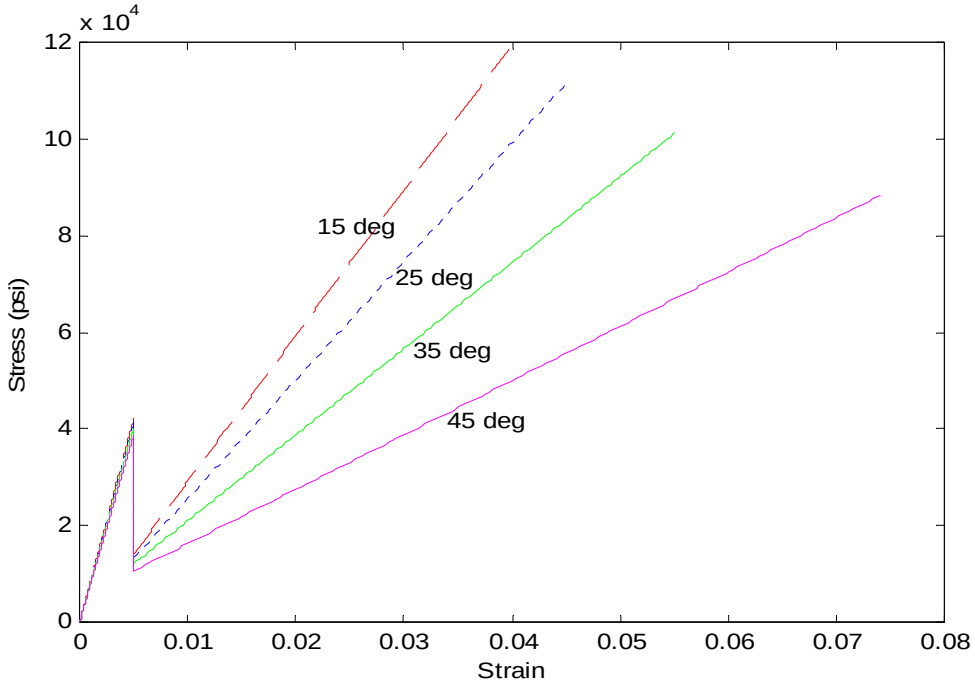

Figure 5.9: Variation in Braiding Angles, Kevlar 29 / P-55S 4K Carbon, 10-mm Bars.

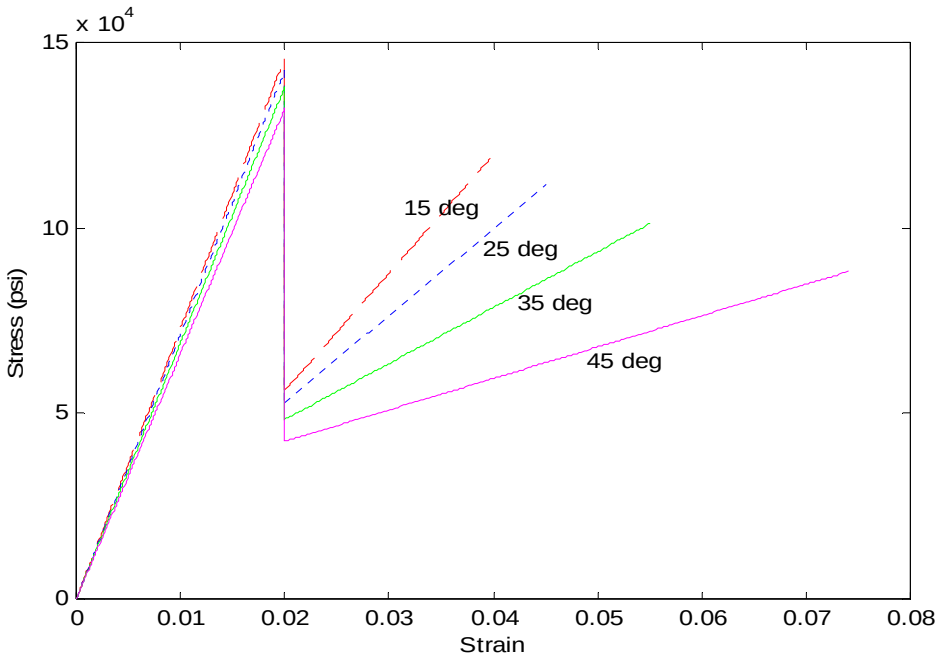

Figure 5.10: Variation in Braiding Angle, Kevlar 29 / IM-7 12K Carbon, 10-mm Bars.

Table 5.1: Estimated Tensile Properties of 10 mm Composite Rebar with Kevlar 29 Sleeve and IM7-12K Core. (2 Rib Yarns)

Properties	**Kevlar 29**	**IM7-12K**	**(Epon 9500/Epi-Cure Curing Agent 9550)**
Denier	1500	4014	—
Density (g/cc)	1.44	1.78	—
Number of yarns	176.0	43.0	—
Total denier	264000	172602	—
Braid angle (degrees)	30	0	—
Area (1 yarn) (in^2)	0.000207	0.000389	—
Total yarn area (in^2)	0.0365	0.0167	—
Ultimate tensile strength (psi)	400305	790250	9200
Elastic modulus (ksi)	8992	40030	450
Manufacturer	DuPont	Hexcel	Shell
Composite Properties			
Volume fraction (estimate)	0.41680	0.16534	0.41786
Diameter (in^2) (Nominal 9-mm dia.)	Area (in^2)	Area of yarns (K49 & IM7) (in^2)	
0.358902	0.10112	0.05322	
Elastic modulus (ksi)	Ultimate strength (psi)	Breaking load (lbs)	
10554.5	301352.1	30471.6	

Table 5.2: Estimated Tensile Properties of 10mm Composite Rebar with Kevlar 29 Sleeve and IM7-12K Core. (4 Rib Yarns)

Properties	**Kevlar 29**	**IM7-12K**	**(Epon 9500/Epi-Cure Curing Agent 9550)**
Denier	1500	4014	—
Density (g/cc)	1.44	1.78	—
Number of yarns	256.0	43.0	—
Total denier	384000	172602	—
Braid angle (degrees)	45	0	—
Area (1 yarn) (in^2)	0.00025	0.000389	—
Total yarn area (in^2)	0.06502	0.0167	—
Ultimate tensile strength (psi)	400305	790250	9200
Elastic modulus (ksi)	8992	40030	450
Manufacturer	DuPont	Hexcel	Shell
Composite Properties			
Volume fraction (estimated)	0.62478	0.11359	0.26163
Diameter (in^2) (Nominal 11-mm dia.)	Area (in^2)	Area of yarns (K49 & IM7) (in^2)	
0.43300	0.14718	0.08174	
Elastic modulus (ksi)	Ultimate strength (psi)	Breaking load (lbs)	
10282.9	342275.5	50375.7	

Table 5.3: Estimated Tensile Properties of 10 mm Composite Rebar with Kevlar 49 and P55S-4K Carbon Core. (4 Rib Yarns)

Properties	**Kevlar 49**	**P-55S, 4K**	**(Epon 9500/Epi-Cure Curing Agent 9550)**
Denier	1140	6429	—
Density (g/cc)	1.45	2.00	—
Number of yarns	320.0	30.0	—
Total denier	364800	192870	—
Braid angle (degrees)	45	0	—
Area (1 yarn) (in^2)	0.0001917	0.0005542	—
Total yarn area (in^2)	0.061344	0.016627	—
Ultimate tensile strength (psi)	400305	249400	9200
Elastic modulus (ksi)	17840	60191	450
Manufacturer	DuPont	Amoco	Shell
Composite Properties			
Volume fraction (estimated)	0.58945	0.11297	0.29759
Diameter (in^2) (Nominal 9-mm dia.)	Area (in^2)	Area of yarns (K49 & IM7) (in^2)	
0.43300	0.14718	0.07797	
Elastic modulus (ksi)	Ultimate strength (psi)	Breaking load (lbs)	
17449.4	266870.2	39277.7	

5.1.4 Discussion

The predicted tensile stress-strain behavior of the 10-mm diameter bar comprised of a sleeve of Kevlar 49 and a core of P55-S carbon was shown in Figure 5.4. As seen in Figure 5.4, a bilinear stress-strain curve resulted with an ultimate level above yield. Yield was assumed to occur when the core yarns broke, since the strain

capacity of P55-S was only 0.5%. Once the carbon core fractures, the load is picked up by the sleeve and any remaining core yarns. The predicted yield stress was approximately 49 ksi with a corresponding yield strain of 0.5%. The ultimate strain was 3.7% with a corresponding ultimate stress of approximately 82 ksi. The strain of unidirectional Kevlar 49 yarns is only 1.9%. However, since the yarn was braided, the translational efficiency of the yarn (i.e., braid angle effect) must be accounted for. When this was considered, the ultimate strain of the sleeve became 3.7%.

Figure 5.5 showed the predicted stress-strain behavior for the Kevlar 29/ P55-S material system. The strengths at yield and ultimate were 39 ksi and 85 ksi, respectively. The strain at yield was again 0.5% (fracture of core yarns) since P55-S was still used, and the ultimate strain was 7.4%. Again, this strain was achieved by means of the translational efficiency of the braid yarns. Also, the ultimate strain of Kevlar 29 was 3.7% in the unidirectional orientation compared to 1.9% of Kevlar 49.

Figure 5.6 showed the predicted behavior for the Kevlar 29/ IM7-12K material system. The strengths at yield and ultimate were given as 126 ksi and 85 ksi, respectively. The strain at yield was 2% and the ultimate strain was again 7.4%. The ultimate strain of IM7 carbon is 2% which is four times greater than the ultimate strain of P55-S which is 0.5%. However, the ultimate strength of IM-7 is 790 ksi compared to 249 ksi of P55-S. This explains the large increase in strength of the bar with a core of IM7-12K carbon. This was verified experimentally. Since the strength of the core was so high, once the core yarns broke, the Kevlar 29 sleeve picked up the load until complete bar failure. This ultimate load of the sleeve (and the composite bar) was lower than the ultimate load of the core as shown in Fig. 5.6. Even though this bar

was very ductile, the fact that the ultimate load capacity was lower than the yield load was not as desirable. However, since the yield load was so large, and therefore, might not be reached in service conditions, the added ductility past yield would function as reserve strength and ductility in the event of extreme overloading. The main concern of this bar would be the stiffness, since the stiffness of IM7-12K is 33 Msi while P55-S has a stiffness of 55 Msi.

Figure 5.7 showed all three examined material systems plotted together. It is evident from this figure that the strength increase of the IM-7 bar is significant over the P55-S core bar. The IM-7 bar behaved almost as high strength steel up to yield, but then had a zone of ductility past yield. Even though the ultimate strength of the IM-7 bar was lower than the yield strength, the post-yield region was still consistent with the other two systems used (Kevlar 29 or 49 with a P55-S core), and therefore, shows promise. It should be noted that by changing the volume fraction, the composite bar with a core of IM-7 can be designed to have a higher ultimate strength than its yield strength.

The major differences between using Kevlar 29 or Kevlar 49 with a core of P55-S are twofold. First, the ductility was increased significantly using Kevlar 29 since the unidirectional ultimate strain of Kevlar 29 was 3.7% compared to 1.9% of Kevlar 49. However, the stiffness of Kevlar 29 is about half of Kevlar 49. Therefore, once the core yarns yielded, the stress drop was greater for the bar using Kevlar 49 as illustrated in Figure 5.7. This drop is explained later in Figures 5.8 through 5.10.

Shown in Figure 5.8 was the variation in strength properties for the Kevlar 49/ P55-S system with variations of braid angle between 15 and 45 degrees. The braid

angle has three main effects on the strength properties of the bar. First, by lowering the braiding angle, as seen in Figure 5.8, the ultimate strain of the bar was reduced. As the braid angle approached 45 degrees, the ultimate strain was increased by a factor of $1/\cos^2\theta$ where θ is the braid angle. At 45 degrees, the yarn was off axis by 45°, so the strain was increased by two times since $1/\cos^2(45°) = 2$. A bar braided at 15° had much less ultimate strain capacity than a bar braided at 45°.

However, since the yarn was more off axis (i.e., away from the unidirectional orientation), the strength of the bar decreased, as seen in Figure 5.8. The strength of a bar braided at 15° was significantly larger than a bar braided at 45°. Therefore, as the braid angle increased, the overall strength of the bar decreased.

Thirdly, the stress drop at yielding (i.e., fracture of the core yarns) was effected by the braid angle. As seen in Figures 5.8 through 5.10, the stress drop was less for bars with low braid angles. This stress drop was particularly more severe for the case of the bars using Kevlar 29 since the stiffness was about half of Kevlar 49. This strength drop effect should be minimized.

Shown in Figures 5.9 and 5.10 was variation in strength properties with variation in braid angle for the Kevlar 29/ P55-S and Kevlar 29/ IM7-12K systems, respectively. The same trends existed for the latter as that for the Kevlar 49/ P55-S system.

Finally, the braid angle effects the size, height, and spacing of the deformation pattern or ribs produced by the four rib yarns. As the braid angle decreased towards 15°, the bar had very little deformation pattern, since the rib height was decreased and the rib spacing was increased. A braid angle of 45° gave much closer rib spacing and

greater rib height. Therefore, even though the strength properties were reduced, for sufficient bond to concrete, the braid angle cannot be too low. Otherwise, the bar can never develop its full strength since reinforced concrete beams will always fail by bar pullout failure.

5.2 Scanning Electron Microscopy (SEM) of 10-mm DHFRP Bars

Before testing was conducted to obtain the mechanical properties of the DHFRP bars, the microstructure was studied. This microstructure characterization included the use of Scanning Electron Microscopy (SEM) as a technique to examine the microstructure of the DHFRP bars. A good microstructure should predict sufficient mechanical properties, while a poor microstructure with dry fibers and discontinuous interfaces indicates inferior mechanical properties.

5.2.1 Sample Preparation

In order to obtain a good representation of the bar's internal structure, one-inch long samples were cut from various locations along the bar length. Each bar was produced in a length sufficient to be used as a piece of beam or column rebar, one or two tension specimens, and several SEM samples. Therefore, actual bars used for in-situ applications were investigated. The samples were taken from many bars at various locations to get a statistical sample. Each sample was marked and mounted in a polyester resin system for sample mounting. The sample was placed on its end in the sample cup (1.5 inches diameter and 1.5 inches high) and properly marked. A mixture of 60 mL of polyester resin and 30 drops of hardener was mixed thoroughly at room temperature. This amount was enough to cast 3 samples. The mixture was then

gently poured around the sample, as care was be taken to avoid knocking the sample over. Also, caution was exercised that the samples did not float to the surface during pouring the resin. The mounted samples were allowed to cure for 24 hours at room temperature before they were ground and polished.

Once the resin had completely cured, the samples were placed in the sample holder of an automatic polisher (Struers Rotopol-22). Grinding and polishing were carried out in accordance with the schedule in Table 5.4. Aluminum oxide powder (1 micron particle size) was used in polishing the samples. Polishing was done in multiples of 10 minute increments with a 30N force applied. After each cycle, the samples were removed, washed with cold water, and air dried. An optical microscope set at 100X magnification was used to examine the surface of the samples. The polishing process was repeated until all scratches were completely removed. They were then gold coated in a Denton Vacuum Desk II system according to the manufacturer's recommendations. Shown in Figure 5.11 are the polishing and gold coating machines.

Figure 5.11: Polishing Machine and Gold-Coating Machine for SEM Sample Preparation.

Table 5.4: SEM Samples Grinding and Polishing Schedule.

Sand Paper (grid)	Force (N)	Time (min.)
400	25	1
800	20	1
1200	15	1

SEM photographs were taken at various magnifications and locations such as the core, sleeve, core-sleeve interface, and the entire cross-section of the rebar. The purpose of SEM observations was to verify the fiber wet out, void content, and continuity in sleeve-core interface. The micrographs were taken with an AMRAY 1830D4 Scanning Electron Microscope system with the intensity setting at 20 Kev. Shown in Figure 5.12 is the AMRAY system.

Figure 5.12: AMRAY SEM System, Drexel University.

5.2.2 SEM Observations

Three series of SEM tests were conducted. Series 1 contained bars made with the new preform design (four rib yarns) using a P-55S 4K carbon core and Kevlar 49 for the sleeve yarns. Series 2 were bars made using the new preform design using an IM-7 12-K carbon core and Kevlar 29 for the sleeve yarns. Finally, Series 3 were bars using the original preform design (two rib yarns) using P-55S 4K carbon core and Kevlar 49 (1500 denier) for the sleeve yarns. Comparisons were made between the three series of data. These results determined the efficiency of the various preform designs and manufacturing processes of the DHFRP bars.

5.2.2.1 Series 1: SEM of P-55S 4K Bars with New Preform

Series 1 of the SEM characterization was conducted on bars produced using P-55S 4K carbon for the core yarns and Kevlar 49 for the sleeve yarns. The improved dieless pultrusion process was used (see Fig. 4.22). For this bar, two different denier yarns were used for the general braiding yarns and the rib yarns, but the total denier of the bar was similar to the other 10-mm bars used. Again, the larger denier yarn was used for the ribs for ease of yarn winding and bar production.

Shown in Figures 5.13 through 5.16 are SEM scans of the bar at lower magnifications (15 – 25 times). These scans show the entire interface between the carbon core and the Kevlar sleeve yarns. The purpose of showing the entire carbon core cross section was to determine whether or not the interface between the core and the sleeve was continuous without voids and that the shape of the core was circular. The shape of the core theoretically should be circular, but dependent on the pressure exerted by the sleeve yarns, the shape of the core may vary as will be seen later.

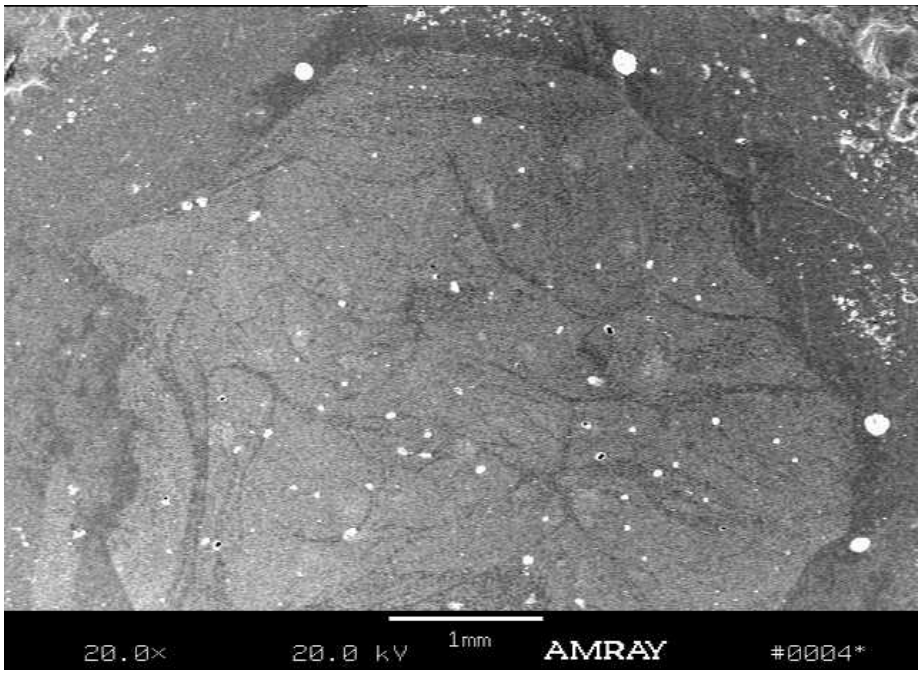

Figure 5.13: SEM Scan of P-55S 4K Carbon Core with Kevlar 49 Sleeve, 20X Magnification.

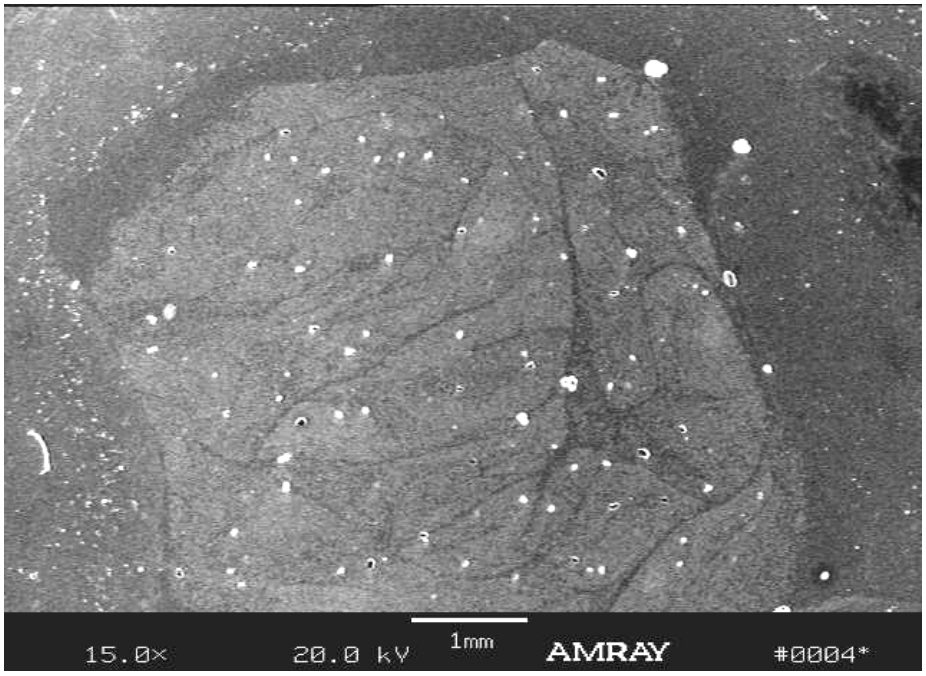

Figure 5.14: SEM Scan Showing Entire Interface Between P-55S 4K Carbon Core and Kevlar 49 Sleeve Yarns, 15X Mag.

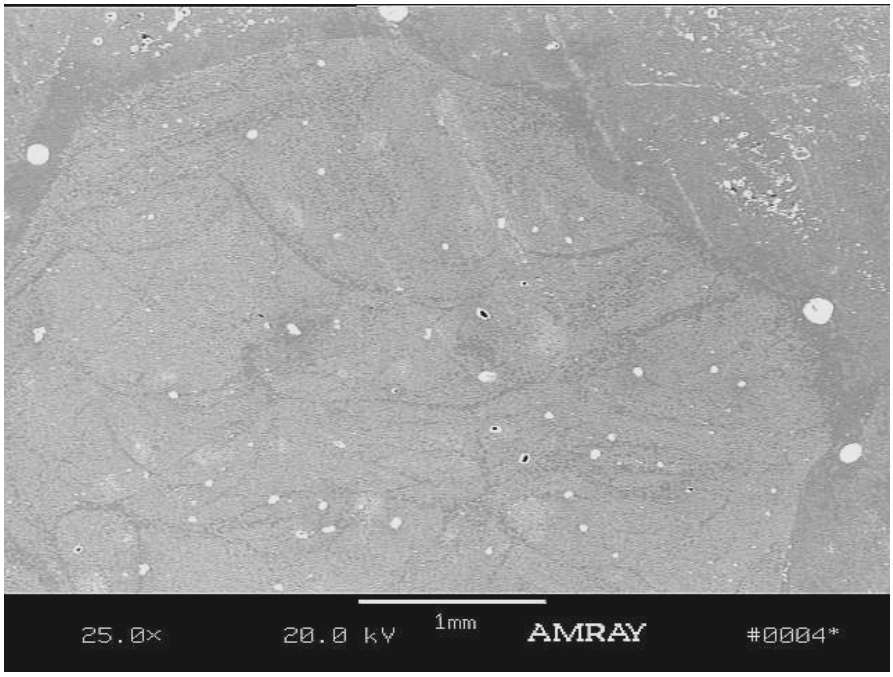

Figure 5.15: SEM Scan Showing Entire Interface Between P-55S 4K Carbon Core and Kevlar 49 Sleeve Yarns, 25X Mag.

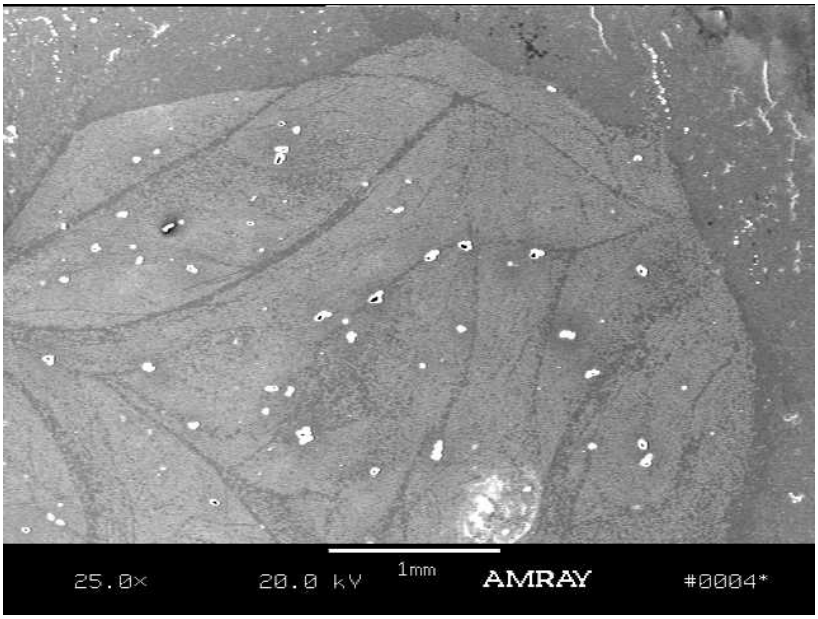

Figure 5.16: SEM Scan Showing Entire Interface Between P-55S 4K Carbon Core and Kevlar 49 Sleeve Yarns, 25X Mag.

Figure 5.13 showed the cross section of the bar at 20 times magnification. Shown was approximately 80 % of the cross section of the core with the interface between the sleeve and core. The shape of the carbon core was generally circular except for the right side of the core. The bottom center right had some core yarns that protruded from the circular shape and above that, the yarn was compressed inward from a circular shape. This is explained by the amount of pressure that is exerted by the sleeve yarns. The general braiding yarns should exert uniform pressure on the core since the yarns are symmetrically and continuously braided around the core. The rib yarns, however, depending on the desired rib pattern and location along the length, may or may not exert uniform pressure on the bar. If the rib pattern is symmetric, the exerted pressure on the core is fairly uniform, as shown in Figures 5.13 through 5.16. The bottom center right area of the core yarns shown in Figure 5.13 did not have as much pressure exerted on it since this was probably a braiding yarn, and therefore, the core yarns protruded outward from the circular shape. In contrast, the area above this had too much pressure exerted on the core, probably by a rib yarn, and therefore, the core was compressed inward from the ideal circular shape.

The dark area on the top left center of the scan was a resin rich area between the core and sleeve. Again, this was a region where less pressure was exerted by the sleeve, again probably by a braiding yarn. These resin rich regions were evident along some length of the core-sleeve interface in all of the bars manufactured using dieless pultrusion. Also, seen in Figure 5.13 and especially Fig. 5.14, many of the white spots on the SEM scans were not voids but particles on the surface of the mounted specimen. The white marks on the bar were particles that were on the gold coating.

Looking closely, these marks are above the actual surface of the sample. Also, these marks have a shadow cast on one side of them. Other dirt particles were on the sample before the surface was gold coated, and were impossible to prevent. These were black marks on the specimen. The voids were typically described as marks that are black and had a white ring around them (Fig. 5.14). These markings for either dust particles or actual voids in the composite were more evident at higher magnifications shown later.

Similar observations can be made for the other cross sections shown in Figures 5.14 through 5.16 as discussed above for Figure 5.13.

Shown in Figures 5.17 through 5.24 are SEM images of the interface between the core and the sleeve yarns at higher magnifications. These images illustrated good interface between the P-55S and the Kevlar 49 yarns. It was evident from these figures that good wet out occurred since these images were almost void-free. An example of a void is shown in Figure 5.22. The white marks on the right side are voids in the Kevlar yarns. These white marks follow along the outline of the surrounding yarns. The black mark with the white outline in the center of Figure 5.20 is not a void since this is above the surface of the bar, and rests on top of the surrounding yarns.

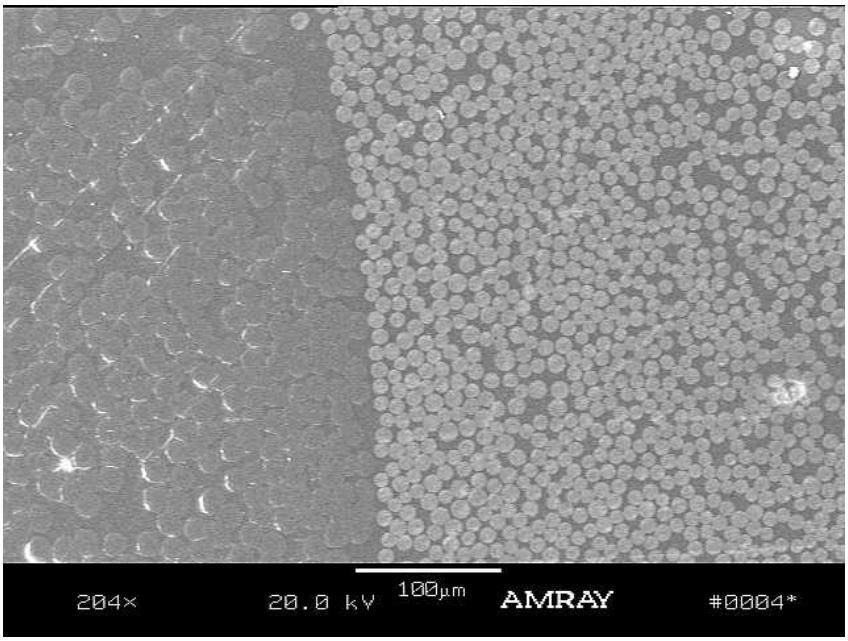

Figure 5.17: Good Interface Between P-55S Carbon Core and Kevlar Sleeve, 204 X Mag.

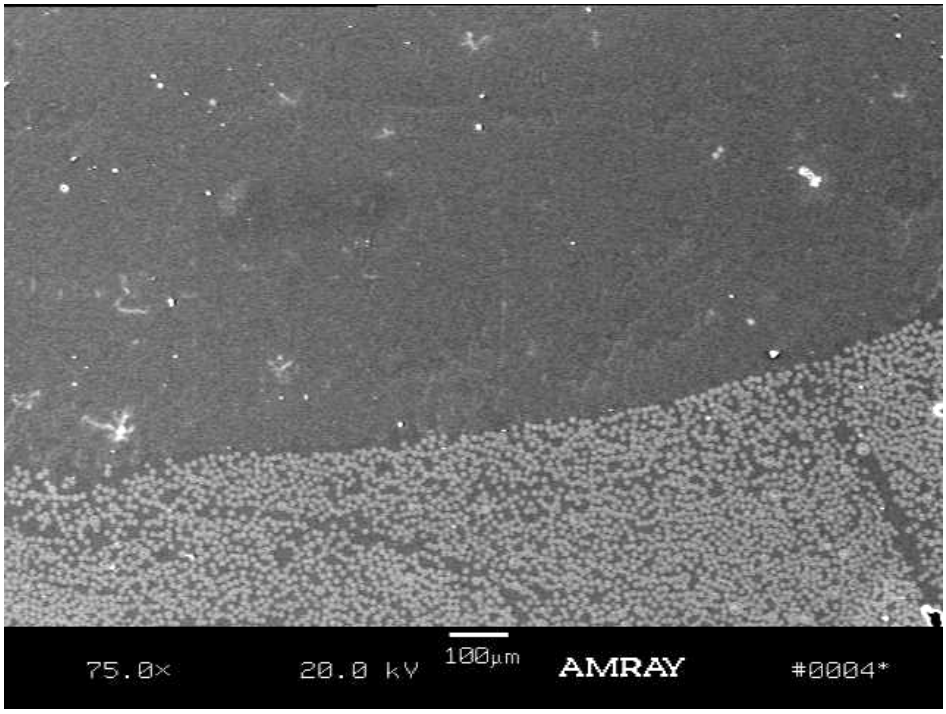

Figure 5.18: Good Interface Between P-55S 4K Carbon Core and Kevlar Sleeve, 75 X Mag.

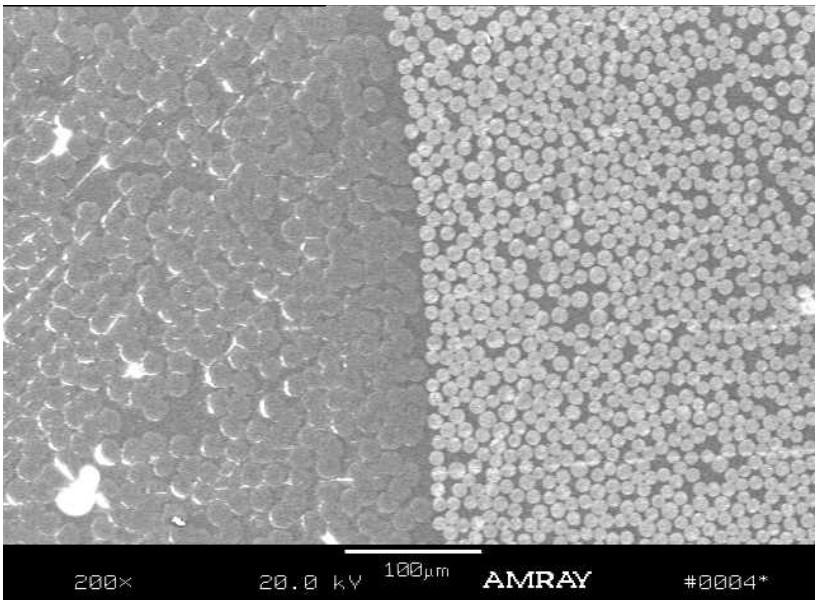

Figure 5.19: Good Interface Between P-55S 4K Carbon Core and Kevlar Sleeve, 200 X Mag.

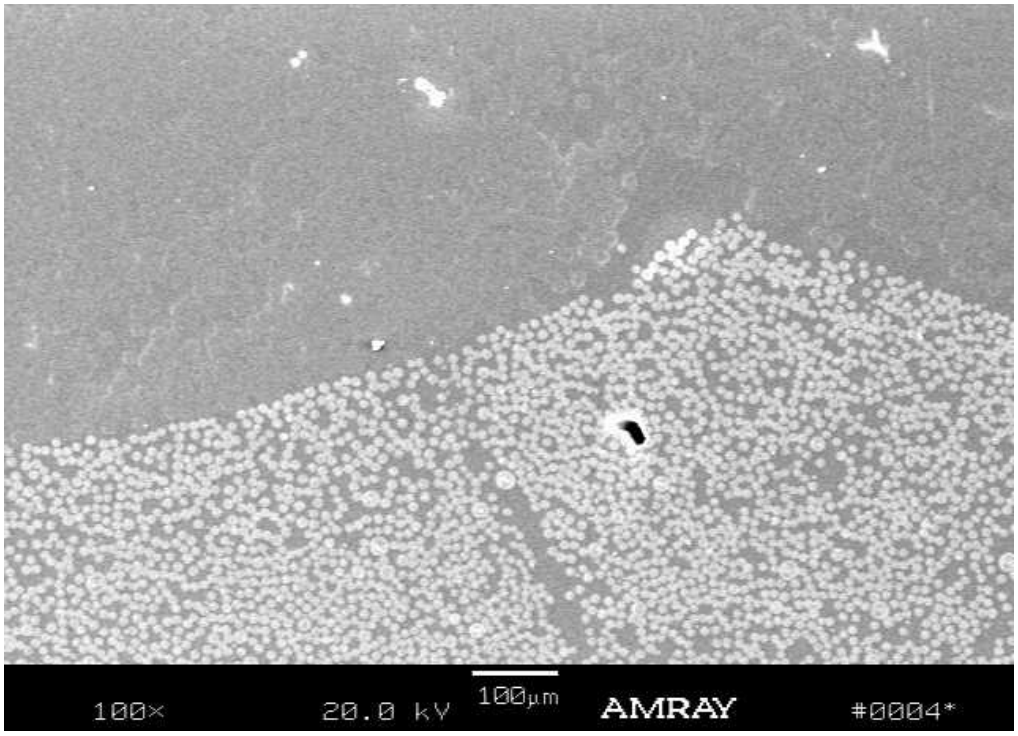

Figure 5.20: Good Interface Between P-55S 4K Carbon Core and Kevlar Sleeve, 100 X Mag.

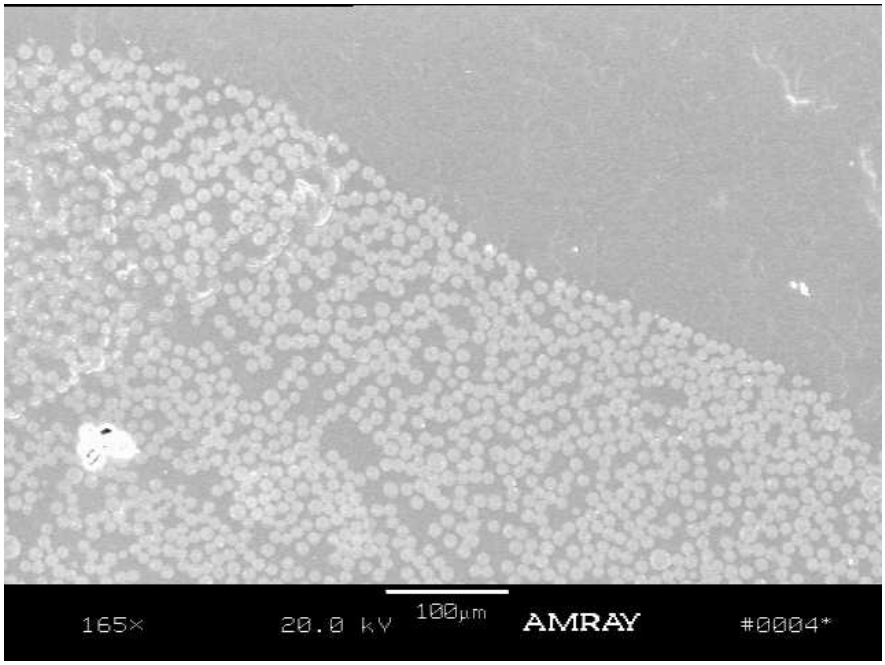

Figure 5.21: Good Interface Between P-55S 4K Carbon Core and Kevlar Sleeve, 165 X Mag.

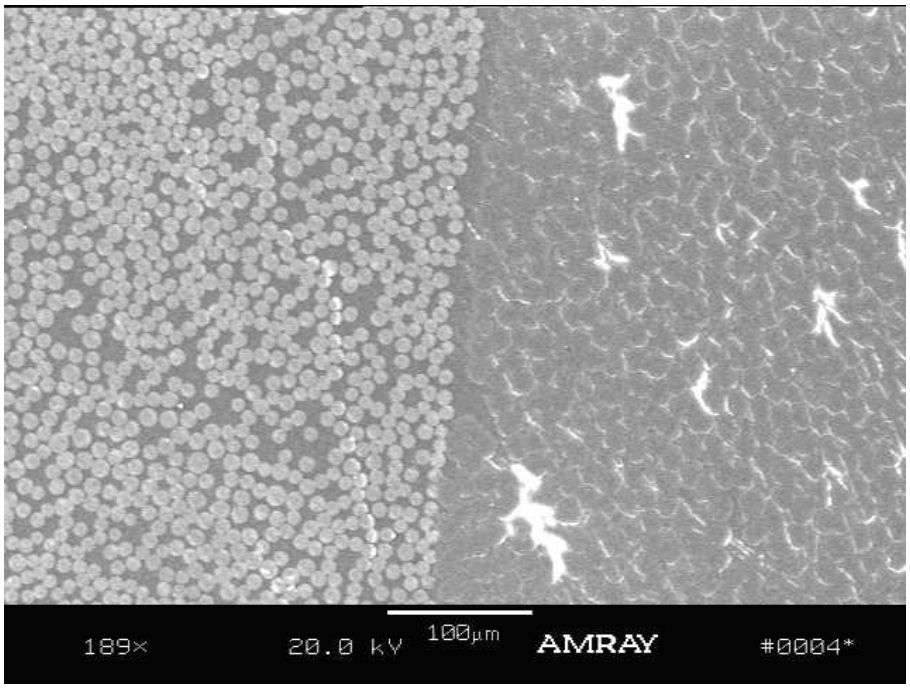

Figure 5.22: Good Interface Between P-55S 4K Carbon Core and Kevlar Sleeve, 189 X Mag.

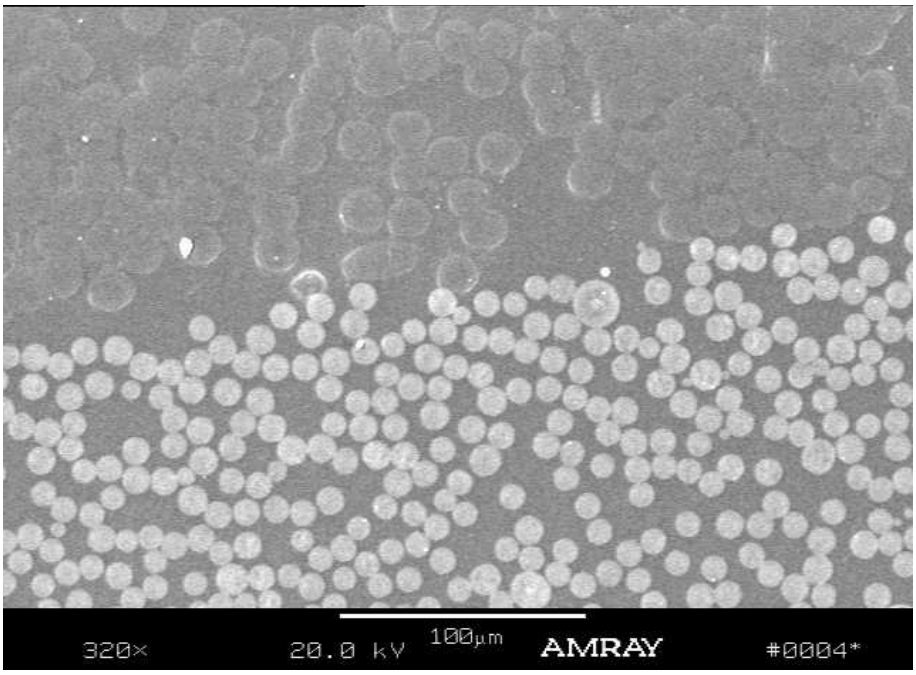

Figure 5.23: Close Up of Good Interface Between P-55S 4K Carbon Core and Kevlar Sleeve, 320 X Mag.

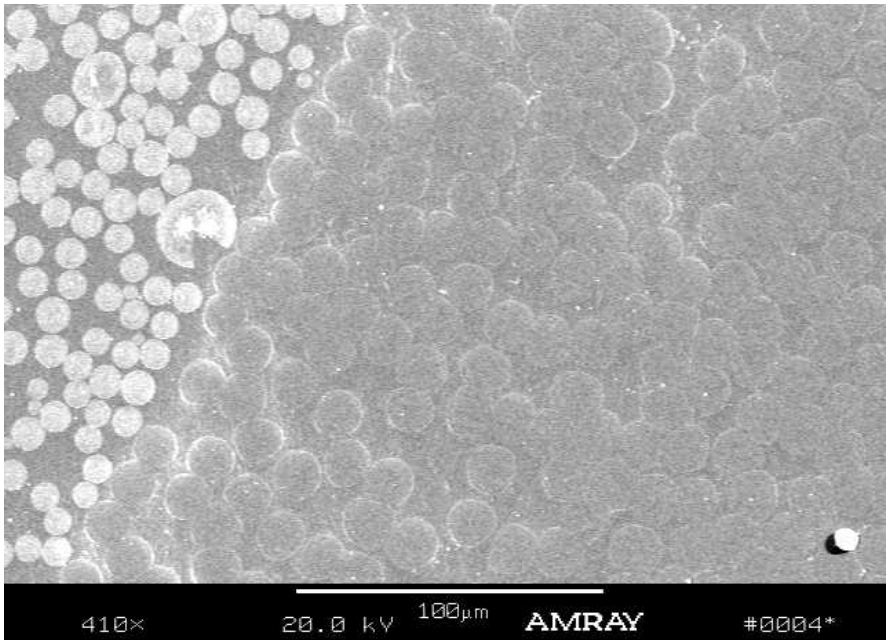

Figure 5.24: Close Up of Good Interface Between P-55S 4K Carbon Core and Kevlar Sleeve, 410 X Mag.

Figure 5.17 at approximately 200 times magnification showed the core/ sleeve interface with the Kevlar sleeve yarns on the left (darker yarns) and the P-55S core yarns on the right (lighter yarns). As seen, the interface was good due to the absence of voids. Also the fiber packing was very uniform and tight, thereby preventing resin rich areas from developing. The striations or lines on the left side (Kevlar yarns) are not defects but scratches on the surface of the sample that incurred during polishing the SEM sample.

Figure 5.18 at 75 times magnification also showed good interface without significant void content or resin-rich regions. At 75 times magnification, a much larger length of the interface was shown, still showing good wetting. This was again evident in Figure 5.20 which was at 100 times magnification. Figure 5.19, shown at 200 times magnification, was similar to Figure 5.17 showing good interface over a shorter distance.

Figure 5.20 showed the interface at 100 times magnification. At this magnification, the distortion in shape of the carbon core was more noticeable. Again, this was caused by uneven braid pressure caused by the heavier rib yarns. Minor distortion was also evident in Figure 5.21, but when viewed at lower magnification, would not be evident. Figure 5.22 showed the interface at 189 times magnification. Even though the core-sleeve interface was very good here, on the right side (in the Kevlar braiding yarns) were white areas which were voids. These were more obvious since the marks followed the shape of surrounding yarns and were in the same plane of the yarns.

Shown in Figures 5.23 and 5.24 were scans of the interface at 320 times and 410 times magnification, respectively. These scans showed much detail of the interface, but only over a very small portion of the bar. Again, good fiber packing and good fiber wetting was evident, free of voids. The Kevlar yarn packing in Figure 5.24 was tighter than the yarns in Figure 5.23. If the yarn packing gets too tight, the yarn bundles will not be impregnated properly, thereby causing dry fibers. However, this was not evident in either of these scans.

Figures 5.25 through 5.28 show regions of the core-sleeve interface where good wetting is still evident but the consolidation or fiber packing was not as tight. This resulted in resin-rich regions between the core and rib yarns. This occurred in regions where the braiding yarns, not rib yarns, consolidated the core. The braiding yarns did not have as much tension as the rib yarns, and therefore, did not exert as much pressure on the core as the regions around the rib yarns. In these regions around the cross section of the core, resin-rich regions existed. Even though these regions look much more dramatic in Figures 5.25 through 5.28 due to the higher magnifications (from 60.5 times to 200 times), when Figures 5.13 through 5.16 are reviewed (the entire cross section at lower magnifications, 15 times to 25 times), the resin-rich regions are not as large when compared to the entire core-sleeve interface.

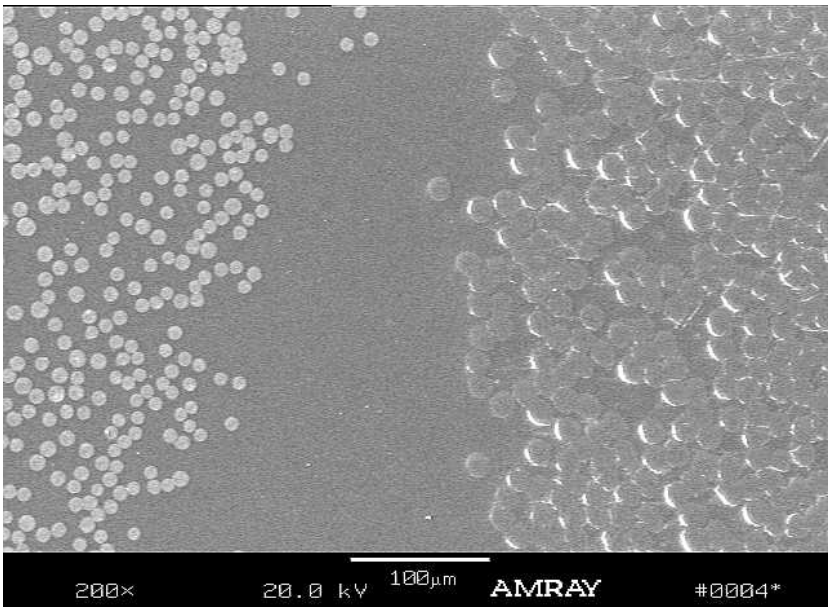

Figure 5.25: Interface Between P-55S 4K Carbon Core and Kevlar Sleeve Showing Resin-Rich Regions, 200 X Mag.

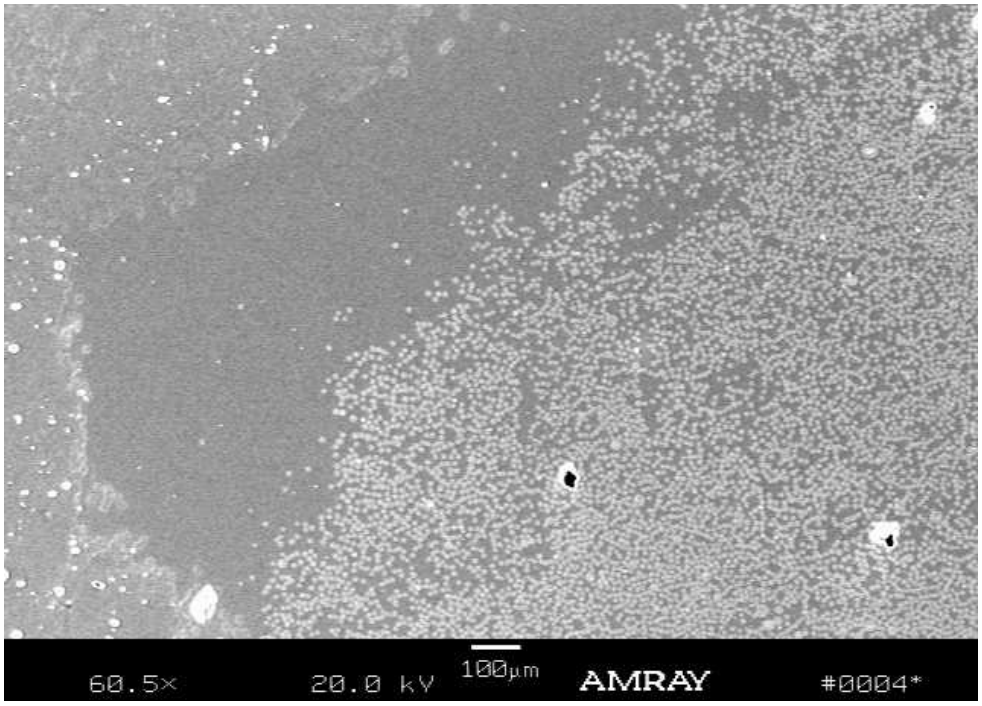

Figure 5.26: Interface Between P-55S 4K Carbon Core and Kevlar Sleeve Showing Resin-Rich Regions, 60.5 X Mag.

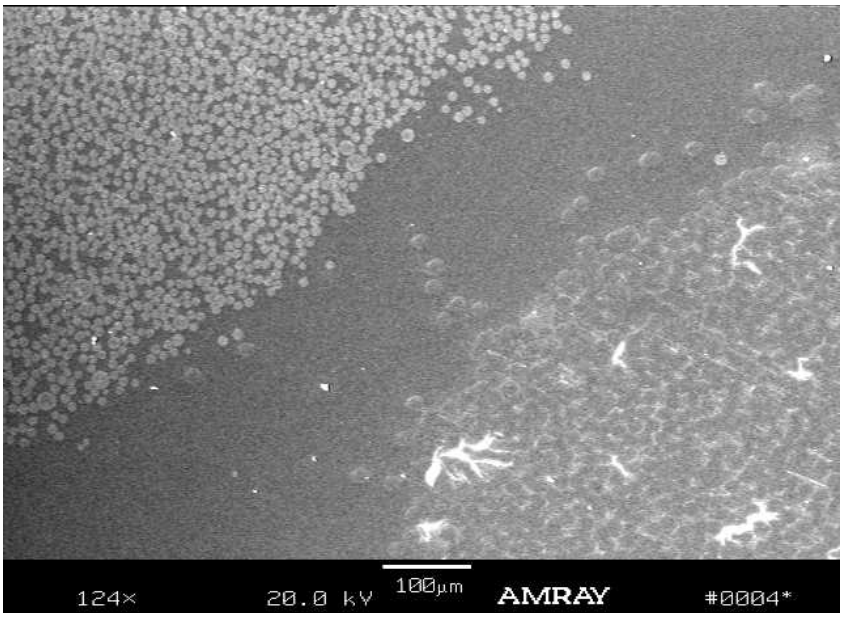

Figure 5.27: Interface Between P-55S 4K Carbon Core and Kevlar Sleeve Showing Resin-Rich Regions, 124 X Mag.

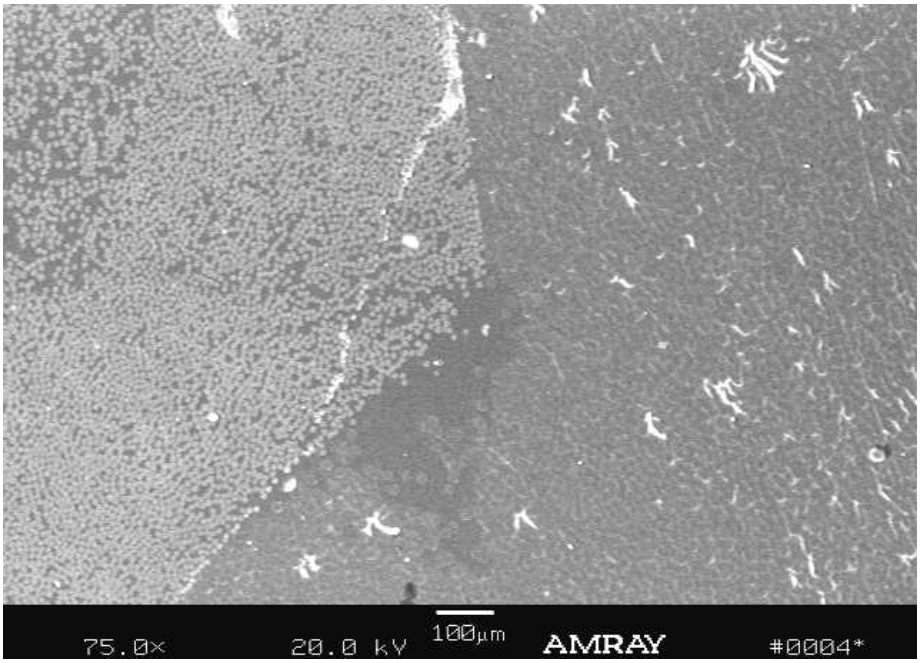

Figure 5.28: Interface Between P-55S 4K Core and Kevlar 49 Sleeve Showing Both Good Interface and Resin-Rich Regions, 75 X Mag.

Figure 5.25 showed a short segment of the core-sleeve interface at 200 times magnification where a resin-rich interface existed. Figure 5.26, shown at 60.5 times magnification, showed a much larger segment of this resin rich interface. In Fig. 5.26, the shape of the resin rich area followed the shape of the braiding yarns. Above and below the resin rich region were segments of good interface (where rib yarns exerted sufficient pressure). This was also evident in Figure 5.27, shown at 124 times magnification.

Shown in Figure 5.28 was the interface magnified 75 times showing both regions of good fiber packing under higher pressure and resin-rich regions. This was also an example of core distortion from being completely circular shaped. Around the resin-rich regions, the core was distorted in shape resulting from less pressure provided by the sleeve yarns at this location. One solution to remedy this problem would be to use a die for the bar that would exert a more uniform pressure on the bar. However, the use of a die had other significant problems which are explained later.

Shown in Figure 5.29 is a portion of the Kevlar sleeve at 600 times magnification. Shown in Figure 5.30 is the carbon core shown at 1000 times magnification. Figure 5.31 shows a microscopic scan of the outside bar edge along the Kevlar braiding yarns while Figure 5.32 shows the intersection of three braiding yarns.

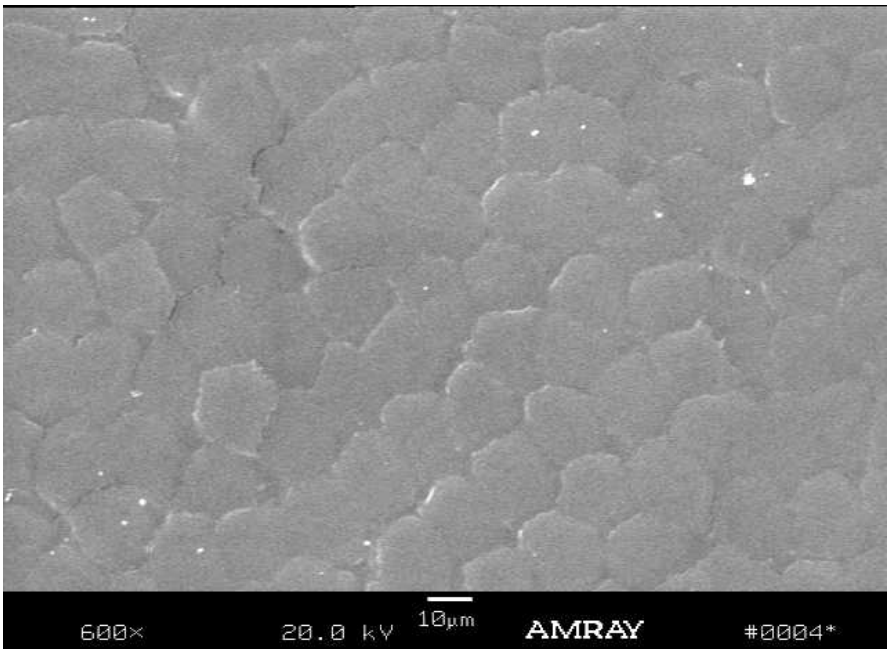

Figure 5.29: Kevlar 49 Braiding Yarns, Showing Good Fiber Packing, 600 X Magnification.

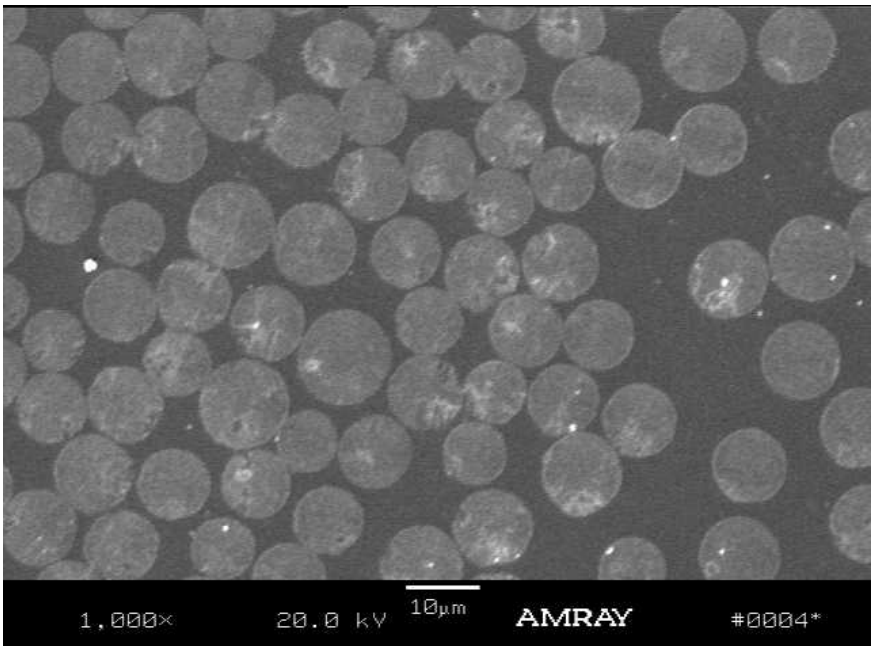

Figure 5.30: Carbon P-55S 4K Core Yarns, Showing Good Fiber Packing, 1000 X Magnification.

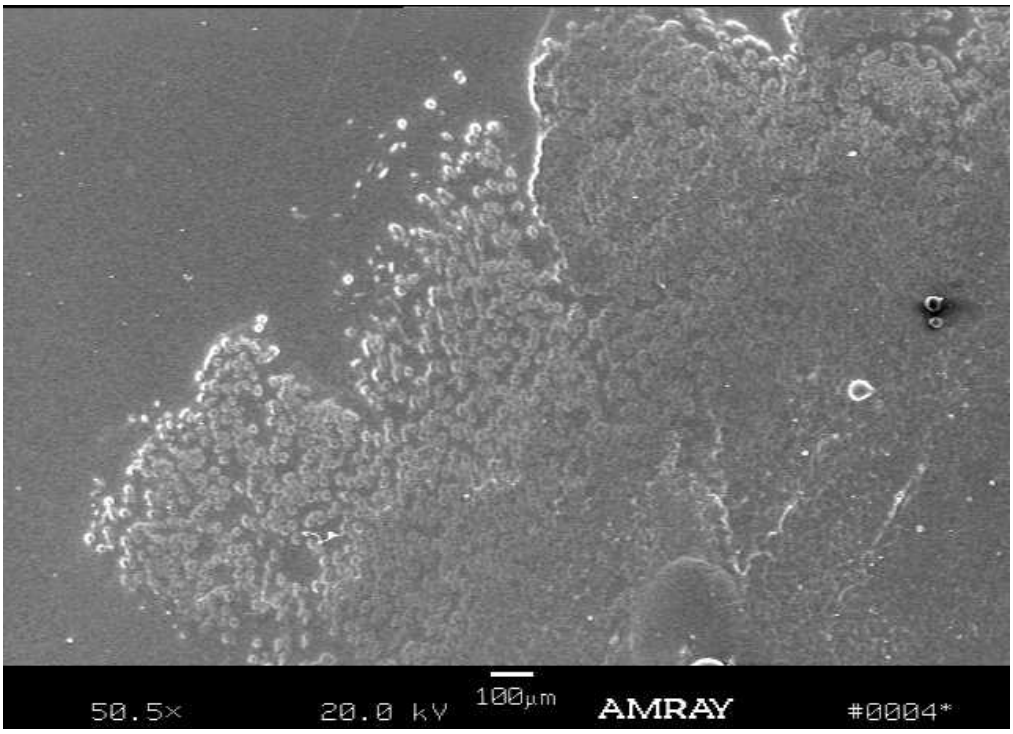

Figure 5.31: Edge of 10-mm Bar Showing the Edge of the Braiding Yarns, 50.5 X Magnification.

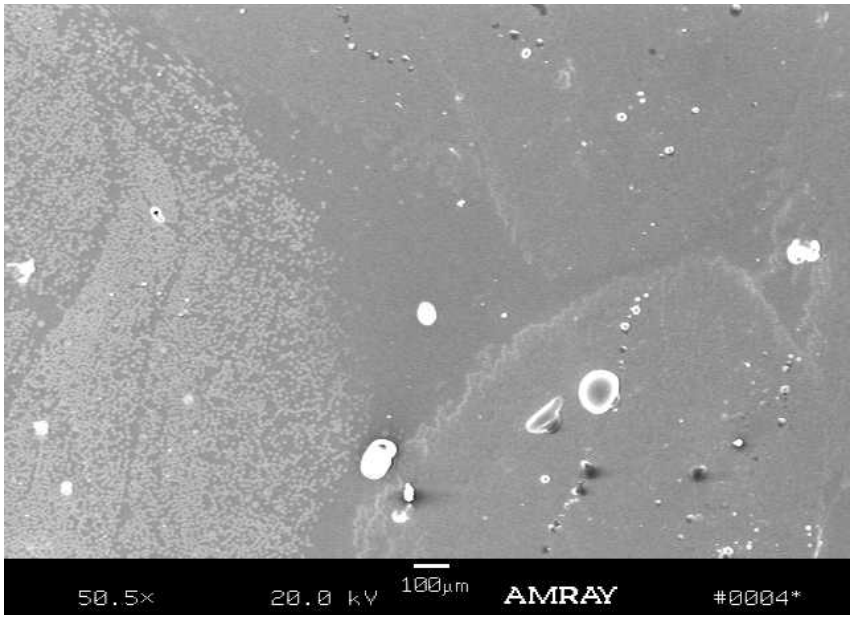

Figure 5.32: Intersection of Three Braiding Yarns, Showing Yarn-Resin Interface, 50.5 X Mag.

Figure 5.29, showing the Kevlar yarns magnified at 600 times, showed uniform and tight yarn packing. This sample also showed good yarn wetting evidenced by the lack of voids. However, if the fiber packing was much tighter, poor wetting might result in dry fibers due to a very high fiber volume fraction.

Figure 5.30 showed the carbon core yarns at 1000 times magnification. The P-55S yarns were very circular in shape and had a smooth surface texture as seen in this figure. Again, good yarn packing and uniform yarn distribution was evident. Good wetting was evident by the lack of voids. This microscan of the carbon demonstrated a more ideal condition for complete yarn wetting compared to the Kevlar microscan of Figure 5.29 since there was sufficient space around each yarn to ensure proper yarn wetting.

Figure 5.31 showed a section of the bar edge at approximately 50 times magnification. From the scan, the surface roughness of the bar was evident. Again, good fiber wetting was shown as well as good yarn packing.

Figure 5.32 showed the intersection of the carbon core on the left and three braiding yarns at approximately 50 times magnification. Within the yarn bundles, good yarn packing and wetting was evident. However, at the intersection point of the three yarns, a resin-rich area existed. This was the dark region in the middle of the scan. These resin-rich regions were typical of braiding yarn intersections throughout the bar. They existed due to a lack of confining pressure by the braiding yarns. This could be remedied by the use of a die.

5.2.2.2 Series 2: SEM of IM-7 12K Bars with Original and New Preforms

Series 2 of the SEM characterization was conducted on 10-mm bars consisting of a carbon core of IM-7 12K yarn and a braided sleeve of Kevlar 29 yarns. Again, these materials were used during the improvement of the braidtrusion process due to their availability; however, interesting properties and characteristics resulted with this material system. In this series, both the original preform using two rib yarns and the new preform using four rib yarns was used. It was during this trial manufacturing series that the preform was changed from two rib yarns to four rib yarns. Also, the effects of using a die at the manufacturer's curing recommendations (fully heated) and at a modified curing schedule (partially-heated) and the effects of dieless braidtrusion were investigated.

SEM photographs indicated good resin infiltration in both 2-rib yarn bars using the die, and 4-rib yarn bars without a die. This was true since both preforms used the resin bath to infiltrate the core yarns. The braiding yarns or braided sleeve imposed sufficient pressure to force the resin to flow outward and penetrate the braiding and rib yarns (approximately 73% of the total fiber volume fraction).

The 2-rib yarn bars were investigated first. Shown in Figure 5.33 is the entire cross section of a 2-rib yarn rebar. This bar was fabricated with a heated die and a post- cure oven. The shape of the core is considerably distorted, due to uneven pressure caused by the rib yarns. Since there were only two rib yarns, the cross section was unsymmetrical, with resulting unsymmetrical pressure. Also, DHFRP rebars with 2-rib yarns produced with a die contained a large number of voids, larger void size, and the voids were clustered into a region where there was no rib yarn as seen on the

left in Figure 5.33. There are more voids for the 2-rib yarn bars than the 4-rib yarn bars (P-55S/ Kevlar 49) presented in Section 5.2.2.1.

Figure 5.34 shows good fiber wet out at various locations in the cross section and along the length of the pultruded rebar. Again, at such high magnifications, the bar looks good locally, but this does not give a good macroscopic representation of the bar. Figure 5.35 shows various locations of the core-sleeve interface around the circumference of the core. Large voids were scattered throughout the cross section even in the braided sleeve. The core cross section was highly distorted along the length as predicted in Figure 4.15 and also observed in SEM photographs of the actual composite. This void concentration and core distortion can be explained by the effect of a pressure rise inside the die as the preform is pulled through. This is explained later in section 5.2.2.4.

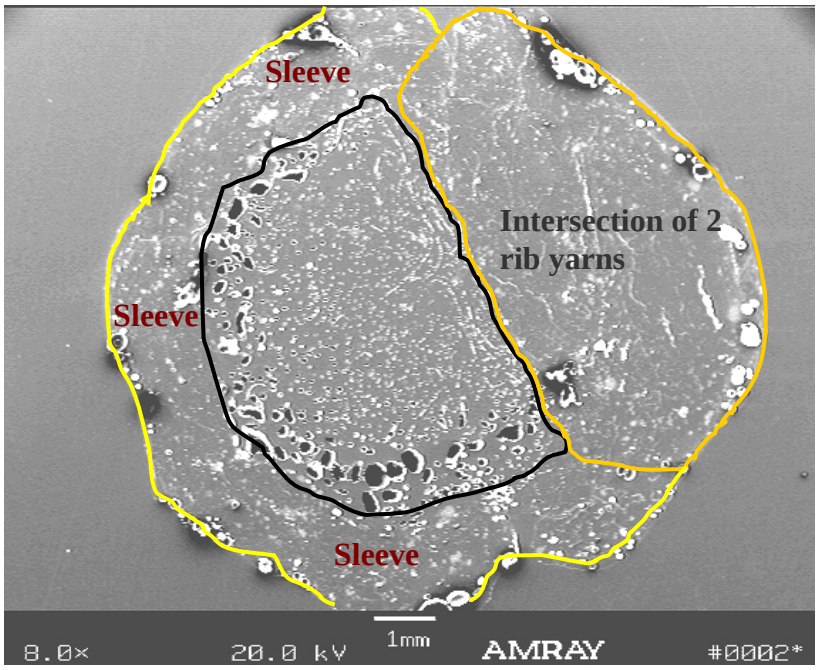

Figure 5.33: Cross Section of 2-Rib Yarn Bar Produced with Die. (8x Magnification).

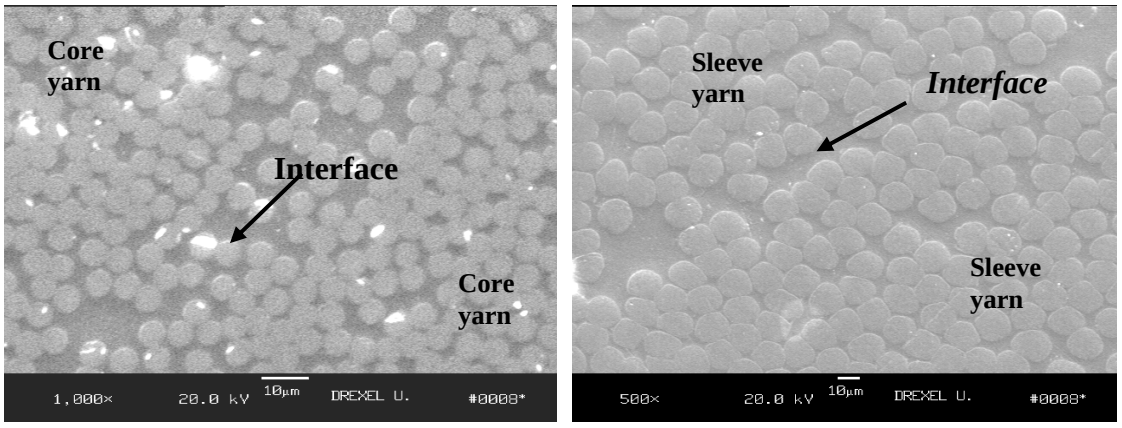

(a) IM7 carbon core at 1,000x magnification. (b) Kevlar 29 sleeve at 500x magnification.

Figure 5.34: Good Fiber Wet Out in Both Core and Sleeve; 2 Rib Yarn Bar Produced with Die.

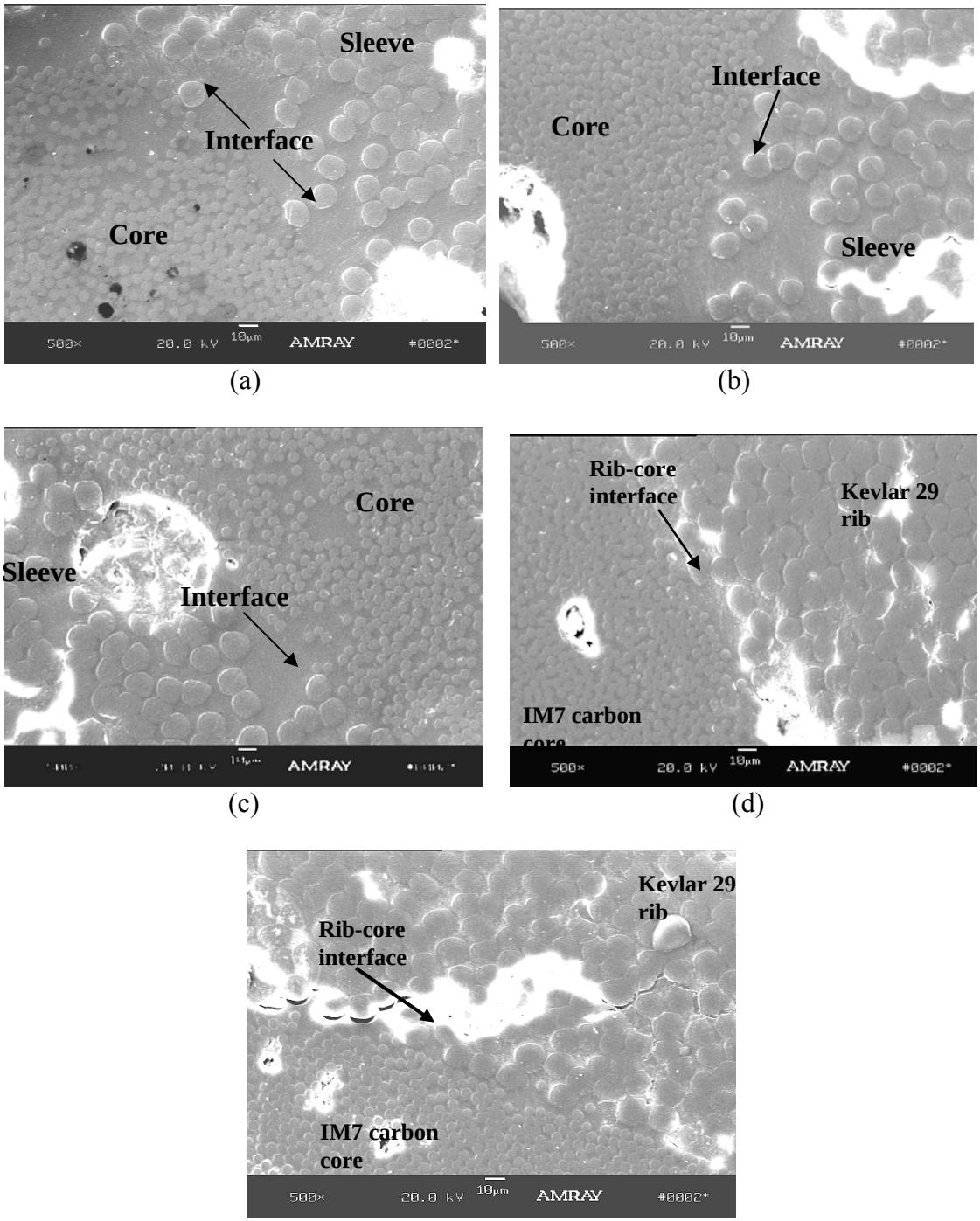

Figure 5.35: Core-Sleeve Interface of 2 Rib Yarn Bars (500x mag.) at Various Locations Around the Circumference of the Core. (a-c) Core-Sleeve Interface Away from Rib Yarns; (d and e) Discontinuity in Core-Sleeve Interface at Rib Yarn Crossing.

Next, the microstructure of the new preform (4-rib yarns) was analyzed. Shown in Figure 5.36 is the entire cross section of the 4-rib yarn bar. Again, the 4-rib yarn bar was fabricated without either a die or a post-cure oven. It can be seen that the 4-rib yarns rebar produced without the die had better quality than the 2-rib yarn bar manufactured with a die (Fig. 5.33). The void content was much less, smaller in size, and uniformly distributed within the core. The carbon core was slightly distorted but still relatively circular. The 4-rib yarns kept the core much more uniform and symmetric, especially compared with the 2-rib yarn bar (Fig. 5.33). The non-uniform hoop pressure that was evident in the 2-rib yarn case (and caused the core distortion), was eliminated by using four rib yarns.

Figures 5.37 and 5.38 are SEM micrographs representing various regions in the cross section. Examination of the cross sections of the rebar revealed good resin infiltration throughout the bar. From SEM analysis of the cross sections, it can be concluded that the tension on the braiding yarns provided sufficient pressure to force the resin in the core to flow outward and penetrate the Kevlar 29 sleeve. In addition to this finding, the pressure applied by yarn tension was uniformly distributed around the circumference of the rebar. This indication was observed from the shape of the carbon core in Figure 5.36. Changes in core geometry for both the 2-rib and 4-rib cases were previously demonstrated in Figures 4.15 and 4.16. These proposals for the use of a new preform, namely the 4-rib yarn bar, were verified by the microscopy results. It is evident that the use of four ribs greatly improves the microstructure than using the previous two- rib yarn design.

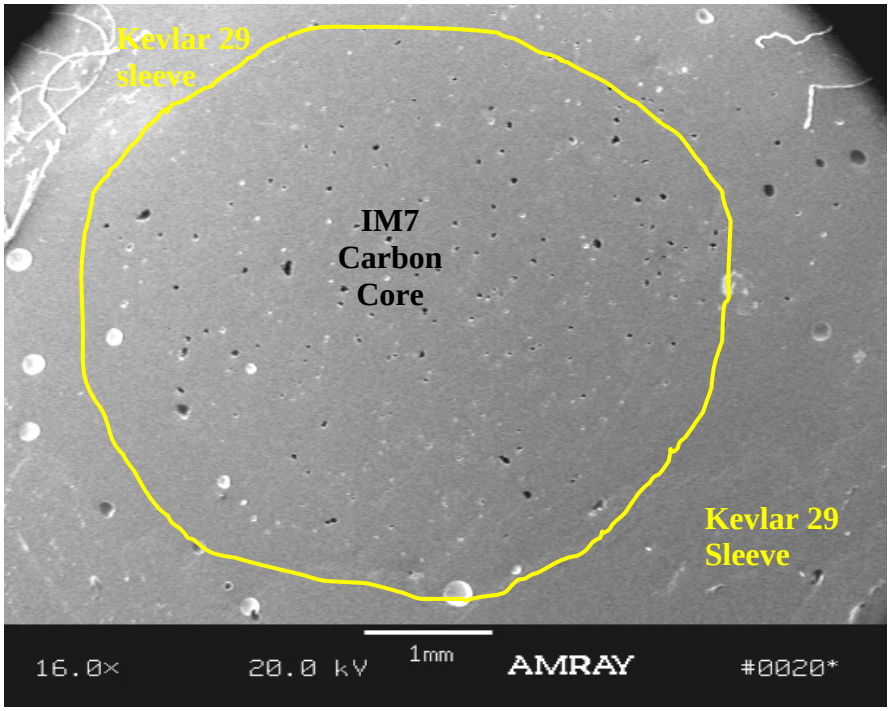

Figure 5.36: SEM Photograph of 4-Rib Yarn Rebar Cross Section at 16x Magnification.

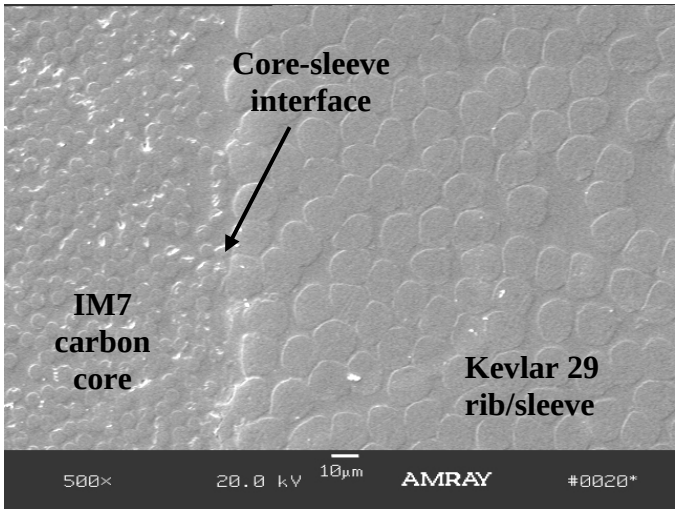

(a) Interface between IM7 carbon core and Kevlar 29 rib yarn at 500x magnification.

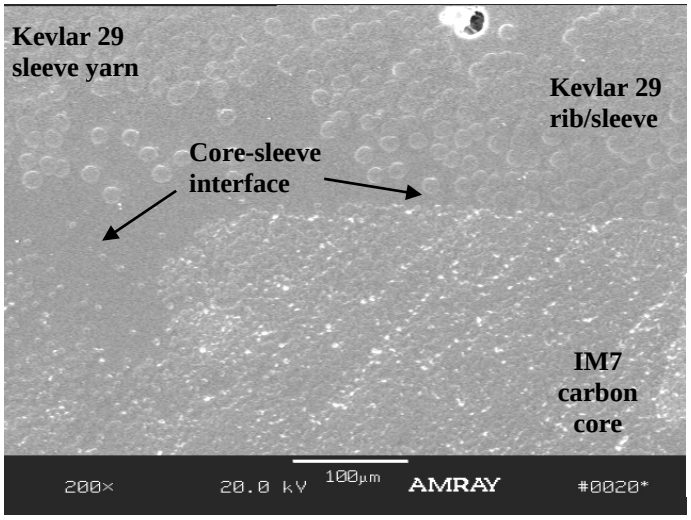

(b) Interface between IM7 carbon core and Kevlar 29 rib and Kevlar 29 rib at 200x magnification.

Figure 5.37: Core-Sleeve Interface of 4-Rib Yarn Bar Produced Without Die.

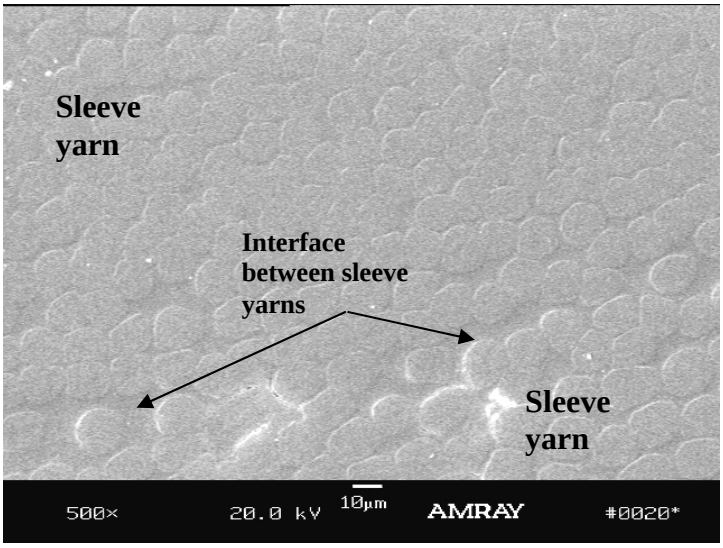

(a) Interface between 2 sleeve yarns at 500x magnification.

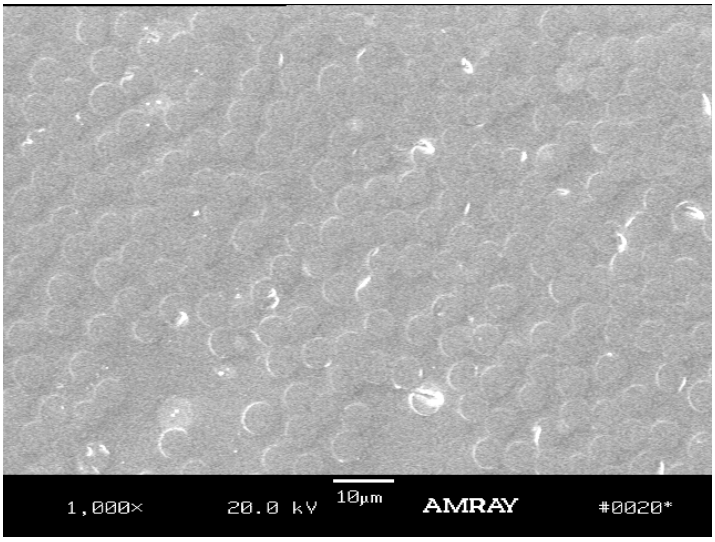

(b) IM7 carbon core at 1,000x magnification.

Figure 5.38: SEM Micrographs Showing Good Fiber Wet Out in Both Sleeve and Core Yarns; 4 Rib Yarns Produced Without Die.

5.2.2.3 Series 3: SEM of P55-S Bars with Original Preform and Manufacturing Process

The original manufacturing process of braidtrusion was to either pour or spray the resin at the fell point of the braid. Also, the original preform design was the unsymmetrical design using two rib yarns. This process appeared to work sufficiently well for the small diameter model bars, but for prototype-size bars, did not result in proper fiber wetting or consolidation.

Figure 5.39 shows the entire cross section of a bar at 15.9 times magnification manufactured using the original preform and process. First, there is an extremely large void in the core-sleeve interface in the bottom left corner of the bar and also some smaller but significant interfacial voids in the upper right corner. The width of the interfacial voids in the bottom left is up to ¼ of the entire core diameter. This demonstrates very poor consolidation of the sleeve and the core. Such a large defect would probably cause premature failure, since the strength of the resin is much lower than either fibrous system. Also, distributed throughout the core are many smaller voids (small black dots). This is also an indication that the core yarns were not sufficiently impregnated. Resin was either sprayed (model bars) or poured onto the sleeve just prior to the braiding point. While the sleeve yarns show good fiber wetting, it was impossible for the resin to penetrate the large rib yarn bundles and the entire core yarn, especially for the prototype-size bars. Finally, the shape of the core is extremely distorted, due to the uneven pressure of the unsymmetrical braided preform.

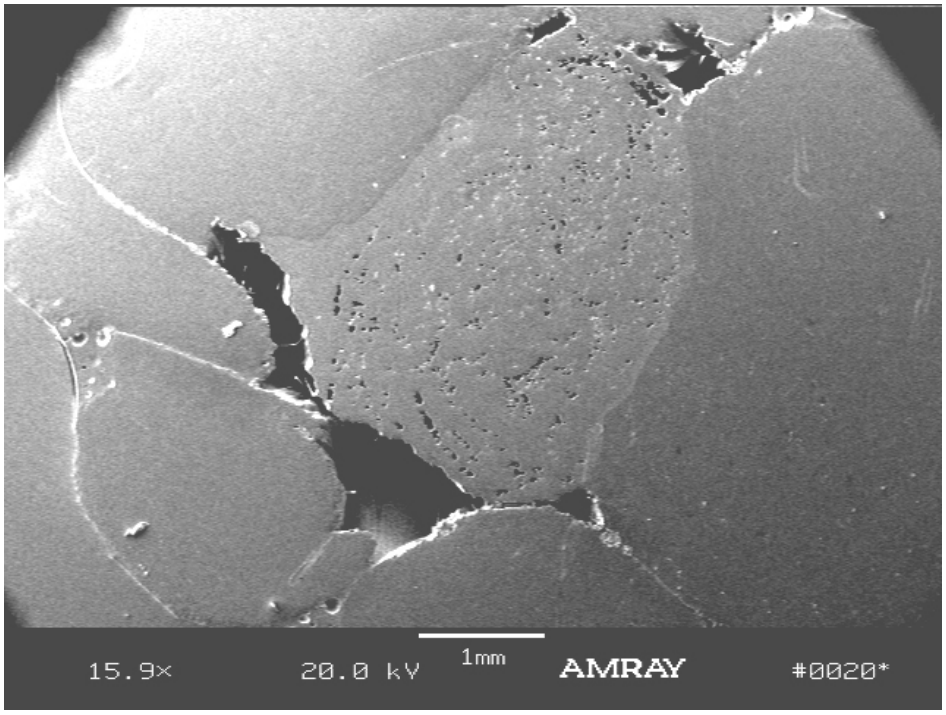

Figure 5.39: Entire Cross Section of Bar with Original Preform and Manufacturing Technique, 15.9 X Magnification.

Figure 5.40 shows the core-sleeve interface at 500 times magnification. This shows uniform yarn consolidation and good fiber wetting. However, this can be misleading since a high magnification factor was used and shows only a small segment of the interface. This was taken from the same bar as Figure 5.39, which had the large voids. Therefore, it is important to demonstrate scans at both low and high magnification for the DHFRP bars.

Shown in Figure 5.41 are the core yarns at 500 times magnification. Again there is good yarn consolidation. However, there are significant voids on the left and bottom portions of the scan demonstrating poor fiber wetting.

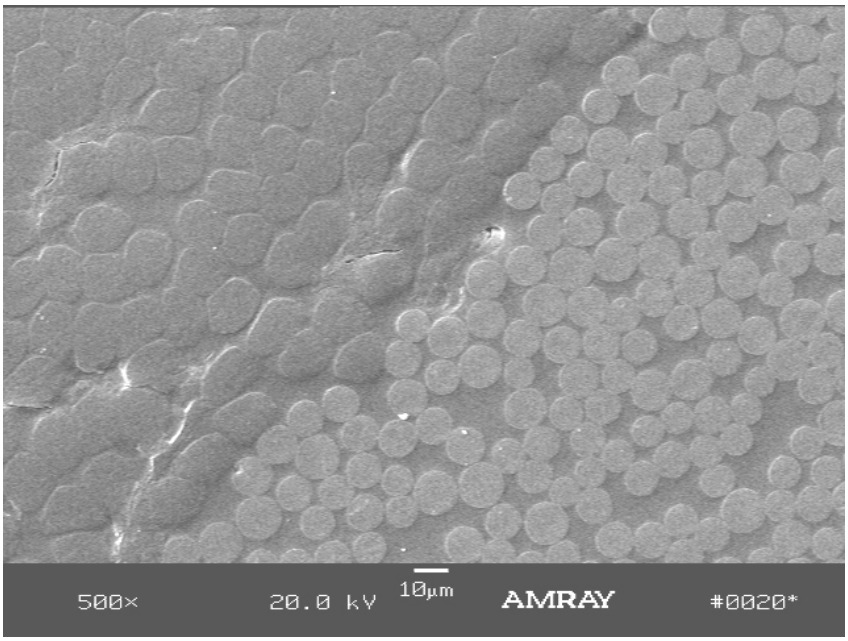

Figure 5.40: Core-Sleeve Interface of Originally Manufactured Bar, 500X Magnification.

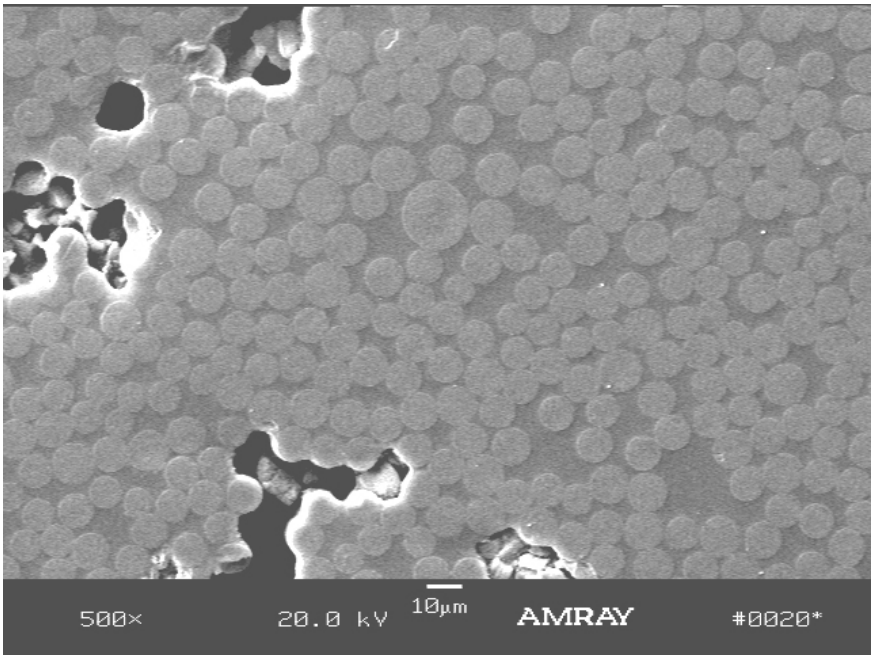

Figure 5.41: Core Yarns of Originally Manufactured Bars, 500 X Magnification.

It can be seen from these scans that the original preform and manufacturing process needed to be changed for the prototype-size DHFRP bars. This uncertainty in microstructure would result in uncertainty of material and mechanical properties.

5.2.2.4 Justification and Verification of Dieless Braidtrusion Process

Shown in Figure 5.33 was the cross section of a 2-rib yarn rebar, which was fabricated using a heated die and a post cure oven. As seen, these bars contained more voids, larger void size, and the voids were clustered into a region where there were no rib yarns. The core cross section was highly distorted along the length as predicted in Figure 4.15. Contrary to this was the use of 4-rib yarn bars manufactured using dieless braidtrusion. These bars showed good interface with good wetting and minimal core distortion (Figures 5.13 through 5.16 and 5.36).

This void concentration and core distortion can be explained by the effect of a pressure rise inside the die as the preform is pulled through. Consider a 10-mm diameter die with a tapered entrance shown in Figure 5.42. The main purpose of the tapered entrance was to generate a pressure rise inside the die, which assisted in removing excess resin and consolidating the preform. The braided preform was approximately 13-mm in diameter (measured from rib to rib). As it entered the die, the diameter of the preform gradually decreased by the tapered section of the die inlet. With pultrusion of a constant cross sectional profile, this theory is applicable since the composite has already cured as it exits the die. In braidtrusion of non-constant cross sectional profile such as a rebar, however, the composite cannot be cured inside the die. Partial curing was preferred at the die exit as this allowed the braided preform to spring back slightly in order to preserve the rib pattern on the surface. Expansion of

the preform relieved the pressure and since the composite was not fully cured the fibers loosened up, thus generating voids in the structure and separation along the core-sleeve interface at some regions. Regions of high void contents were found along the core-sleeve interface where there were only sleeve yarns, whereas along the rib yarns the void content was much less because of the pressure difference. Again, the model shown in Figure 5.42a, b and the cross sections in Figures 4.15 and 4.16 can explain this. A cross section of the die showing intimate contact between the rebar surface and the die wall demonstrates the pressure at this location is much greater. Higher pressure provided better compaction, and hence, lower voids content. However, as the composite exited the die this highly compressed area tended to spring back more leaving a discontinuity across the interface and distorted core shape as illustrated in Figures 5.33 and 5.42c. In regions of lower pressure or regions in the absent of rib yarns, high concentrations of voids along the core-sleeve interface were likely to occur. There was no contact between the die wall and the rebar itself, and therefore, the pressure was not enough to eliminate the entrapped air pockets. These regions underwent absolutely no or very small pressure throughout the process, so bar spring-back at the die exit did not exist, and hence separation across the core-sleeve interface was not likely to happen.

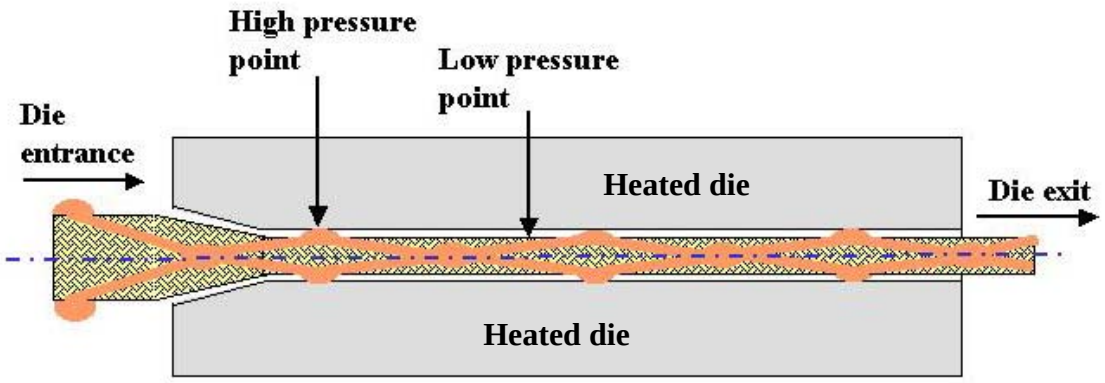

(a) Schematic diagram of preform inside heated die

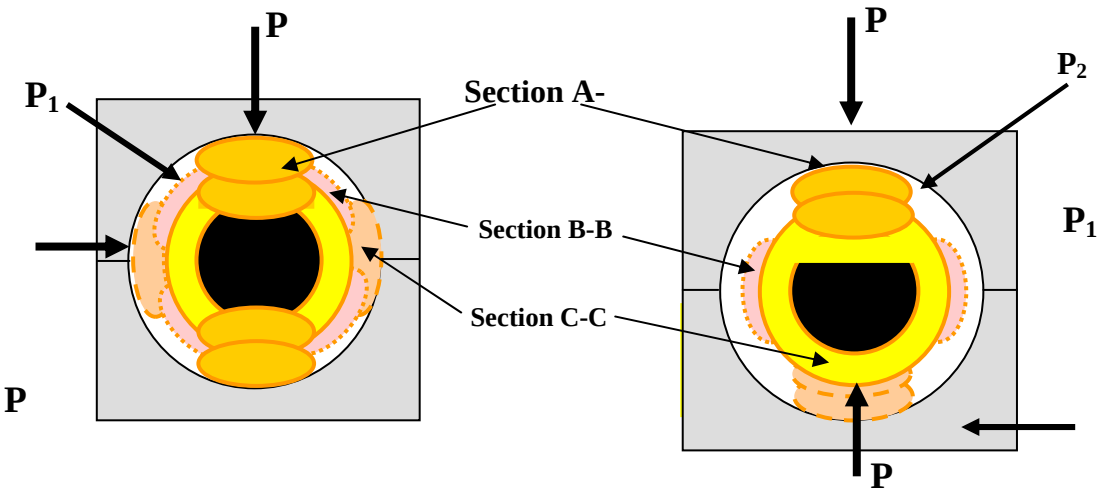

$(P > P_1)$ $(P > P_1 > P_2)$

(b) End view of 4-rib yarns rebar

(c) End view of 2-rib yarns rebar

Figure 5.42: Effects of Pressure on Rebar at Various Locations Inside the Die (Lam, 2001).

From the above observations it can be concluded that manufacturing of rebar by braidtrusion is possible without the present of a heated die. SEM verified enormous improvements in rib symmetry when 4-rib yarns were used. The void content was noticeably less as a result of uniform pressure during consolidation. Proper yarn tension provided adequate hoop pressure that functioned similar to a metal die. Dieless braidtrusion or pultrusion is highly favorable since the processing cost can further be reduced due to lower tooling cost and time-savings cost due to the periodic die cleaning.

5.3 Comparison of Previous and New 10-mm Diameter DHFRP Bars

Three series of 10-mm rebars were compared on a micro-structural basis. These various bar types are compared in the flowchart shown in Figure 5.43. It is possible to also compare the bars on a visual inspection basis as well. Many of the previous conclusions can be confirmed by inspecting the outside surface condition of the various types of 10-mm DHFRP bars made. As shown in Figure 5.43, bar variation parameters included geometry (two versus four rib yarns), material (different core/ sleeve systems), and processing (die and dieless pultrusion). These variations are shown visually in the following figures.

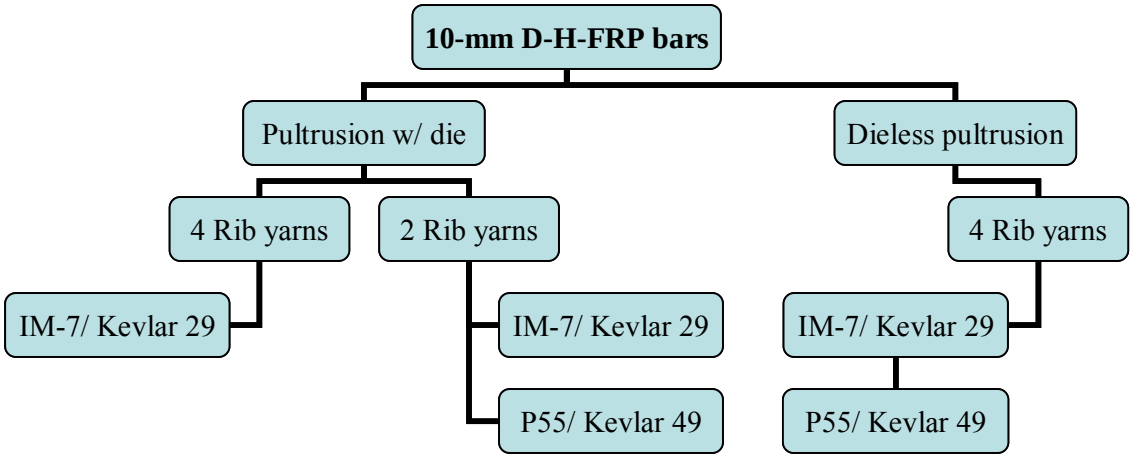

Figure 5.43: Flowchart of the Various Types of 10-mm DHFRP Bars Developed.

Before the bars were manufactured, the yarn could be compared on a visual basis. Kevlar yarn is influenced by ultraviolet light. Even though the strength properties do not change much, the color of the yarn changes with exposure to light. Shown in Figures 5.44 and 5.45 are yarn bundles of Kevlar 49 yarn. The color of the yarn depended on the duration of the exposure to sunlight. The two yarn bundles shown in Figure 5.44 have various colors, dependent on the exposure to sunlight. Kevlar yarn with no exposure to sunlight was bright yellow. As the duration of the exposure to sunlight increased, the color became darker as shown in the figure. This was more evident in Figure 5.45 which is a close up of the yarn bundle. The left and center portion of the yarn bundle was yarn with little or no ultraviolet exposure while the right side of the bundle had moderate exposure. This variation in exposure caused

the color of the final DHFRP bar to vary; however, this exposure was inevitable since the yarn bundles remained on the yarn carriers for an extended period of time.

Figure 5.44: Yarn Bundles of Kevlar 49 Yarn Showing Color Variation Due to Ultraviolet Light.

Figure 5.45: Kevlar 49 Yarn Bundle Showing Unexposed Yarn (left side) and Exposed Yarns (right side).

Various processing parameters were evident when the bar was examined after manufacturing. These included the use of two rib yarns versus four yarns, the use of a die and various die heating parameters versus dieless braidtrusion, and the use of a post-curing oven.

Shown in Figure 5.46 is a bar manufactured using an IM-7 carbon core and a sleeve of Kevlar 29 yarn. This was a two-rib yarn bar using a fully-heated die and post-cure oven. The die heating profile provided by Shell Chemical for the Epon 9500/ EPICURE 9550 Resin system was used. Details of the heating profile were given in Chapter 4. For traditional pultrusion, when the composite part exits the heated die, the part is almost fully cured. It will not change shape upon exiting the die. Also, pultruded parts traditionally have constant cross section. As seen in Fig. 5.46, the DHFRP bar is circular and smooth with a constant cross section. There is no deformation pattern on the bar produced by the ribs. When the bar entered the die, the pressure provided by the die consolidated the bar into a smooth, circular cross section. The heat provided by the die then cured the bar so when the bar exited the die, a cured smooth circular bar of constant cross section resulted. From a composites manufacturing viewpoint, this bar was a correctly pultruded part; however, since there is no surface deformation, it is impractical to be used for rebar since the bond strength is very low. Therefore, a heated die using the resin manufacturer's specifications could not be used, and therefore, the specifications were modified.

Figure 5.46: Two Rib-Yarn Bar Made with Fully-Heated Die, IM-7/ Kevlar 29 System.

The die heating schedule was experimented with and modified to produce a bar that was both cured and had a deformation pattern. The higher the die temperature, very little deformation pattern existed on the bar surface, while if the temperature was too low, a good deformation pattern existed on the bar surface, but little consolidation of the bar occurred. Shown in Figure 5.47 is a bar with two rib yarns made of IM-7 carbon and Kevlar 29 using a die with a lower die temperature. As explained earlier in this chapter, this allowed the bar to partially cure when exiting the die, but also provided for some rebound of the bar to produce some deformation pattern. As shown by the microstructure of the bar, this process lead to a bar that had the most number of voids due to this expansion of the bar after exiting the die. This expansion pulled the sleeve away from the core, therefore causing large voids to exist. This was more evident when the die temperature was lower and more post-die expansion was allowed.

Figure 5.47: Two Rib-Yarn Bar Made with Partially-Heated Die, IM-7/ Kevlar 29 System.

Shown in Figures 5.48 and 5.49 are two rib-yarn bars of IM-7 and Kevlar 29 manufactured using both a die and a post-curing oven. Only a partial curing was performed since there is still a deformation pattern on the bar. The large white bubbles are resin that cured on the underside of the bar in the post-cure oven. These white resin drops did not exist when the bar exited the die, but appeared when the bar exited the post-cure oven. When the bar entered the oven, the viscosity of the resin decreased due to the increase in temperature. This decrease in viscosity caused the resin to flow again since the bar was not fully cured exiting the die. The flowing resin began to drip on the underside of the bar due to gravity. However, as it dripped, the heat in the post-cure oven was sufficiently high to cause the resin to cure while flowing (i.e., dripping) out of the bar. The resin was then heated by the post-cure oven and froze into large cured droplets on the underside of the bar. Note the large amount of air contained in the resin evidenced by the large air bubbles present. This created an aesthetic problem for the bar as well as a wetting problem since resin was flowing out of the bar. This release of the resin caused dry fiber and voids to exist, resulting in poor interface between yarns. The post-cure oven temperature was modified to

minimize this effect, but the temperature increase produced by the post-cure oven always produced the resin bubbles to form.

Figure 5.48: Two Rib-Yarn Bar Made With Partially-Heated Die and Post-cure Oven, IM-7/ Kevlar 29 System.

Figure 5.49: Detail of Two Rib-Yarn Bar Made With Partially-Heated Die and Post-cure Oven, IM-7/ Kevlar 29 System.

Shown in Figures 5.50 through 5.53 are bars consisting of P-55S 4K carbon and Kevlar 49. These bars consisted of four rib yarns. These bars were made using the dieless pultrusion process, explained in Chapter 4. As previously described, the

use of four rib yarns provided enough confining pressure to squeeze out the resin from the core. The symmetric rib-yarn pattern acted as a spring die or coil that compressed the bar. As seen in the SEM micrographs, resin-rich regions existed in these bars due to less confining pressure that a die would exert on the preform. Since no post-cure oven was used for these bars, there were no frozen resin bubbles on the underside of the bar. Some resin flow did occur, however, due to gravity, but not as much as the flow in the post-cure oven since the resin viscosity was higher.

Figure 5.50: Four Rib-Yarn Bar Made Using Dieless Pultrusion, P55/ Kevlar 49 System.

Figure 5.51: Closeup of Four Rib-Yarn Bar Made Using Dieless Pultrusion, P55/ Kevlar 49 System.

Figure 5.52: Cross-Sectional View of 4-Rib Yarn Kevlar 49 Bar with P-55S Carbon Core.

Figure 5.53: View of 4-Rib Yarn Kevlar 49/ P55S Bar Showing Deformation Pattern.

CHAPTER 6. STATIC CHARACTERIZATION OF DHFRP BARS

6.1 Background

The microstructure of the DHFRP bars was quantified by SEM microscopy (Chapter 5). This analysis was a first order verification of the quality of the bar. Since the microstructure was good with excellent fiber wetting and interface between the core and sleeve, good mechanical properties should result.

Short-term testing of materials is required to get fundamental material properties. As mentioned earlier, several parameters needed for proper design using DHFRP were sufficient strength, elongation, and stiffness, and sufficient bond and development length when placed in concrete elements. The first set of properties and general mechanical behavior are developed from testing the bar in static axial tension. This test provides the general behavior of the bar, and therefore, is crucial. Bond and pullout tests are used to get the bond strength and development length data. This is also dependent on the deformation pattern and rib properties. Therefore, these properties and the bar surface geometry must be quantified to compare the DHFRP bar with conventional steel reinforcement.

Two tests, the uniaxial tension test and the bond strength test were conducted. Results were compared to conventional steel reinforcement and with theoretically predicted values. The values were then compared to the model 5-mm diameter DHFRP bars to evaluate the scale-up and modeling effects.

6.2 Tensile Characterization

The tensile behavior of the DHFRP was previously characterized for 3-mm and 5-mm diameter model bars by Somboonsong (1997). The current research was to characterize the tensile behavior of prototype bars with a nominal diameter of approximately 10-mm. Tension testing of various FRP bars was conducted by Vermeeren and Tsang (2001), Gerritse (2000), and Castro and Carino (1998) and was discussed in Chapter 2. From the tension test, many crucial mechanical properties of the material are derived. The fundamental design concept of DHFRP was to develop an FRP bar that behaves similarly to conventional steel rebar. Shown in Figure 6.1 is a typical stress-strain curve for mild steel (Gere, 2000) which shows these basic material properties. Since the predicted behavior was that the DHFRP should behave similar to steel, these same material properties and behaviors should also be evident. The desired material properties that should result from the experimental DHFRP stress-strain behavior are summarized in Table 6.1.

As seen in Figure 6.1, three distinct regions exist for the stress-strain behavior of steel up to the ultimate load: linear elastic region, perfect plasticity or yielding region, and the strain hardening region. Since composite materials do not neck, the third region is not necessary for comparison. At least two of these regions are desired for the behavior of DHFRP, namely the linear elastic region and the yielding region, with an ultimate strength greater than the yield strength. From the theoretical analysis performed in Chapter 5, the DHFRP bar should have a definite yield point followed by an increase in load to an ultimate strength higher than yield. This should result in a bilinear stress-strain curve.

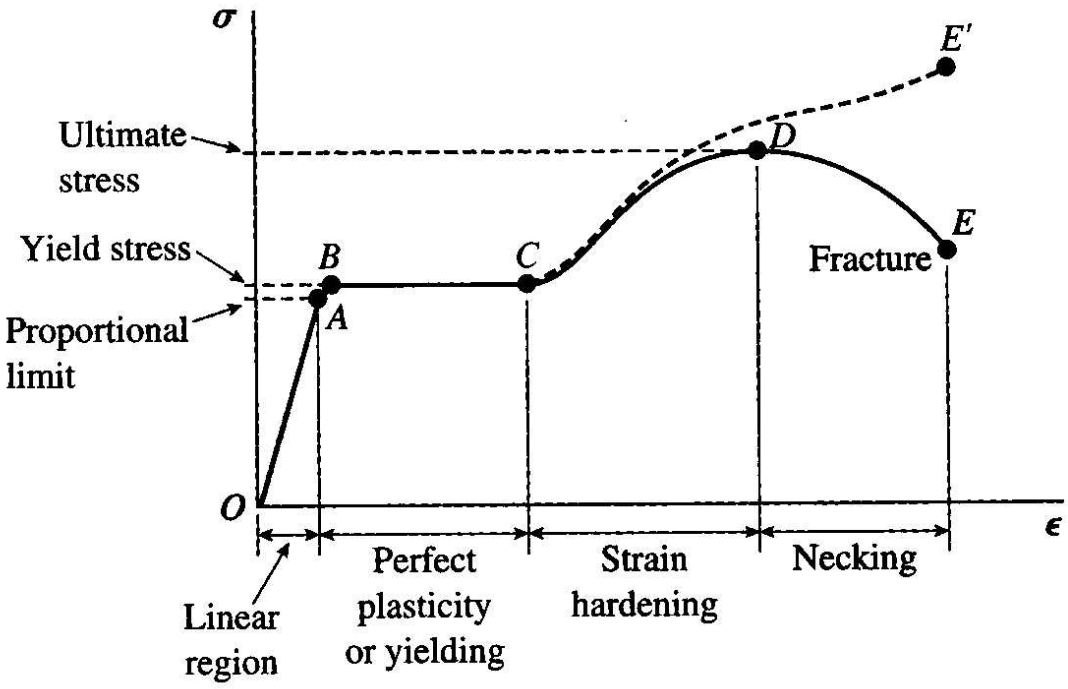

Figure 6.1: Typical Stress-Strain Behavior for Mild Steel (from Gere, 2000).

Table 6.1: Steel Material Properties to be Duplicated by DHFRP.

Material Property	Symbol	Comments
Modulus of elasticity	E	
Yield stress	σ_y	
Yield strain	ε_y	
Stress @ strain hardening	σ_{sh}	Point *C* in Fig. 6-1
Strain @ strain hardening	ε_{sh}	"
Ultimate stress	σ_u	
Ultimate strain	ε_u	

6.2.1 Definitions of Cross-Sectional Area of DHFRP Bars

Since composites materials are comprised of oriented fibers and resin, the material behavior is anisotropic. Specifically, the DHFRP bar is comprised of two different fibers and resin and has an uneven or rough surface geometry, creating a non-uniform cross-sectional area along the bar length. Therefore, for stress calculations, the gross cross-sectional area cannot be used since this assumes the entire cross-sectional area resists the load uniformly (i.e., isotropic behavior). Two areas were defined for the cross-sectional area of the DHFRP bar: the specific area, A_{sp}, and the volumetric area, A_{vol}.

The specific area, A_{sp}, defined in Chapter 5 (Eqns. 5-11, 5-12 and 5-16), was defined as the area of each yarn times the number of yarns, considering any yarn orientation if present. This area is based on the denier of the yarn. For the total bar it is given as

$$A_f = \left[\frac{N_y(\theta) A_{sp}(\theta)}{\cos\theta} + N_y(0°) A_{sp}(0°) \right] = A_b + A_{core} \qquad 6\text{-}1$$

where $A_{sp}(\theta)$ and $A_{sp}(0)$ were defined in Equations 5-11 and 5-12, respectively. For the prototype DHFRP bar, the A_{sp} was 0.0758 in^2 (48.9 mm^2). This included the area of the unidirectional core yarns and the oriented braid and rib yarns.

The volumetric area was based on the change in volume of water when a piece of DHFRP was placed in a graduated cylinder. A piece of bar of known length was placed in a graduated cylinder filled with a known volume of water. The change in volume of the water was measured. From this, the diameter of the DHFRP bar is given as

$$d = \sqrt{\frac{4}{\pi} \frac{\Delta V}{l}} \qquad 6\text{-}2$$

where ΔV is the change in volume of the water and l is the length of the bar specimen. This method produced an average bar diameter of 0.373 in (9.47-mm) and an average area of 0.1092 in^2 (70.45 mm^2). The average values are shown in Table 6.2. Also shown is the nominal area of the bar, taking diameter readings from rib to rib and from braid yarn to braid yarn, and averaging the results to get a nominal diameter.

Table 6.2: Definitions of DHFRP Cross-Sectional Areas.

Measurement	**Bar diameter, in (mm)**	**Area, in^2 (mm^2)**	**Percent difference from A_{vol}**
Specific area	N/A	0.0758 (48.9)	- 30.6%
Volumetric area	0.373 (9.47)	0.1092 (70.45)	—
Nominal area	0.441 (11.2)	0.1524 (98.3)	+ 40%

6.2.2 Sample Preparation

The 10-mm diameter DHFRP bars needed to be prepared before they could be tested. First, since composite materials are weak in the transverse direction, if the bar was directly gripped into a testing machine, the bar would fail prematurely due to a large stress concentration factor at the grips. Therefore, a way to grip the bars needed to be developed. End grips or tabs were developed for this purpose.

Once the tension specimens were cut to length, the ends of the bars were sanded using 60-grit sandpaper. Sanding made the surface of the bar inside the end grips rough, thereby increasing the frictional bond between the bar and the material used for the end tabs. A detailed discussion of the use of end tabs is discussed in the next section. Shown

in Figure 6.2 is the bar preparation for end tab casting. The bar was manually sanded two times and then sprayed with isopropyl alcohol to clean the surface.

Figure 6.2: Sanding of the Bar Ends for End Tab Casting.

6.2.3 End Tab Development

The gripping of prototype-size DHFRP bar for tensile tests was very difficult. Various end tab types and methods were tried before two methods were chosen. Table 6.3 shows the various types of end tabs that were developed for the 10-mm bars. Some of these tabs were successful and some were not as indicated.

Table 6.3: Various End Gripping Methods for Prototype Size DHFRP Bars.

Tab Type	**Machine Used**	**Results**
3" x 6" concrete cylinders	Adaptable for any machine	Unusable for moderate to high load levels
Trapezoidal end tab, unreinforced	Tinius Olsen 10000 lb Bench-type	Failure—debonding and lateral confinement failure
Reinforced trapezoidal tab	" "	Work—necessary for high load levels
Cylindrical pipe tab	Any machine with wedge action grips	Work—necessary for high load levels

6.2.3.1 Cylindrical Concrete End Tabs

Earlier DHFRP bars were tested using a Tinius Olsen 10000 lb capacity Universal bench-type machine. Cylindrical concrete end tabs were used to grip the ends of the bar. A special mounting device was designed to fit in the Tinius Olsen machine or any other universal machine. The bars were cast in 3" x 6" concrete cylinders as shows in Figure 6.3. This figure shows the mounting device which consisted of a set of plates connected by threaded rods. The concrete mixture consisted of gypsum, sand, and water as listed in Table 6.4. Gypsum was used rather than regular cement since it sets rapidly (24 hours) compared to cement. After the concrete was thoroughly mixed the end of the bar was carefully centered inside a plastic cylinder as shown in Figure 6.4. The concrete mixture was slowly poured into the cylinder and allowed to set overnight.

This gripping device was initially used for the first series of 10-mm diameter prototype bars manufactured using the original preform design and manufacturing process. These bars had lower strength, and therefore, the cylinders provided adequate embedment and anchorage for these bars.

The next set of bars tested were Kevlar 29/IM7 bars with 2 rib yarns. These bars were originally manufactured using pultrusion with a die, and therefore, the rib profile was low. During testing the concrete tabs showed weak bonding between the rebar and concrete. Pullout failure occurred during these tests. This pullout failure is evident in Figure 6.5. This gave impetus in modifying the preform to include a symmetric pattern with closer rib spacing for increased bonding. During testing of the higher-strength materials, the plates began to flex at higher load levels. This caused both axial and bending effects. Because of these second order effects, the use of gypsum-concrete end tabs was discontinued.

Figure 6.3: Tensile Testing of Prototype DHFRP Bar Using Concrete Cylinder End Tabs and Steel Plate Mounting Device.

Table 6.4: Formulation for Gypsum Concrete Mix.

Materials	**Ratio (pbw)**	**Batch Mix (lb)**
Gypsum	1.0	1.8
Sand	1.2	6.0
Water	0.3	7.2
Note: Each batch is enough to fill 4 end tab cylinders.		

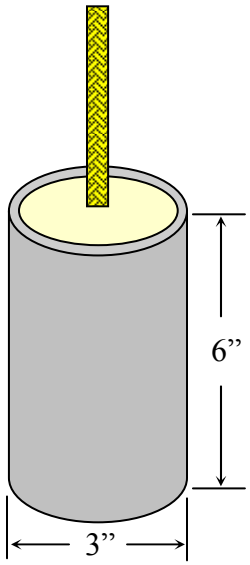

Figure 6.4: Cylindrical Concrete End Tab Casting.

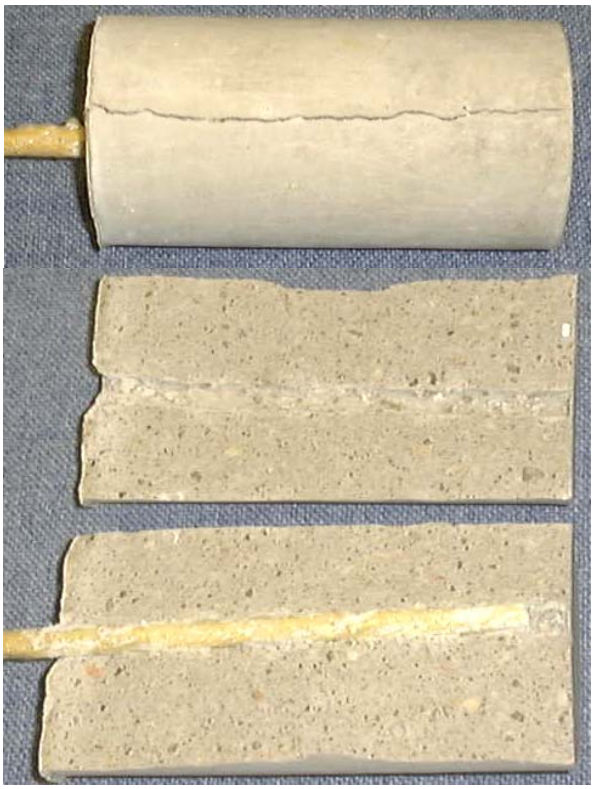

Figure 6.5: Pullout Failure of Bars Embedded in Cylindrical Concrete End Tabs.

6.2.3.2 Trapezoidal Epoxy End Tabs

The next type of end tab used was an epoxy end tab using a trapezoidal geometry. These trapezoidal end tabs were successfully used for 5-mm diameter DHFRP model bars. The geometry of these tabs fit the existing grips of the Tinius Olsen machine, and therefore, was used again.

Molds for casting the end tabs were built from GI-1000 Silicone Rubber (Plastic Tooling Supplies). The end tab was originally designed for 3-mm and 5-mm rebars and seemed to work well. A wooden box with a trapezoidal shape was built and an epoxy end tab was placed at the center of the box (Figure 6.6). A mixture consisting of 10 parts

by weight (pbw) GI-1000 base and 1 pbw GI-1000 initiator as recommended by the supplier was used. Each mold required 450 grams of GI-1000 base and 45 grams of GI-1000 initiator. The rubber mixture was poured and cured 24 hours at room temperature for setting. These end tab molds were made to fit in the Tinius Olsen grips with dimensions shown in Figure 6.7.

Figure 6.6: Wooden Form Containing Plug for End Tab Mold Casting.

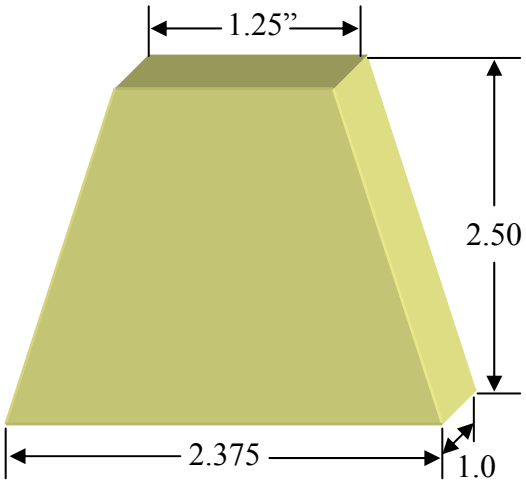

Figure 6.7: Dimensions for Glass-Reinforced Epoxy End Tab.

The first series of prototype bars were cast using these end tabs. The bars were cast horizontally in aluminum molds. Shell Epon Resin 9500/ Epi-Cure 9550 curing agent without internal mold release was used. Chopped E-glass fibers were mixed into the resin during casting. The samples were placed into the Tinius Olsen 10000 machine as shown in Figure 6.8. The tests were ended prematurely due to failure of the end tabs. The end tabs did not provide enough confinement, and therefore, failed outward due to lateral pressure. Therefore, if this end tab was to be used, modifications needed to be made.

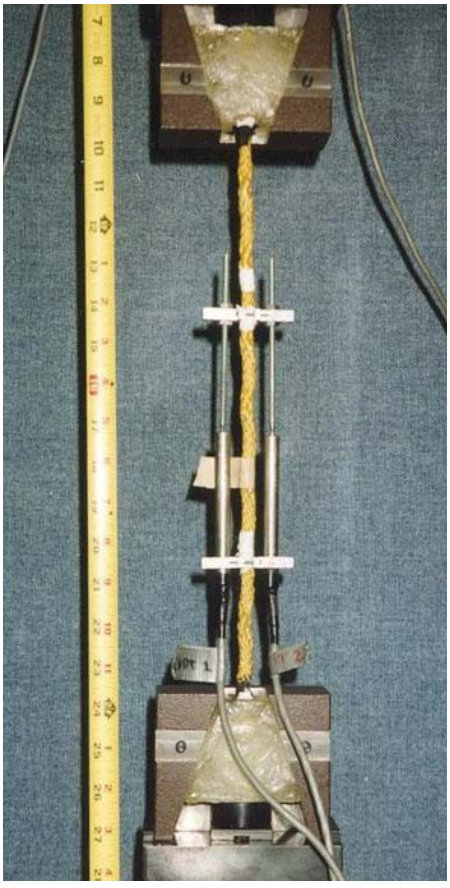

Figure 6.8: Original Epoxy End Tab for Prototype Tension Testing of DHFRP Bars.

Since this end tab geometry fit the existing grips of the available testing equipment, this same geometry was used. However, the end tab instead of being just an epoxy tab with a limited amount of chopped fiber was now designed as a composite part itself. The end tab was reinforced with layers of continuous braided fabric. Chopped fiber was placed inside this tube of fabric to arrest cracking of the epoxy matrix. The idea is similar to concrete columns that are wrapped with E-glass fabric to increase the confinement and ductility. The braided fabric would increase the hoop strength of the end tab, thereby preventing premature failure. Also, by using the new DHFRP preform, which had twice as many deformations as the original preform, the bond strength of the bar would be increased, thereby preventing pullout failure.

Casting of the end tabs was done by standing the mold upright on its end. An aluminum plate was placed in front of the mold and fixed with C-clamps (Figure 6.9). The edges were sealed with Silicon sealant to avoid resin leakage during casting. Since earlier studies indicated failure of end tabs due to lack of confinement, three layers of E-glass braided sleeves (Figure 6.10) were used to line the inside of the mold. The rebar end was inserted and carefully centered and additional E-glass chopped strand mat were added into the mold, around the end of the bar. Glass mat pieces were added until the mold cavity was filled. Shell Epon Resin 9500/Epi-Cure 9550 curing agent without internal mold release was mixed and slowly poured in from the top of the mold (Figure 6.11). Curing took place at room temperature for 24 hrs before the cast was removed from the mold. Figure 6.11 shows the finished end tab with braided glass reinforced.

A horizontal cast was tried but did not work well with the layers of braided fabric. Large air voids were trapped under the fabric since the fabric was on the free surface of

the molds. When the casting was vertical, the free surface was the top of the end tab, which had no reinforcing, and therefore, air could escape. This provided the most uniform and void-free reinforced-epoxy end tab.

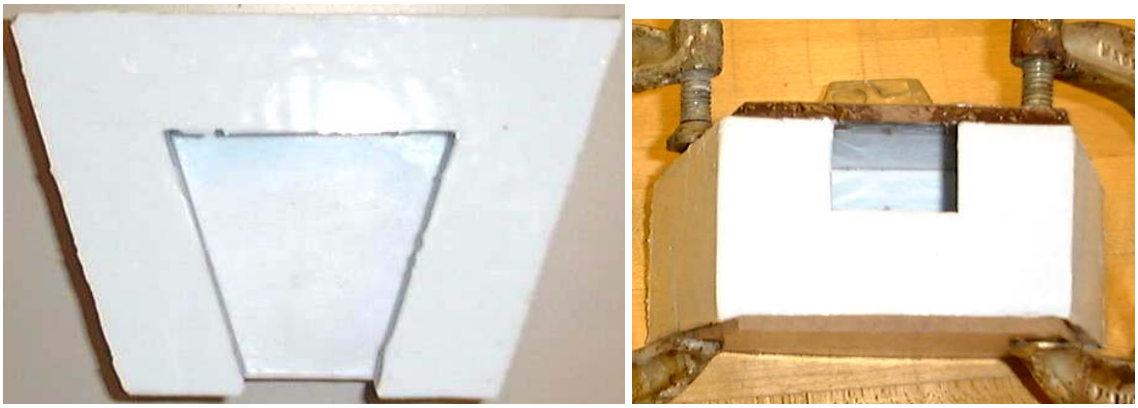

(a) (b)

Figure 6.9: (a) Silicon Rubber Mold for End Tab; (b) Mold in Upright Position with Front Covered.

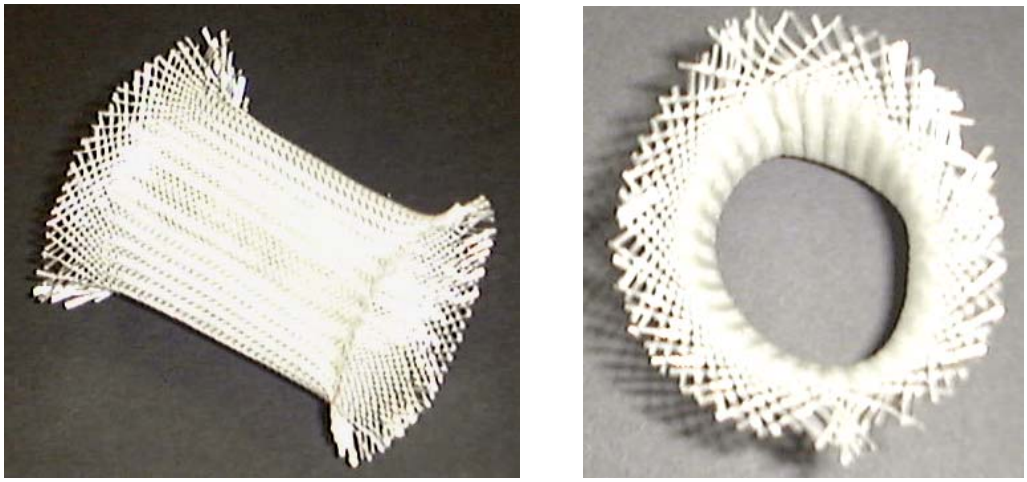

Figure 6.10: E-Glass Braided Glass Sleeve for Reinforcing End Tabs.

Figure 6.11: Setup for End Tab Casting.

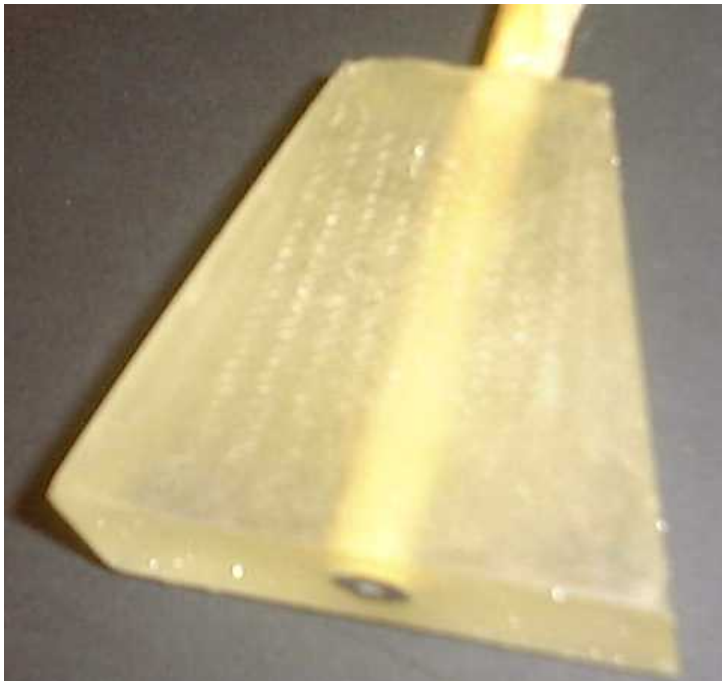

Figure 6.12: Braided Glass Sleeve-Reinforced End Tab.

6.2.3.3 Cylindrical Steel Pipe End Tabs

The third type of end tab developed to test prototype-size DHFRP bars was a pipe-type end grip. These end tabs could be used in any machine that has a wedge-action type grip, such as a 120K Universal Tinius Olsen machine. These end grips provided a circular pressure that was continuous and uniform around the circumference of the pipe.

A diagram of the ¾" pipe end tab used for 10-mm DHFRP bars is shown in Figure 6.13. Schedule 160 pipe was used with an outside diameter (O.D.) of 1.05" and an inner diameter (I.D.) of 0.614". One end of the end tab was threaded using a standard thread. These were then threaded into an articulation device so the bar was tested under purely axial loading conditions, with pin connections on both ends. The inside of the pipes were roughened using a dull drill bit to increase the bond strength between the pipe and the grout used for the end tab. The pipes were cleaned using M-1 Remover metal cleaner (Jomaps, Inc.).

Shown in Figure 6.14 is the device to mount and cast the pipe end tabs. An epoxy grout was used, Sikadur 34 (Sika Inc.). This is a commercial-grade epoxy grout used in construction for anchor bolts. The properties and mix ratio of Sikadur 34 are given in Table 6.5. The epoxy was mixed in an aluminum can.

The open end of the pipe was sealed with duct tape. The pipe was approximately half filled with epoxy. The bar was then placed in the pipe and centered. This ensured that the epoxy was in the bottom of the pipe. The pot life of the resin was approximately 30 minutes so pouring had to commence immediately after mixing occurred. The manufacturer's specifications stated that the annular space around the hole should not exceed 1/8-in (3.17-mm). This was to keep the epoxy layer between the DHFRP bar and

the inside pipe wall small. Each end was cured for 12 hours before the other end was cast. Shown in Figure 6.15 is the casting of the epoxy-filled pipe end tabs.

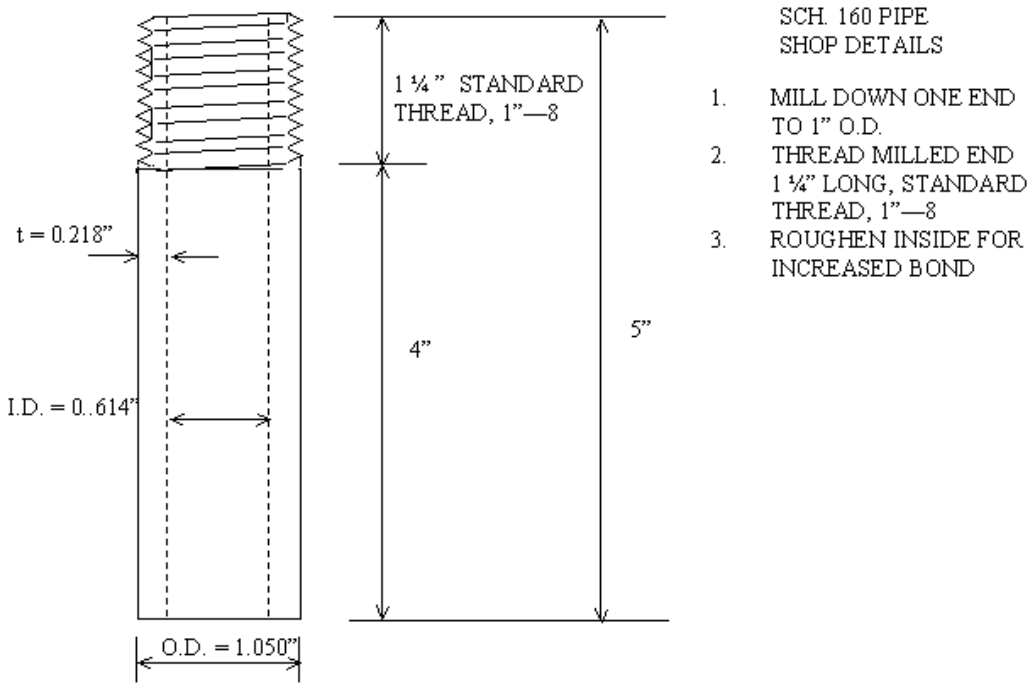

Figure 6.13: Detail of Pipe End Tab for Test Series II.

Table 6.5: Properties of Sikadur 34 Epoxy Grout.

7 day Tensile Strength	8,900 psi (61 MPa)
Elongation at Break	5.4%
14 day Flexural Strength	14,000 psi (97 MPa)
14 day Shear Strength	5,100 psi (35 MPa)
2 day (dry cure) Bond Strength	2,800 psi (19 MPa)
7 day Modulus of Elasticity	21.5 X 104 (1,500 MPa)
Mixing Ratio Component A : Component B	2:1 by volume

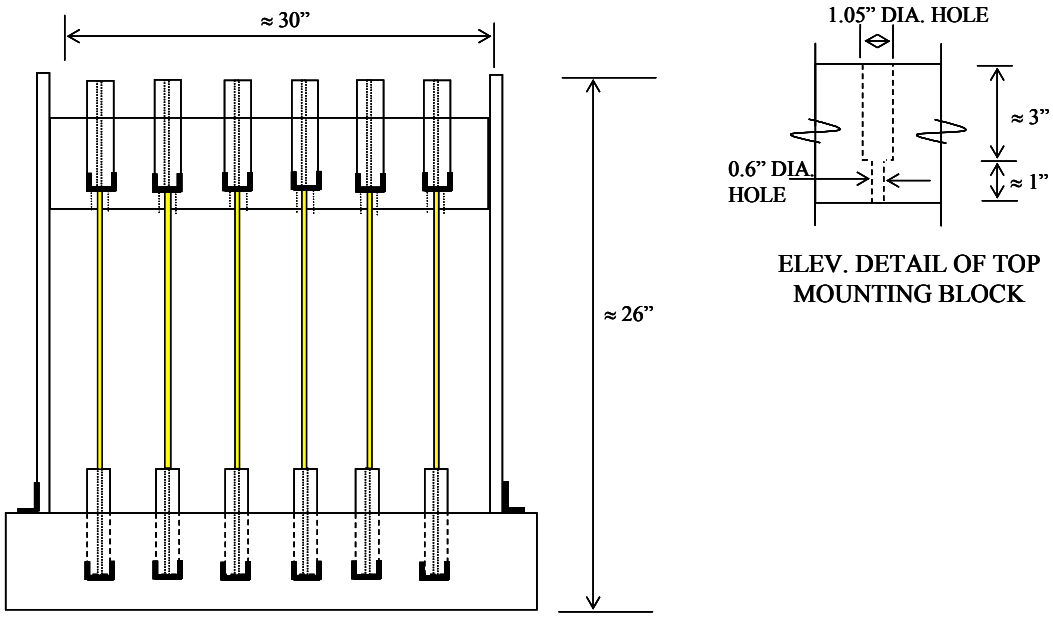

Figure 6.14: Detail of Tension Specimen Mounting Device for Series II Tests.

Figure 6.15: Placement of 10-mm Bars in End Tab Mounting Device, Series II.

6.2.4 Test Procedure

The test setup and procedure was different for each type of end tab used. Only the reinforced-epoxy end tabs (Sec. 6.2.3.2) and the epoxy-grouted pipe end tabs (Sec. 6.2.3.3) were used. Since different machines were needed for each type of tab, the testing setup and procedures are described for each test series.

Test Series I was conducted using a Tinius Olsen 10000 lb (50 kN) capacity universal bench-type machine. The reinforced trapezoidal end tab fit into the existing grip of this machine. A System 4000 data acquisition system (Measurements Group, Inc.) was used to collect data. Three channels were used, one for load and two for extension measurement. Two linear variable differential transducers (LVDT) gauges to measure extension were attached to the test specimen. Figure 6.16 shows a schematic of the LVDTs used for the testing. Figure 6.17 shows the mounting of the LVDTs onto the 10-mm DHFRP bars. Mounting was difficult due to the uneven surface of the bar. Once the LVDTs were mounted to the bar, the bar was placed into the grips of the testing machine. The LVDTs were then connected to the System 4000 data acquisition system. Steel plates were placed over the machine grips and secured with C-clamps to provide additional confinement and to prevent injury if any sudden failure of the end tabs occurred. This is shown in Figure 6.18.

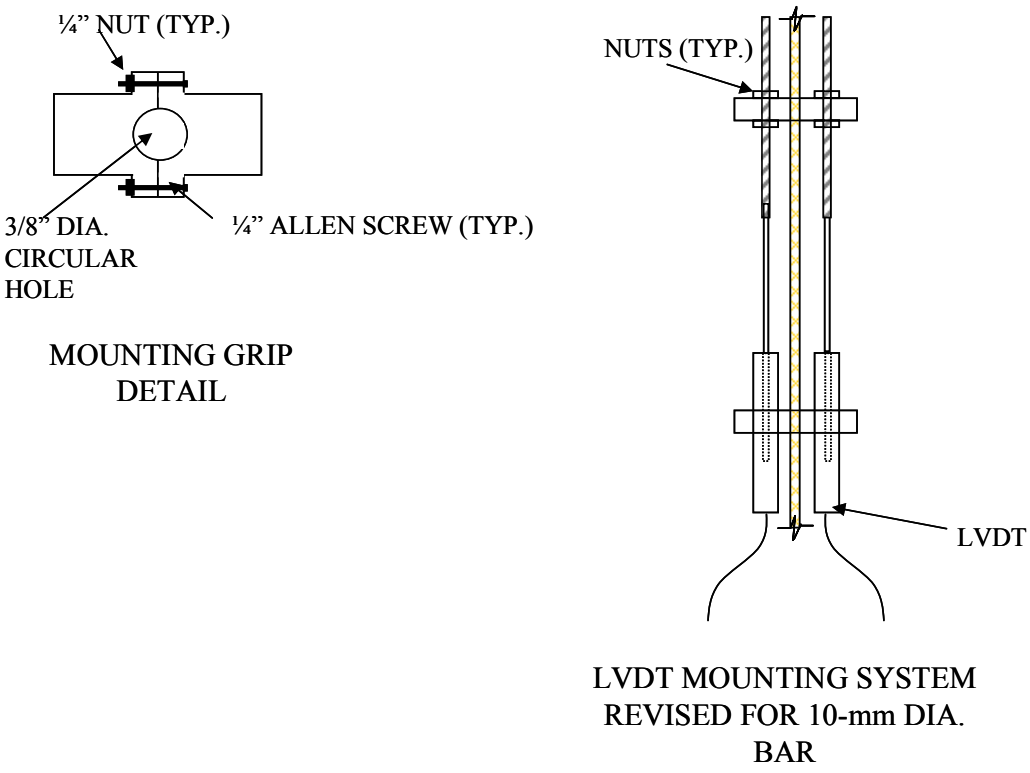

Figure 6.16: Diagram of Revised LVDT System for 10-mm Tension Test, Series I.

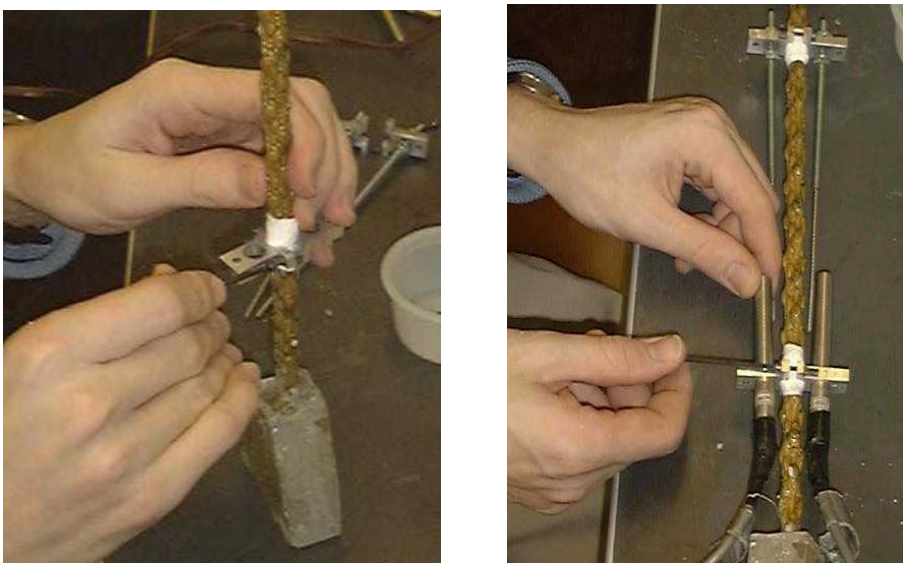

Figure 6.17: Details of Mounting LVDT To 10-mm Bars, Series I.

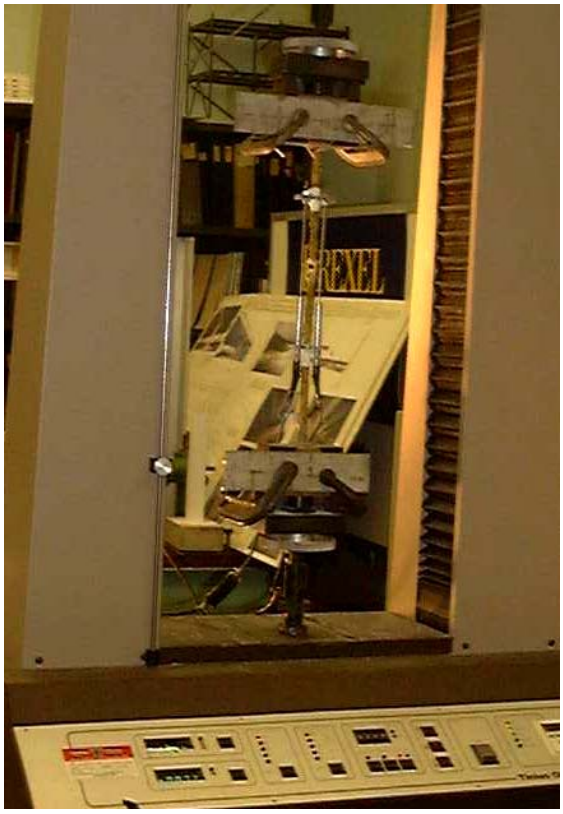

Figure 6.18: Overall View of Tension Test, Series I.

Test Series II was conducted on a Tinius Olsen 120 kip (534 kN) capacity universal testing machine. Wedge-action type grips were used for the pipe end tabs. The bar specimens could be directly placed into the wedge grips; however, care needed to be taken to get accurate alignment of the specimen. Any misalignment could lead to the introduction of flexure in addition to axial effects. The specimens were long (25”-30”) to minimize any bending effects that might occur.

To minimize the bending effects, a special test setup was developed. Articulations were provided on either end of the bar, resulting in two pin-ended connections. This eliminated any bending effects and misalignment that might occur

during testing. The articulation setup is shown in Figure 6.19. The setup consisted of the use of one 7/8” diameter steel eyebolt, one 1” diameter steel eyebolt, a 1” diameter standard chain connector, and a 1” diameter coupling nut. The chain connector was opened up and both eye bolts were placed inside the connector and the connector was re-closed. This setup was then placed into the wedge grips and tightened. This created an articulation that was free to rotate in all directions, thereby creating a pin connection. This articulation was placed on both ends of the bar to prevent bending moments from developing in either end of the bar, as shown in Figure 6.19. The articulation was designed for high-strength DHFRP bars, such as the IM7-12K bar, which has a design strength of approximately 13500 lb (60.05 kN).

Once the articulations were placed into the vee-type grips, 1” coupling nuts were threaded on to the 1” diameter eyebolt. The DHFRP with pipe grips was then threaded onto the coupling nuts. Shown in Figure 6.20 is a detail of the articulation connection.

Extension was measured using a laser extensometer (Model 500L, Hounsfield Test Equipment Inc.). Two pieces of magnetic tape were placed on the bar specimen and the gauge length was measured. During testing, the laser, located on the top of the machine, measured the extension between the two pieces of tape. Shown in Figure 6.21 is a schematic of the entire test setup.

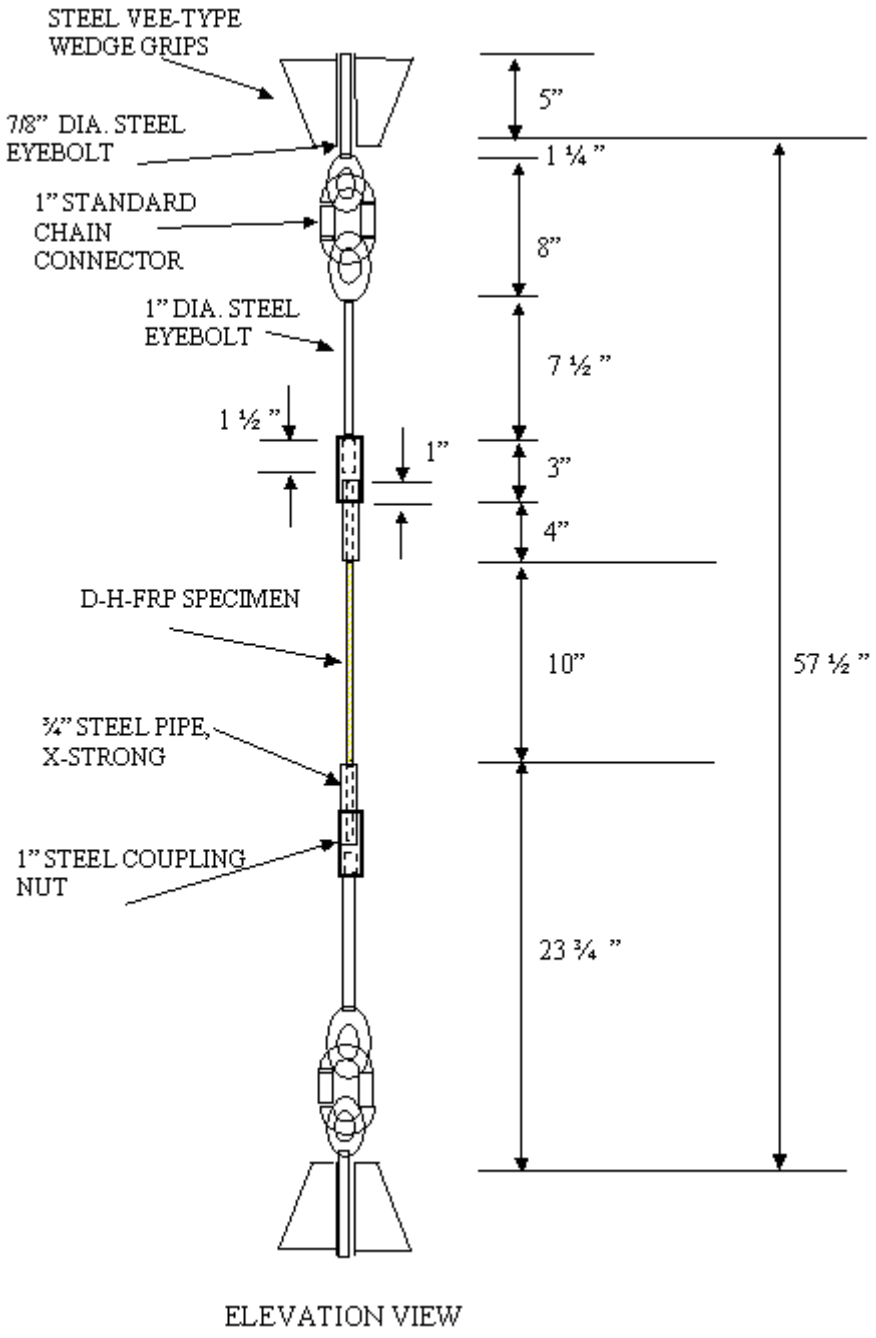

Figure 6.19: Detail of Articulation for Series II Prototype DHFRP Tension Test.

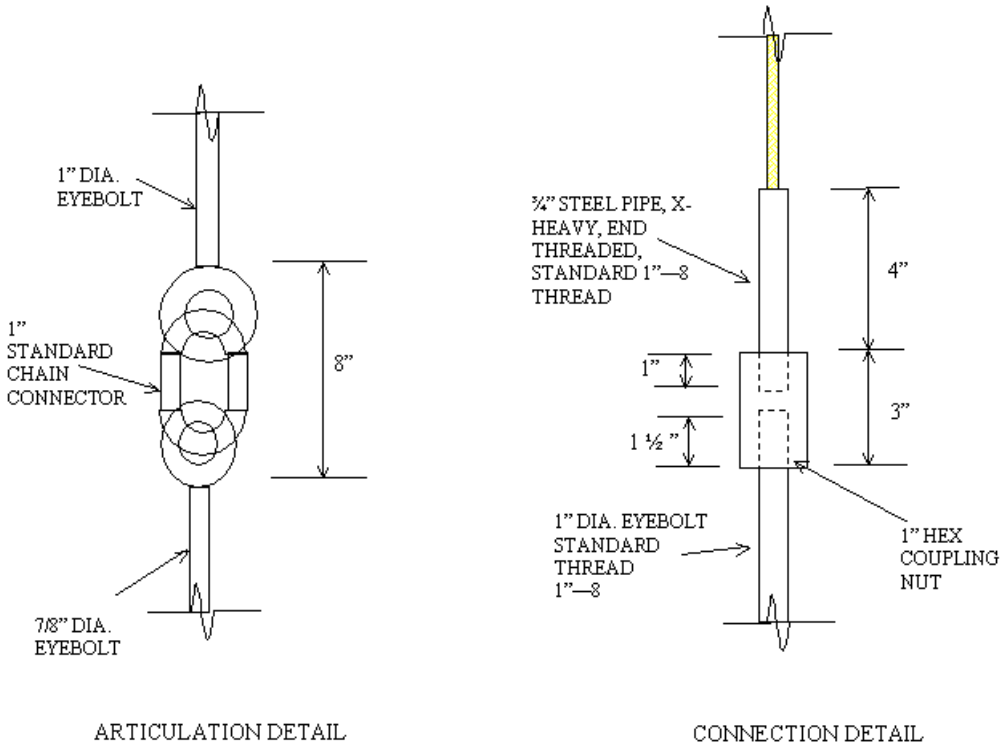

Figure 6.20: Detail of Articulation Device and Connection Detail.

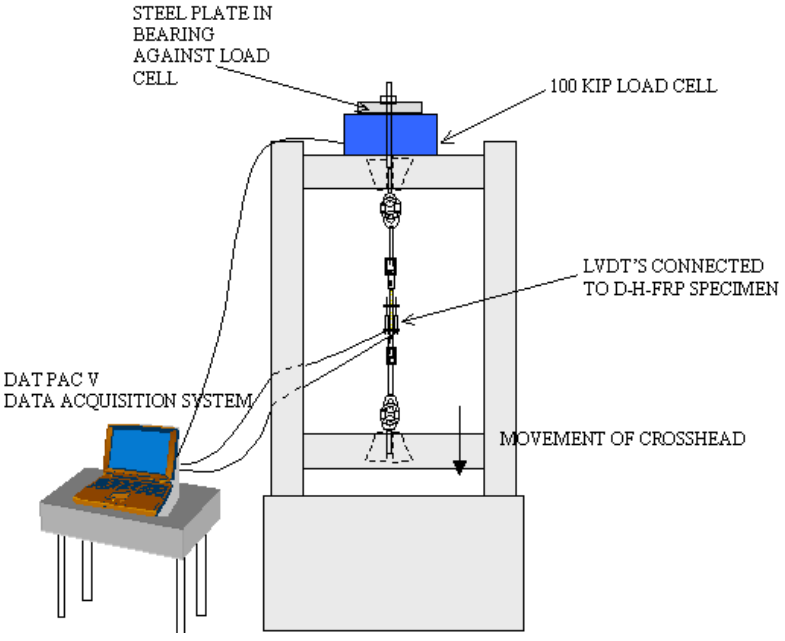

Figure 6.21: Tension Test Setup in 120 K Tinius Olsen Universal Machine for 10-mm DHFRP Bars.

6.2.5 Results

The results of Series I tension tests are presented below. These were tests conducted on the Tinius Olsen 10000 lb capacity universal machine. The reinforced trapezoidal end tabs were used to grip the ends of the bar.

Shown in Figure 6.22 is the bar after failure. Shown are the two LVDTs mounted to the DHFRP bar. Figure 6.23 shows the reinforced-epoxy end tab at the end of the bar. A piece of masonite, cut to the shape of the tab, was placed on top of the tab; then a steel plate was clamped onto the end grip box of the machine. This was to provide additional confinement and prevent damage if a sudden, brittle failure occurred.

Figure 6.24 shows the load-strain curves for all of the tests of 10-mm diameter prototype bars. Load is presented instead of stress since there are various ways to present stress. For design purposes of R/C structures, only the strain and the load are necessary for proper design (Chapter 8). Figure 6.25 shows only the yield zone of the bar. This is the region at the yield point and the beginning of strain hardening. This was presented to show this region of progressive failure in detail. Figure 6.26 through Figure 6.31 are individual plots of the load-strain for each specimen. These are presented to give more detail of each specimen. For comparative purposes, it is better to present all specimens together; however, detail of the failure process is difficult to discern, and therefore, individual plots are presented. Table 6.6 summarizes the results from all tests. Figure 6.32 shows all of the plots together with an average load-strain curve. This is the proposed design curve for prototype DHFRP bars. Figure 6.33 shows the stress-strain curves for all bars. The area used in the stress calculation is based on the area obtained from volumetric calculations (Table 6.2). Figure 6.34 shows a stress-strain curve using the volumetric area and one using the specific area, A_{sp}. The results from Figures 6.33

and 6.34 are tabulated in Table 6.7. The theoretical results from the FADM are compared to the experimental tensile results in Figure 6.35.

Figure 6.22: Failed DHFRP Specimen (a) Overall View,
(b) Detail of Failed Section, Series I.

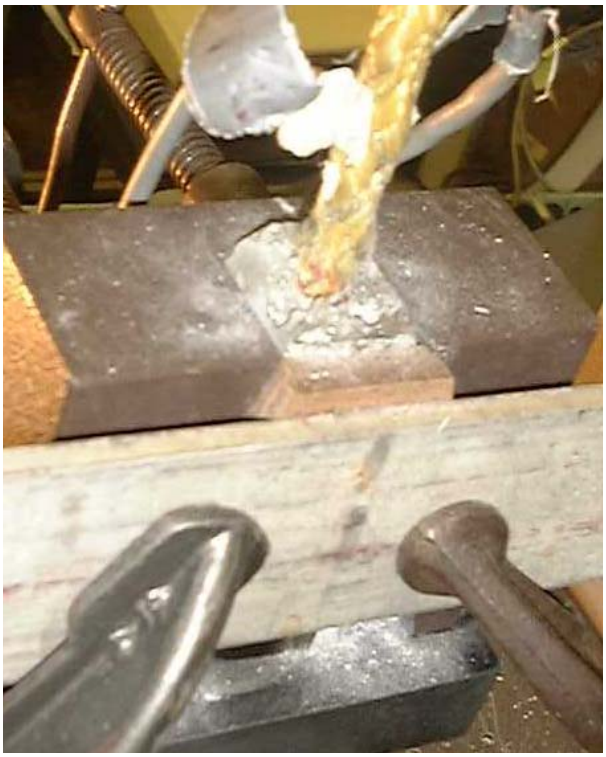

Figure 6.23: Closeup of Epoxy End Tab After Testing, Series I.

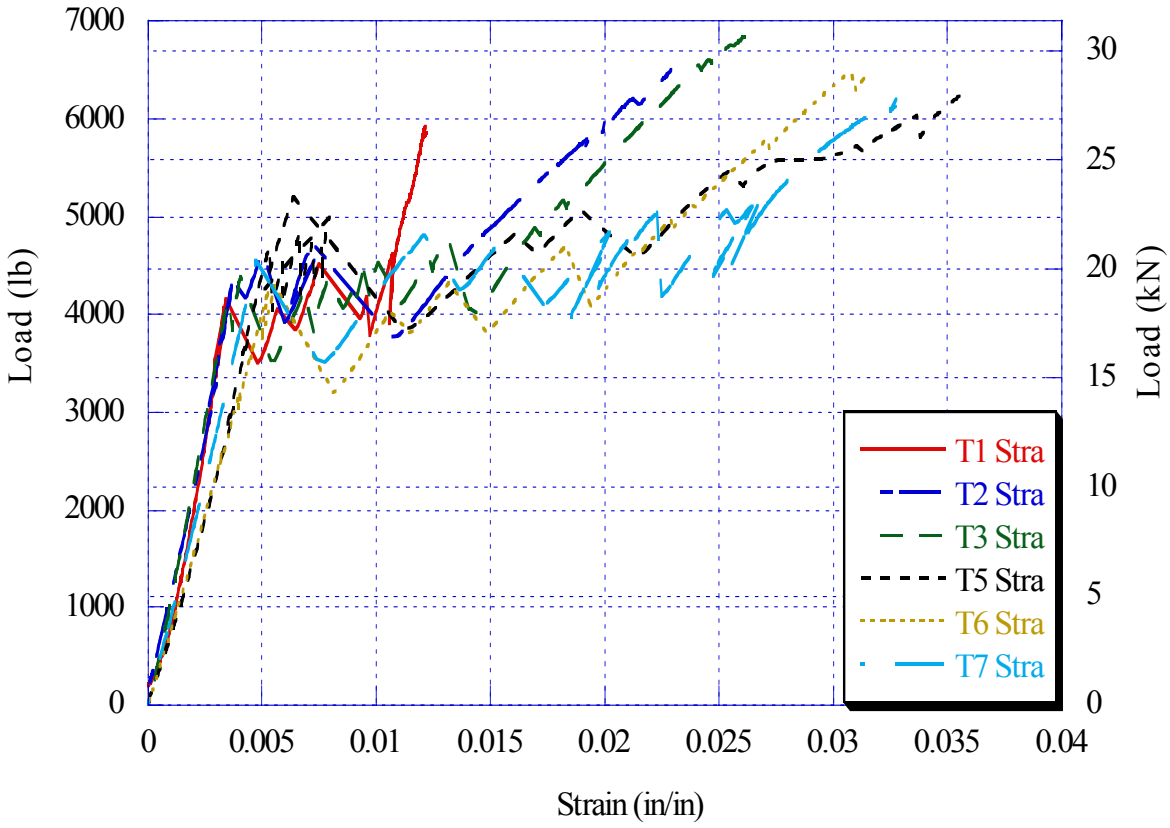

Figure 6.24: Load-Strain Curves for Tension Test of Prototype DHFRP Bars, Series I.

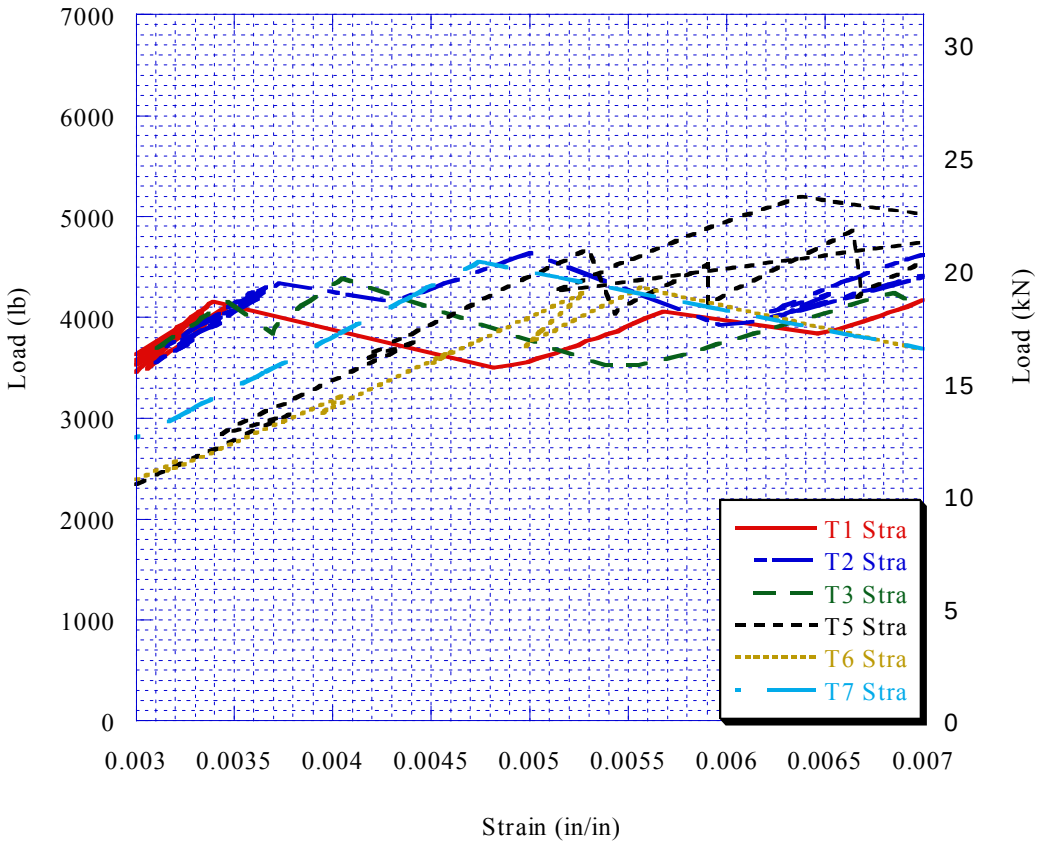

Figure 6.25: Yield Zone for Load-Strain Data, Prototype DHFRP Bar, Series I.

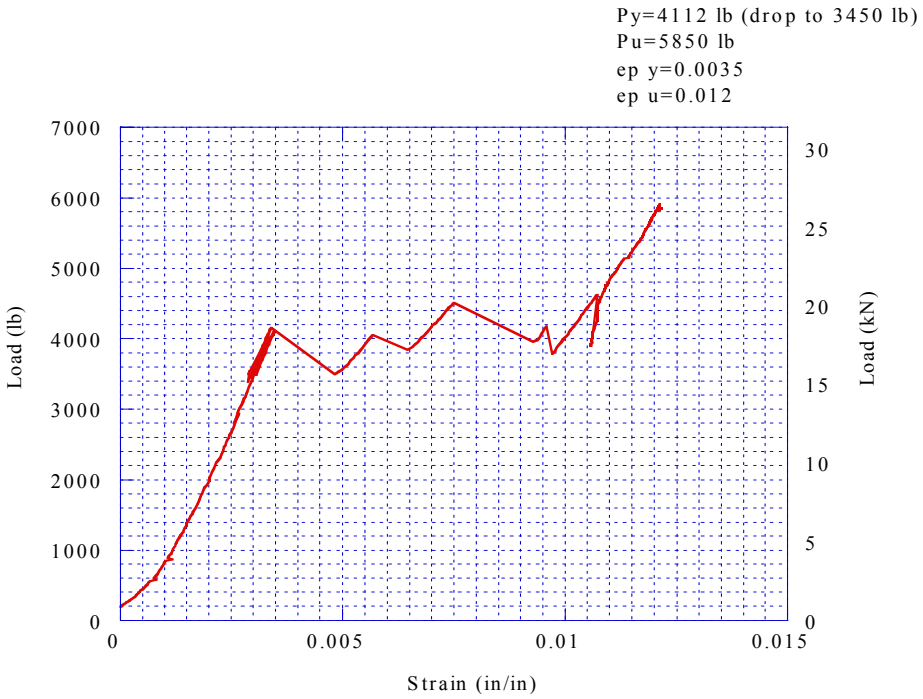

Figure 6.26: Load-Strain Behavior of Prototype DHFRP Bar, Specimen T-1N.

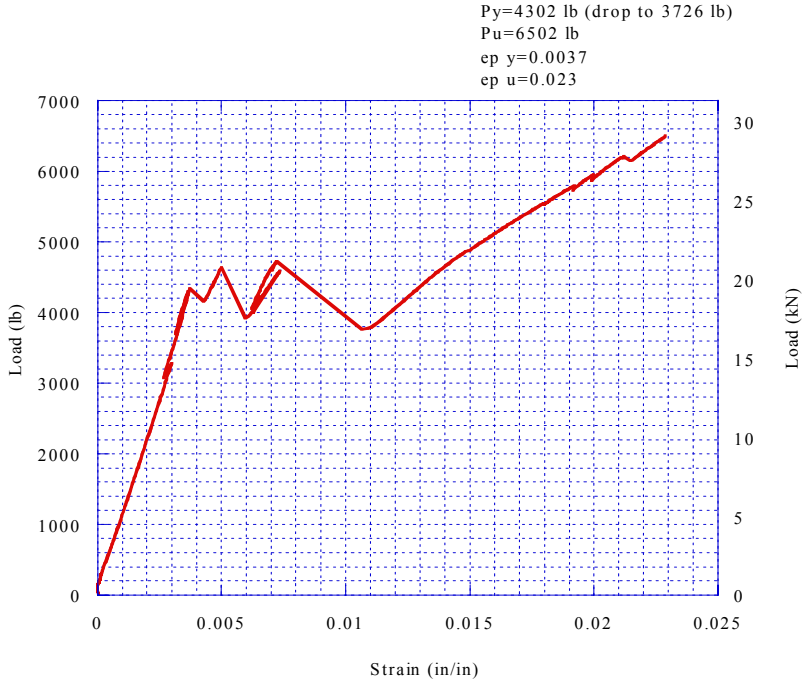

Figure 6.27: Load-Strain Behavior of Prototype DHFRP Bar, Specimen T-2N.

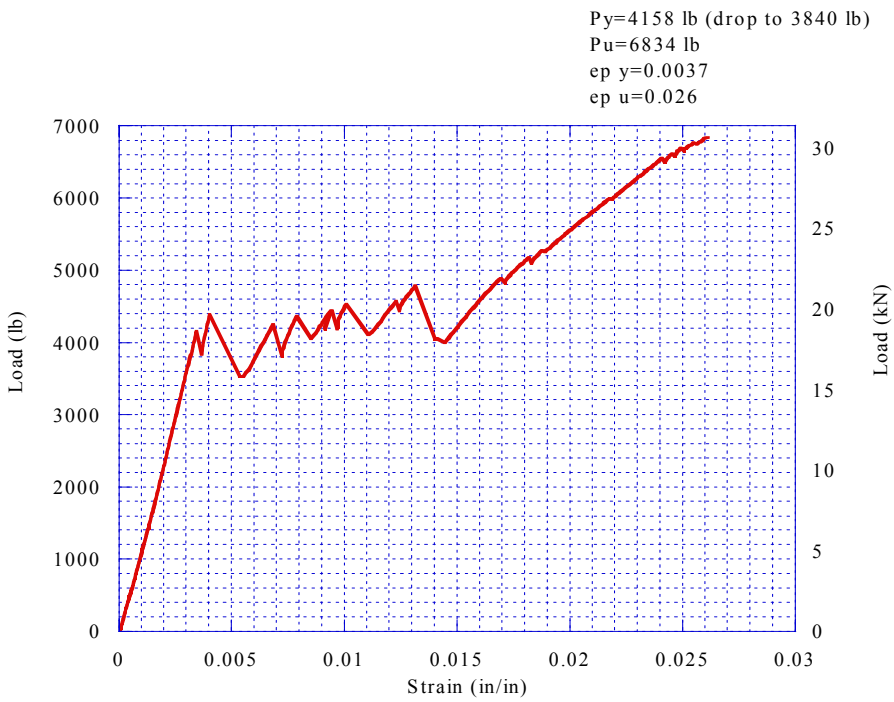

Figure 6.28: Load-Strain Behavior of Prototype DHFRP Bar, Specimen T-3N.

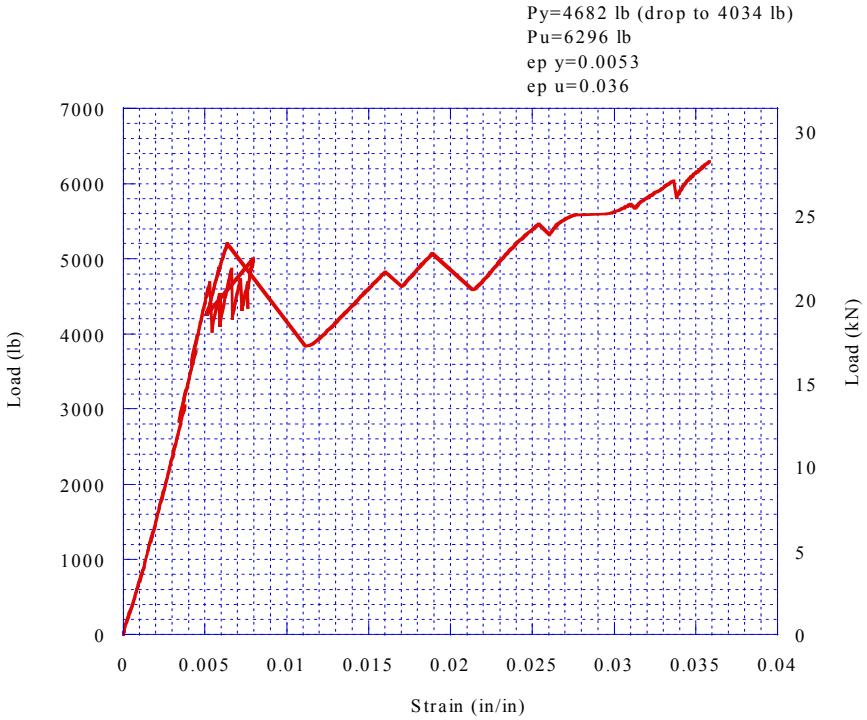

Figure 6.29: Load-Strain Behavior of Prototype DHFRP Bar, Specimen T-5N.

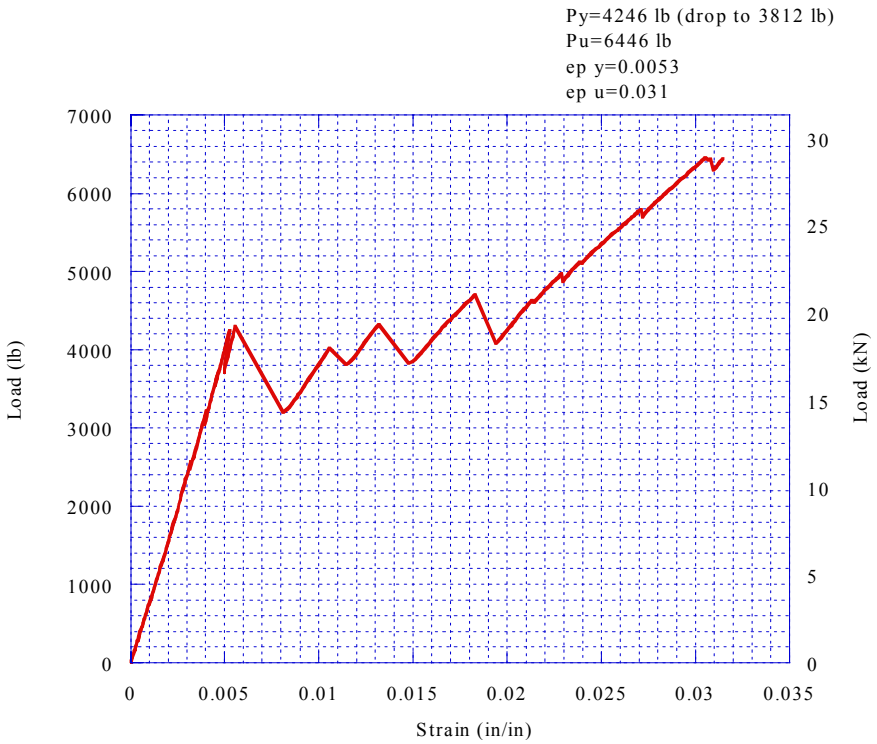

Figure 6.30: Load-Strain Behavior of Prototype DHFRP Bar, Specimen T-6N.

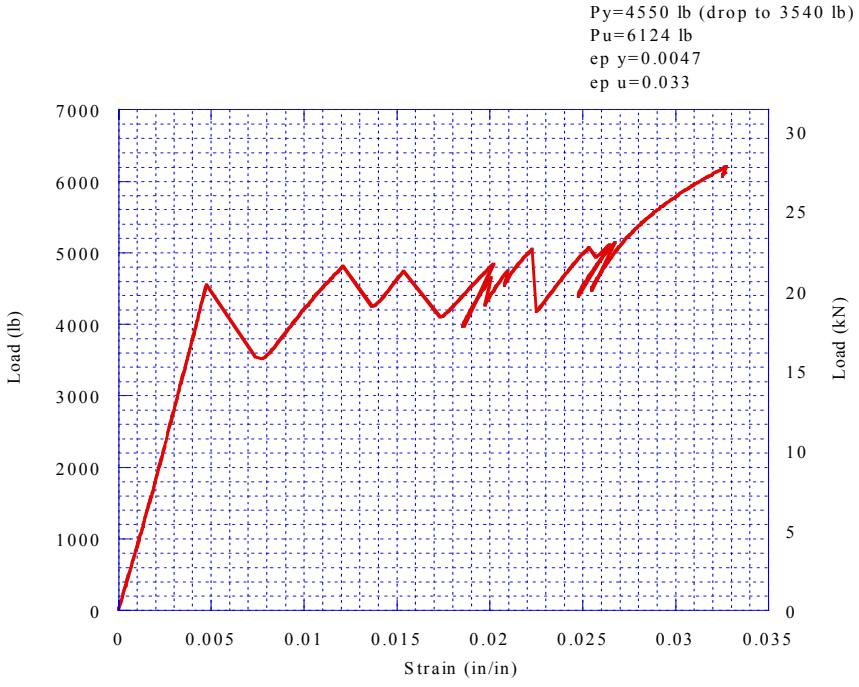

Figure 6.31: Load-Strain Behavior of Prototype DHFRP Bar, Specimen T-7N.

Table 6.6: Results of Tension Tests of 10-mm DHFRP Bars.

Specimen	Yield load, lb (kN)	Ultimate load, lb (kN)	Yield strain	Ultimate strain
T-1N	4112 (18.29)	5850 (26.02)	0.0035	0.012
T-2N	4302 (19.14)	6502 (28.92)	0.0037	0.023
T-3N	4158 (18.50)	6834 (30.40)	0.0037	0.026
T-5N	4682 (20.83)	6296 (28.01)	0.0053	0.036
T-6N	4246 (18.89)	6446 (28.67)	0.0053	0.031
T-7N	4550 (20.24)	6124 (27.24)	0.0047	0.033
Average values	**4342 (19.31)**	**6342 (28.21)**	**0.0044**	**0.0298**

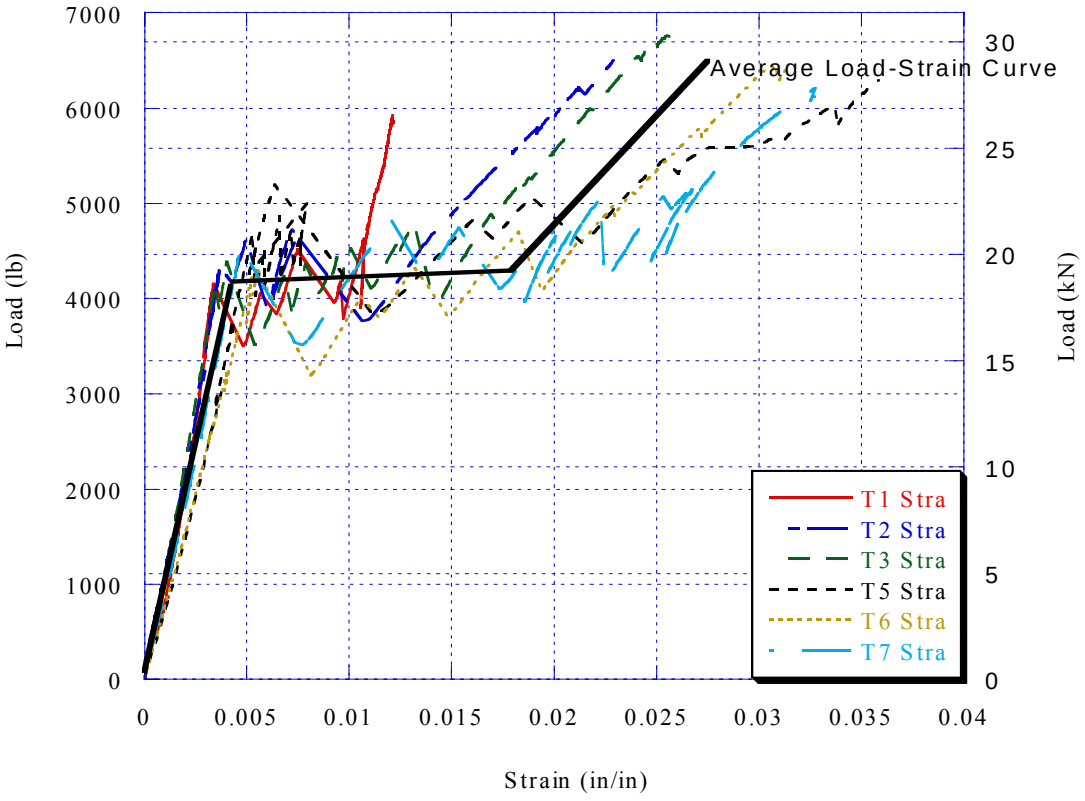

Figure 6.32: Design Load-Strain Data for Prototype DHFRP Bars.

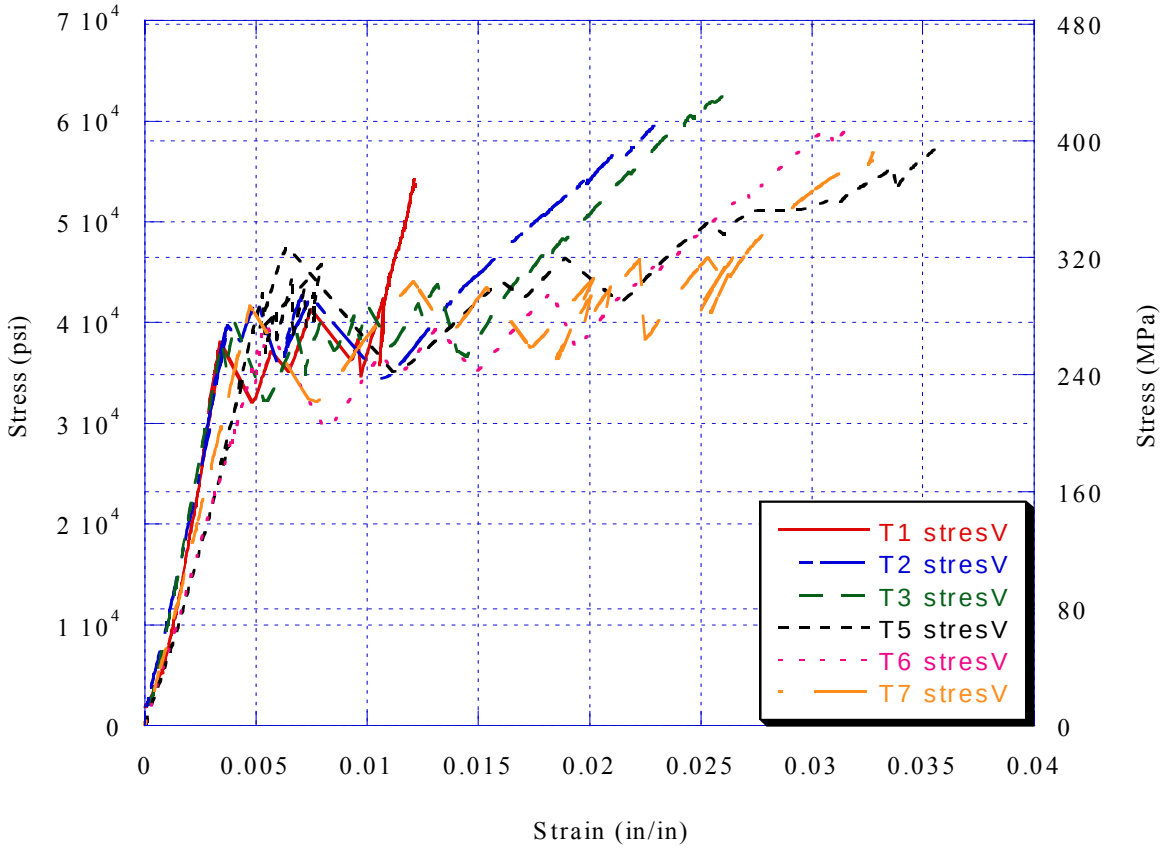

Figure 6.33: Volumetric Stress-Strain for All 10-mm DHFRP Bars.

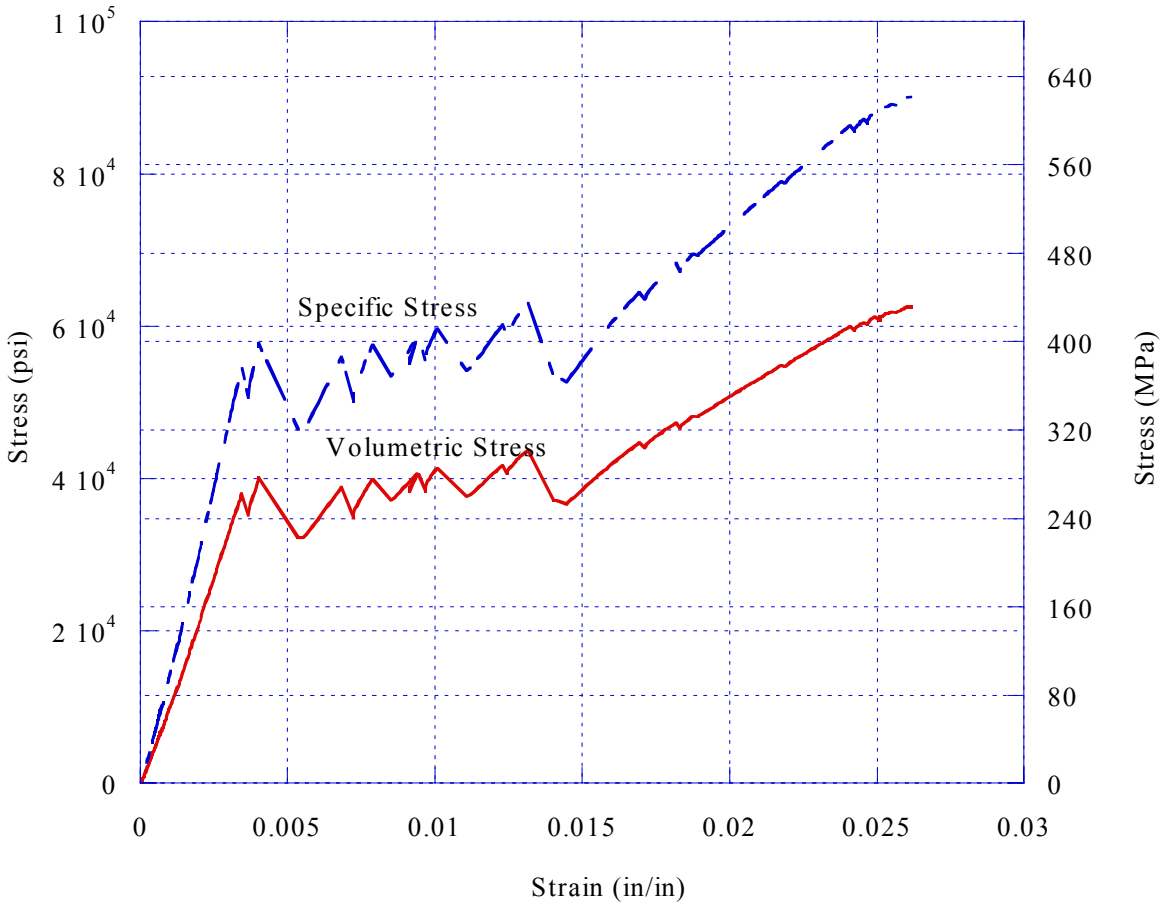

Figure 6.34: Comparison Between Volumetric and Specific Stress Versus Strain.

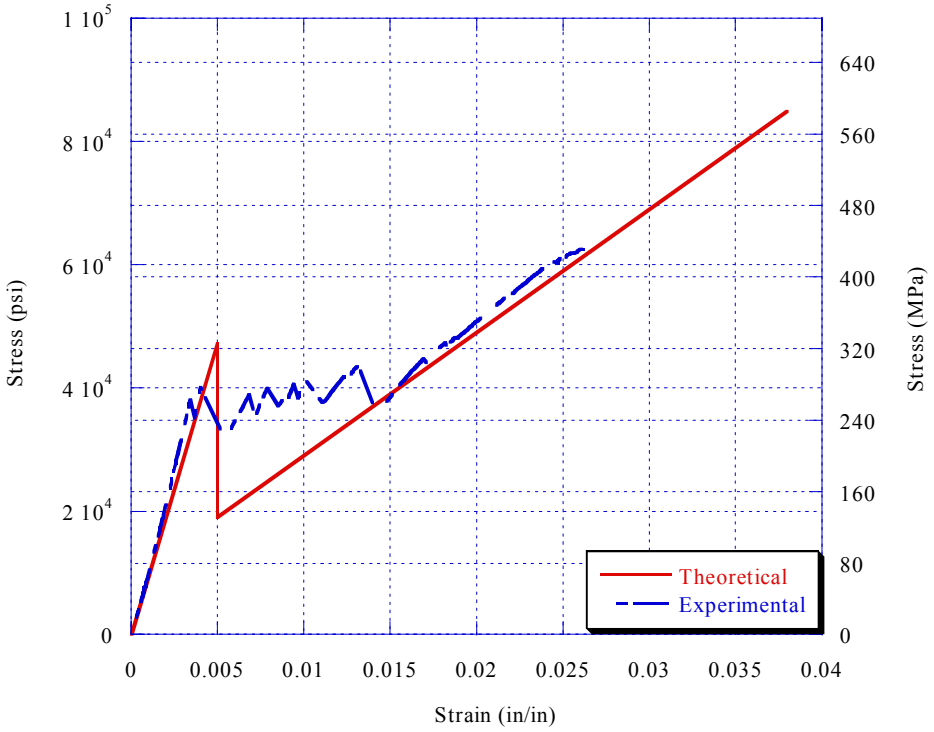

Figure 6.35: Comparison Between FADM Theoretical Results and Experimental Stress-Strain Results.

Table 6.7: Values of Stress and Strain from 10-mm DHFRP Tension Tests.

	Using A_{sp}			Using A_{vol}		
Specimen	Yield stress, ksi (MPa)	Ultimate stress, ksi	Modulus, ksi (GPa)	Yield stress, ksi	Ultimate stress, ksi	Modulus, ksi
T-1N	54.25	77.18	15499.4	37.66	53.57	10758.8
T-2N	56.75	85.78	15339.1	39.40	59.54	10647.5
T-3N	54.85	90.16	14825.6	38.08	62.58	10291.1
T-5N	61.77	83.06	11654.3	42.88	57.66	8089.7
T-6N	56.02	85.04	10569.0	38.88	59.03	7336.4
T-7N	60.03	80.79	12771.6	41.67	56.08	8865.2
Average values	**57.88 (399.1)**	**84.97 (585.8)**	**16131.8 (111.2)**	**40.18 (270.0)**	**58.98 (406.7)**	**10140.6 (69.9)**

6.2.6 Discussion

Shown in Figure 6.22 was the 10-mm DHFRP bar with LVDTs after rupture. The failure plane was localized with rupture of the braid yarns at one cross-section of the bar. The failure mechanism is explained in detail in the next section. Figure 6.23 showed the epoxy end tab after rupture of the DHFRP bar specimen. There was some minor cracking of the end tab at high load levels, but all end tabs were examined after testing and there was no sign of bar pullout. Some of the cracked epoxy resulted from the core yarns breaking. Energy was released through the bar and into the end tabs when core yarn bundles broke, thereby causing minor spalling of the outer layer of epoxy from the tabs.

In Figure 6.24, all load-strain curves were shown. All specimens showed consistent behavior. Several of the specimens had slightly lower stiffness than the first four specimens. These can be attributed to using carbon that was less stiff for some specimens. P-55S 4K carbon was donated by BP Amoco; this carbon had a stiffness of 52 Msi (358.5 GPa), not 55 Msi (379.2 GPa), and therefore, resulted in a slight stiffness decrease and larger strain capacity of these specimens.

Figure 6.25 shows the yield zone of all failed specimens. The load decrease from first yield to stress redistribution was around 500-700 pounds (2.22-3.11 kN). This was consistent for all bars tested. This load drop also was consistent throughout the entire plastic region of behavior. The magnitude of the load drop did not get larger at any point before the strain hardening region commenced. The cause and magnitude of this load drop is explained in the next section.

Shown in Figures 6.26 through 6.31 were the load-strain curves for the 10-mm diameter DHFRP bars. All of these figures showed the same mode of failure resulting in a tri-linear load-strain or stress-strain behavior. The tri-linear effect was a result of the

high initial stiffness of the carbon until failure of some carbon yarns (elastic region), failure of the carbon core (plastic region), and a strain hardening region where the Kevlar sleeve carried additional load until final bar rupture. The load at initial yield ranged from 4112 lb (18.29 kN), Fig. 6.26, to 4682 lb (20.83 kN), Fig. 6.29. The ultimate load ranged from 5850 lb (26.02 kN), Fig. 6.26 to 6834 lb (30.40 kN), Fig. 6.28. The strain at yield ranged from 0.0035 (Fig. 6.26) to 0.0053 (Fig. 6.29) and at ultimate ranged from 0.012 (6.26) to 0.036 (6.29). The theoretical strain at yield based on the failure of core yarns was 0.005. It was impossible during the manufacturing process to align all of the yarns in the zero direction, and therefore, the complete properties of the carbon could not be realized. The values of strain that were over 0.005 (Figs. 6.29 and 6.30) were manufactured with the less stiff carbon (E = 52 Msi). Since the stiffness decreased, the ductility or strain capacity increased slightly, as shown in the curves. A summary of the results with the average loads and strains at yield and ultimate were shown in Table 6.6.

Figure 6.32 showed the design load-strain curve for 10-mm diameter DHFRP bars. This curve was taken as the average of all properly-failed load-strain curves. Since the load drop in the plastic region was very consistent, an average curve was used instead of lower-bound or upper-bound curves. From this curve, the design parameters of 10-mm DHFRP bars were shown.

Figures 6.33 and 6.34 showed the stress-strain curves for the DHFRP bars. The stress shown in Figure 6.33 was defined using the volumetric area, as explained in Section 6.2.1. Figure 6.34 showed both stress-strain curves using the definitions of specific stress and volumetric stress (based on A_{sp} and A_{vol}, respectively). These curves demonstrate the difference in stress capacity depending on how the cross sectional area of

the bar was defined. Using A_{sp}, the yield stress was 57.88 ksi (399.1 MPa), and the ultimate stress was 84.97 ksi (585.8 MPa), similar to Grade 60 reinforcement; when the area was define using A_{vol}, the yield stress was 40.18 ksi (277.0 MPa), and the ultimate stress was 58.98 ksi (406.7 MPa), similar to Grade 40 reinforcement. The strength of the bar was defined using A_{vol} since this appeared to give more realistic strength values. However, for design of R/C flexural members, the load can be used directly, and therefore, the strength of the bar becomes unnecessary.

Shown in Figure 6.35 was the comparison between the theoretical stress-strain curve and the experimental stress-strain curve. Good correlation existed between the two curves, verifying the FADM model. The FADM model did not show a plastic region, it only modeled the linear elastic region up to yielding followed by a strain-hardening region, resulting in a bilinear curve. This was because the FADM model assumed that the core yarns were completely impregnated and unidirectional, and therefore, failed compositely at a strain of 0.005. This was not what physically happened, as explained in the next section of the bar failure mechanism. The second portion of the theoretical stress-strain curve, assuming that the entire load was carried by the Kevlar sleeve, was verified by the experimental results.

6.3 DHFRP Failure Mechanism

Unlike conventional FRP bars which are linear elastic until failure, the DHFRP bar has a unique failure mechanism which fails progressively but controlled until final bar rupture. This failure mechanism for model bar sizes was discussed in Somboonsong (1997). However, since many processing parameters were studied and changed for the

manufacture of prototype-size bars, the failure mechanism of the new DHFRP bar is discussed.

The DHFRP bar has a progressive failure due to two unique inherent features: first, the bar is a hybrid material system, and second, the bar has a unique geometry including unidirectional and off-axis yarns. Using a first-order analysis, these two features control the overall behavior of the bar when loaded. Shown in Figure 6.36 is a load-strain curve for a 10-mm diameter DHFRP bar under uniaxial tension. Five important points or regions of interest are shown. On the right is a cross section of the bar shown at each of the five points of interest.

Region 1 is the bar under axial load before any fiber failure. In this region, the entire bar, carbon yarns, Kevlar yarns, and resin are working compositely to resist the load.

At a certain load level, point two (Fig. 6.36) occurs. This is where the carbon yarns begin to break. This is shown by the one white yarn on the right figure. The white yarns show that this region carries no load. The yield point is actually strain controlled. The ultimate strain of P-55S 4K carbon is 0.5%. At around this strain, carbon yarns or tows (yarn bundles) begin to break. The first carbon yarn or yarn bundle to break defines the yield point of the bar. This exact strain or load value of this point can not be easily controlled using the current braidtrusion manufacturing process since the carbon core yarns are not under uniform tension. When the carbon core yarns were plied, they were manually cut to length and tensioned before winding onto a creel. The yarns were 30-ply with 4K filaments per yarn. It was impossible for all 30 yarns to have uniform tension. This was obvious during the manufacturing of the DHFRP bars as the carbon yarn passed

under the resin bath and into the braiding machine. This caused some yarn bundles to be 'pretensioned', and therefore, these yarns had initial prestress before the bar was externally loaded. These yarns or yarn bundles failed first, causing the initial yield of the DHFRP bar.

Region 3 is the yield region of the bar. This is caused by breaking of yarns or yarn bundles in the carbon core, as shown in the right side of the figure. Each drop in the load-strain curve is caused by another yarn bundle failing. This behavior of the bar in this region is again controlled by core yarn tension and is explained in Figures 6.37 and 6.38. Figure 6.37 shows the stress-strain behavior of a monolithic continuous rod of a given cross section, for example, steel. As the rod is pulled in axial tension, the rod yields and eventually fractures. Since the rod works monolithically, the stress-strain curve is smooth without any abrupt jumps. Theoretically, a perfect composite material would do this. Shown in Figure 6.38 is the stress-strain behavior of a discrete fibril system; for comparison, say a rod of the same cross section as Fig. 6.37 made of steel wires. As this wire bundle is pulled in tension, some wires carry more load because of nonuniform tension on the wire bundle. The wires that carry more load yield first and eventually fracture, causing a drop in load. After this drop, the load is carried by the surrounding wires until another one fails. This progressive failure continues until all wires fail. This mechanism is shown by region 3 of Figure 6.36. These drops in load are caused by uneven core yarn tension. For fibrous systems, uneven tension causes the yarns to be of different length. The yarns under highest tension fail first. Since there is a matrix, the load is carried by the other yarns. This causes a progressive failure. If all of the carbon yarns were under uniform tension with no prestress, they should all

theoretically fail at a strain around 0.5%. This progressive failure mechanism does produce additional ductility of the bar. Since there were only seven drops on this curve but 30 yarns in the core, carbon yarn bundles and not individual yarns failed. Also, the height of the drops was controlled by how well the core yarns worked compositely. The largest drop for the 10-mm bar was around 800 pounds (3.56 kN). Most load drops were much less than this. This was verified by good fiber wetting shown in the SEM scans (Chapter 5). Earlier DHFRP bars with poor wetting had many more and much larger load drops due to improper load transfer. This will be explained in the next paragraph.

Once all of the core yarns fail, the load is carried by the sleeve, illustrated by point four in Fig. 6.36. The curve is again smooth with a new stiffness. This is the 'strain hardening' portion of the curve. This is primarily the sleeve yarns and matrix working. Comparing the slope and strain of this curve to the theoretical curve for only a Kevlar 49 sleeve (without core) braided on a 45° ± 5° angle verifies this conclusion.

The failure of the Kevlar sleeve yarns had a different audio pitch or frequency than the carbon core yarns. It had a higher pitch. Also, the cracking of the matrix had a different audio pitch (frequency). The three components had distinct pitches during failure. This made it apparent which component was failing at which time.

A new and unique feature of the 10-mm DHFRP bar made using the modified dieless pultrusion was the smooth strain-hardening region. All other DHFRP bars made prior to this (Somboonsong, 1997) had load drops until final bar rupture. This was caused by poor wetting of the core yarns. When the core yarns failed, load was not transferred since the matrix was discontinuous. This mechanism continued until final bar rupture. There were many more load drops, demonstrating that more individual carbon

core yarns and not large yarn bundles failed. The number and magnitude of the load drops were minimized in the new bar using dieless pultrusion, thereby creating a smoother, tighter, and more controlled yield region.

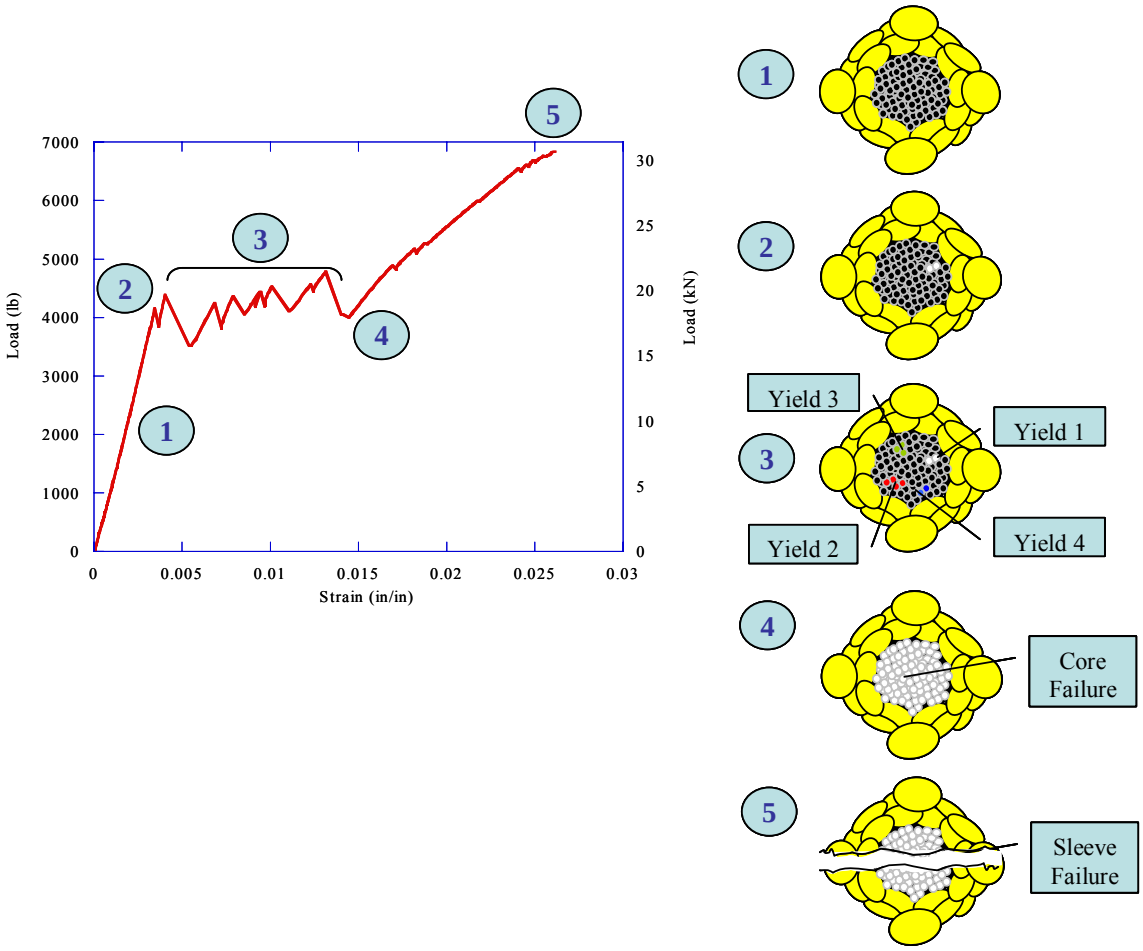

Figure 6.36: Failure Mechanism of DHFRP Manufactured By Dieless Braidtrusion.

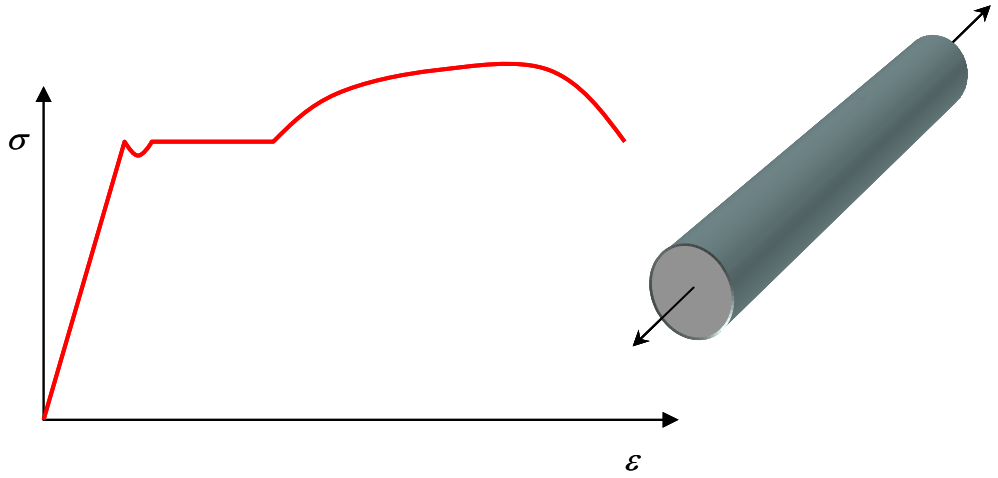

Figure 6.37: Stress-Strain Behavior of a Monolithic Continuous Structure.

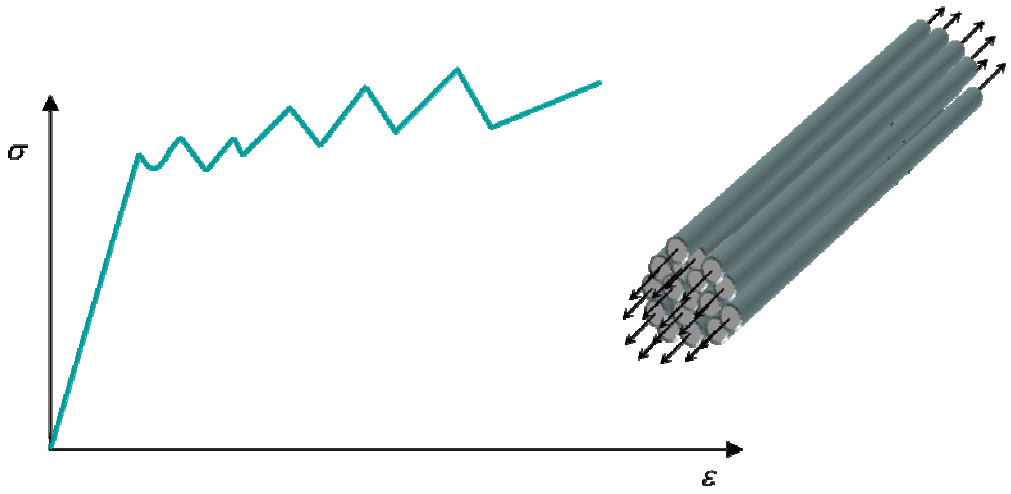

Figure 6.38: Stress-Strain Behavior of Discontinuous Fibril Structure.

6.4 Bond Characterization

In addition to having sufficient strength and stiffness, the bond strength of reinforcing materials is equally important. The strength and performance of R/C structures depend on the development of adequate bond between the bars and the concrete. The bond and strength characteristics of FRP bars depend on many variables. These variables include the following: size, shape, surface configuration (e.g., ribs) and surface roughness, position of the bars in the concrete element, confinement pressure, compressive strength of the concrete, embedment length, environmental conditions, temperature change, moisture absorption, mechanical interlock of bars against the concrete, chemical adhesion, and hydrostatic pressure against the FRP bars due to shrinkage of hardened concrete. Most commercially available FRP bars cannot be modeled after the bond behavior of steel reinforcing bars because of the fundamental differences between the physical and mechanical properties of two materials and their interaction with concrete. However, as shown in the previous sections, DHFRP have a tri-linear stress-strain behavior similar to steel with an integrated rib pattern similar to steel bars, and therefore, should be able to be modeled in a similar manner as conventional steel rebars.

The bond behavior of R/C structures is described. The importance of the deformation pattern, the rib height, and rib spacing was investigated for the DHFRP bar. Finally, experimental results were presented for the 10-mm prototype bars and compared with other commercially used FRP bars.

6.4.1 Background and Theory

The reinforcement in concrete receives its portion of the load only from the surrounding concrete. The bond stress is the shear stress at the bar-concrete interface. The stresses in the bar are modified by this load transfer occurring between the bar and the surrounding concrete. When the bond stress develops, a composite structure is created. The bond strength is an important parameter when detailing reinforcement in structural components (Park, 1975).

The bond force is measured by the rate of change in the force in the reinforcing bars, and does not exist unless the steel stresses change between any two sections along the bar. The bond stress is defined as the shear force per unit area of bar surface and is given as

$$u_{avg} = \frac{q}{\sum o} = \frac{\Delta f_s A_b}{\sum o} = \frac{d_b}{4}\Delta f_s \qquad 6\text{-}3$$

where q = change of bar force over unit length

Σo = nominal surface area of a bar of unit length

d_b = nominal diameter of the bar

Δf_s = change of steel stress over unit length

A_b = area of the bar

The bond stresses in R/C members occur from two distinct situations: first, from the anchorage of bars and second, from the change of bar force along its length, due to a change in bending moment along the member.

6.4.1.1 Anchorage Bond and Flexural Bond

A bar must extend a distance l_d beyond any section at which it is required to develop a given force, where the distance l_d is required to transmit the bar force to the concrete by bond. Shown in Figure 6.39 is a pullout specimen used in testing the bond strength of DHFRP bars. The stress distributions for both the bar and the bond along the length of the specimen are shown.

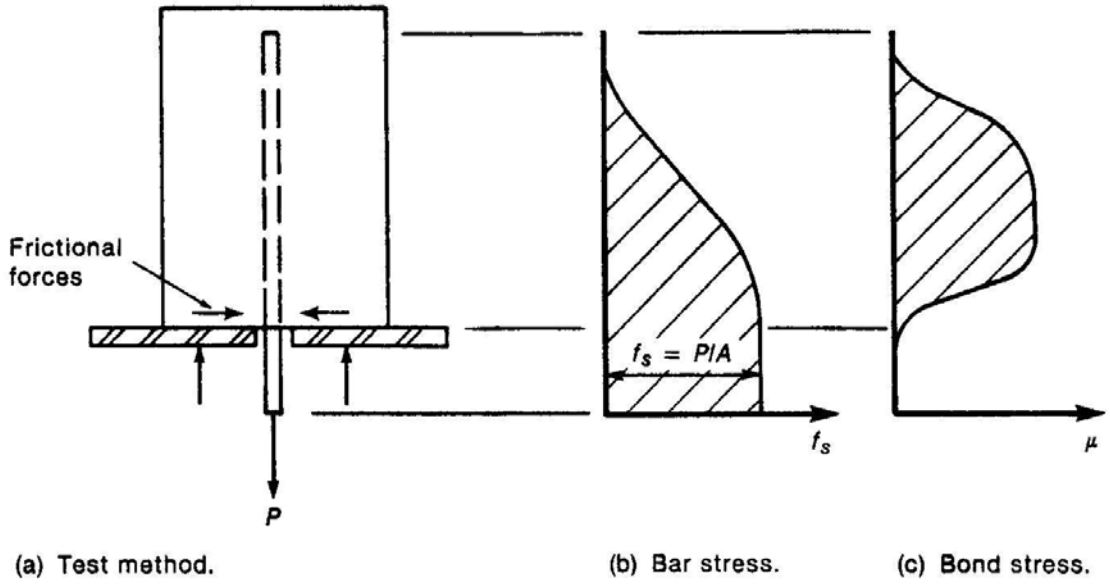

Figure 6.39: Distribution of Bar and Bond Stresses in a Pullout Specimen (from MacGregor, 1997).

Shown in Figure 6.40a is the generation of anchorage or development bond. In the figure, the average bond stress, u_{avg}, is assumed to be uniformly distributed over the length l_d. Considering equilibrium yields the following:

$$T = A_b f_s = u\left(\sum o\right) l_d \qquad 6\text{-}4$$

Rearranging and plugging in the area of a circular bar ($\pi d^2/4$) and plugging in πd for Σo yields an expression for the development length in terms of the bond strength, bar diameter, and bar tensile strength f_s

$$l_d = \frac{d_b}{4u_{avg}} f_s \qquad 6\text{-}5$$

Shown in Figure 6.40b is the development of flexural bond. Bond forces ΔT are developed along the flexural reinforcement in the shear span of any beam. Assuming that the bond stresses u are uniformly distributed between any two sections close to each other, the equilibrium of a short length of bar requires that $\Delta T = u\ \Sigma o\ \Delta x$. However, for beam action to occur, the internal tension force T must vary at the same rate as the external bending moment M. Therefore

$$\Delta T = \frac{\Delta M}{jd} = \frac{V}{jd}\Delta x \qquad 6\text{-}6$$

and

$$u = \frac{V}{jd\sum o} \qquad 6\text{-}7$$

Equation 6-6 shows that when the rate of change of external bending moment (i.e., the shear force) is high, the flexural bond stress can also be very large. However, Equation 6-6 oversimplifies the physical situation because the presence of cracks in the concrete at discrete intervals along a member results in additional bond stresses due to the tension carried by the concrete between the cracks as shown in Figure 6.41. Even where the shear force is zero (i.e., constant bending moment), bond stress will be developed. However, provided that sufficient anchorage length is available for the bars, failure from

flexural bond stress does not occur. Flexural bond concerns require that the anchorage length must be checked in regions of members where the bending moment is zero (supports and points of contraflexure). In these regions, the shear force is high and the tension steel area is small, resulting in high flexural bond stresses.

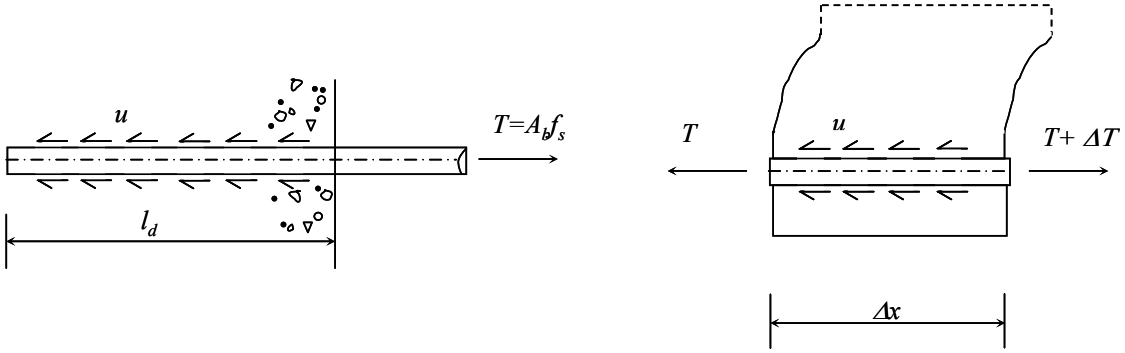

Figure 6.40: Development of Anchorage and Flexural Bond.

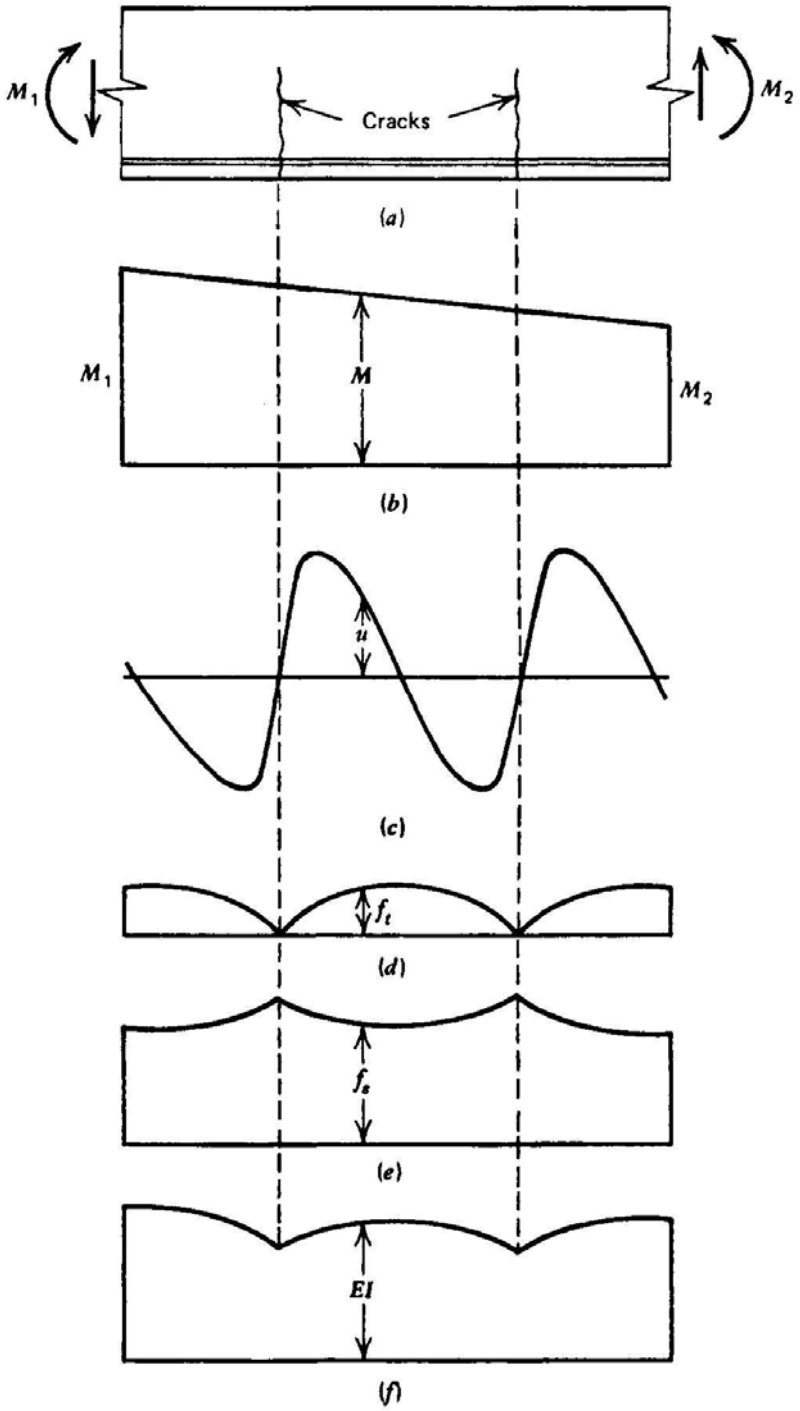

Figure 6.41: Effect of Cracking of a R/C Flexural Element; (a) Element of Beam; (b) Bending Moment Distribution; (c) Bond Stress Distribution; (d) Concrete Tensile Stress Distribution; (e) Steel Tensile Stress Distribution; (f) Flexural Rigidity Distribution in Elastic Range.

6.4.1.2 General Features of Bond Resistance

The bond resistance of bars is mainly developed through chemical adhesion, frictional resistance, and mechanical interlock. Chemical adhesion occurs between the mortar paste and the bar surface; however, even low stresses cause sufficient slip to break the adhesion between the concrete and the reinforcement. Once slip occurs, bond can be developed only be means of friction and by mechanical interlock. The frictional resistance depends on the surface conditions of the reinforcement. For steel bars, the variation in pitting can be significant for mildly rusted bars. However, for FRP bars, the surface condition can vary due to the manufacturing process. Smooth FRP bars can only depend on these two types of bond resistance since there are no surface deformations. To increase frictional resistance, many FRP bars are sand coated. If this is not done, most of the bond resistance is only chemical adhesion which would result in low bond resistance.

Deformed bars have much higher bond capacity because of the interlocking of the ribs with the surrounding concrete. Figure 6.42 shows the bond stress developed between two ribs of a bar; these bond stresses are associated with the following stresses:

1. Shear stresses, v_a, developed through adhesion along the surface of the bar
2. Bearing stresses f_b, against the face of the rib
3. Shear stresses v_c, acting on the cylindrical concrete surface between adjacent ribs

From equilibrium, the relation between these stresses and the forces to be transferred to the concrete by bond over a short length of bar between the centers of ribs is

$$\Delta T = \pi d_b^{'}(b + c)v_a + \pi \frac{d_b^{''2} - d_b^{'2}}{4} f_b \approx \pi d_b^{''} c v_c \qquad 6\text{-}8$$

where each term in 6-8 is defined in Figure 6.42.

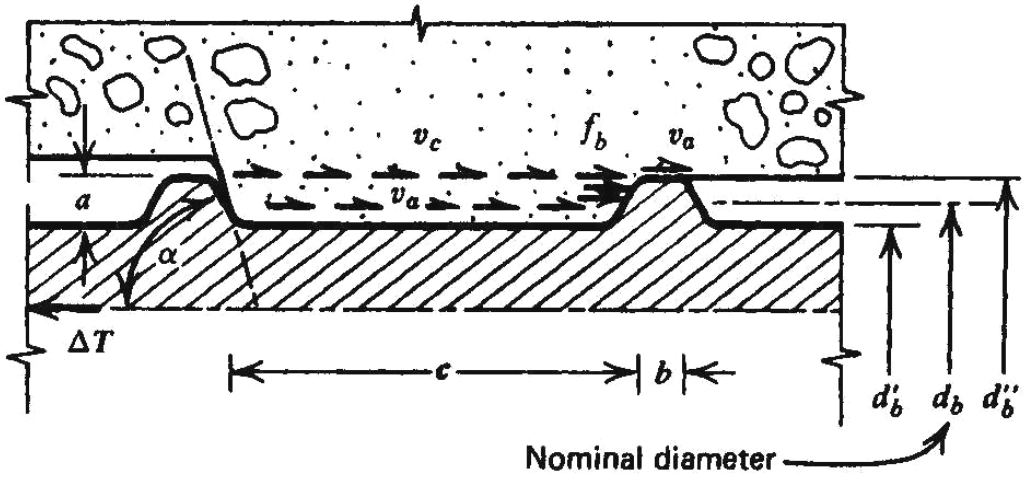

Figure 6.42: Stresses Between Two Ribs of a Deformed Bar (Park and Paulay, 1975).

As the load is increased, the adhesion along the bar surface breaks down. The remaining frictional shear strength is very small in comparison with the bearing strength developed around the ribs. Therefore, v_a can be ignored for practical purposes. The remaining components of bond force development, f_b and v_c, can be simplified as follows:

- Since $b \approx 0.1c$, the rib spacing is approximately equal to c.
- Since $a \approx 0.05d'_b$, the bearing area of one rib is

$$\pi \frac{d_b''^2 - d_b'^2}{4} \approx \pi d_b a \qquad 6\text{-}9$$

From Equation 6-8, $\Delta T = \pi d_b a f_b \approx \pi d_b c v_c$; therefore

$$v_c \approx \frac{a}{c} f_b \qquad 6\text{-}10$$

Rehm (1968) related issues involved with bond to the geometric parameter a/c. Rehm's work found that the most satisfactory performance of a bar embedded in concrete over the short length c was when a/c was around 0.065. ASTM A-305 states that the

deformation requirements are such that $0.057 < a/c < 0.072$. When the ribs are high and are spaced too closely, the shear stress v_c governs the behavior and the bar pulls out. Also, when the rib spacing is larger than approximately 10 times the rib height, the partially crushed concrete may form a wedge in front of the rib, and failure occurs by splitting of the surrounding concrete. The concrete in front of the rib can sustain a bearing pressure several times the cylinder crushing strength because of the confined condition of the concrete (Park and Paulay, 1975). Shown in Figure 6.43 are the two types of failure mechanisms associated with the rib. The failure mode in Figure 6.43a is a shear pullout failure mode, which must be prevented by defining a proper geometry of the deformed bars. Figure 6.43b shows the failure mode that is desirable to develop sufficient bond resistance.

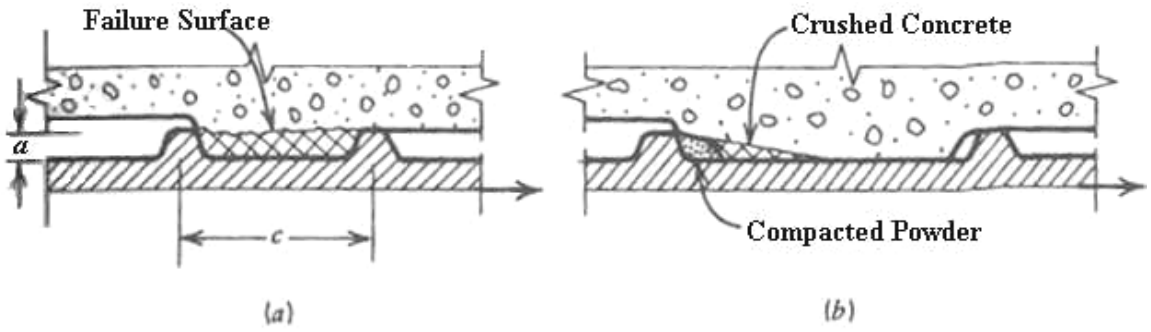

Figure 6.43: Failure Mechanism at the Ribs of Deformed Bars (a) a/c > 0.15. (b) a/c < 0.10.

The load-bond slip relationship for deformed bars is primarily affected by the behavior of the concrete immediately in front of the ribs. The quality of the concrete in

this region depends on its relative position when cast. Water gain and sedimentation under reinforcing bars can occur and under coarse aggregate particles. A soft and spongy layer of concrete can form under the ribs. Large slips can occur when bearing stresses of high intensity are developed against such a soft zone.

As shown in Figure 6.42, the rib profile made an angle α with the longitudinal axis of the bar. The variation of this angle between the face of the rib and the axis of the bar does not seem affect the bond strength provided that this angle is more than 70° (Park and Paulay (1975). When α is between 45° and 70°, the deformations must be reversed in direction on each side or on opposite sides of the bar (ASTM A-615). Special pullout tests, using bar specimens with a single rib, indicated that if the angle α is greater than 40°, the friction between the rib face and the concrete is sufficient to restrict slip along this interface (Gergely, 1969). Slip of the bar is then likely to be mainly attributable to the crushing of the concrete in front of the ribs (Fig. 6.43b). Contrary to this, if α is small and the surface is smooth, slip can occur along the face of the rib, and the rib tends to push the concrete away from the bar (Lutz and Gergely, 1967). This wedging action can be a major cause of longitudinal splitting along the bar (Park and Paulay, 1975).

6.4.1.3 Bond Performance of Pullout Specimens

Shown in Figure 6.44 is the typical bond stress versus slip curve for a short embedded FRP bar (Tamuzs, 2001). There are several distinct regimes of the bond-slip curve that must be defined. Section *OA*: as loading commences, the main bond mechanism is chemical adhesion between the FRP bar and the concrete. No measurable slip is observed at this stage.

Section *AB*: as the load is increased, the adhesion breaks down, and the bond mechanism changes. The slip at the local end of the bar increases and the deformations (lugs) of the bar develop bearing stresses due to reaction against the surrounding concrete. When the principal tensile stress caused by bond stresses reach the tensile strength of the concrete, micro cracking occurs at the tips of the bar deformations. For some FRP bars, instead of cracking, a soft layer might form, which has some tension transfer capacity since the deformations of FRP bars are softer than steel deformations (Tamuzs, 2001).

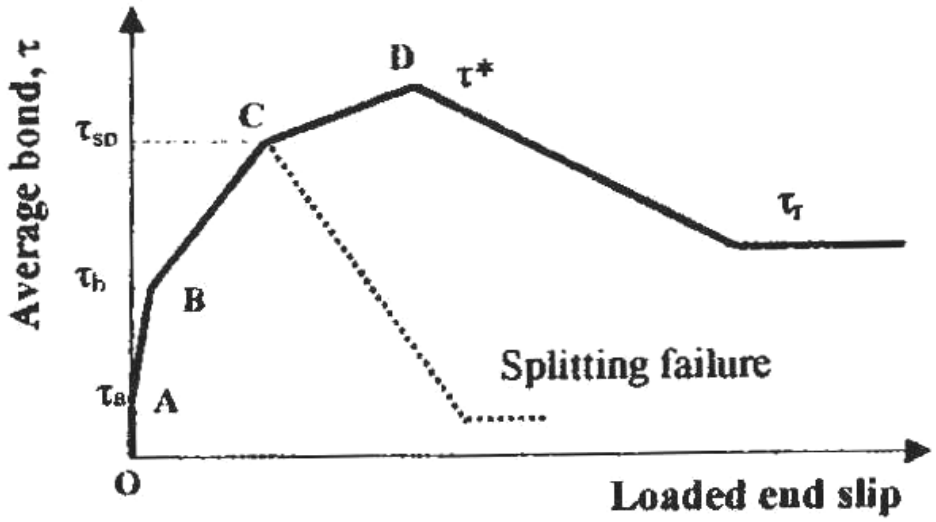

Figure 6.44: Bond Stress Versus Slip Curve for an FRP Short Embedment (Achillides, 1998).

Section *BC*: As slip increases, the principle direction of compressive forces in the concrete act at an angle α to the bar as shown in Figure 6.45. The value of α depends on

the value of the modulus of the bar, the type of bar surface, and the slip (Tamuzs, 2001). The radial component from the bond forces is balanced against rings of tensile stresses developed in the concrete. The splitting resistance of the concrete ring around the bar is critical in forming a crack along the bar. If this does not result in failure, the possible ultimate crack pattern giving minimum splitting resistance against the radial pressure generated by bond force determines the anchorage capacity. The splitting resistance is influenced by the confinement by the surrounding concrete mass, the transverse reinforcement and pressure (if present). When the splitting crack along the bar propagates through the entire cover of the embedment, the displacement between the bar and the concrete increases considerably (i.e., slip), and this results in evenly distributed bond stress along the anchorage length.

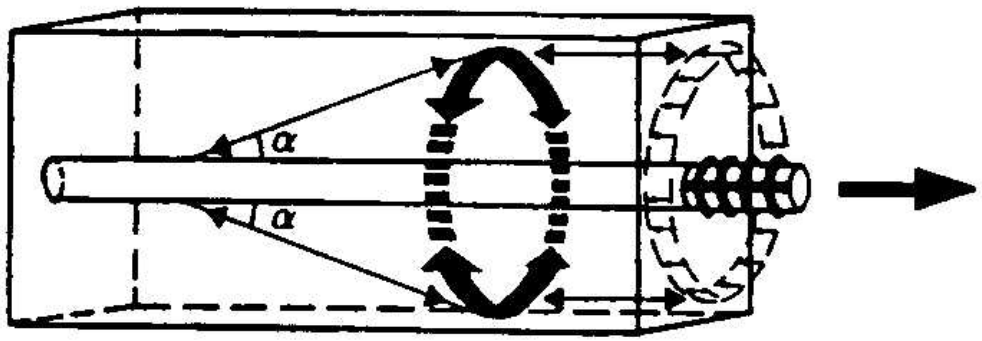

Figure 6.45: Schematic Representation of the Radial Components of Bond Forces and Balanced Against Tensile Stress Rings in the Concrete (Tepfers, 1973).

Section *CD*: If sufficient resistance to splitting is provided by the surrounding concrete mass, the bond stress can reach the maximum bond stress. At this stage, both the loaded and unloaded (free) ends of the bar are slipping and bond stiffness is significantly decreased. Depending on the relative magnitude of the concrete strength as compared to the shear strength of the surface deformations of the bar, various failure modes may result.

Section *DE*: After attaining maximum bond stress, τ^*, the residual bond strength mainly depends on the frictional resistance, τ_r, at the failure interface.

6.4.2 Development Length and Theoretical Modeling of Bond Behavior

The concept of development length is based on the average bond strength attained over the embedment length of the reinforcement. The development length is critical because highly stressed bars have the tendency to split relatively thin sections of restraining concrete. This is especially important when a row of bars, even in mass concrete, can create a weakened plane with longitudinal splitting along the plane of the bars. This is not as critical for a single bar embedded in a sufficiently large mass of concrete.

The basic equations for the development length, l_d, is given in terms of the bar diameter, d_b for deformed bars in tension. For number 6 bars and smaller, the development length in inches is given in ACI 318-02 as either

$$\frac{l_d}{d_b} = \frac{f_y \alpha \beta \lambda}{25\sqrt{f_c'}} \text{ or } \frac{l_d}{d_b} = \frac{3 f_y \alpha \beta \lambda}{50\sqrt{f_c'}} \qquad \text{6-11 a, b}$$

where α = reinforcement location factor, β = coating factor, λ = lightweight aggregate concrete factor, f_y is the yield strength of the reinforcement (psi), and f'_c is the concrete compressive strength (psi). Equation 6-11a is valid when 1) the clear spacing of bars being developed or spliced is not less than d_b, the clear cover is not less than d_b, and the stirrups or ties throughout l_d are not less than the code minimum or 2) the clear spacing of bars being developed or spliced is not less than 2 d_b and the clear cover is not less than d_b. Eqn. 6-11b is valid for all other cases. The theoretical development lengths for the 5-mm and 10-mm DHFRP bars and corresponding epoxy-coated Number 3 steel rebars are given in Table 6.8 using Eqns. 6-11 a, b. For these equations, the α = 1.0, β = 1.2 (all other epoxy-coated bars or wires), and λ = 1.0 (normal-weight concrete). The epoxy-coated factor was taken into account since the DHFRP does have a layer of epoxy on the bar surface. Epoxy coated steel was used for comparison of the β parameter.

Table 6.8: Theoretical Development Lengths for 5-mm and 10-mm DHFRP Bars.

	Eqn. 6-11a		**Eqn. 6-11b**	
For f'_c **= 4000 psi**	l_d / d_b	l_d, **in (mm)**	l_d / d_b	l_d, **in (mm)**
5- mm DHFRP	28.46	5.60 (142.3)	42.69	8.40 (213.5)
10-mm DHFRP	30.49	11.43 (290.4)	45.74	17.15 (435.7)
Gr. 40 steel	30.36	11.38 (289.2)	45.54	17.08 (433.7)
Gr. 60 steel	45.54	17.08 (433.8)	68.31	25.61 (650.6)
For f'_c **= 6000 psi**	l_d / d_b	l_d, **in (mm)**	l_d / d_b	l_d, **in (mm)**
5- mm DHFRP	23.24	4.57 (116.2)	34.86	6.86 (174.3)
10-mm DHFRP	24.90	9.34 (237.2)	37.35	14.01 (355.7)
Gr. 40 steel	24.79	9.30 (236.1)	37.18	13.94 (354.1)
Gr. 60 steel	37.18	13.94 (354.1)	55.77	20.91 (531.2)

The development length can be expressed in terms of the ultimate value of the average bond stress by setting in Eqn. 6-5 Δf_s equal to f_y

$$l_d = \frac{f_y d_b}{4\mu_{avg,ult}} \qquad 6\text{-}12$$

Equation 6-12 can be used to obtain a value of the development length from experimental data.

The development length of rebars is compared for both steel rebars and various FRP bars. The expressions for development length for FRP bars are modified from steel due to two features of most commercially manufactured FRPs: linear-elastic behavior until failure and relatively smooth bar surfaces (compared with conventional steel bars). Therefore, the development length equations are modified to reflect these differences.

In the design of concrete reinforced with conventional steel bars, adequate load transfer is insured by providing a development length long enough to hold the bar against the force that produces yield in the bar. Using ACI 318-02, the development length in terms of a constant and the cross sectional area of the bar is

$$l_d = 0.04 \frac{A_b f_y}{\sqrt{f_c'}} \qquad 6\text{-}13$$

where

l_d = development length (in)

A_b = bar cross sectional area (in^2)

The optimum bond length is defined as the minimum embedment length required to develop the ultimate load of the rebar. Equation 6-13 expressed the development length in terms of the bar area and a numerical constant. This is the same equation as 6-

11a, but written in terms of the bar area instead of the bar diameter. The basic equation of this form for development length given by ACI for steel bars is

$$l_{db} = KA_b \frac{f_u}{\left(f_c'\right)^{1/2}} \qquad 6\text{-}14$$

A complete modeling of the bond constitutive relationship (i.e., bond-slip relation), which is modeled for steel bars, must be developed for FRP bars and the DHFRP bar. Three theoretical bond-slip relationships were proposed for linear elastic GFRP bars, 1) the Malvar model, 2) the EBP model used for steel and 3) the CMR model.

The Malvar model (Malvar 1994) was the first model proposed for FRP bars. The model is represented by the following relationship:

$$\frac{\tau}{\tau_m} = \frac{\left[F\left(s/s_m\right) + (G-1)\left(s/s_m\right)^2\right]}{\left\{1 + (F-2)\left(s/s_m\right)A + G\left(s/s_m\right)^2\right\}} \qquad 6\text{-}15$$

with

$$\frac{\tau_m}{f_t} = A + B\left(1 - e^{-C\sigma/f_t}\right)$$
$$s_m = D + E\sigma \qquad 6\text{-}16a, b$$

Where τ_m = peak bond stress, s_m = slip at peak bond stress, s = confining axi-symmetric radial pressure, f_t = tensile concrete strength, σ = confining axi-symmetrical radial pressure, and *A, B, C, D, E, F, G* are empirical constants.

The EBP model (Eligehausen et al., 1983) was proposed for steel bars, and expresses the ascending branch of the bond-slip curve ($s_1 < s_2$)

$$\frac{\tau}{\tau_1} = \left(\frac{s}{s_1}\right)^{\alpha} \qquad 6\text{-}17$$

where τ_1 = maximum bond strength, s_1 = corresponding slip at τ_1, and a is curve fitting parameter.

A model (CMR) for the ascending branch was proposed by Cosenza (1997). This model represents an alternative to the EBP model and is defined as

$$\frac{\tau}{\tau_m} = \left[1 - e^{(-s/s_r)}\right]^{\beta} \qquad 6\text{-}18$$

where τ_m = peak bond stress and s_r and β are parameters based on curve-fitting of the experimental data.

Based on experimental results, Tighiouart et al. (1998) calibrated the parameters s_r and α of the CMR model. A new model proposed for the ascending branch of the bond-slip relationship was defined

$$\frac{\tau}{\tau_m} = \left[1 - e^{4s}\right]^{0.5} \qquad 6\text{-}19$$

where τ_m = peak bond stress and s = slip corresponding to the bond stress τ.

6.4.2.1 Theoretical Development Length for DHFRP Bars

Since DHFRP has a tri-linear stress-strain behavior similar to steel and not linear elastic until failure like other FRP bars, the bond behavior of DHFRP will be modeled using the basic equations for steel. For the development length, the value of the numerical constant K must be determined (Eqn. 6-14). Using this equation for DHFRP, and equating 6-12 with 6-14, the factor K is expressed as

$$K = \frac{\left(f_c'\right)^{1/2}}{\mu_{avg,ult}\,\pi d_b} \qquad 6\text{-}20$$

where K is a coefficient and f'_c is the concrete compressive strength. For steel, $K = 0.05$. Researchers have found that K varies between 0.047 and 0.064 for various FRP bars (Tighiouart, 1998). From experimental data, a value of K will be computed for the 10-mm diameter DHFRP bar.

6.4.3 Deformation Pattern Design and Analysis

The bond strength of the DHFRP bar is an equally important property in addition to ductility. Without sufficient bond strength, the full strength of the bar will never be developed. Integral to good bond strength is the deformation pattern of the rebar. The deformation patterns of commercially available steel rebar are shown in Figure 6.46. Shown are eight different deformation patterns. Tests conducted by Clark (1946) showed that bars develop higher bond strength when the spacing of lugs was closer (bars 4, 5, and 7, Figure 6.46). ASTM A615, Standard Specification for Deformed and Plain Billet-Steel Bars for Concrete Reinforcement, gives deformations as a function of bar diameter as shown in Table 6.9. Also specified are the maximum spacing of deformations and the minimum height. These values should be taken into consideration when evaluating the deformation pattern of the 10-mm DHFRP bar.

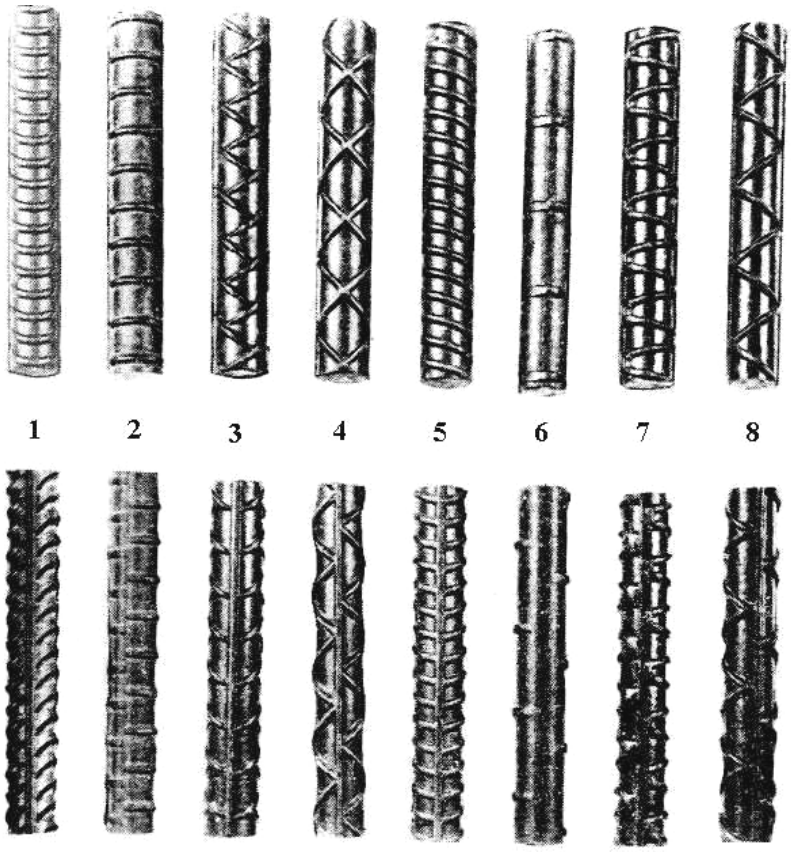

Figure 6.46: Comparison of Conventional Steel Rebar Deformations.

Table 6.9: Deformation Requirements Per ASTM A615.

Bar Number	Max. avg. spacing, in.	Min. height, in.	Max. gap, in.
3	0.262	0.015	0.143
4	0.350	0.020	0.191
5	0.437	0.028	0.239
6	0.525	0.038	0.286
7	0.612	0.044	0.334
8	0.700	0.050	0.383
9	0.790	0.056	0.431
10	0.889	0.064	0.487
11	0.987	0.071	0.540

As seen in Figure 6.46, various types of deformation patterns exist, from spiral to diamond to triangular patterns. The DHFRP's manufacturing flexibility can be utilized to produce various deformation patterns. For example, to produce a spiral deformation pattern, two rib yarns are used, placed in the same rotational direction. For a diamond pattern, four rib yarns are used rotating in opposite directions where four rib yarn crossings occur for each rotation of the braiding ring.

The deformation pattern of the original DHFRP preform is similar to case eight in Figure 6.46. This pattern is an unsymmetrical rib pattern. This pattern is shown in Figure 6.47 for the DHFRP bar. Two rib yarns moving in opposite directions were used to create this deformation pattern. In one unit cell of the deformation pattern (Fig. 6.47), the two rib yarns crossed twice in one complete rotation of the braiding ring. This is shown in Figure 6.48a, where 1, 2, 3, and 4 refer to positions of each rib yarn as it traveled around the braiding ring. As seen in Fig. 6.47, along the length of the bar, three rib crossings or lugs were created in the unit cell.

The deformation pattern of the modified 10-mm DHFRP bar used four rib yarns, as shown in Figure 6.49. By placing four rib yarn carriers on the braiding ring, four crossings occurred at quarter rotations of the braiding ring (Figure 6.48 b). This created eight rib crossings or lugs in the unit cell, Figure 6.49. This was an increase from three ribs to eight ribs per unit cell, thereby increasing the mechanical bond between the bar and the concrete.

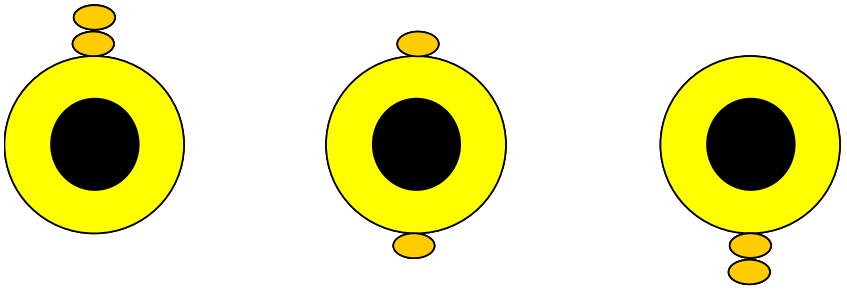

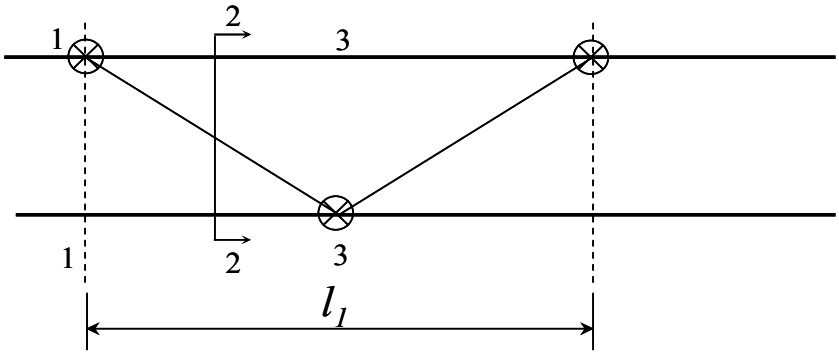

Figure 6.47: Original DHFRP Deformation Pattern and Deformation Unit Cell.

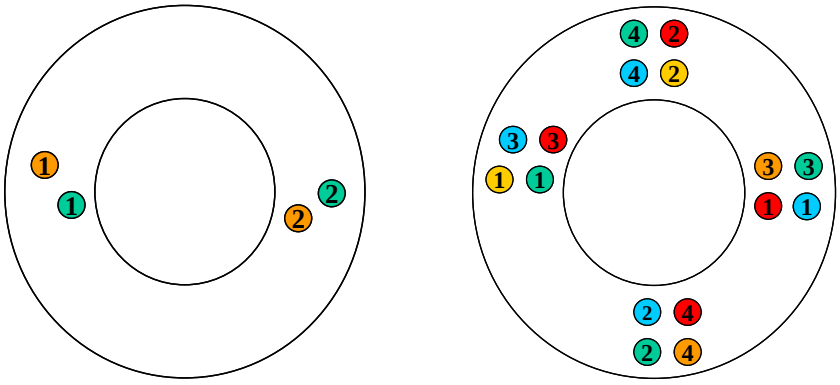

Figure 6.48: Movement of Rib Yarns Around Braiding Ring: (a) Original Preform Design and (b) Symmetric Preform Design.

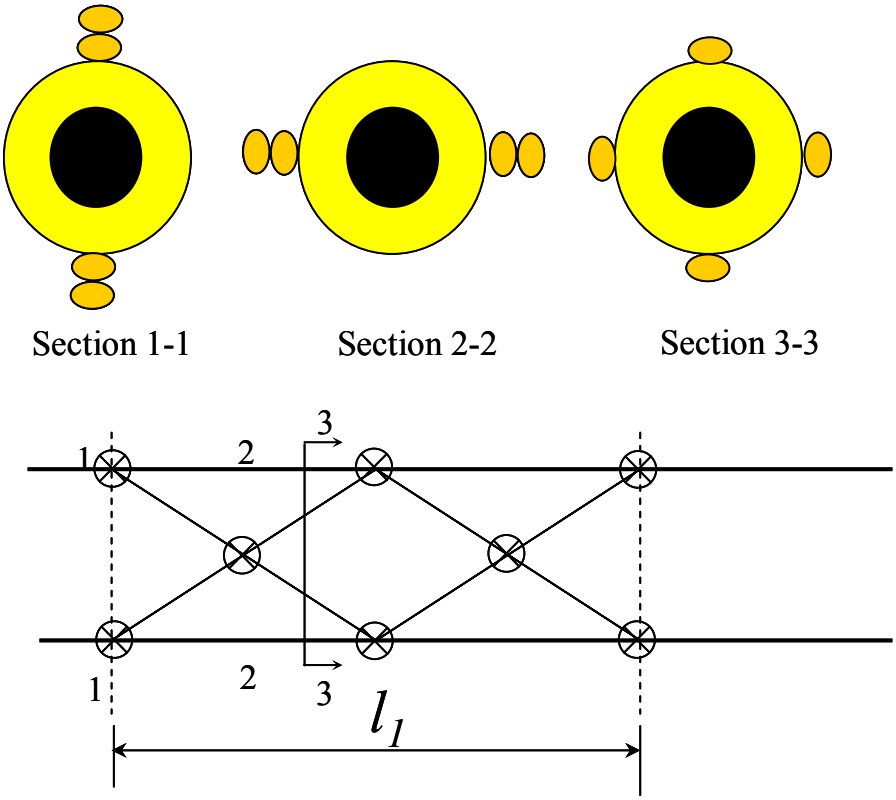

Figure 6.49: New DHFRP Deformation Pattern and Deformation Unit Cell.

For the DHFRP bar, the spacing between deformations and the pitch angle of the diamond deformation pattern are both functions of the braid angle, θ. The height of the deformations is a function of the size of the rib yarns and the braiding angle. For moderate to high braid angles (approaching ±45-50 degrees), the rib-yarn lugs were more closely spaced. For example, for a constant braiding angle for both two and four rib yarn bars, the lug spacing was decreased from 1.5" and 3.0" (high to low braid angle) for the two rib yarn bar to 0.75" and 1.5" (high to low angle) for the four rib yarn bar. Also, due to the intermediate crossing at the center of the helical pattern for the four rib yarn bar

(Figure 6.49), the actual spacing between lugs on the new bar is between 0.375" and 0.75", which is much closer to the standard values given by ASTM A615, Table 6.9.

Figure 6.50 shows the rib height for the four rib yarn DHFRP bar. The rib height was obtained by taking readings of the bar diameter at different locations along the bar, measuring from rib to rib and off the ribs. The rib height is given by

$$a = \frac{1}{2}\left(d_{rib} - d_{braid}\right) \qquad 6\text{-}21$$

Table 6.10 compares the bar deformation parameters for Number 3 and 4 steel rebars per ASTM A615 to the parameters for both two and four rib yarn DHFRP 10-mm bars. Shown in Figure 6.51 is the 10-mm DHFRP bar showing the actual deformation pattern and surface roughness. Due to the inter-lacing of the twenty braid yarns, the bar maintains surface roughness even away from the rib yarn pattern. Since the number of general braiding yarns were doubled from 10 to 20 using the modified braidtrusion, the number of yarn interlacings was also doubled, thereby increasing the surface roughness.

The deformation pattern for the new DHFRP is symmetrical with respect to the centroidal axis of the bar. Thus the moment of inertia of the bar is identical for all bar orientations. The previous DHFRP bars had both a weak and strong axes of bending depending on the orientation of the ribs with respect to the axis of bending. This was due to the fact that the moment of inertia, I_z changed depending on whether the ribs were oriented vertically or horizontally since the bar was asymmetric. As seen by the SEM micrographs of the bar (Chapter 5), this modified rib yarn pattern created a more uniform pressure profile on the bar as the resin was squeezed out from the impregnated core yarns. The symmetric rib pattern acted as a spring-coil die. Past DHFRP bars using the unsymmetrical rib pattern had a pressure gradient with the highest pressure being applied

at the ribs and rib crossings. This problem was corrected using the four rib yarn symmetric bar.

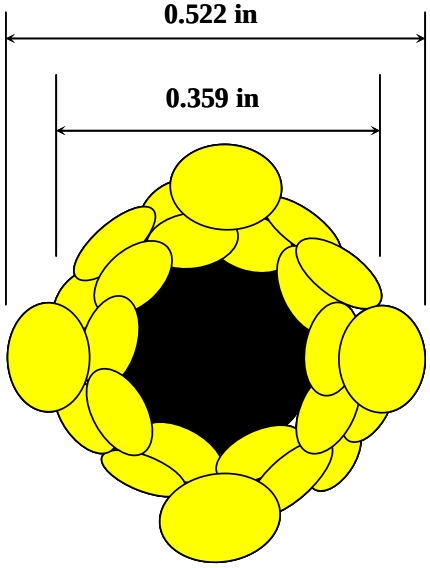

Figure 6.50: Average Height of Rib Deformations on 10-mm Diameter DHFRP Bars.

Table 6.10: Comparison of Bar Deformation Parameters for Steel and DHFRP Bars.

	ASTM A615		Old DHFRP Design	New DHFRP Design
Pattern/Size	No. 3	No. 4	Unsymmetrical	Symmetric diamond
Rib Spacing, in (mm)	0.262 (6.65)	0.350 (8.89)	1.5-3.0 (38.1-76.2)	0.375-0.75 (9.525-19.05)
Rib Height, in (mm)	0.015 (0.381)	0.020 (0.508)	0.035 (0.889)	0.081 (2.06)

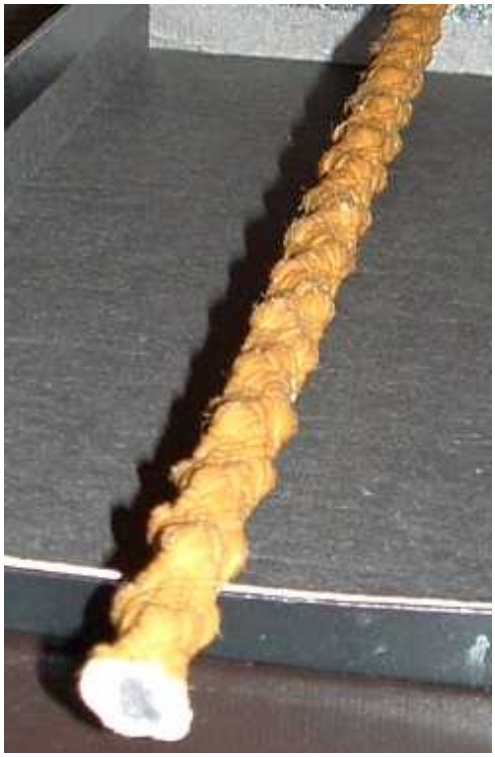

Figure 6.51: 10-mm DHFRP Bar Showing Deformation Pattern and Surface Roughness.

6.4.4 Sample Preparation

Shown in Figure 6.52 is a detailed schematic of the bond pullout specimens for 10-mm DHFRP bars. The specimen consisted of a 6-in by 12-in (152.4-mm by 304.8-mm) concrete cylinder with the bar placed in the center. Standard plastic cylinder molds were used as forms. A one inch thick foam disk was placed at the bottom of the mold. The foam was dense enough as to not compress under the weight of the concrete or to absorb moisture. The bar was extended through the foam disk to the bottom of the mold. This allowed the bar to be centered and provided a one inch piece of bar to be exposed that was needed to measure free-end slip. Inside the form, a 5 ¾" (146.05-mm) paper

tube was placed around the bar. This was used to break the bond between the concrete and the bar over a specified length. The position of the tube was varied depending on the desired bond length. The tube was held in place by duct tape on the exterior and Teflon tape inside the tube, and the bottom was sealed with clay to prevent concrete slurry from leaking into the tube.

Attached to the end of the bar specimen was a piece of Schedule 160 steel pipe. This was the same pipe used for the tension test series 2 specimen grips. This end of the bar was gripped into the Tinius Olsen universal machine, similar to the tension tests described in Section 6.2.3.3.

A steel frame constructed from Unistrut was used to align the specimens during casting, Figure 6.53. The specimens were aligned and taped onto the frame during the casting of the concrete. The concrete mix used is given in Table 6.11. The concrete was mixed using a drum 5 cubic foot drum mixer (Imer Minuteman). Additional 4-in by 8-in (101.6-mm by 203.2–mm) cylinders were made to obtain the compressive and tensile strength of the concrete. The specimens were cured in a water bath until tested.

Shown in Table 6.12 are the embedment lengths used for the test. The bar was cut into 24 inch (609.6-mm) lengths. The embedment length was varied by changing the height the paper tube was placed in the cylinder. This range of embedment lengths encompassed the theoretical development length computed in section 6.4.2.1.

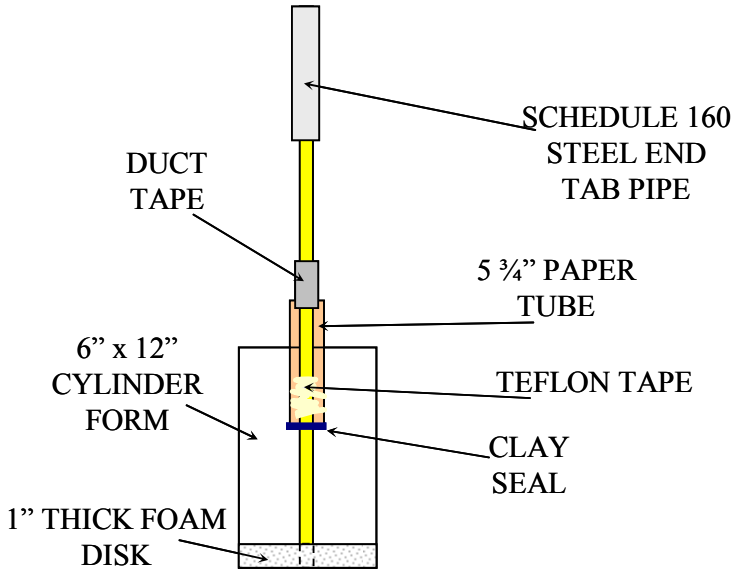

Figure 6.52: Bond Specimen Detail for 10-mm DHFRP Bars.

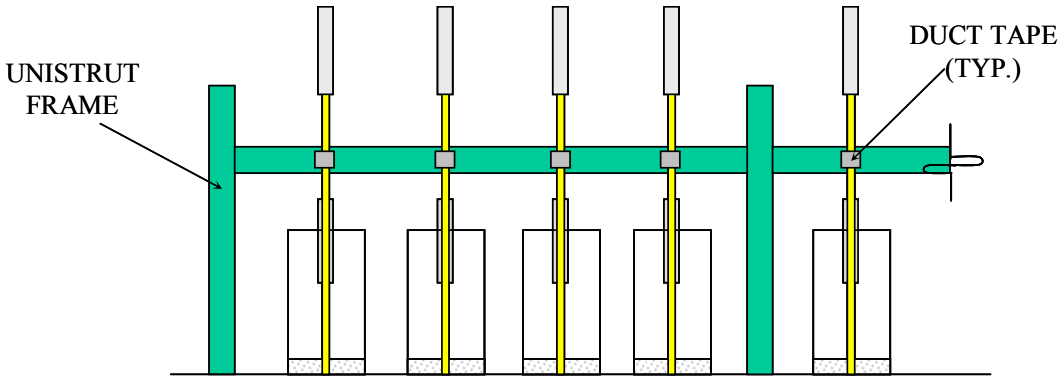

Figure 6.53: Bond Casting Setup for 10-mm DHFRP Bars.

Table 6.11: Concrete Mix Design Used for Bond Pullout Specimens.

Material	Ratio by weight	Weight for mix, lb (kg)
Coarse aggregate 3/8" dia.	3	351.76 (159.56)
Sand	2	234.51 (106.37)
Cement (Type III)	1	117.26 (53.19)
Water	0.45	52.77 (23.94)

Note: This mix is for 3—6" x 12" and 6—4" x 8" cylinders

Table 6.12: Embedment Lengths Used for Bond Pullout Specimens.

Embedment length, in (mm)	Number of DHFRP Specimens
2.5 (63.5)	3
5.0 (127.0)	3
7.5 (190.5)	3
10.0 (254.0	3
12.0 (304.8)	2

6.4.5 Test Procedure

The testing program for bond strength consisted of test specimens subjected to monotonic tensile load to failure. The setup is shown schematically in Figure 6.54. A Tinius Olsen 120K capacity Universal machine was used. The concrete specimen was placed on top of the stationary cross-head. The concrete specimen was placed on a 1/2" steel bearing plate. The plate was slotted to allow the bar to be placed in it. The bar was aligned downward through the hole in the cross-head. The pipe end tab was placed in an articulation device, similar to that used for tension specimens, Series II (Section 6.2.3.3).

The articulation device was placed in the vee-grip in the lower movable cross-head. The overall setup is also shown in Figure 6.55.

The free end and forced end slip were measured. For the free-end slip, an LVDT was placed on the 1-in piece of bar sticking out of the concrete cylinder. The LVDT was spring loaded as to not lose contact with the bar. The LVDT was mounted on a separate supporting structure. The forced-end slip was not measured directly. It was impossible to mount the LVDT at the interface of the forced-end of the concrete. A mounting bracket was placed on the bar as close as possible to the surface. Two LVDTs were used to eliminate any possible bending effects. The LVDTs are shown in Figure 6.56.

The load was applied at a rate of 0.04 in/ min. The load and LVDT displacements were measured using the System 10 DataPAC (Daytronics Inc.) data acquisition system.

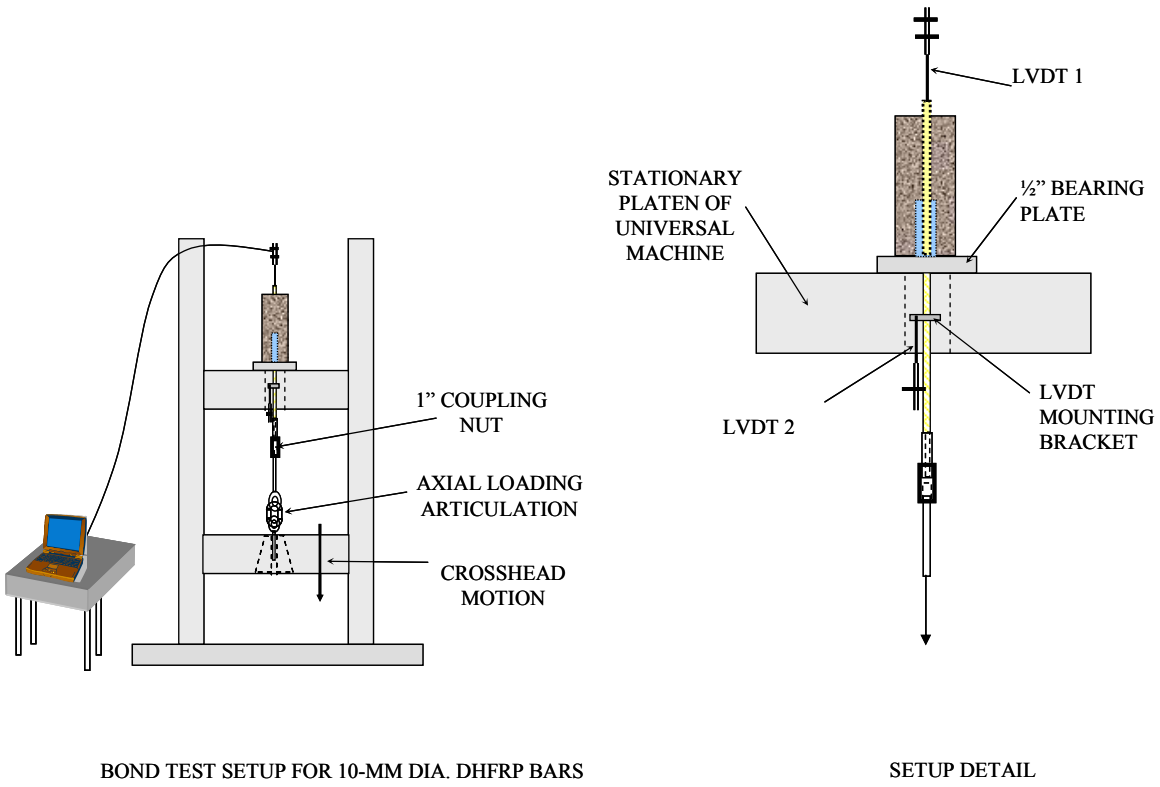

Figure 6.54: Bond Test Setup for 10-mm DHFRP Bars.

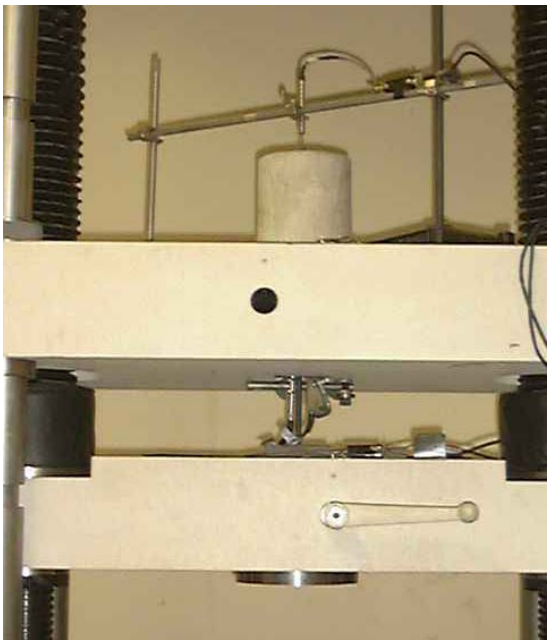

Figure 6.55: Bond Pullout Test Specimen in Tinius Olsen 120K Universal Machine.

Figure 6.56: Slip Measurement: (a) Free-End Slip on Bar and (b) Forced-End Slip on Bar.

6.4.6 Results

The results of the pullout tests included the measured slip at both the free end and the forced end of the embedded bar. Two embedment lengths were tested, 2.5 inches and 5.0 in. Shown in Figures 6.57 through 6.60 is the free end slip versus load for each individual specimen. Figure 6.61 shows the free end load-slip behavior for all DHFRP bars for both embedment lengths. The forced end load-slip behavior is shown in Figures 6.62 through 6.65 for each individual specimen and the forced-end behavior is shown for all specimens in Fig. 6.66.

The bond stress was then calculated based on the bar diameter. Figure 6.67 shows the free end bond stress versus slip behavior for all specimens. The forced end bond stress versus slip is shown in Figure 6.68. Figure 6.69 shows the average free end stress-slip behavior for both embedment lengths. The average forced end stress-slip behavior

for both embedment lengths is given in Figure 6.70. A comparison between the free end and forced end behaviors for both embedment lengths is shown in Figure 6.71. The bond test results are presented in Table 6.13 with average design values given.

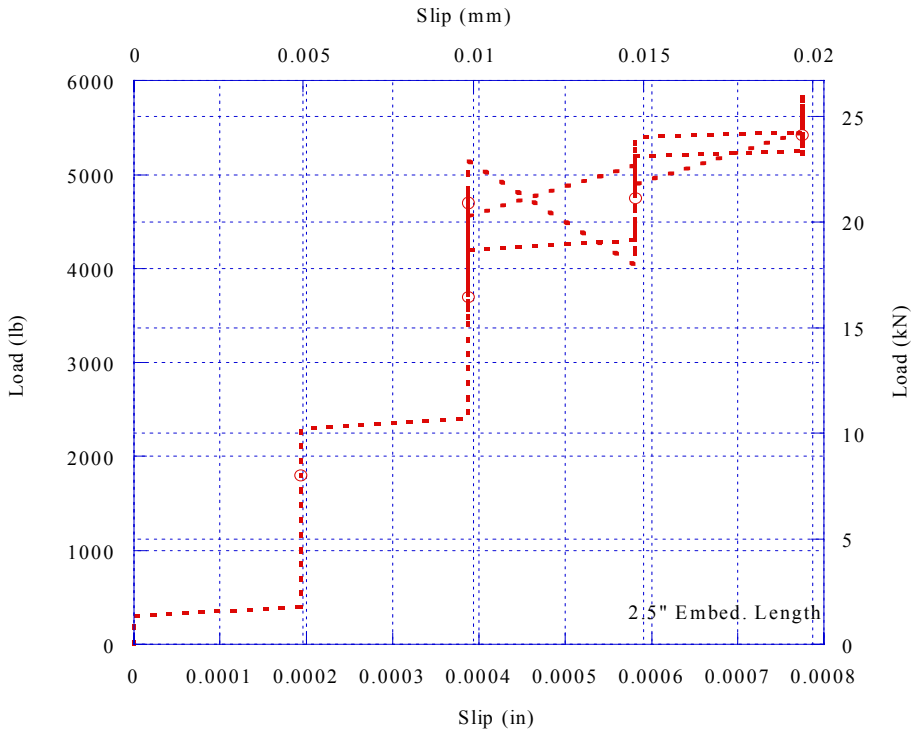

Figure 6.57: Free-End Load-Slip Behavior, Bond Specimen B3.

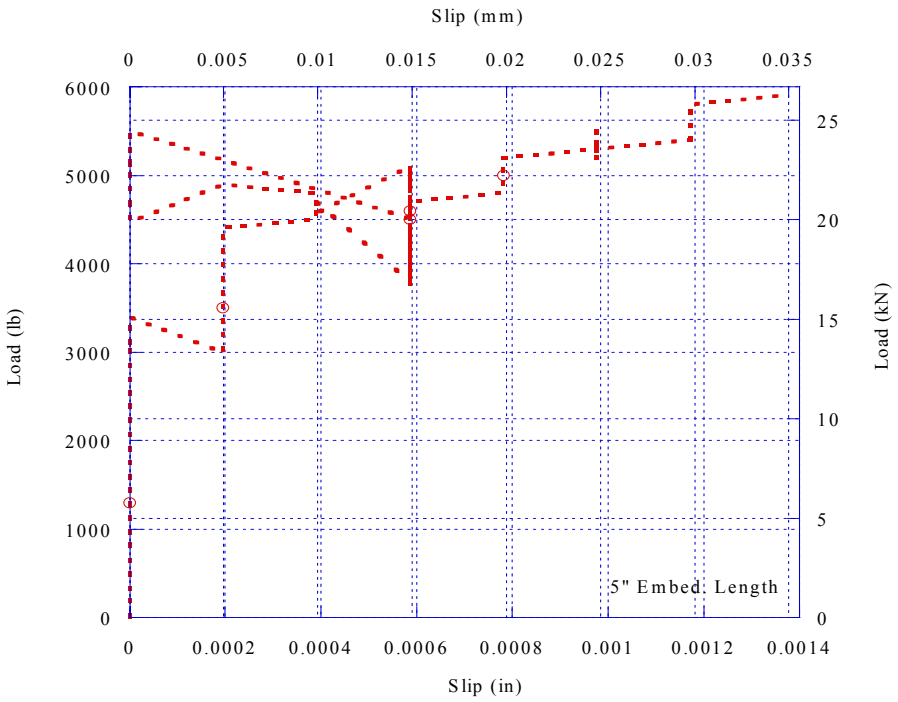

Figure 6.58: Free-End Load-Slip Behavior, Bond Specimen B5.

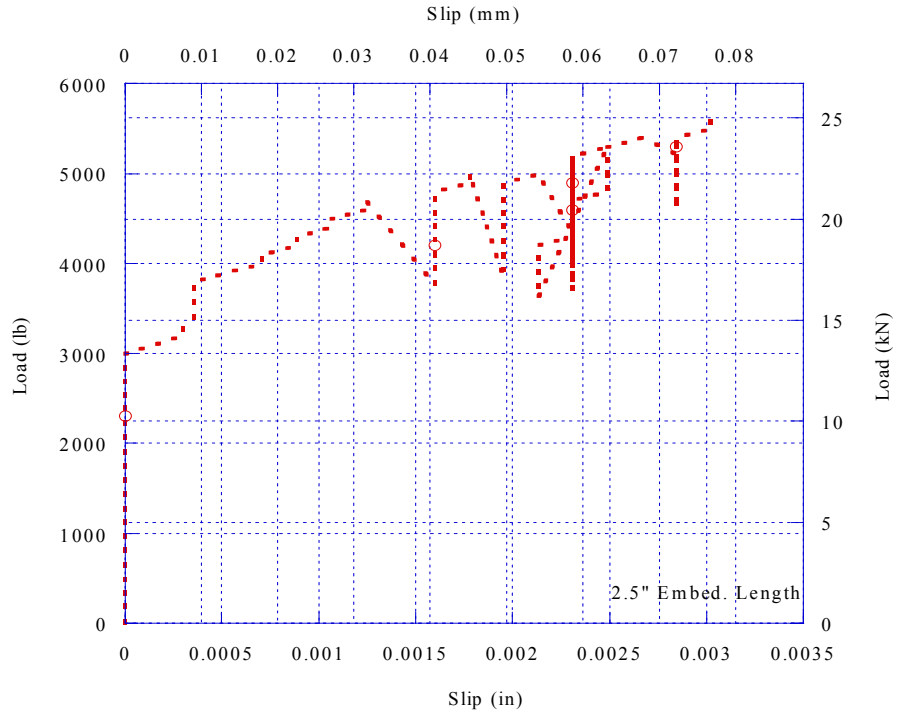

Figure 6.59: Free-End Load-Slip Behavior, Bond Specimen B6.

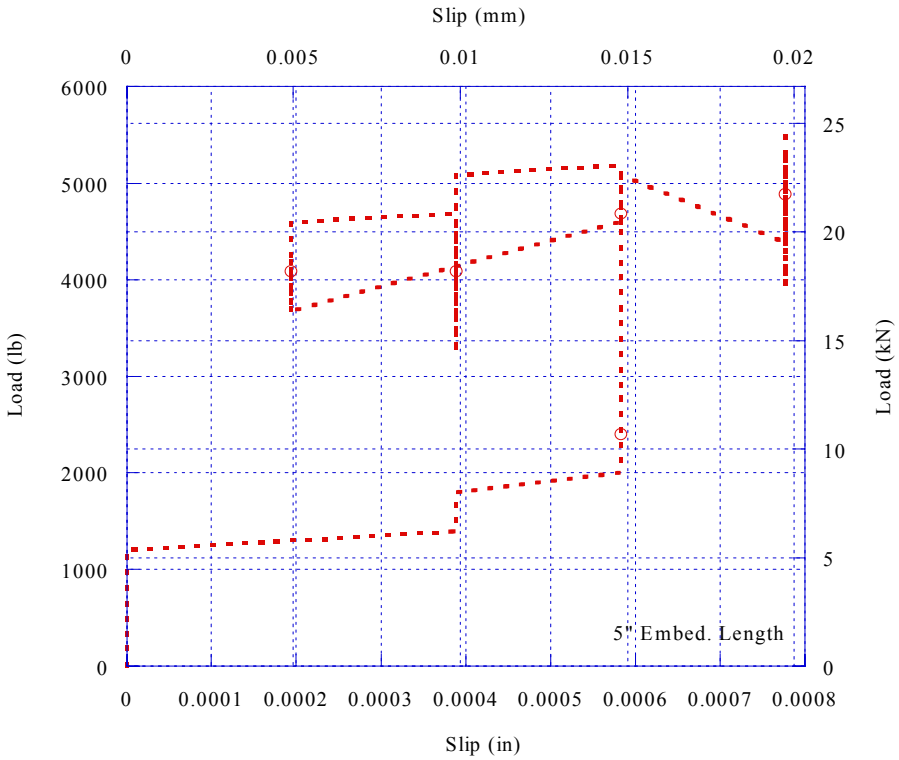

Figure 6.60: Free-End Load-Slip Behavior, Bond Specimen B7.

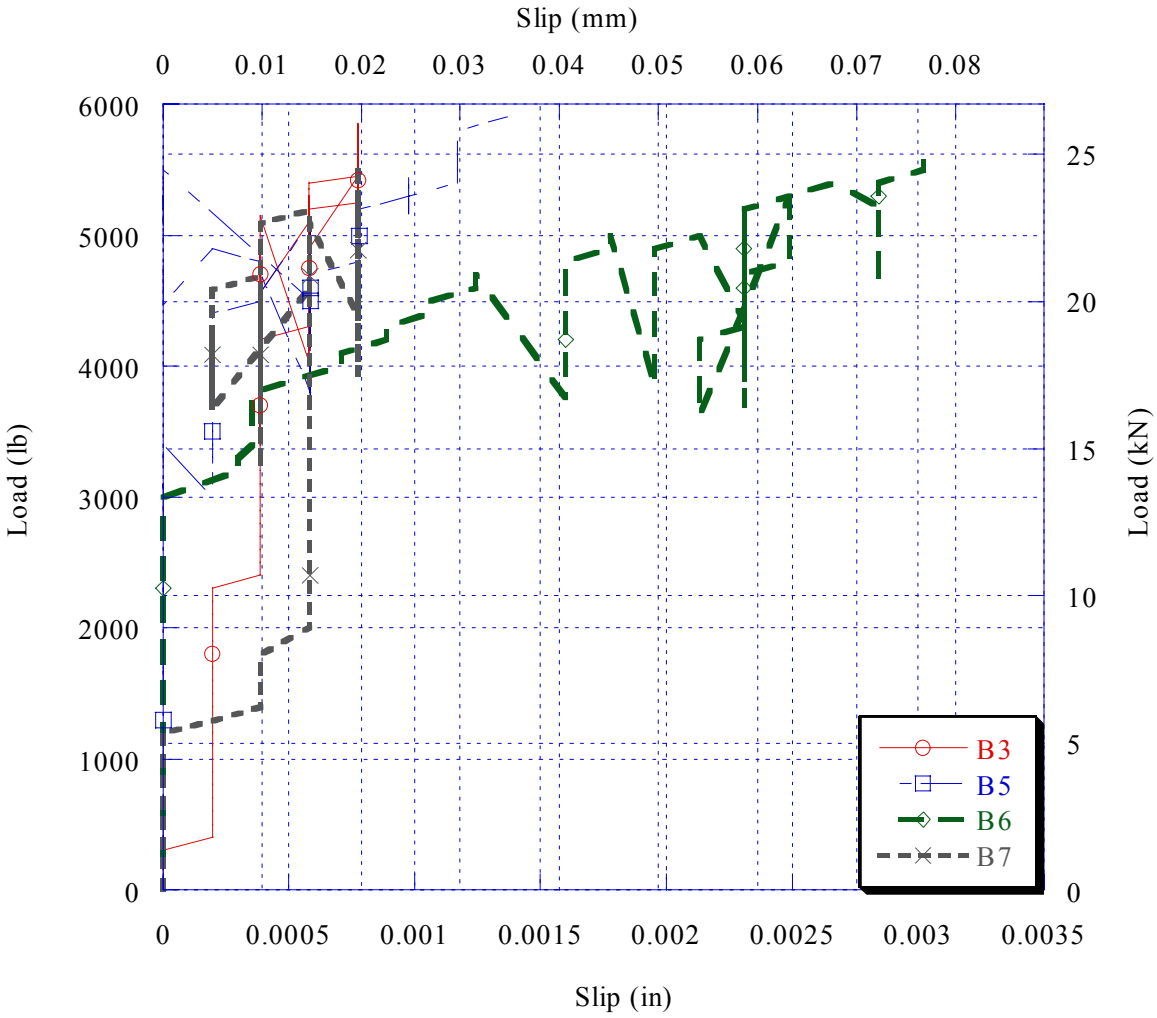

Figure 6.61: Free-End Load-Slip Behavior for 10-mm Diameter DHFRP Bars with Various Embedment Lengths.

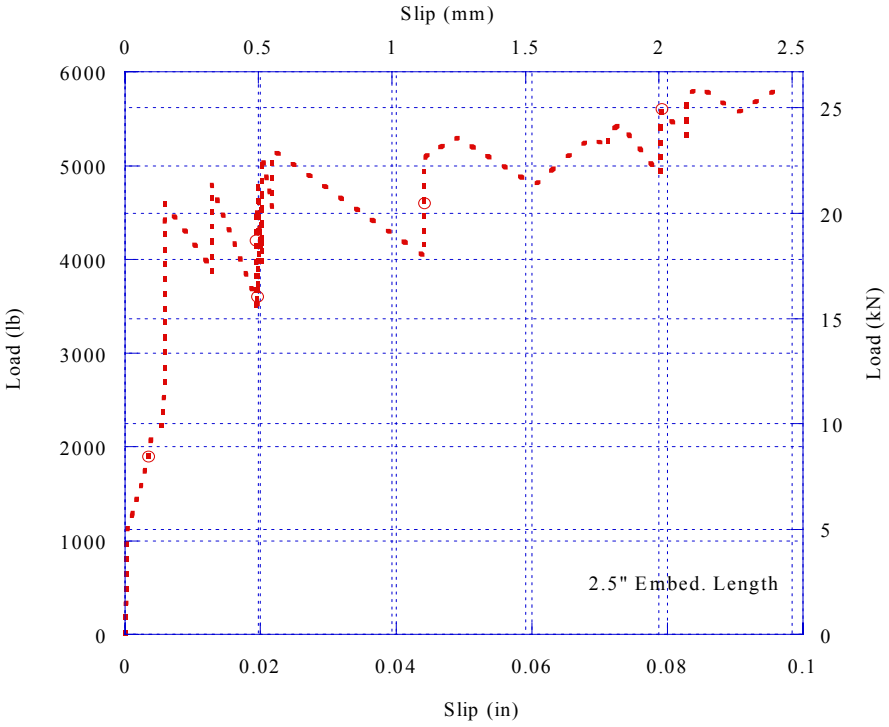

Figure 6.62: Forced-End Load-Slip Behavior, Bond Specimen B3.

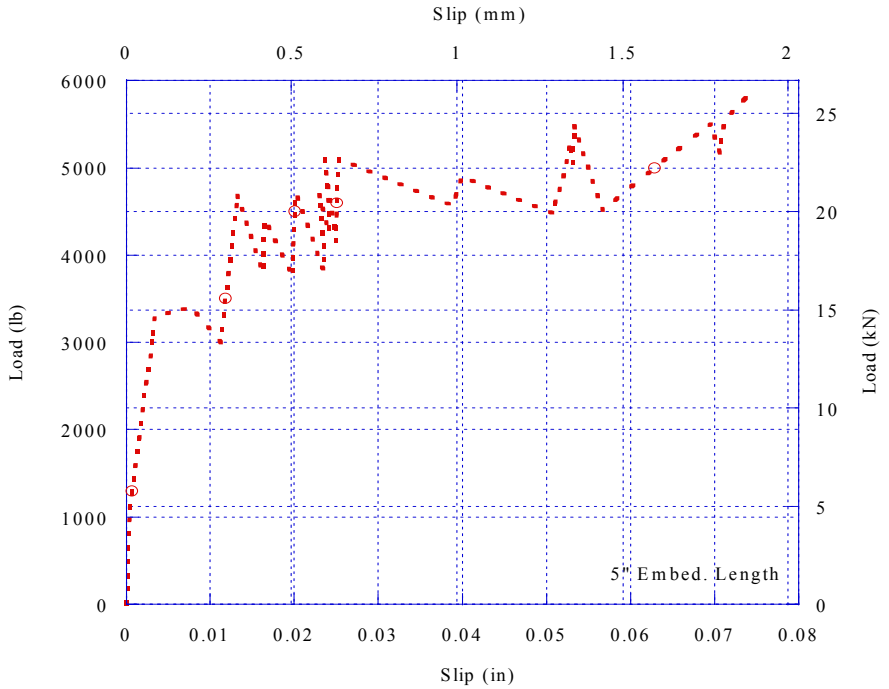

Figure 6.63: Forced-End Load-Slip Behavior, Bond Specimen B5.

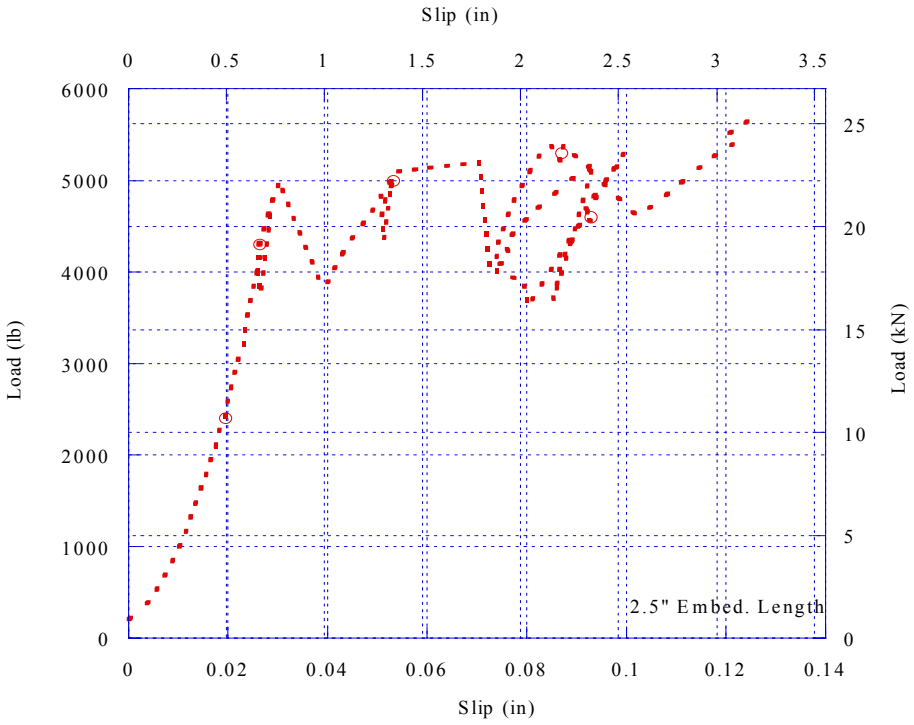

Figure 6.64: Forced-End Load-Slip Behavior, Bond Specimen B6.

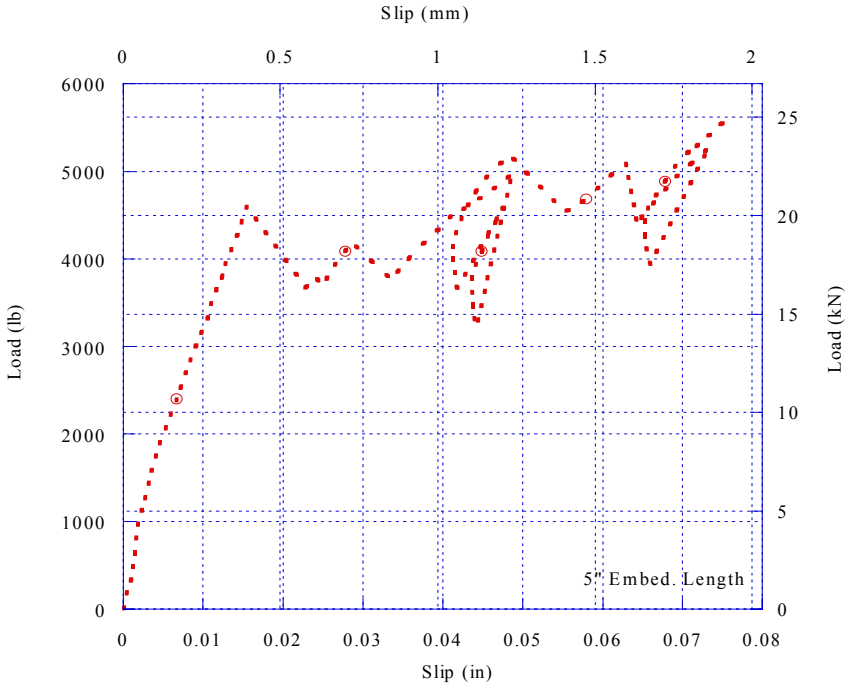

Figure 6.65: Forced-End Load-Slip Behavior, Bond Specimen B7.

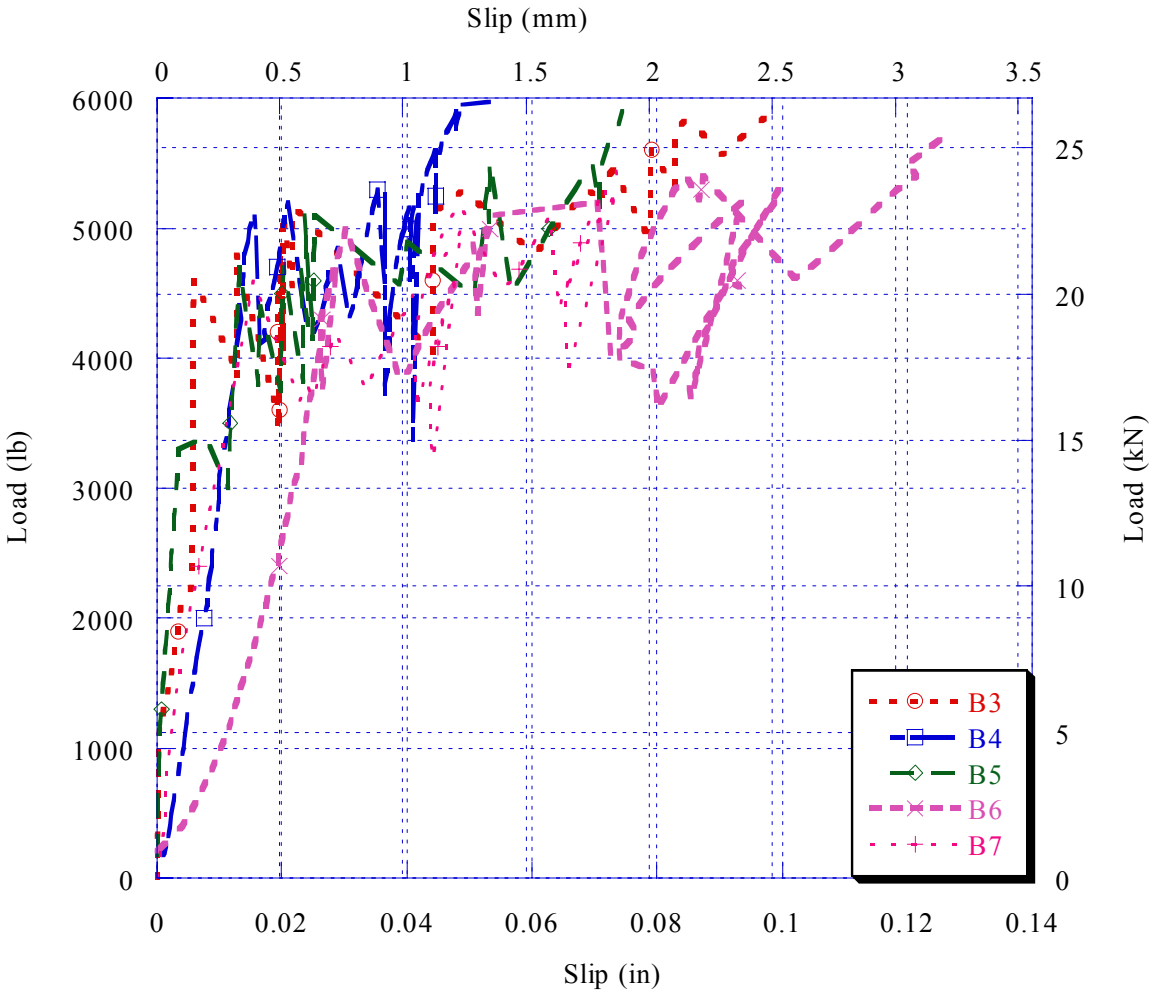

Figure 6.66: Forced-End Load-Slip Behavior, 10-mm DHFRP Bond Specimens, Embedment Lengths = 2.5” (63.5 mm) and 5.0” (127 mm).

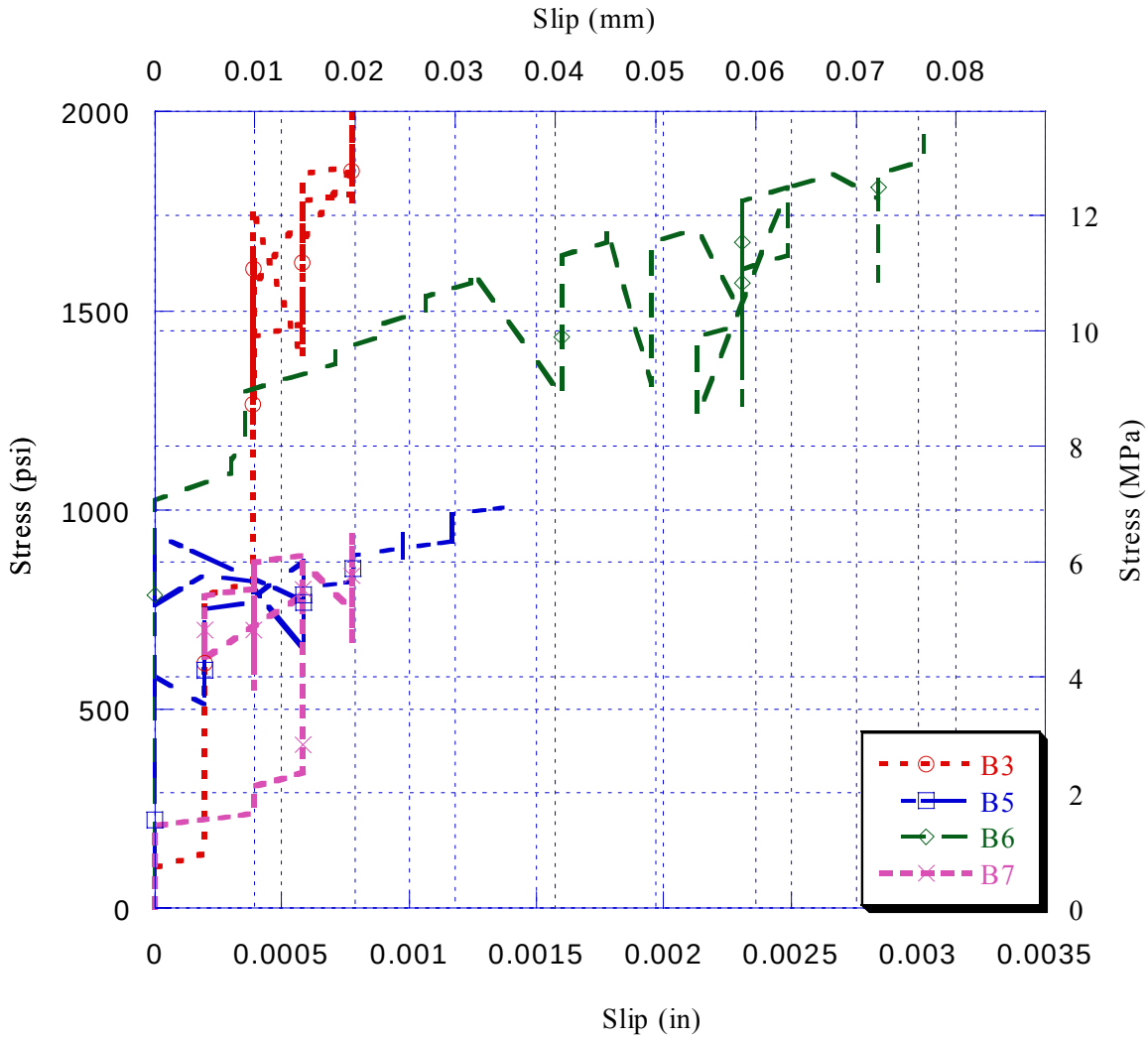

Figure 6.67: Free-End Stress-Slip Behavior, 10-mm DHFRP Bond Specimens, Embedment Lengths = 2.5" (63.5 mm) and 5.0" (127 mm).

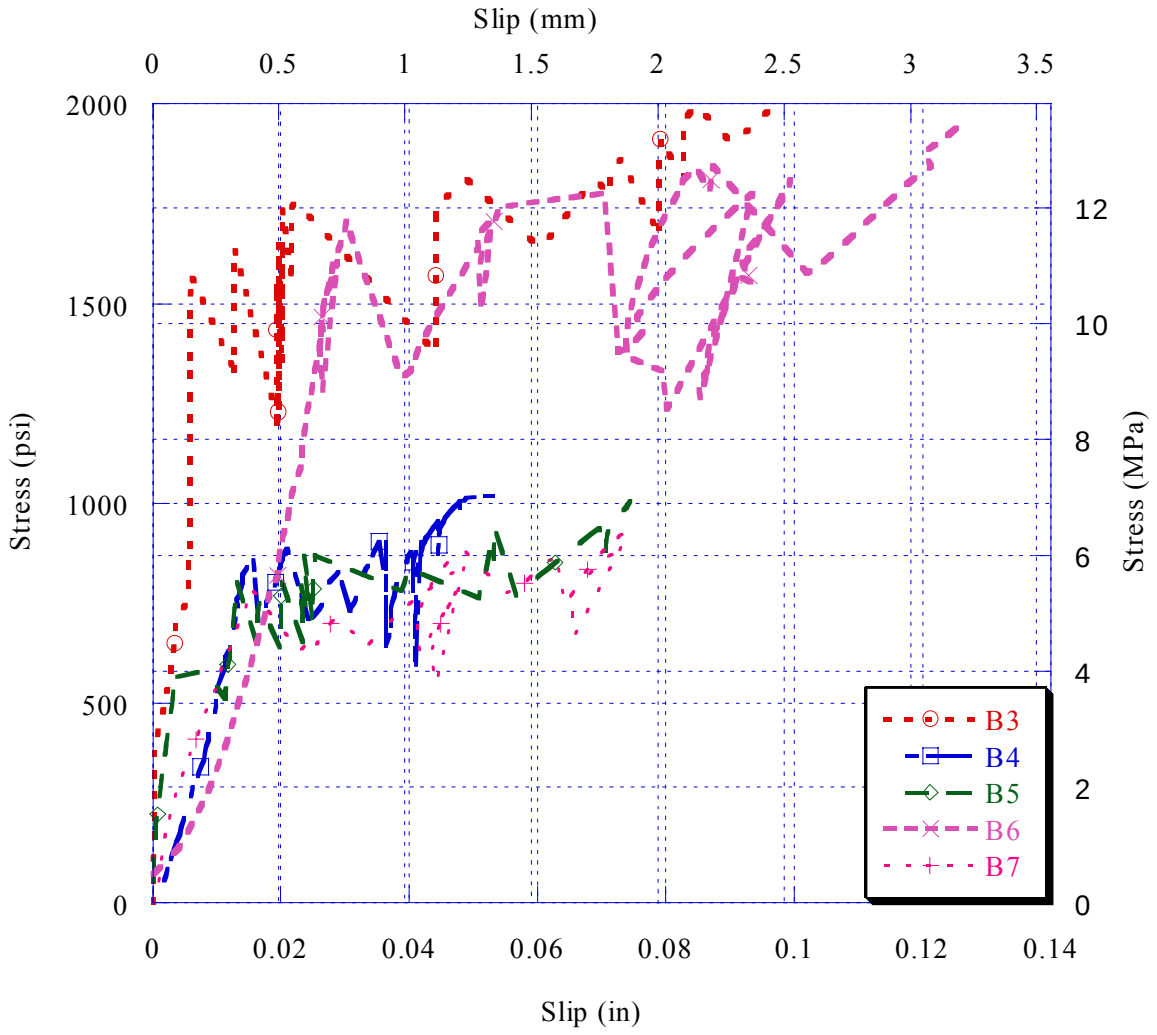

Figure 6.68: Forced-End Stress-Slip Behavior, 10-mm DHFRP Bond Specimens, Embedment Lengths = 2.5" (63.5 mm) and 5.0" (127 mm).

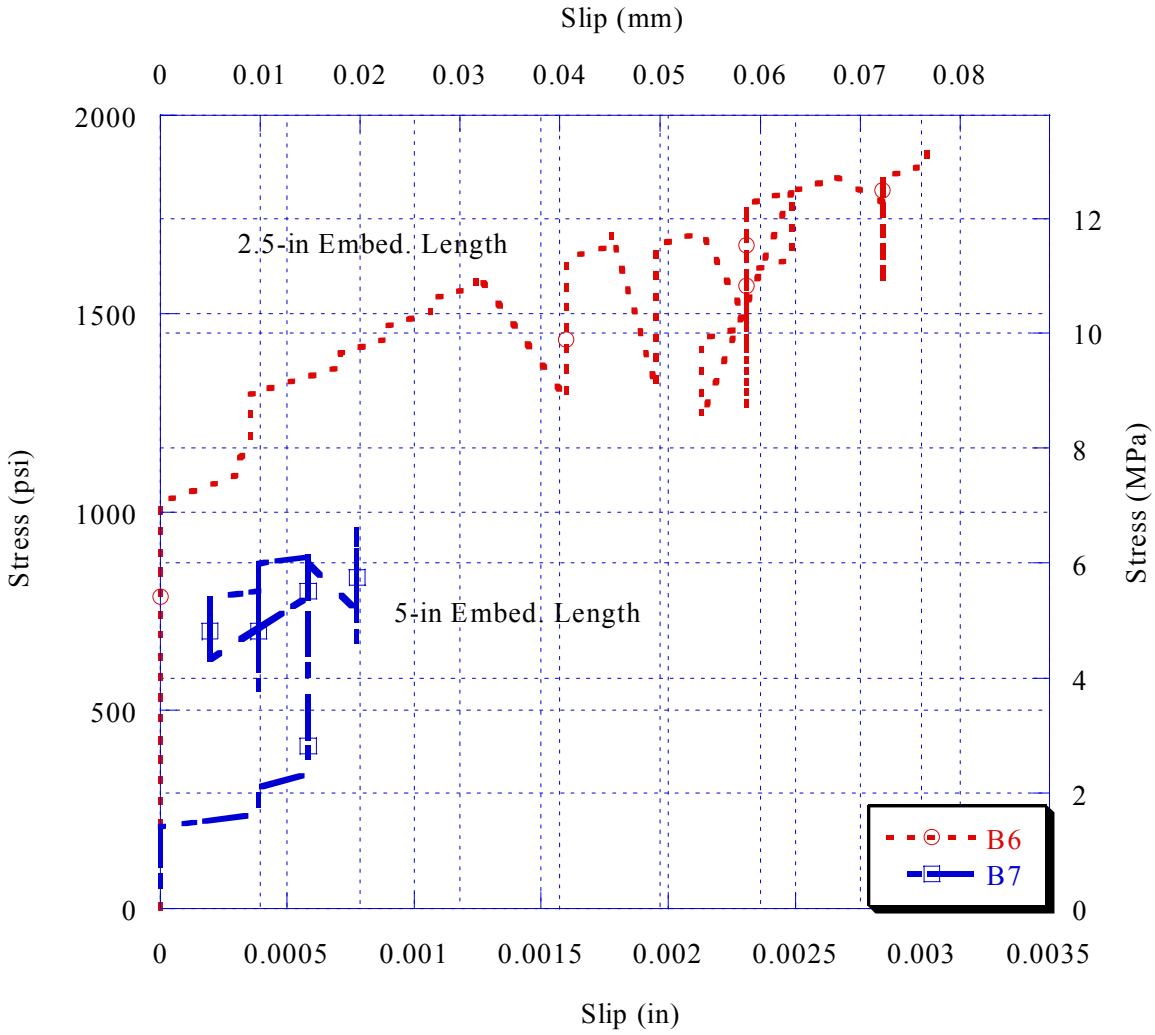

Figure 6.69: Average Free-End Stress-Slip Behavior for 2.5" (63.5 mm) and 5.0" (127 mm) Embedment Lengths, 10-mm DHFRP Bars.

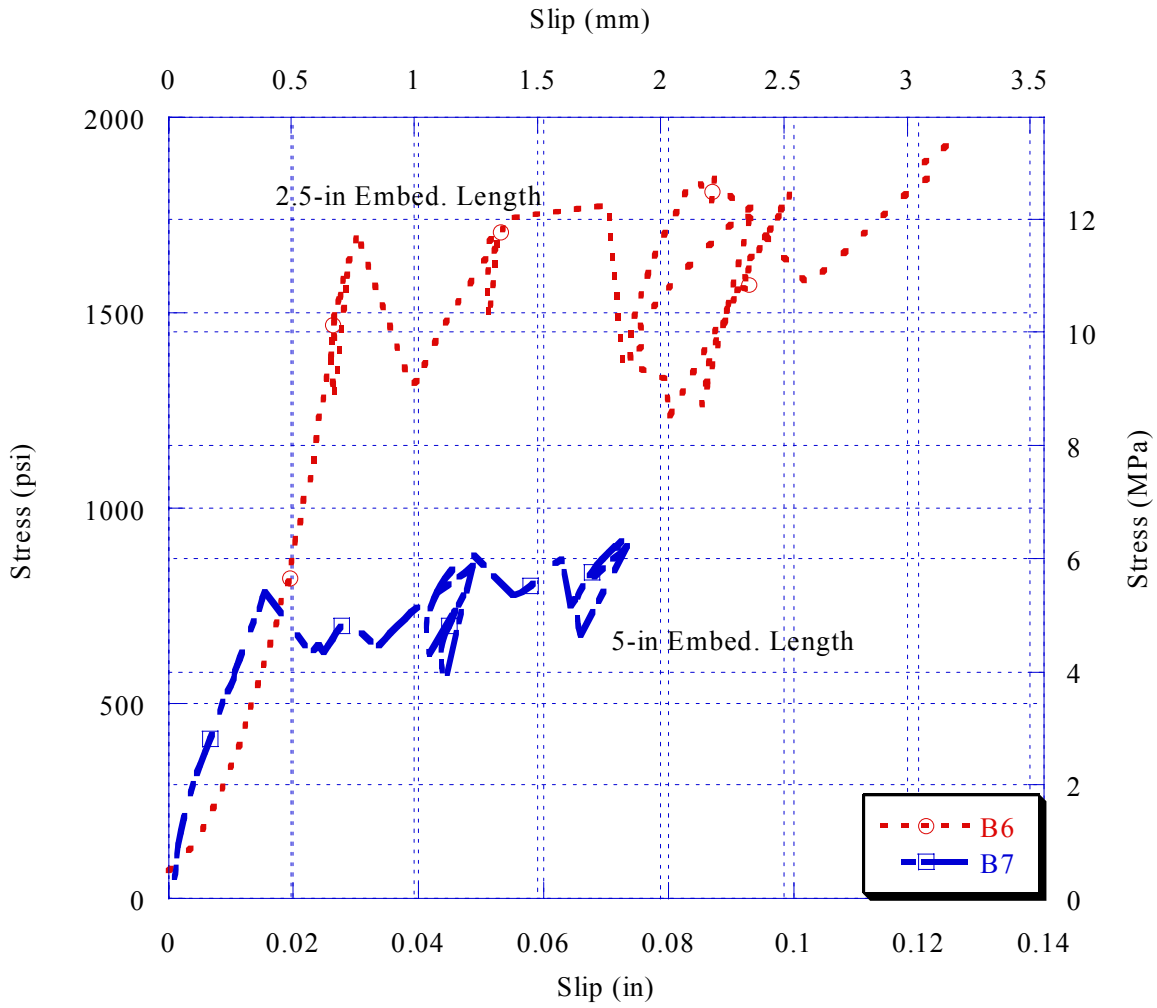

Figure 6.70: Average Forced-End Stress-Slip Behavior for 2.5" (63.5 mm) and 5.0" (127 mm) Embedment Lengths, 10-mm DHFRP Bars.

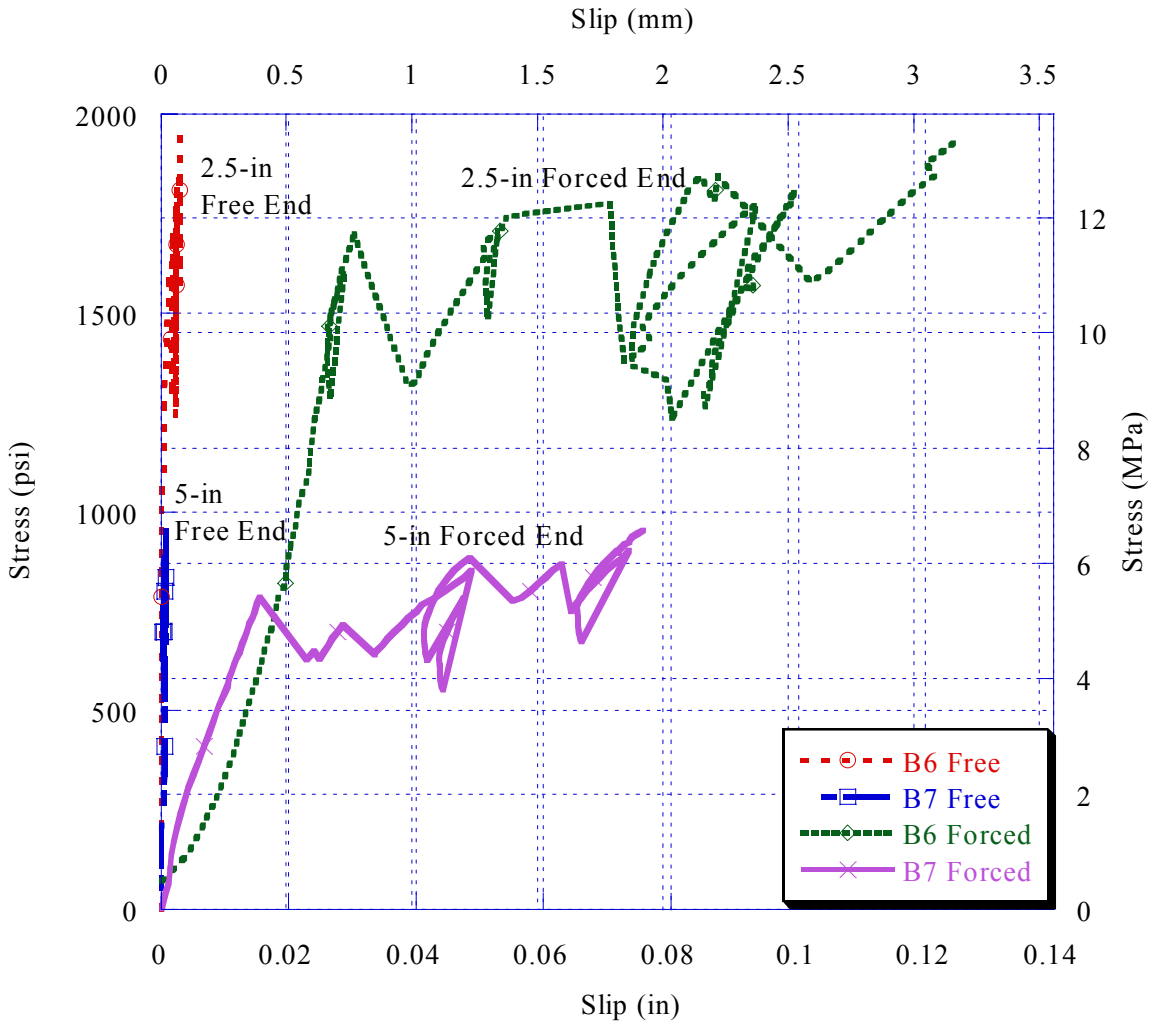

Figure 6.71: Comparison of Average Free-End and Forced-End Stress-Slip Behavior for 2.5" (63.5 mm) and 5.0" (127 mm) Embedment Lengths, 10-mm DHFRP Bars.

Table 6.13: Summary of Results from Bond Tests of 10-mm DHFRP Bars.

Specimen ID	Embedment length, in (mm)	Total free end slip, in (mm)	Average forced-end slip, in (mm)	Failure load, lb (kN)	Failure stress, psi, (MPa)
B3	2.5 (63.5)	0.0008 (0.02)	0.0971 (2.47)	5846 (26.0)	1996.1 (13.8)
B4	5.0 (127)	0.0205 (0.52)	0.0532 (1.35)	5970 (26.6)	1019.21 (7.0)
B5	5.0 (127)	0.0013 (.03)	0.0744 (1.89)	5900 (26.2)	1007.26 (6.9)
B6	2.5 (63.5)	0.003 (0.08)	0.1252 (3.18)	5680 (25.3)	1939.4 (13.4)
B7	5.0 (127)	0.0008 (0.02)	0.0756 (1.92)	5590 (24.9)	954.33 (6.6)
Avg. values for 2.5" emb.		0.002 (.05)	0.111 (2.82)	5763 (25.6)	1967.7 (13.6)
Avg. values for 5.0" emb.		0.007 (0.19)	0.068 (1.72)	5820 (25.9)	993.6 (6.9)
dia_{bar} = 0.3729 in (9.47)		$A_{bond\ 2.5"} = \pi\, dia_{bar}\, L$ =2.93 in^2		$A_{bond\ 2.5"}$ = 5.86 in^2	

6.4.7 Discussion

Shown in Figures 6.57 through 6.61 were the free end load versus slip relationships for 10-mm DHFRP bars. Results for embedment lengths of 2.5 in and 5.0 in were presented. Specimens with embedment lengths of 7.5 in, 10.0 in, and 12.0 in were cast, but since all bond specimens with embedment lengths of 2.5 in and 5.0 in failed by bar rupture and not by bar pullout, the longer embedment length specimens were not tested. Figures 6.57 through 6.60 showed each test result individually to show the detailed pullout of each specimen and the combined results were shown in Figure 6.61.

As seen in Figures 6.57 through 6.61, all DHFRP had a similar slip mechanism. For all embedment lengths, failure occurred by bar rupture, not by bar pullout. The DHFRP slip mechanism is extremely unique, and is directly dependent on the failure mechanism of the bar, as described in section 6.3. The load-slip curve for DHFRP is a stepped curve until bar rupture. When the load was increased, very little free-end slip

was recorded. This is indicated by the vertical line in Figs. 6.58 through 6.60. When the load became sufficiently large, the core yarns yielded. At this fracture of a core yarn bundle, slip was recorded. However, the load level decreased simultaneously when the core yarns broke as indicated by the curve. As the load was again increased after yielding, virtually no slip was detected until another yarn bundle of core yarns broke. This pattern continued until rupture of the DHFRP bar, thereby causing the stepped appearance of the load-slip curve.

The slip of the DHFRP bar was caused by progressive fracture of the core yarns. When a group of core yarns fractured, a stress wave or shock wave was released into the bar. This energy release was also observed in the tension tests of DHFRP bars. In the tension test, this energy wave caused spalling of the outer surface of the epoxy end tabs at the ends of the bar. For the bond test, this stress wave caused the bar to suddenly pull or tug for the duration of the wave. This was instantaneous with the core yarn breakage. This energy release caused a sudden and instantaneous slip of the bar. After the stress wave passed through the bar, the slip was again negligible until the next stress wave passed through the bar (i.e., core yarn bundle failure). This bond-slip mechanism is unique to the DHFRP bar based on its design, and does not exist for other FRP bars or steel.

The forced end load versus slip behavior was shown Figures 6.62 through 6.64 for each individual specimen and the combined results were presented in Figure 6.66. The forced end slip was greatest for the shortest embedment length (2.5 in). The behavior for all specimens was very consistent and repeatable as shown in Figure 6.66. The forced end slip behavior was governed by the failure mechanism of the DHFRP bar itself. These

curves are similar to the tensile curves for the DHFRP bars (Figs. 6.26 through 6.31). Slip occurred continuously throughout the entire test until bar rupture. Slip also occurred when the carbon core yarn bundles broke, similar to the free end slip behavior. Again, when the core yarns broke, the load dropped and the rate of slip decreased until the load reached the previous maximum level. This behavior was governed by the failure behavior of the bar. The forced end behavior was more consistent than the free-end slip behavior and followed more closely the actual failure of the bar instead of the energy wave that pulled on the bar which influenced the free-end slip.

The bond stress versus slip was shown in Figure 6.67 for the free end and in Figure 6.68 for the forced end. The experimental bond stress is defined as

$$u_{avg} = \frac{F_{bond}}{\pi dL} \qquad 6\text{-}22$$

By plotting the stress instead of the load, the values are normalized by a factor of the embedment length, as given in Eqn. 6-22. This is especially evident for the forced end slip, Fig. 6.68, where the bond stress is almost double for the shorter embedment length. Shown in Figure 6.69 was the average free end stress-slip behavior for both embedment lengths. This figure showed the step behavior that is typical in the free-end slip, and the variation in stress values for the two embedment lengths. Figure 6.70 showed the average bond stress-bar slip behavior for the forced end. These two curves would be used to derive experimental design values for development lengths and bond stress values. Figure 6.71 compared the average free and forced end stress-slip curves for both embedment lengths. This figure shows that the forced-end slip is much more significant than the free end slip. When plotted together, it is evident that the free end slip is almost

negligible compared with the forced end slip. However, both values of slip are extremely small for an embedment length of only 2.5 in.

Concrete cylinders (4" x 8", 101.6 x 203.2 mm) were tested to obtain values of the concrete compressive strength f'_c. The average compressive strength of the concrete used for the bond specimens was 4731 psi (32.6 MPa).

The values of the average free end slip, forced end slip, failure load, and failure stress were tabulated in Table 6.13. These values and the experimental concrete compressive strength are used to compute various quantities for the DHFRP bars. The development length based on the experimental bond stress data (Eqn. 6-12) is computed. Also, the K factor to compute the development length as a function of the bar cross-sectional area (Eqn. 6-20) is computed. The K factor for steel bars is 0.04 and the development length equation was given as Eqn. 6-13. These experimental results are given in Table 6.14. The theoretically computed development lengths given in Table 6.9 are compared with the values obtained using bond stress data.

Table 6.14: Experimental Values of Development Length Parameters and Comparison with Theoretical Values.

K (Eqn 6-20)	l_d, (Eqn. 6-12), in (mm)	Theoretical l_d, (Eqn. 6-11a)	Theoretical l_d, (Eqn. 6-11a)	% Diff, Eqns. 6-12 and 6-11a
u_{avg} for 2.5"	1.90 (48.26)	10.46 (265.7)	15.68 (398.3)	550.5
0.027				
u_{avg} for 5.0"	3.77 (95.76)	10.46 (265.7)	15.68 (398.3)	277.5
0.054				

The *K* value for DHFRP used in equation 6-14 compares well to the value for steel (0.04). Since both embedment lengths resulted in bar rupture and not bar pullout, the ultimate load values were almost identical. Since the bond stress is the load divided by the bar surface area (i.e., divided by the embedment length), the stress values for the 5.0 in embedment length are half for the 2.5 in embedment lengths. Therefore, the *K* factor and experimental development lengths were computed twice, corresponding to each value of the bond stress (Table 6.14). The experimental development length values are much lower than the theoretical values (Tables 6.14 and 6.9). Section 12.2.1 of the ACI 318-02 code states that the development length should not be less than 12 in or 300 mm. The experimental values obtained for DHFRP were much below the theoretical values. Additional testing of embedment lengths less than 2.5 inches was not conducted since embedment lengths this short would have little practical value in actual construction. A conservative value of 5.0 in development length (2.6 times the experimental value obtained) could be used for design purposes.

The DHFRP bars ruptured at embedment lengths as short as 2.5". This was because of the new symmetric preform design using more rib yarns. Also, keeping the braid angle at approximately 45 degrees increased the rib height and spacing, thereby improving the mechanical interlock. Also, the general surface of the DFRP bar away from the rib was rough since the bar was manufactured without a die. This greatly improved the bond strength of the DHFRP bars. From the bond pullout tests, the development length computed using the ACI 318-02 code results in very conservative values for the DHFRP bar.

CHAPTER 7. LONG-TERM CHARACTERIZATION OF DHFRP BARS

7.1 Background

The short-term material behavior must be quantified before any predictions or testing on long-term behavior can be made. The short-term behavior of DHFRP was described in Chapters 5 and 6 and included microscopy of the DHFRP cross section, tensile characterization, bond strength, and bending strength. Long-term behavior includes creep and stress-rupture behavior for life-cycle design of structures and high-cycle fatigue strength for the proper design in highway bridges. The creep and stress-rupture behavior was quantified for 5-mm diameter DHFRP bars.

7.2 Creep and Stress-Rupture Characterization

Creep is a visco-elastic effect that is manifested as a polymer deforms under constant load. For steel, this effect occurs at elevated temperatures, but for polymers, creep can occur at room temperature. Data on the creep-rupture capacity of materials is needed for proper life-cycle design of structures. The creep-rupture strength and behavior is well known for materials such as steel, but is less defined for newly manufactured composite materials. For steel, a sustained tensile load of 75% or lower of the ultimate load is considered safe for creep rupture failure (Dowling, 1999). For the proper life-cycle design of reinforced-concrete structures with DHFRP reinforcing, it is mandatory to know the long-term time-dependent properties such as creep-rupture strength for the 50-year design life of the structure. A test was conducted to determine the creep-rupture behavior of 5-mm diameter DHFRP bars.

7.2.1 Sample Preparation

The 5-mm diameter DHFRP bars were cut to 16" lengths and each end was embedded in 2" by 4" (50.8-mm x 101.6-mm) concrete cylinders. Type III cement was used to accelerate the cure time. A mix of 3:2:1 of sand: cement: water was used. Sufficient embedment length was provided to prevent pullout failure of the bars. A creep specimen is shown in Figure 7.1.

7.2.2 Test Procedure

A test was conducted to determine the creep-rupture behavior of 5-mm DHFRP bars. The test setup is shown in Figure 7.2. The test was conducted on a plumb lever-type creep testing device built at Drexel University. It consisted of two twin aluminum W-shape towers. The lever arm was a cold-rolled steel piece of Unistrut (Unistrut Philadelphia) that was pinned to the towers. This pin connected the specimen to the load point. The load to dead weight ratio was 1:10. Two timers were mounted to the specimen in series to record the time until failure, one a 24-hour timer measuring increments of 15 minutes, and the other a 12-hour timer, with seconds as the smallest time gradation.

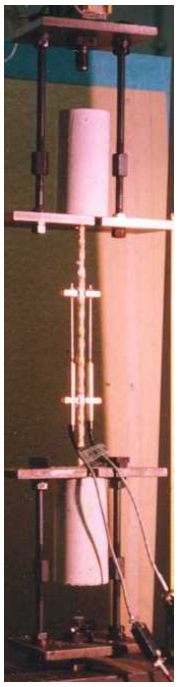

Figure 7.1: Creep-Rupture Test on 5-mm Diameter DHFRP Bars.

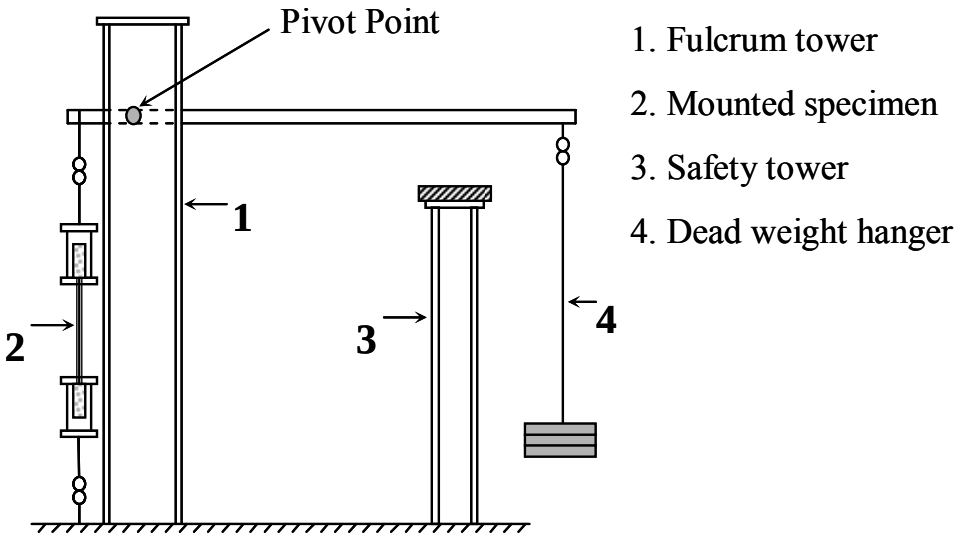

Figure 7.2: Creep-Rupture Test Setup for 5-mm DHFRP Bars.

Shown in Figure 7.3 is the specimen detail. The specimens were mounted in a double-plate system, both top and bottom. ¼" cold rolled steel plates were used. The plates were slotted to allow placement of both ends of the specimen. The set of two plates (one at each end) was held together by 3/8" diameter threaded rod. Four pieces of rod connected the two plates, one at each corner. This plate system was articulated at each end using eyebolts. A ¼" open eyebolt was pried open, and a ¼" closed eyebolt was placed in it. The open eyebolt was then welded closed. This acted as a universal joint which compensated for any misalignment that might occur when loaded.

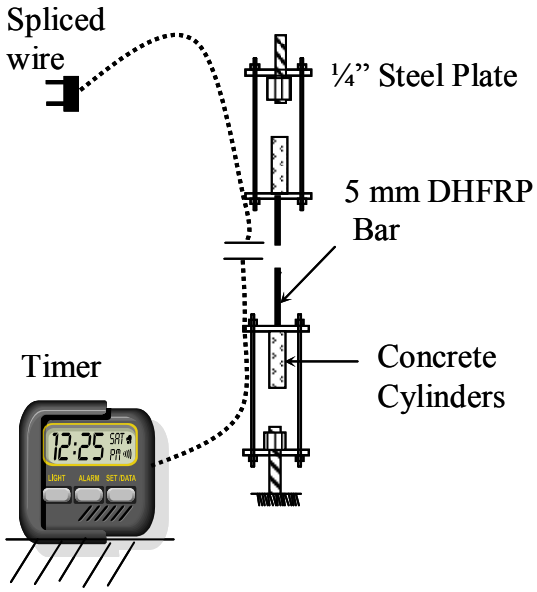

Figure 7.3: Detail of Creep-Rupture Test Setup.

The bars used were 5-mm bars with the original preform design and manufacturing process (Somboonsong, 1997). The material load-strain and stress-strain curves for the 5-mm bars are shown in Figure 7.4.

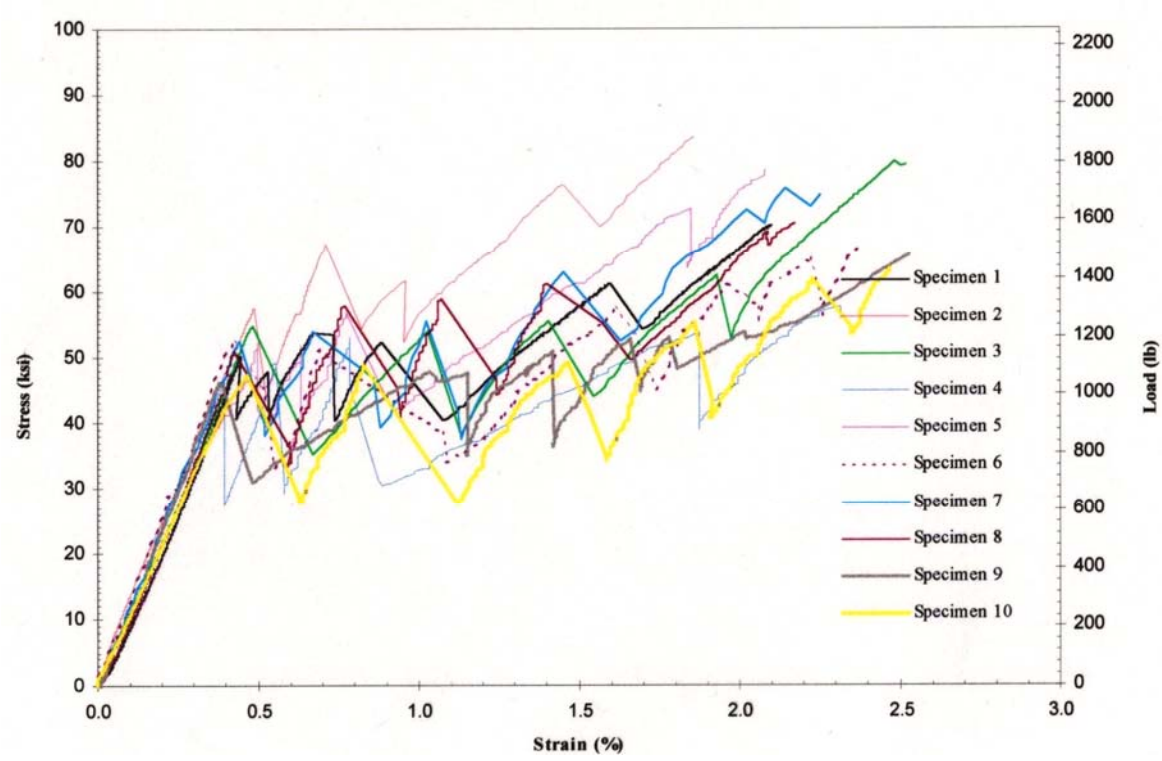

Figure 7.4: DHFRP Material Stress-Strain and Load-Strain for 5-mm DHFRP Bars (Somboonsong, 1997).

The specimens were placed in the double plate system without dead weight. Dead weight was then quickly placed on the weight hanger at the opposite end of the fulcrum. The weights used were 20, 10, and 5 lb (9.07, 4.54, and 2.27 kg) steel weights. Timing of the test commenced when all the dead weight was placed on the hanger. The time to

failure was then recorded. Failure was defined as either bar rupture or a prolonged amount of time (e.g., over 100 hours).

Approximately 20 specimens were tested at four different load levels. The four load levels were based on a percentage of the average ultimate tensile load, $P_{ult,\ shown}$ in Figure 7.4. From tension tests, the ultimate load capacity of the 5-mm bar was 5.34 kN (1.2 kips). The load levels chosen were 3.56, 4.00, 4.23, and 4.45 kN (0.8, 0.9, 0.95, 1.0 kips); these values corresponded to 90 %, 85 %, and 80 % of the ultimate tensile load, respectively. To initially get the system in horizontal equilibrium, an additional 0.31 kN of preload was added. The maximum sustained load and time to failure were then recorded for each specimen.

7.2.3 Results

Shown in Figure 7.5 is a plot of the load ratio $P_{rupture}/P_{ult}$ (rupture load to ultimate load ratio) versus time until failure. The results are tabulated in Table 7.1. Since the data is nonlinear, the semi-logarithmic plot was constructed, taking the log of time. A best fit logarithmic function was placed through the data using a built-in logarithmic function generator using the KaleidaGraph™ software (Synergy Software). This resulted in an equation of the form

$$Y = a - b \log T \qquad 7\text{-}1$$

The characteristic endurance line generated from the test data using KaleidaGraph is given by the logarithmic function

$$Y = 0.863 - 0.035 \log x \qquad 7\text{-}2$$

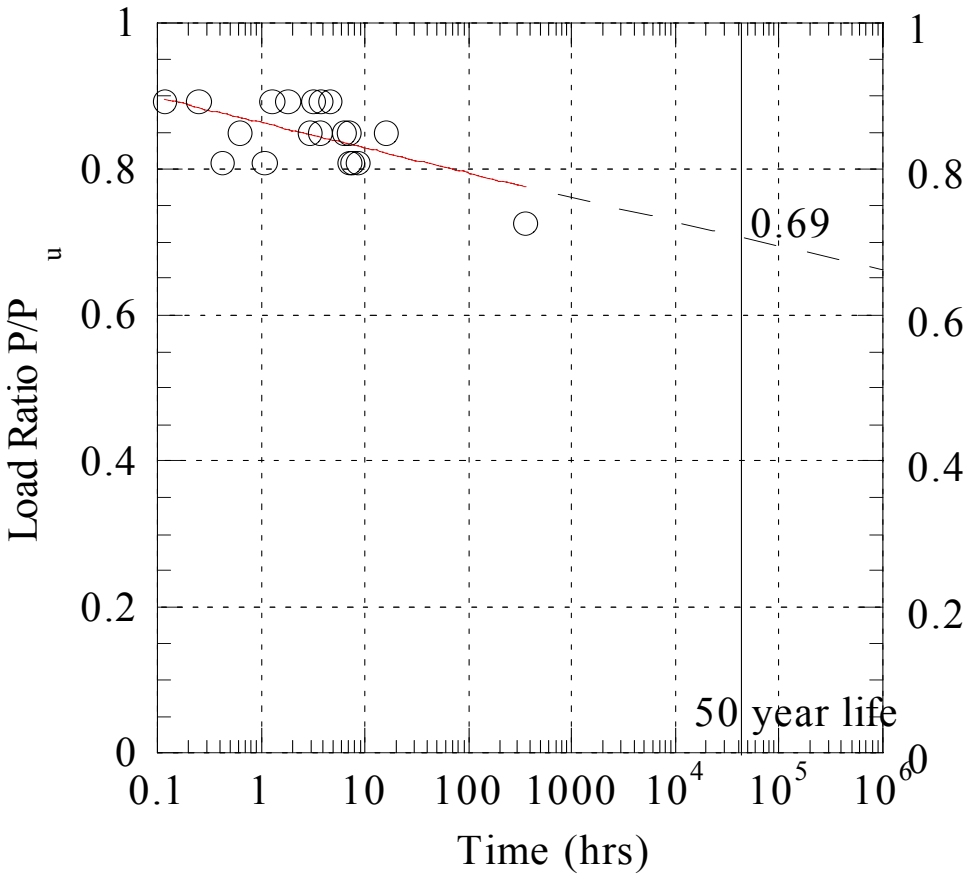

Figure 7.5: Stress-Rupture for 5-mm DHFRP Bars.

Table 7.1: Creep-Rupture Results for 5-mm DHFRP Bars.

Specimen ID	Force on Specimen (lb)	(kN)	Time to Failure (hours)	Mode of Failure
CR-1	1070	4.76	0.117	Bottom at cylinder
CR-2	1070		1.23	Top 1/3 point
CR-3*	1070		12 hr 25’	Center
CR-4	1070		4.683	Center
CR-5*	1070			Top @ cylinder
CR-6	1070		3.75	Top, 2” from cylinder
CR-7	1070		3.25	Center
CR-8	1070		0.25	Bottom @ cylinder
CR-9	1070		1.067	Bottom @ cylinder
CR-10	970	4.31	8.73	Bottom @ cylinder
CR-11	970		168	No Failure
CR-12	970		124.317	No Failure
CR-13	1020	4.54	6.25	Center
CR-14	1020		2.97	Center
CR-15	1020		0.0103	Bottom @ cylinder
CR-16	1020		0.0106	Bottom @ cylinder
CR-17	1020		7.03	Center
CR-18	1020		3.7	Bottom @ cylinder
CR-19	1070		2.8	Bottom @ cylinder
CR-20*	870		Instant	Top @ cylinder
CR-21*	1070		Instant	Top cylinder failed
CR-22*	1070			
CR-23	970		7.1	
CR-24	970		7.58	Center
CR-25	1020		15.85	Center
CR-26	970		0.42	Center
CR-27	870		350.25	Center

* These specimens were not included in the data reduction set due to failure time discrepancies.

7.2.4 Discussion

The creep-rupture results for 5-mm DHFRP bars were shown in Figure 7.5. As expected, the data shows decreasing load ratio with increased failure time. Two specific

failure times are noted in Fig. 7.5. First, failure at 50 years is shown. The load ratio value at this time is 0.69or 69 % of the ultimate load. The load ratio value at 10^6 hours, the value documented by the Japanese Code (JSCE, 1995) is 0.61 or 61 % of the ultimate. These values are very promising when compared to other results from creep test as shown in Table 7.2. Results by Mukae et al. (1994) for aramid FRP rods show that the creep failure capacity at 100 years is 61 % of the standard tensile strength of the material. Budelmann and Rostasy (1993) found that sustained stress is limited to 60% of the short-term ultimate strength for GFRP. Also, Anigol (1991) and Khubchandani (1991) reported no loss in strength for 50% of the ultimate for CFRP and GFRP. Therefore, the obtained results for DHFRP are either superior or comparable with other FRP materials.

Table 7.2: Comparison of Creep Rupture Strengths at 100 Years.

Material	Percent of Ultimate Load Capacity	Reference
DHFRP	0.63	Drexel University
Aramid FRP (AFRP)	0.61	Mukae
GFRP	0.60	Budelmann and Rostasy
GFRP/ CFRP	0.50	Anigol
GFRP/ CFRP	0.50	Khubchandani

CHAPTER 8. FLEXURAL TESTING OF REINFORCED CONCRETE BEAMS

8.1 Background

Two types of load deflection behavior for reinforced concrete (R/C) members are brittle and ductile failure modes and are shown in Figure 8.1. The load-deformation characteristics of members are necessary for three main reasons. First, brittle failure should be prevented. Linear elastic FRP materials presented by Theriault et al. (1998), Aiello and Ombres (2000) and Jost et al. (2001) fail in a brittle mode. In the extreme event of a structure being loaded to failure, it should be able to undergo large deflections near maximum load carrying capacity. This may save lives by giving warning of failure and preventing a total collapse.

Second, for statically indeterminate structures, the possible distribution of internal forces (moments and shear) depends on the ductility of the member at the critical sections. A different distribution of moments than obtained from a linear elastic analysis is possible if moment redistribution can take place. As ultimate load is approached, some sections reach their ultimate resisting moments before others; however, if plastic rotation occurs at these critical sections while the ultimate moment is maintained, additional load can be carried as the moments elsewhere increase to their ultimate values. The ultimate load of the structure is reached when, after the formation of sufficient plastic hinges, a collapse mechanism is developed. However, this is only applicable for under-reinforced members where the reinforcement behaves in a ductile manner with sufficient ductility.

Third, in areas of earthquakes, a critical design consideration is the ductility of the structure when subjected to seismic-type loading. The seismic design philosophy for R/C

structures relies on the energy absorption and dissipation by post-elastic deformation during major seismic events. Structures incapable of behaving in a ductile manner must be designed for much higher seismic forces to avoid collapse. This would be true for most FRP bars which are linear elastic to failure.

The load-deflection and moment-curvature analyses of R/C flexural members were investigated for prototype-size beam and slab elements reinforced with DHFRP. The stress-strain behavior of DHFRP (Chapter 6) showed significant ductility, and therefore, the flexural R/C members should fail in a gradual ductile mode. The energy absorption capability of DHFRP will be verified by the load-deflection and moment-curvature behaviors of the R/C beams.

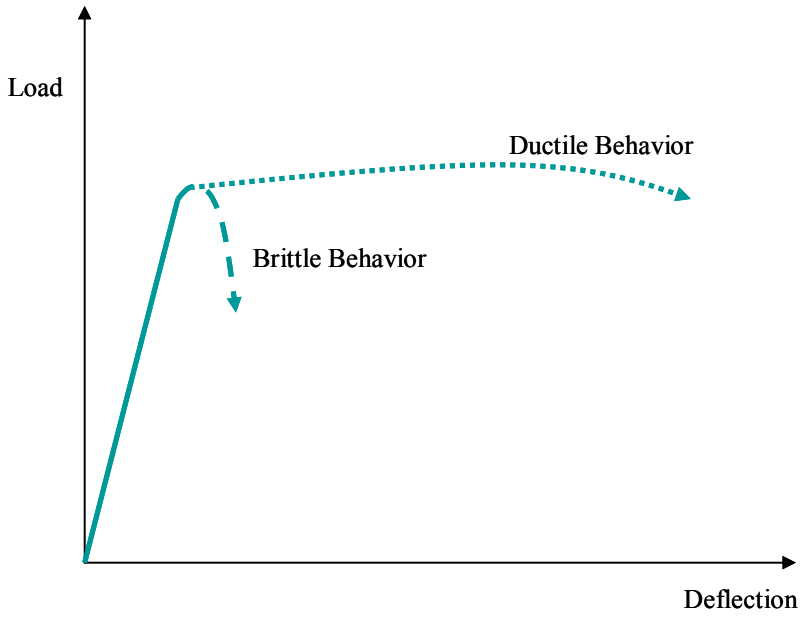

Figure 8.1: Possible Load-Deflection Behaviors of a Flexural Member.

8.1.1 Theoretical Moment-Curvature and Load-Deflection Analyses

The load-deflection and moment-curvature relationships for R/C beams are important to quantify the overall structural behavior. Shown in Figure 8.2 is the deformation of an R/C element under pure bending with the corresponding strain distribution. The radius of curvature R, neutral axis depth kd, concrete strain in the extreme compression fiber ε_c, and tension steel strain ε_s, will vary along the length of the member since between cracks the concrete can still carry some tension load. Defining the curvature of the element as the rotation per unit length of member, and referring the strain diagram of Figure 8.2, the curvature is given as

$$\varphi = \frac{\varepsilon_c}{kd} = \frac{\varepsilon_s}{d(1-k)} = \frac{\varepsilon_c + \varepsilon_s}{d} \qquad 8\text{-}1$$

where the curvature is the gradient of the strain profile at the element, as shown in Figure 8.2. In the linear range, the classical elastic equation relating the moment and curvature can be used:

$$EI = MR = \frac{M}{\varphi} \qquad 8\text{-}2$$

In limit and seismic design, the ductility of a member is expressed as the ratio of the ultimate deformation to the deformation at first yield. Also, the ratio of the ultimate curvature to the curvature at yield is a measure of the strain capacity of a member in flexure. These quantities are critical in determining the ductility of a member, and this is directly related to the ductility of the reinforcement.

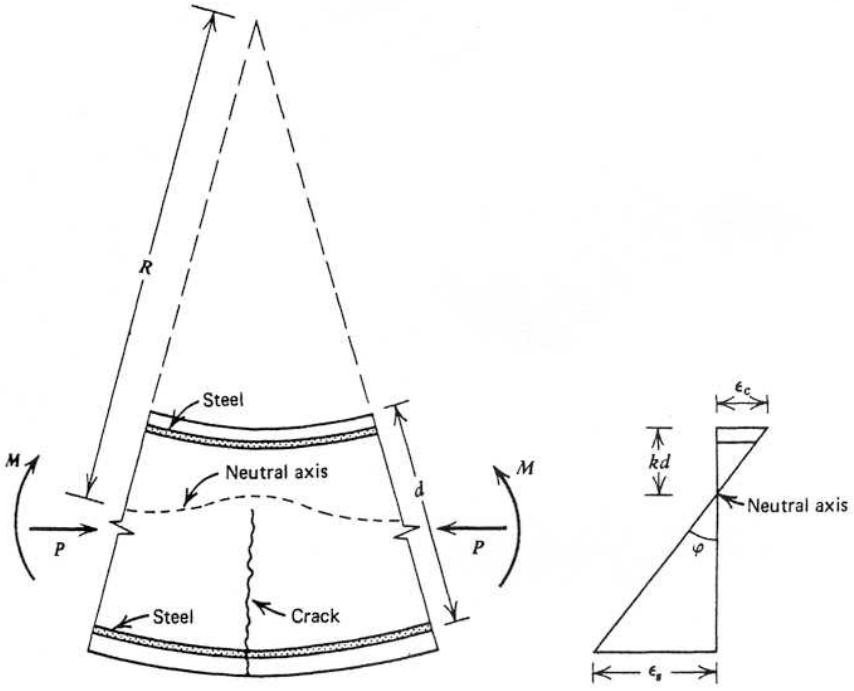

Figure 8.2: Section of R/C Under Pure Bending and Corresponding Linear Strain Distribution (Park and Paulay, 1975).

For moment-curvature analysis of concrete elements, three regions of behavior were investigated: linear elastic region up to cracking of the concrete, linear post-cracking region up to first yield of the reinforcement, and post-yield behavior to failure.

The first regime of behavior is the region including service loading before cracking. In this regime, the section was analyzed using elastic theory and the transformed section method. Shown in Figure 8.3 is the general case of a doubly reinforced rectangular section at cracking of the concrete in tension. In this section, the modular ratio is defined as

$$n = \frac{E_s}{E_c} \qquad 8\text{-}3$$

Where E_s is the modulus of reinforcement and E_c is the concrete modulus.

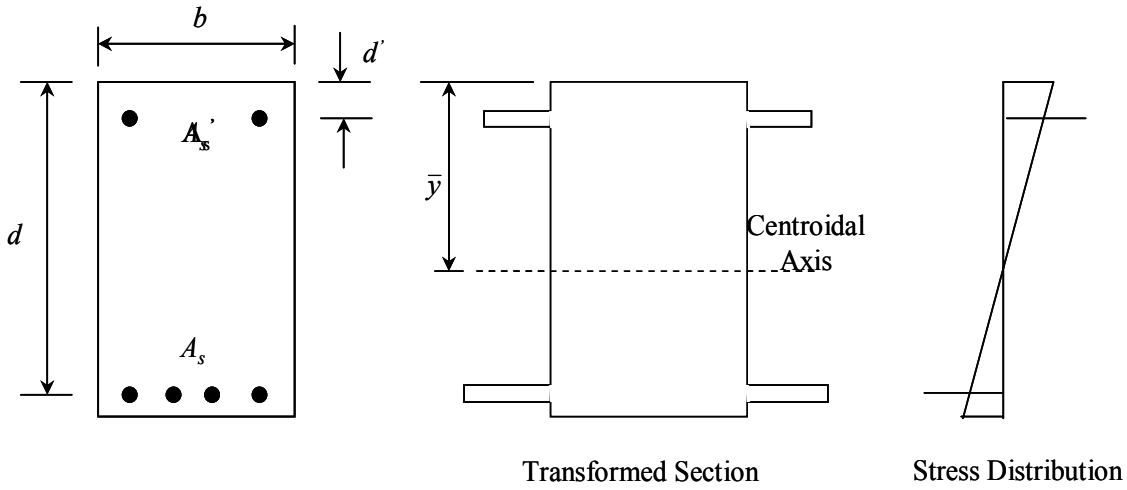

Figure 8.3: Beam Section Analysis Before Cracking: Elastic Behavior.

The total transformed area is defined as

$$A_{transformed} = bh + (n-1)\left(A_s + A_s^{'}\right) \tag{8-4}$$

Where A_s, $A_s^{'}$, and b, are defined in Figure 8.3 and h is the depth of the section. The centroid of the transformed section was found by taking moments of the areas about the top edge of the section

$$\bar{y} = \frac{bh + (n-1)A_s d + (n-1)A_s^{'} d^{'}}{A_{transformed}} \tag{8-5}$$

The moment of inertia is then given as

$$I = \frac{1}{12}bh^3 + bh\left(h/2 - \bar{y}\right)^2 + (n-1)A_s\left(\bar{y} - d\right)^2 + (n-1)A_s^{'}\left(\bar{y} - d^{'}\right)^2 \tag{8-6}$$

The term 1/12 bh^3 was dropped for the areas of steel since these are very small compared to the Ad^2 terms. Cracking occurs when the modulus of rupture, f_r, is reached in the bottom fiber. The cracking moment is thus

$$M_{crack} = \frac{f_r I}{y_{bottom}} \tag{8-7}$$

The cracking curvature, as defined in equation 8-1, at the cracked level is

$$\varphi_{crack} = \frac{f_r / E_c}{y_{bottom}} \tag{8-8}$$

Where ϕ_{crack} is in rad/ in or rad/m and y_{bottom} is defined as

$$y_{bottom} = h - \bar{y} \tag{8-9}$$

Next, the values of moment and curvature when the tension reinforcement first yielded were considered. The compressed concrete of the members was considered unconfined. Concrete is generally regarded as unconfined unless positive measures are taken to confine it by closely spaced transverse reinforcement.

Figure 8.4 shows the stress and strain diagrams for the general case of a doubly reinforced rectangular section at first yield of the tension reinforcement. The curvature at first yield of the tension steel is found from equation 8-1 in terms of the strain in the steel at yield. However, when the steel yields, the stress in the extreme fiber of the concrete may be much less than the cylinder strength, f'_c. The stress-strain curve for concrete is approximately linear up to $0.7f'_c$, and therefore, if the concrete stress does not exceed this value when the steel yields, the depth of the neutral axis can be calculated using the straight line (elastic) theory (Park and Paulay, 1975).

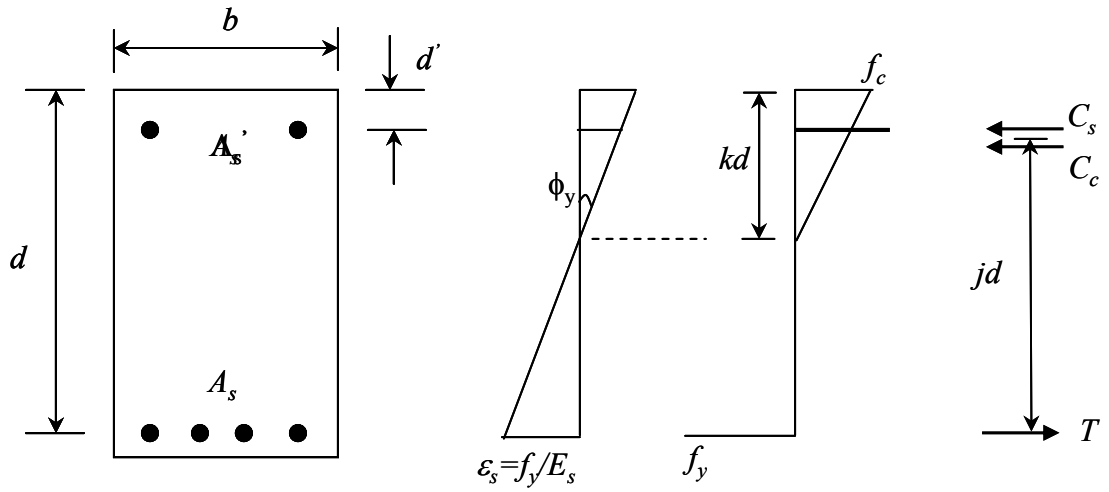

Figure 8.4: Doubly Reinforced Beam Section at First Yield: Strain Distribution, Stresses, and Force Resultants.

The neutral axis depth factor, k, was determined, and the magnitude of the forces and the centroid of the compressive forces in the steel and concrete were determined. The neutral axis depth factor, k, is given as

$$k = \left[\left(\rho + \rho'\right)^2 n^2 + 2\left(\rho + \frac{\rho' d'}{d} \right) n \right]^{1/2} - \left(\rho + \rho'\right) n \qquad 8\text{-}10$$

The moment at yield is

$$M_y = A_s f_y jd \qquad 8\text{-}11$$

and the curvature at yield is given as

$$\varphi_y = \frac{f_y / E_s}{d(1-k)} \qquad 8\text{-}12$$

where A_s = area of tension steel, A_s' = area of compression steel, b = width of section, d = effective depth of tension steel, d' = distance from extreme compression fiber to centroid of compression steel, E_c = modulus of concrete, E_s = modulus of steel, f_y = yield strength

of steel, *jd* = distance from centroid of compressive forces in the steel and concrete to the centroid of tension. The reinforcement ratios for both the tension and compression steel, respectively, are

$$\rho = \frac{A_s}{bd} \qquad \rho' = \frac{A_s'}{bd} \qquad \text{8-13 a, b}$$

The third and final region of the beam behavior is the ultimate curvature and moment capacity of the doubly reinforced section for the case where the compression steel yields. This is shown in Figure 8.5.

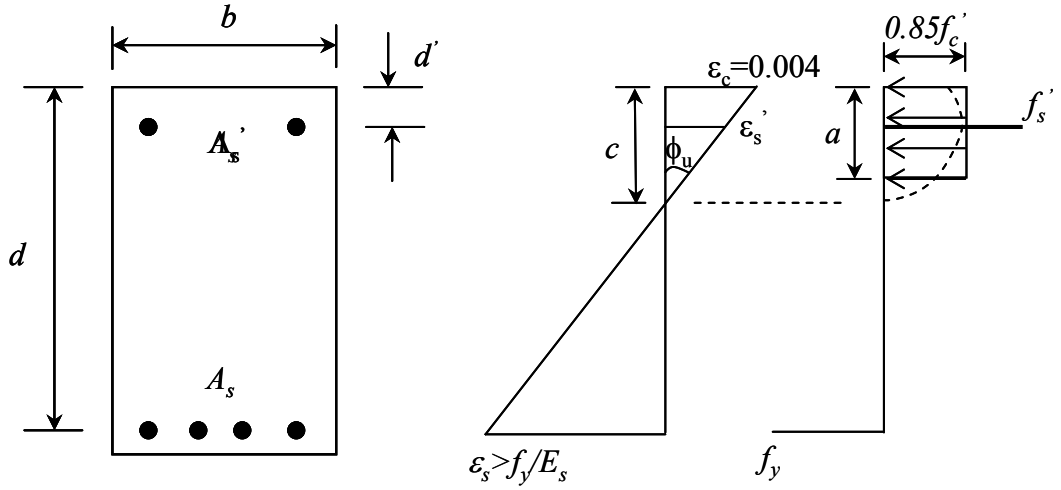

Figure 8.5: Doubly Reinforced Beam at Ultimate: Strain and Stress Distributions.

The design equations at ultimate for the depth of the compression block, *a*, the ultimate moment, and the ultimate curvature are given as

$$a = \frac{A_s f_y - A_s^{'} f_y}{0.85 f_c^{'} b} \tag{8-14}$$

$$M_u = 0.85 f_c^{'} ab\left(d - \frac{a}{2} \right) + A_s^{'} f_y \left(d - d^{'} \right) \tag{8-15}$$

$$\varphi_u = \frac{\varepsilon_c}{c} = \frac{\varepsilon_c \beta_1}{a} \tag{8-16}$$

The strain in the compression steel, shown in the strain diagram of Figure 8.5, is given as

$$\varepsilon_s^{'} = \varepsilon_c \left(\frac{c - d^{'}}{c} \right) = \varepsilon_c \left(1 - \frac{\beta_1 d^{'}}{a} \right) \tag{8-17}$$

Substituting equation 8-14 into 8-17 shows that the compression steel is yielding when

$$\varepsilon_c \left[1 - \beta_1 d^{'} \left(\frac{0.85 f_c^{'} b}{A_s f_y - A_s^{'} f_y} \right) \right] \geq \frac{f_y}{E_s} \tag{8-18}$$

Equation 8-18 must be satisfied for equations 8-14 to 8-16 to be applicable. If this is not satisfied, the actual value for the compressive steel stress must be used and not the yield stress in finding the ultimate moment. In this case, the value of *a* calculated in Eq. 8-14 is incorrect, and the actual steel stress and *a* have to be calculated from the equilibrium equation and the strain diagram. The equilibrium equation in general form is

$$a = \frac{A_s f_s - A_s^{'} f_s^{'}}{0.85 f_c^{'} b} \tag{8-19}$$

and from the strain diagram,

$$f_s^{'} = \varepsilon_s^{'} E = 0.003 \frac{a - \beta_1 d^{'}}{a} E_s \qquad \text{or} \qquad f_s^{'} = f_y \tag{8-20a, b}$$

Solving equations 8-19 and 8-20 simultaneously gives

$$\frac{1}{2}\left(\frac{a}{d} \right)^2 + \frac{a}{d}\left(\frac{\rho' \varepsilon_c E_s - \rho f_y}{1.7 f_c^{'}} \right) - \frac{\rho^{'} \varepsilon_c E_s \beta_1 d^{'}}{1.7 f_c^{'} d} = 0 \tag{8-21}$$

This gives the value of a. Substituting equation 8-20 into the general ultimate moment equation for beams with compression steel yields

$$M_u = 0.85 f_c^{'} ab\left(d - \frac{a}{2}\right) + A_s^{'} E_s \varepsilon_c \frac{a - \beta_1 d^{'}}{a}\left(d - d^{'}\right) \qquad 8\text{-}22$$

A value of ε_c = 0.004 can be used in ultimate curvature calculations because a value of ε_c = 0.003 is conservative (Park and Paulay, 1975). The ratio ϕ_u/ϕ_y gives a measure of the curvature ductility of the section. Using equations 8-16 and 8-12

$$\frac{\varphi_u}{\varphi_y} = \frac{\varepsilon_c}{f_y / E_s} \frac{d(1-k)}{a/\beta_1} \qquad 8\text{-}23$$

Substituting equations 8-10 and 8-14 into equation 8-23 gives the curvature ductility factor for a doubly reinforced beam as

$$\frac{\varphi_u}{\varphi_y} = \frac{0.85\beta_1 E_s \varepsilon_c f_c^{'}}{f_y^2\left(\rho - \rho^{'}\right)}\left\{1 + \left(\rho + \rho^{'}\right)n - \left[\left(\rho + \rho^{'}\right)^2 n^2 + 2\left(\rho + \frac{\rho^{'} d^{'}}{d}\right)n\right]^{1/2}\right\} \qquad 8\text{-}24$$

The load-deflection behavior is calculated from the moment-curvature results. For a beam in four-point bending, the load as a function of the moment is given as

$$P = \frac{M}{a} \qquad 8\text{-}25$$

where a is the shear span of the loaded beam. The loads P_{crack}, P_y, and P_u were calculated corresponding to M_{crack}, M_y, and M_u. The deflections were calculated from the curvature since for four-point bending, the center region is under pure bending, and therefore, undergoes constant curvature and is bent into a circular arc. From the deformed geometry, the deflection based on the curvature is given as

$$\delta = \frac{(1-\cos\theta)}{\varphi} \qquad 8\text{-}26$$

where θ is the angle measured at the center of curvature of the circular arc of the beam. From the deformed geometry (Gere, 2000),

$$\sin\theta = \frac{L}{2}\varphi \qquad 8\text{-}27$$

noting that $\phi = 1/\rho$, where ρ is the radius of curvature and L is the span length of the beam.

A program to determine the moment-curvature and load-deflection for doubly reinforced rectangular beam sections applicable for both steel and DHFRP reinforced beams was written using MATLAB (MathWorks, Inc.). The results are presented in Section 8.1.3 and discussed in Section 8.1.4. The MATLAB program is in Appendix E.

8.1.2 Beam Design Model for DHFRP R/C Beams

A MATLAB program was developed that designed various beams using 10-mm DHFRP bars. This program is valid for any beam dimensions, DHFRP and steel moduli, and concrete compressive strengths. The program designs the area of reinforcement required based on $0.5\rho_b$, half the balanced reinforcement ratio. The flexural and shear capacities are then computed in addition to the applied load capacity of the beam. Details of this program are given in Appendix E.

A program was developed using MATLAB that analyzed beams with given cross sections and number of bars. This program calculated the ultimate moment capacity of the cross section. This program was developed based on ACI-318-02 design for steel R/C flexural members. Details of this program are given in Appendix E.

8.1.3 Results

The theoretical results developed from Section 8.1.1 are given for both the moment-curvature and load-deflection behavior of DHFRP and steel beams and then for the general beam design using program *beam_design* coded in MATLAB. Two areas of reinforcement were used in the calculations: the volumetric area (A_{vol}) and the specific area (A_{sp}), as described in Section 6.25. Figure 8.6 shows the load versus deflection behavior for both steel and prototype DHFRP using A_{vol} and Figure 8.7 shows the load versus deflection behavior using A_{sp}. The moment-curvature relations for both steel and DHFRP R/C beams are shown in Figures 8.8 and 8.9, again using the two reinforcement areas, respectively. Figures 8.10 through 8.13 show the results from the beam design program. Parameters that were varied included different rectangular cross sections of the beams, DHFRP moduli, and concrete compressive strengths. The results are tabulated in Table 8.1. Beams of 4" x 6" (101.6 mm x 152.4mm) and 4" by 8" (101.6 mm x 203.2 mm) cross sections and lengths of 96" (2438.4 mm) were used in the design program.

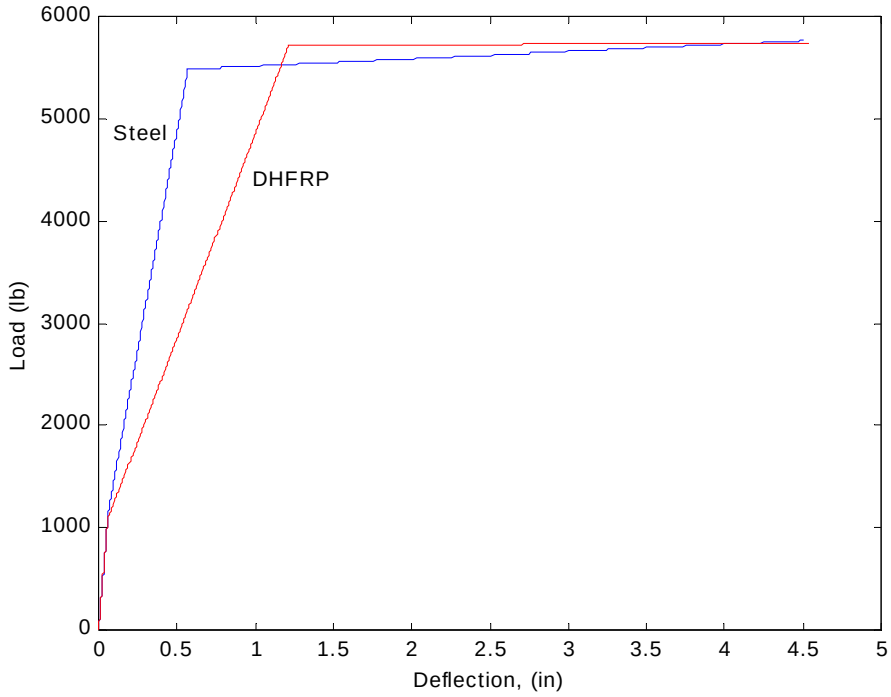

Figure 8.6: Theoretical Load-Deflection Relationship for Prototype Steel and DHFRP Reinforced Beams Using Volumetric Area.

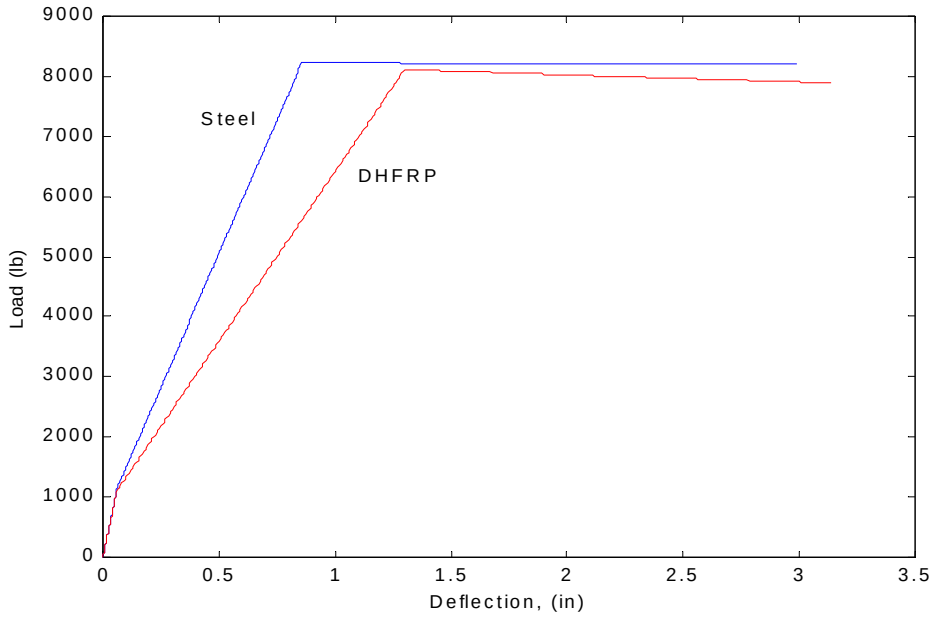

Figure 8.7: Theoretical Load-Deflection Relations for Prototype Steel and DHFRP Reinforced Beams Using Specific Area.

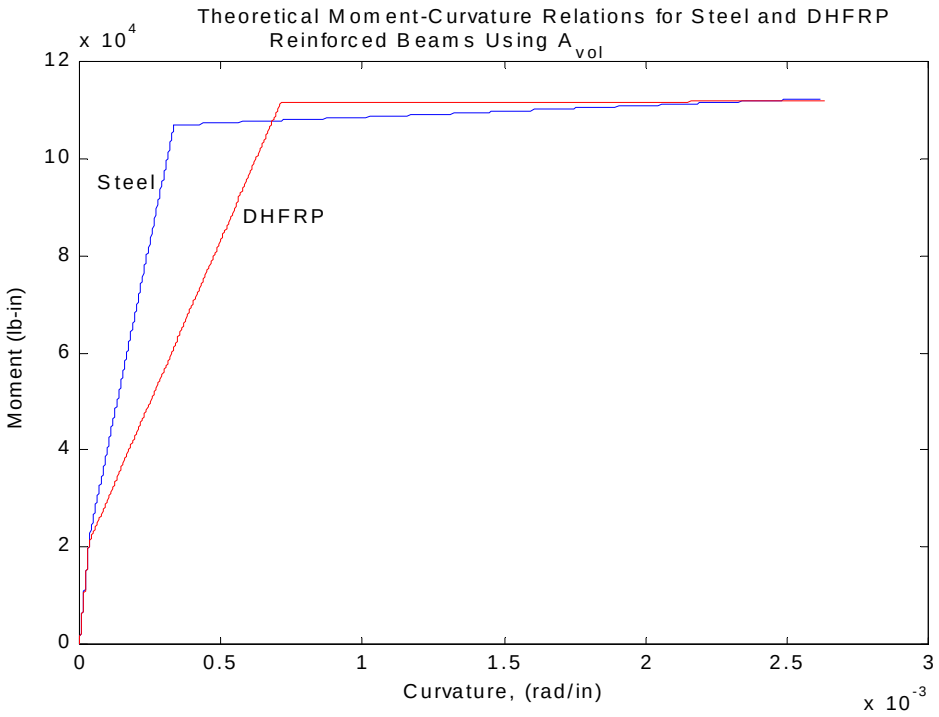

Figure 8.8: Theoretical Moment-Curvature Relationship for Steel and DHFRP Reinforced Beams Using Volumetric Area.

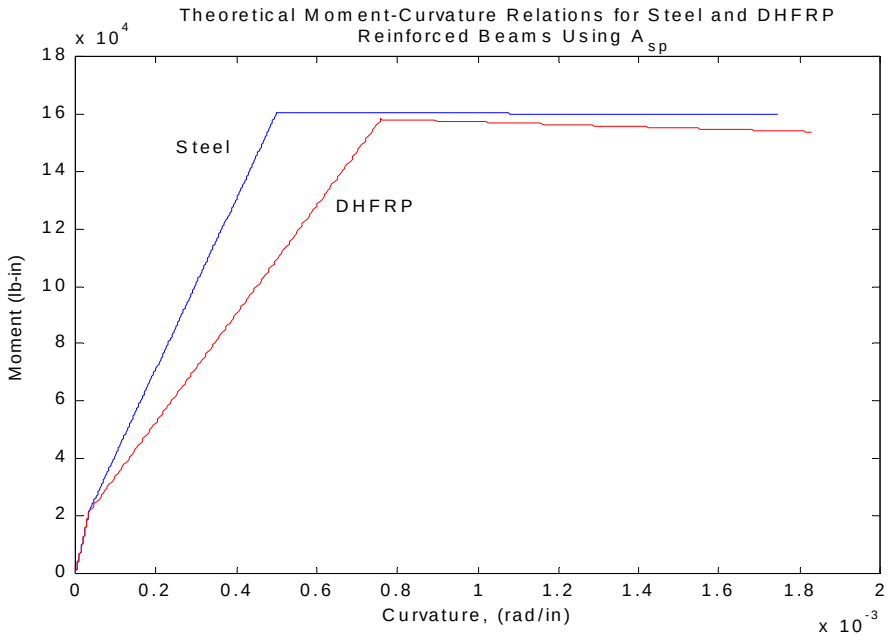

Figure 8.9: Theoretical Moment-Curvature Relationship for Steel and DHFRP Reinforced Beams Using Specific Area.

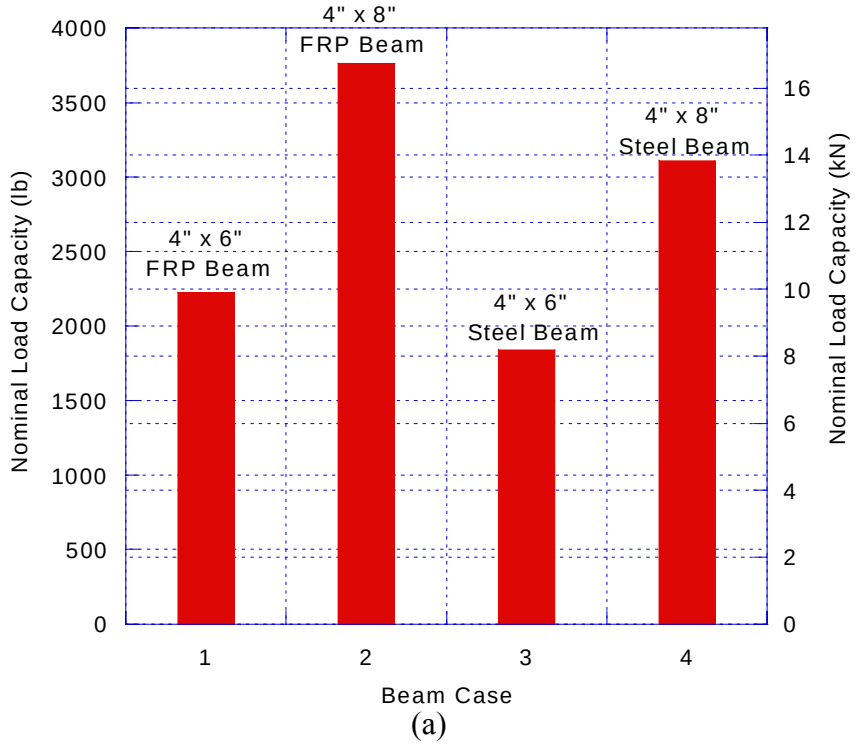

Figure 8.10: (a) Nominal Load, (b) Nominal Moment, and (c) Number of Bars for Various R/C Beams; $f_{y\,DFRP}$ = 30 000 psi, f'_c = 3500 psi.

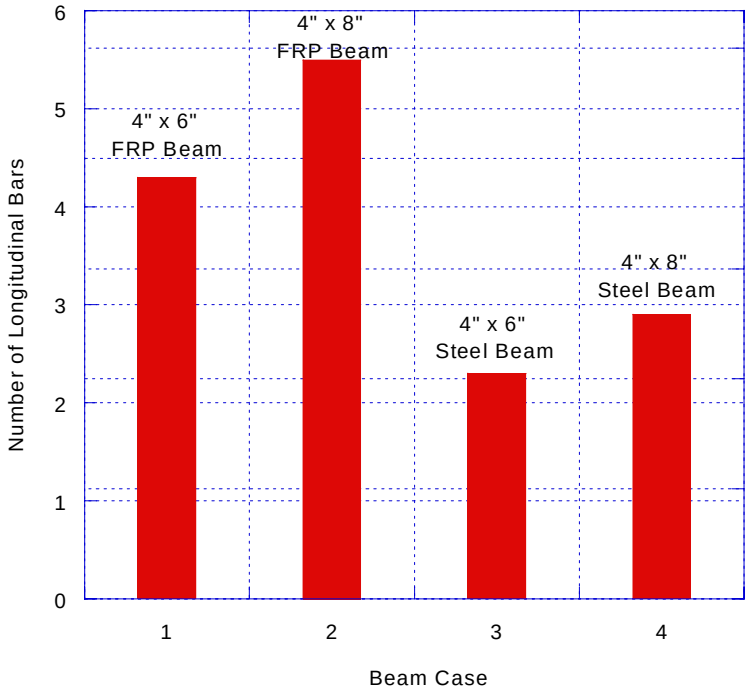

(c)

Figure 8.10 (continued)

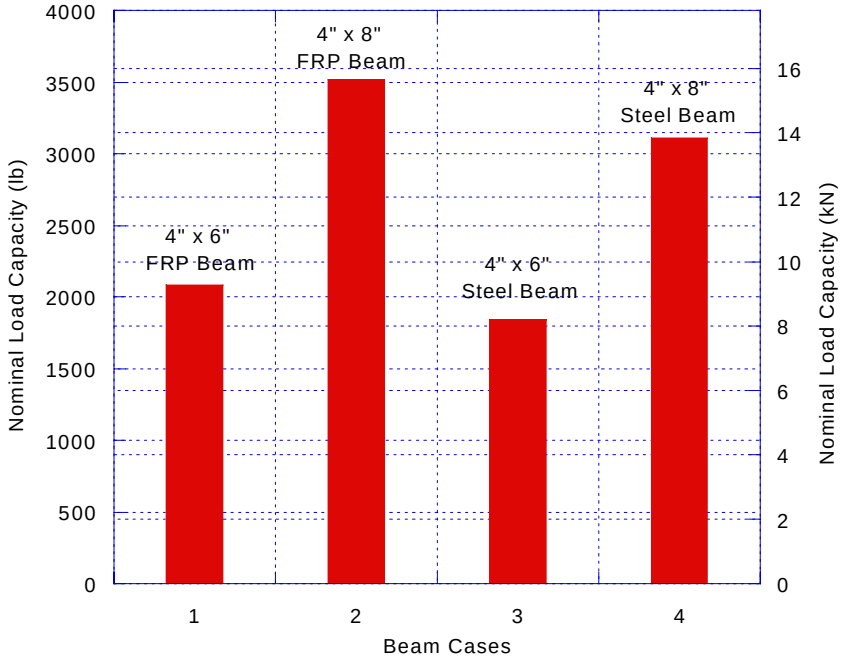

(a)

Figure 8.11: (a) Nominal Load, (b) Nominal Moment, and (c) Number of Bars for Various R/C Beams; f_{y_DFRP} = 40 000 psi, f'_c = 3500 psi.

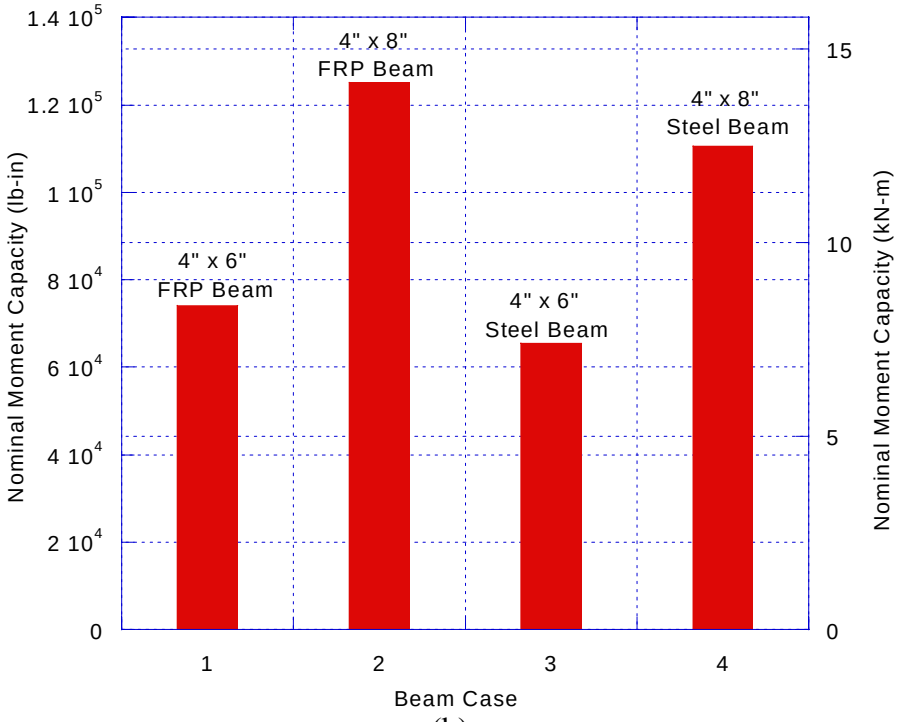

(b)

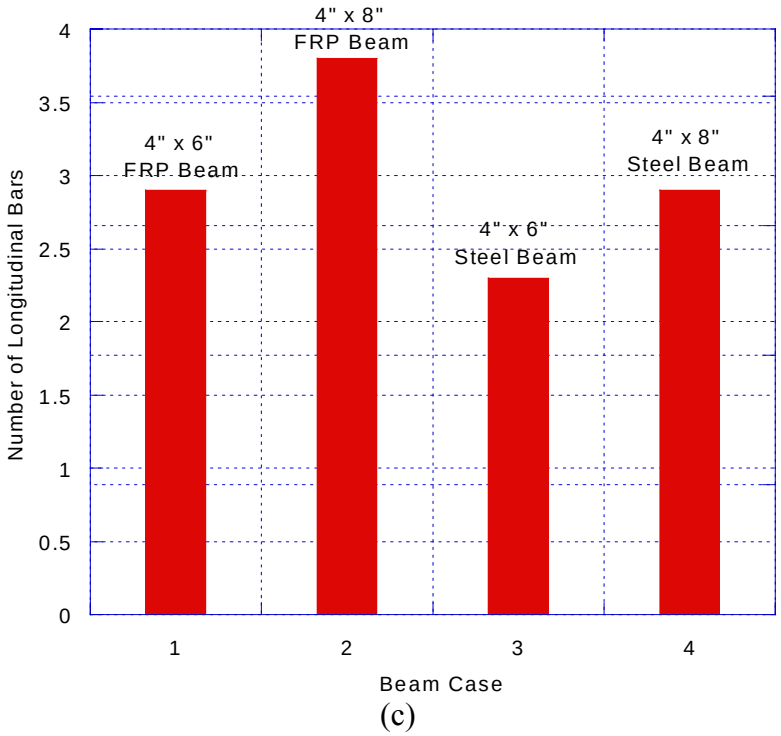

(c)

Figure 8.11 (continued)

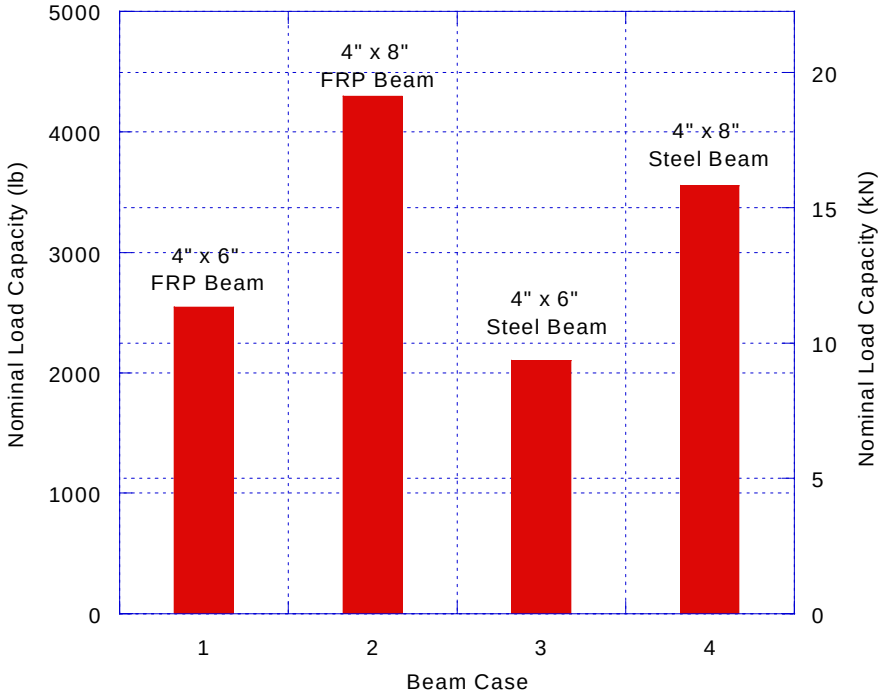

(a)

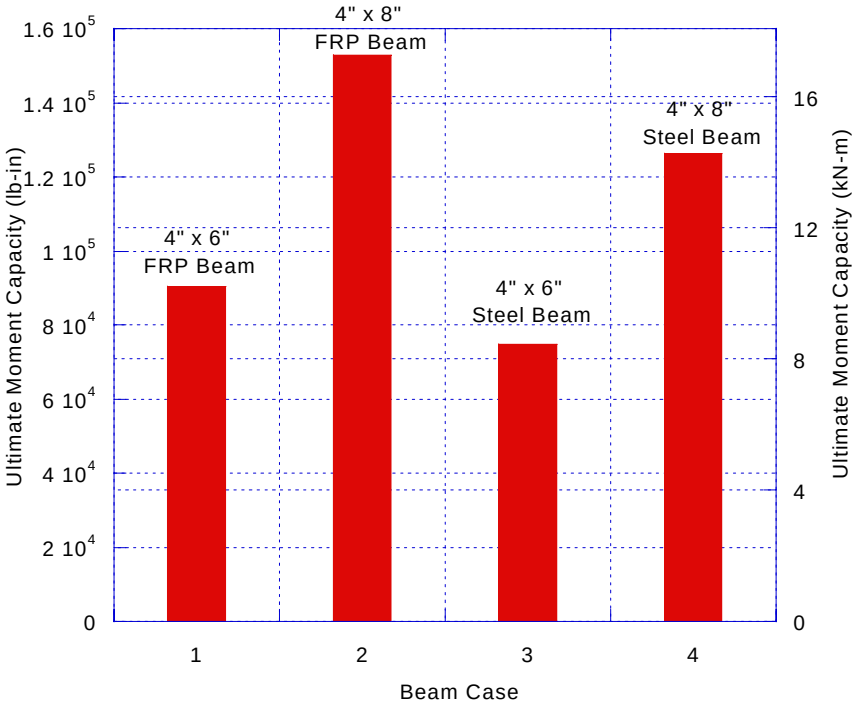

(b)

Figure 8.12: (a) Nominal Load, (b) Nominal Moment, and (c) Number of Bars for Various R/C Beams; $f_{y\,DFRP}$ = 30 000 psi, f'_c = 4000 psi.

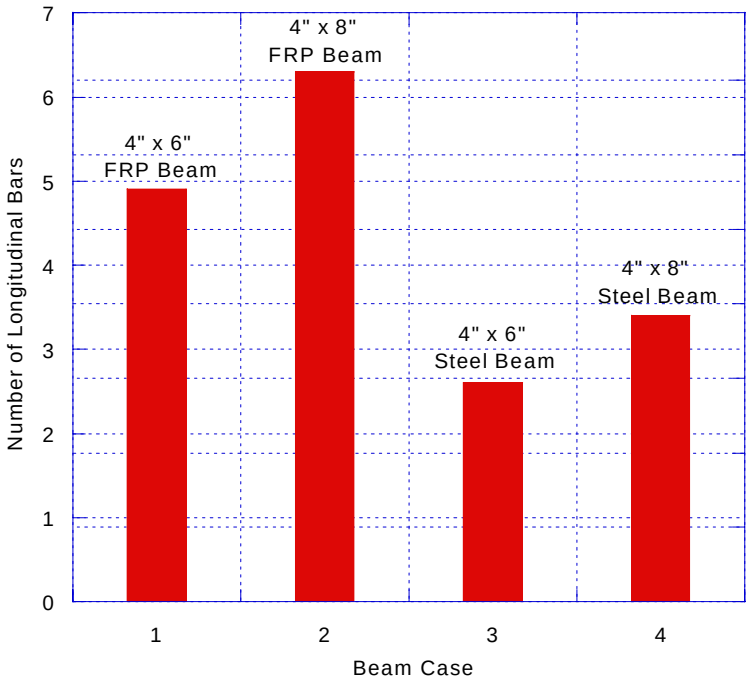

(c)

Figure 8.12 (continued)

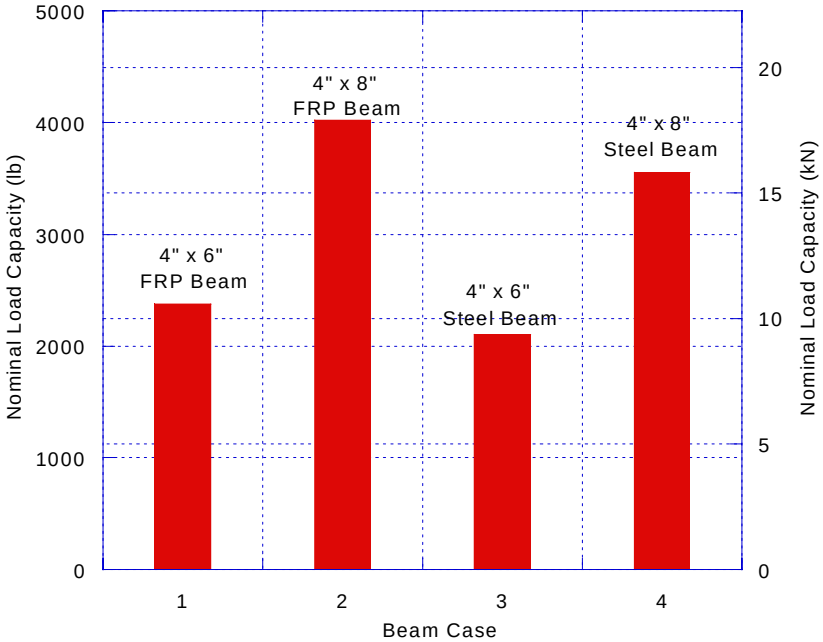

(a)

Figure 8.13: (a) Nominal Load, (b) Nominal Moment, and (c) Number of Bars for Various R/C Beams; f_{y_DFRP} = 40 000 psi, f'_c = 4000 psi.

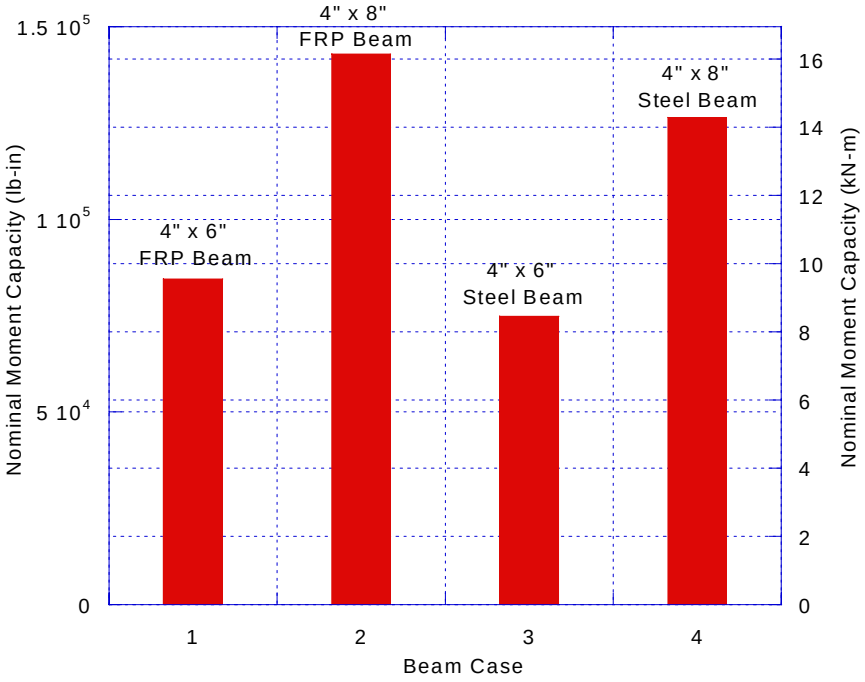

(b)

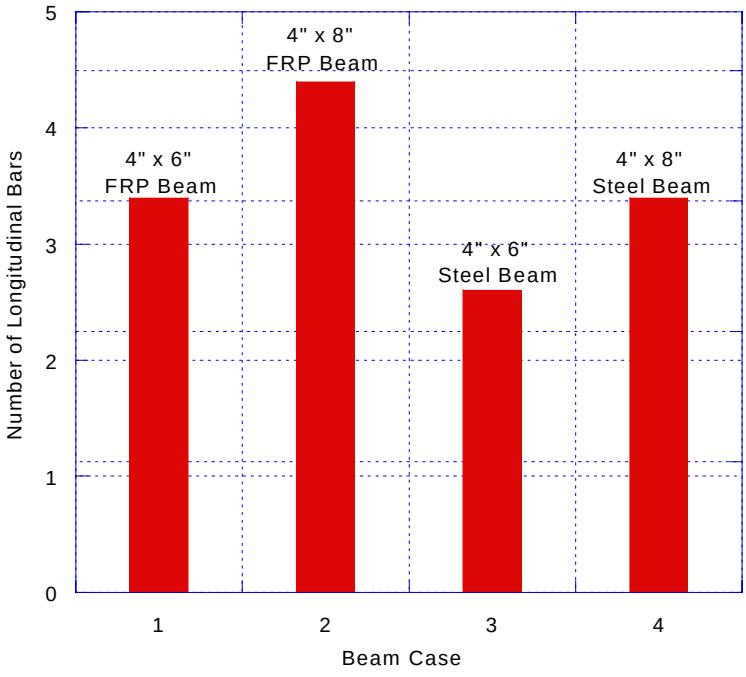

(c)

Figure 8.13 (continued)

Table 8.1: Results of R/C Beam Design for Various Values of DHFRP Yield Strength and Concrete Compressive Strength.

Reinf. Type	A_{req} **(in^2)**	**Number of Bars**	ρ	M_n **(lb-in)**	P_n **(lb)**	V_n **(lb)**	s_{max} **(in)**
Case 1: $f_{y\,DFRP}$ = 30 000 psi, f'_c = 3500 psi							
DHFRP 1	0.6268	4.3	0.3160	79162	2226.4	2619.3	2.50
DHFRP 2	0.8148	5.5	0.3160	133780	3762.7	4426.6	3.25
Steel 1	0.2494	2.3	0.2515	65419	1839.9	2164.6	2.50
Steel 2	0.3243	2.9	0.2515	110560	3109.5	3658.2	3.25
Case 2: $f_{y\,DFRP}$ = 40 000 psi, f'_c = 3500 psi							
DHFRP 1	0.4331	2.9	0.2911	74006	2081.4	2448.7	2.50
DHFRP 2	0.5630	3.8	0.2911	125070	3517.6	4138.4	3.25
Steel 1	0.2494	2.3	0.2515	65419	1839.9	2164.6	2.50
Steel 2	0.3243	2.9	0.2515	110560	3109.5	3658.2	3.25
Case 3: $f_{y\,DFRP}$ = 30 000 psi, f'_c = 4000 psi							
DHFRP 1	0.7163	4.9	0.3160	90470	2544.5	2993.5	2.50
DHFRP 2	0.9312	6.3	0.3160	152900	4300.2	5059.0	3.25
Steel 1	0.2851	2.6	0.2515	74765	2102.8	2473.8	2.50
Steel 2	0.3706	3.4	0.2515	126350	3553.7	4180.8	3.25
Case 4: $f_{y\,DFRP}$ = 40 000 psi, f'_c = 4000 psi							
DHFRP 1	0.4949	3.4	0.2911	84578	2378.8	2798.5	2.50
DHFRP 2	0.6434	4.4	0.2911	142940	4020.1	4729.5	3.25
Steel 1	0.2851	2.6	0.2515	74765	2102.8	2.4738	2.50
Steel 2	0.3706	3.4	0.2515	126350	3553.7	4180.8	3.25

8.1.4 Discussion

Shown in Figures 8.6 and 8.7 were the theoretical load-deflection relationships for prototype steel and DHFRP R/C beams using both volumetric and specific areas of DHFRP. Shown in Figures 8.8 and 8.9 were the theoretical moment-curvature

relationships for prototype steel and DHFRP beams using the two DHFRP bar areas. As explained in Chapter 6, since a standard method of measuring the cross-sectional area of a fibrous composite does not exist, the two areas mentioned give upper and lower bound solutions of the area.

The load-deflection relationships are critical in finding the loads at cracking, yield, and ultimate. This was critical when testing the DHFRP beams and for designing the beam test setup. The load-deflection analysis in this program is defined for a beam under four-point loading, where each point load on the beam is defined as $P/2$. For both the steel and the DHFRP, the curves are tri-linear with three slopes defined at cracking, yielding, and failure. From the figures, the DHFRP beam had larger deflections at cracking and yielding since the bars are less stiff than steel bars. Also, the steel R/C load-deflection curve was terminated at the same location as the DHFRP curve for comparison, but the steel R/C beam has additional ductility. These curves illustrate that the DHFRP R/C beam behaves similar to the steel R/C beam with a controlled yield point followed by significant inelastic deflections until failure. As seen in Figure 8.7 using the specific DHFRP bar area which is less than the volumetric area, the yield load is approximately 40 percent higher and the ultimate deflection is approximately 30 percent less compared to the A_{vol} (Fig. 8.6). Using $A_{specific}$ gives the bar a higher stiffness. These two cases represent the lower and upper bound load-deflection solutions, and therefore, the experimental results should lie between these two cases.

Figures 8.8 and 8.9 showed the theoretical moment-curvature relationships. Again the DHFRP demonstrated a similar result to the steel R/C beams with a tri-linear relationship defined by the cracking, yield, and ultimate points. Again, since the stiffness

of the DHFRP is approximately 47 percent of steel, the curvatures are larger for the DHFRP R/C beams. Again, these two curves represent the lower and upper bounds, respectively for moment-curvature behavior of DHFRP R/C beams. Since the strain capacity of a section under pure bending is dependent on the curvature of the section, these graphs represent the amount of strain capacity a section can obtain, resulting in either a ductile or brittle failure mode.

Figures 8.10 through 8.13 showed results form the beam design program. Two cross sections of beams were used, 4" x 6" (101.6 mm x 152.4mm) and 4" by 8" (101.6 mm x 203.2 mm) cross sections and lengths of 96" (2438.4 mm). Beams reinforced with either DHFRP or steel were considered. The beams used in the experimental portion of the program had a cross section of 101.6 mm x 152.4mm (4" x 8"). Beams of this size are reasonable for 10-mm DHFRP bars. Larger cross sections would require either two layers of reinforcement or larger diameter DHFRP bars. For the four beams shown, the nominal load capacity, the nominal moment capacity and the number of bars were calculated. Two other parameters were varied, namely the DHFRP yield strength and the concrete compressive strength. The yield strength was taken as either 30000 psi (206.84 MPa), Figs. 8.10 and 8.12 or 40000 psi (275.79 MPa), Figs. 8.11 and 8.13 and the concrete compressive strength was taken as 3500 psi (24.13 MPa), Figs. 8.10 and 8.11 or 4000 psi (27.58 MPa), Figs. 8.12 and 8.13. These two parameters have variability from beam to beam, and therefore, these various cases gave upper bound and lower bound solutions.

For each case considered, the DHFRP beams required more bars than a steel beam designed for the same capacity. This is because the DHFRP bars are less stiff than steel

bars, and therefore, more bars are needed to withstand the same moment capacity. The results for each of the four cases were tabulated in Table 8.1. This table shows the area of reinforcement required, the number of bars, the reinforcement ratio, ρ, the nominal moment, load, and shear capacities, and the maximum stirrup spacing.

8.2 Flexural Testing

An experimental program was conducted on prototype beam members reinforced with 10-mm DHFRP bars. The tests confirmed the theoretical predictions made for prototype DHFRP and similitude relationships of strength and ductility derived for DHFRP-reinforced members. Work on model-size flexural members was conducted by Somboonsong (1997) and included beam members reinforced with 3-mm and 5-mm DHFRP bars. In order to compare scaling relations, the prototype beams reinforced with 10-mm bars had geometric relationships derived through similitude from the model sizes. The scale-up relations are shown in Table 8.2. Since the bar diameter was doubled, the areas were increased by a factor of four. Therefore, all lengths were increased by a factor of two. The similitude relationships were shown in Chapter 3. The length of the prototype beam was increased more than two times to prevent shear failures that occurred in previous model beams (Somboonsong, 1997).

Table 8.2: Scale Up of Beam Geometric Properties from Model to Prototype Sizes.

Beam	Nominal Bar Diameter (mm)	Beam Dimensions (mm) [in]	Number of Bars Used
Model 1	3.0	25.4 x 50.8 x 609.6 [1 x 2 x 24]	4
Model 2	5.0	50.8 x 101.6 x 1219.2 [2 x 4 x 48]	4
Prototype	10.0	101.6 x 203.2 x 2895.6 [4 x 8 x 114]	4

Shown in Figure 8.14 is the loading configuration for the flexural beam tests. The beam was subjected to four-point loading. The shear and moment diagrams are also shown. The center span of the beam has constant bending moment, and therefore, constant curvature. Figure 8.15 shows the span in elevation with the locations of the loading and reaction points. Also, to prevent shear failure, stirrups were spaced at the distances shown. Two DHFRP beams were constructed and tested.

Prior to this test series, a series of slab sections were tested including three DHFRP sections and one steel section. The DHFRP prototype-size bars used to reinforce the slabs were not manufactured using dieless braidtrusion, and therefore, a bar-rupture failure mode occurred. The details of this test series is given in Appendix D. The following discussion is about Series II R/C beams using DHFRP manufactured using dieless braidtrusion.

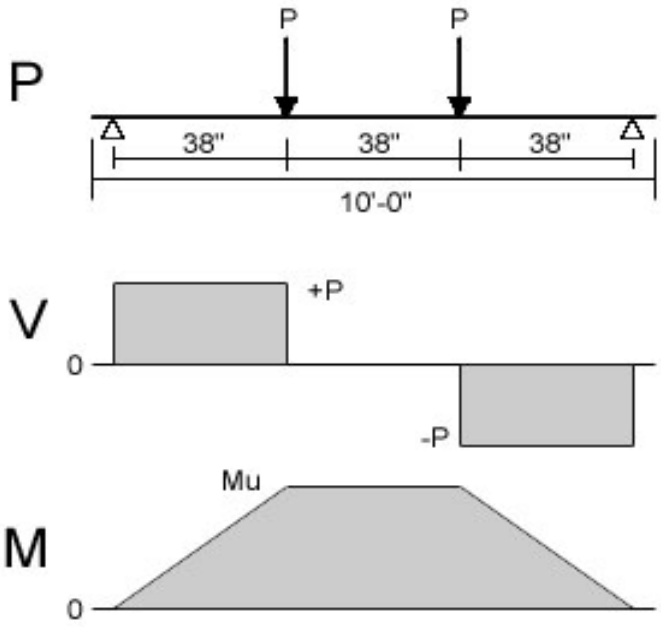

Figure 8.14: Four-Point Loading Configuration for Prototype Beam Tests.

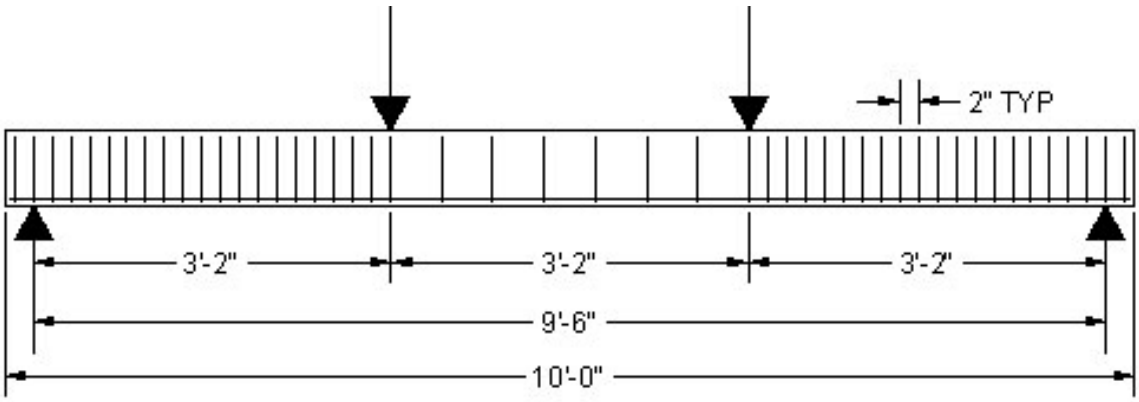

Figure 8.15: Beam Dimensions, Shear Reinforcement, and Loading.

8.2.1 Sample Preparation

Once the DHFRP bars were manufactured, they were cut to length for the longitudinal bars. Stirrups were manufactured to prevent a shear failure mode. 0.119 in (3.023 mm) diameter smooth steel annealed wire (Number 11 wire) was used for the stirrups. Tests by Somboonsong (1997) initially used DHFRP stirrups but were unsuccessful. Modifications to the current braidtrusion process would have to be developed. Therefore, steel wire was used as shear reinforcement. Figure 8.16 shows the wire used for the shear reinforcement. A wooden jig with steel pins and guides was built to bend the stirrups to the proper dimensions and is shown in Figure 8.17. The finished stirrups used as shear reinforcement are shown in Figure 8.18. A 135° closed hook was used for the stirrups. The steel used was Grade 40 with f_y = 41179.56 psi (283.92 MPa). Stirrup steel samples were tested in tension to get the actual stress-strain properties. These curves are shown in Figure 8.19. The steel properties are given in Table 8.3.

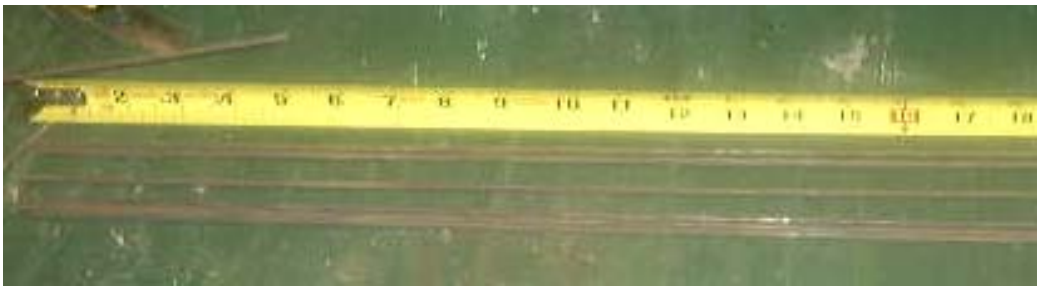

Figure 8.16: Plain Steel Wire Used for Shear Reinforcement for Prototype DHFRP Reinforced Beams.

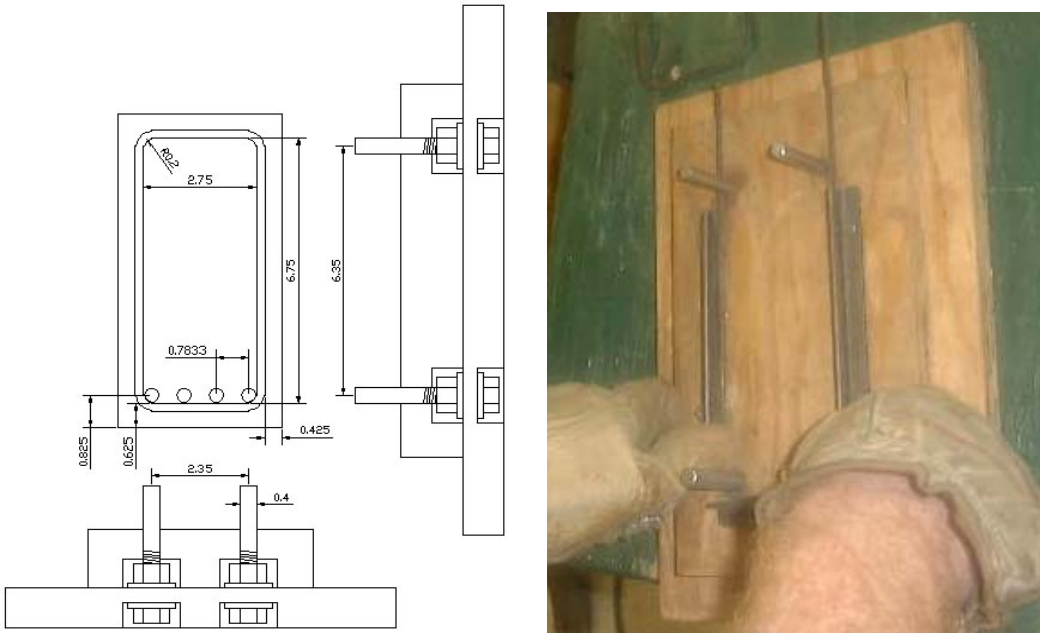

Figure 8.17: Jig Design and Bending of Steel Shear Reinforcement in Jig for Prototype Beams.

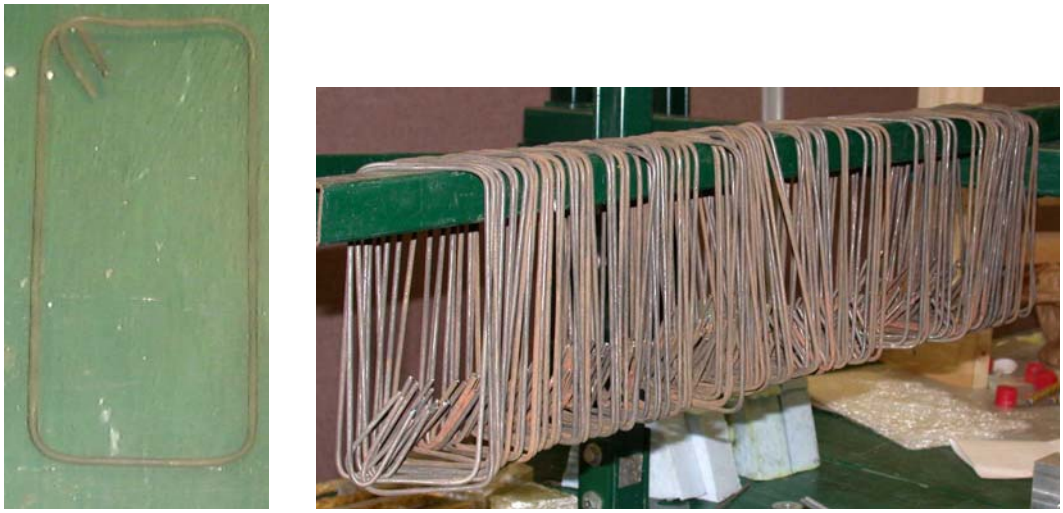

Figure 8.18: Stirrups Used as Shear Reinforcement for Prototype DHFRP Reinforced Beams.

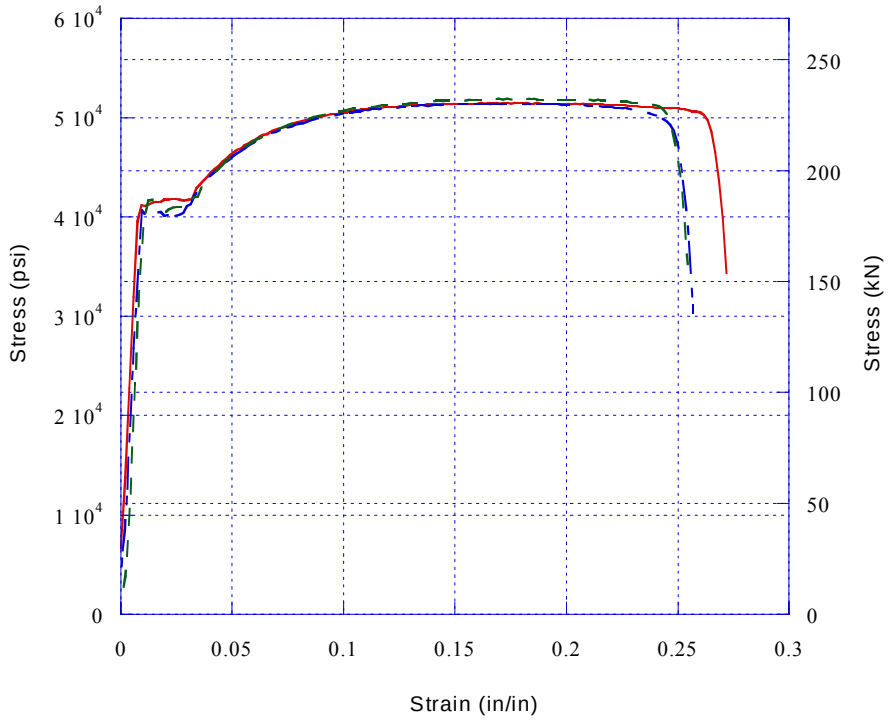

Figure 8.19: Stress-Strain Behavior of 0.119 in Diameter Steel Wire Used as Stirrups for Prototype Beams.

Table 8.3: Stirrup Steel Stress-Strain Properties.

σ_y, psi (MPa)	ε_y	σ_u, psi (MPa)	ε_u
41179.56	0.009225	51519.4	0.2619
40640.09	0.0094	51429.49	0.2448
41719.03	0.014292	51789.14	0.2434
Avg.= 41179.56 (283.9231)	0.011	51579.34 (355.627)	0.250

Next, the reinforcing cage was constructed. This is shown in Figure 8.20. The stirrups were tied to the longitudinal bars using Number 18 (0.0478 in, 1.21-mm dia.) annealed steel wire. A saddle hook was used. Two pieces of Number 9 (0.1495 in, 3.80-

mm dia.) steel wire were used in the top corners of the stirrups to hold the cage in place. These wires were not considered as compression reinforcement, and therefore, were ignored in the design calculations. The finished reinforcing cages are shown in Figure 8.21. The finished cages and forms are shown in Figure 8.22. The forms were made out of plywood and were braced using 2" x 4" (50.8 mm x 101.6 mm) diagonal braces and stiffeners along the top edge of the form. Plywood diaphragms were placed at the ends of the forms to prevent any torsional effects while the concrete was being poured.

Two of the four bars used for beam Series II were cut 0.5 feet too short, and therefore, additional bars were spliced at the ends of the beam, as shown in Figure 8.23. The spliced bars were placed such that only one splice was located at each end of the beam. Therefore each end of the beam had three bars continuous over the reaction. The length of the spliced bars was 20 in (508 mm).

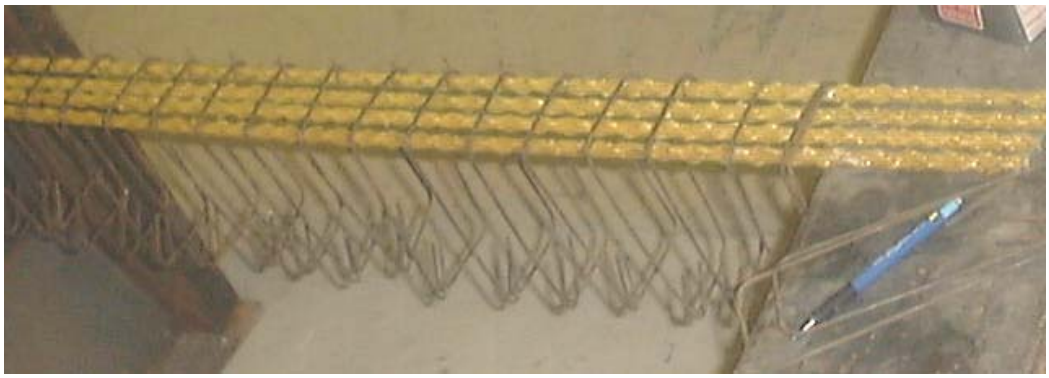

Figure 8.20: Construction of Reinforcement Cage for Prototype DHFRP Reinforced Beams.

Figure 8.21: Finished Reinforcing Cages Used for Prototype DHFRP Reinforced Concrete Beams.

Figure 8.22: Finished Reinforcing Cage (Left) and Forms Used for Prototype DHFRP Reinforced Concrete Beams.

Figure 8.23: Splice Used for Prototype Beam II.

The forms were lubricated using releasing oil. The oil used to lubricate the forms during casting consisted of 2/3 parts boiled linseed oil and 1/3 part turpentine. Chairs and

spacers made from Number 11 wire were spaced 12" apart to support the reinforcing cage and to align the cage properly. The mixed used for the prototype beams is shown in Table 8.4. Type III high-early cement was used to gain strength quickly. A drum mixer (Imer Minuteman, 5 ft^3 capacity) was used to batch the concrete since the volume needed did not warrant the use of ready-mix concrete. Two batches were used per beam. 3" x 6" (76.2 x 152.4 mm) test cylinders were made to obtain both the compressive and tensile strength of the concrete. A 1.25" (31.75 mm) flex shaft vibrator (11" head length, Denver Concrete Vibrator) was used to consolidate the concrete. Figure 8.24 shows the beams being cast.

Table 8.4: Concrete Mix Used for Prototype DHFRP R/C Beams.

Material	**Ratio by weight**	**Weight for mix, lb (kg)**
Coarse aggregate 3/8" dia.	3	351.76 (159.56)
Sand	2	234.51 (106.37)
Cement (Type III)	1	117.26 (53.19)
Water	0.45	52.77 (23.94)

Note: This is enough mix for 2 beams and 18—3" x 6" cylinders

Figure 8.24: Casting and Vibrating of Prototype DHFRP Reinforced Concrete Beams.

8.2.2 Test Procedure

The prototype beams were loaded under four point loading to obtain a region of constant moment. The test setup is shown in Figure 8.25. A hydraulic loading jack (Lehigh, Model HP325, 12 in max. stroke) was mounted onto the existing loading frame. A 50 kip load cell (Honeywell Sensotec) was threaded onto the end of the loading jack. A structural steel tube (5” x 3” x ¼”) was used as a spreader beam to distribute the load

to the two loading points. Pin and roller reactions were placed at each of the supports of the spreader beam and the DHFRP beam. A System 10 DataPAC Data Acquisition System (Daytronic Corporation) was used to obtain load and displacement data.

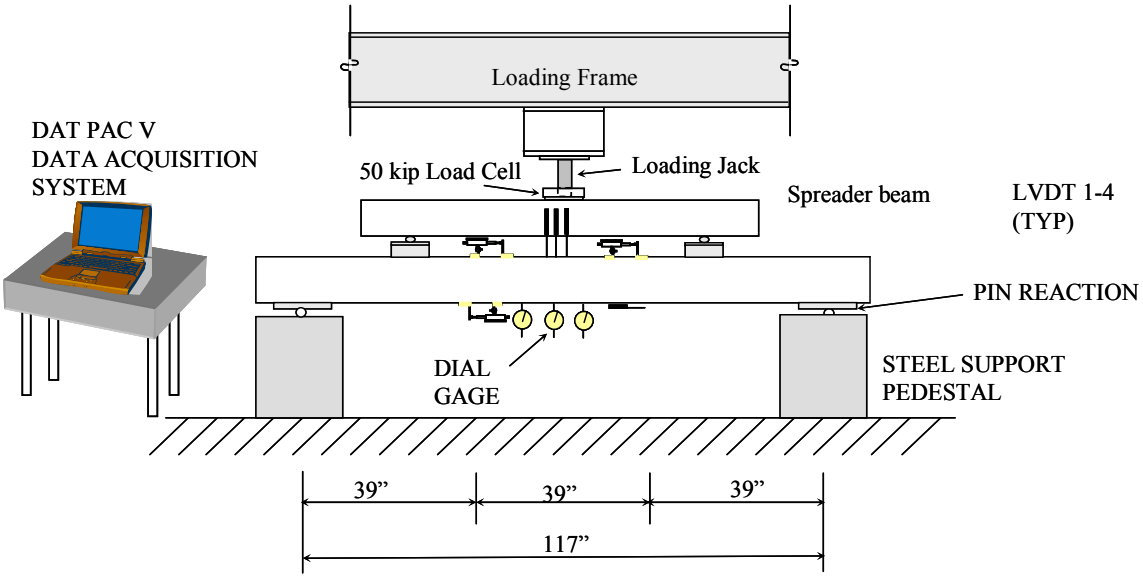

Figure 8.25: Test Setup for Prototype DHFRP Beams.

Figures 8.26 and 8.27 show the instrumentation used on the beam to measure deflections and strains. The beam was whitewashed for clearer visibility of cracking and crack propagation. Also, a 2” x 2” grid was drawn on the center portion of the beam undergoing constant bending. To measure vertical deflections, three LVDTs and three dial gauges were used (Figure 8.26); three LVDTs placed on top of the beam and the dial gauges under the beam. The dial gauges were used as a mechanical backup system to verify the readings of the LVDTs. Both sets of gauges were placed symmetrically about

the center line of the beam, the outer two LVDTs placed 0.9-in from the centerline and the outer two dial gauges placed 3-in from the center line. Three LVDTs and gauges were used to check the symmetry of the deflections and later used to calculate curvatures at the centerline based on finite differences of deflections. From the side view, the LVDTs were placed off center since the spreader beam was on top of the R/C beam. The strain measurement instrumentation is shown in Figure 8.27 and consists of dial gauges and 1 LVDT. These were mounted on the sides of the beam near the extreme tension and compression fibers. Aluminum angles were mounted onto the beam surface using epoxy. The gauges were mounted onto the angles. The initial gauge length was measured before loading and increments of deflection were measured. Three gauges were used to check the symmetry of loading and to get average values of strain and curvature. The strains were then calculated. Due to large anticipated deflections and crack widths, strain gauges were not placed on the beam. Figure 8.28 shows the detail of a dial gauge used for strain measurement and Figure 8.29 shows the detail of an LVDT used for strain measurement.

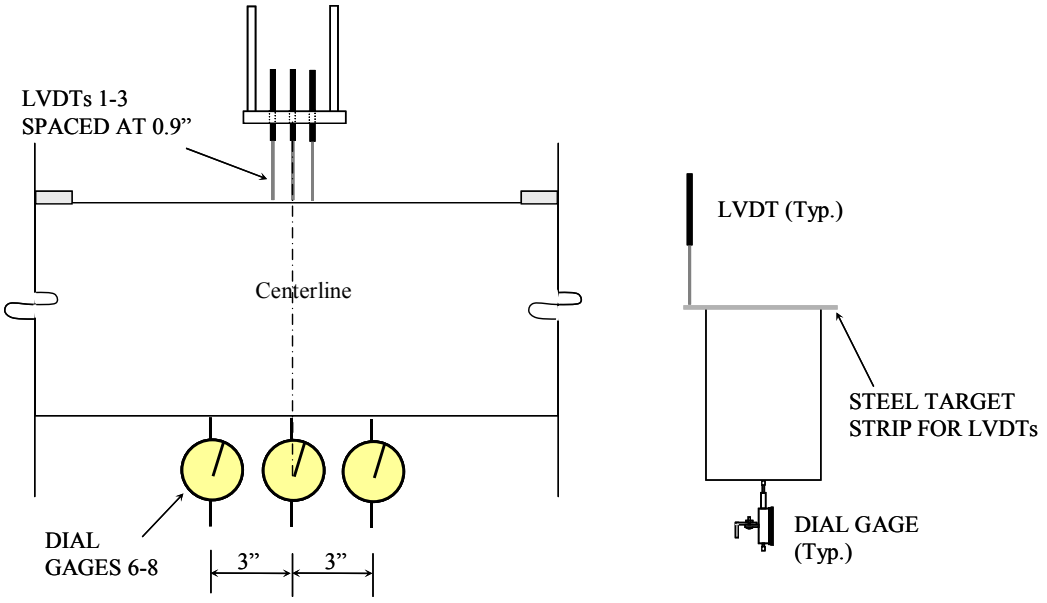

Figure 8.26: Instrumentation for Deflection Measurements: LVDTs and Dial Gauges.

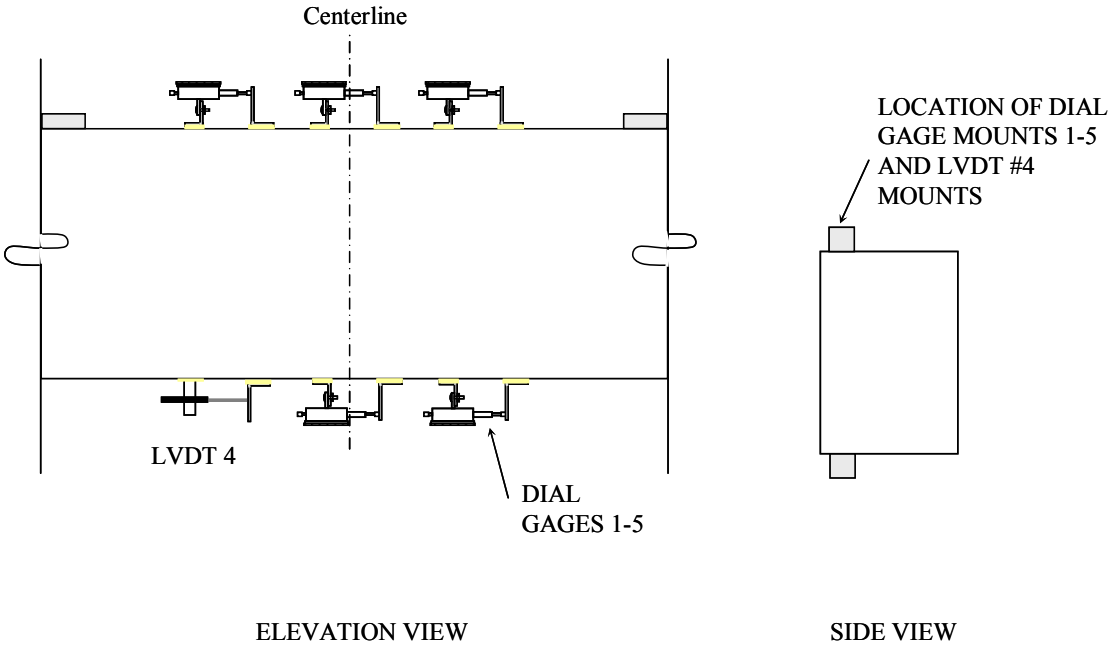

Figure 8.27: Instrumentation for Strain Measurements: LVDTs and Dial Gauges.

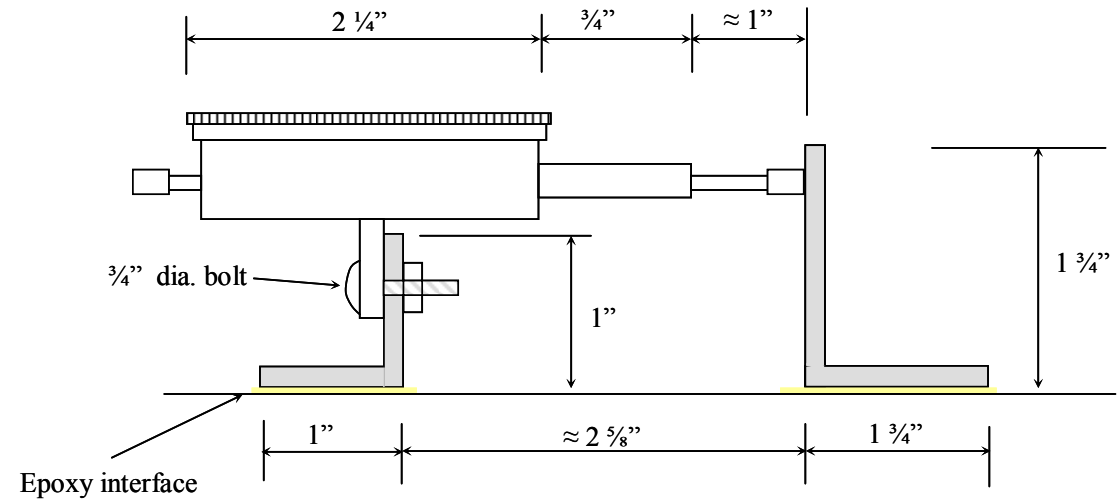

Figure 8.28: Detail of Dial Gauge Used for Strain Measurement.

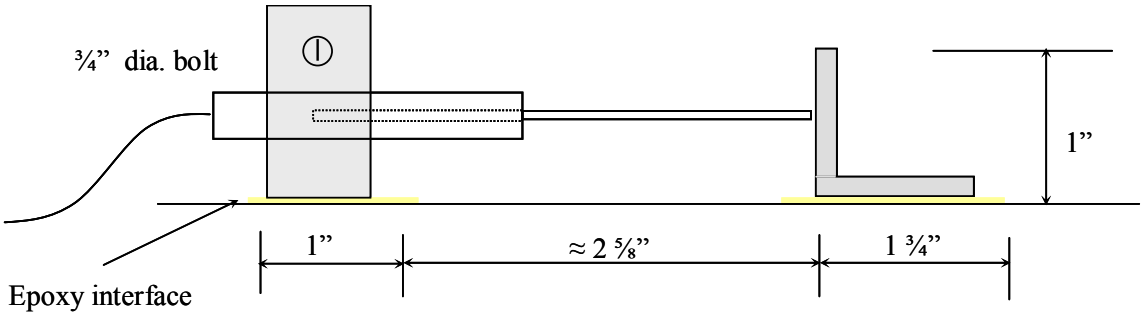

Figure 8.29: Detail of LVDT Used for Strain Measurement.

The test was conducted under load control. The load was applied using a hydraulic hand pump. The loading increments were 100 lb increments until initial cracking. After cracking the load was applied at 200 lb increments until first yield. During the yielding portion, the load increments were varied between 50 and 200 lb increments. Immediately after core yarn breaking (i.e., a load drop), the increment was

200 lb; however, when the load was approaching the previous maximum value (just prior to another anticipated core yarn breakage), the increment was decreased to 50 lb in order to get better resolution. At each load level, the load was held and the readings of displacement were recorded. During testing the cracking, yield, and ultimate loads were noted. Also, the cracking pattern and crack growth was documented at various load levels during the test.

8.2.3 Results

The results for prototype beam P-1 and beam P-2 are presented. These include photographs of the test setup and the progression of cracking until failure for both beams. The load-displacement and moment-curvature were plotted and compared.

8.2.3.1 Prototype Beam P-1

Shown in Figure 8.30 is the overall beam setup. The LVDTs and dial gauges to measure deflections were mounted on a separate frame constructed of steel rods that reacted directly against the floor, separate from the beam system. Figure 8.31 shows a detail of the dial gauge instrumentation where the vertical dial gauges measured deflection and the horizontally mounted gauges on the side of the beam measured deflections which were used for strain readings. The gauges were mounted on the side for ease of reading. The bottom center gauge was an LVDT. Figure 8.32 shows a detail of the load actuator and load cell, the spreader beam, and the vertical LVDTs for deflection measurements. Since the spreader beam was aligned directly over the R/C beam, thin steel plates were epoxied onto the concrete surface and the LVDTs were mounted to the plates. This enabled the LVDTs to be aligned vertically, thereby

preventing erroneous data. Shown in Figure 8.33 is the System 10 DataPAC data acquisition system. The data from the load cell and the four LVDTs was simultaneous recorded to Microsoft Excel using a laptop computer.

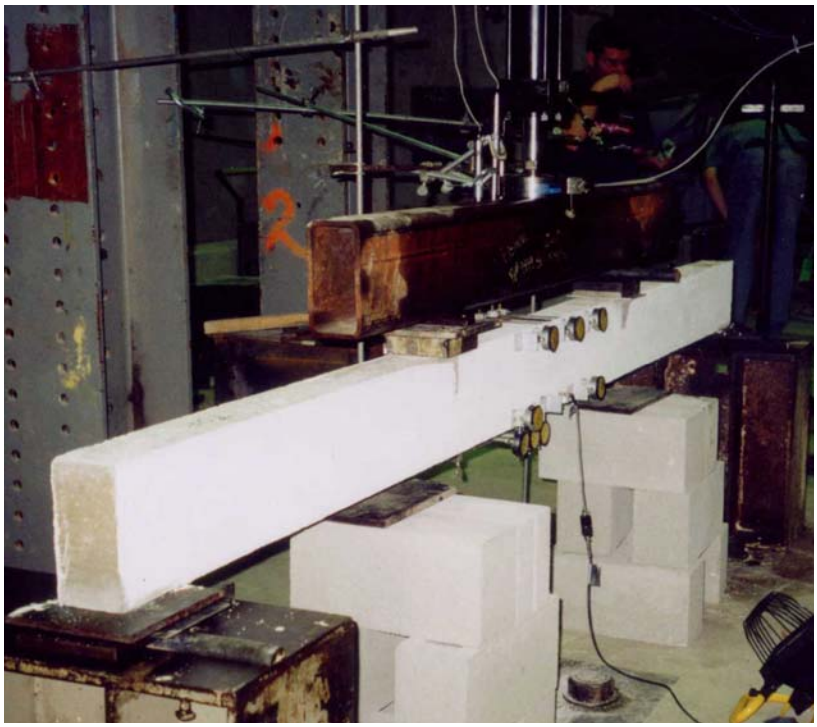

Figure 8.30: Prototype DHFRP Beam Test Setup.

Figure 8.31: Detail of Instrumentation for Deflections and Strains.

Figure 8.32: Detail of (a) Load Actuator, Load Cell, and Spreader Beam and (b) Detail of LVDTs for Deflection Measurements.

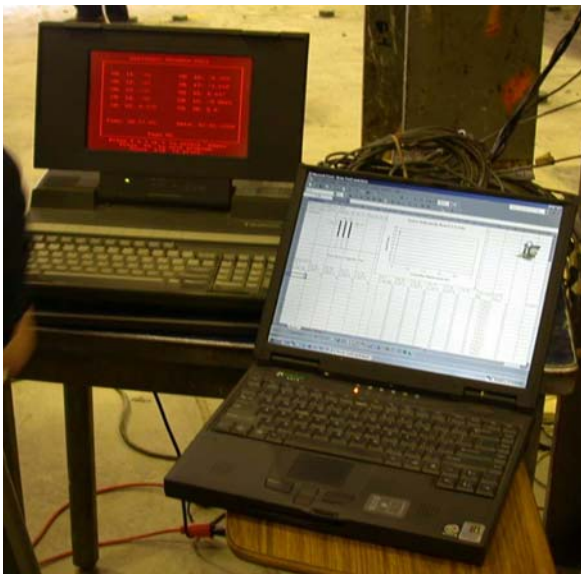

Figure 8.33: DataPAC System 10 Data Acquisition System.

Shown in Figures 8.34 through 8.38 are photographs of the progressive failure of beam P-1 from initial cracking to failure of the compression side of the beam. Shown in Figure 8.34 is the beam cracking at around 1800 lb, before yielding of the reinforcement. Figure 8.35 shows the cracking at approximately 4000 lb, just prior to yielding. Figure 8.36 shows flexural cracking along the length of the span near failure. Shown in Figure 8.37 is the crushing failure of the concrete on the compressive side of the beam. Figure 8.38 shows the cracking pattern at failure and the compressive failure (top left of photograph).

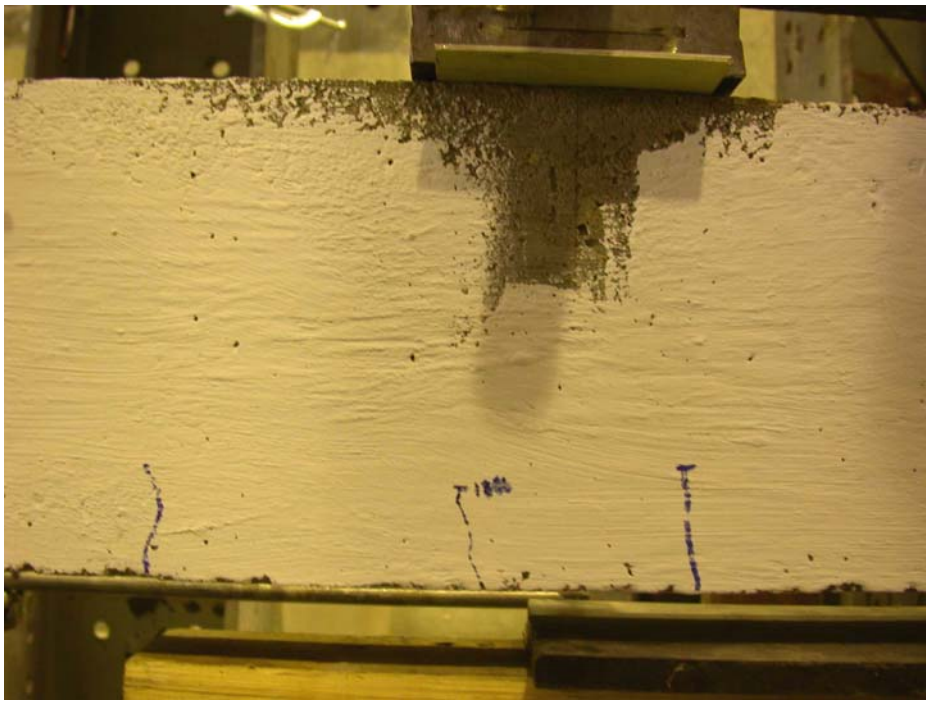

Figure 8.34: Beam P-1 Cracking at 1800 lb.

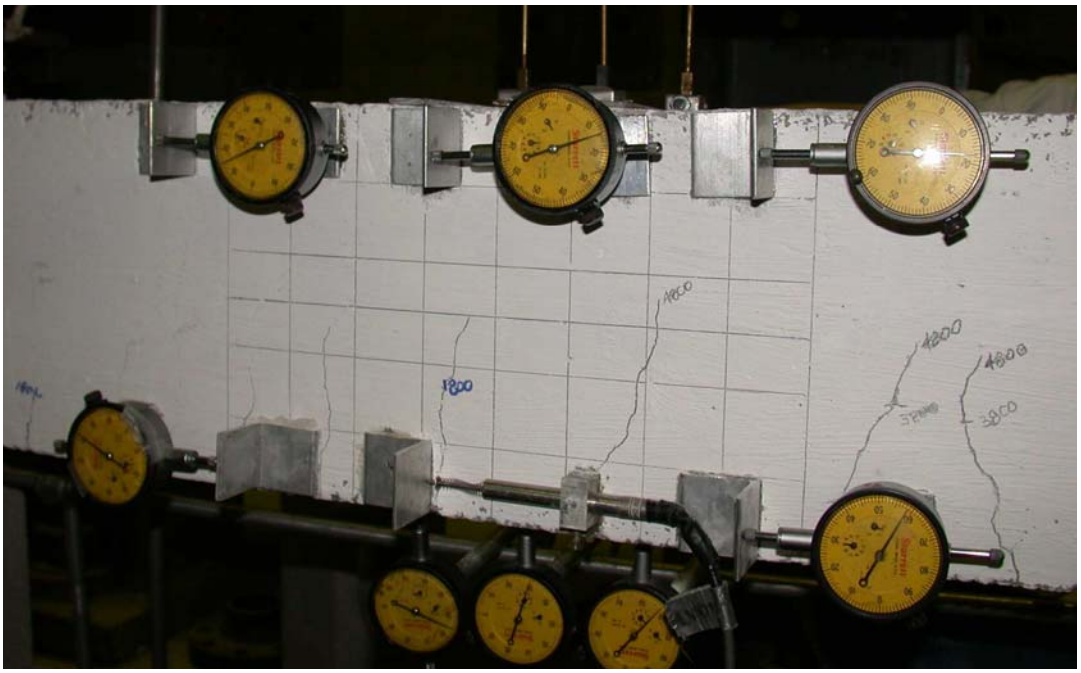

Figure 8.35: Beam P-1 Cracking at Approximately 4000 lb.

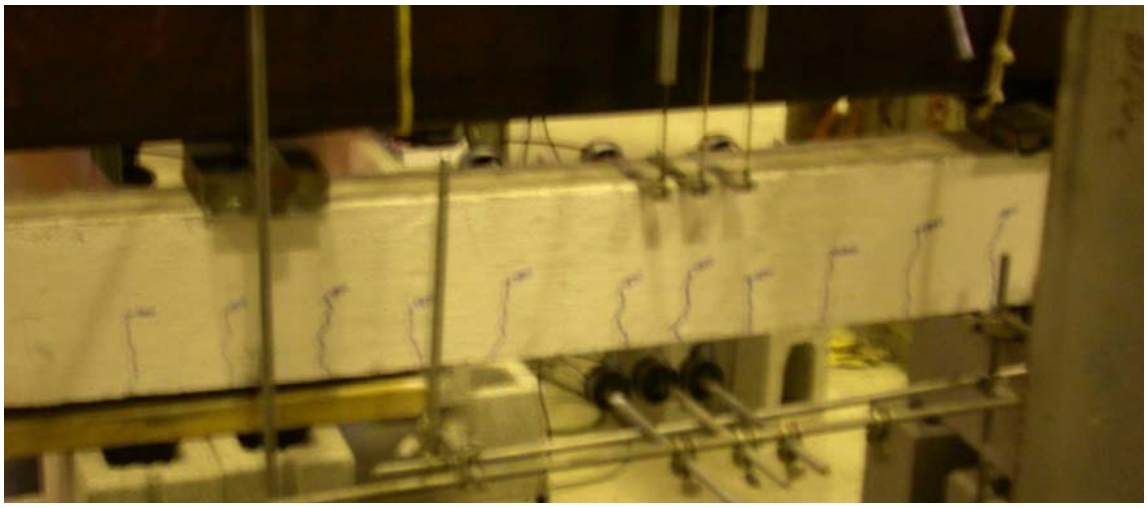

Figure 8.36: Beam Cracking Along the Length of Beam P-1 Near Failure.

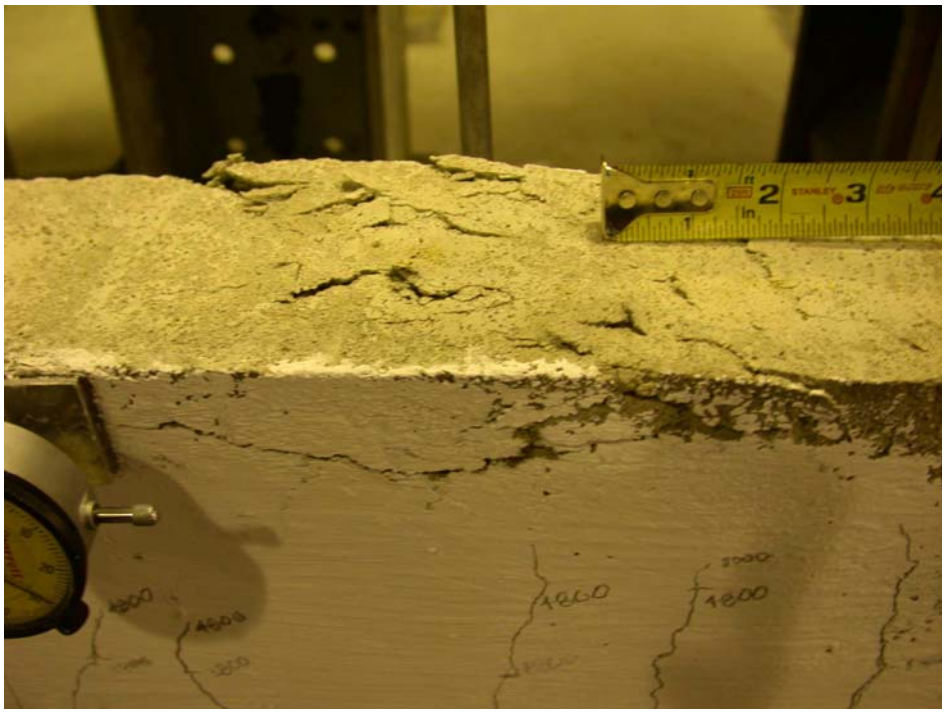

Figure 8.37: Crushing Failure of Compression Side of Beam P-1.

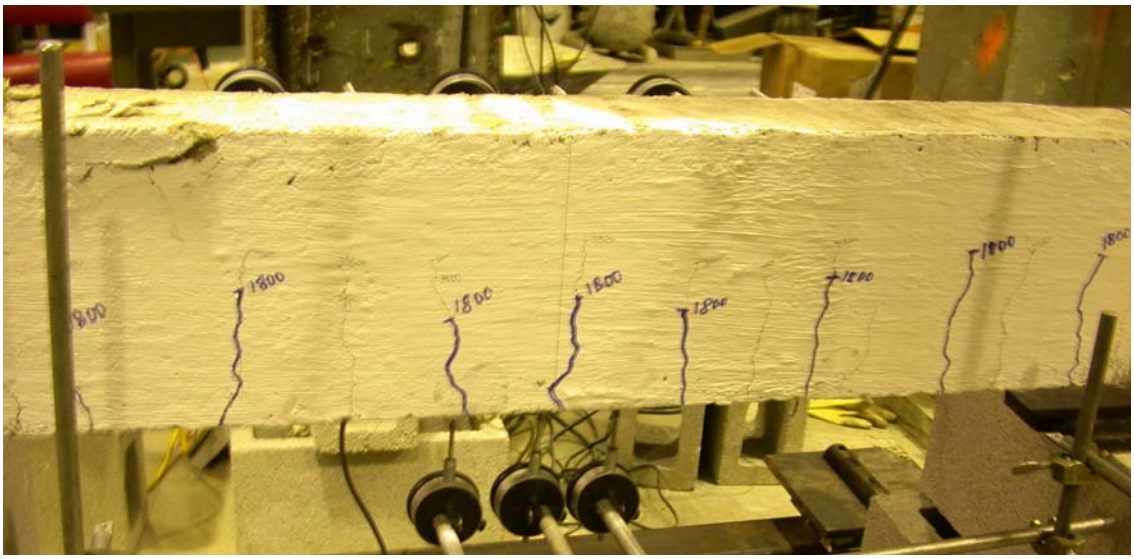

Figure 8.38: Crushing of Compression Side of Beam and Cracking at Failure, Beam P-1.

Shown in Figures 8.39 and 8.40 is the load-deflection behavior of beam P-1. Figure 8.39 shows the portion of the curve around the cracking load. This is shown for greater resolution of this point. Figure 8.40 shows the entire curve until concrete compression failure.

The curvature was obtained from the deflections of the LVDTs and the dial gauges. The moment was obtained from the load values recorded and the curvature values were obtained using a finite difference of deflections. Figure 8.41 shows the center portion of a beam where there deflections are measured at the centerline, a distance h to the left of the centerline, and a distance h to the right. Using finite differences, the curvature is given as

$$\phi = \frac{y_{i+1} - 2y_i + y_{i-1}}{h^2} \qquad 8\text{-}28$$

where y_{i+1}, y_i, y_{i-1}, and h are defined in Fig. 8.41. These points are locations where the vertical dial gauges and LVDTs were located. This procedure is valid for a beam section under constant curvature. Shown in Figure 8.42 is the moment-curvature behavior for beam P-1.

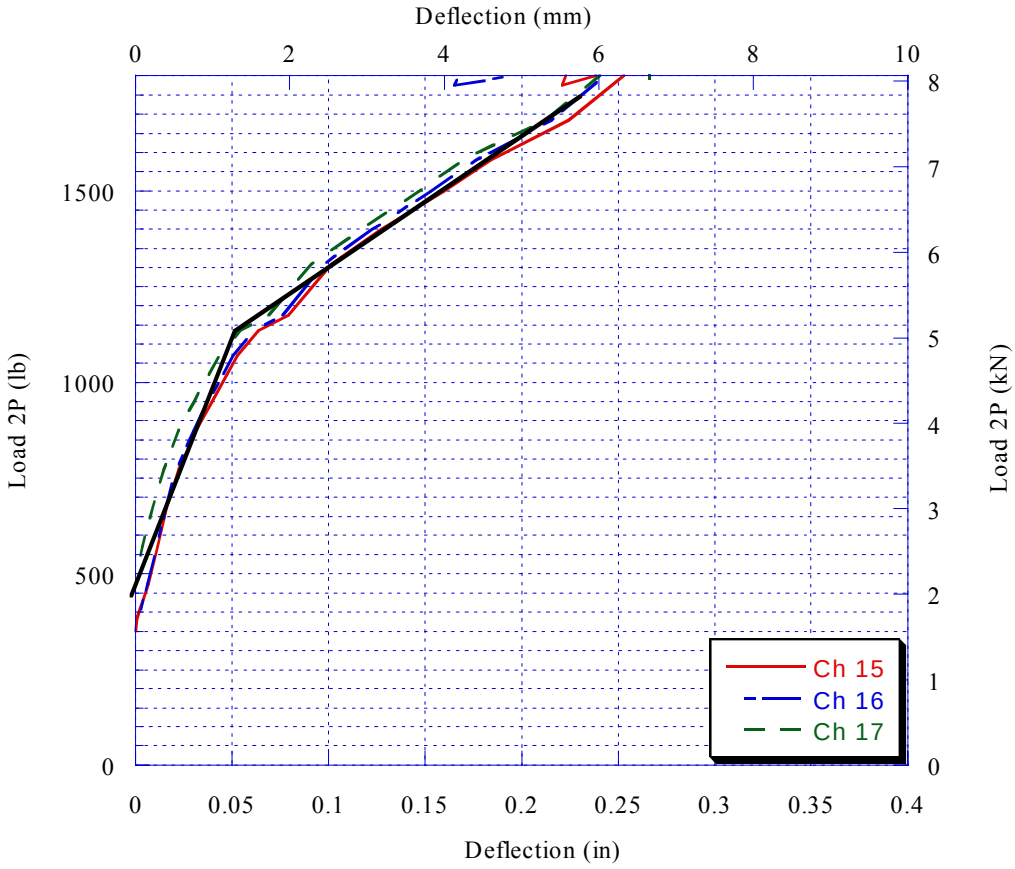

Figure 8.39: Load-Deflection Behavior at Cracking of Beam P-1.

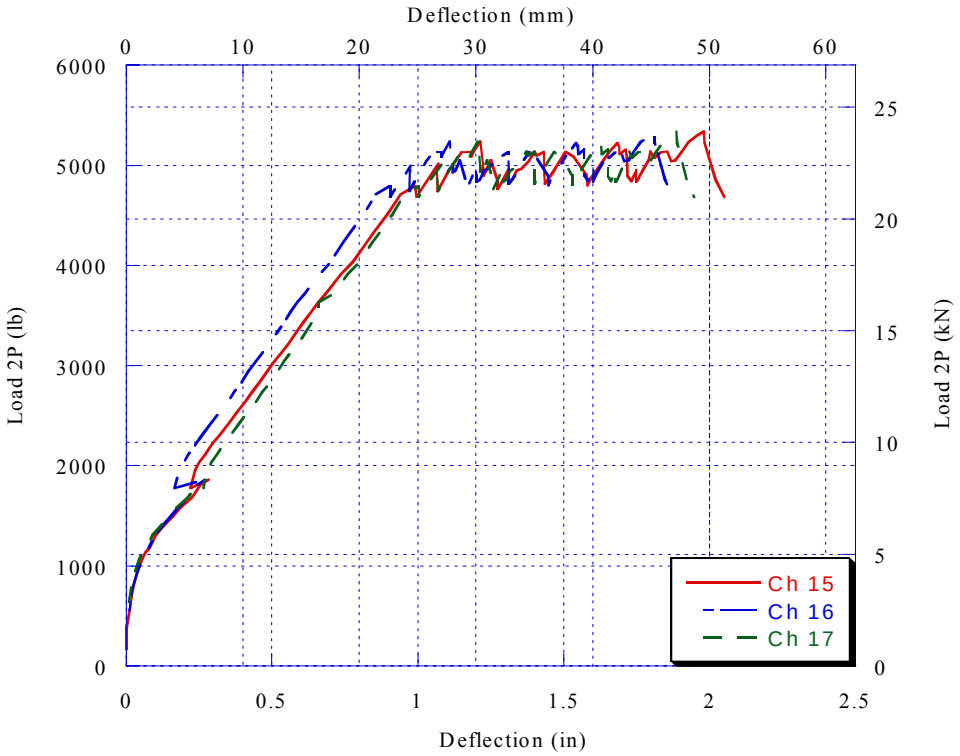

Figure 8.40: Load-Deflection Behavior to Failure of Beam P-1.

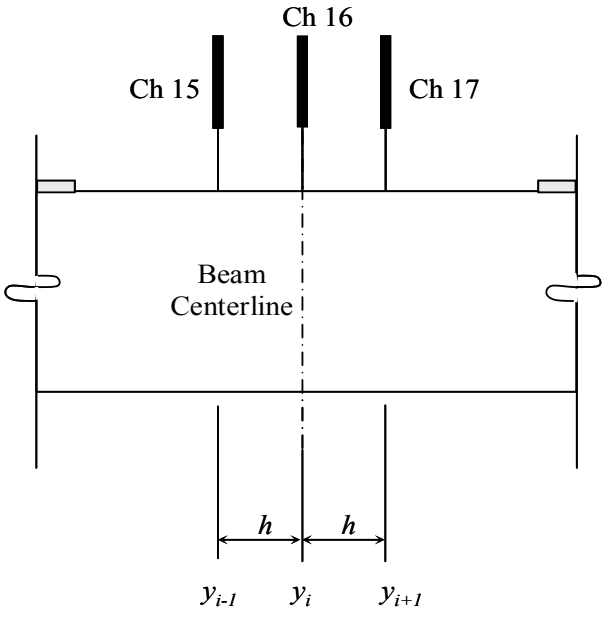

Figure 8.41: Definitions for Calculating Curvature from Finite Differences of Deflections.

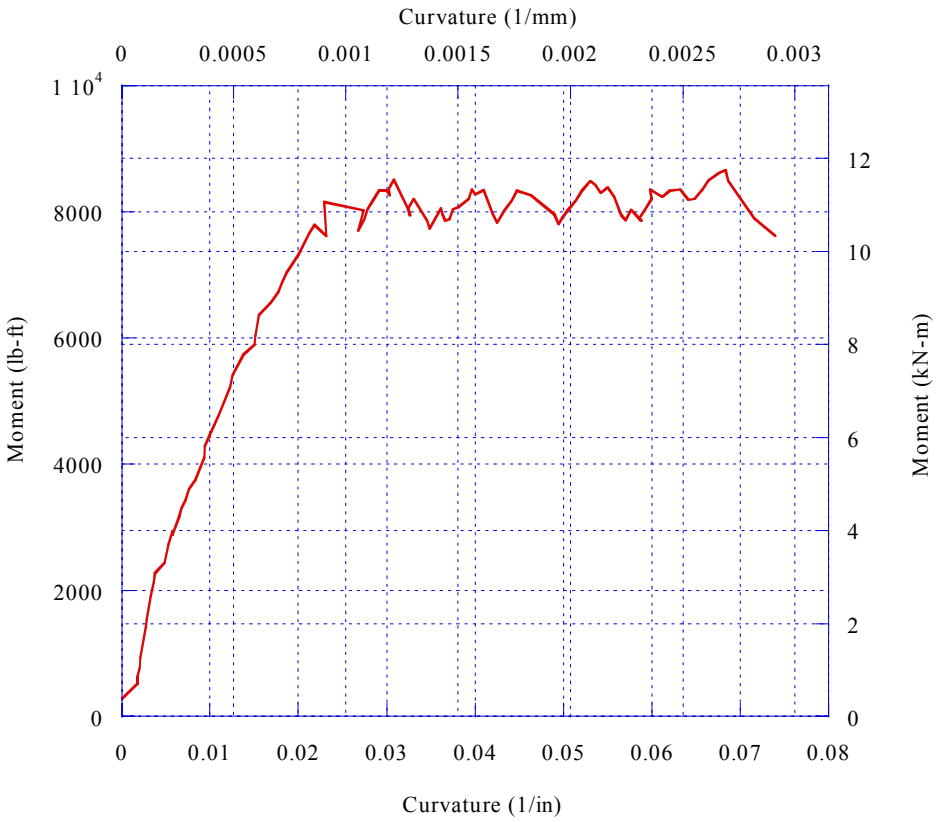

Figure 8.42: Moment-Curvature Behavior to Failure of Beam P-1.

8.2.3.2 Prototype Beam P-2

Shown in Figures 8.43 through 8.54 is the progression of cracking of beam P-2. Figure 8.43 shows the development of flexure cracks at around 3000 pounds and Figure 8.44 shows cracking at load levels of 4000 lb and 5700 lb. Figure 8.45 shows cracking of the right portion of the span at a load level of 5700 lb. Shown in Figures 8.46 through 8.48 is the crack development of the center of the beam at increasing load levels. Figure 8.49 shows the crushing failure of the compression side of the beam and the flexural cracking below the failure area. Shown in Figures 8.50 and 8.51 is the failed concrete

compression zone. Figure 8.52 is a top view of the beam showing the crushed concrete compression zone on the top of the beam and the spalled concrete. The final cracking pattern of the entire beam is shown in Figure 8.53 at failure (i.e., beam is still loaded). Figure 8.54 shows the inelastic deformations of the beam after the load was taken off. Figure 8.55 and 8.56 show the load-deflection behavior of beam P-2 at both the cracking load (8.55) and up to failure (8.56). Figure 8.57 shows the moment-curvature behavior of beam P-2. Shown in Figures 8.58 and 8.59 are comparisons of results from both beam tests; 8.58 compares the load-deflection of beams P-1 and P-2 and 8.59 compares the moment-curvature behavior.

Shown in Figures 8.60 and 8.61 are the concrete compressive stress-strain curves for the concrete used in beams P-1 and P-2, respectively. The tensile (split-cylinder) stress-strain behaviors are shown in Figures 8.62 and 8.63.

The load-deflection and moment-curvature results are given in Table 8.5. The concrete strengths are presented in Table 8.6. Figure 8.64 compares the experimental load deflection behavior to the theoretical behavior predicted in Figure 8.6.

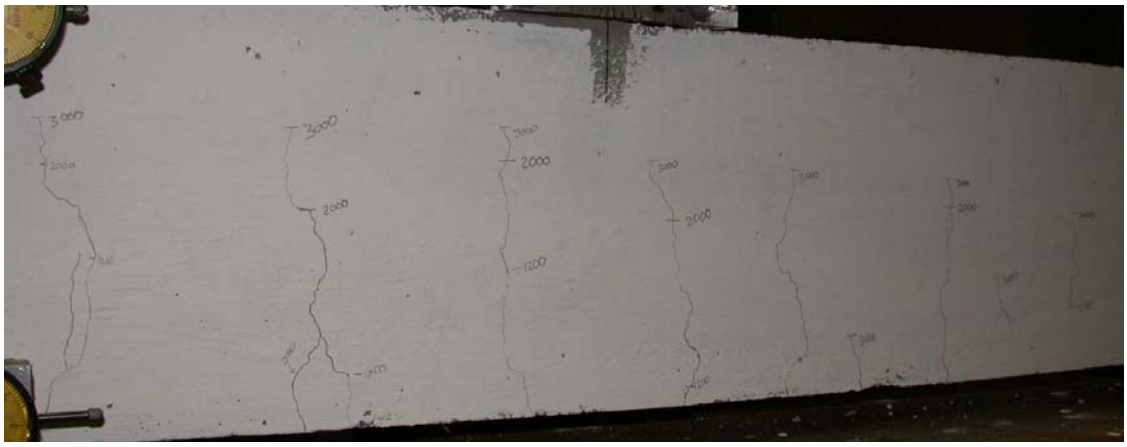

Figure 8.43: Beam P-2 Cracking at 3000 lb.

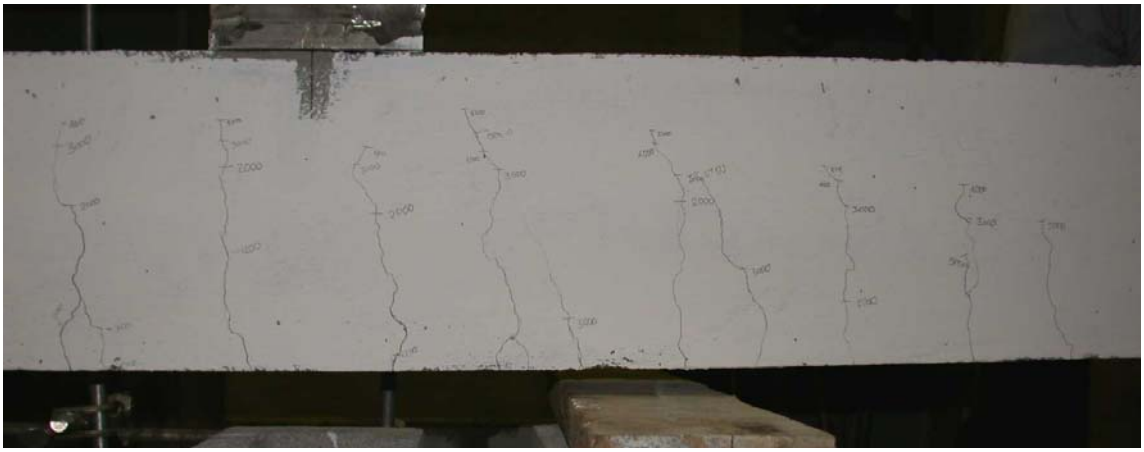

Figure 8.44: Beam P-2 Cracking Marked at 4000 and 5700 lbs.

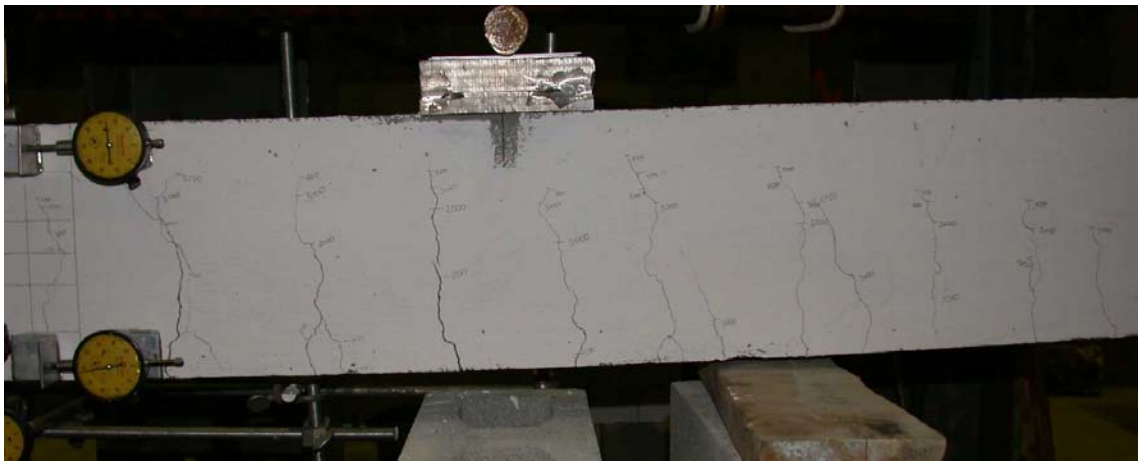

Figure 8.45: Right Side of Beam P-2: Cracking at Loads Up to 5700 lbs.

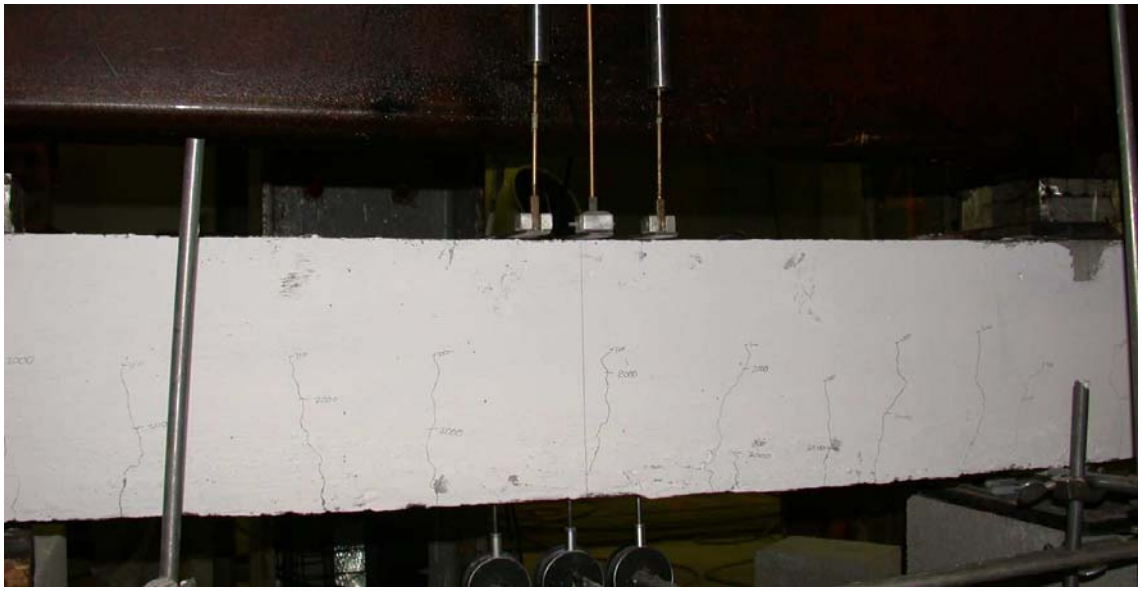

Figure 8.46: Cracking in Center of Span of Beam P-2 at 2000 and 3000 lbs.

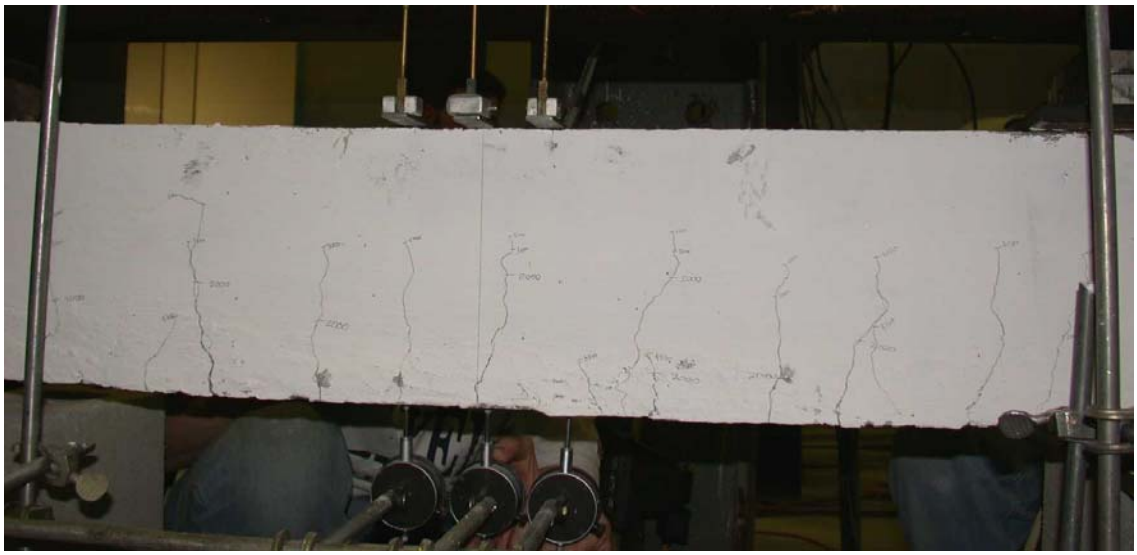

Figure 8.47: Cracking in Center of Span of Beam P-2 at Load Levels Up to 5200 lbs.

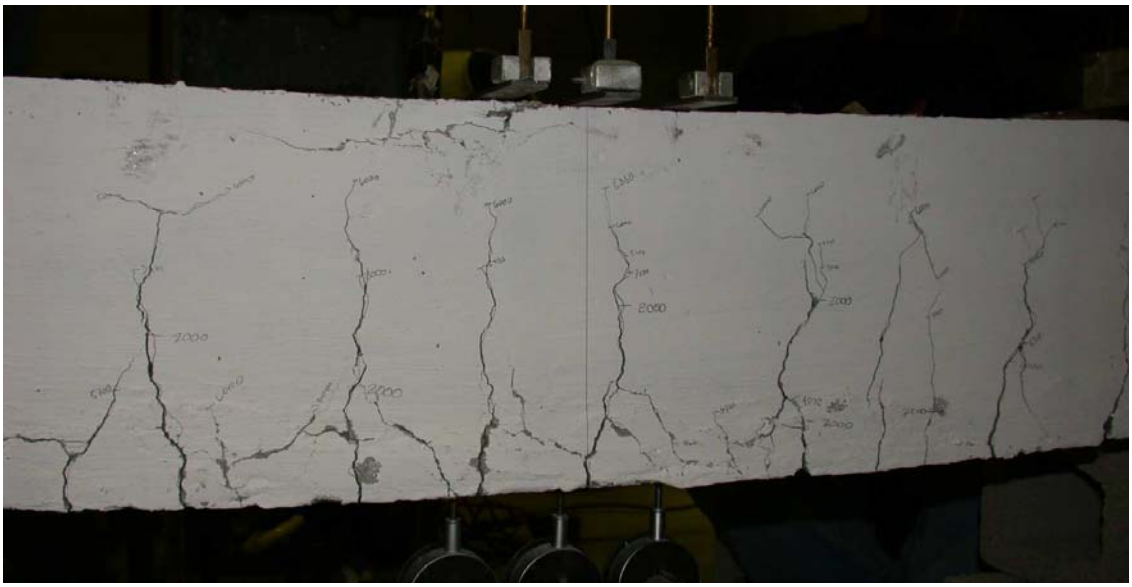

Figure 8.48: Cracking in Center Span of Beam P-2 at Load Levels above 6000 lbs., Near Failure.

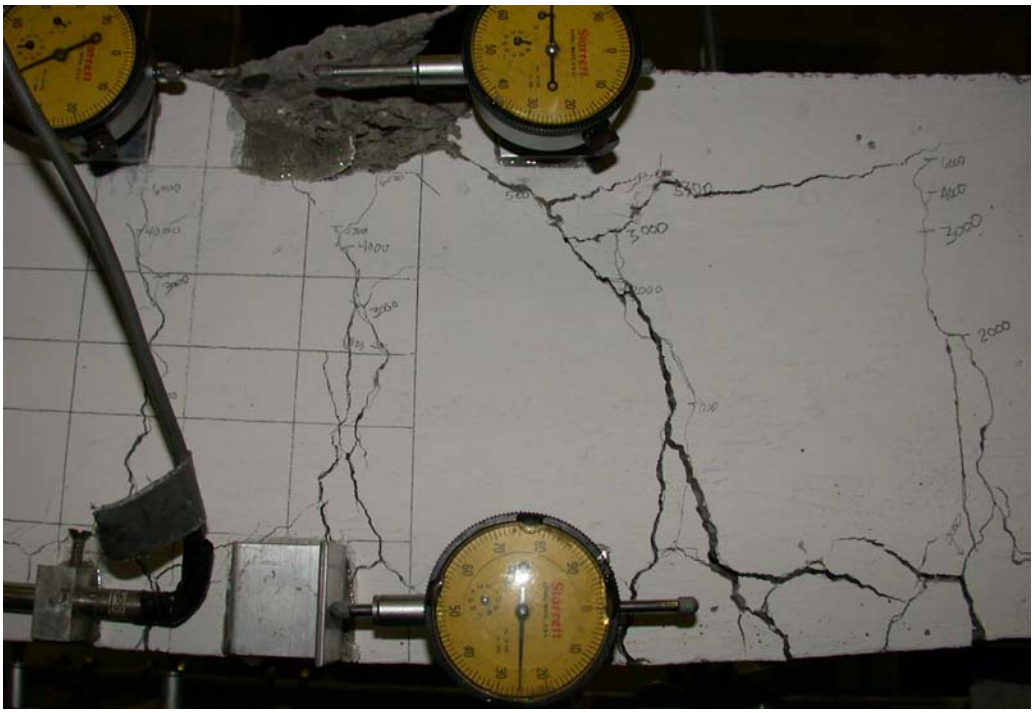

Figure 8.49: Crushing Failure of Compression Zone of Beam P-2 and Flexural Cracking.

Figure 8.50: Side View of Crushing Failure of Compression Zone of Beam P-2.

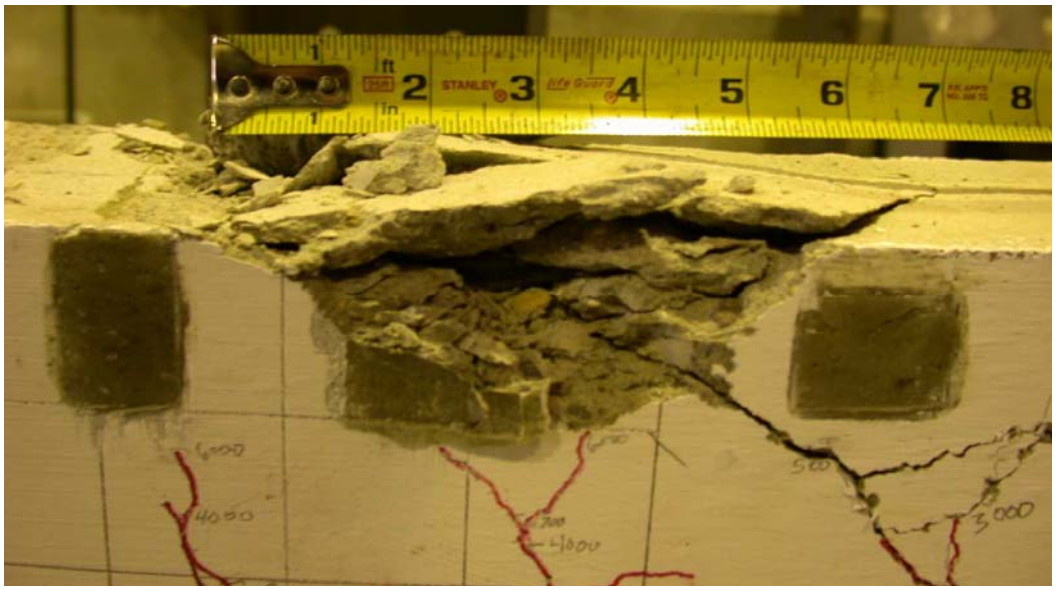

Figure 8.51: Failure of Beam P-2: Crushing and Final Flexural Cracking Pattern.

Figure 8.52: Top View of Crushed Compression Zone of Beam P-2 at Failure.

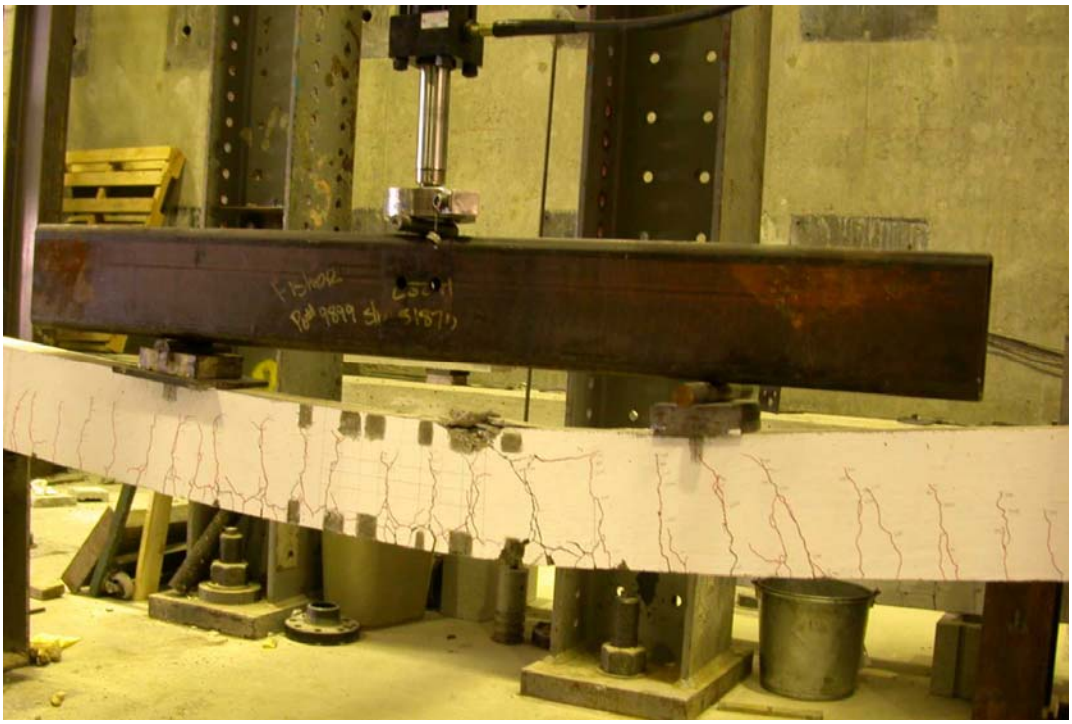

Figure 8.53: Final Cracking Pattern of Beam P-2 at Failure.

Figure 8.54: Large Inelastic Deflections of Beam P-2 at Failure.

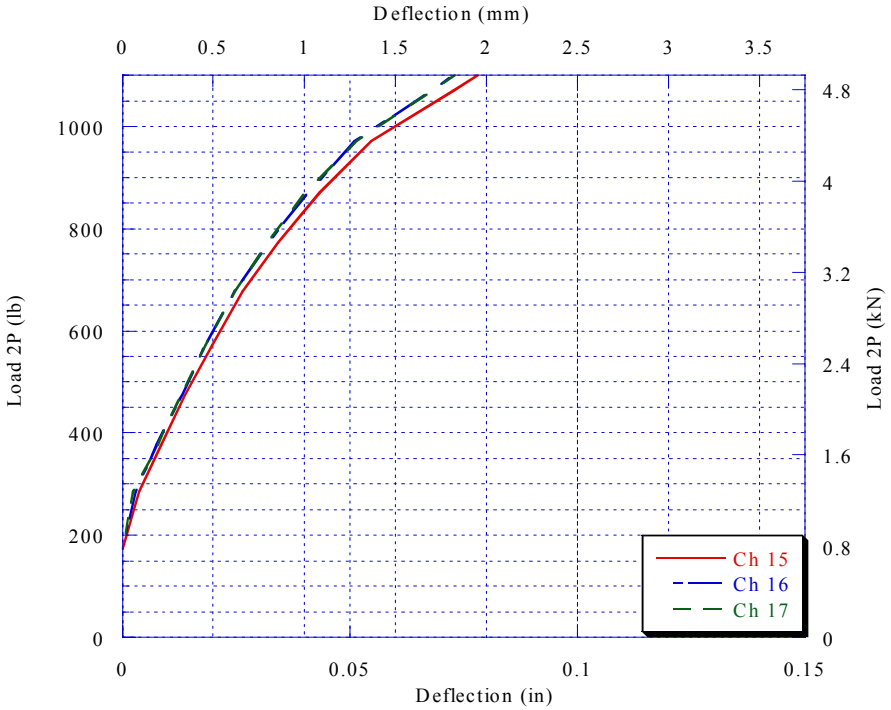

Figure 8.55: Load-Deflection Behavior Up to Cracking of Beam P-2.

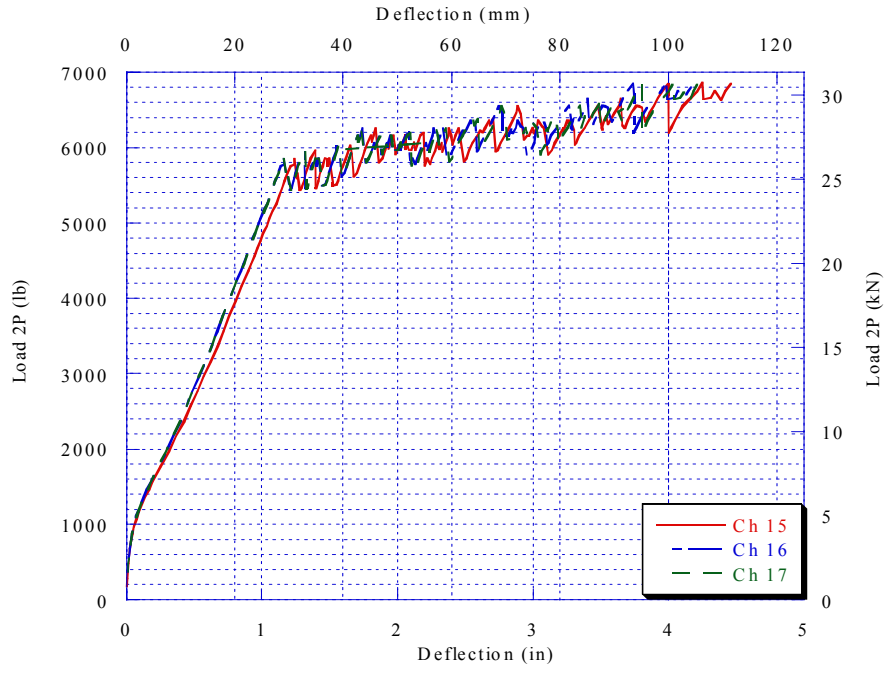

Figure 8.56: Load-Deflection Behavior to Failure of Beam P-2.

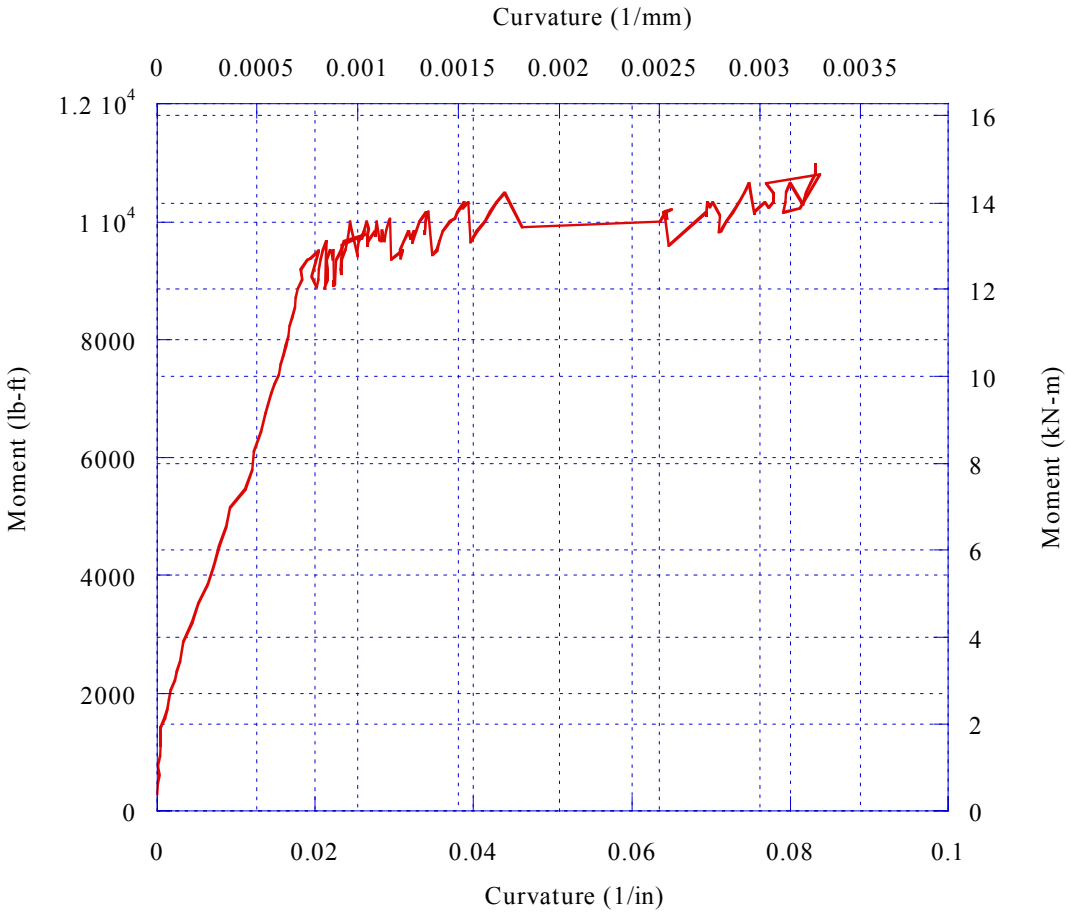

Figure 8.57: Moment-Curvature Behavior of Beam P-2.

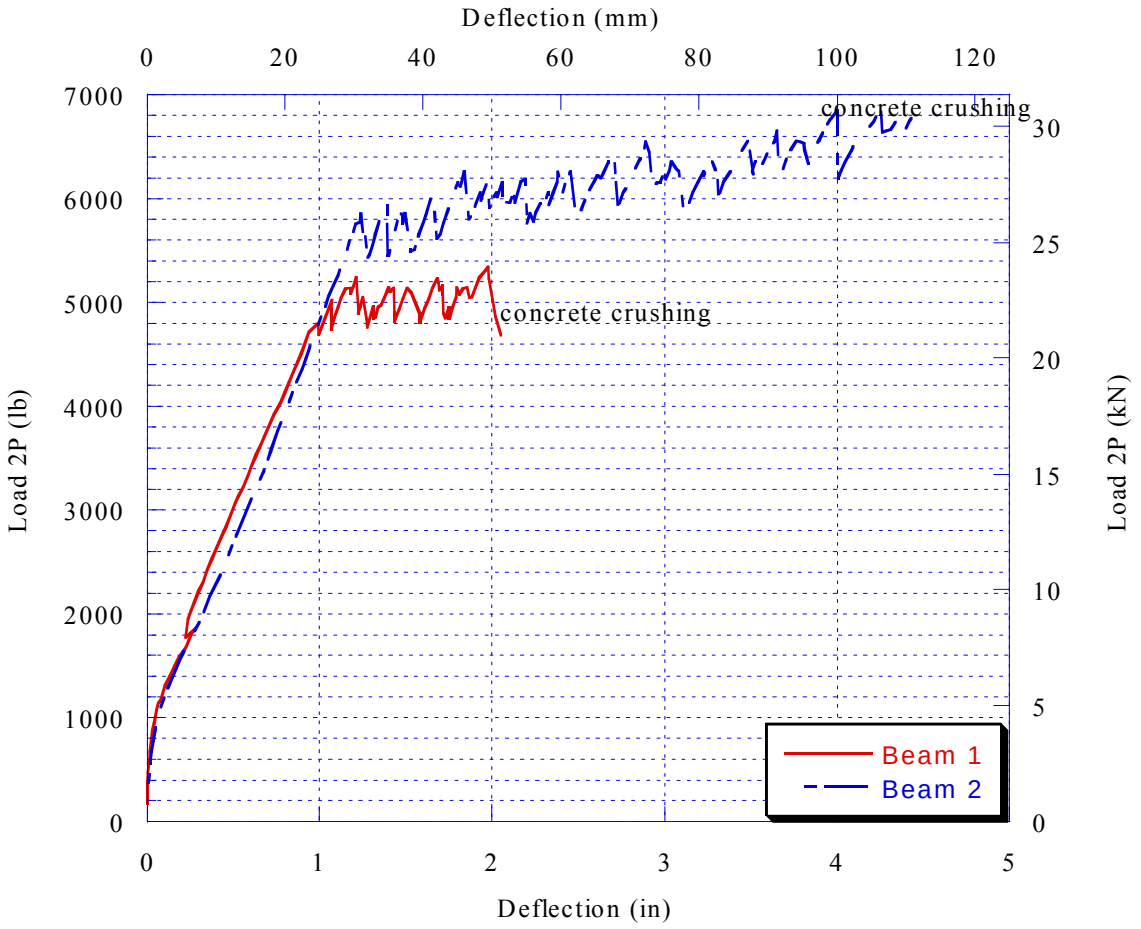

Figure 8.58: Load-Deflection Behavior of Beams P-1 and P-2 to Failure.

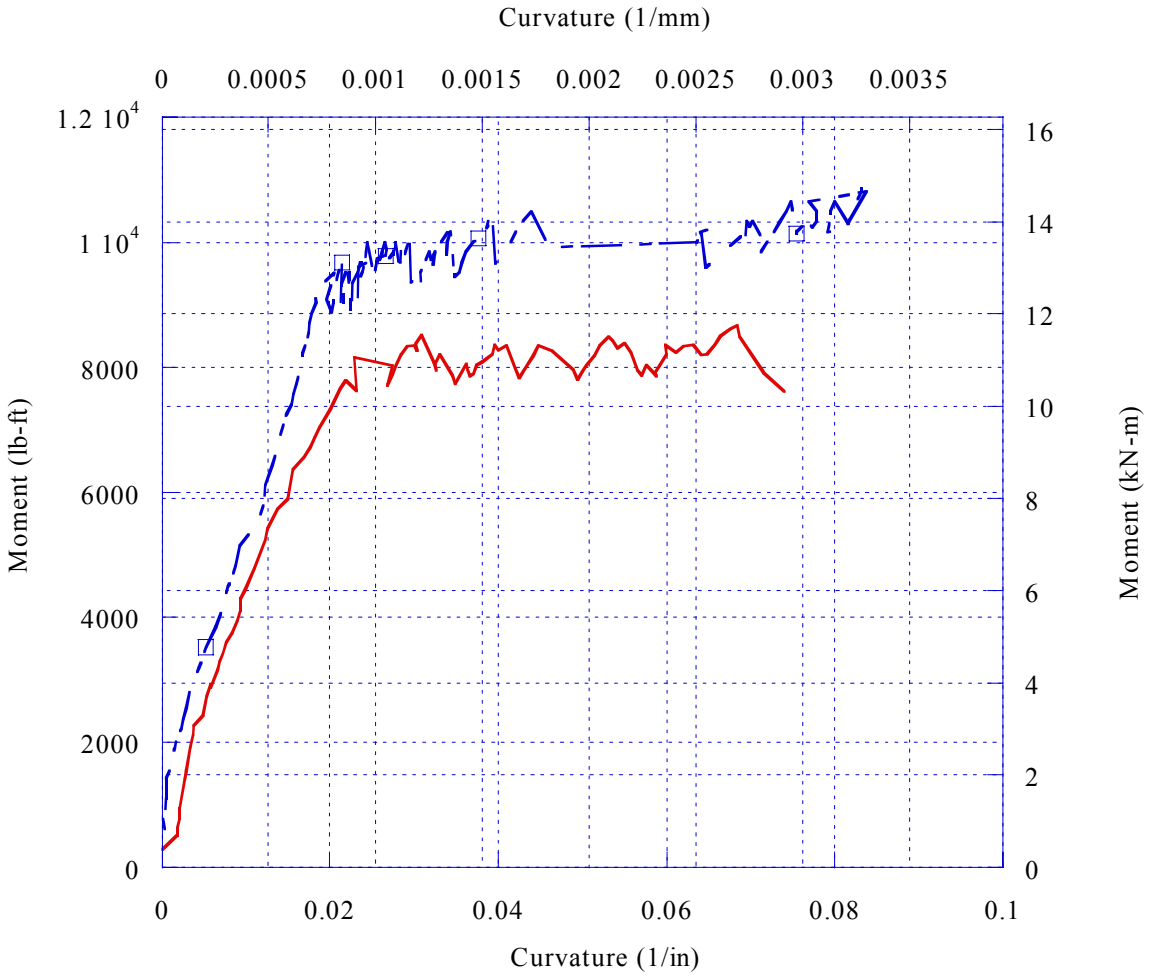

Figure 8.59: Moment-Curvature Behavior of Beams P-1 and P-2 to Failure.

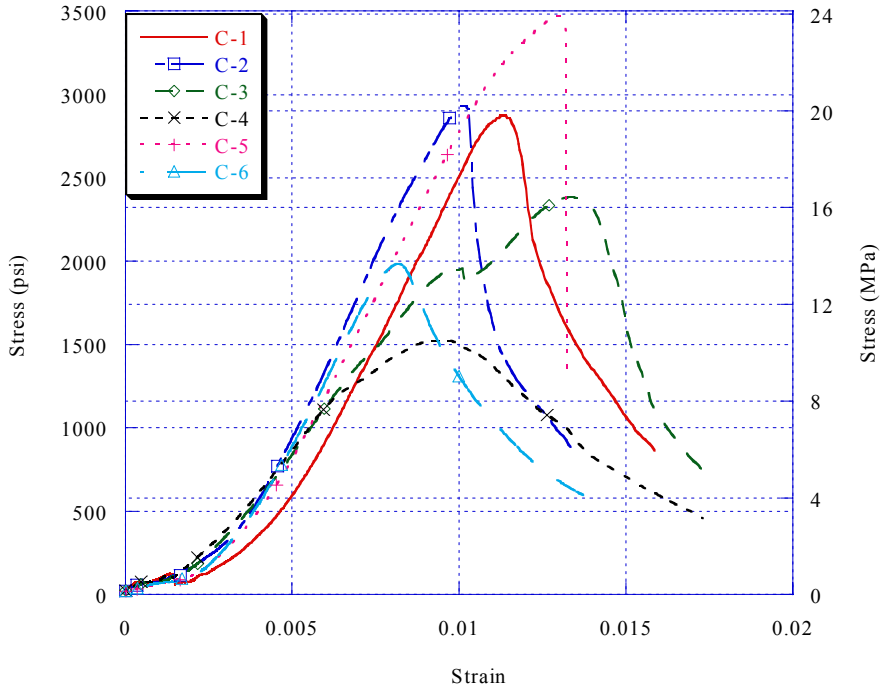

Figure 8.60: Compressive Stress-Strain Behavior of Concrete Used in Beam P-1.

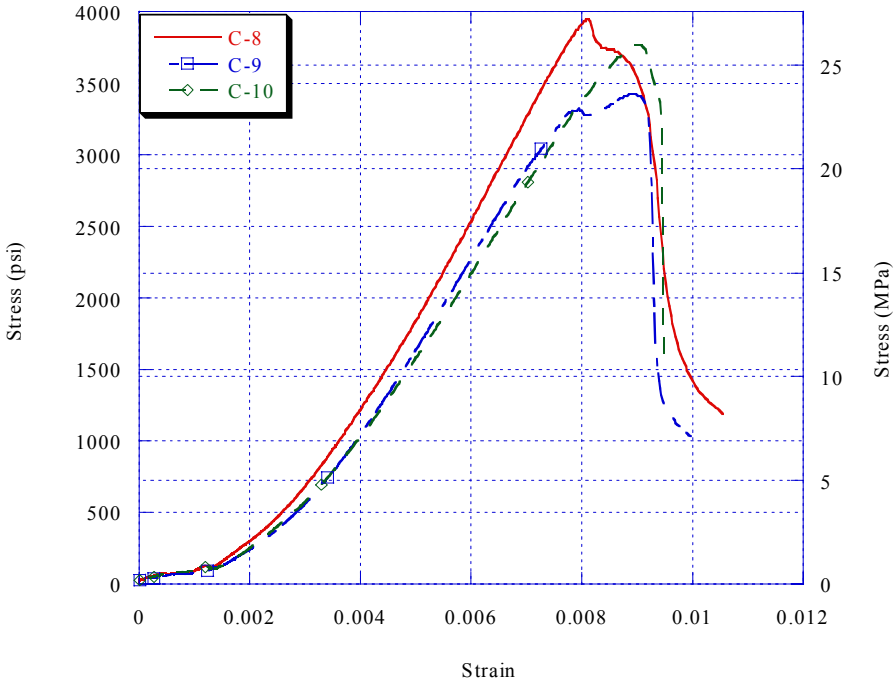

Figure 8.61: Compressive Stress-Strain Behavior of Concrete Used for Beam P-2.

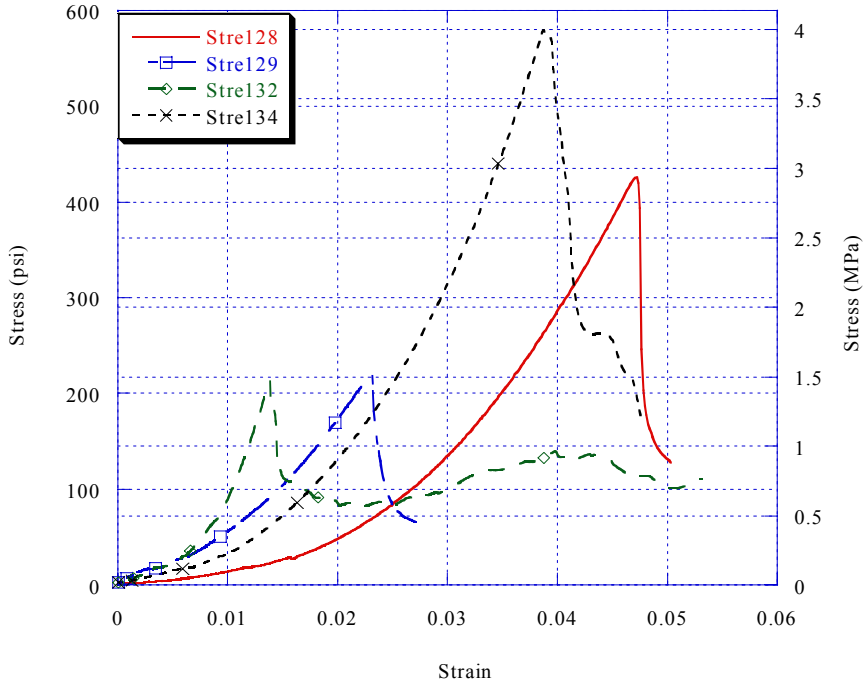

Figure 8.62: Split-Cylinder Tensile Behavior of Concrete Used in Beam P-1.

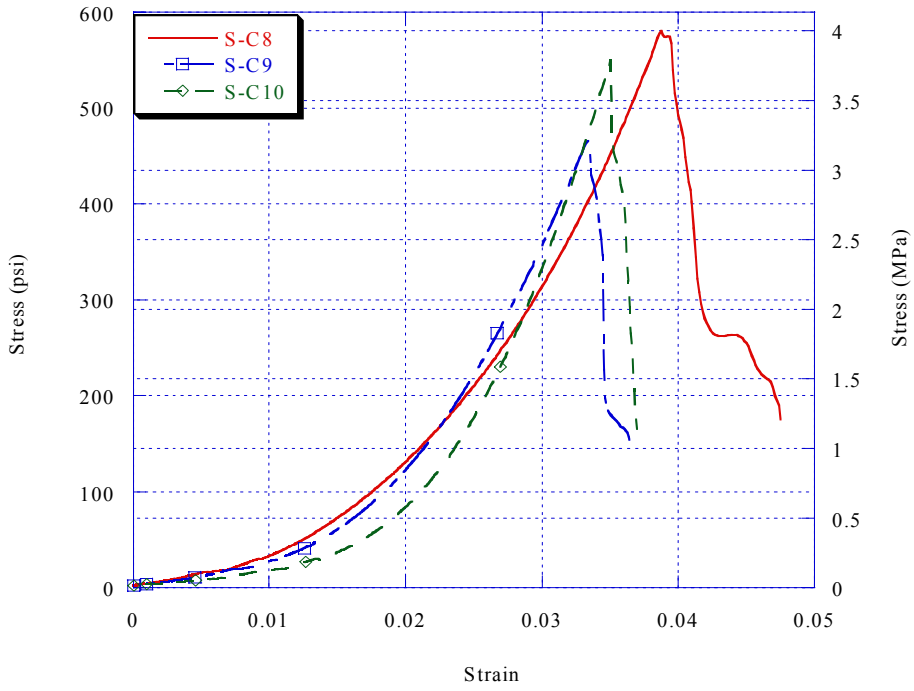

Figure 8.63: Split-Cylinder Tensile Behavior of Concrete Used in Beam P-2.

Table 8.5: DHFRP Prototype Beam Results.

Beam	Load, lb (kN)	Deflection, in (mm)	Moment, lb-ft (N-m)	Curvature, 1/in (1/mm)
P-1				
Cracking	1135.1 (5.0)	0.062 (1.57)	2274.8 (3.1)	0.0038 (0.0002)
Yield	4940.2 (22.0)	0.972 (24.7)	8155.3 (11.1)	0.0229 (0.0009)
Failure	5335.7 (23.7)	1.81 (46.0)	8670.6 (11.8)	0.074 (0.003)
failure/ yield ratios	1.08	1.86	1.06	3.23
P-2				
Cracking	1370.5 (6.1)	0.13 (3.3)	2375.7 (3.2)	0.0038 (0.0002)
Yield	5855.5 (26.0)	1.16 (29.5)	9515.2 (12.9)	0.033 (0.002)
Failure	6849.3 (30.5)	4.19 (106.4)	11130.1 (15.1)	0.13 (0.005)
failure/ yield ratios	1.17	**3.61**	1.17	**3.94**

Table 8.6: DHFRP Prototype Beam Concrete Properties.

Compression Tests	Beam 1	Beam 2
f'_c, psi (MPa)	2871.86 (19.80)	3451.89 (23.80)
	2928.44 (20.19)	3947.03 (27.21)
	2382.37 (16.43)	3423.59 (23.60)
	1525.05 (10.51)	3763.12 (25.95)
	3466.03 (23.90)	
	1983.42 (13.68)	
Average f'_c	**2526.20 (17.42)**	**3646.41 (25.14)**
Split-Cylinder Tests f_{ct} psi (MPa)	231.31 (1.59)	580.03 (4.00)
	426.18 (2.94)	466.85 (3.22)
	220.34 (1.52)	550.68 (3.80)
	213.27 (1.18)	450.59 (3.11)
	218.93 (1.47)	
Average f_{ct}	**262.01 (1.74)**	**512.037 (3.53)**

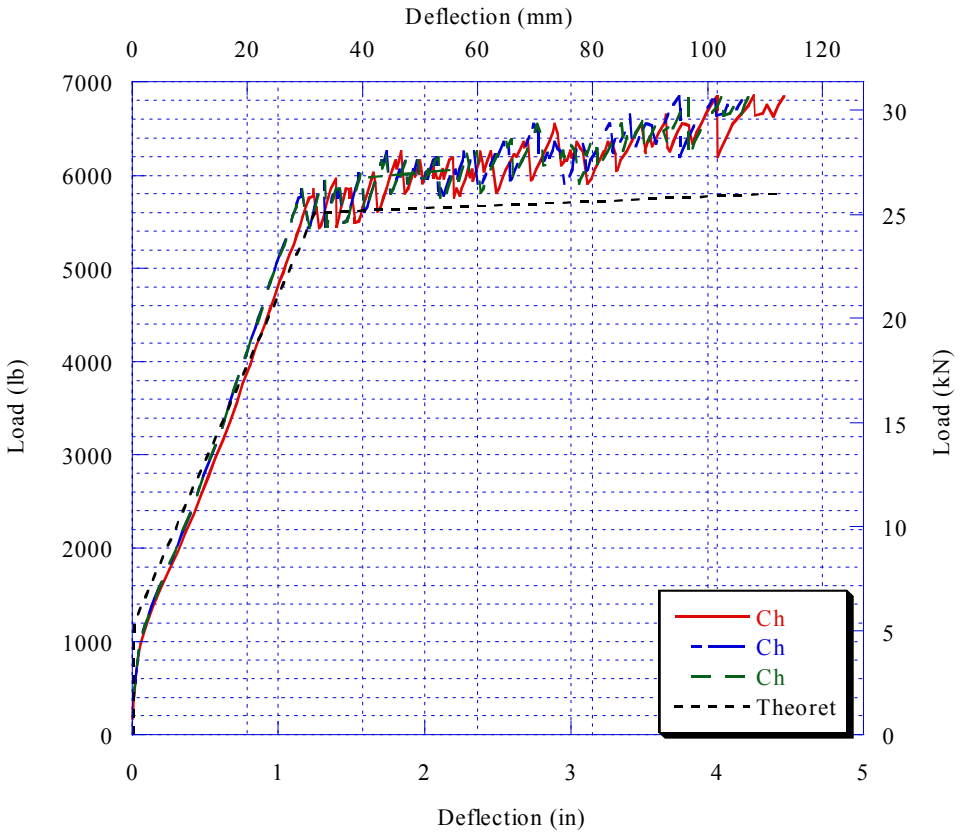

Figure 8.64: Experimental Versus Theoretical Load-Deflection Behavior for 10-mm DHFRP Beams.

8.2.4 Discussion

The performance of R/C beams with prototype DHFRP bars was measured in four ways: (1) the crack progression to failure, the (2) failure mode, (3) the load-deflection behavior and (4) moment-curvature behavior. These measures indicated the ductility, bond strength, and energy absorption of DHFRP.

Shown in Figure 8.34 was the cracking of beam P-1 at 1800 lb. This showed three small vertical flexural cracks that began near the right load point from the spreader beam. This was at the edge of the region of constant maximum moment. Figure 8.35

showed cracking at approximately 4000 lb. It was observed that flexural cracks had progressed half-way up the side of the beam in the center span of constant moment. Figure 8.36 showed the crack propagation near failure. The cracks were closely spaced and symmetric. This was an indication of good bonding between the DHFRP bars and the surrounding concrete. Also noted was the absence of diagonal cracks which indicated sufficient shear resistance by the stirrups.

At a load of approximately 5335 lb, the beam failed by crushing of the compression face of the beam. Figure 8.37 showed this failure with spalling of the concrete. Figure 8.38 showed this failure along with the final cracking pattern of beam P-1. The cracks were very closely spaced, similar to steel longitudinal reinforcement, indicating good bond behavior. Also, there were no diagonal shear cracks. Therefore, beam P-1 failed in flexure, a favorable mode for ductile behavior.

The load-deflection behavior and moment-curvature behavior was shown in Figures 8.39 through 8.41. Figure 8.39 showed the load-deflection behavior around cracking. This was plotted to show the sudden change in stiffness when the concrete cracked in tension. The cracking load for beam P-1 was 1135.1 lb. Figure 8.40 showed the entire load deflection behavior for beam P-1. This curve shows a well-defined tri-linear load deflection behavior for a DHFRP R/C beam, as predicted by the theoretical models. This behavior is very similar to steel and not typical for an FRP-reinforced beam. The change in stiffness is defined at the cracking load, the load at first yield, and the ultimate load. The behavior after yield was similar to the uniaxial tensile behavior of DHFRP with load drops and increases until either bar rupture or concrete compression failure (Chapter 6). This series of load drops was very symmetric and controlled, similar

to the tensile test behavior. After the test was completed, the cracked R/C beam was jack hammered to remove the DHFRP bars. One of the four DHFRP bars was ruptured. However, the load capacity of the remaining three bars was still large enough for the beam to fail by concrete crushing before complete bar rupture. Figure 8.41 showed moment-curvature behavior of beam P-1. This was obtained by using finite difference of displacements (Eqn. 8-28). The moment curvature is again tri-linear and defined at cracking, first yield, and beam failure.

Figure 8.43 showed the cracking of beam P-2 at 3000 lb. This again occurred over the right support, similar to beam P-1. This might indicate unsymmetrical loading of the beam, but the cracking occurred at the edge of the region of constant maximum moment. As the load was increased to 4000 lb and 5700 lb (Fig. 8.44), more closely spaced vertical flexural cracks were observed. At 5700 lb (Fig. 8.45), the cracking over the right support (i.e., the location of crack initiation) was more significant with larger crack width opening. There was no sign of diagonal cracking at this load level.

The center span cracking was observed to verify the symmetry of the applied load. Figure 8.46 showed the center span cracking at 2000 lb and 3000 lb and Figure 8.47 showed the cracking at levels up to 5200 lb. When looking at the complete center span (region of constant maximum moment), the cracking pattern was very symmetric about the centerline of the beam. Therefore, the effect of more cracking over the right loading point was not as significant when looking at the entire center span. Figure 8.48 showed the cracking at center span near beam failure. Many secondary cracks were observed connecting the larger flexural cracks. This figure also showed the beginning of concrete crushing failure on the compression face of the beam. This compression failure

occurred at a load of 6849 lb. The crushing failure was viewed from the side in Figures 8.49 and 8.50. Figure 8.51 showed the length of concrete spalling on the compression face. The length of the compression zone failure was approximately 7 in. The top view of the compression failure was shown in Figure 8.52. The top steel wire used to hold the cage together buckled at failure (left side of beam). This occurred at the location of concrete spalling which was the location of highest compressive stresses.

The final cracking pattern was shown in Figure 8.53 while the load was held at failure. The crack pattern was very closely spaced and symmetric, similar to beam P-1 and to steel R/C beams. All of the cracks were vertical flexural cracks, and no signs of diagonal shear cracks were evident. The close spacing of the cracks indicated good bond strength. The failure mode of this beam was ductile, similar to beam P-1. Figure 8.54 showed the beam when the load was released. Large inelastic deformations resulted as indicated by the deformed shape of the beam. This behavior was verified by the load-deflection and moment-curvature behaviors (Figures 8.56 and 8.57). The cracking load was 1370.5 lb (Figure 8.55) and the load at failure was 6849.5 lb. The load deflection behavior and moment-curvature behavior was tri-linear. Similar to beam P-1, the bars were extracted from beam P-2. None of the four bars ruptured along the length of the beam indicating additional residual strength remaining in the DHFRP bars.

A comparison of the results between beams P-1 and P-2 were shown in Figure 8.58 for load deflection and Figure 8.59 for moment-curvature. The behaviors were very similar, but the load and moment capacities and the total deflection and curvature were greater for beam P-2. This can be explained by comparing concrete strengths, Figures 8.60 through 8.63 and Table 8.6. The same mix design was used for both beams;

however the strength of the concrete used for beam P-2 was 44% greater in compression and almost double the tensile strength than beam P-1 (Table 8.6). Therefore, beam P-1 failed prematurely, still by concrete crushing, but at a lower load level. Therefore, the entire strength of the DHFRP bars was not utilized for beam P-1. Figure 8.64 showed the comparison between the experimental results of beam P-2 with the theoretical models for beam behavior developed in Section 8.1.1. There was very good correlation between the theoretical model developed an the experimental results.

The load-deflection and the moment-curvature results were presented in Table 8.5. The loads, deflection, moments, and curvatures were provided at cracking, first yield of the reinforcement, and failure of the beam (concrete crushing). Two definitions were used to indicate the ductility of a R/C concrete member. These are based on definitions of displacement and curvature. Additionally, ductility can be based on rotation. The displacement ductility ratio of the beams is defined as

$$\mu_{\Delta} = \frac{\Delta_u}{\Delta_y} \qquad 8\text{-}29$$

where Δ_u is the ultimate deflection and Δ_y is the deflection at yield. The curvature ductility ratio is defined as

$$\mu_{\phi} = \frac{\phi_u}{\phi_y} \qquad 8\text{-}30$$

where ϕ_u is the ultimate curvature and ϕ_y is the curvature at yield.

The ductility ratio is a measure of the beam's capacity to develop ductility. Table 8.5 gave both displacement and curvature ductility factors. The results from beam P-2 were used since beam P-1 failed prematurely. The displacement ductility factor was 3.61 and the curvature ductility factor was 3.94. This is very promising since most current

FRPs have ratios closer to 2-3, whereas the DHFRP factors are closer to 4. This indicates significant ductility capacity which is essential to obtain the full plastic strength of the section (Paulay and Priestley, 1992). Also, since the bars did not rupture at failure, there was still residual strength in the DHFRP bars. If higher strength concrete was used, the full strength and ductility of the DHFRP could be realized, and therefore, the ductility factors would higher, indicating higher ductility capacity of DHFRP R/C beams.

Slab sections reinforced with 10-mm DHFRP bars made prior to dieless braidtrusion were tested. These slab sections failed by bar rupture, a brittle failure mode, but ductility indices on the order of 4-5 were achieved before bar rupture. Details of the test and results are given in Appendix D.

CHAPTER 9. REVERSE CYCLIC TESTING OF REINFORCED CONCRETE BEAM-COLUMNS

The flexural strength of DHFRP R/C beams was investigated for beams subjected to monotonic loading (Chapter 8). These tests demonstrated the ductility capacity of DHFRP and illustrated that an FRP system that possesses ductility could be designed using the same design philosophy of steel R/C members.

Another measure of the ductility and energy absorption capability of DHFRP is to subject columns reinforced with longitudinal DHFRP bars to fully-reversed cyclic loading. Again, since the behavior of DHFRP is similar to steel reinforcement, the load-deformation response of the columns under cyclic loading should exhibit a stable hysteretic behavior similar to steel with significant energy absorption capacity.

9.1 Background

Post-elastic behavior of reinforced concrete members is critical in the proper design for seismic response of R/C structures (Paulay and Priestley, 1992). Reverse cyclic loading (i.e., reversed cycles of tension and compression) is a method to simulate the loading due to earthquakes.

Early theoretical work on cyclic loading of R/C members was conducted by Agrawal, Tulin, and Gerstle (1965), Park, Kent, and Sampson (1972), and Bertero and Bresler (1969). Most of these theories are based on an assumed linear strain profile down the depth of the section and idealized stress-strain curves for concrete and steel. The moment-curvature loop for each cycle is obtained by calculating the moment and curvature corresponding to a range of strains in the extreme fiber of the member. First,

the neutral axis depth is determined for a given strain value in the extreme fiber. This depth value is adjusted until the stresses in the concrete and steel result in internal forces that balance the external forces acting on the section. For this, the strain profile from the section and the stress-strain curves for the materials (concrete and steel) are utilized, considering the previous strain history. The method used by Park, Kent, and Sampson (1972) is described.

9.1.1 Repeated and Reversed Stress Behavior

The stress behavior studied thus far was monotonic loading in axial tension or compression. For steel, if the load is released before failure, the specimen recovers along a path parallel to the initial slope of the stress-strain curve. When reloaded, the specimen follows the same path and returns to the original monotonic stress-strain curve. The original curve is then closely followed. This indicates that the monotonic stress-strain curve is an envelope curve for repeated loading of the same sign (tension or compression).

If axial loading is reversed (cycles of tension and compression), the stress-strain behavior for steel is given in Figure 9.1. This figure shows the Bauschinger effect where the stress-strain behavior of steel under reversed loading becomes nonlinear at a stress much lower than the initial yield strength.

An idealization used by Kato et al. (1973) obtained the cyclic stress-strain curve for reversed loading from the monotonic curves for tension and compression. This method was based on experimental stress-strain data and is shown in Figure 9.2. Figure 9.2a shows the skeleton curves for monotonic tension and compression. Also shown is the repeated load stress-strain behavior. The specimen is loaded to a certain strain level,

then unloaded. The specimen is then reloaded to another strain level and unloaded. This figure shows four complete load cycles. The monotonic and repeated load curves show good agreement. These monotonic curves show the nonlinear Bauschinger effect, illustrated by the dotted lines. The reversed load diagram is divided into curves corresponding to various monotonic load cycles either in compression or tension (Fig. 9.2a). The monotonic load cycles are superimposed together to generate the reversed cyclic diagram.

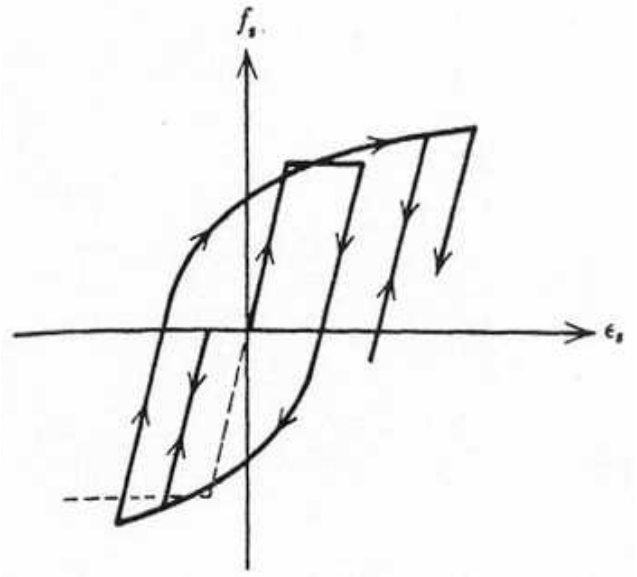

Figure 9.1: Stress-Strain Curve for Steel with Cyclic Loading Including the Bauschinger Effect (Park and Paulay, 1975).

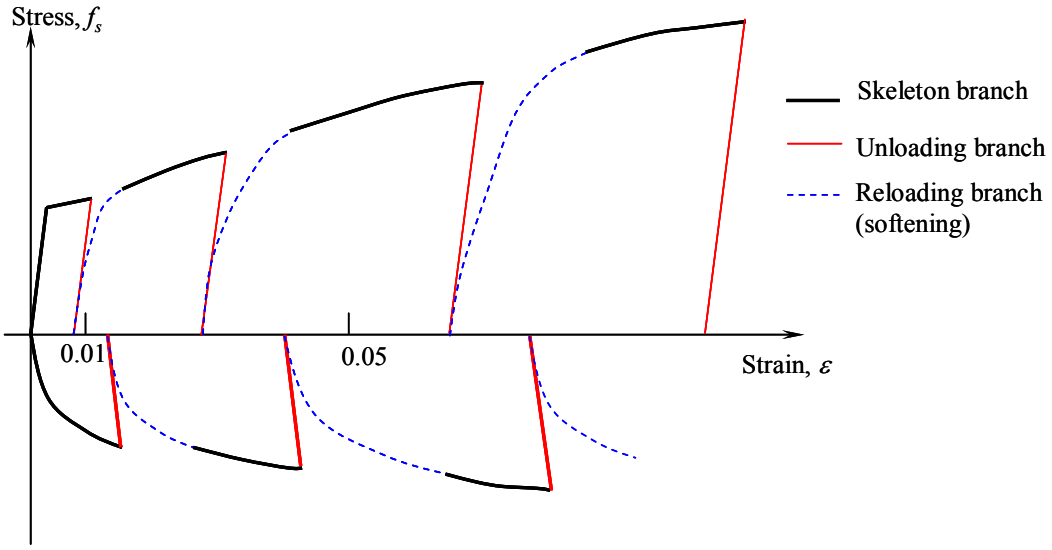

(a)

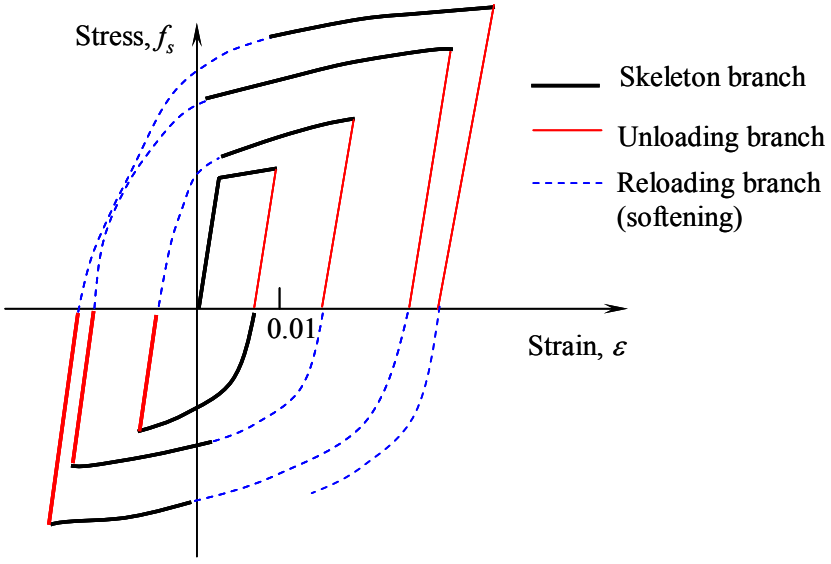

(b)

Figure 9.2: Stress-Strain Curves for Steel Under Reversed Cyclic Loading; (a) Expanded Monotonic Curves in Tension and Compression, (b) Superimposed Reversed Loading Curve.

9.1.2 Theoretical Modeling and Hysteretic Behavior

The determination of the theoretical moment-curvature relationships by the procedure developed by Park, Kent, and Sampson is described. The stress-strain curve for steel under cyclic loading was shown in Figure 9.1. The unloading path for stresses, both positive and negative, follows the initial elastic slope. After the first yield excursion, the loading parts of the stress-strain curve can be represented by the Ramberg-Osgood relationship

$$\varepsilon_s - \varepsilon_{si} = \frac{f_s}{E_s}\left(1 + \left|\frac{f_s}{f_{ch}}\right|^{r-1}\right) \qquad 9\text{-}1$$

with the following empirical values determined by Kent and Park (1973) for intermediate grade steel

$$f_{ch} = f_y\left[\frac{0.744}{\ln\left(1+1000\varepsilon_{ip}\right)} - \frac{0.071}{1-e^{1000\varepsilon_{ip}}} + 0.241\right] \qquad 9\text{-}2$$

This relationship is used to idealize the shape of the softened braches of the stress-strain curve. For odd-numbered loading cycles (n = 1, 3, 5, …)

$$r = \frac{4.49}{\ln(1+n)} - \frac{6.03}{e^n - 1} + 0.297 \qquad 9\text{-}3$$

For even-numbered loading cycles (n = 2, 4, 6,…)

$$r = \frac{2.20}{\ln(1+n)} - \frac{0.469}{e^n - 1} + 3.04 \qquad 9\text{-}4$$

where ε_s = steel strain

ε_{si} = the steel strain at the beginning of a loading run

f_s = the stress in the steel

E_s is the modulus of steel

ε_{ip} = the plastic strain in the steel produced in the previous loading run

n = the loading run number

The first yield occurs at $n = 0$, $n = 1$ is the first postyield stress reversal, $n = 2$ is the second postyield stress reversal up to failure of the specimen. The model assumes that buckling of the compression steel is prevented by closely spaced transverse steel around the longitudinal steel.

The stress-strain curve for concrete subjected to cyclic loading is shown in Figure 9.3. This figure shows the envelope curve *ABCD* for compressive stress represented by the relationships determined by Kent and Park (1971) for concrete confined by rectangular hoops under monotonic loading. The curve is defined as:

Region *AB*: $\varepsilon_c \leq 0.002$

$$f_c = f_c^{'}\left[\frac{2\varepsilon_c}{0.002} - \left(\frac{\varepsilon_c}{0.002}\right)^2\right] \qquad 9\text{-}5$$

assuming that the confining steel has no effect on the shape of this part of the curve or the strain at maximum stress. It also assumed that the maximum stress reached by the confined concrete is the cylinder strength, f'_c.

Region *BC*: $0002 \leq \varepsilon_c \leq \varepsilon_{20c}$

$$f_c = f_c^{'}\left[1 - Z\left(\varepsilon_c - 0.002\right)\right] \qquad 9\text{-}6$$

where

$$Z = \frac{0.5}{\varepsilon_{50u} + \varepsilon_{50h} - 0.002}$$

$$\varepsilon_{50u} = \frac{3 + 0.002 f_c^{'}}{f_c^{'} - 1000} \qquad \text{9-7a, b, c}$$

$$\varepsilon_{50h} = \frac{3}{4} \rho_s \sqrt{\frac{b''}{s_h}}$$

where f'_c = concrete cylinder strength in psi, ρ_s = ratio of volume of transverse reinforcement to volume of concrete core measured to outside of hoops, b'' = width of confined core measured to outside hoops, and s_h = hoop spacing. The parameter Z defines the slope of the assumed linear falling branch. The slope of the falling branch is specified by the strain when the stress has fallen to $0.5f'_c$ (Kent and Park, 1971).

Region CD: $\varepsilon_c \geq \varepsilon_{20c}$

$$f_c = 0.2 f_c^{'} \qquad \text{9-8}$$

where 9-8 takes into account the ability of the concrete to sustain some stress at very large strains. Results by Kent and Park (1971) showed that the envelope curve for unconfined concrete undergoing repeated inelastic loading is approximately identical to the monotonic curve. The same behavior is assumed for confined concrete. A linear stress-strain curve for concrete in tension is assumed, with the same slope as the curve for compression at zero stress.

Referring to Figure 9.3, on unloading from point E, it is assumed that 0.75 of the previous stress is lost without a decrease in strain, where a linear path of slope $0.25E_c$ is followed to point G. If the concrete is uncracked, it can still carry tensile stress to point K; however, if the concrete has already cracked or cracks during this stage, the tensile strains increase but no tensile stress develops. On reloading, the strain must regain the

value at *G* before compressive stress can be sustained again. If reloading commences before unloading produces zero compressive stress, reloading follows one of the paths *IJ*. The average slope of the assumed loop between *E* and *G* is parallel to the initial tangent modulus of the stress-strain curve.

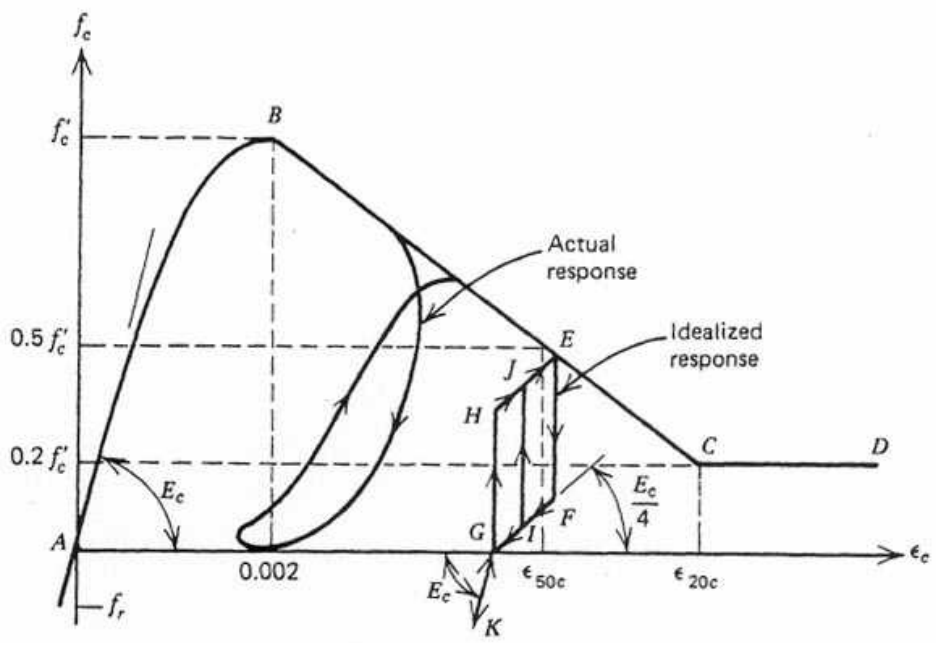

Figure 9.3: Stress-Strain Behavior of Concrete with Cyclic Loading (Park et al., 1972).

The stress-strain curve for the cover concrete outside of the hoops in compression is assumed to follow the curve for the confined core at strains less than 0.004. The cover concrete, at strains greater than 0.004, is considered to have spalled with zero strength. The cover concrete might become ineffective after several reversals of high-intensity

loading, because the transverse steel leads to a plane of weakness between the core and the cover concrete (Park and Paulay, 1975).

9.1.2.1 Method of Theoretical Moment-Curvature Analysis

The determination of the theoretical moment-curvature curves for cyclically loaded R/C sections is defined between given limits of curvature. Since the concrete compressive stress distributions are complicated during cyclic loading cycles, the stresses acting on discrete elements of the section are summed to determine the magnitude and position of the internal forces acting on the section. Shown in Figure 9.4 is the discretized cross section of a square column. The section is divided into a number of horizontal elements, each having the width of the section at that level. The section is discretized into *n* elements, numbered from the top. The depth of each is *h/n* where *h* is the depth of the section. The top reinforcement is located in element *nd'/h* and the bottom reinforcement is located in element *nd/h*. If the strain in the top element is defined as ε_{cm} and the neutral axis depth is *kd*, the average strain in element *i* (Fig. 9.4) is defined as

$$\varepsilon_i = \varepsilon_{cm} \frac{n(kd/h) - i + 0.5}{n(kd/h)} \qquad 9\text{-}9$$

Using the assumed stress-strain curves for both the concrete and reinforcement, the stress in the concrete and the reinforcement for each element is computed and is taken as the stress corresponding to the average strain in the element. From the stresses and the areas of the concrete and reinforcement in each element, the forces on the section may be determined.

To generate the moment-curvature curve, an iterative technique is utilized to calculate points on the curve. The strain ε_{cm} in the top concrete fiber is adjusted by a fixed amount. For each value of ε_{cm}, the neutral axis depth kd is estimated, and stresses in the elements are computed for this strain profile. The forces acting on the elements are then calculated, and the equilibrium of the forces is checked by using the requirement that

$$\sum C - \sum T = P \qquad 9\text{-}10$$

where C and T are the compressive and tensile forces acting on the elements, respectively, and P is the compressive load acting on the section. P is zero in the case of a beam but has a value in the case of columns. If the equilibrium of Equation 9-10 is not satisfied, the estimated neutral axis position is incorrect and must be adjusted until equilibrium of forces is achieved. Having obtained equilibrium, the bending moment M and curvature ϕ are calculated for the particular value of ε_{cm} and P.

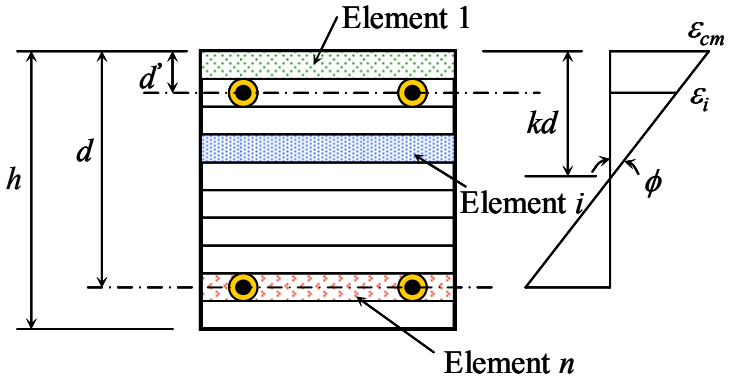

Figure 9.4: Discretized Cross Section with Elements for a Square R/C Column Section.

The load-deformation response for cyclically loaded members can be determined from the moment-curvature response using relationships between curvatures, rotations, and deflections. Since the curvature is defined as the rotation per unit length of member, the rotation between any two points A and B is defined as

$$\vartheta_{AB} = \int_{A}^{B} \phi \, dx \qquad 9\text{-}11$$

Shown in Figure 9.5 is a cantilever beam with deformation due to rotation $d\theta$ over the element of length dx only. The rotation $d\theta$ is equal to ϕdx, where ϕ is the curvature at the element dx. The vertical deflection $d\Delta$ at point A from the tangent at the fixed end B due to rotation $d\theta$ between the ends of the element is $x\ d\theta$ or $x\phi dx$. The deflection of point A from the tangent at point B due to curvature along the whole length of the member between these two points is defined as

$$\Delta_{AB} = \int_{A}^{B} x \, \phi \, dx \qquad 9\text{-}12$$

Equations 9-11 and 9-12 are valid for both elastic and plastic curvatures. If the moment-curvature relationships for a member are known, the rotations and deflections can be calculated.

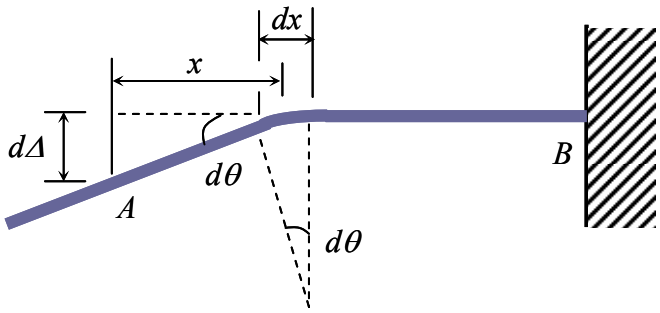

Figure 9.5: Deflection Due to Flexural Deformation of an Element.

For the cantilever beam-column, the theoretical moment-curvature curves are used to determine the theoretical maximum tip deflection, where the cyclic transverse load is applied at the end of the cantilever. The member is divided into a number of short longitudinal elements as shown in Figure 9.6, where the moment at the center of each element is assumed to be constant over the length of that element. Changes of deflection are obtained by adjusting the concrete strain ε_{cm} at the extreme fiber at the end element of the cantilever and by using the iterative technique used for the moment curvature to find the neutral axis depth, bending moment, and curvature for that value of ε_{cm} for the element. The load producing this bending moment could be established and the bending moments in the remaining elements determined. For each of the remaining elements, the value of ε_{cm} is adjusted from the previous incremental value, then the location of the neutral axis corresponding to strain compatibility and equilibrium is determined, and the value of the moment for the trail value of ε_{cm} is computed. The computed value is compared with the required value of moment, and ε_{cm} is adjusted until the computed and required values of bending moment are equal. This method computes the curvatures

corresponding to the moments for all sections, and the deflection profile is computed from the curvatures.

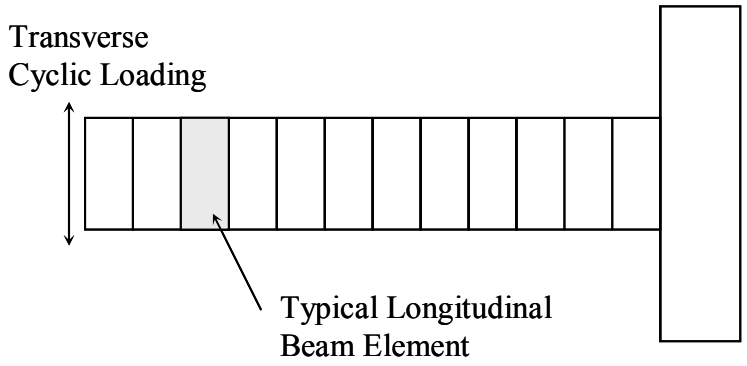

Figure 9.6: Longitudinal Discretization of Column for Theoretical Deflection Calculations.

9.1.2.2 Theory of Hysteretic Behavior

The performance of R/C columns reinforced with ductile reinforcing bars (i.e., steel or DHFRP) can be based on three criteria:

1. Column moment capacity
2. Displacement ductility
3. Overall hysteresis behavior, degradation, and energy dissipation characteristics

These criteria are obtained from the lateral load-deflection plots (applied lateral load versus tip displacement). Shown in Figure 9.7 is a typical hysteresis curve for a steel-reinforced concrete column subjected to reverse cyclic lateral load and axial load until failure (Lim, 1990).

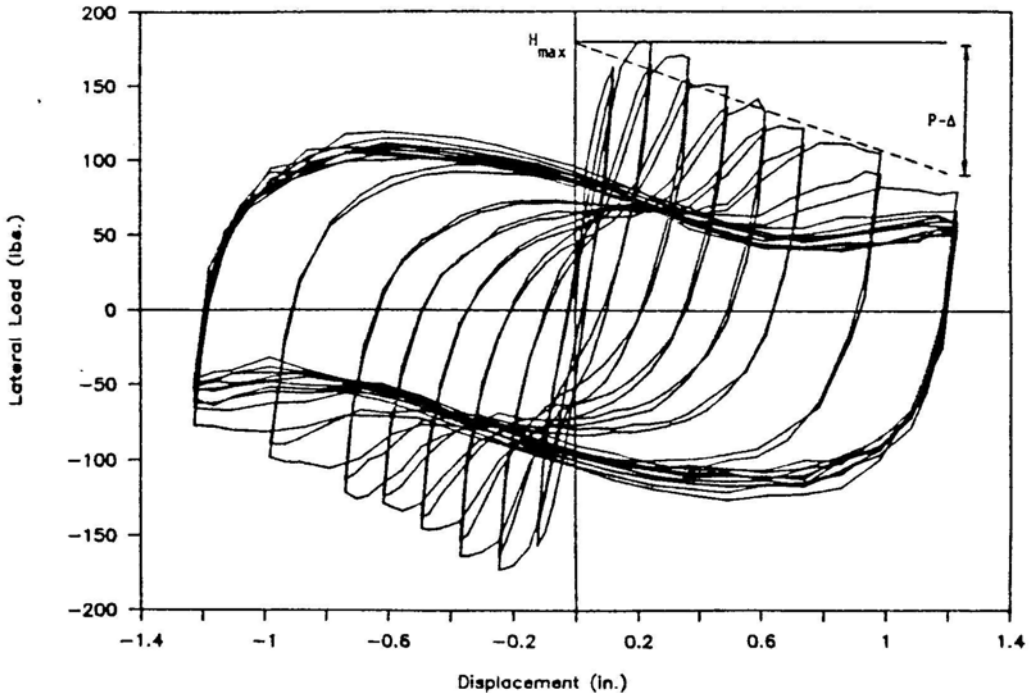

Figure 9.7: Typical Load-Displacement Hysteresis Curves for Members Subjected to Reversed Cyclic Transverse and Axial Compressive Loads (Lim, 1990).

The hysteresis curves provide several important quantifications including:

1. Stiffness (slope of the curve)
2. Peak values of lateral load and deflection
3. The shape of the hysteresis loops

The area under the hysteresis loops gives the total energy dissipated by the column under cyclic loading. This is given as

$$E_{dissipated\,/\,cycle} = \int A_{cycle} \qquad 9\text{-}13$$

And the total energy dissipated for the entire test is

$$E_{dissipated\ \text{total}} = \sum_{1}^{n} E_{dissipated\ /\ cycle} \qquad 9\text{-}14$$

where n is the total number of cycles. Much of this energy dissipation is a result of the reinforcing material to yield. Therefore, if the reinforcing material has elasto-plastic behavior, as in the case of DHFRP bars, the amount of energy dissipation in the case of severe overloading should be significant.

As seen in Figure 9.7, the lateral load capacity decreases as the inelastic displacement level is increased. This is due to changes in the geometry of the column during testing, thus producing secondary P-Δ moments. These are a result from the applied axial load. As the column experiences large inelastic deformations, the P-Δ moments become more significant. The magnitude of the P-Δ moments can be seen in the load-deflection curves (Fig. 9.7) by measuring the distance between the horizontal line drawn at the peak of the first load cycle, and the downward sloping line, drawn through the previous point and the peak of the last load cycle.

These plots can be non-dimensionalized by taking the total moment (including the P-Δ moment) and normalizing it with respect to the yield moment, M_y. Also, the measured displacement is normalized with respect to the yield moment, Δ_y. This shows the displacement ductility factor directly. The degree of strength degradation is readily seen in these relationships since this shows drops between the value of the normalized moment and the value at the previous ductility factor.

9.1.3 Shear Deterioration

To evaluate the column shear deterioration occurring during testing as the number of load cycles increase, the ratio of the applied shear, V, to the yield shear (i.e., the shear at the prescribed yield displacement), V_y, can be plotted versus the displacement ductility factor ($\mu = \Delta/\Delta_y$). The ratio V/V_y is defined as the relative shear strength index (Lim, 1990). These plots give the shear deterioration envelope curves, showing the reduction in peak shear capacity with increasing displacement ductility and increasing number of loading cycles at a given displacement level. The shear is constant and equal to the applied load at that load level for a cantilever beam loaded with a transverse tip load.

9.1.4 Energy Dissipation Characteristics

During an earthquake, without undue damage a structure must be able to temporarily store part of the input energy as strain energy, and then dissipate the energy by inelastic deformation in the members. The energy dissipated in this way is equal to the area enclosed by the hysteresis loops. Shown in Figure 9.8 is a member with perfectly elasto-plastic response. The energy dissipated during a complete displacement cycle is the shaded area of the parallelogram *BCDE*. For a particular displacement level, μ, the ideal plastic energy dissipated, E_p, is given as

$$E_P = 4(\mu - 1)V\Delta_y \qquad 9\text{-}15$$

where μ is the displacement ductility factor, V is the maximum shear force attained at that given displacement factor, and Δ_y is the prescribed yield displacement. In this equation, V is used instead of V_y for each value of μ in order to eliminate inconsistency of values of

Δ_y and variations in the steel and concrete strengths (Lim, 1990). The actual dissipated plastic energy is less than that given in equation 9-15

$$E_{P\,\text{actual}} < E_P \qquad 9\text{-}16$$

To evaluate the energy dissipation effectiveness, the energy ratio is defined

$$\frac{E}{E_P} \qquad 9\text{-}17$$

which is the relative energy dissipation index at each ductility factor. This ratio is an indication of the energy dissipation effectiveness of the column and is also a measure of the pinching effect present in the hysteresis curves. The energy dissipation index can be plotted against the displacement ductility factor to obtain a direct relationship of the dissipation capacity of a member at various ductility levels.

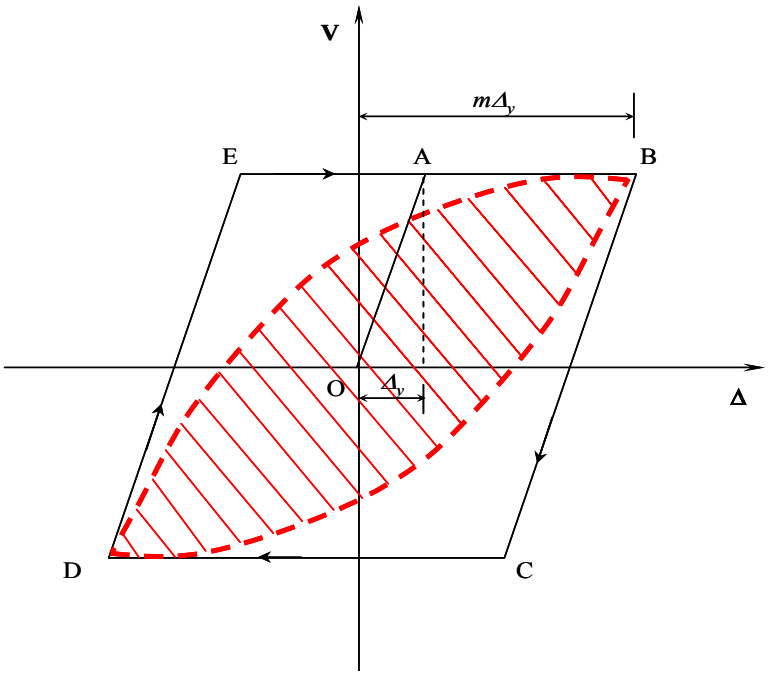

Figure 9.8: Theoretical Hysteretic Energy Dissipation Model (Lim, 1990).

A decrease in the energy dissipation index signifies pinching in the hysteresis behavior. Pinching is defined as the tendency of the stiffness to decrease appreciably when the member is unloaded (Lim, 1990). The loss of stiffness, near the zero lateral load position, results in low energy dissipation. The causes of pinching include bond deterioration along the longitudinal bars, sliding shear, and flexural cracks. The flexural cracks are formed by tension steel yielding which do not close until the compression steel yields when the load is reversed. Until the cracks close to permit the concrete to act in compression, only the tension and compression steel act to resist the applied moment. The stiffness of the steel couple is much less than that provided by the combined concrete and steel couple. This results in pinching and lower energy dissipation.

One means of measuring the ability of a structure to withstand an earthquake is to calculate the structure's energy dissipation capacity. The energy dissipated by a column during a particular load cycle is determined by integrating the area within the lateral load-deflection curve (Equation 9-13). The energy absorbed per cycle can be presented as shown in Figure 9.8.

Test results from Lim (1990) showed that in all tests, the energy dissipated during any second cycle of loading at a given displacement ductility level decreased by some amount with respect to that dissipated during the first cycle. This was due to the concrete deterioration and loss of bond between the concrete and reinforcement.

The study of low-cycle fatigue characteristics was investigated. The stability of the hysteretic behavior when specimens were loaded under many cycles of repeated loadings was studied. The repeated cycles of inelastic loading produced concrete deterioration and modified steel properties. This caused changes in the cyclic energy

absorption and the load-deflection characteristics. At high displacement levels, deterioration was more rapid than for specimens at lower displacement levels. Therefore, test specimens at a large number of loading cycles at a high ductility demand were tested, say at $\mu = 10$. The specimens were first cycled up to $\mu = 10$, then cycled 10 times at this level. At this high level, the loops either will remain relatively stable or show significant degradation by decreased energy capacity. This same procedure will be used to study the effects of reinforcing columns with DHFRP longitudinal bars instead of conventional steel bars.

9.1.5 Aspects of Ductile Response, Energy Dissipation, and Design Limit States for R/C Bridge Columns

Ductility is an essential property of a structure during inelastic response during severe seismic events. The ductile behavior of a typical R/C bridge column or pier is explained. Shown in Figure 9.9 is a concrete bridge column subjected to transverse loading. Satisfactory response of the bridge in Figure 9.9a relies on the capacity of the bridge pier to undergo several cycles of inelastic displacement without significant degradation of strength or stiffness. This response is defined as ductility. Without ductility, significant strength or stiffness degradation would occur, and the response displacements would increase significantly beyond those corresponding to elastic response, the load capacity of the structure decreases, and the structure may therefore collapse. Mathematically, ductility is defined as the ratio of deformation at a given response level to the deformation at yield, as shown in Figure 9.10. The ductility ratios can also be defined in terms of strain, rotation, and curvature and are given in Section 9.3.2.

If the level of inelastic deformation is low, inelastic strains induced in critical parts of the structures form plastic hinges (at the base of the columns), thereby limiting the damage to specific areas of the structure. The response of the structure depends on the severity of the seismic event. For moderate serviceability-level earthquakes, the structural response may be similar to an equivalent elastic response. After the earthquake, only hairline cracks would be evident. This is because the peak compression strains in the plastic hinge region at the base of the column are smaller than the crushing strain (Priestley et al., 1996). The elastic response to the excitation would require a base shear strength of V_{me}, and the actual response would correspond to ductile response with base shear force V_{md} and a peak displacement Δ_M, Fig. 9.9b. Therefore, it is possible to design for a base shear strength that is less than 50% of the true linear elastic response level (Priestley et al., 1996).

For more intense ground excitations, concrete strains in the plastic hinge region exceed the crushing strain, resulting in spalling of the concrete cover. The reinforcement strains are large and flexural cracks remain open after the excitation. If the hinge reinforcement is designed properly, the core concrete remains relatively intact, and post-earthquake repair is possible by epoxy injecting the flexural cracks and replacing the spalled cover concrete. For this level of inelastic loading, the base shear strength required is V_{de} (Fig. 9.9b), and the reduction in the design level of base shear force given by the ratio V_{de} / V_{md} may be as large as five. The penalty in not designing the bridge column to behave elastically during a severe earthquake is that the possibility of minor, repairable damage must be accepted during the design life of the bridge. However, the initial cost is greatly reduced since extra strength is not provided.

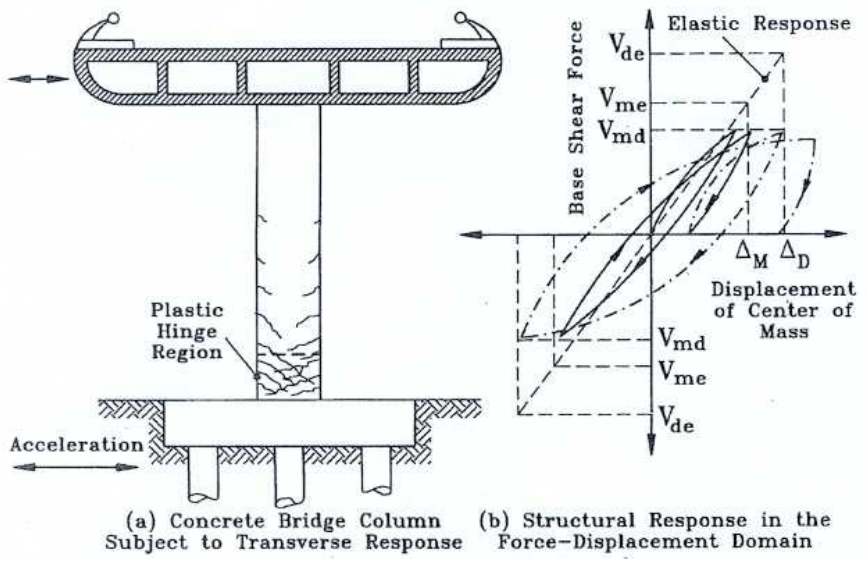

Figure 9.9: Ductile Response of a R/C Bridge (Priestley et al., 1996).

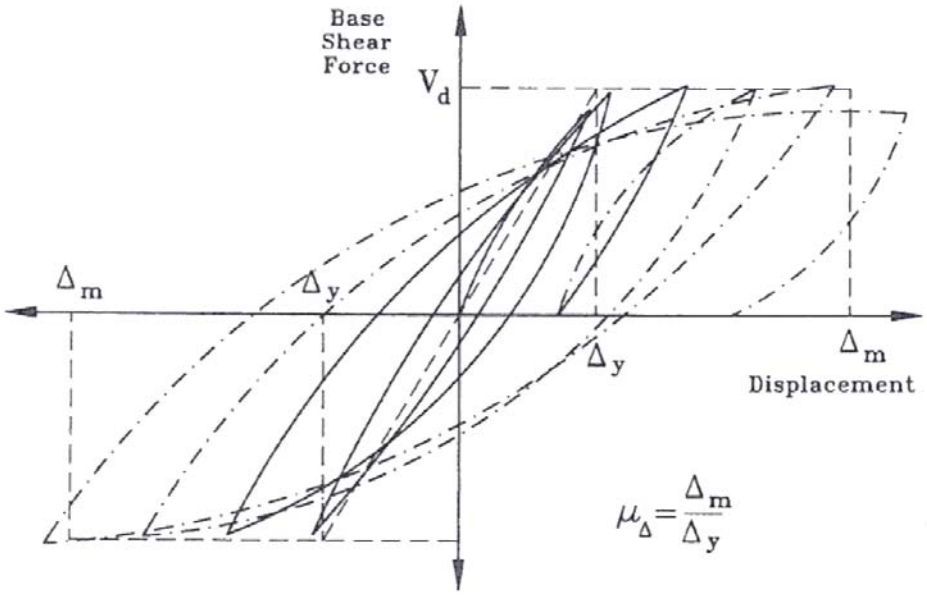

Figure 9.10: Definition of Displacement Ductility for Reverse Cyclic Loading (Priestley et al., 1996).

The design philosophy is to define limit states of member and structural response as shown in Figure 9.11. Figure 9.11a shows member limit states and Figure 9.11b shows structure limit states. The member limit states are cracking, first-yield, spalling, and ultimate. Significant changes in stiffness occur at the cracking and yield limit states. For unconfined concrete, the spalling limit state may be significant (Priestley et al., 1996).

The structure limit states are defined as the serviceability limit state, the damage-control limit state, and the survival limit states, and are based on levels of structural displacements. For the serviceability limit state, crack widths should be small so grouting is not needed, spalling should not have occurred, and the displacement ductility factor should be around $\mu_\Delta = 2$ (Priestley et al., 1996). For the damage-control state, the ductility factor is around $\mu_\Delta = 4$, with crack injection grouting and replacement of cover concrete, but the damage is repairable. The survival limit state is to ensure that reserve capacity exists above the damage control state in the case of severe ground shaking to prevent collapse of the structure.

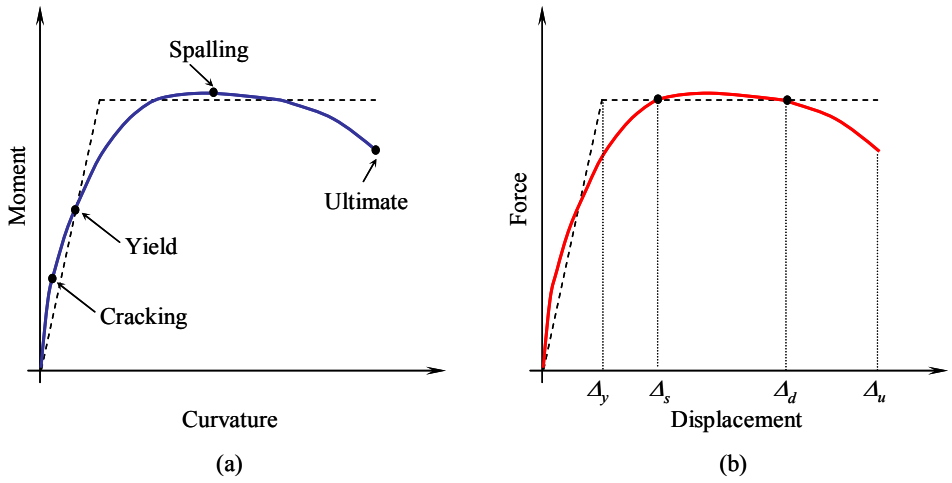

Figure 9.11: Design Limit States: (a) Member Limit State and (b) Structure Limit State.

9.2 Geometric and Material Parameters for Small and Large-Scale Model R/C Columns

Before any theoretical modeling can commence, the geometric and material properties for both the small and large-scale columns must be defined. These include the dimensions of the column and footing, the number of longitudinal bars, the bar spacing and arrangement, the hoop size and spacing, and material properties including the concrete and reinforcement properties. Two size columns were constructed and tested. The column dimensions were partially influenced by the currently available DHFRP bars, either 5-mm or 10-mm diameters. Testing was conducted on small-scale model columns and large-scale model columns. Model sizes were also chosen since the fabrication and testing was easier than for prototype size specimens. The results obtained in the model tests will be scaled up using the theory presented in Chapter 3 for prototype-size bridge columns.

9.2.1 Small-Scale Model Columns

Small-scale model columns were constructed to study the reverse cyclic loading capacity of R/C columns reinforced with DHFRP. These columns were reinforced with 5-mm DHFRP bars manufactured by Somboonsong (1997). The scale used was sufficient using 5-mm longitudinal reinforcing bars to replicate a prototype column with a scaled moment and shear capacity. Also, since there was a limited amount of 5-mm DHFRP bar remaining, the smaller scale could utilize the remaining material most efficiently.

9.2.1.1 Column Design

Small-scale rectangular columns were constructed. The model dimensions are given in Figure 9.12. The columns were reinforced with four 5-mm diameter DHFRP longitudinal bars. These bars were manufactured using the original preform and manufacturing process. The column reinforcing cages were manufactured before the preform and process were modified, and therefore, were used for this testing program. Two companion columns were reinforced with deformed steel wire. The longitudinal bars extended into the 2.5 inch (63.5 mm) thick base. The thickness of the base was designed to ensure a rigid end connection and prevent pullout of the longitudinal bars. The cross section of the columns was 1.5” by 1.5” (38.1 mm by 38.1 mm). These dimensions were chosen to ensure failure of the column, not the base. The length of the columns varied from 10 to 15.5 inches (254 to 393.7 mm). This gave aspect ratios (L/d) ranging from 6.67 to 10.33.

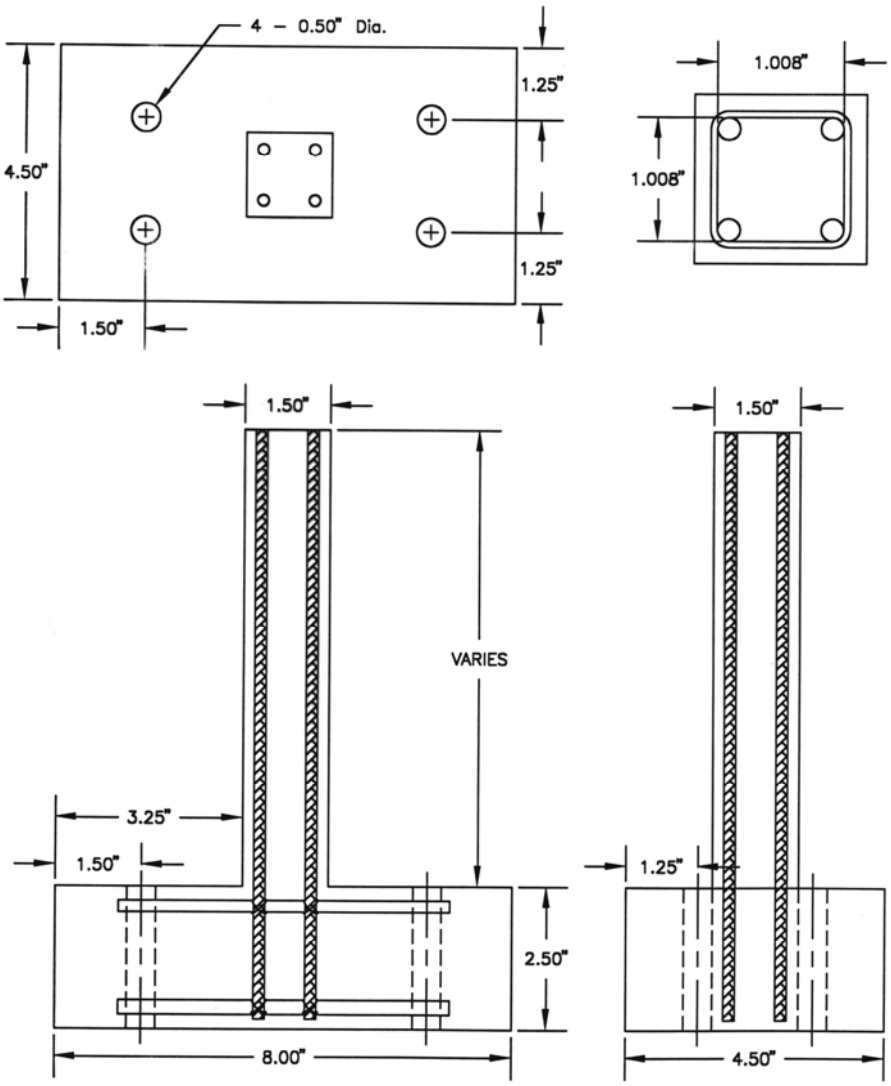

Figure 9.12: Small-Scale Model Column Dimensions.

9.2.1.2 Material Properties

The 5-mm diameter DHFRP longitudinal bars were tested in tension by Somboonsong (1997). The material stress-strain and load-strain curves for these bars were shown in Figure 7.4. For the companion steel reinforced columns, heat-treated deformed steel bars with a diameter of d_b = 0.1126 in (2.86 mm) were used. The steel

columns were designed for the same capacity as the DHFRP columns. Therefore, six steel longitudinal bars were needed for the steel reinforced section.

The transverse reinforcement was 0.045 inch (1.14 mm) deformed steel wire. Double leg ties were used to prevent shear failure. The hoop spacing varied between 0.25 and 1.0 inches (6.35 and 25.4 mm). A seismic detail in the plastic hinge region according to ACI 318-02 was not used for these columns. Steel hoops were chosen instead of FRP hoops to eliminate an additional variable. Shown in Figures 9.13 and 9.14 are the reinforcing details for a typical model DHRP reinforced column and steel reinforced column, respectively.

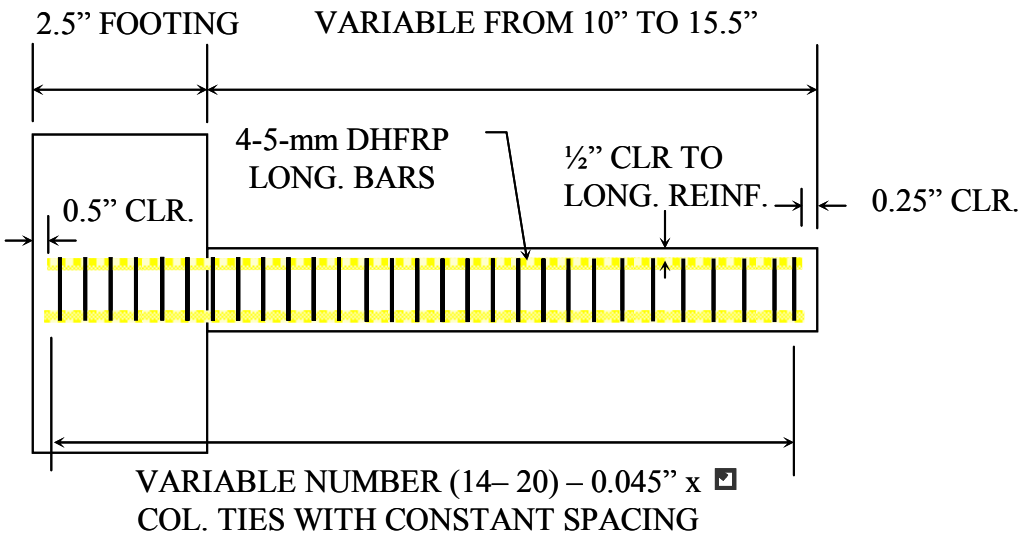

Figure 9.13: Reinforcing Details for Model DHFRP R/C Columns.

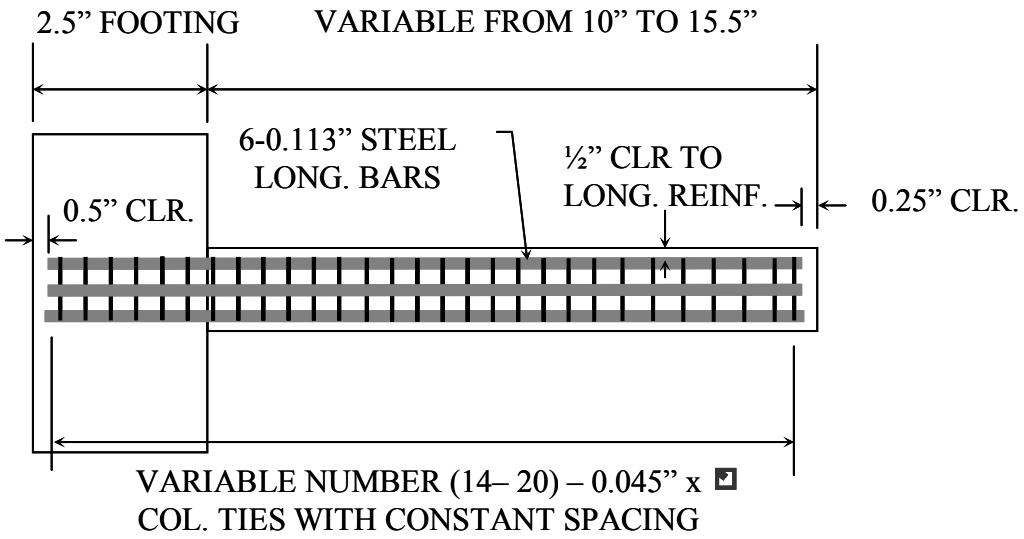

Figure 9.14: Reinforcing Details for Model Steel R/C Columns.

A mix of model concrete was used for the testing. The mix consisted of concrete sand, cement, and water. Model concrete was used following similitude relationships described in Chapter 3. Type III cement (high early) was used for the columns to enable quicker curing time. The model aggregate used consisted of sand passing a standard #4 sieve. 2”x 4” (50.8 x 101.6 mm) and 1” x 2” (25.4 x 50.8 mm) cylinders were used to get the compressive and split cylinder strength of the concrete. The mix ratios used and amounts needed per column are given in Table 9.1. The average compressive strength was 4500 psi (31.03 MPa).

Table 9.1: Type III Concrete Mix Design for Small-Scale Model R/C Columns.

Material	Ratio (pbw)	Amount needed, lb (kg)
Sand	3.0	13.85 (6.28)
Cement	1.0	4.61 (2.09)
Water	0.6	2.77 (1.26)
This is enough mix for 1 column, 8—2”x 4” and 8—1” x 2” cylinders		

9.2.2 Large-Scale Model R/C Columns with Prototype DHFRP Bars

Large-scale model columns reinforced with 10-mm DHFRP bars were constructed to study the reversed cyclic loading capacity of R/C columns reinforced with DHFRP. These columns were reinforced with 10-mm DHFRP bars with the symmetric preform and manufactured using the modified braidtrusion process. A scale factor of two was used between the model and prototype since the longitudinal DHFRP bar diameter was doubled. This scale was sufficient using 10-mm longitudinal reinforcing bars to replicate a prototype column with a scaled moment and shear capacity.

9.2.2.1 Column Design

Large-scale model rectangular columns were constructed. The column dimensions are given in Figure 9.15. The columns were reinforced with four 10-mm diameter DHFRP longitudinal bars. These bars were manufactured using the modified braidtrusion manufacturing process. The longitudinal bars extended into the 10.0 inch (254 mm) thick base. The thickness of the base was designed to ensure a rigid end connection and prevent pullout of the longitudinal bars. The cross section of the columns was 3.0” by 3.0” (76.2 mm by 76.2 mm). These dimensions were chosen to ensure

failure of the column, not the base (i.e., slender column). The length of the columns was constant at 29 inches (736.6 mm); this was governed by the length of the DHFRP available. This gave an aspect ratio (*L/d*) of 9.67.

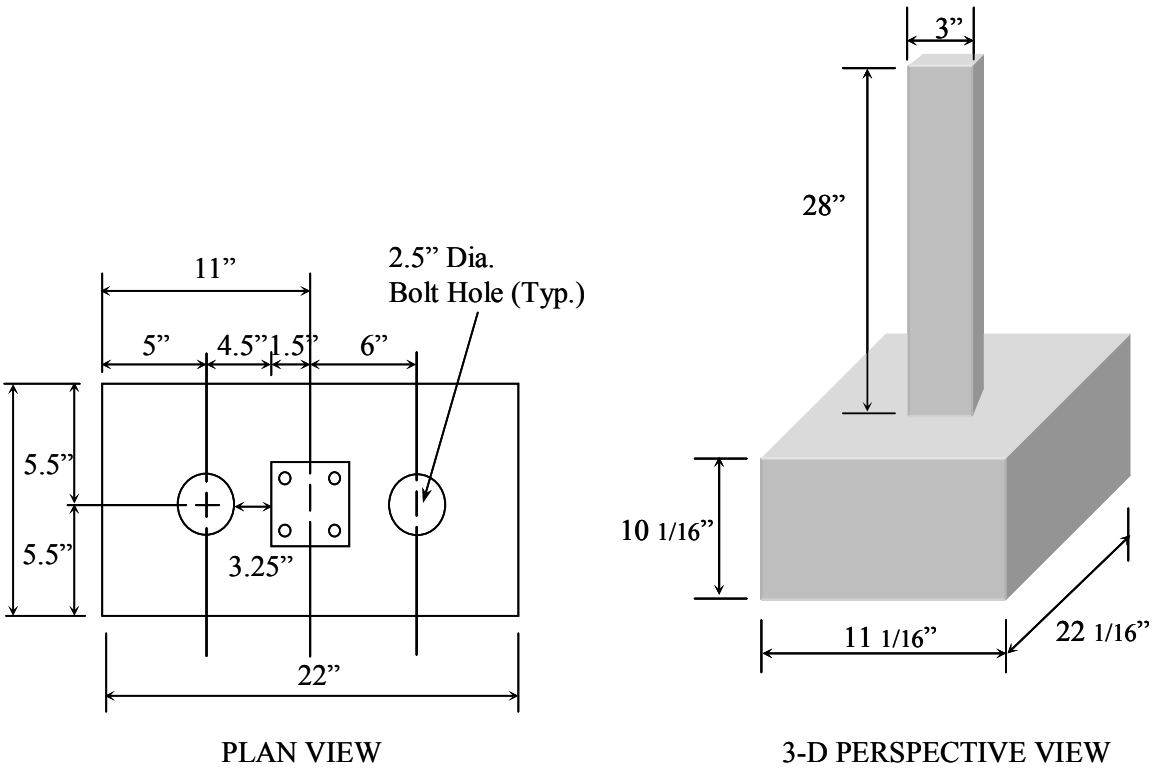

Figure 9.15: Dimensions of Large-Scale Model DHFRP R/C Columns.

9.2.2.2 Material Properties

The 10-mm diameter DHFRP longitudinal bars were tested in tension (Section 6.2.5). The material stress-strain and load-strain curves for these bars were shown in Figures 6.24 through 6.33.

The transverse reinforcement was 0.125 inch (3.175 mm) plain steel wire. Double leg ties were used to prevent shear failure. Contrary to the model columns, the hoop spacing was variable along the length of the column but was the same for all columns constructed. The hoop spacing was designed using ACI 318-02 (Sections 21.1 through 21.4) using special provisions for seismic design. The hoop spacing was smaller for the plastic hinge region of the column and was increased away from the plastic hinge region to the free-end of the column. Two spacings were used: nine hoops were spaced at 0.75" (19.05 mm) and 17 hoops were spaced at 1.125" (28.5 mm). Steel hoops were chosen instead of FRP hoops to eliminate an additional variable. Shown in Figures 9.16 are the reinforcing details for a typical large-scale model DHRP reinforced column.

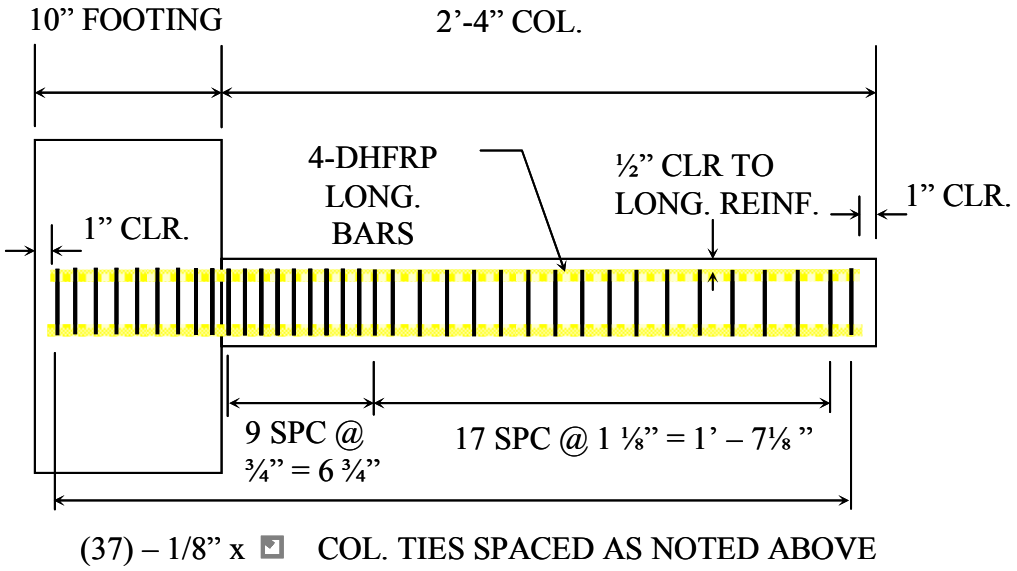

Figure 9.16: Reinforcing Details for Large-Scale Model DHFRP R/C Columns.

A mix of prototype concrete was used for the testing. The mix was comprised of 3/8" diameter stone, concrete sand, cement, and water. The mix design used for the bond and beam specimens was used again for the large-scale model columns. Type III cement (high early) was used for the columns to enable quicker curing time. 4"x 8" (101.6 x 203.2 mm) cylinders were used to get the compressive and split cylinder strength of the concrete. The mix ratios used and amounts needed per column are given in Table 9.2. The average compressive strength was 4600 psi (31.72 MPa).

Table 9.2: Concrete Mix Design for Large-Scale Model DHFRP R/C Columns.

Material	Ratio (pbw)	Amount needed, lb (kg)
3/8" Stone	3.0	144.2 (65.4)
Sand	2.0	96.1 (43.6)
Cement	1.0	48.1 (21.8)
Water	0.45	24.0 (10.9)
This is enough mix for 1 column and 8—4"x 8" cylinders		

9.3 Theoretical Moment-Curvature Analysis

The moment-curvature analysis and moment-rotation analysis for reverse cyclic loading was performed using the program SEQMC (SEQAD Moment Curvature Analysis Tools Version 1.0, SC Solutions, Inc.). This program conducted a moment curvature analysis based on Mander's confined concrete model. The program was valid for either circular or rectangular columns, fixed at the base (i.e., bridge pier) with varying levels of

axial load. The program computes three things: 1) the section analysis, 2) the moment-curvature analysis, and 3) the moment-rotation analysis and plastic hinge length.

9.3.1 Mander Confined Concrete Stress-Strain Model

A model for the stress-strain relationship for confined concrete was developed by Mander et al. (1988) and is used in seismic evaluation of structures. The model is shown in Figure 9.14 and is applicable to different section shapes and confinement levels. The equations used in the model to describe the state of stress and strain are:

$$f_c = \frac{f_{cc}^{'} xr}{r - 1 + x} \tag{9-18}$$

$$f_{cc}^{'} = f_c^{'}\left[2.254\left(1 + 7.94\frac{f_l^{'}}{f_c^{'}}\right)^{1/2} - 2\frac{f_l^{'}}{f_c^{'}} - 1.254\right] \tag{9-19}$$

$$x = \frac{\varepsilon_c}{\varepsilon_{cc}} \tag{9-20}$$

$$\varepsilon_{cc} = 0.002\left[1 + 5\left(\frac{f_{cc}^{'}}{f_c^{'}} - 1\right)\right] \tag{9-21}$$

$$r = \frac{E_c}{\left(E_c - E_{\text{sec}}\right)} \tag{9-22}$$

$$E_c = 60000\left(f_c^{'}\right)^{1/2} \tag{9-23}$$

$$E_{\text{sec}} = \frac{f_{cc}^{'}}{\varepsilon_{cc}} \tag{9-24}$$

In these equations, f'_{cc} is the maximum value of concrete stress with corresponding strain ε_{cc} and f'_l is the effective lateral confining stress. For rectangular sections the effective lateral confining stress can be estimated as

$$f'_{lx} = K_e \rho_x f_{yh} \quad 9\text{-}25$$

$$f'_{ly} = K_e \rho_y f_{yh} \quad 9\text{-}26$$

The effective lateral confining stress is dependent on the ratio of transverse reinforcement in the principal directions, ρ_x and ρ_y. In equations 9-25 and 9-26, K_e is the confinement effectiveness coefficient, which is assumed to by 0.75 for rectangular sections.

The ultimate value of compressive strain of confined concrete ε_{cu} is defined as that corresponding to fracture of confining transverse steel. By equating the strain energy capacity of the transverse steel at maximum strength (f_{yh}) to the energy absorbed by the concrete, the ultimate concrete strain can be estimated as

$$\varepsilon_{cu} = 0.004 + 1.4 \rho_s f_{yh} \frac{\varepsilon_{su}}{f'_{cc}} \quad 9\text{-}27$$

where for rectangular sections

$$\rho_s = \rho_x + \rho_y \quad 9\text{-}28$$

For a section to provide strains given by Eqn. 9-27, the transverse reinforcement should be tensioned to failure as a result of the expanding concrete core. Values of ε_{cu} can be 4 to 16 times (i.e., 0.012 to 0.05) the value of ε_{cu} = 0.003, the value for unconfined concrete (Paulay and Priestley, 1992). The value of ultimate strain given in Eqn. 9-27 is valid for confined sections subjected to direct axial compression; however, for sections subjected to compression by flexure and axial compression, the value given by 9-27 can

be up to 50% less than the actual strain value. Therefore, the ultimate curvature defined as ε_{cu}/c is also conservative.

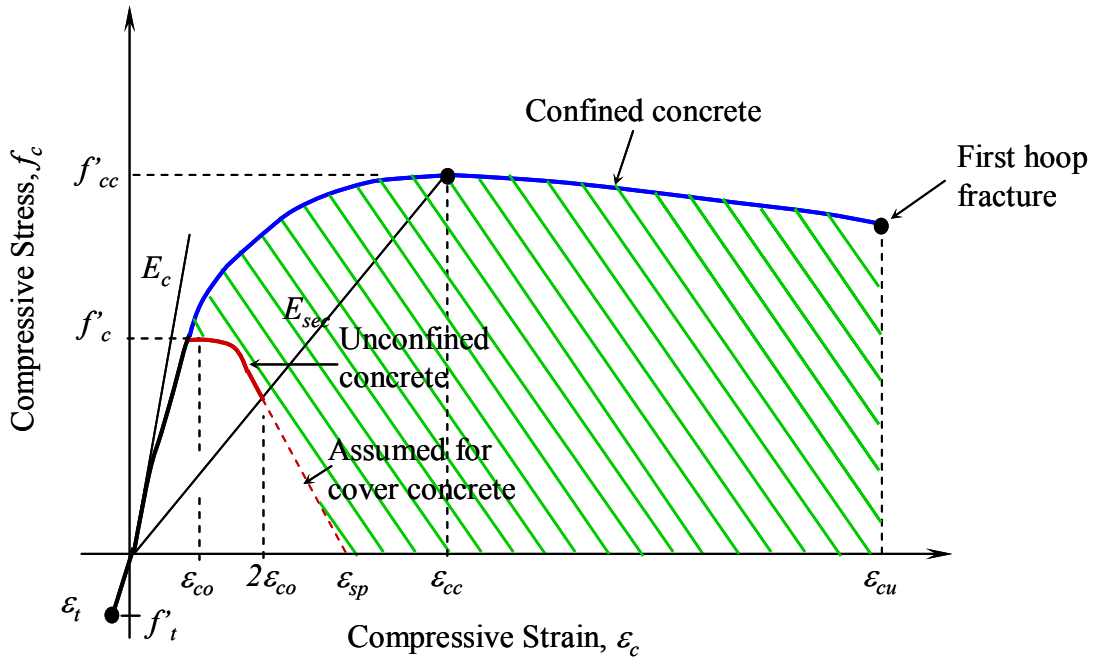

Figure 9.17: Mander Stress-Strain Model for Monotonic Loading of Confined and Unconfined Concrete in Compression (Paulay and Priestley, 1992).

9.3.2 Ductility Relationships: Curvature, Rotation, Displacement, and Plastic Hinge Length

The amount of ductility a structure possesses depends on the constituent materials of the structure (strain capability) and the overall response of the structure. The ductility factors of the structure can be quantified by strains, curvatures, rotations, and displacements. Shown in Figure 9.18 is an R/C cantilever subjected to transverse

loading. For a ductile member, the inelastic failure behavior of the column is for a plastic hinge to form at the base of the column. The available plastic rotation capacity and resulting member ductility capacity depends on the section geometry and the amount and distribution of transverse reinforcement in the plastic hinge region (Priestley et. al., 1996). Figure 9.18b shows the elastic moment diagram for the cantilever. Figure 9.18c and 9.18d show the curvatures at two levels of response, at yield of the critical section (9.18c) and at the maximum response of the column (9.18d). At the maximum response, the curvature can be divided into two portions, yield curvature and plastic curvature. Also, the extent of plasticity can be defined by the length of the plastic hinge. The curves are not smooth due to cracking along the length of the member. The deflections are shown in 9.18e and are divided into two portions, elastic deflections and plastic deflections. As seen in the figure, a significant contribution to the plastic deflections is the rotation about the base of the cantilever, the location of the plastic hinge.

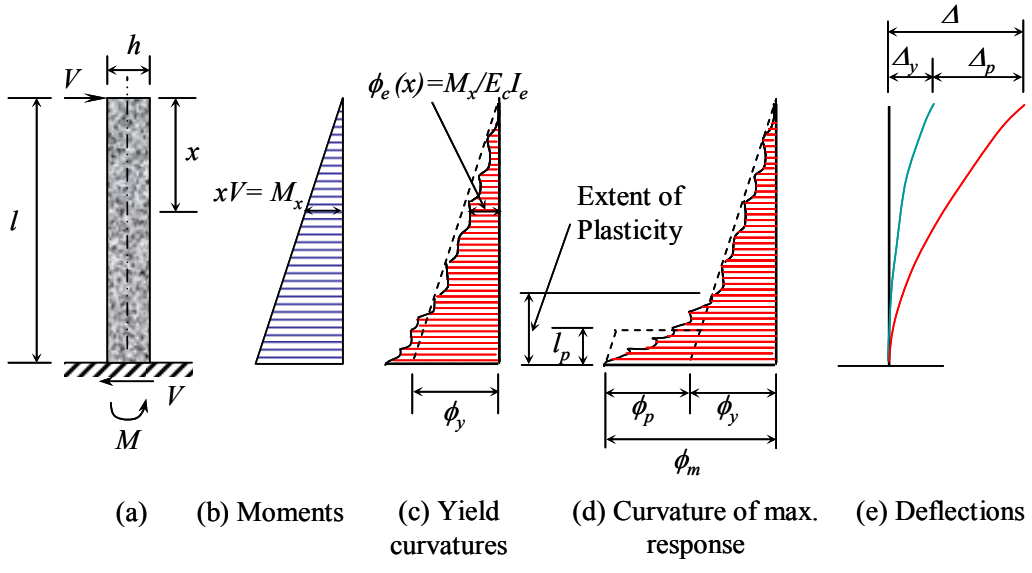

Figure 9.18: Moment, Curvature, and Deflection Relationships for a Prismatic R/C Cantilever.

For the plastic rotation capacity, a bilinear approximation of the moment-curvature relationship for the critical section is required, as shown in Figure 9.19. The equivalent yield curvature, ϕ_y, is found by taking the intersection point of the bilinear approximation, namely the first yield point (M_n, ϕ_y). The plastic curvature capacity, ϕ_p is defined as the difference between the ultimate curvature ϕ_u corresponding to the limit compression strain ε_{cu}, and the yield curvature. Therefore

$$\phi_p = \phi_u - \phi_y \tag{9-29}$$

This plastic curvature is assumed to be constant over the length of the plastic hinge, defined as l_p. The length of the plastic hinge is

$$l_p = \begin{cases} 0.08L + 0.15 f_{ye} d_{bl} \geq 0.3 f_{ye} d_{bl} & f_{ye} \text{ in ksi} \\ 0.08L + 0.022 f_{ye} d_{bl} \geq 0.044 f_{ye} d_{bl} & f_{ye} \text{ in MPa} \end{cases} \tag{9-30a, b}$$

where L is the distance from the critical section of the plastic hinge to the point of contraflexure and d_{bl} is the diameter of the longitudinal reinforcement. From the geometry, the plastic rotation is

$$\vartheta_p = l_p \phi_p = l_p \left(\phi_u - \phi_y \right) \tag{9-31}$$

The member ductility capacity is defined by the section curvature ductility capacity

$$\mu_\phi = \frac{\phi_u}{\phi_y} \tag{9-32}$$

To obtain the member displacement ductility factor, the displacement at yield is defined as

$$\Delta_y = \frac{\phi_y L^2}{3} \tag{9-33}$$

In Figure 9.18, the ultimate displacement was defined as $\Delta_y + \Delta_p$. The plastic displacement included the component due to the plastic rotation, θ_p and the additional elastic moment due to the increase in moment from M_n to M_u (Fig. 9.19). Δ_p is defined as

$$\Delta_p = \left(\frac{M_u}{M_n} - 1\right)\Delta_y + l_p\left(\phi_u - \phi_y\right)\left(L - 0.5l_p\right) \qquad 9\text{-}34$$

The member displacement ductility μ_Δ is given as

$$\mu_\Delta = \frac{\Delta_u}{\Delta_y} = 1 + \frac{\Delta_p}{\Delta_y} = \frac{M_u}{M_n} + 3\left(\mu_\phi - 1\right)\frac{l_p}{L}\left(1 - 0.5\frac{l_p}{L}\right) \qquad 9\text{-}35$$

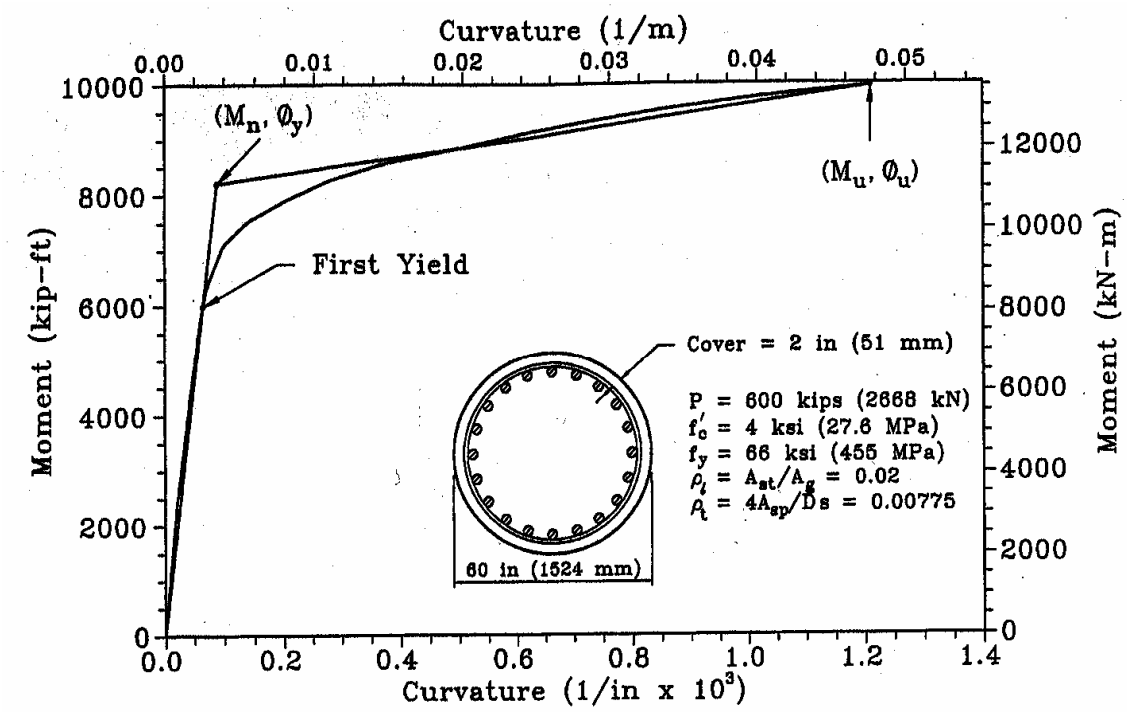

Figure 9.19: Bilinear Approximation of a Column Moment-Curvature Relationship (Priestley, et al., 1996).

9.3.3 Model Parameters

The reinforcing material and material properties must be defined for the moment-curvature analysis. In SEQMC, four possible steel models were given. These models included 1) mild steel, 2) high strength steel, 3) elasto-plastic steel (ACI model), and 4) user defined model. When one of the four models is chosen, the program generates the corresponding stress-strain curve. For DHFRP bars, the user defined model was chosen. For the user defined model, pairs of strain and stress values, one data pair per line, were read through an ASCII data file. The first data pair was the yield point and all other pairs defined the post-yield and hardening curves.

In this model, certain parameters must be defined. These parameters are shown in Figure 9.20. For the DHFRP reinforcement model, input parameters are listed in Table 9.3 for the small-scale model and in Table 9.4 for the large-scale model.

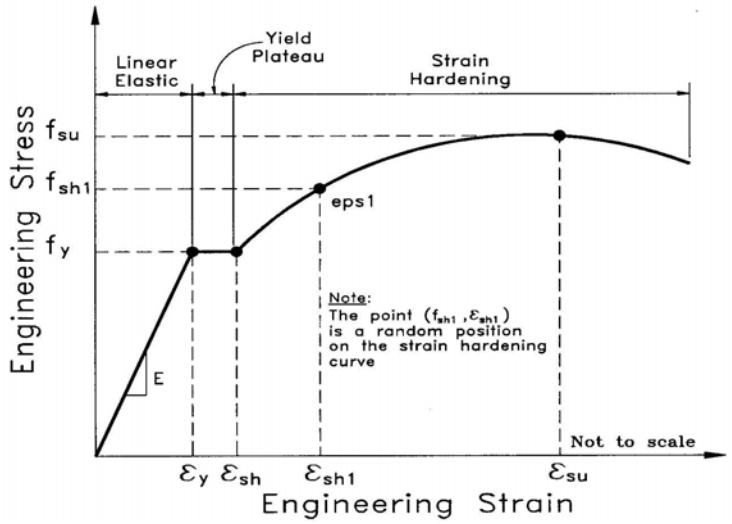

Figure 9.20: User Defined Steel Stress-Strain Curve and Definition of Characteristic Parameters (SC Solutions, 1998).

Table 9.3: Input Information for Small-Scale Columns Theoretical Moment-Curvature Calculations.

Input Information	**Concrete Materials**	**Reinforcing Materials, Steel**	**Reinforcing Materials, DHFRP**
Units = Imperial	Concrete compressive strength ≈ 4000 psi	Transverse Reinforcement	Transverse Reinf.
Column dimension: $w = d$ = 1.5" x 1.5"	Use the Mander defined model	d_t = 0.045 in	″
Column length (variable): L = 10", 12", 15.5"		*Variable spacing* s = 0.25 in, 0.5 in, 1.0 in	″
		Legs in strong direction = 2	″
		Longitudinal reinforcement:	Longitudinal Reinf.
		Use mild steel model, given in SEQMC	E = 10140.6 ksi σ_y = 40.18 ksi ε_y = 0.00453 ε_{sh} = 0.012 (not truly defined for 5-mm bars) σ_u = 58.98 ksi ε_u = 0.0227
		bar diameter d_b = 0.1126 in	bar diameter d_b = 0.197 in

Axial Load Input

Axial Load Levels	**Axial Load, lb (kN)**
0	0 (0)
$0.05\, f'_c\, A_g$	450 (2.0)
$0.1\, f'_c\, A_g$	900 (4.0)
$0.15\, f'_c\, A_g$	1350 (6.01)
$0.2\, f'_c\, A_g$	1800 (8.01)
$0.3\, f'_c\, A_g$	2700 (12.01)

Table 9.4: Input Information for Large-Scale Columns Theoretical Moment-Curvature Calculations.

Input Information	**Concrete Materials**	**Reinforcing Materials, Steel**	**Reinforcing Materials, DHFRP**
Units = Imperial	Concrete compressive strength ≈ 4000 psi	Transverse Reinforcement	Transverse Reinf.
Column dimension: $w = d$ = 3" x 3"	Use the Mander defined model	d_t = 0.125 in	″
Column length L = 29" (736.6 mm)		s = 0.75 in	″
		Legs in strong direction = 2	″
		Longitudinal reinforcement:	Longitudinal Reinf.
		Use mild steel model, given in SEQMC	E = 10140.6 ksi σ_y = 40.18 ksi ε_y = 0.00453 ε_{sh} = 0.012 σ_u = 58.98 ksi ε_u = 0.0227
		bar diameter d_b = 0.1126 in	bar diameter d_b = 0.375 in

Axial Load Input

Axial Load Levels	**Axial Load, lb (kN)**
0	0 (0)
0.05 $f'_c A_g$	1800 (8.0)
0.1 $f'_c A_g$	3600 (16.0)
0.15 $f'_c A_g$	5400 (24.0)
0.2 $f'_c A_g$	7200 (32.03)
0.3 $f'_c A_g$	10800 (48.04)

9.3.4 Results

The results of the moment-curvature analysis are presented. The program performed a section analysis, a moment-curvature analysis, a moment-rotation analysis including the plastic hinge length, and a moment-curvature analysis for various axial load levels. The parameters in Tables 9.3 and 9.4 were used. The analysis was first performed for a model column with DHFRP reinforcement with normal parameters

defined as a hoop spacing of 0.5" (12.7 mm) and a column length of L = 12" (304.8 mm). These were the most common parameters used when constructing the column specimens. The section analysis was performed, followed by a moment-curvature analysis with low axial load, $0.05 f'_c A_g$. A level of axial load was needed to run the analysis. The moment-curvature analysis generated a trace of the moment-curvature curve with a superimposed bilinear elasto-plastic approximation. This analysis assumed the formation of a plastic hinge, and the plastic curvature was assumed constant over the equivalent plastic hinge length, l_p. Figure 9.21 tabulates the section properties for this column. Figure 9.22 shows the moment-curvature relationship and Figure 9.23 gives the moment-rotation curve. The plastic hinge length was calculated as 2.3 in (58.42 mm). Figure 9.24 provides a parametric study on the effects of axial load for a given section. Five axial load levels were defined (maximum limit of the program): $0.05 f'_c A_g$, $0.1 f'_c A_g$, $0.15 f'_c A_g$, $0.2 f'_c A_g$, and $0.3 f'_c A_g$, given in Table 9.3. Shown in Figure 9.25 is the moment-curvature analysis for zero axial load and various axial load levels.

The length of the column L and the hoop spacing s were studied parametrically for the ranges used in testing. The moment-curvature and moment-rotation analyses were conducted for a column length of L = 15" (381 mm). The moment-curvature relationship is shown in Figure 9.26 and the moment-rotation relationship is given in Figure 9.27. Since there was variability in the hoop spacing in the physical specimens, upper and lower bound values of hoop spacing were used. Figures 9.28 and 9.29 show the moment curvature and moment-rotation, respectively, for a hoop spacing s = 0.25" (6.35 mm). Shown in Figures 9.30 and 9.31 are the moment curvature and moment-rotation, respectively, for a hoop spacing s = 1.0" (25.4 mm).

As a comparison, an equivalent-capacity model steel R/C column was analyzed. The section properties are shown in Figure 9.32. Six longitudinal bars were used. The resulting moment-rotation is shown in Figure 9.33 and the moment-curvature for various axial load levels (including no axial load) is shown in Figure 9.34.

The properties for the large-scale model DHFRP columns were given in Table 9.4. The analysis was first performed for a column with DHFRP reinforcement with normal parameters which included a hoop spacing of 0.75" (19.05 mm) and a column length of L = 29" (736.6 mm). This was the hoop spacing used in the plastic hinge region of the column specimens. The section analysis was performed, followed by a moment-curvature analysis with low axial load, $0.05\ f'_c\ A_g$. Figure 9.35 tabulates the section properties for this column. Figure 9.36 shows the moment-curvature relationship and Figure 9.37 gives the moment-rotation curve. The plastic hinge length was calculated as 4.5 in (114.3 mm). Figure 9.38 provides a parametric study on the effects of axial load for a given section. Five axial load levels were defined (maximum limit of the program): $0.05\ f'_c\ A_g$, $0.1\ f'_c\ A_g$, $0.15\ f'_c\ A_g$, $0.2\ f'_c\ A_g$, and $0.3\ f'_c\ A_g$, given in Table 9.4.

The hoop spacing was not uniform along the length of the column. In the plastic hinge region, the spacing was s = 0.75 in (19.05 mm), which was used in the previous analysis. Outside of the plastic hinge length, the spacing was increased to 1.125 in (28.58 mm) in accordance to ACI 318-02. Shown in Figures 9-39 and 9-40 are the moment-curvature and moment-rotation behaviors for a hoop spacing of s = 1.125 in (28.58 mm).

Finally, a companion steel R/C column was analyzed. This column was reinforced with four No. 3 longitudinal bars using the same hoop spacing. Shown in Figure 9.41 are

the section properties. Figure 9.42 shows the moment-rotation behavior and Figure 9.43 shows the moment-curvature for various axial load levels.

SECTION PROPERTIES:

Section Depth	= 1.5 in.		
Section Width	= 1.5 in.		
Cover to Main Steel	= 0.3 in.		
Concrete Model	= Mander		
Concrete Strength	= 5.00 ksi		
Steel Model	=		
Steel Strength	= 38.1 ksi		
Young's Modulus	= 11004.9 ksi		
Tension Side Reinforcement	= 2 Bars (0.197 Bars)		
Compression Side Reinforcement	= 2 Bars (0.197 Bars)		
Hoop Size	= 0.0449999 Bars	Average Number of Legs	= 2.0
Hoop Spacing	= 0.5 in.	Hoop Strength	= 40.0 ksi

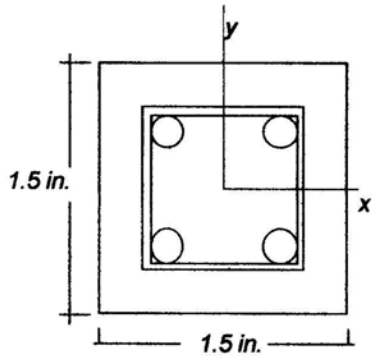

Figure 9.21: Section Properties for Model DHFRP R/C Columns.

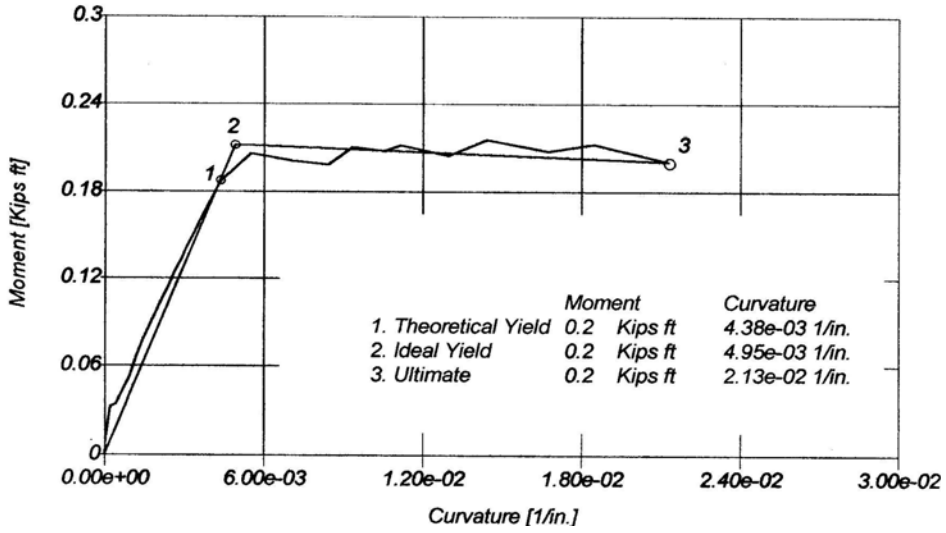

Figure 9.22: Moment-Curvature Relationship for Model DHFRP R/C Columns: Standard Parameters.

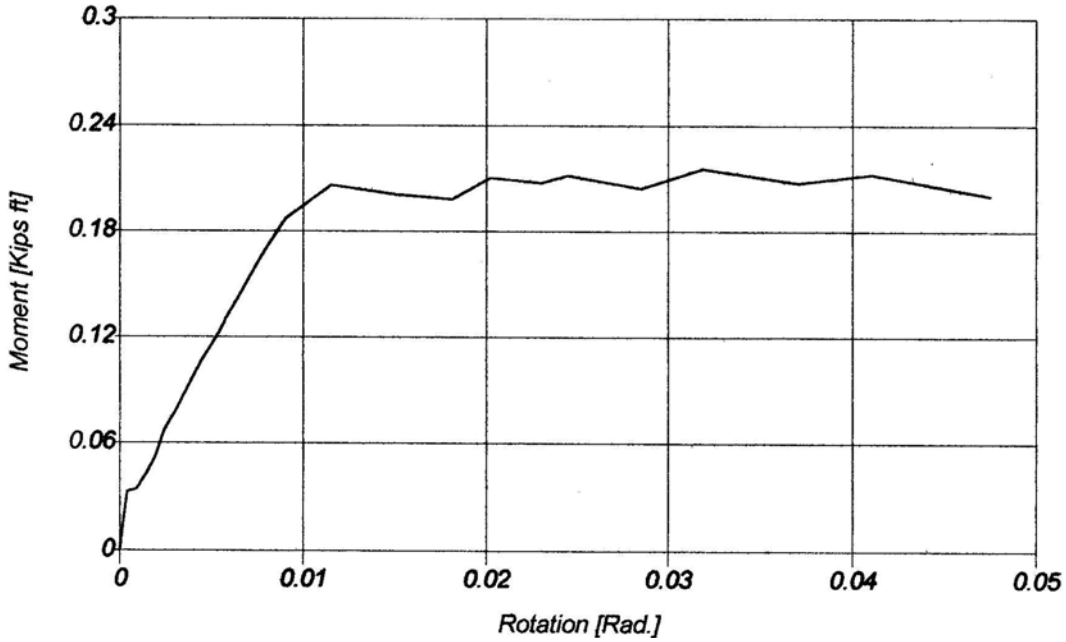

Figure 9.23: Moment-Rotation Relationship for Model DHFRP R/C Columns: Standard Parameters.

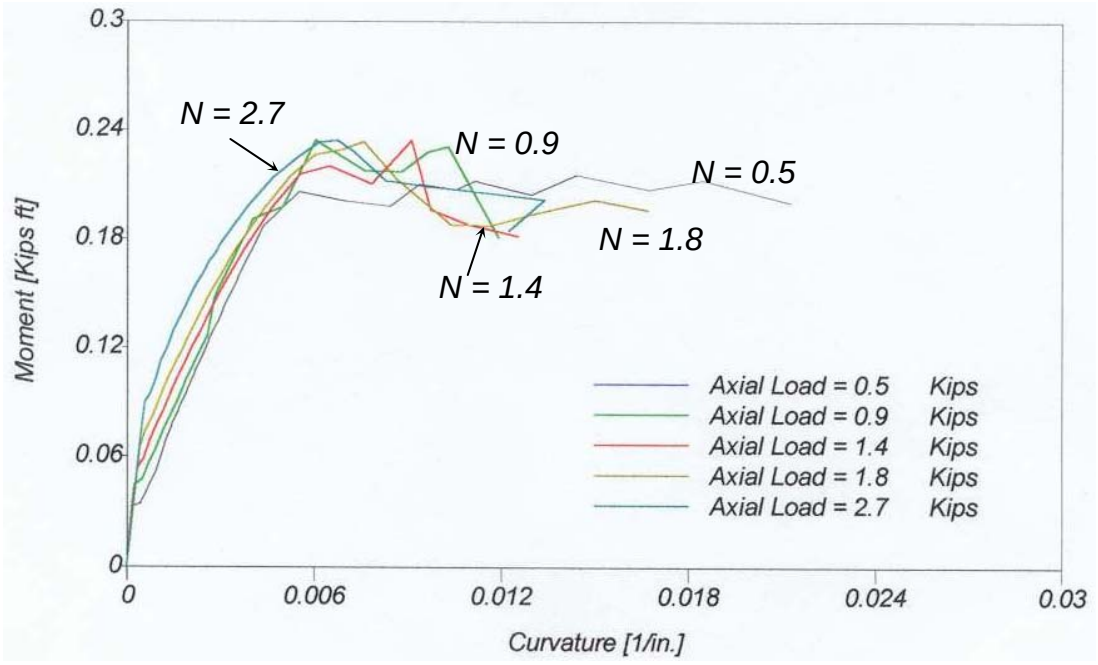

Figure 9.24: Moment-Curvature Relationships for Various Axial Load Levels for Model DHFRP R/C Columns: Standard Parameters.

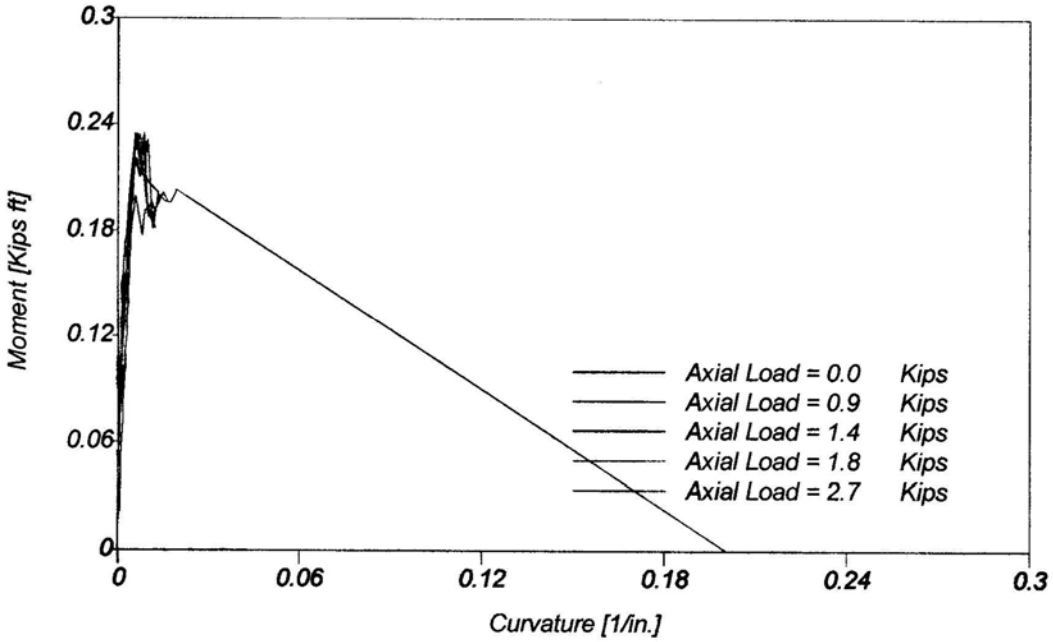

Figure 9.25: Moment-Curvature Relationships with and without Axial Load for Model DHFRP R/C Columns: Standard Parameters.

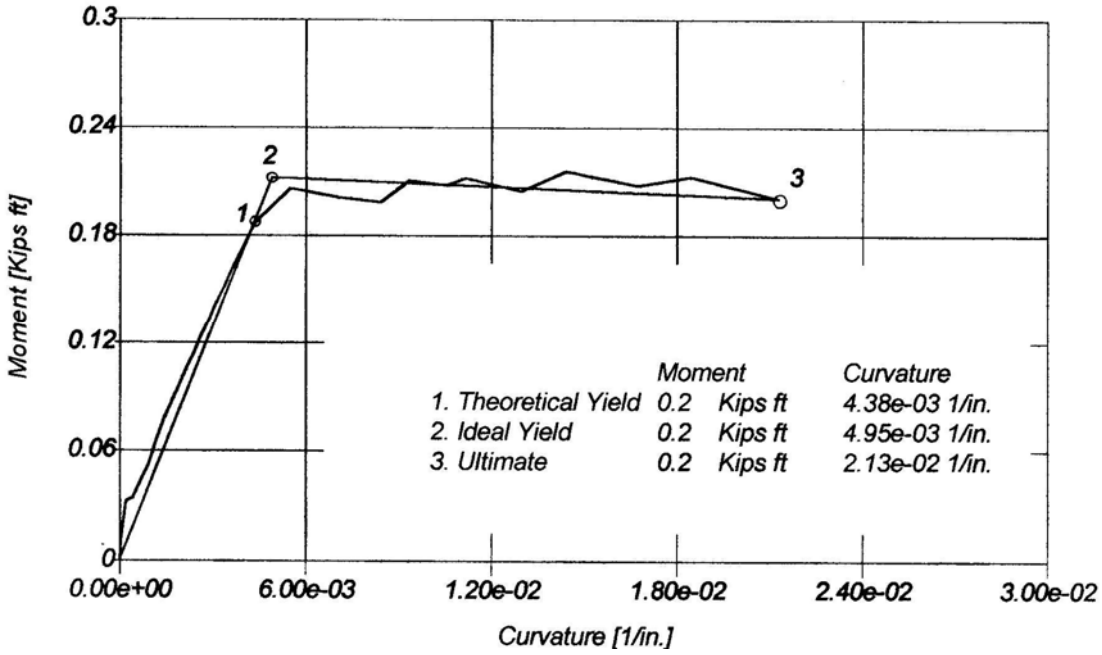

Figure 9.26: Moment-Curvature Relationship for Model DHFRP R/C Columns: L = 15".

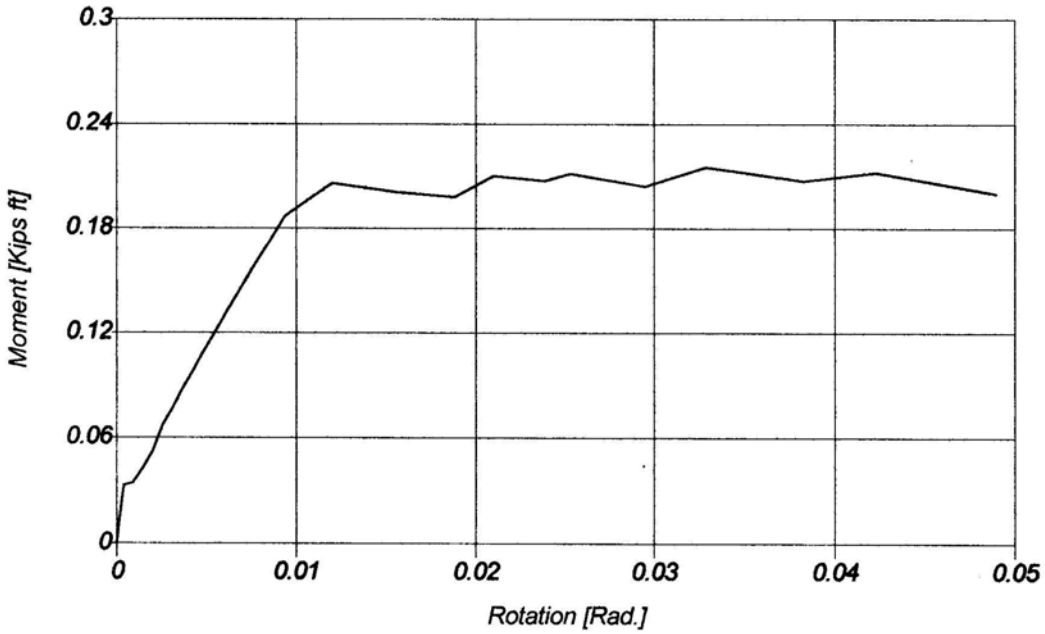

Figure 9.27: Moment-Rotation Relationship for Model DHFRP R/C Columns: L = 15".

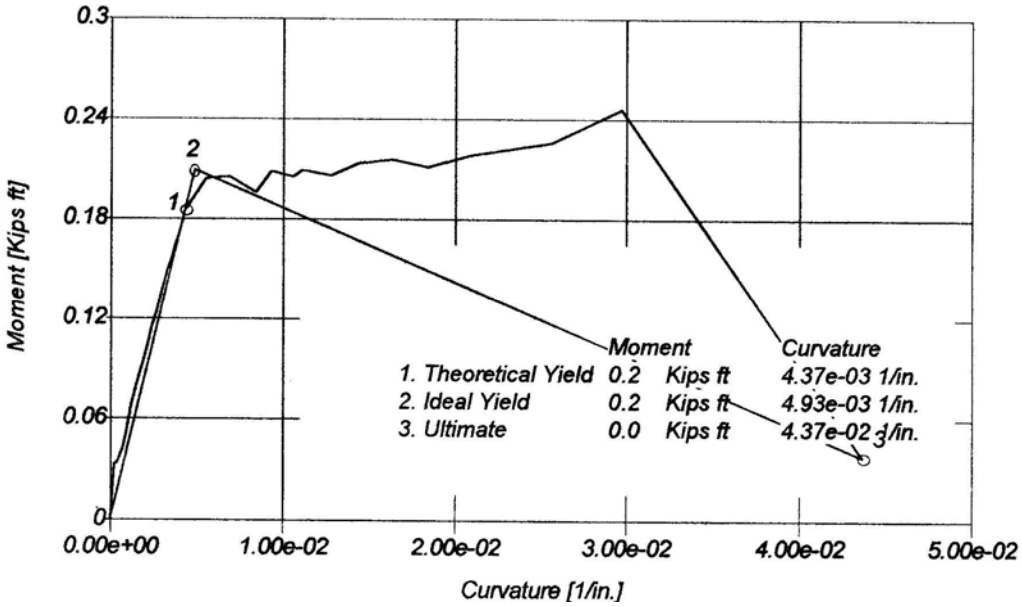

Figure 9.28: Moment-Curvature Relationship for Model DHFRP R/C Columns: s = 0.25".

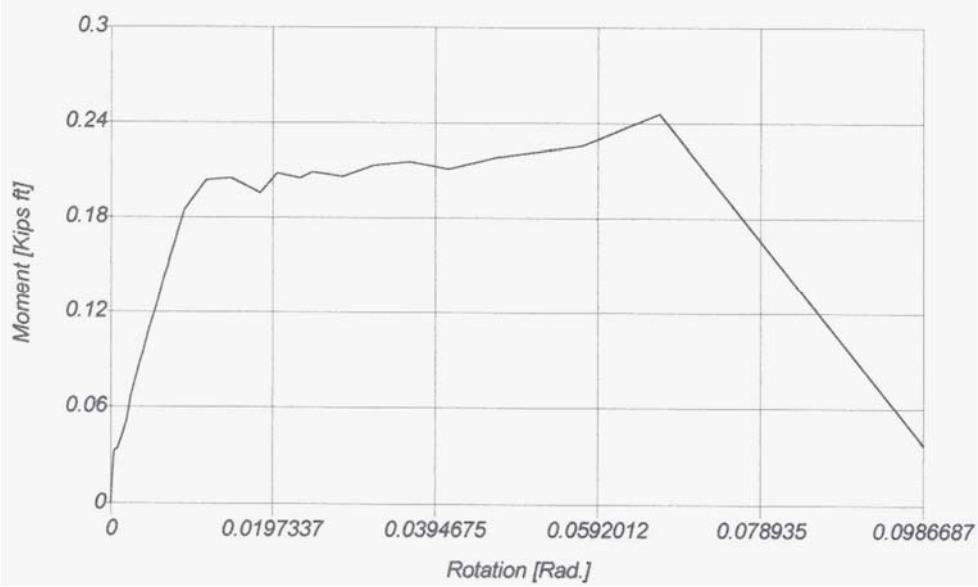

Figure 9.29: Moment-Rotation Relationship for Model DHFRP R/C Columns: s = 0.25".

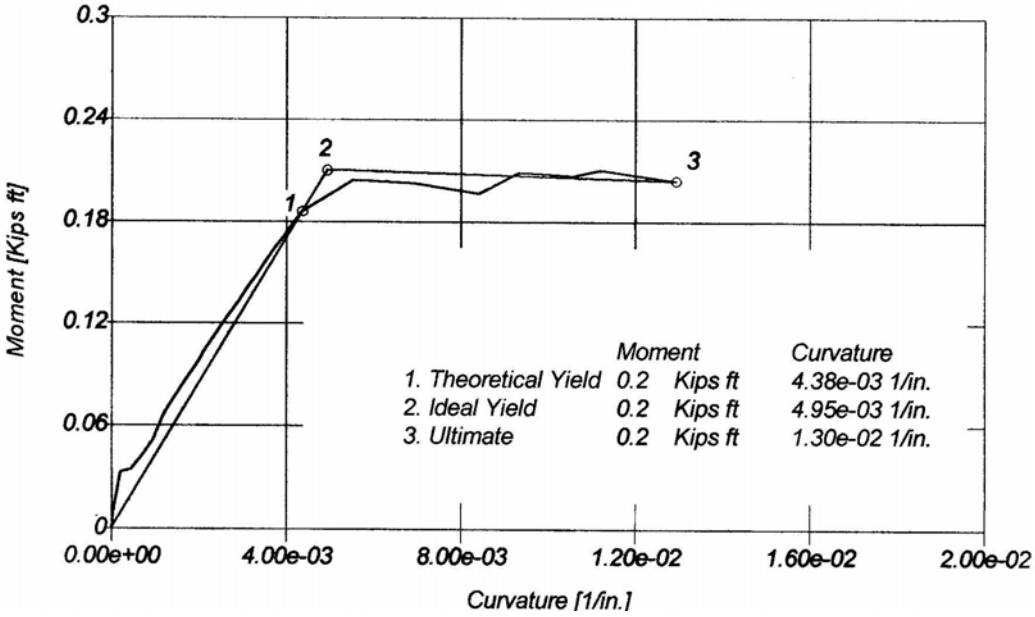

Figure 9.30: Moment-Curvature Relationship for Model DHFRP R/C Columns: s = 1.0".

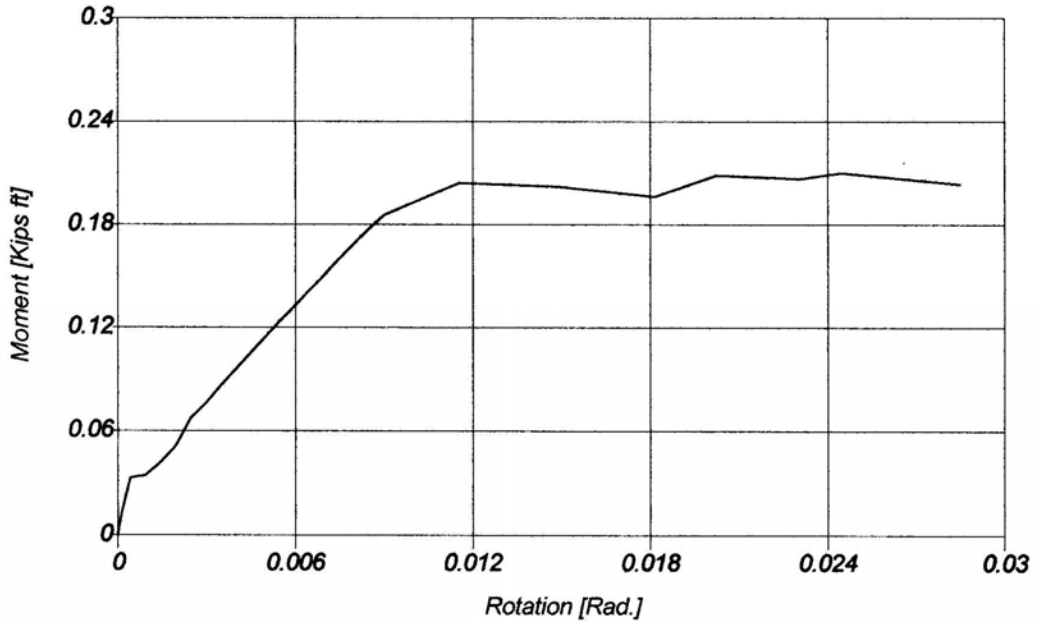

Figure 9.31: Moment-Rotation Relationship for Model DHFRP R/C Columns: s = 1.0".

SECTION PROPERTIES:

Section Depth	*= 1.5 in.*
Section Width	*= 1.5 in.*
Cover to Main Steel	*= 0.3 in.*
Concrete Model	*= Mander*
Concrete Strength	*= 5.00 ksi*
Steel Model	*= Mild Strength Steel*
Steel Strength	*= 66.0 ksi*
Young's Modulus	*= 29000.0 ksi*
Tension Side Reinforcement	*= 2 Bars (0.1126 Bars)*
Compression Side Reinforcement	*= 2 Bars (0.1126 Bars)*
Side Reinforcement	*= 1 Bars (0.1126 Bars) each side*

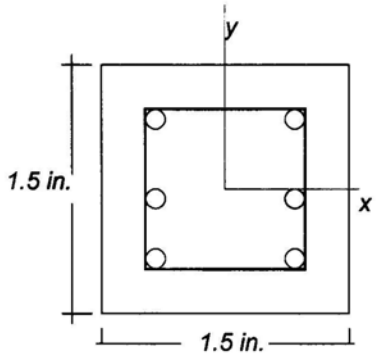

Hoop Size	*= 0.00449999 Bars*	*Average Number of Legs*	*= 2.0*
Hoop Spacing	*= 0.5 in.*	*Hoop Strength*	*= 40.0 ksi*

Figure 9.32: Section Properties for Model Steel R/C Columns.

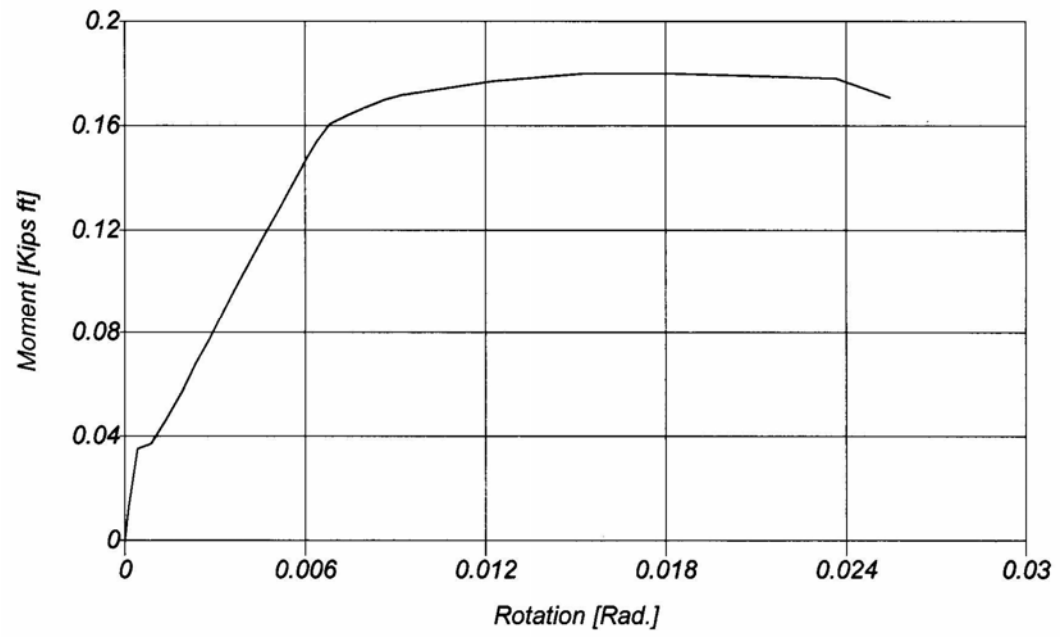

Figure 9.33: Moment-Rotation Relationship for Model Steel R/C Columns.

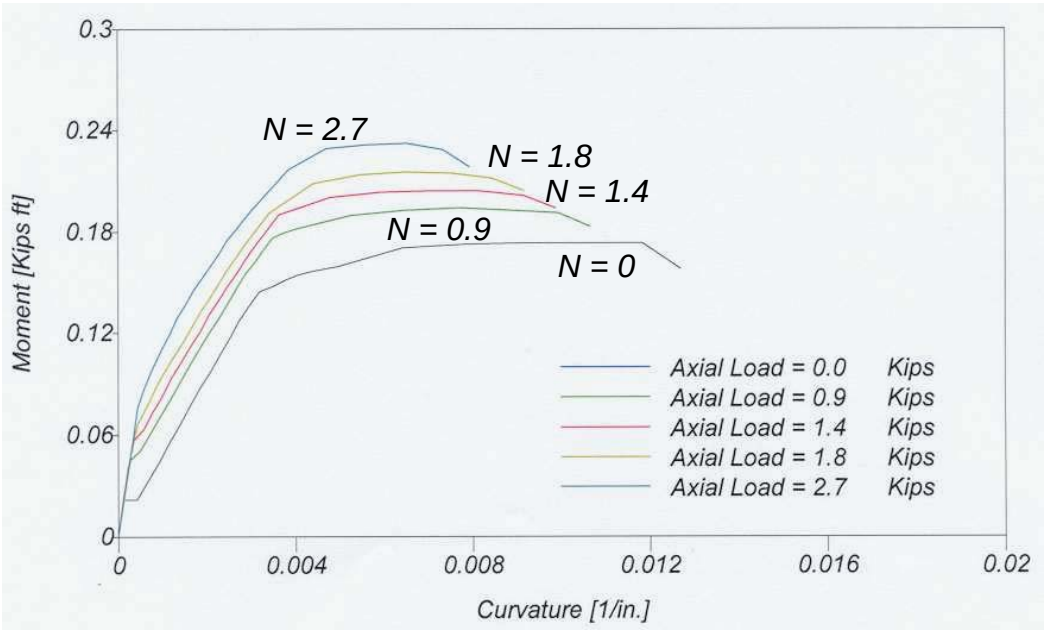

Figure 9.34: Moment-Curvature Relationships with and without Axial Load for Model Steel R/C Columns.

SECTION PROPERTIES:

Section Depth	= 3.0 in.		
Section Width	= 3.0 in.		
Cover to Main Steel	= 0.5 in.		
Concrete Model	= Mander		
Concrete Strength	= 5.00 ksi		
Steel Model	=		
Steel Strength	= 38.1 ksi		
Young's Modulus	= 11004.9 ksi		
Tension Side Reinforcement	= 2 Bars (#3 Bars)		
Compression Side Reinforcement	= 2 Bars (#3 Bars)		
Hoop Size	= 0.125 Bars	Average Number of Legs	= 2.0
Hoop Spacing	= 0.7 in.	Hoop Strength	= 41.2 ksi

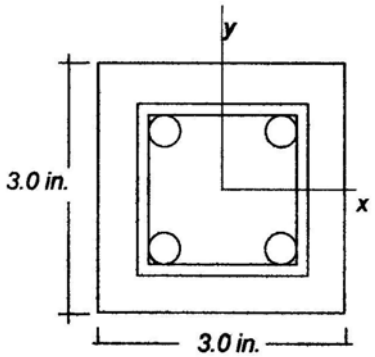

Figure 9.35: Section Properties for Large-Scale Model DHFRP R/C Columns.

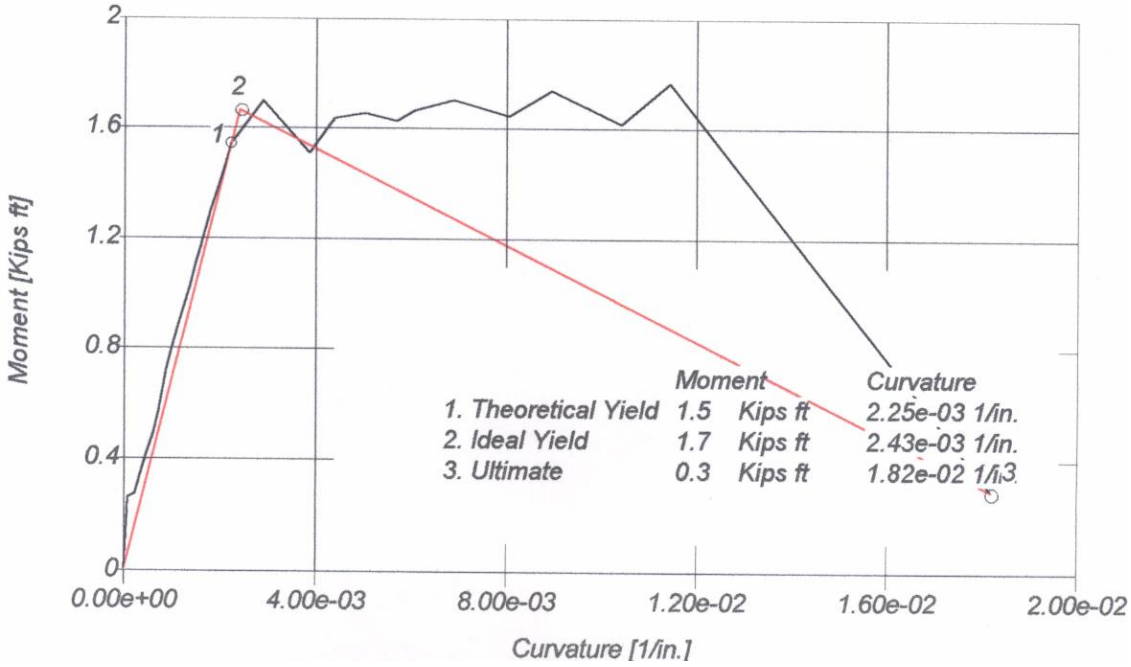

Figure 9.36: Moment-Curvature Relationship for Large-Scale Model DHFRP R/C Columns: Standard Parameters.

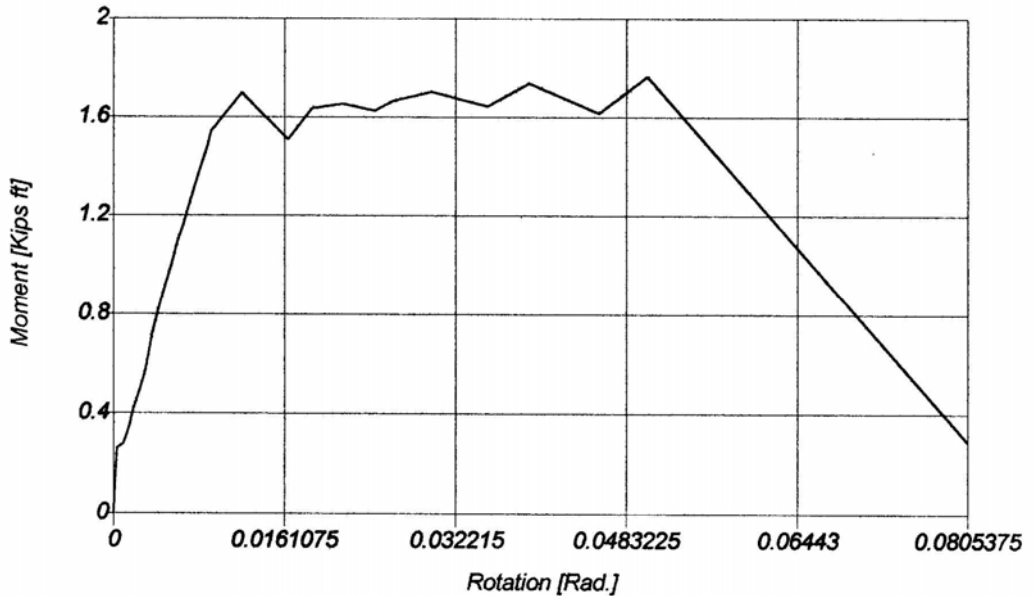

Figure 9.37: Moment-Rotation for Large-Scale Model DHFRP R/C Columns: Standard Parameters.

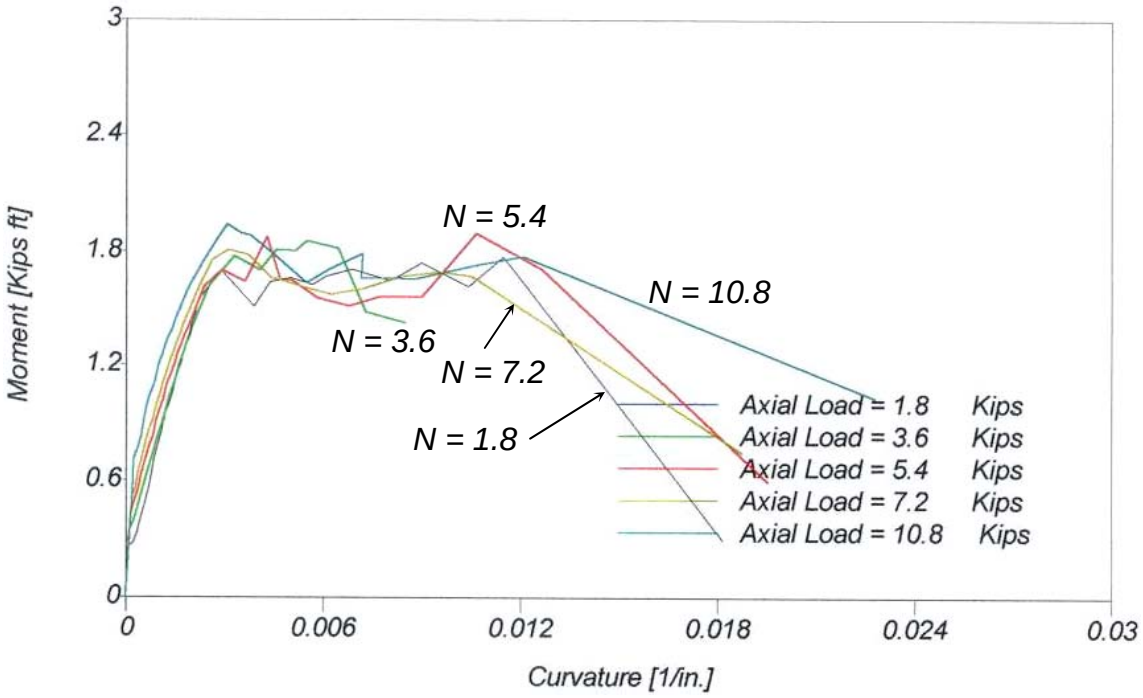

Figure 9.38: Moment-Curvature Relationships for Various Axial Load Levels for Large-Scale Model DHFRP R/C Columns: Standard Parameters.

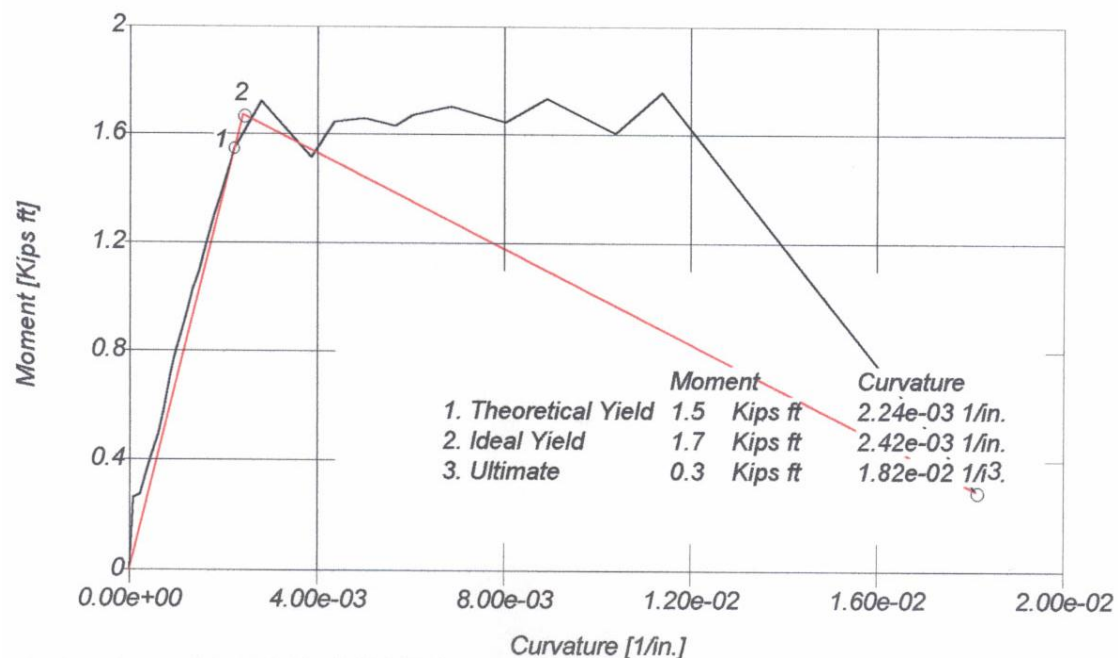

Figure 9.39: Moment-Curvature for Large-Scale Model DHFRP R/C Columns: s = 1.125".

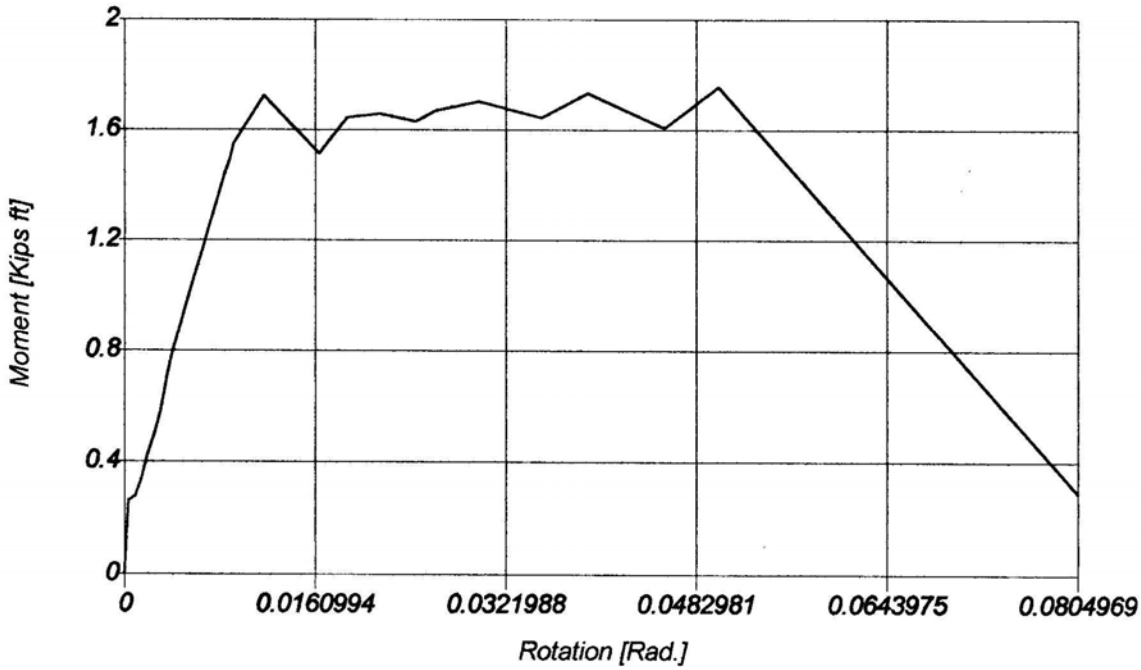

Figure 9.40: Moment-Rotation for Large-Scale Model DHFRP R/C Columns: s = 1.125".

SECTION PROPERTIES:

Section Depth	*= 3.0 in.*		
Section Width	*= 3.0 in.*		
Cover to Main Steel	*= 0.5 in.*		
Concrete Model	*= Mander*		
Concrete Strength	*= 5.00 ksi*		
Steel Model	*= Mild Strength Steel*		
Steel Strength	*= 66.0 ksi*		
Young's Modulus	*= 29000.0 ksi*		
Tension Side Reinforcement	*= 2 Bars (#3 Bars)*		
Compression Side Reinforcement	*= 2 Bars (#3 Bars)*		
Hoop Size	*= 0.125 Bars*	*Average Number of Legs*	*= 2.0*
Hoop Spacing	*= 0.7 in.*	*Hoop Strength*	*= 41.2 ksi*

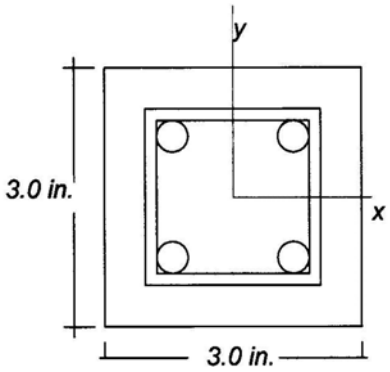

Figure 9.41: Section Properties for Large-Scale Model Steel R/C Columns.

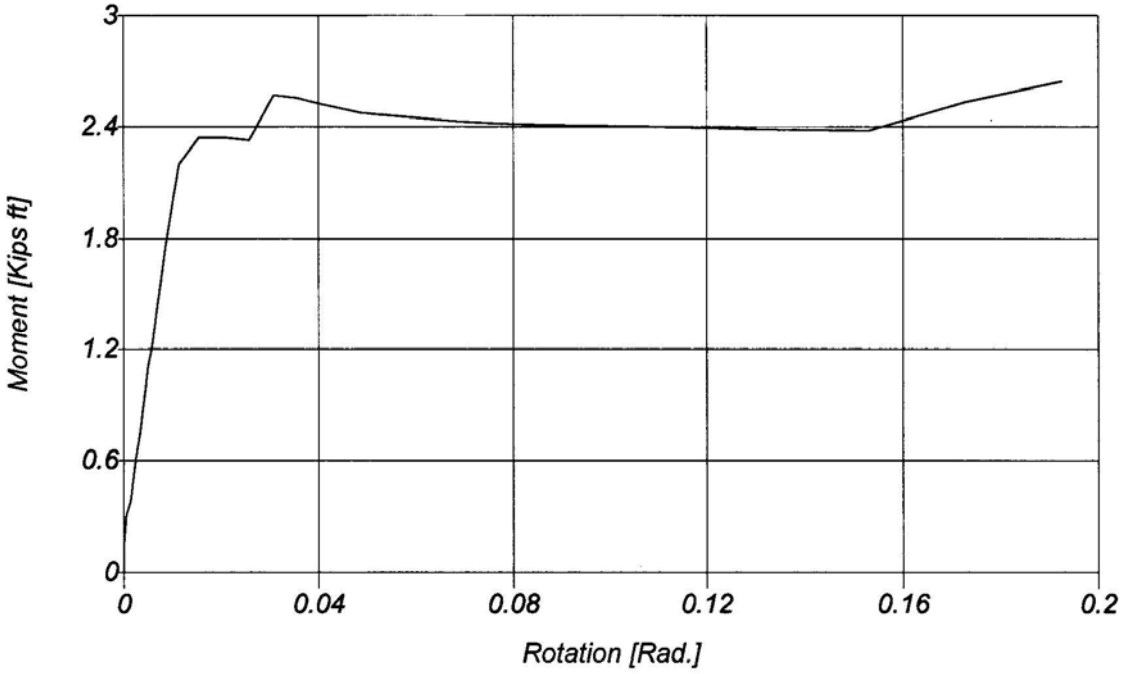

Figure 9.42: Moment-Rotation Relationship for Large-Scale Model Steel R/C Columns.

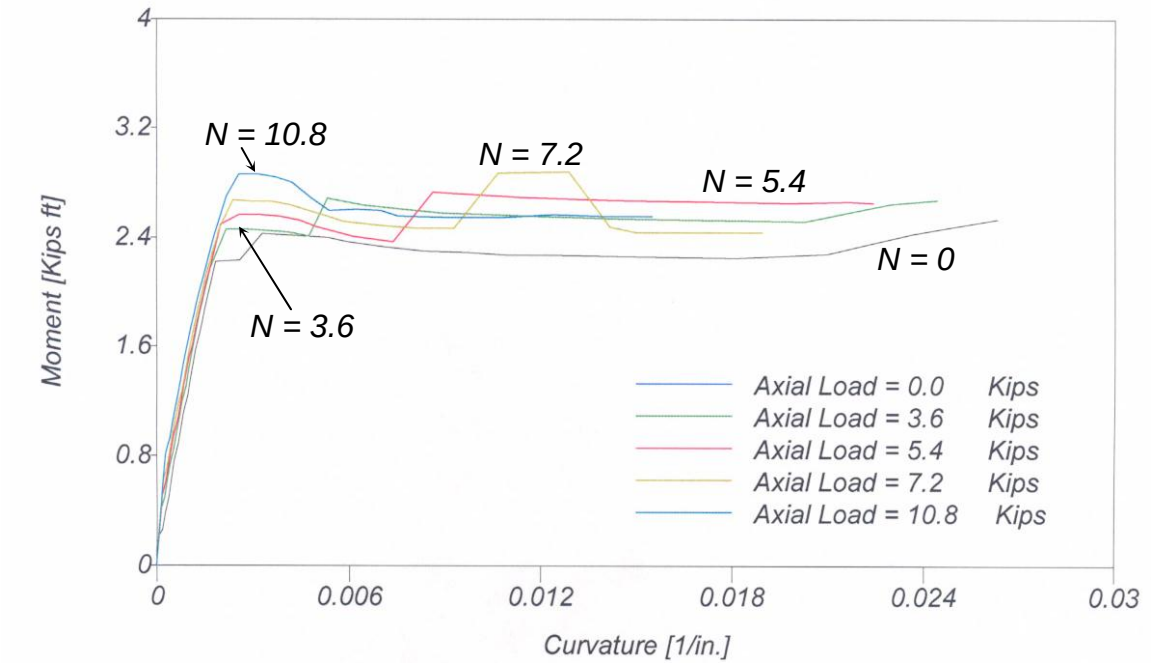

Figure 9.43: Moment-Curvature Relationships with and without Axial Load for Large-Scale Model Steel R/C Columns.

9.3.5 Discussion

Shown in Figures 9.21 through 9.43 were the moment-curvature analyses for both small and large-scale model columns reinforced with both DHFRP and steel using the SEQMC moment-curvature program. The analyses for the small scale columns were presented in Figures 9.21 through 9.34. The hoop spacing was 0.5" (12.7 mm) and the column length was L = 12" (304.8 mm). The moment-curvature relationship for an axial load level of 0.45 kips ($0.05\, f'_c\, A_g$) was presented in Figure 9.22. For this applied axial load level, the theoretical yield curvature was 0.000438 1/in, the ultimate curvature was 0.0213 1/in, resulting in a curvature ductility factor of 4.3. The yield moment was 0.185 kip-ft (0.25 kN-m) with an ultimate moment of approximately 0.19 kip-ft (0.26 kN-m).

A bilinear relation is evident, similar to steel. From the moment-rotation results of Figure 9.23, a plastic hinge length of 2.3 in (58.42 mm) was computed based on a shear span of 12 in (304.8 mm). From this plot, a rotation ductility factor of 4.6 was computed.

Shown in Figures 9.24 and 9.25 was a parametric study of axial load on moment–curvature response. As seen in Figure 9.24, the curvature ductility was greatest for low values of axial load ($0.05\ f'_c\ A_g$). For higher levels of axial load, the lowest ultimate curvatures resulted, and therefore, the lowest ductility factors. Figure 9.25 showed no axial load and four values of axial load. It appears that the curvature ductility is greatest for no axial load; however, the strength decrease is significant, and this could not be considered in the analysis.).

Shown in Figures 9.26 and 9.27 was the moment-curvature and moment-rotation behavior for a column length of 15". Both of these curves indicate that a small increase in the column length (12" to 15", a 20% increase) resulted in a negligible change in the rotation or curvature capacities. The plastic hinge zone increased from 2.3 in to 2.7 in.

Variations in the hoop spacing were studied. Shown in Figures 9.28 and 9.29 were the moment-curvature and moment-rotations for a smaller hoop spacing of s = 0.25". The ductility of the member increased significantly with a smaller hoop spacing. The curvature ductility increased from 4.3 to 8.9, a 106 % increase, and the rotational ductility factor increased from 4.6 to 7.4, a 62 % increase. The moment capacities were similar to values using a hoop spacing of s = 0.5". For a hoop spacing of 1 inch, the ductility of the member decreased significantly. The curvature ductility decreased from 4.3 to 2.9, a 48.3 % decrease, and the rotational ductility factor decreased from 4.6 to 2.7, a 70.4 %

decrease. Several model column specimens had a hoop spacing of 1 inch, and therefore, this spacing was investigated.

The results for a model steel column were presented in Figures 9.33 through 9.34. The tri-linear moment-curvature and moment-rotation responses were observed. The model column was designed to have the same moment capacity as the DHFRP columns and was reinforced with six 0.1126" (2.86-mm) diameter bars. The curvature ductility was 3.48 and the rotational ductility factor was 3.72. The plastic hinge length decreased to 2.2" (55.9 mm). The ductility was not as great for the steel R/C column. This could be attributed to the small size of the reinforcement which was wire and not actual bar.

The analyses for the mid scale columns were presented in Figures 9.35 through 9.38. The hoop spacing was 0.75" (19.05 mm) and the column length was L = 29" (736.6 mm). The moment-curvature relationship for an axial load level of 0.45 kips ($0.05\, f'_c\, A_g$) was presented in Figure 9.36. For this applied axial load level, the theoretical yield curvature was 0.000225 1/in, the ultimate curvature was 0.0182 1/in, resulting in a curvature ductility factor of 7.5. This value is greater than that obtained for the small-scale model column. From the moment-rotation results of Figure 9.37, a plastic hinge length of 4.5 in (114.3 mm) was computed based on a shear span of 29 in (736.6 mm). From this plot, a rotation ductility factor of 5.4.

The variation of moment-curvature behavior with axial load was presented in Figure 9.38. This figure shows that the largest ultimate curvature resulted for the largest value of axial load (10.8 kips, $0.3\, f'_c\, A_g$) and the smallest ultimate curvature results from an axial load level of 3.6 kips ($0.1\, f'_c\, A_g$). This result was not the same as for the model columns.

The hoop spacing along the length of the column varied from s = 0.75 in the plastic hinge region to s = 1.125" outside of the plastic hinge. Figures 9.39 and 9.40 showed the resulting moment-curvature and moment-rotation behaviors. The results showed virtually no effect on curvature and rotational ductilities. For the large-scale model columns, the hoop spacing was designed using ACI 318-02 seismic provisions both within and outside the plastic hinge region. The seismic provisions were not used for the model columns.

The moment-rotation and moment- curvature with various axial load levels was presented in Figures 9.42 and 9.43, respectively. The column was reinforced with four No. 3 rebars. This did not give match the DHFRP moment capacity exactly, but these bars were used since No. 3 bars are the most readily available. The curvature ductility factor was 12.7, the rotational ductility factor was 14.9, and the plastic hinge length was 7.5. These values are much larger than the DHFRP values. Also, Figure 9.43 clearly shows that the ultimate curvature decreases as the level of axial load increases.

Shown in Table 9.5 is a summary of results from the moment-curvature analysis.

Table 9.5: Summary of Theoretical Moment-Curvature Results for R/C Columns.

Model	Plastic Hinge Length , in (mm)	Curvature Ductility, μ_ϕ	Rotation Ductility, μ_θ
M1: normal	2.3 (58.42)	4.8	4.6
M2: L = 15" (381mm)	2.6 (66.04)	4.8	4.6
M3: s = 0.25" (6.4 mm)	2.3 (58.42)	8.9	7.4
M4: s = 1.0" (25.4 mm)	2.3 (58.42)	2.9	2.7
M5: steel	2.2 (55.88)	3.5	3.7
P1: normal	2.3 (114.3)	7.5	5.4
P2: s = 1.125" (28.6 mm)	2.3 (114.3)	7.5	5.4
P3: steel	2.3 (190.5)	12.7	14.9

9.4 Theoretical Interaction Diagrams

Since bridge columns are subjected to combined loading, the interaction between bending moment and axial load must be determined. The interaction diagrams are computed using the strain compatibility solution determining key points on the interaction diagram (MacGregor, 1997). The sign convention used in the calculation of interaction diagrams is compression is positive and tension is negative.

The theoretical top point on the interaction diagram is calculated using

$$P_0 = 0.85 f_c^{'}\left(A_g - A_{st}\right) + f_y A_{st} \qquad 9\text{-}36$$

where A_g = gross area of the column, A_{st} = area of reinforcement. The maximum usable axial load as defined in ACI Sec. 10.3.5.1 and 10.3.5.2 is given as

$$\phi P_{n(\max)} = \phi\left[0.85 f_c^{'}\left(A_g - A_{st}\right) + f_y A_{st}\right] \qquad 9\text{-}37$$

where ϕ = 0.85 for spiral columns and 0.8 for tied columns.

The general case involves the calculation of $\underline{P_n}$ acting at the centroid, and M_n about the centroid, assuming a strain distribution of ε_{cu} = 0.003. The column cross

section and the assumed strain distribution are shown in Figure 9.44. Three layers of reinforcement are shown, with layer 1 having strain ε_{s1} and area A_{s1}; also, layer 1 is closest to the least compressed surface, and is a distance d_1 from the most compressed surface. The strain distribution shown is defined by setting $\varepsilon_{cu} = 0.003$ and assuming a value of ε_{s1}. Since ε_{s1} was arbitrarily chosen, an iterative procedure is used to get the correct value. Therefore, set $\varepsilon_{s1} = Z\,\varepsilon_y$, where Z is an arbitrarily chosen value. Positive values of Z correspond to positive compressive strains.

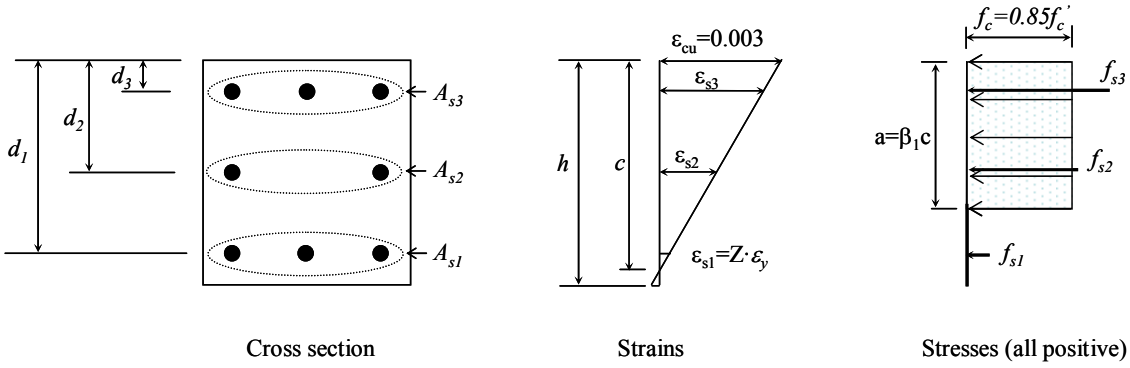

Figure 9.44: Column Cross Section and Strain and Stress Profiles.

From Figure 9.44b, using similar triangles,

$$c = \left(\frac{0.003}{0.003 - Z\varepsilon_y} \right) d_1 \qquad 9\text{-}38$$

and

$$\varepsilon_{si} = \left(\frac{c - d_i}{c} \right) 0.003 \qquad 9\text{-}39$$

where ε_{si} and d_i are the strain in the i^{th} layer of steel and the depth to that layer. Once the values of c and ε_{s1}, ε_{s2}, and so on, are known, the stresses in the concrete and in each layer of steel can be computed. For elastic-plastic reinforcement such as DHFRP,

$$f_{si} = \varepsilon_{si} E_s \quad \text{but} \quad -f_y \le f_{si} \le f_y \qquad 9\text{-}40$$

The stresses in the concrete are represented by the equivalent rectangular stress block.

The next step is to compute the compressive force in the concrete, C_c, and the forces in each layer of reinforcement, F_{s1}, F_{s2},..., F_{sn}. This is done by multiplying the stress by the corresponding areas giving

$$C_c = \left(0.85 f_c^{'}\right)(ab) \qquad 9\text{-}41$$

for a rectangular section.

If a is less than d_i,

$$F_{si} = f_{si} A_{si} \qquad 9\text{-}42$$

where F_{si} is positive in compression. If a is greater than d_i for a particular layer of steel, the area of the reinforcement in that layer must be included in the area used to compute C_c. Therefore, equation 9-42 would become

$$F_{si} = \left(f_{si} - 0.85 f_c^{'}\right) A_{si} \qquad 9\text{-}43$$

The axial load capacity, P_n, for the assumed strain distribution is the summation of the axial forces:

$$P_n = C_c + \sum_{i=1}^{n} F_{si} \qquad 9\text{-}44$$

The moment capacity M_n for the assumed strain distribution is found by summing the moments of all the internal forces about the centroid of the column. Figure 9.45 shows the internal forces and moment arms. All the forces are shown positive (compressive) in Figure 9.45. The moment is given as

$$M_n = C_c\left(\frac{h}{2}-\frac{a}{2}\right)+\sum_{i=1}^{n} F_{si}\left(\frac{h}{2}-d_i\right) \qquad 9\text{-}45$$

where a positive internal moment corresponds to a compression at the top face.

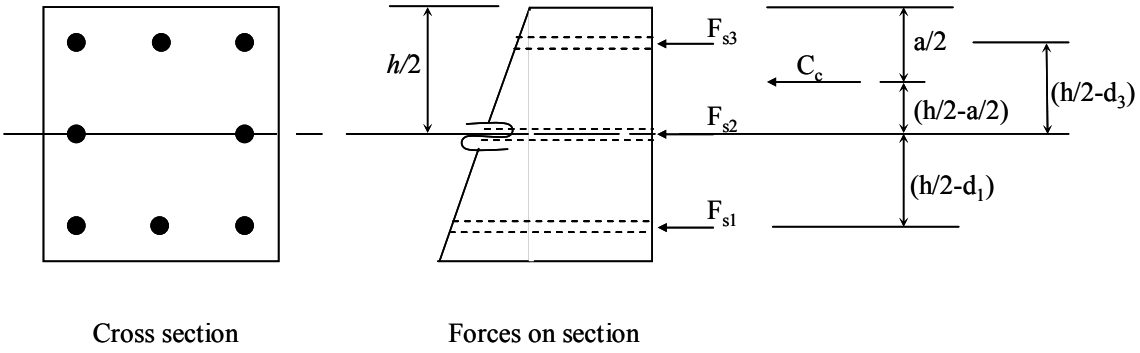

Figure 9.45: Internal Forces and Moment Arms About the Column Centroid.

9.4.1 Results

The column interaction diagrams are presented in Figures 9.46 through 9.50. Both actual and design interaction diagrams are presented using both steel and DHFRP longitudinal reinforcement. Figure 9.46 shows the actual and design interaction diagrams for model columns reinforced with 5-mm DHFRP bars. Figure 9.47 compares the actual (unfactored) DHFRP diagram with equivalent model steel reinforcement. Shown in

Figure 9.48 are the actual and design interaction diagrams for large-scale model columns reinforced with 10-mm DHFRP bars. Figure 9.49 compares the actual (unfactored) DHFRP diagram with a R/C column reinforced with four number 3 steel bars. Figure 9.50 compares the unfactored interaction diagrams for 5-mm and 10-mm DHFRP R/C columns.

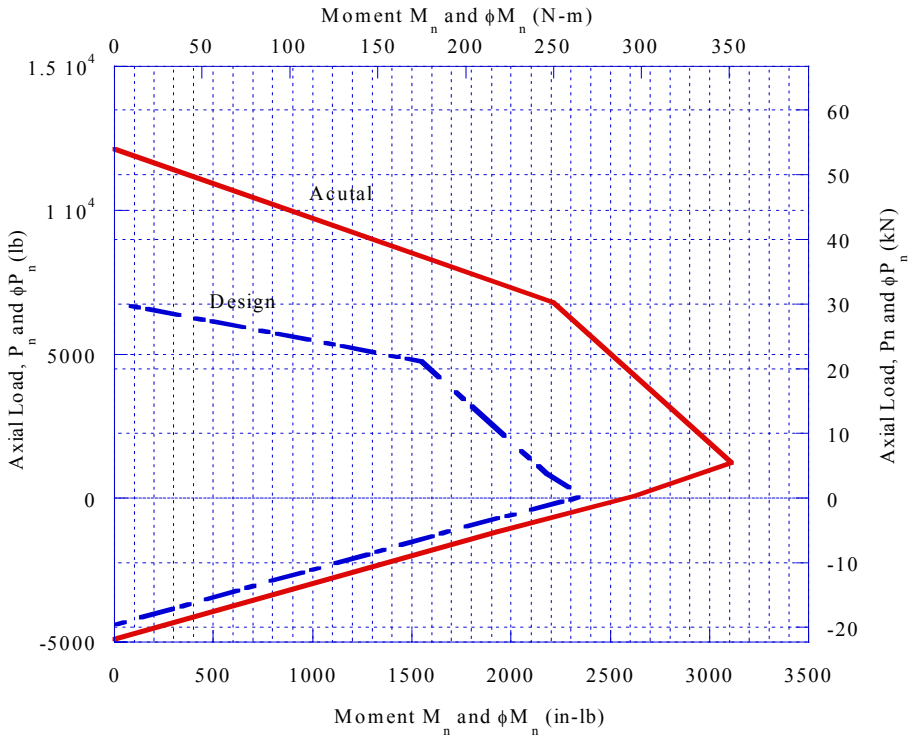

Figure 9.46: Interaction Diagram for 5-mm DHFRP R/C Column.

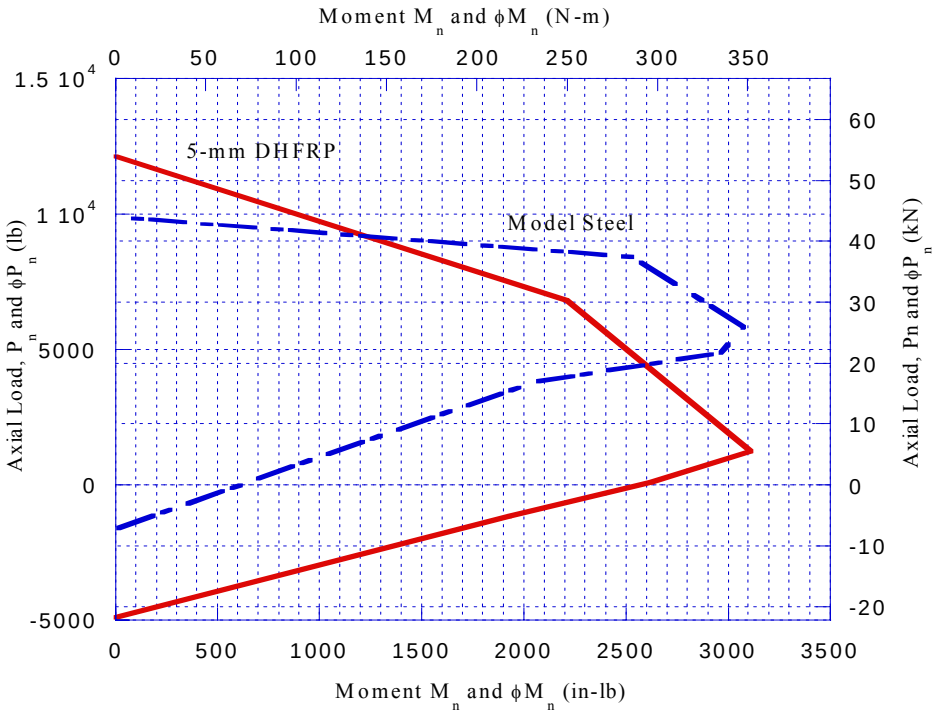

Figure 9.47: Interaction Diagram for 5-mm DHFRP and Companion Model Steel R/C Columns.

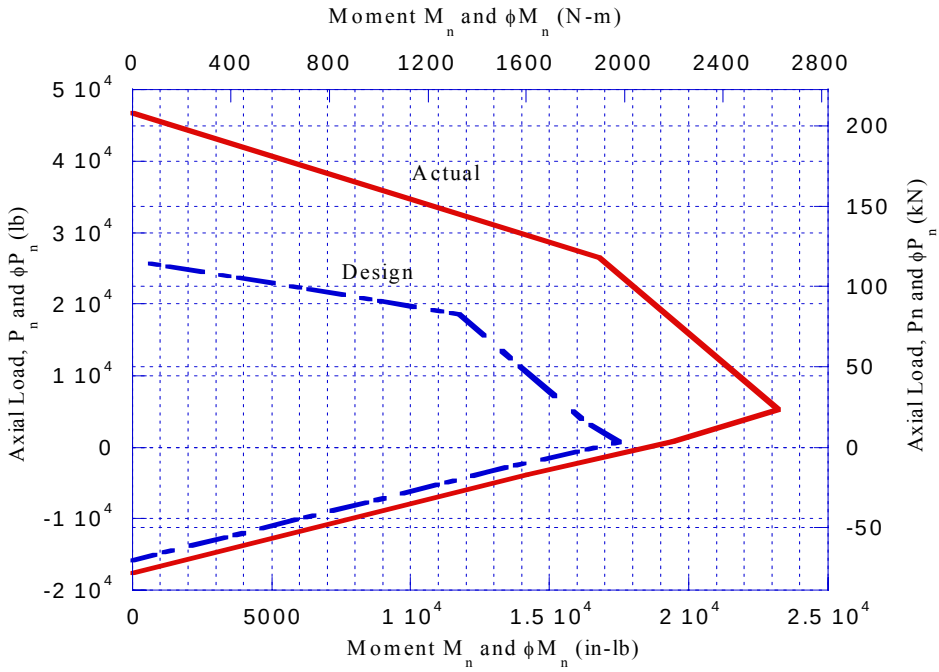

Figure 9.48: Interaction Diagram for 10-mm DHFRP R/C Column.

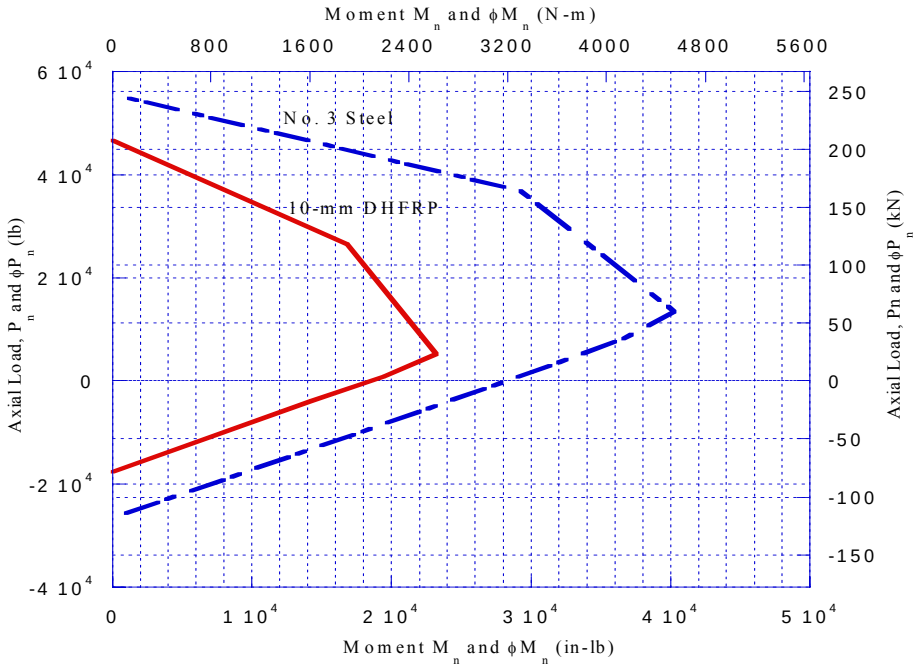

Figure 9.49: Interaction Diagram for 10-mm DHFRP and Companion No. 3 Steel R/C Columns.

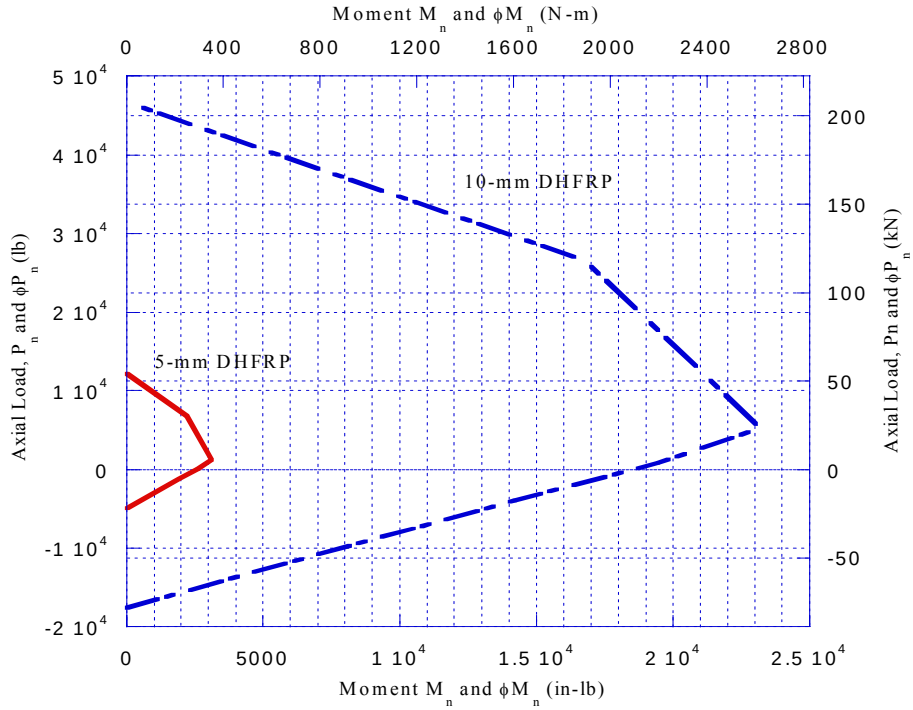

Figure 9.50: Interaction Diagrams for 5-mm DHFRP and 10-mm DHFRP R/C Columns.

9.4.2 Discussion

Shown in Figures 9.46 through 9.50 were the interaction diagrams for R/C columns reinforced with either DHFRP or steel longitudinal bars. Figure 9.46 showed the actual and design interaction diagrams for model columns reinforced with 5-mm DHFRP bars. The design interaction curve is more conservative since a design factor of $\phi = 0.7$ is used. Using the design factor, the largest axial force reduced from 12140 lb (54 kN) to 6744 lb (30 kN), and the moment was reduced from 3100 in-lb (13.8 N-m) to 2300 in-lb (10.2 N-m). Figure 9.47 compared the actual (unfactored) DHFRP diagram with equivalent model steel reinforcement. The steel-reinforced section was designed to have the same moment capacity as the DHFRP section. The moment capacity was similar for both columns, but the axial load capacity was larger for the DHFRP columns. Both the axial compression and tension capacities were larger for the DHFRP column. The axial compression increased from 10116 lb (45 kN) to 12140 lb (54 kN), an increase of 20%. Also, the balanced failure point had the same moment capacity for both types of reinforcement; however, since the steel had lower tensile capacity, the balanced axial load in the steel was 5620 lb (25 kN) and for the DHFRP was 1349 lb (6 kN). The low tensile capacity for the steel is probably attributed to the fact that the bars used were wire.

Shown in Figure 9.48 were the actual and design interaction diagrams for large-scale model columns reinforced with 10-mm DHFRP bars. Using the design factor, the largest axial force reduced from 46500 lb (207 kN) to 26000 lb (116 kN), and the moment was reduced from 23200 in-lb (2650 N-m) to 17500 in-lb (1950 N-m).Figure 9.49 compared the actual (unfactored) DHFRP diagram with a R/C column reinforced with four number 3 steel bars. The moment capacity of these two sections was not the

same as in the model columns. Four No. 3 bars were used since these would most readily available for columns of this size. The balanced failure points had similar axial load capacities, but the moment capacity of the steel R/C column was significantly greater (40500 in-lb versus 21000 in-lb, an increase of 93%). The maximum axial compressive and tensile capacities were similar for both columns, however.

Figure 9.50 compared the unfactored interaction diagrams for 5-mm and 10-mm DHFRP R/C columns. This figured compares the scaling effects on moment and axial load capacities from the small and large-scale model columns. The unfactored axial load was 12140 lb (54 kN) for the small-scale model columns and 46500 lb (207 kN) for the large scale model columns (an increase of 3.8 times), while the moment capacity was 3100 in-lb (13.8 N-m) for the model columns and was 23200 in-lb (2650 N-m) for the large-scale model columns (an increase of 7.5 times). These increases are consistent with the similitude values given in Table 3.1. The concentrated force increases with the length squared from model to prototype. Since the length is doubled, the axial force in the prototype should be approximately 4 times that of the model. The results from the analysis had an increase of 3.8 times. The moment increases by the length cubed, which would be $(2)^3 = 8$. The result obtained was an increase in moment capacity of 7.5 from model to prototype, which is consistent to the similitude results.

CHAPTER 10. EXPERIMENTAL PROGRAM OF SMALL-SCALE MODEL REINFORCED CONCRETE BEAM-COLUMNS

Small-scale model columns were constructed to quantify the energy absorption capability of DHFRP as longitudinal reinforcing. The small-scale models enabled the improvement of testing procedures of R/C beam-columns under both cyclic lateral and constant axial loads. The samples were fabricated, the test setup designed and constructed, and the specimens were tested.

10.1 Sample Preparation

Sample preparation of the model columns included the design and construction of a reusable mold, fabricating rectangular hoops, and assembling the reinforcing cages. The column form was designed to be reusable and to be easily disassembled after the concrete hardened. Figure 10.1 shows the form used with a model DHFRP reinforcing cage in the form. The form was constructed from pine and painted with three coats of polyurethane sealer to minimize water intrusion. As seen in this figure, at the base of the column a clay gasket was made to prevent leakage of the wet concrete. Shown in Figure 10.2 is an extension cap that was used for constructing columns longer than 12 inches (304.8 mm). The extension cap was made of four pieces of aluminum angle that were screwed onto the existing wood form.

During casting, four holes were placed through the footing form to allow the finished footing to be bolted directly to a strong table. Four oversized holes were drilled into the bottom of the footing form. Figure 10.3 shows the footing form with the four holes. 3/8” (9.53 mm) copper tubing was used for inserts. The bottoms of the tube were

lubricated with Vaseline and placed into the bottom of the form. This allowed the bottom piece of the form to be removed after casting. The tops of the tubes were sealed with clay. This prevented the holes from filling with concrete slurry during casting.

The transverse reinforcement hoops were fabricated by cutting pieces of 0.045 in (1.14 mm) deformed wire and forming them around a jig with needle-nose pliers. The hoops were then tied to the longitudinal bars with small wire and spaced uniformly along the column length. The spacing was varied for different columns and varied between 0.25 inches (6.35 mm) and 1.0 inch (25.4 mm). The longitudinal DHFRP bars with the cage being fabricated are shown in Figure 10.4 and the completed cage is shown in Figure 10.5. Two layers of steel mat reinforcing were used for the footing to prevent failure of the footing. These were constructed of steel wire instead of DHFRP to eliminate an additional variable.

Figure 10.1 Model Column Form with DHFRP Cage Inside.

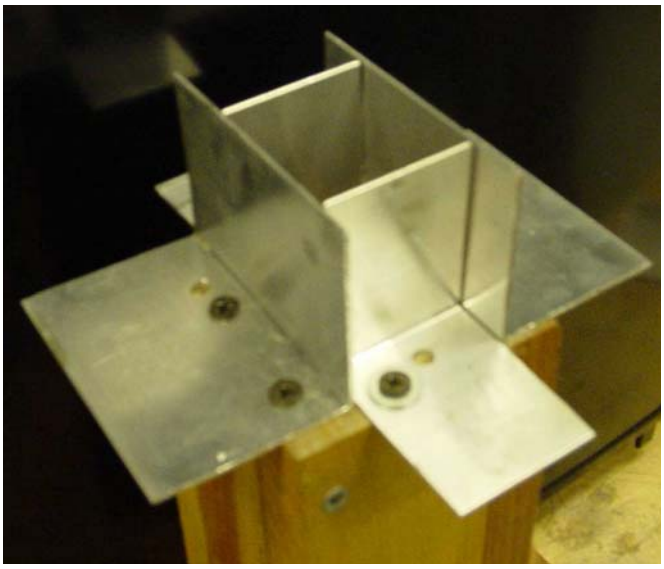

Figure 10.2: Aluminum Column Form Extension Cap for Longer Model Columns.

Figure 10.3: Copper Pipe Inserts for Anchor Rods, DHFRP Model Columns.

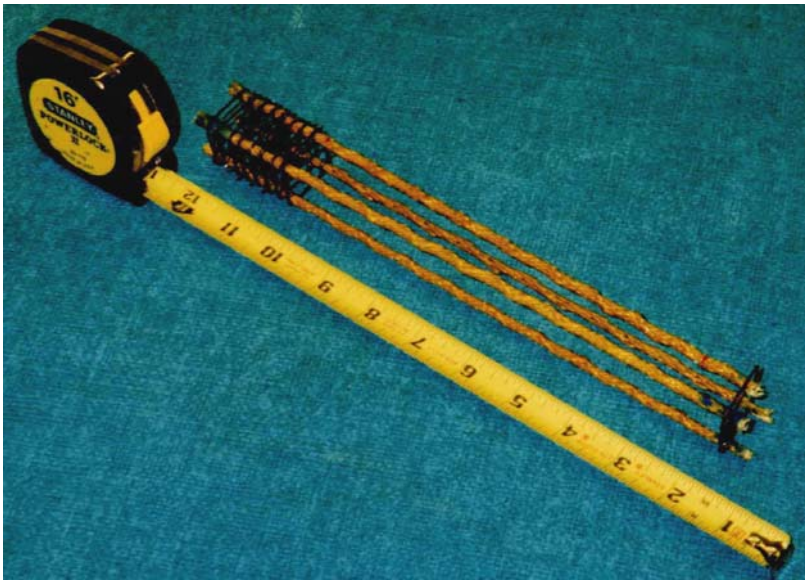

Figure 10.4: Longitudinal DHFRP Reinforcing Bars with Some Hoops.

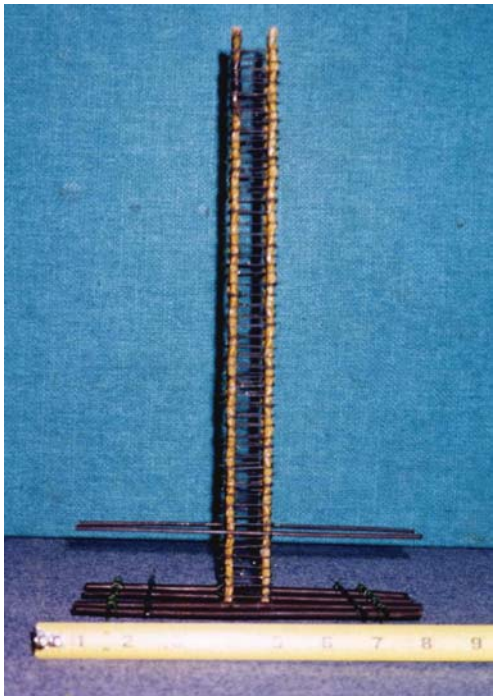

Figure 10.5: Completed Reinforcing Cage for Column and Base.

For the model columns, the best casting procedure was to cast the columns in two parts, using two smaller batches of concrete. This was manageable for one person. The forms were lightly oiled using the same oil used for the beams (Chapter 8). The cage was placed and centered into the base portion of the form. The concrete was placed in the base; a small rod was used to compact the concrete. Once the base was filled, the top portion of the mold was secured and the mold was placed on a small variable frequency vibrating table to consolidate concrete and release any entrapped air. This was the first part of the casting. Another batch using the same materials and mix ratio was immediately made. For the second casting, the column was then filled through the opening at the top of the column. The same compaction method used for the base (rodding followed by vibration) was used for the column. Also, six 2" x 4" (50.8 mm x 101.6 mm) cylinders and six 1" x 2" (25.4 mm x 50.8 mm) model cylinders were made for each column specimen. Clay gaskets were used to prevent slurry from leaking during vibration of the footing and column, as shown in Figure 10.6. Figure 10.7 shows the casting of the column footing and Figure 10.8 shows the casting of the column.

Figure 10.6: Form with Clay Gaskets Between Column and Base.

Figure 10.7: Casting of the Footing Concrete.

(a)

(b)

Figure 10.8: Horizontal Casting of the Column Concrete.

10.2 Test Setup

The model columns were tested at John Barry Laboratory, Villanova University. The setup was mounted onto the existing test frame. The capacity of the frame is 500000 lb (2224 kN), and the load values for this and the large-scale model-scale tests were well below the limits for both member stresses and deflections. Shown in Figure 10.9 is the general test setup. The existing column and bottom beam of the test frame were used. A steel W 10 x 26 beam was cantilevered from the existing W 14 x 61 column. Two pieces of 7/8" (22.2 mm) diameter all thread were placed between the far end of the cantilevered beam and the bottom beam of the frame and attached by nuts top and bottom. This supported the cantilevered beam at the far end and provided more support when the lateral load was applied. The model DHFRP column was mounted to the top flange of the test-frame bottom beam by using a system of 3/8" (9.53 mm) thick steel plates and ½" (12.7 mm) diameter threaded bar. Four pieces of all thread were placed in the holes in the footing and through four matching holes in the flange of the support beam. A piece of steel plate was placed on top of the footing and the all thread was tensioned with nuts and washers, placed above the plates and below the bottom of the beam flange and tensioned to sufficiently clamp down the specimen.

Both lateral load and axial compression were applied to the free end of the column. Devices were designed to apply the combined loading. Care was taken to have all connections articulated, so as to not introduce secondary unknown loading effects. Shown in Figure 10.10 is the detail of the axial load application device. The axial loading device consisted of two rectangular steel struts that were connected to a cap plate. The bottom of the struts had a hole that connected to the loading cap of the specimen using a bolt. This allowed for rotation. The axial loading yoke threaded into the end of

the load jack. The load cell was placed between the jack and the top beam of the frame. A 30000 lb capacity pancake-type load cell was used. Translation of the loading system was provided by using a block and rail assembly (McMaster Carr ®, 2004). A ½" (12.7 mm) thick mounting plate was bolted onto the guide block, and the load cell was bolted onto the mounting plate. A plate was bolted onto the loading jack. This plate was placed against the load cell and the two mounting plates were connected together using. four pieces of ¼" (6.35 mm) threaded rod. This kept the entire system from shifting until axial load was applied to the specimen. The block and loading assembly was then placed on the rail. The block had ball bearings and allowed the loading assembly to move as the column was cycled. To prevent excessive movement, a rail tensioning system was provided. This consisted of a piece of 5/16" (7.94 mm) threaded rod with 3 nuts and two pieces of angle. The nuts were tightened and loosened depending on the cyclic loading direction. The nuts were loose enough, and therefore, did not induce any additional lateral force. This enabled fine control of the translational movement.

Figure 10.11 shows a detail of the connection between the axial loading jack and the axial loading yoke. The tip of the loading actuator was 3/8" fine thread. A 7/8" piece of threaded rod was used to connect the loading jack to the loading yoke. As seen in the figure, a 3/8" hole was tapped into the 7/8" rod and the other end was threaded into the cap of the loading yoke. This allowed the entire loading system to be mechanically fastened.

Shown in Figure 10.12 is the detail of the lateral load application device. A hinging arm was connected to the loading cap by two pins. This provided a rotational articulation for the lateral load, thereby applying the load normal to the surface of the

column. A 5000 lb (22.2 kN) tension/ compression S-type load cell was placed between the hinge arm and the loading actuator. The system was connected using threaded rod to provide mechanical connection of all parts of the loading system. Figure 10.13 shows a detail of connection between the lateral load cell and the actuator and the connection between the actuator and the loading cap. All connections were made using threaded rod. The larger pieces of threaded rod were tapped so that smaller pieces could be screwed into them.

Shown in Figure 10.14 is a detail of the instrumentation used for the testing. Five LVDTs were used and two load cells. An LVDT was placed at the column tip to measure the lateral deflections of the column. Four LVDTs were used at the base to measure the displacements at the base. From this, the rotations, strains, and curvatures at the base could be calculated. Shown in Figure 10.15 is the mounting device for the LVDTs at the base. This device was made of ¼" (6.35 mm) aluminum angle, and mechanically screwed onto the base of the column using four Allen bolts. Since the largest cracking and deterioration was expected at the base, adhesively-mounted devices were avoided. Shown in Figure 10.16 is the calculation of various strain, rotation, and curvature quantities based on the LVDT displacement readings. These will be discussed in more detail in the next section.

Shown in Figures 10.17 through 10.28 are photographs of the test setup used for the 5-mm DHFRP R/C columns tests. Figure 10.17 shows the overall test setup without the application of axial load. The loading cap used to mount the lateral loading device to the column is shown in Figure 10.18. The mounting plates and all thread system used to secure the specimen to the test frame are shown in Figure 10.19. Shown in Figure 10.20

is the lateral loading system, including the lateral load cell, the loading actuator, and the threaded connection pieces. The LVDTs used to measure displacements are shown in Figures 10.21 through 10.23. Figure 10.21 shows the lateral LVDT used to measure the tip lateral displacement at the top of the column. This LVDT was mounted on a steel column that was part of the test frame. Shown in Figure 10.22 is the articulation between the loading cap and the horizontal LVDT. A door hinge mechanism was used. This allowed the LVDT to rotate relative to the column, and therefore, remained transverse to the surface of the column face during the test. The other end of the LVDT was also articulated allowing for its free rotation. Shown in Figure 10.23 are the four LVDTs that measured vertical displacement at the base of the column. These displacement values were used to calculate the rotations, strains, and curvature at the base of the column.

Figures 10.24 through 10.28 show the test setup including the application of axial load. Figure 10.24 is the overall setup with axial load. Figure 10.25 shows a closeup of the entire axial loading device. Figure 10.26 shows the loading cap with the application of both axial and lateral loads. The axial load cell and block and rail system used to articulate the axial load application is shown in Figure 10.27 The tensioning system used to control the amount of translational articulation needed for the axial load application system is shown in Figure 10.28.

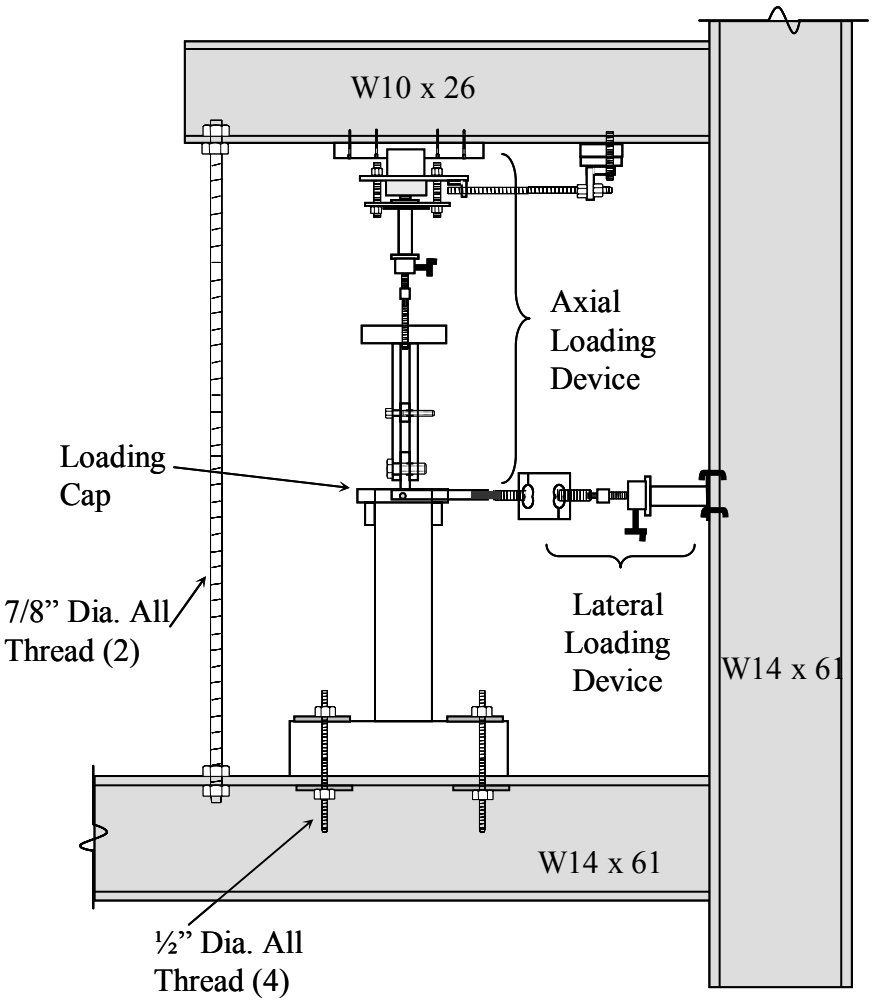

Figure 10.9: Setup for Model Column Tests.

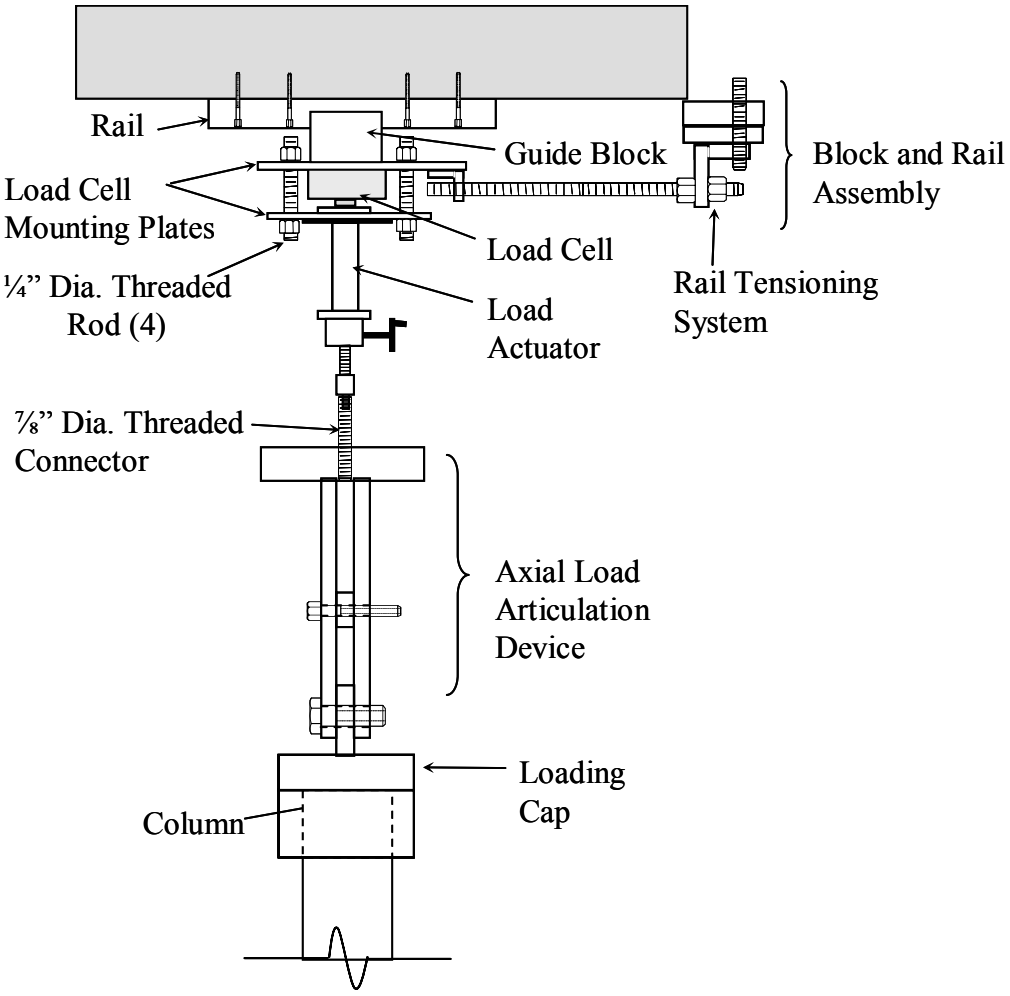

Figure 10.10:Detail of Axial Load Application Device.

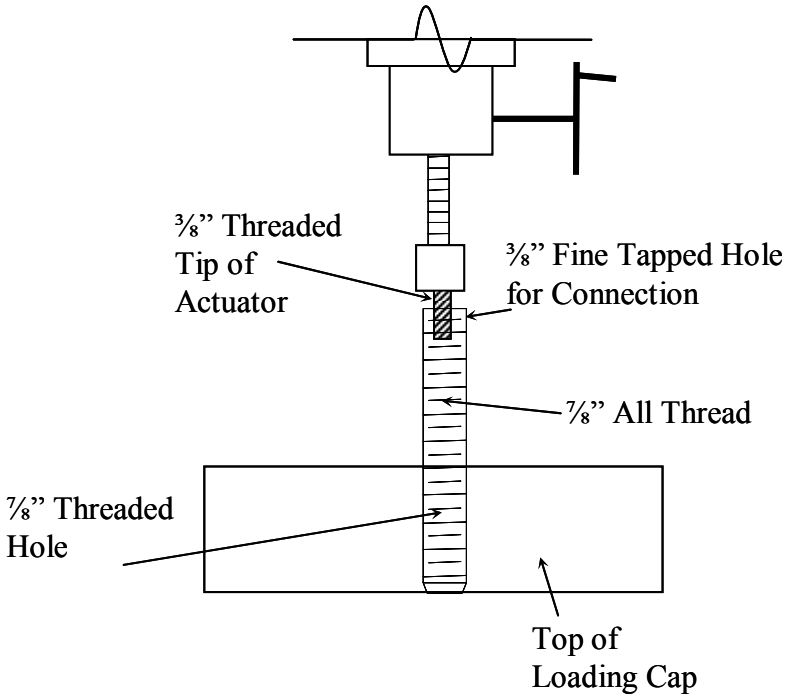

Figure 10.11:Detail of Connection Between Axial Loading Jack and Axial Articulation Device.

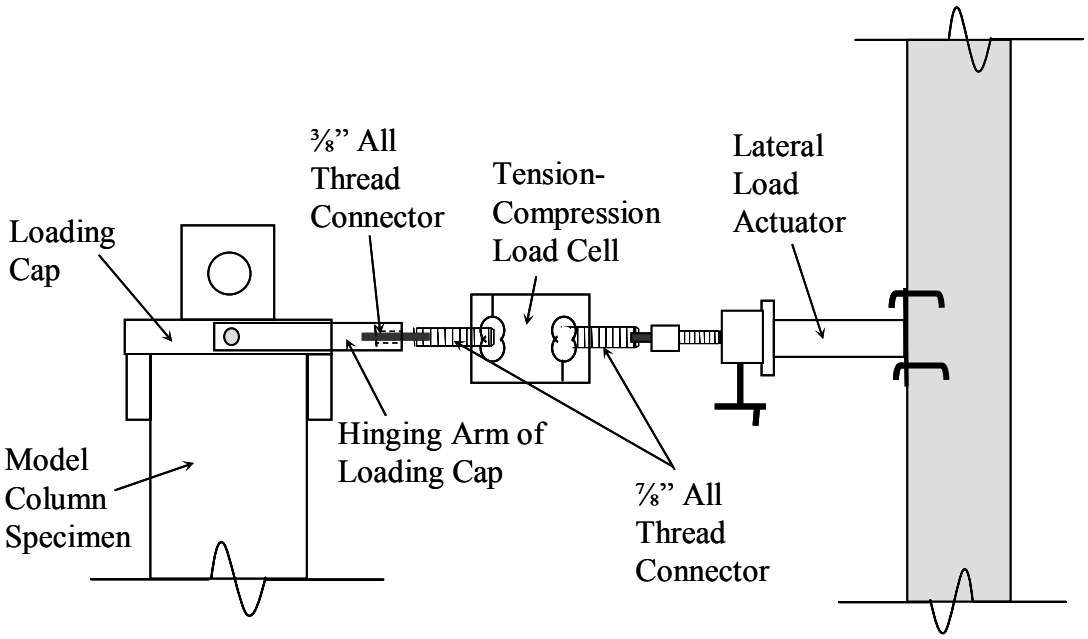

Figure 10.12:Detail of Lateral Load Application Device.

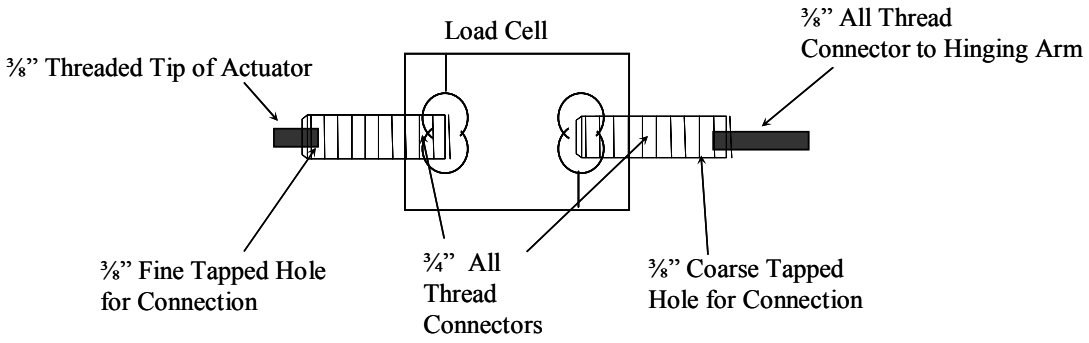

Figure 10.13:Detail of Connections Between Lateral Load Cell and Actuator and Lateral Loading Cap.

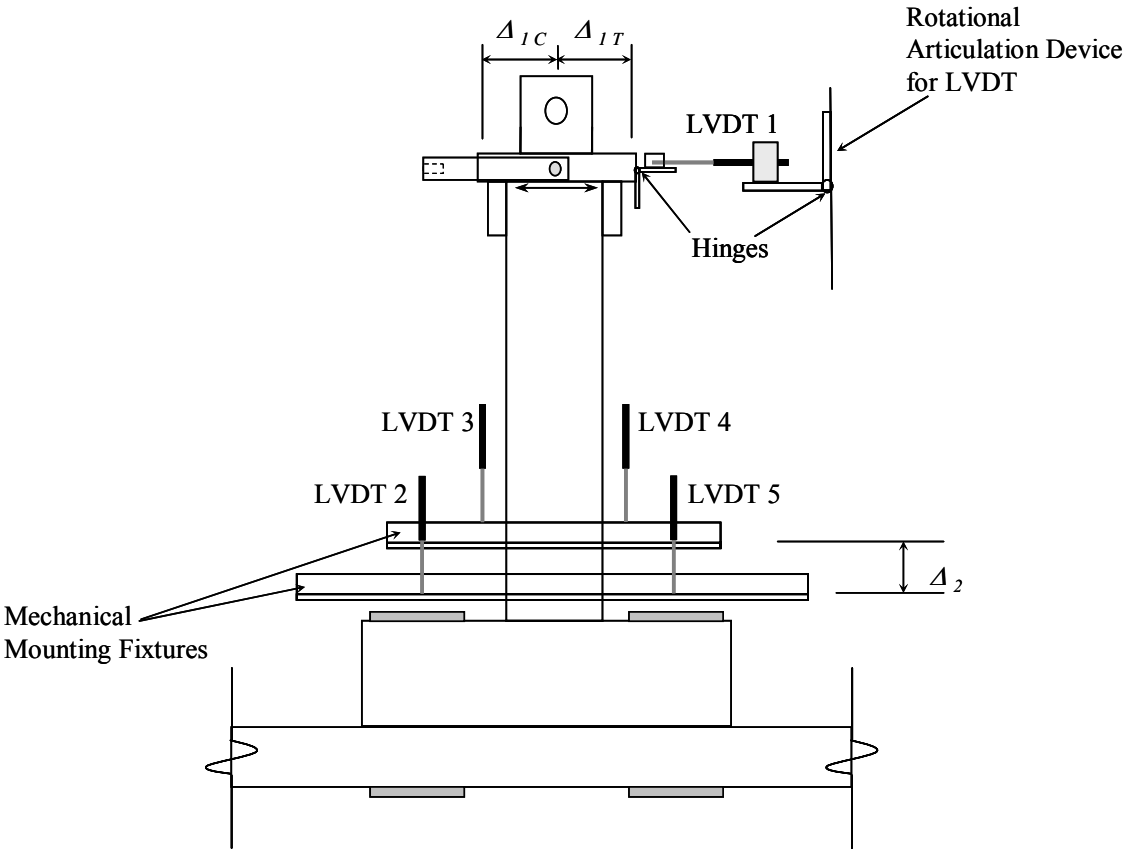

Figure 10.14:Detail of Instrumentation for Model Column Tests.

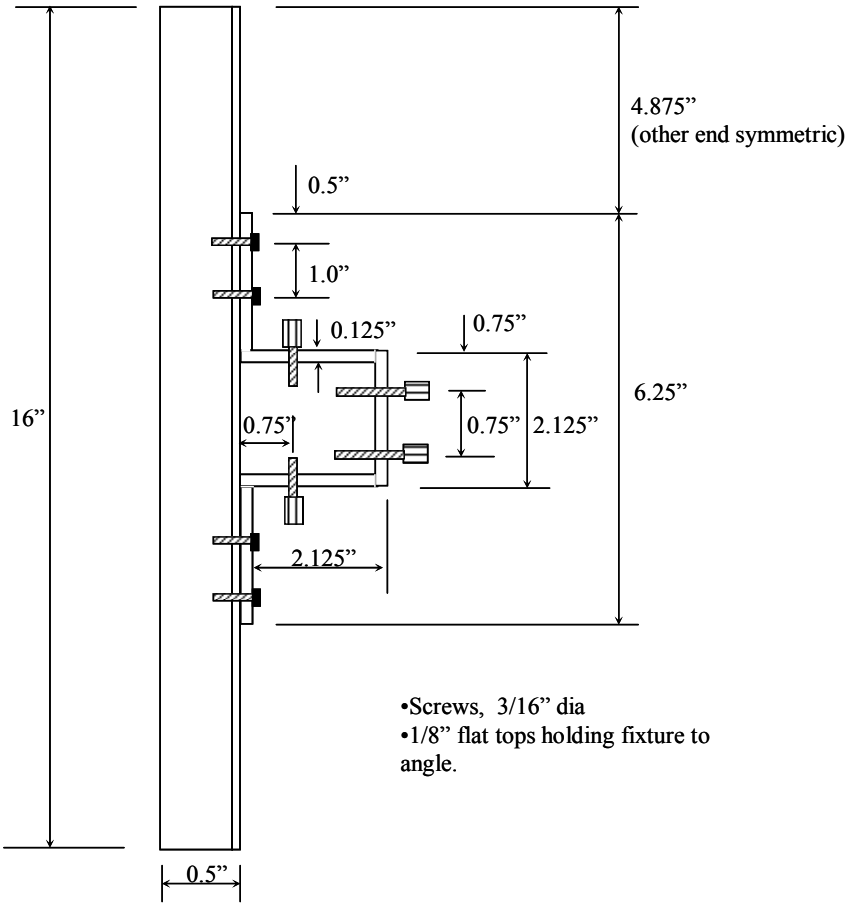

Figure 10.15:Mounting Device for LVDTs for Base of Model Column.

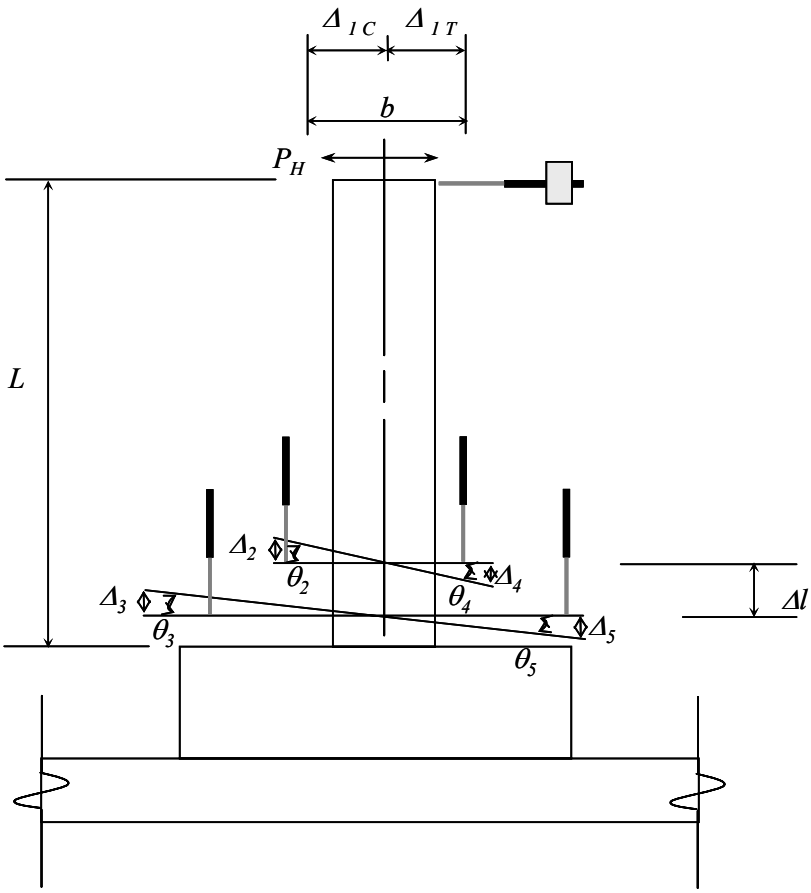

$$\theta_i = \frac{\Delta_i}{\left(\frac{b}{2}\right)} \quad \text{for } i = 2, 3, 4\,5$$

$$M = P_H L$$

$$\varepsilon_L = \frac{\Delta_2 - \Delta_3}{\Delta l}$$

$$\varepsilon_R = \frac{\Delta_4 - \Delta_5}{\Delta l}$$

(a)

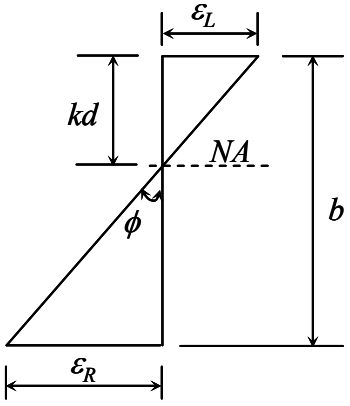

$$\phi = \frac{\varepsilon_L}{kd} = \frac{\varepsilon_R}{b - kd} = \frac{\varepsilon_L + \varepsilon_R}{b}$$

(b)

Figure 10.16:(a) Measurements Obtained from Instrumentation of Model Column and (b) Strain Profile Measurements.

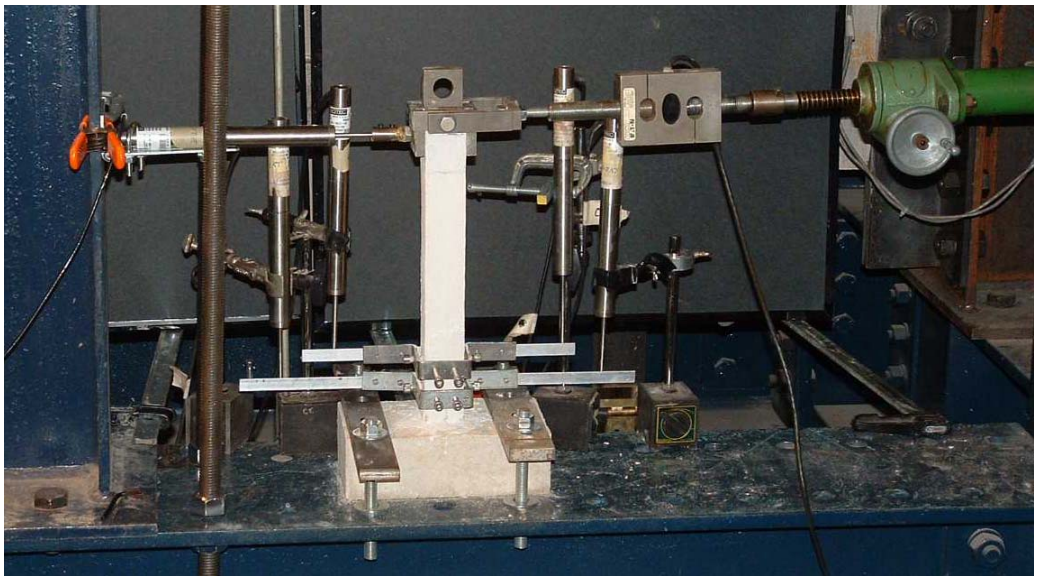

Figure 10.17:Overall Test Setup Without Axial Load for 5-mm R/C DHFRP Columns.

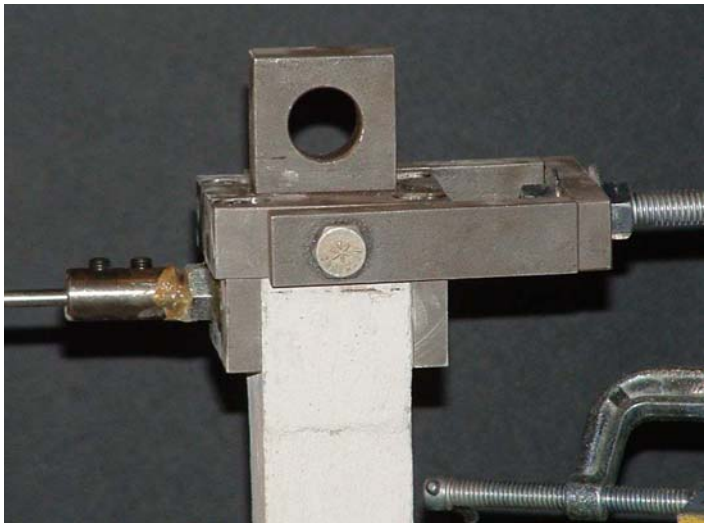

Figure 10.18:Loading Cap Used for 5-mm R/C DHFRP Columns.

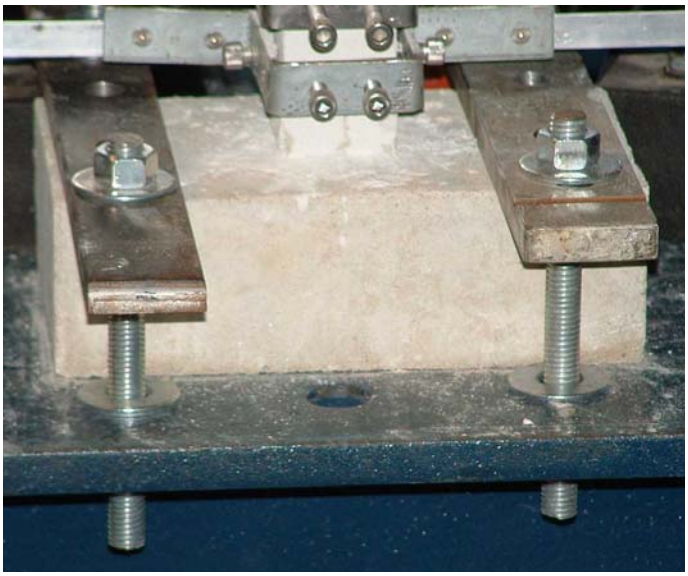

Figure 10.19:Mounting Plates and All Thread for 5-mm R/C DHFRP Columns.

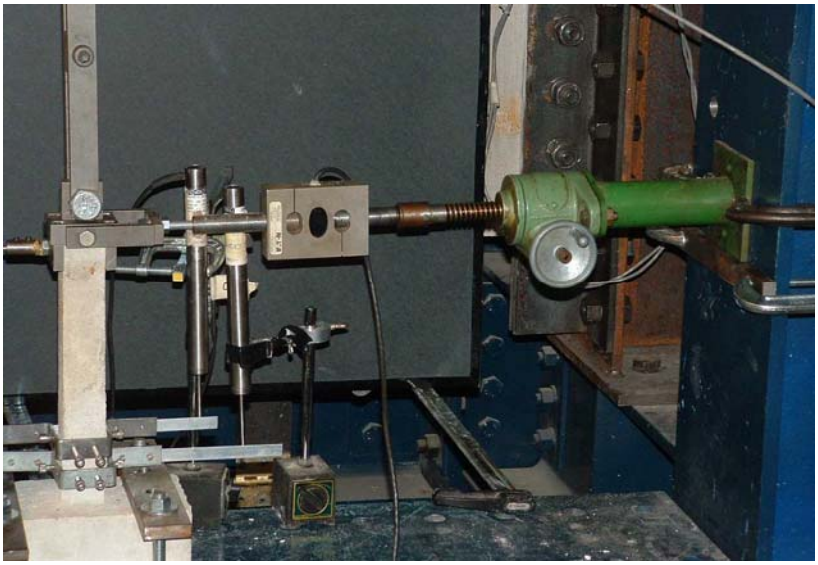

Figure 10.20:Lateral Load Cell and Lateral Loading Device for 5-mm R/C DHFRP Columns.

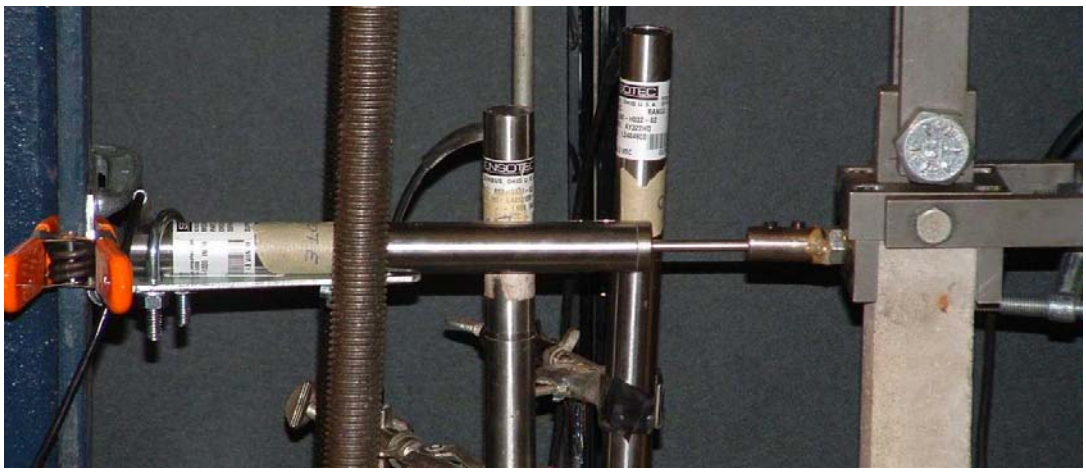

Figure 10.21: Lateral LVDT to Measure Tip Displacement for 5-mm R/C DHFRP Columns.

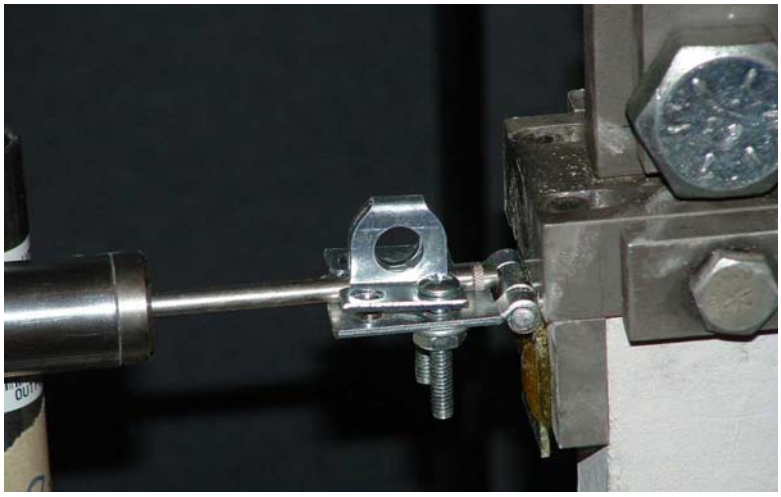

Figure 10.22: Articulation Between Loading Cap and Horizontal LVDT for 5-mm R/C DHFRP Columns.

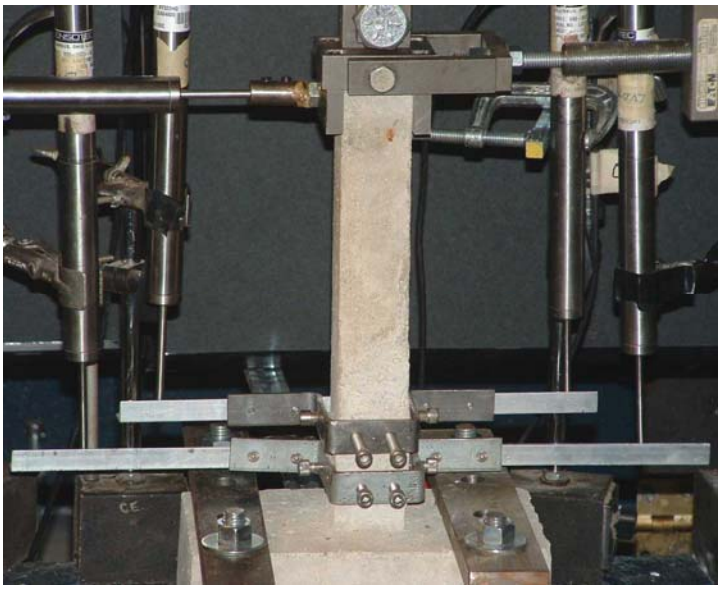

Figure 10.23: Vertical LVDTs Used for Rotation and Curvature Calculations for 5-mm R/C DHFRP Columns.

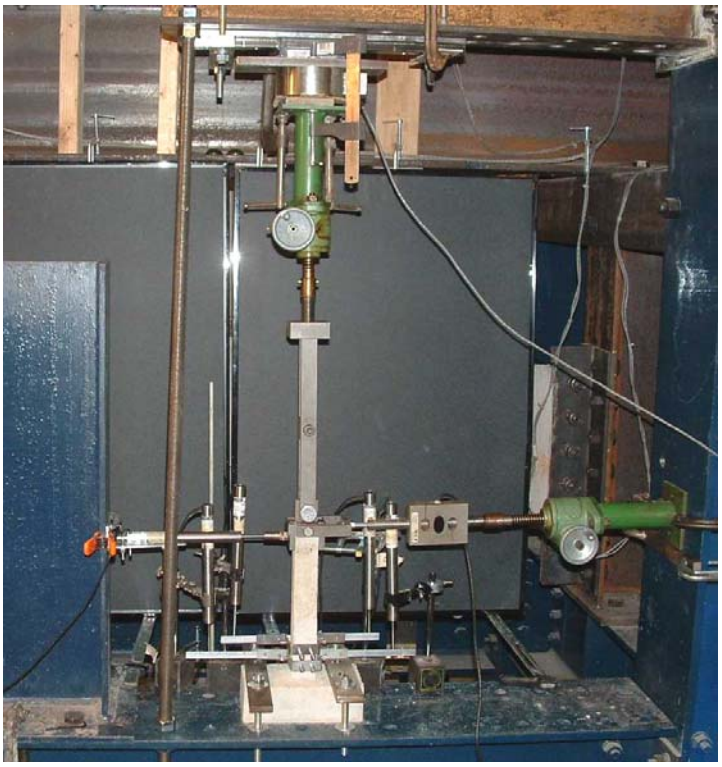

Figure 10.24: Overall Test Setup with Axial Load for 5-mm R/C DHFRP Columns.

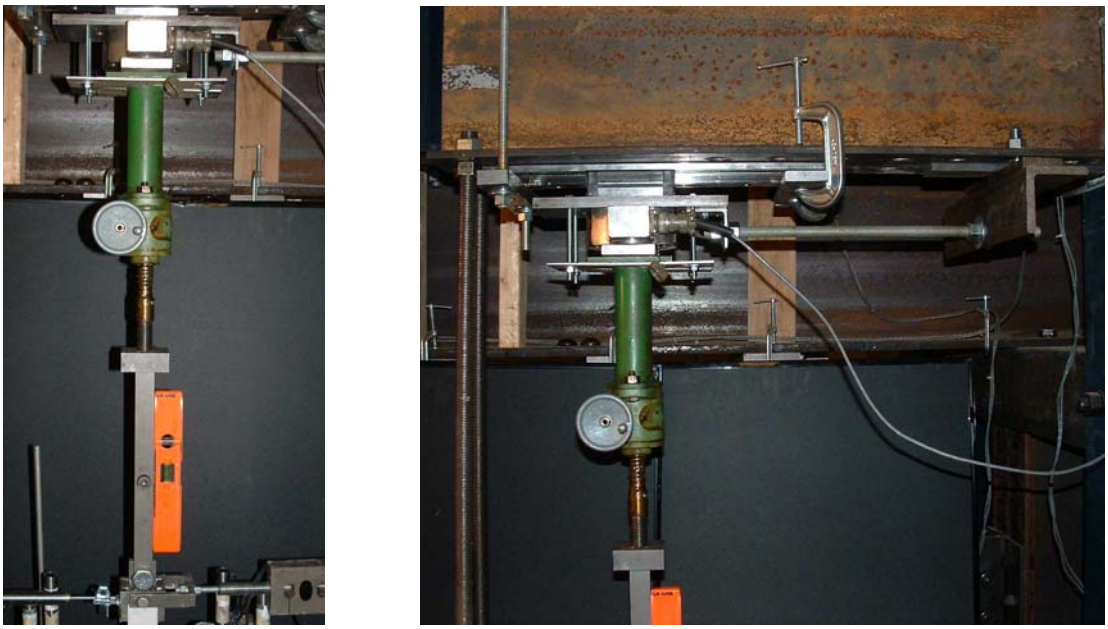

Figure 10.25:Axial Loading Device and Test Setup for 5-mm R/C DHFRP Columns.

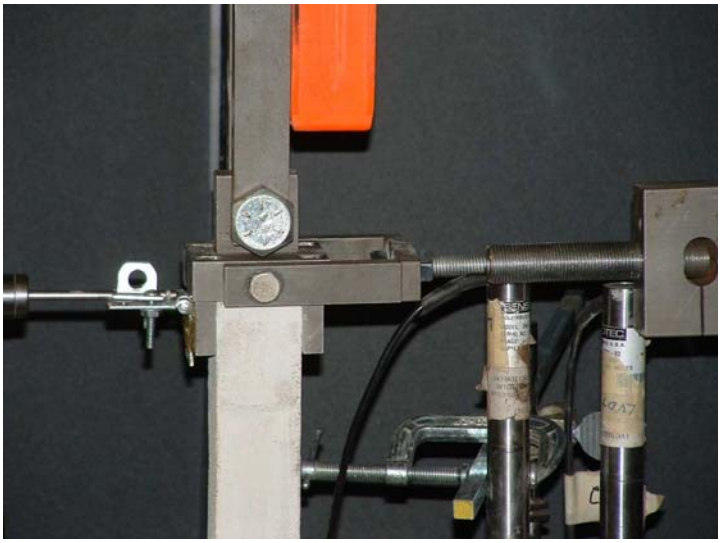

Figure 10.26:Loading Cap with Axial Loading Device for 5-mm R/C DHFRP Columns.

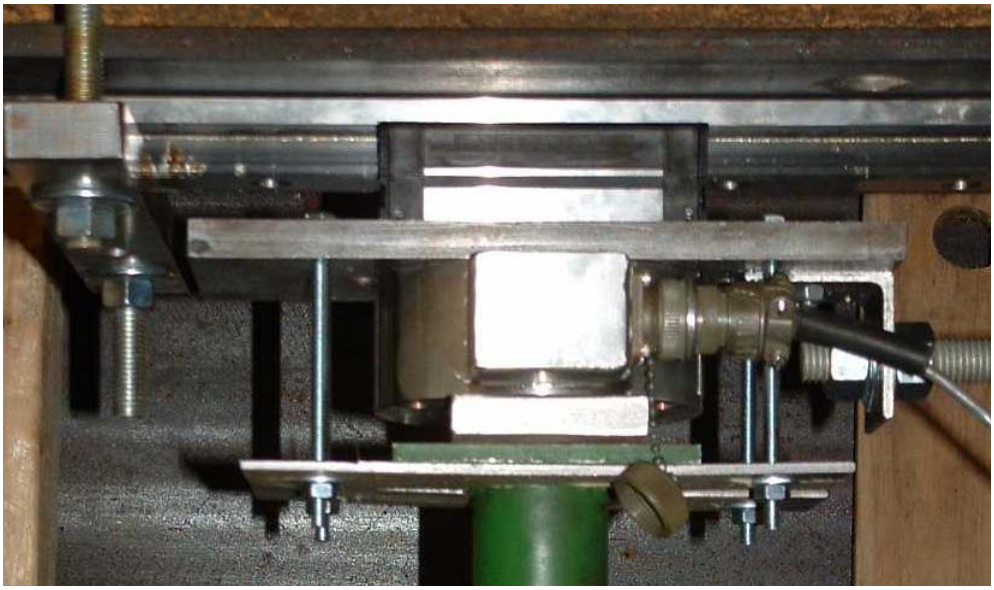

Figure 10.27:Axial Load Cell and Block and Rail System Used for 5-mm R/C DHFRP Columns.

Figure 10.28:Tensioning System for Axial Load Rail for 5-mm R/C DHFRP Columns.

The column was set into position and bolted down to the test frame. The axial load was applied first. The various levels of axial load are given in Table 10.1. These values of axial load were based on percentages of the gross compressive strength of the concrete section. A hand-operated screw-gear actuator was used to apply the constant axial compression load. The maximum load capacity of the jack was 2000 lb (8.9 kN) and the maximum stroke was 6.5 in (165.1 mm). Recording of data began when the axial load was first applied.

Once the desired level of axial load was achieved, the simulated lateral seismic load was applied to the loading cap on top of the column using a similar hand operated actuator. The column was loaded at its tip and was cycled through both tensile and compressive loads. The load was applied in increasing levels based on the definition of the displacement ductility factor which is

$$\mu = \frac{\Delta_{actual}}{\Delta_{yield}} \qquad 10\text{-}1$$

Where Δ_y is the calculated yield displacement of the column tip. Once the yield displacement was determined, the specimen was loaded in a complete cycle at each level of the displacement ductility factor. The loading cycles were increased based on cyclic deflections referenced to the first lateral yield displacement, Δ_y.

There are two approaches to determining the cyclic loading sequence. The first approach is to cycle the load between prescribed deflection limits until failure or severe distress occur. The second method is to determine the number of cycles performed at a particular deflection level. The deflection levels increase until failure or severe distress occur. Another method to determine Δ_y was devised by Priestly (1987). This method

requires first loading the specimen to ¾ of the calculated lateral capacity of the specimen, V_p, and measuring the specimen lateral displacement. The measured displacement is considered as ¾ Δ_y of the specimen from which the yield displacement can be calculated. Subsequently, the specimen was subjected to a cyclic loading pattern consisting of increasing multiples of Δ_y to demonstrate the ductility and hysteretic behavior.

Once Δ_y was found, the loading was controlled by displacement increments to predetermined values of displacement ductility levels (i.e., multiples of Δ_y). Since the failure mechanism of DHFRP is much different than steel, one loading cycle at each displacement ductility level was used; these were at levels of $\mu = 1$ through $\mu = 8$.
The cyclic loading sequence used in the model tests is given in Table 10.2. This loading sequence was used for all model tests. This was done to keep the loading uniform for comparative purposes. The displacement-controlled loading sequence is shown in Figure 10.29.

Six small-scale model DHFRP columns were tested. A companion model steel column designed for the same moment capacity was tested. Three of the columns were tested without axial load to get the general hysteretic behavior and to optimize the test setup. The final three columns were tested at axial load levels of $0.05 f'_c A_g$, $0.1 f'_c A_g$, and $0.2 f'_c A_g$. These corresponded to levels of low to moderate axial load.

Table 10.1: Axial Load Values Used in Small-Scale DHFRP R/C Column Tests.

Axial Load Level	Load Value, lb (kN)
$0.05\,f'_c\,A_g$	450 (2.0)
$0.1\,f'_c\,A_g$	900 (4.0)
$0.2\,f'_c\,A_g$	1800 (8.0)

Table 10.2: Lateral Loading Sequence Used for Small-Scale DHFRP Column Tests.

Displacement sequence	Displacement values, in (mm)
0.2 Δ_y	± 0.0384 (0.975)
0.4 Δ_y	± 0.0767 (1.948)
0.6 Δ_y	± 0.1151 (2.924)
0.8 Δ_y	± 0.1534 (3.896)
1 Δ_y	± 0.1918 (4.872)
2 Δ_y	± 0.3835 (9.74)
2.5 Δ_y	± 0.4795 (12.18)
3 Δ_y	± 0.5753 (14.61)
3.5 Δ_y	± 0.6713 (17.05)
4 Δ_y	± 0.7671 (19.48)
5 Δ_y	± 0.959 (24.36)
6 Δ_y	± 1.1506 (29.23)
8 Δ_y	± 1.5342 (38.97)

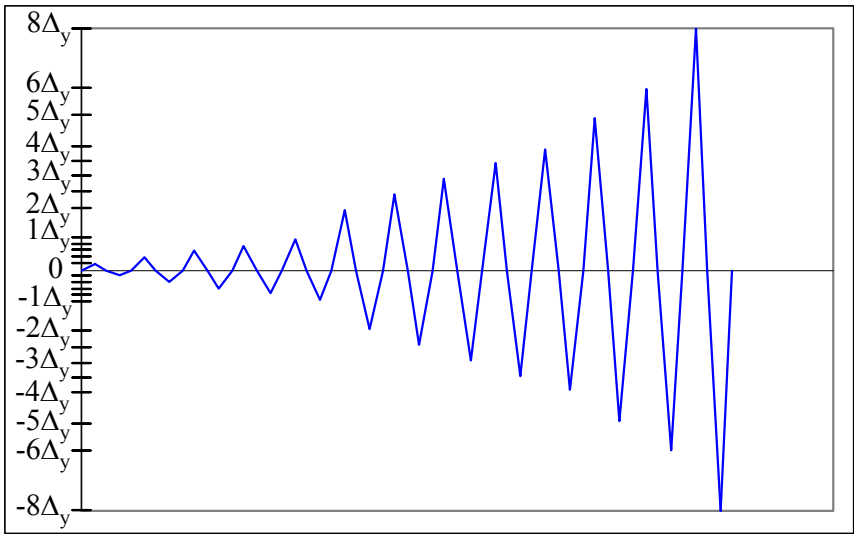

Figure 10.29: Displacement Loading Sequence for Model Columns.

10.3 Results

The results from the small-scale model column tests are presented in two forms. Qualitatively, the failure process was documented by observing the overall response of the columns including cracking patterns, overall displacements at increasing cycles, and plastic hinge formation. The results were presented quantitatively by the load-deflection, moment-rotation, and moment-curvature behaviors.

10.3.1 Qualitative Results of DHFRP Small-Scale Model Column Tests

Model column M-1 was a steel-reinforced column designed for the same moment capacity as the DHFRP columns. However, the column failed prematurely and the results were discarded. Only the stiffness comparison in the initial portion of the load-deflection curve was made between steel and DHFRP-reinforced columns.

Shown in Figures 10.30 through 10.33 is column M-2, reinforced with 5-mm DHFRP bars. This column had no axial load applied. Displacement levels were defined as the cycle number referenced on Δ_y. Figure 10.30 illustrates the cracking patterns at displacement level 4 (this is a level of 4 Δ_y). Shown in Figure 10.31 is the overall lateral displacement at increasing load cycles: displacements 1, 3, and 4 (low to moderate displacements). The plastic hinge formation is shown at high displacements in Figure 10.32, and the permanent inelastic strains or set of the column when unloaded after failure is shown in Figure 10.33.

Shown in Figure 10.34 is column M-3 (0.05 $f'_c A_g$ axial load) at low displacement levels 1 and 2. The plastic hinge formation is detailed for specimen M-3 at displacement levels 2, 3 and 4 (low to high displacement levels) in Figure 10.35.

The overall displacement behavior is well documented from low to high cycles in Figure 10.36 for column M-4 (no axial load). The plastic hinge formation was also shown in Figure 10.37 for displacement levels 2, 3, 5, and 6.

The behavior of column M-5 (0.1 $f'_c A_g$ axial load) is shown in Figures 10.38 through 10.41. The column cracking pattern is shown in Figure 10.38 for low displacements. The overall column displacements and cracking are shown at high displacements in Fig. 10.39. The plastic hinge formation is shown for displacement levels 2, 3, and 4 (Fig. 10.40), and the plastic hinge and column cracking for displacement level 4 are shown in Figure 10.41.

The behavior of column M-6 (0.2 $f'_c A_g$ axial load) is shown in Figures 10.42 through 10.45. The failure of the column and concrete deterioration was more dramatic since the axial load level was highest. The entire failed column showing final cracking

patterns and plastic hinge deterioration is shown in Figure 10.42. The plastic hinge formation at displacement levels 1, 2, and 3 are given in Figure 10.43. The failure of the plastic hinge is shown in Figure 10.44. Figure 10.45 shows the failed column base after all load was removed.

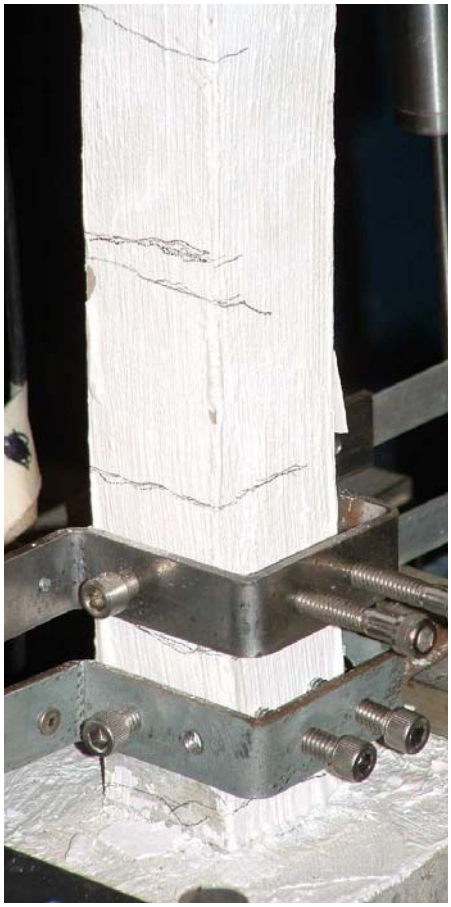

Figure 10.30: Column Cracking Pattern at Displacement Level 4 for Model Column Test M-2, 5-mm DHFRP Reinforced R/C Column.

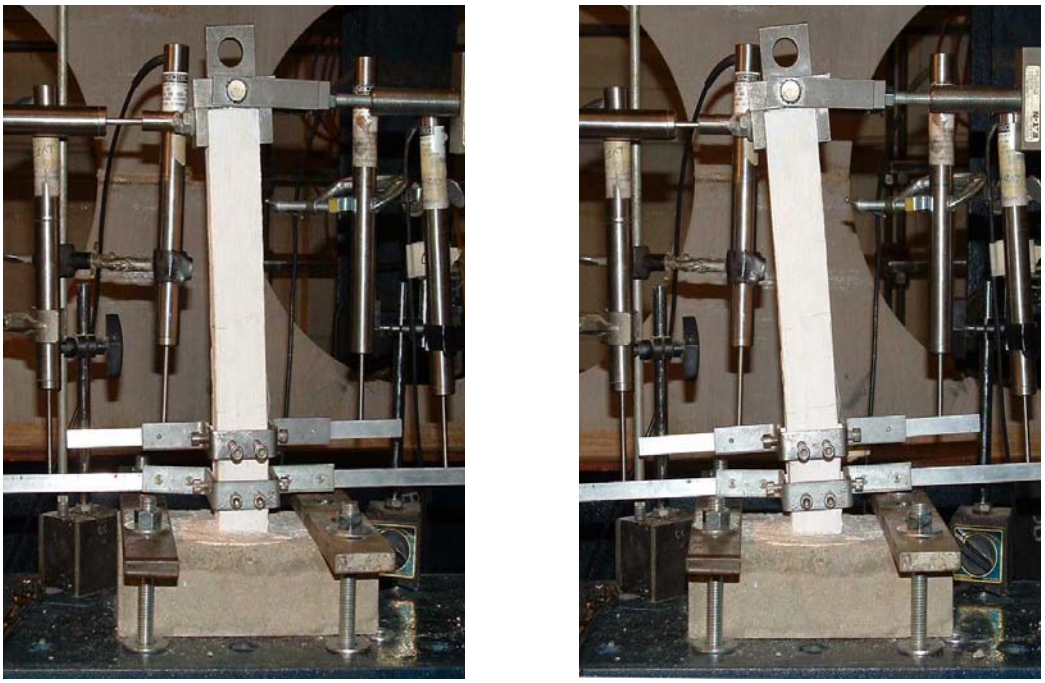

(a) (b)

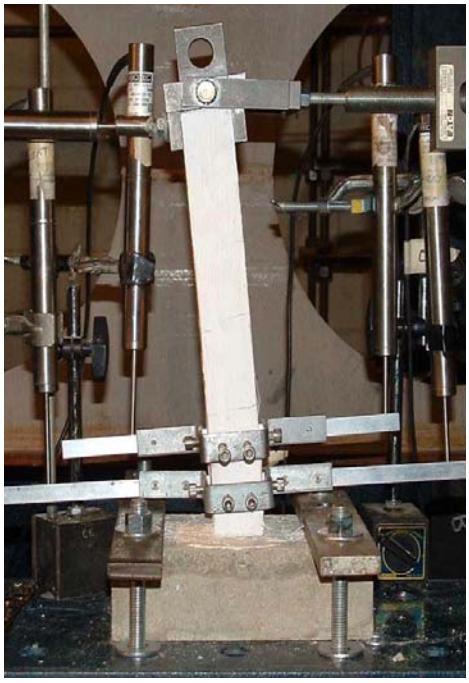

(c)

Figure 10.31: Displacement Levels (a) 1, (b) 3, and (c) 4 for Model Column Test M-2, 5-mm DHFRP Reinforced R/C Column.

Figure 10.32: Plastic Hinge Formation at Displacement Level 5 for Model Column Test M-2, 5-mm DHFRP Reinforced R/C Column.

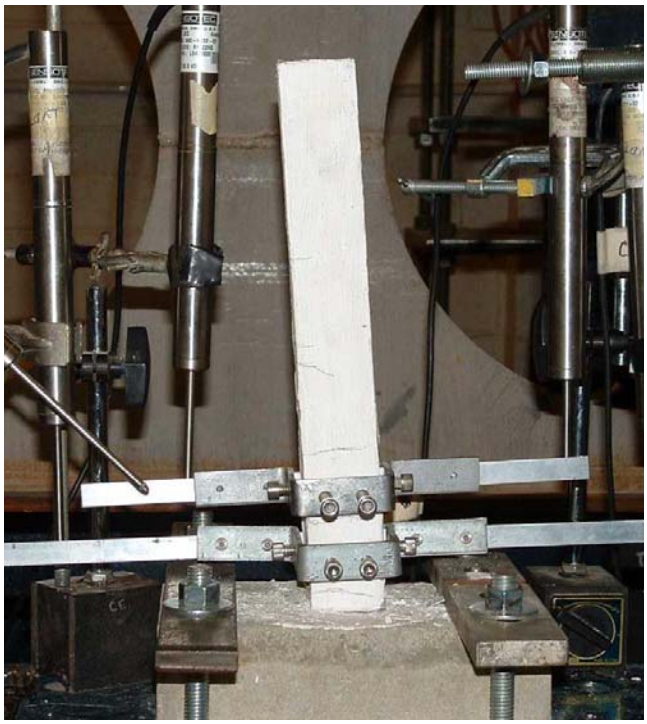

Figure 10.33: Permanent Inelastic Strains for Model Column Test M-2, 5-mm DHFRP Reinforced R/C Column.

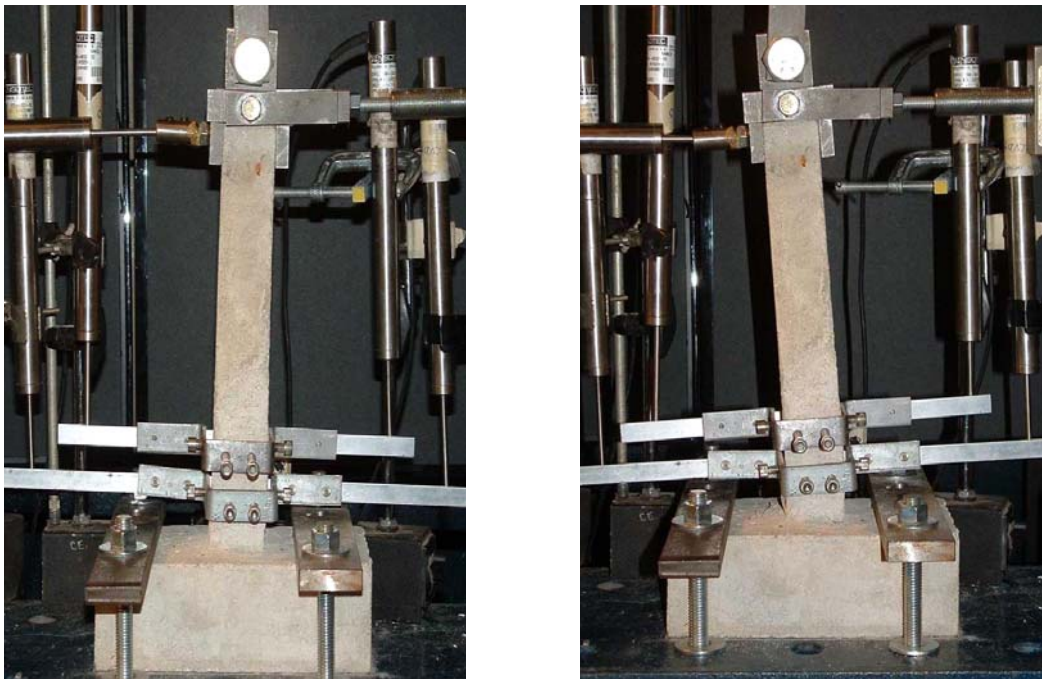

(a) (b)

Figure 10.34: Displacement Levels (a) 1 and (b) 2 for Model Column Test M-3, 5-mm DHFRP Reinforced R/C Column.

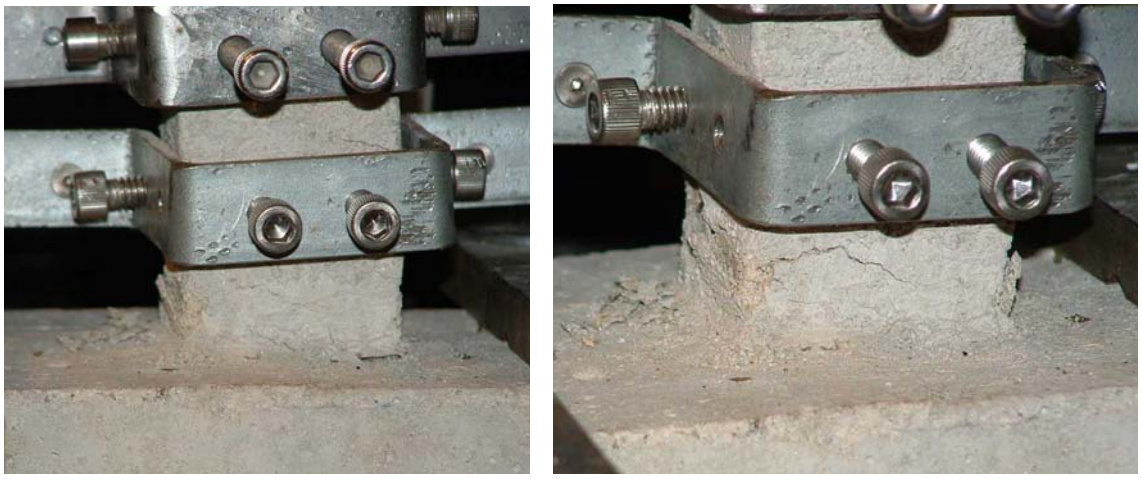

(a) (b)

Figure 10.35: Plastic Hinge Formation for Displacement Levels (a) 2, (b) 3, and (c) 4 for Model Column Test M-3, 5-mm DHFRP Reinforced R/C Column.

(c)

Figure 10.35 (continued)

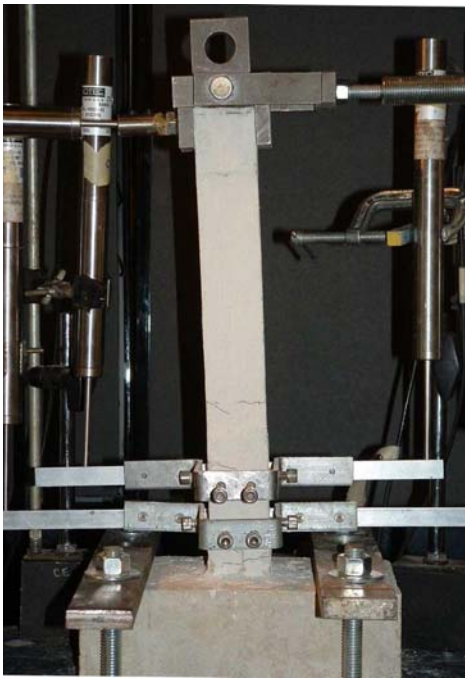

(a)

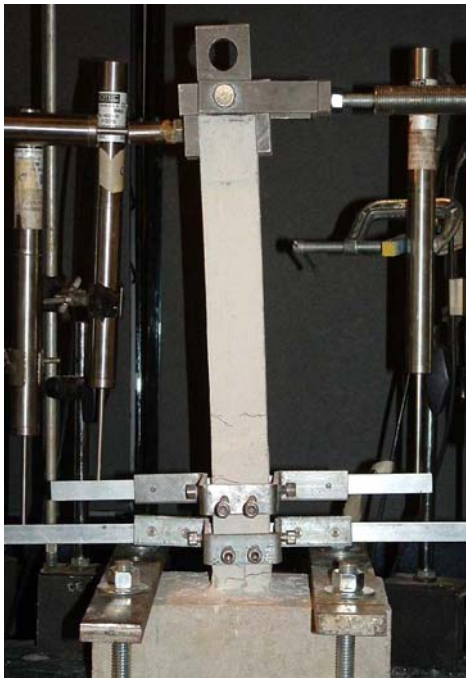

(b)

Figure 10.36: Displacement Levels (a) 2, (b) 3, (c) 4, (d), 5 and (e) 6 for Model Column Test M-4, 5-mm DHFRP Reinforced R/C Column.

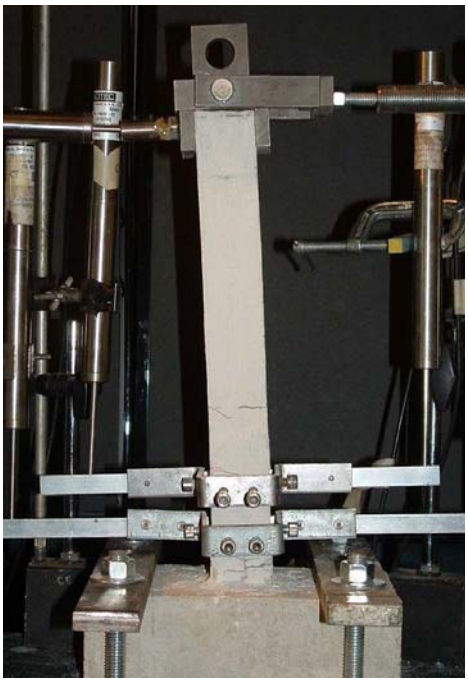

(c)

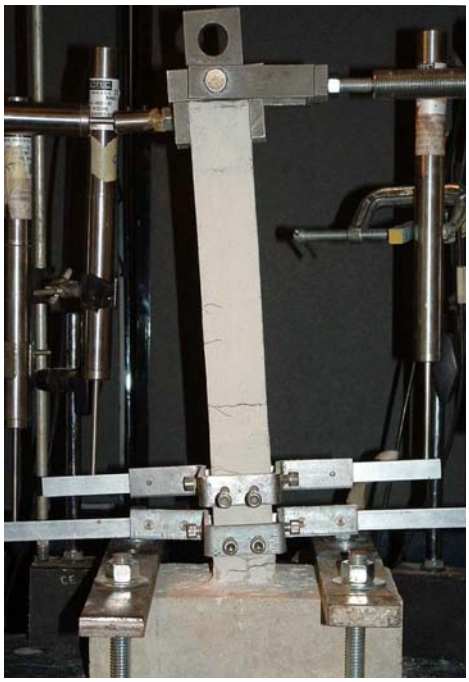

(d)

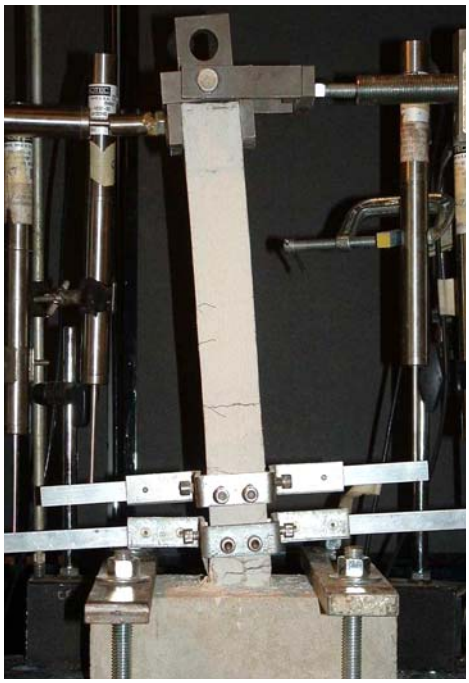

(e)

Figure 10.36 (continued)

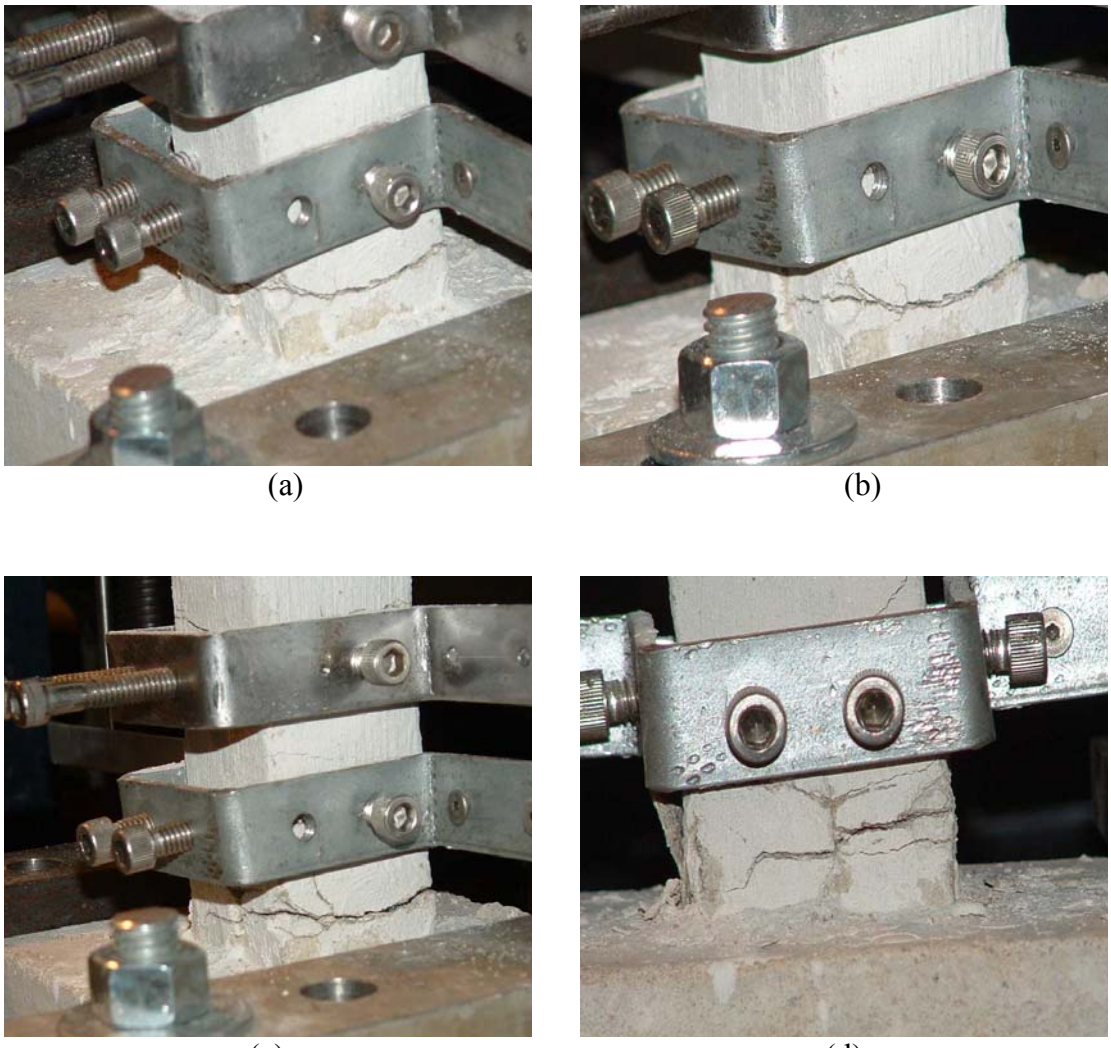

(a) (b)

(c) (d)

Figure 10.37: Plastic Hinge Formation for Displacement Levels (a) 2, (b) 3, (c) 5, and (d) 6 for Model Column Test M-4, 5-mm DHFRP Reinforced R/C Column.

Figure 10.38:Column Cracking at Displacement 2 for Model Column Test M-5, 5-mm DHFRP Reinforced R/C Column.

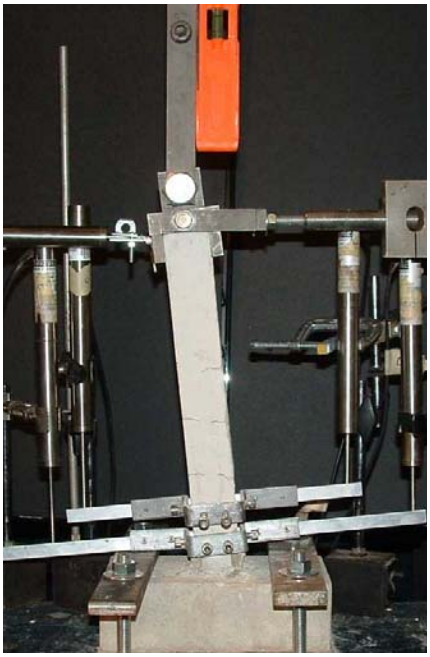

Figure 10.39:Overall Column Displacement and Cracking at Displ. Level 4 for Model Column Test M-5, 5-mm DHFRP Reinforced R/C Column.

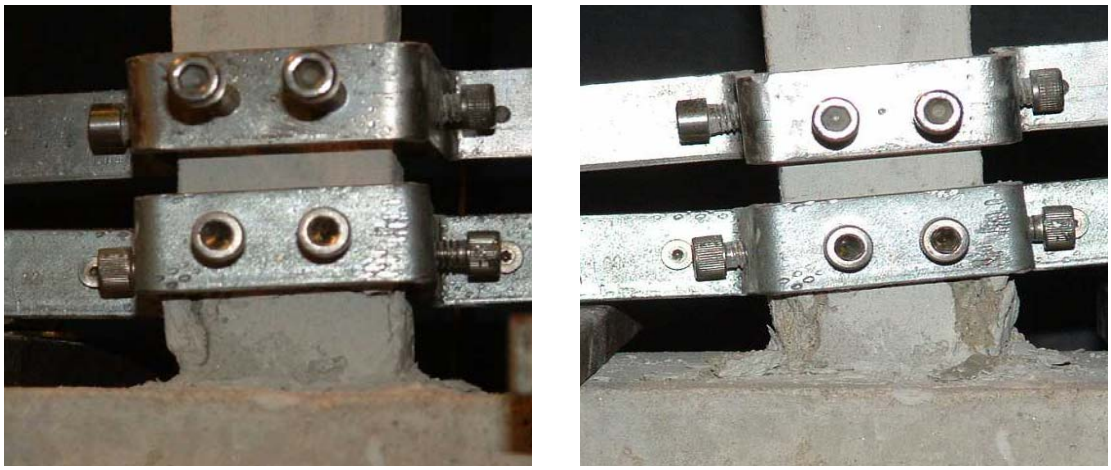

(a) (b)

(c)

Figure 10.40: Plastic Hinge Formation for Displacement Levels (a) 2, (b) 3, and (c) 4 for Model Column Test M-5, 5-mm DHFRP Reinforced R/C Column.

Figure 10.41:Column Cracking and Plastic Hinge for Displacement Level 4 for Model Column Test M-5, 5-mm DHFRP Reinforced R/C Column.

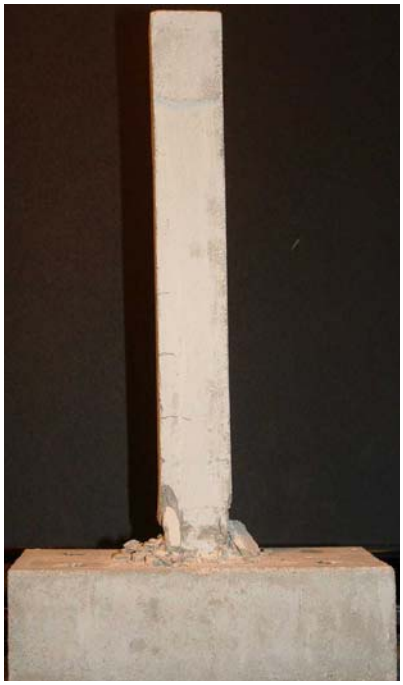

Figure 10.42:Failed Columns After Testing for Model Column Test M-6, 5-mm DHFRP Reinforced R/C Column.

(a)

(b)

(c)

Figure 10.43: Plastic Hinge Formation for Displacement Levels (a) 1, (b) 2, and (c) 3 for Model Column Test M-6, 5-mm DHFRP Reinforced R/C Column.

Figure 10.44:Plastic Hinge at Failure Showing Exposed Longitudinal Bars for Model Column Test M-6, 5-mm DHFRP Reinforced R/C Column.

Figure 10.45:Failed Column Base for Model Column Test M-6, 5-mm DHFRP Reinforced R/C Column.

10.3.2 Quantitative Results of DHFRP Small Model Column Tests

To quantitatively describe the behavior, three sets of data reduction were conducted for the small model column tests. The general cyclic load-displacements are shown in Figures 10.47 through 10.51. These demonstrate the overall hysteretic behavior of the model columns. The energy absorption of the reinforced section was obtained by finding the area under each cycle of the load-displacement curve and summing to get the total area. These results for the model column tests are presented in Table 10.3.

The area under each loop of the load-displacement curve was calculated using the method of coordinates. This method is regularly used in computing irregular land areas in surveying problems (McCormac, 1991). The total area of an enclosed area is given as

$$Area = \frac{1}{2}\sum x_i\left(-y_{i+1} + y_{i-1}\right) \qquad 10\text{-}2$$

where x is the i^{th} displacement data value and y_{i+1} and y_{i-1} are the load values before and after the i^{th} value, respectively. This gives the total area enclosed by all hysteresis loops of the load-deflection curve.

The moment-base rotation behavior is given in Figures 10.52 through 10.56. The moments include both the bending moment due to lateral load and the P-Δ moment due to axial load. The moment-curvature at the base is presented in Figures 10.57 through 10.61.

The rotation and curvature at the base were calculated from the four vertical LVDTs at the base (Fig. 10.23). Shown in Figure 10.46 are the relationships from the column setup and the corresponding strain profile to calculate base rotations, the location of the neutral axis, strains, and curvatures. This figure shows the relationships for the top set of LVDTs (*A* and *D*); however, similar relationships could be developed for the

bottom two LVDTs (*B* and *C*). From the figure, the base rotation is the slope of the arm and is given as

$$\theta = \frac{\Delta_A + \Delta_D}{L_{TOT}} = \frac{\Delta_{Ltop}}{kd} = \frac{\Delta_D}{L_D + kd} \qquad 10\text{-}3$$

From similar triangles, the depth of the neutral axis, *kd*, is defined as

$$kd = \frac{\Delta_D L_{TOT}}{\Delta_A + \Delta_D} - L_D \qquad 10\text{-}4$$

The deflection on the left column surface at the extreme fiber in compression is

$$\Delta_{Ltop} = \frac{\Delta_D kd}{L_D + kd} \qquad 10\text{-}5$$

The corresponding deflection on the right column surface at the extreme fiber in tension is

$$\Delta_{Rtop} = \Delta_A \left[\frac{L_{TOT} - kd - L_D - L_A}{L_{TOT} - kd - L_D} \right] \qquad 10\text{-}6$$

For the bottom two LVDTs, the equations would be identical except the subscripts *A* and *D* would be replaced by *B* and *C*, respectively. The corresponding bottom displacements are defined as $\Delta_{L\ bot}$ and $\Delta_{R\ bot}$. The strains at the left face (compression) and the right face (tension) are given as

$$\varepsilon_L = \frac{\Delta_{Ltop} - \Delta_{Lbot}}{l} \qquad \varepsilon_R = \frac{\Delta_{Rtop} - \Delta_{Rbot}}{l} \qquad 10\text{-}7 \text{ a, b}$$

where *l* is the vertical distance between the two sets of LVDTs. From the strain profile of Figure 10.46, the curvature at the critical section is given as

$$\varphi = \frac{\varepsilon_L + \varepsilon_R}{b} \qquad 10\text{-}8$$

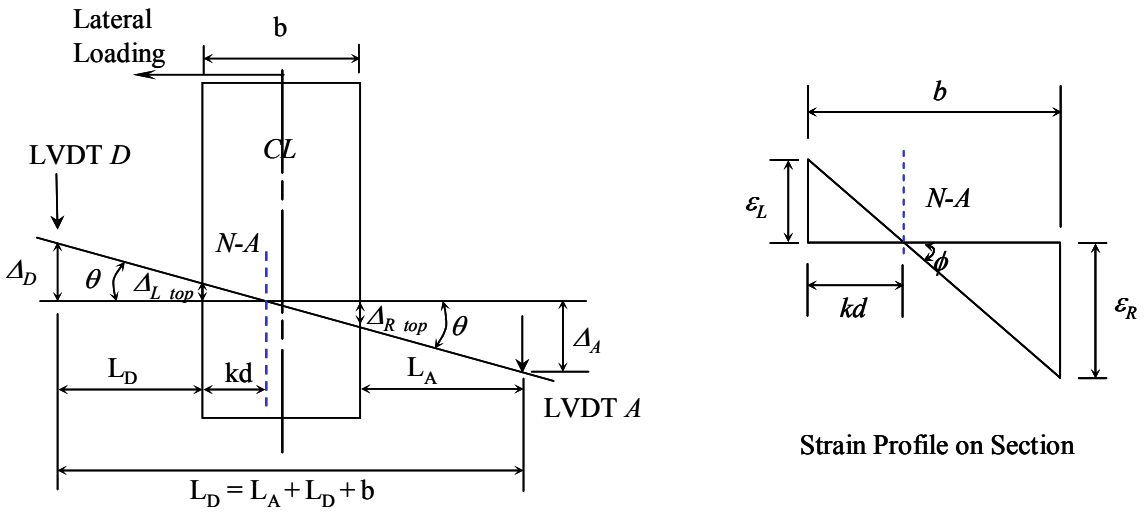

Figure 10.46: Experimental Determination of Base Rotation and Curvature.

The load-deflection behavior of model steel and DHFRP is compared in Figure 10.62. The experimental moment-rotation and moment-curvature behaviors are compared with the theoretical envelope curves in Figures 10.63 and 10.64, respectively.

Comparison of all test results is given in Table 10.4. Values of deflection, rotation, curvature, load, and moment at yield are listed. The drop in load at first yield is given. Also, the maximum values of the listed quantities are given for both compression and tension cycles. The ductility indices are listed in Table 10.5. These include definitions of ductility based on displacement, rotation, and curvature. Cylinders were tested to get the concrete compressive and tensile strengths. These results are tabulated in Table 10.6.

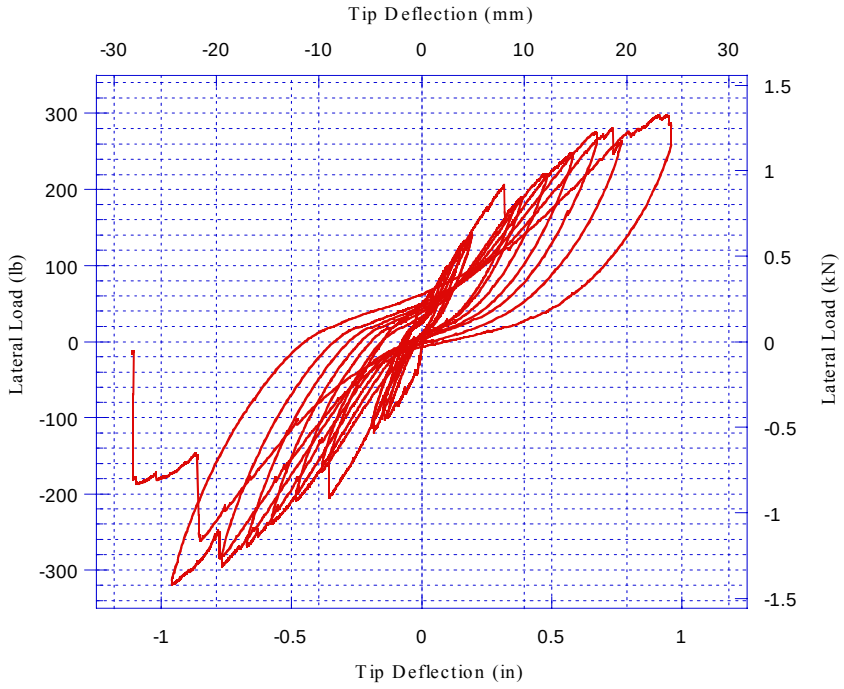

Figure 10.47: Hysteretic Load-Deflection Behavior of Test M-2, Small-Scale DHFRP R/C Col., $N = 0$.

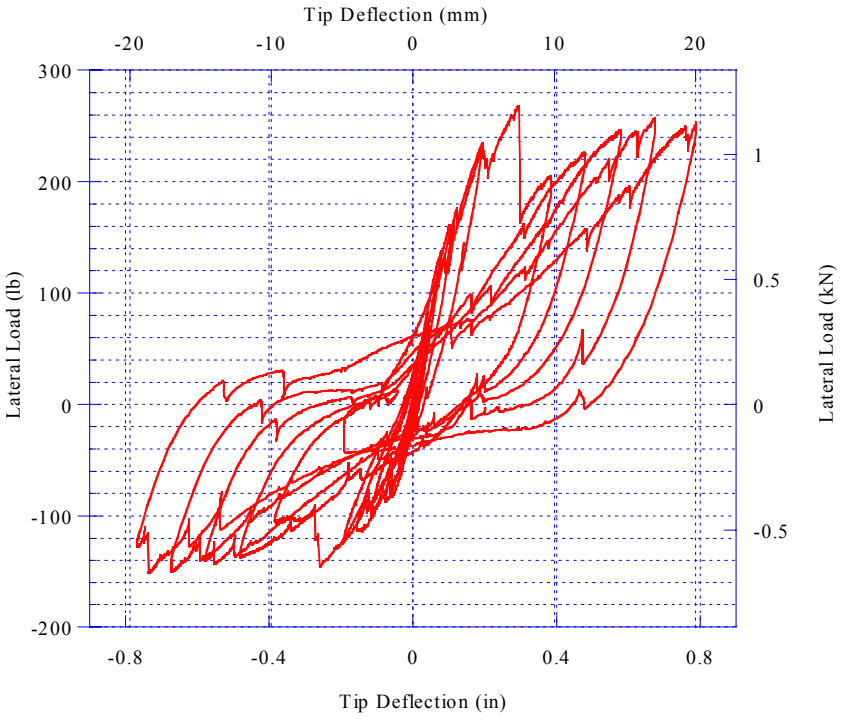

Figure 10.48: Hysteretic Load-Deflection Behavior of Test M-3, DHFRP R/C Col., $N = 0.05 f'_c A_g$.

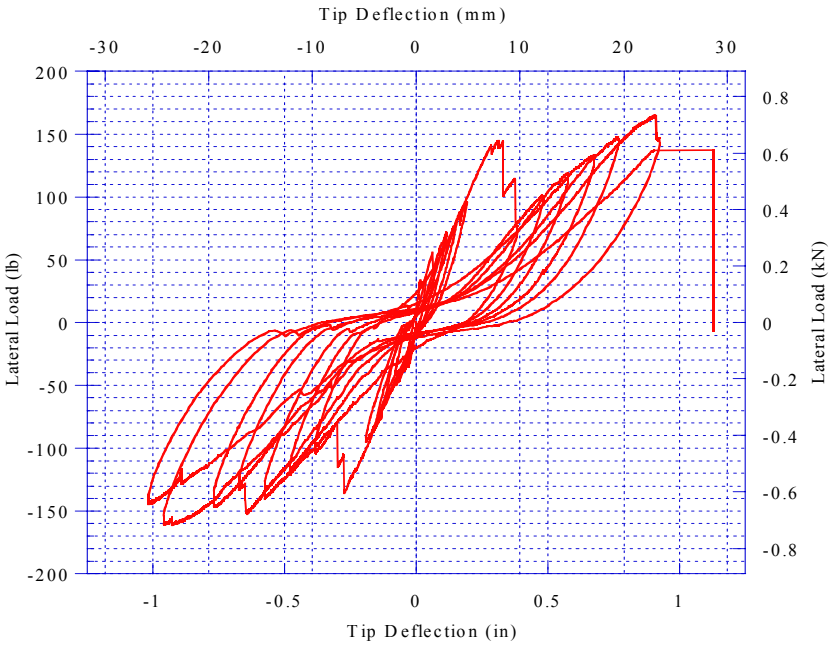

Figure 10.49: Hysteretic Load-Deflection Behavior of Test M-4, Small-Scale DHFRP R/C Col., $N = 0$.

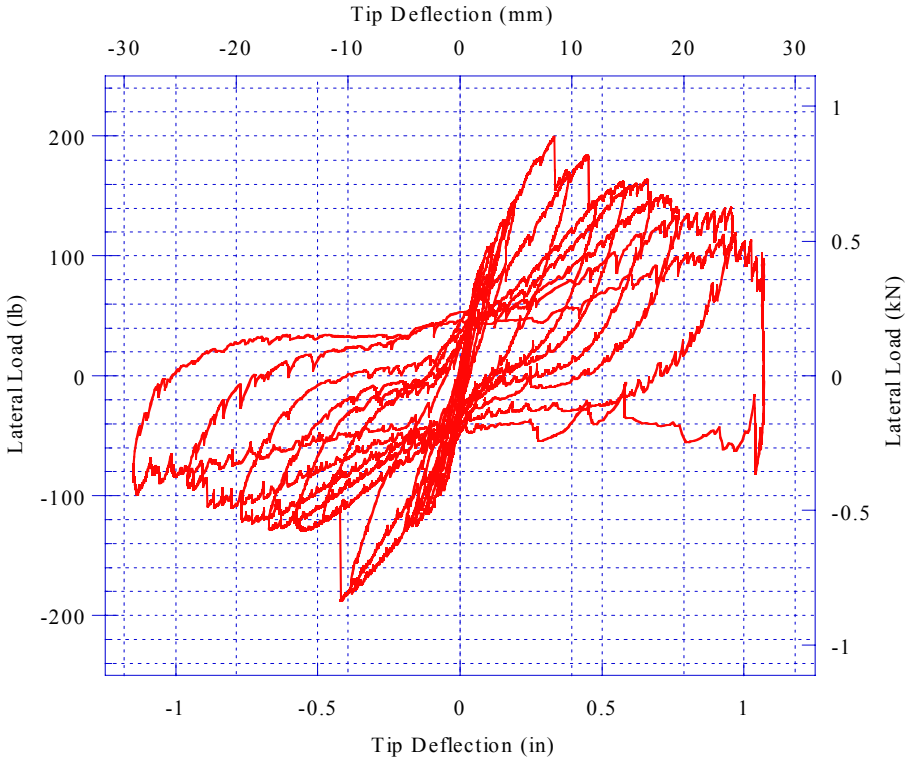

Figure 10.50: Load-Deflection Behavior of Test M-5, Small-Scale DHFRP R/C Col., $N = 0.1\, f'_c\, A_g$.

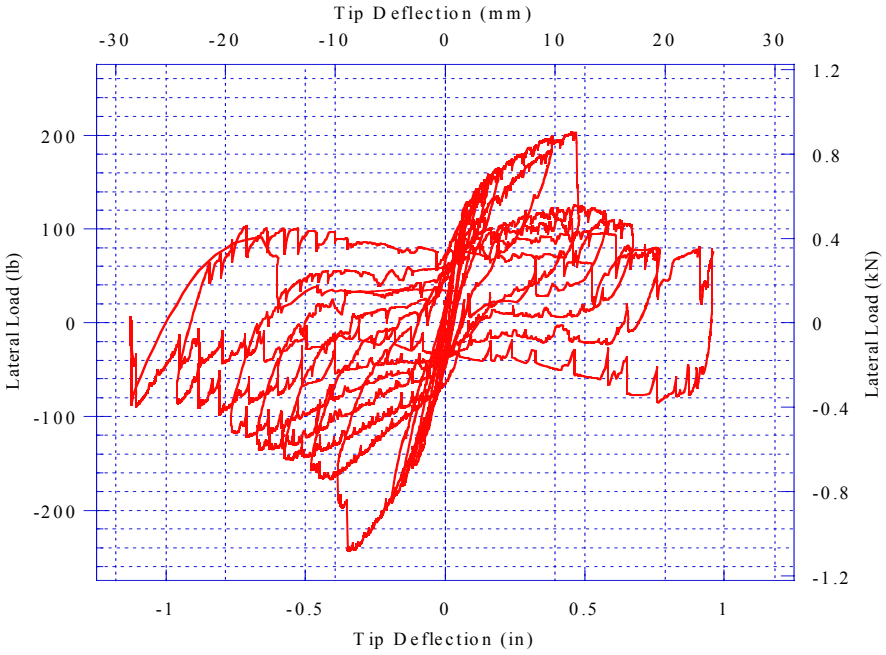

Figure 10.51: Load-Deflection Behavior of Test M-6, Small-Scale DHFRP R/C Col., $N = 0.2 f'_c A_g$.

Table 10.3: Energy Absorption Values for Small-Scale DHFRP Column Tests.

Specimen	Area, lb-in (N-m)	% of Max. Value
M-1	550.37 (62.18)	58.8
M-2	768.55 (86.83)	82.1
M-3	585.55 (66.16)	62.6
M-4	506.91 (57.27)	54.2
M-5	849.14 (95.94)	90.7
M-6	935.85 (105.73)	100

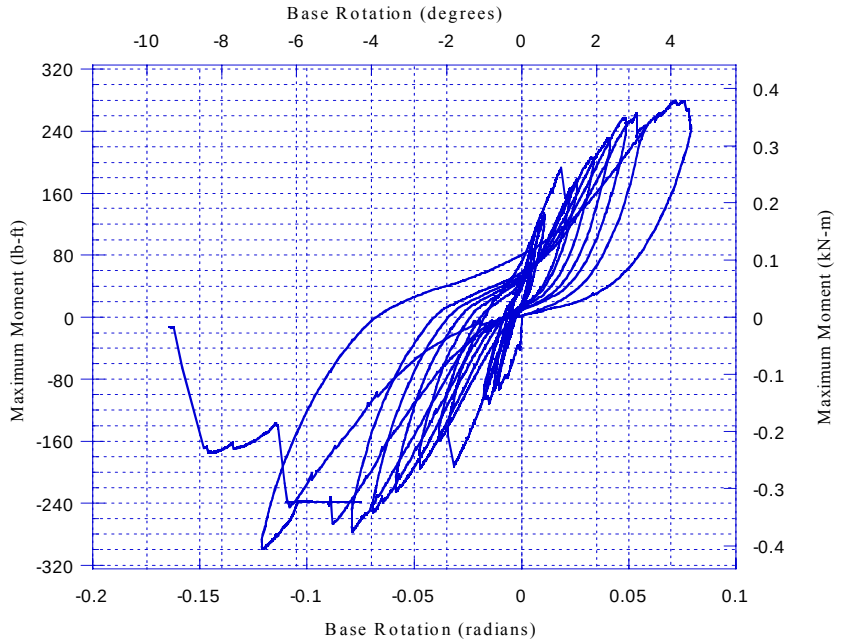

Figure 10.52: Moment-Base Rotation Behavior of Test M-2, Small-Scale DHFRP R/C Col., $N = 0$.

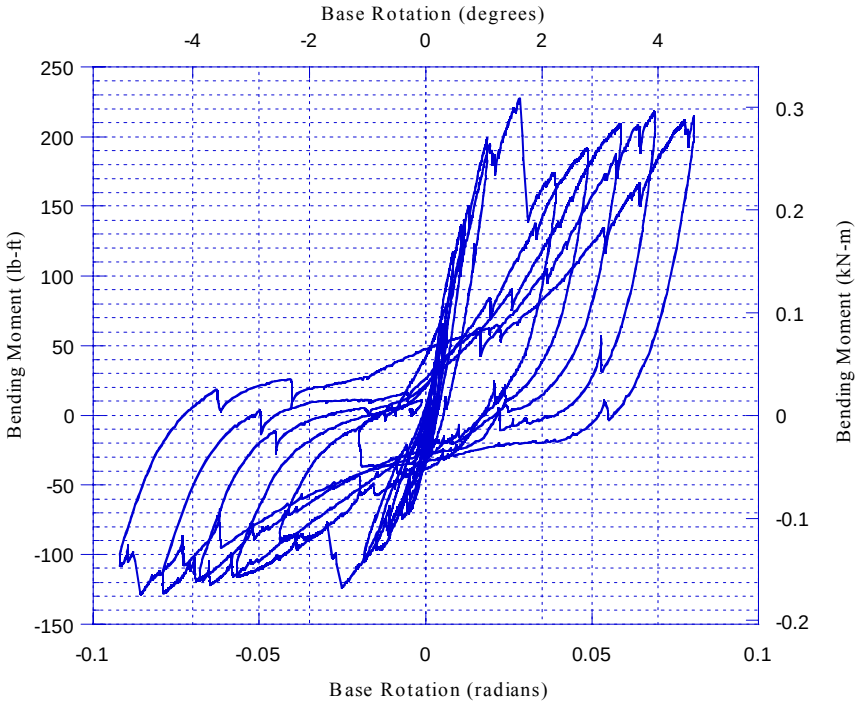

Figure 10.53: Moment-Base Rotation Behavior of Test M-3, Small-Scale DHFRP R/C Col., $N = 0.05 f'_c A_g$.

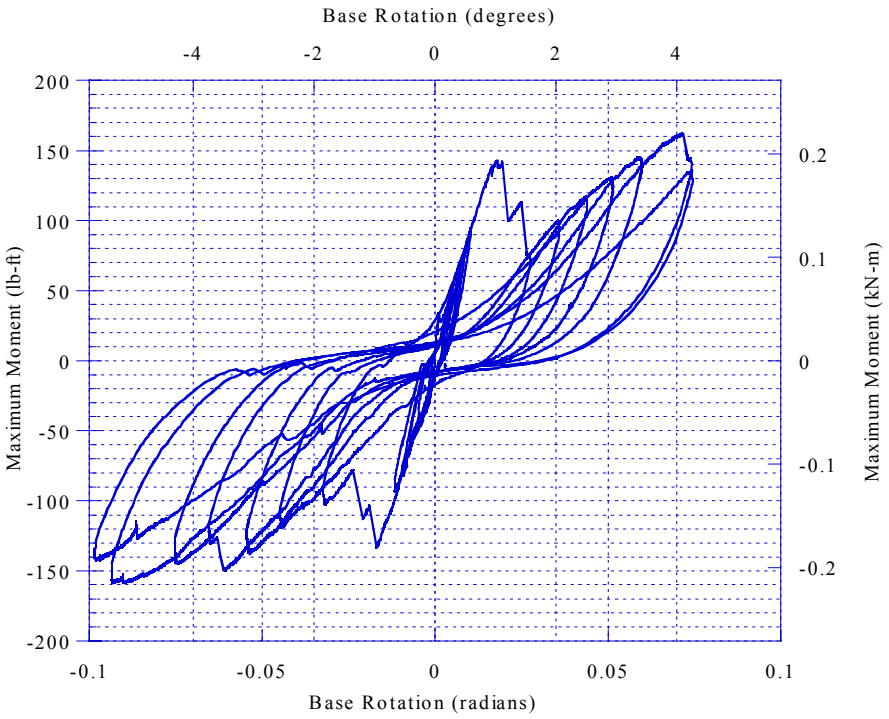

Figure 10.54: Moment-Base Rotation Behavior, Test M-4, Small-Scale DHFRP R/C Column, $N = 0$.

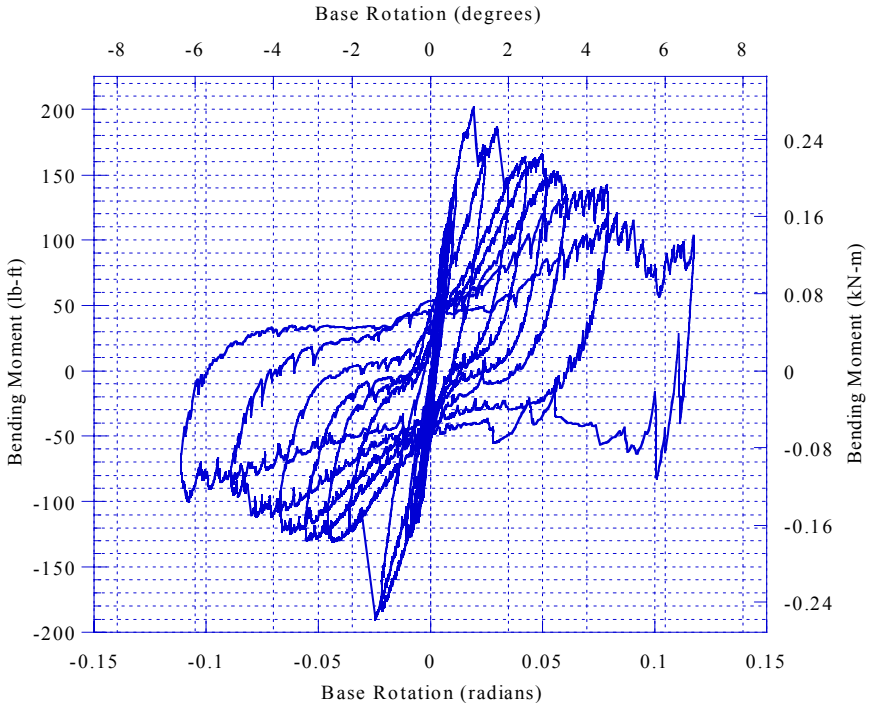

Figure 10.55: Moment-Base Rotation Behavior, Test M-5, Small-Scale DHFRP R/C Col., $N = 0.1\, f'_c\, A_g$.

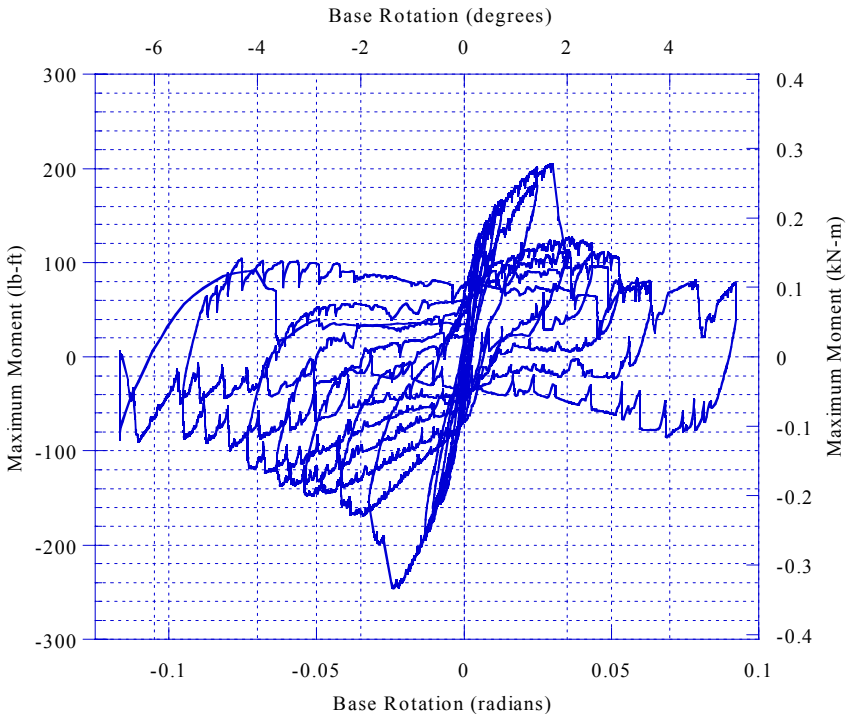

Figure 10.56: Moment-Base Rotation Behavior, Test M-6, Small-Scale DHFRP R/C Col., $N = 0.2 f'_c A_g$.

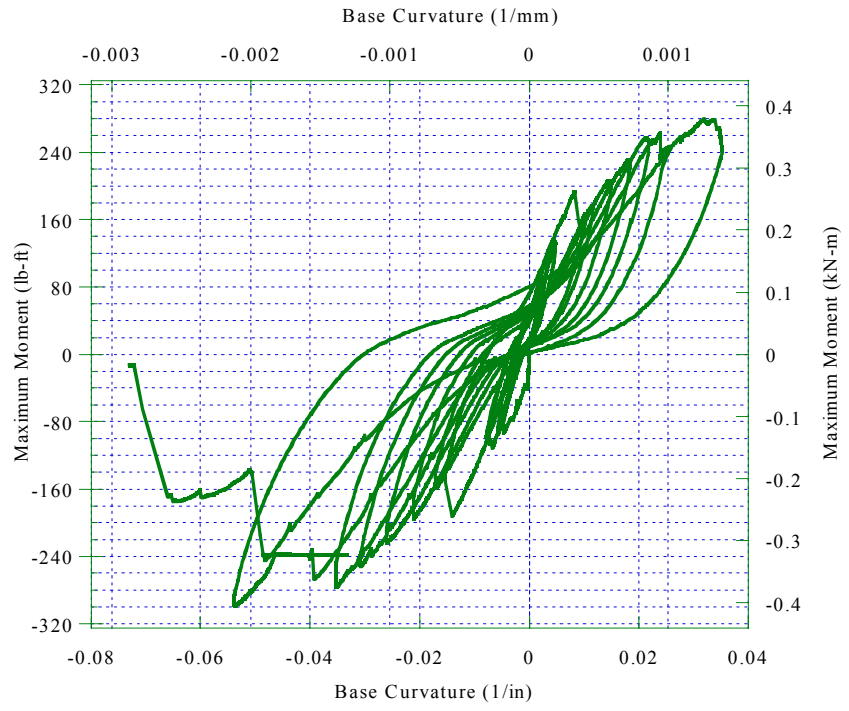

Figure 10.57: Moment-Curvature Behavior of Test M-2, Small-Scale DHFRP R/C Column, $N = 0$.

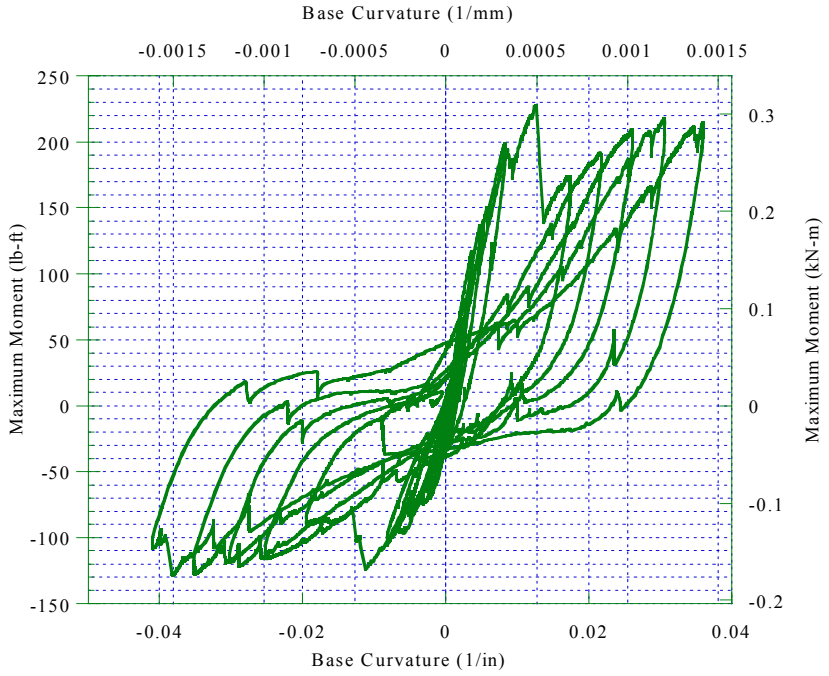

Figure 10.58: Moment-Curvature Behavior, Test M-3, Small-Scale DHFRP R/C Col., $N = 0.05\, f'_c\, A_g$.

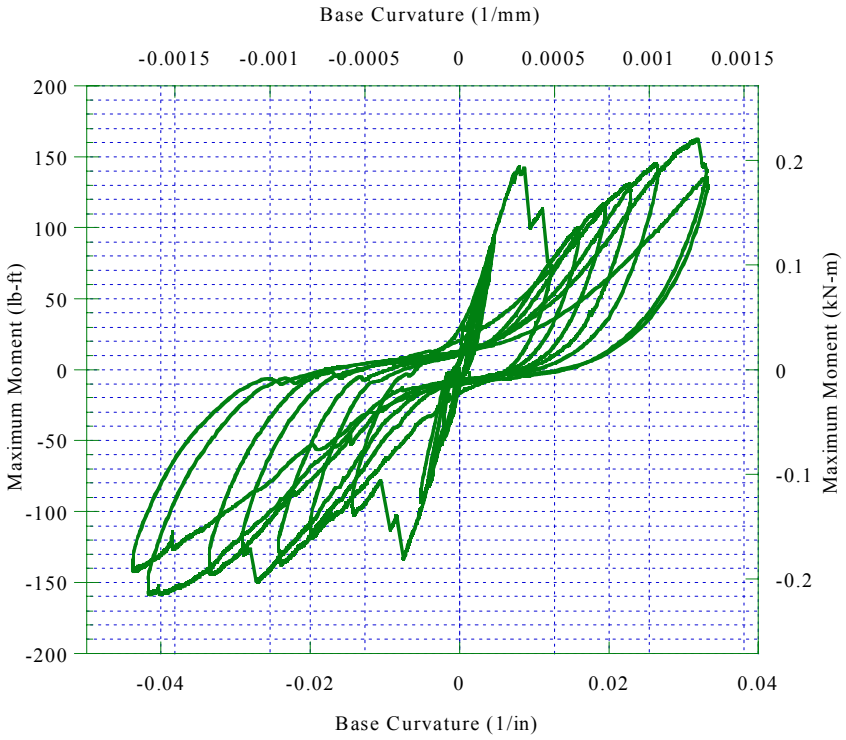

Figure 10.59: Moment-Curvature Behavior of Test M-4, Small-Scale DHFRP R/C Column, $N = 0$.

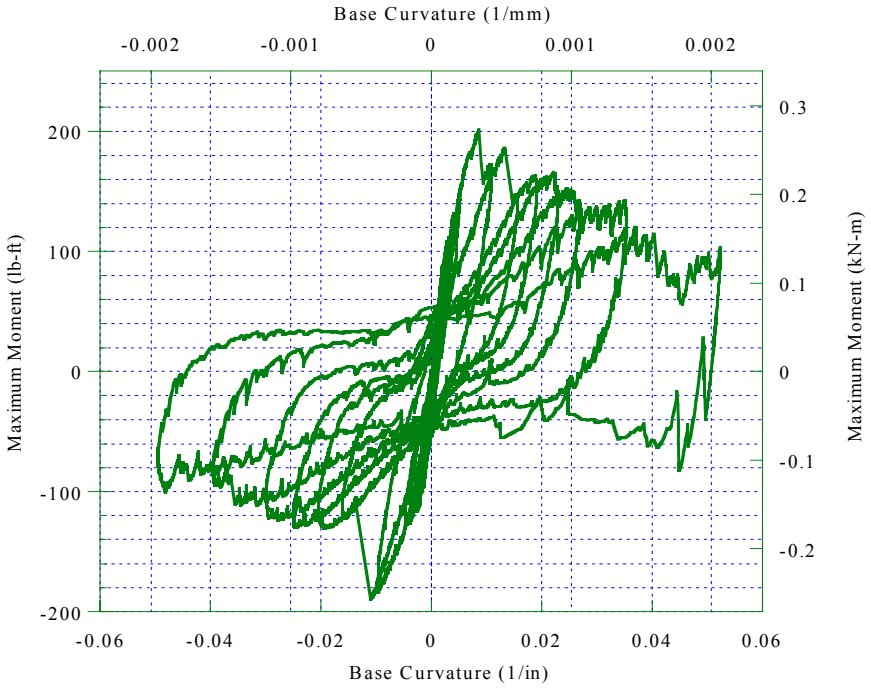

Figure 10.60: Moment-Curvature Behavior, Test M-5, Small-Scale DHFRP R/C Col., $N = 0.1\, f'_c\, A_g$.

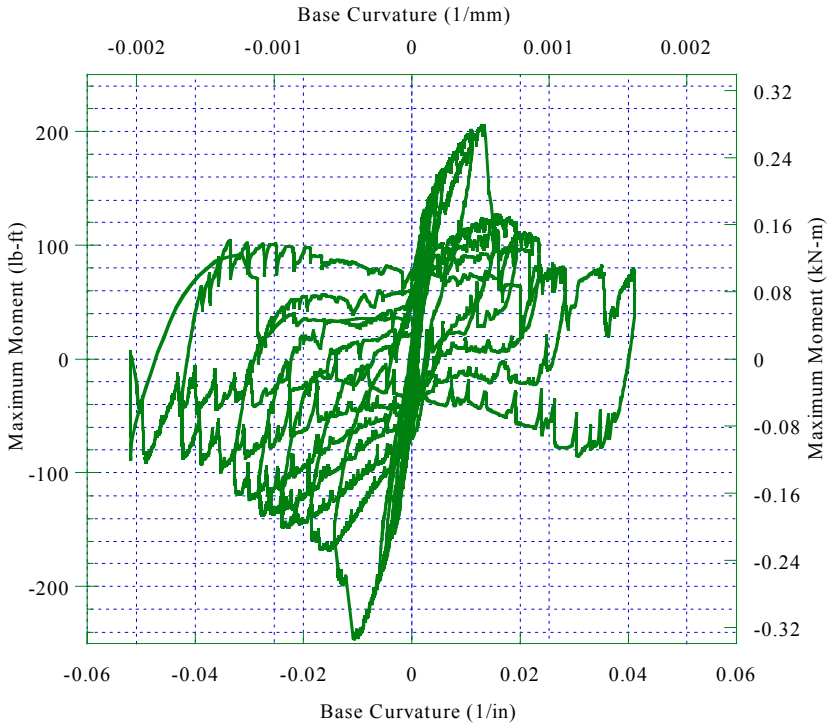

Figure 10.61: Moment-Curvature Behavior of Test M-6, Small-Scale DHFRP R/C Col., $N = 0.2\, f'_c\, A_g$.

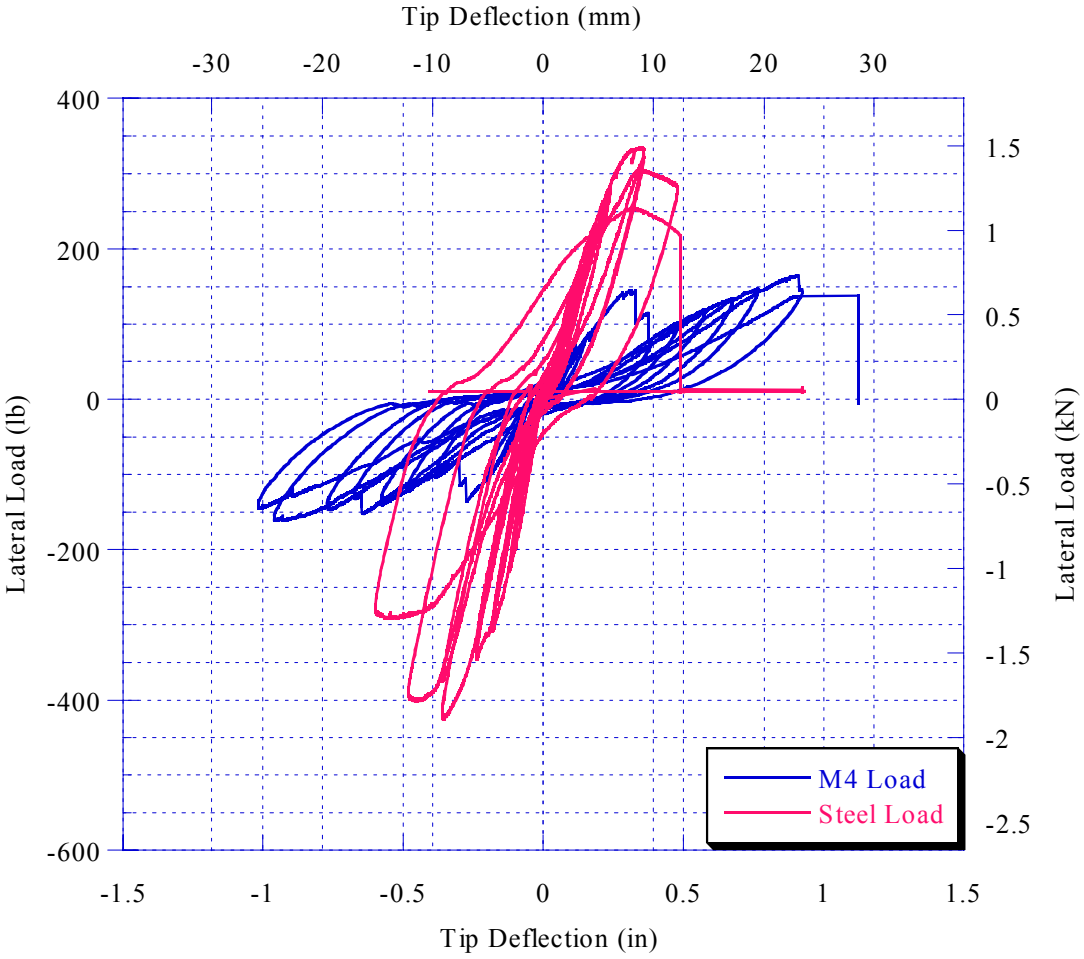

Figure 10.62: Comparison of Model Steel and DHFRP R/C Columns: Hysteretic Load-Deflection Behavior.

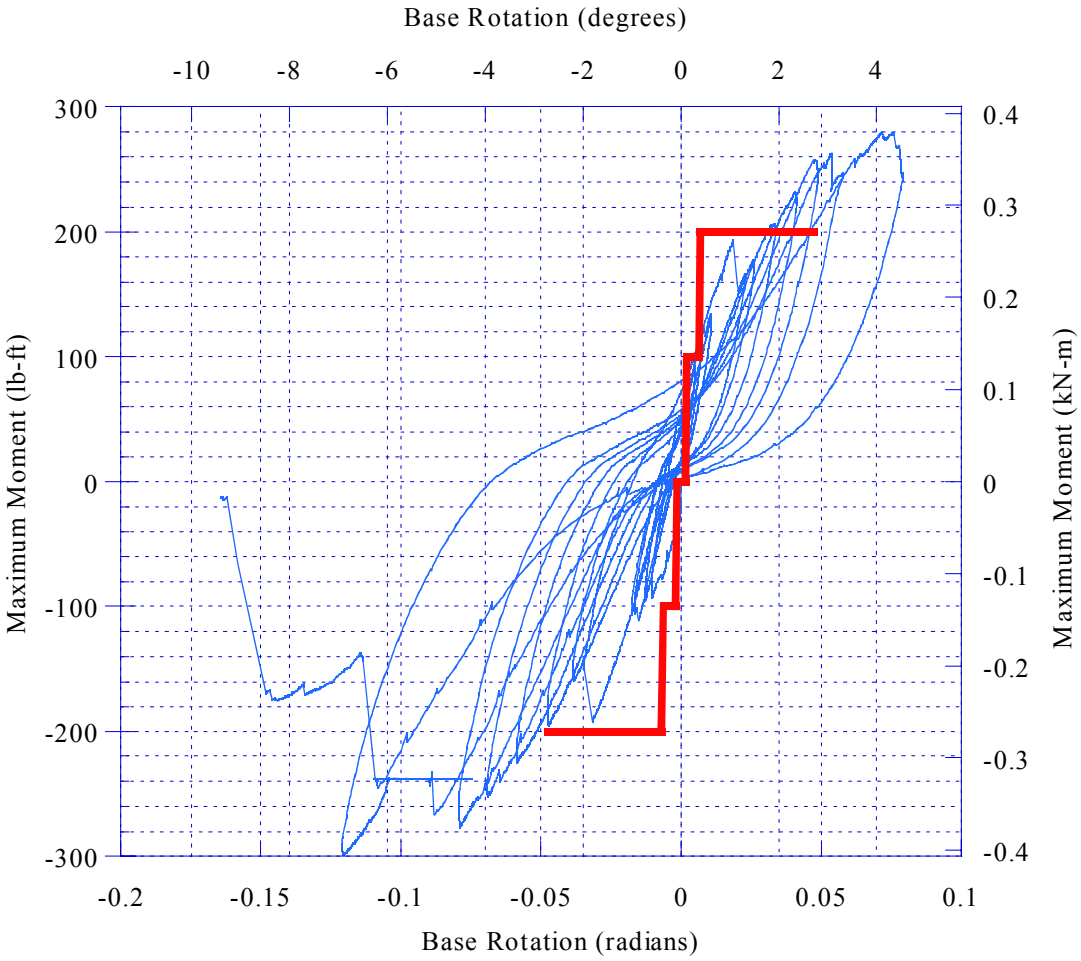

Figure 10.63: Comparison of Small-Scale DHFRP Moment-Rotation Behavior and Theoretical Envelope Curve.

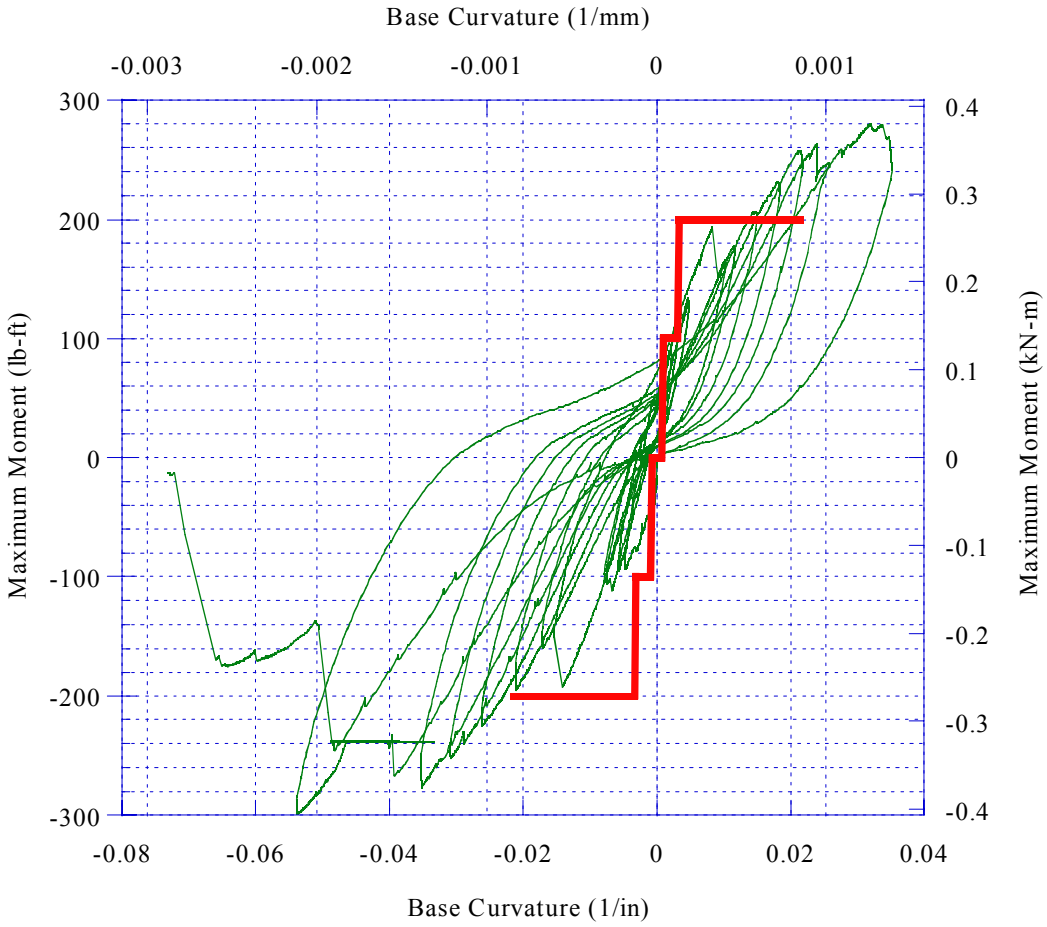

Figure 10.64: Comparison of Small-Scale DHFRP Moment-Rotation Behavior and Theoretical Envelope Curve.

Table 10.4: Results of Cyclic Tests for Small-Scale DHFRP and Steel R/C Columns.

Specimen	**Deflection (in)**	**Rotation (rad)**	**Curvature (1/in)**	**Lateral Load (lb)**	**Moment (lb-ft)**
M-1, yield	0.28	0.033	0.010	314.23	261.86
Maximums	0.93	0.098	0.023	334.74	278.95
Minimums	-0.60	-0.044	-0.031	-425.19	-354.33
M-2, yield	-0.36	-0.032	-0.014	204.84 → 160.58	-192.04
Maximums	0.96	0.079	0.035	298.24	279.60
Minimums	-1.11	-0.164	-0.073	-319.08	-299.14
M-3, yield	-0.26	-0.025	-0.011	145.01 → 125.89	-123.11
Maximums	0.79	0.081	0.036	267.67	227.24
Minimums	-0.77	-0.092	-0.041	-151.96	-129.01
M-4, yield	-0.27	-0.017	-0.008	133.58 → 107.1	-131.49
Maximums	1.13	0.075	0.033	165.22	162.64
Minimums	-1.02	-0.098	-0.044	-161.44	-158.92
M-5, yield	-0.33	0.019	0.009	199.32 → 171.19	201.39
Maximums	1.15	0.118	0.052	199.32	201.39
Minimums	-1.07	-0.111	-0.049	-188.21	-190.17
M-6, yield	-0.35	-0.024	-0.011	241.73 → 194.55	-244.25
Maximums	0.96	0.092	0.041	202.53	204.64
Minimums	-1.13	-0.117	-0.052	-243.82	-246.36

Table 10.5: Ductility Factors from Small-Scale DHFRP and Steel R/C Columns.

Specimen	$\mu_\Delta = \Delta_u / \Delta_y$	$\mu_\theta = \theta_u / \theta_y$	$\mu_\phi = \phi_u / \phi_y$
M-1*	3.37	2.98	3.13
M-2	3.13	5.19	5.18
M-3	3.04	3.65	3.69
M-4	4.12	5.23	5.79
M-5	3.47	5.85	6.08
M-6	3.23	4.50	4.79

Table 10.6: Compressive and Tensile Strength of Concrete Used for Small-Scale DHFRP R/C Columns.

	1" x 2" cylinders		2" x 4" cylinders	
Specimen	Comp. Strength f'_c psi (MPa)	Tensile Strength f_t, psi (MPa)	Comp. Strength f'_c psi (MPa)	Tensile Strength f_t, psi (MPa)
M-1	3842.9 (26.5)	1484.9 (10.2)	4607.0 (31.8)	792.6 (5.5)
M-2	5078.6 (35.0)	650.5 (4.5)	5390.3 (37.2)	393.5 (2.7)
M-3	3321.4 (22.9)	983.6 (6.8)	5056.6 (34.9)	880.9 (6.1)
M-4	4050 (27.9)	1212.8 (8.4)	5060.8 (34.9)	516.9 (3.6)
M-5	5978.6 (41.2)	1002.7 (6.9)	4600.3 (31.7)	743.7 (5.1)
M-6	4542.9 (31.3)	820.5 (5.7)	5265.5 (36.3)	762.5 (5.3)

10.4 Discussion

The column performance was based on three criteria:

1. Column moment capacity
2. Displacement, rotation, and curvature ductilities
3. Overall hysteresis behavior, degradation, and energy dissipation characteristics

Figures 10.30 through 10.33 showed column M-2, reinforced with 5-mm DHFRP bars. This column had no axial load applied. Displacement levels were defined as the cycle number referenced on Δ_y. Figure 10.30 showed the cracking patterns at displacement level 4. All cracks were flexural cracks. Throughout the test, no shear cracking occurred. Shown in Figure 10.31 was the overall lateral displacement at increasing load cycles: displacements 1, 3, and 4 (low to moderate displacements). Significant inelastic deformation is evident in Fig. 10.31c with rotation about the plastic hinge. A close-up of the plastic hinge at displacement level 5 was shown in Figure 10.32, and the permanent inelastic strains or set of the column when unloaded after failure was

shown in Figure 10.33. Some elastic recovery occurred in the column when unloaded; however, significant permanent set remained as evident in Fig. 10.32.

Shown in Figure 10.34 was column M-3 (0.05 f'_c A_g axial load) at low displacement levels 1 and 2. The plastic hinge formation was detailed for specimen M-3 at displacement levels 2, 3 and 4 (low to high displacement levels) in Figure 10.35. At displacement level 4, spalling of the concrete cover occurred. This was more evident for columns with axial load.

The overall displacement behavior was well documented from low to high cycles in Figure 10.36 for column M-4 (no axial load). Fig. 10.36e shows significant inelastic deformation and plastic rotations about the base. The plastic hinge formation was also shown in Figure 10.37 for displacement levels 2, 3, 5, and 6. The hinge region at high displacements still had much less concrete cover spalling than for columns with axial load.

The behavior of column M-5 (0.1 f'_c A_g axial load) was shown in Figures 10.38 through 10.41. The column cracking pattern was shown in Figure 10.38 for low displacements. Again, cracking was limited to flexural cracking. The overall column displacements and cracking were shown at high displacements in Fig. 10.39. Significant inelastic deformation is evident in this figure. The amount of base rotation is evident by observing the rotation of the base LVDT mounting fixtures. The corresponding plastic hinge development was shown for displacement levels 2, 3, and 4 (Fig. 10.40), and the plastic hinge and column cracking for displacement level 4 were shown in Figure 10.41.

The behavior of column M-6 (0.2 f'_c A_g axial load) was shown in Figures 10.42 through 10.45. The failure of the column and concrete deterioration was more dramatic

since the axial load level was highest. The entire failed column showing final cracking patterns and plastic hinge deterioration was shown in Figure 10.42. Significant spalling of the concrete cover was evident in this figure. Large sections of concrete spalled from the center of each side, where the confinement provided by the rectangular hoops was the smallest. The plastic hinge formation at displacement levels 1, 2, and 3 were given in Figure 10.43. Figure 10.43c showed significant spalling and concrete deterioration of the column base. The failure of the plastic hinge was shown in Figure 10.44. At the end of the test, the cover concrete failed, thereby exposing the DHFRP longitudinal bars. Figure 10.45 showed the failed column base after all load was removed. At the plastic hinge, only the core concrete remained.

To qualitatively describe the behavior, three sets of data reduction were conducted for the model column tests. The general cyclic load-displacements were shown in Figures 10.47 through 10.51. These demonstrated the overall hysteretic behavior of the model columns. The energy absorption of the reinforced section was obtained by finding the area under each cycle of the load-displacement curve and summing to get the total area. These results for the model column tests were presented in Table 10.3. The hysteresis loops illustrate two key points. First, by having open loops versus linear behavior, the DHFRP bars showed significant energy absorption capability, unique when compared with most linear-elastic composite materials. Second, the ductility of the DHFRP was further quantified by this energy absorption capacity. This is particularly valuable in design and retrofit of reinforced concrete structures in regions of high seismicity where ductility design is used.

The hysteretic load-deflection behavior of column M-2 was shown in Fig. 10.47. This was a DHFRP R/C column tested without axial load. Symmetric hysteretic behavior was observed. A stable hysteresis was evident with little stiffness deterioration after initial cracking of the section. More pinching was evident than the steel R/C column. The energy absorbed by the column was 768.55 lb-in (86.83 N-m). This was 82.1% of the maximum energy absorbed by a small-scale column (M-6). The displacements at yield and failure were -0.36 in (9.14 mm) and -1.11 in (28.2 mm), respectively. The displacement ductility index was 3.13.

The hysteretic load-deflection behavior of column M-3 was shown in Fig. 10.48. This was a DHFRP R/C column tested with low axial load. Less pinching was evident for a column with a low level of axial load than no axial load. This was due to the fact that the concrete remained in compression due to the axial compression force, thereby suppressing the opening of tension cracks. This enabled the column to absorb more energy. The energy absorbed by the column was 585.55 lb-in (66.16 N-m). This was 62.6% of the maximum energy absorbed. The stiffness degradation was moderate with low axial load due to cracking and hinge deterioration. The displacement ductility index was 3.04.

The hysteretic load-deflection behavior of column M-4 was shown in Fig. 10.49. This column had no axial load. More pinching was again evident for a column without axial load. However, the hysteresis was stable with increasing load cycles without significant stiffness deterioration. The energy absorbed by the column was 506.91 lb-in (57.27 N-m). This was 54.2% of the maximum energy absorbed. Therefore, the column without axial load had lower energy absorption. The displacement ductility index was

4.12. This was due to the fact that the DHFRP yielded at a lower load value than the other specimens.

The hysteretic behavior of column M-5 was shown in Fig. 10.50. This column had moderate axial load. At higher displacement levels, much less pinching was evident than for low or no axial force levels. This increased the compression in the concrete, thereby suppressing the opening of tension cracks. The energy absorbed by the column was 849.14 lb-in (95.94 N-m). This was 90.7% of the maximum energy absorbed. This is much greater than for no axial force. However, the stiffness degradation was more severe than for columns with no axial load. This was caused by the P-Δ moments due to the axial load and large inelastic displacements. As the load cycles increased, the P-Δ moments significantly influenced the overall column behavior. Therefore, the stiffness decreased at high displacement levels with large values of P-Δ moments. The displacement ductility index was 3.47.

The hysteretic behavior of column M-6 was shown in Fig. 10.51. This column had high axial load. At higher displacement levels, much less pinching was evident than for low or no axial force levels. The energy absorbed by the column was 935.85 lb-in (105.73 N-m). This was the maximum energy absorbed, thereby verifying the increased energy absorption for columns with moderate axial load. However, the stiffness degradation was the most severe with large axial load. This was caused by the P-Δ moments due to the axial load and large inelastic displacements. The displacement ductility index was 3.23.

The moment-base rotation behavior was given in Figures 10.52 through 10.56. The moments included both the bending moment due to lateral load and the P-Δ moment

due to axial load. The overall trend of the moment-rotation was very similar to the load-deflection behavior. The same trends regarding pinching, stiffness degradation, and *P-Δ* behavior was similar for the moment-rotation behavior. At the maximum of large displacement cycles, the *P-Δ* moment dominated the value of the total moment because of the large magnitude of the axial load compared to the lateral load. The maximum moments ranged from -158.92 lb-ft (0.22 kN-m) to 354.33 lb-ft (0.48 kN-m). The maximum rotations ranged from -0.092 radians to 0.12 radians. The rotation ductility indices ranged from 2.98 to 5.85. The largest value of rotational ductility was column M-5 which had the largest energy absorption.

The moment-curvature at the base was presented in Figures 10.57 through 10.61. The moments included both the bending moment due to lateral load and the *P-Δ* moment due to axial load. The overall trend of the moment-curvature was very similar to the load-deflection behavior. At the maximum of large displacement cycles, the *P-Δ* moment dominated the value of the total moment because of the large magnitude of the axial load compared to the lateral load. The maximum moments ranged from -158.92 lb-ft (0.22 kN-m) to 354.33 lb-ft (0.48 kN-m). The maximum curvatures ranged from -0.031 1/in to -0.073 1/in. The values of curvature represent the gradient of the strain profile at that section. The curvature ductility indices ranged from 3.13 (M-1, steel) to 6.08 (M-5, DHFRP).

The load-deflection behavior of model steel and DHFRP was compared in Figure 9.116. The steel-reinforced column has much higher initial stiffness which was expected since the modulus is approximately 2.6 times greater. The overall displacement capacity of the 5-mm DHFRP bars was greater than steel wire used as longitudinal bars.

The experimental moment-rotation and moment curvature were compared with the theoretical envelope curves in Figures 9.117 and 9.118, respectively. Even though the theoretical curves were for monotonic loading, they provided the loading envelope for the experimental cyclic data. Good correlation between initial stiffness and rotation and curvature for both theoretical and experimental curves exist. Specimen M-2 was stiffer than M-4, and therefore, would follow the initial stiffness of the theoretical curves. The experimental rotation and curvature was greater than the theoretical. The theoretical curves had a limit on the concrete strain capacity which limited the ultimate rotation and curvature.

Based on the results of the small-scale models, the DHFRP provided sufficient column moment capacity well into the inelastic range, significant displacement ductility, and a stable hysteretic behavior.

CHAPTER 11. EXPERIMENTAL PROGRAM OF LARGE-SCALE MODEL R/C BEAM-COLUMNS WITH PROTOTYPE DHFRP BARS

Large-scale model column specimens were tested based on the results of the small-scale model tests. The columns were designed based on similitude calculations from the model specimens and reinforced with four 10-mm diameter longitudinal DHFRP bars. The test setup was based on the optimized setup for the model tests. The sample preparation, test setup, and results are discussed.

11.1 Sample Preparation

The preparation of the large-scale model columns was similar to that of the model columns. Shown in Figure 11.1 is the construction of the footing reinforcement. Number three and number four steel rebars were used to reinforce the column base. Figure 11.1 shows the guide form used to build the footing cages. Nails were placed in the form to keep the bar placement accurate and the reinforcing mat square. Figure 11.2 shows one layer of footing reinforcement. The reinforcing cage was tied together using Number 18 (0.0478 in, 1.21-mm dia.) annealed steel wire. Figure 11.3 shows the final footing steel reinforcement cage. Based on design, two layers of steel reinforcement was sufficient to prevent failure of the column footing.

Figure 11.1: Guide Form for Building Footing Reinforcing Cage for Large-Scale Model Columns.

Figure 11.2: Building of Footing Reinforcement Layer for Large-Scale Model Columns.

Figure 11.3: Finished Footing Reinforcement Cage for Large-Scale Model Columns.

Next was the construction of the steel hoops. The same steel wire was used as in the beam tests (Chapter 8). This steel had a yield strength of 41.2 ksi (284.1 MPa) and had a diameter of 0.125 in (3.18 mm). The stirrups were bent by hand using a wood jig similar to that used for the beam construction. Once the stirrups were made, the reinforcing cages were constructed. Shown in Figure 11.4 is a guide to construct the reinforcing cages. This guide consisted of a series of nails located in the location of the stirrups placed in a strip of wood. This kept the longitudinal bars parallel and also kept the positioning of the hoops consistent and normal to the axis of the DHFRP longitudinal bars. Shown in Figure 11.5 is the finished reinforcing cage for large-scale model columns. Chairs made of steel wire were placed at the ends and middle of the cage as shown in the figure for proper placement of the cage in the form. Figure 11.6 shows the variation in stirrup spacing. The spacing was designed according to the seismic design provisions of ACI 318-02. The stirrups were spaced 0.75” (19.1 mm) on center in the

plastic hinge region and 1.125” (28.58 mm) on center along the length of the column away from the hinge region. A cross section of the reinforcing cage is shown in Figure 11.7 showing the longitudinal bars and the stirrups. 135° hooks were used, according to the seismic provisions provided in ACI 318-02.

Figure 11.4: Guide Form for Building Longitudinal Reinforcing Cages for Large-Scale Model Columns.

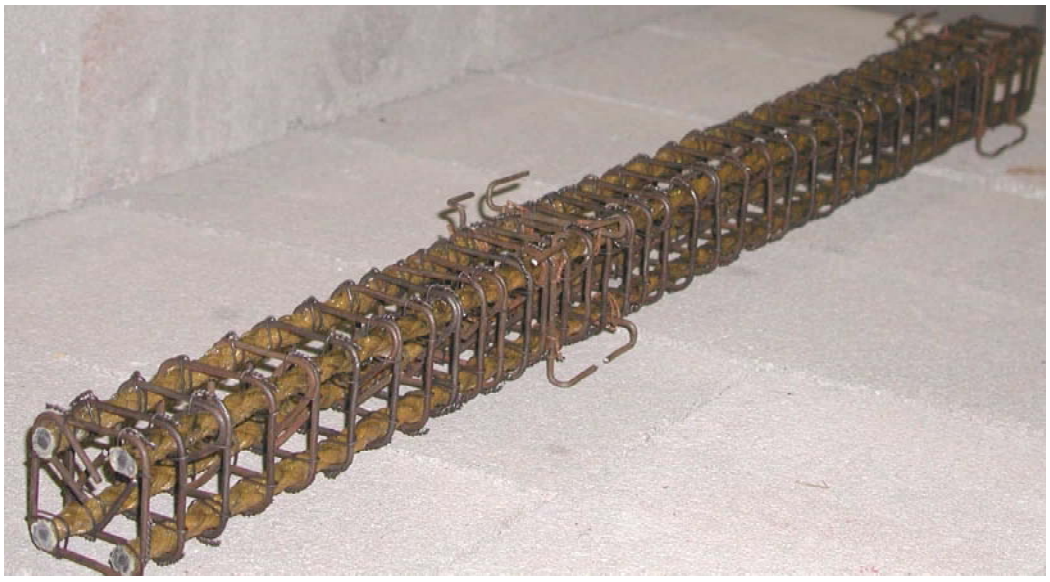

Figure 11.5: Finished DHFRP Reinforcement Cage for Large-Scale Model Columns.

Figure 11.6: Finish DHFRP Reinforcement Cage Showing Closely-Spaced Plastic Hinge Ties.

Figure 11.7: Cross-Sectional View of DHFRP Reinforcement Cage for Large-Scale Model Columns.

Shown in Figure 11.8 is the reinforcing cage and form used for casting the large-scale model columns. The form was built of 0.5" (12.7 mm) thick plywood and 2" (50.8 mm) x 4" (101.6 mm) pine studs. The form was constructed so the column could be cast sideways. This method of casting was used since it was successful for the model columns. Also, the method of casting was used since it was manageable by either one or two people. Since the column was to be bolted to a strong floor, inserts were placed through the footing to create holes in the footing for bolts to be placed. 2.5" (63.5 mm) thick pipe insulation was used. The tubes were wrapped in duct tape and greased with axle grease to break any bonding with the concrete. The inserts are shown in Figure 11.8 and 11.9, and a close-up of the insert is shown in Figure 11.10. Figure 11.9 shows the

plastic hinge region to be cast in the form. From this figure, it is evident that space was very limited, and therefore, care was taken when casting in the hinge region.

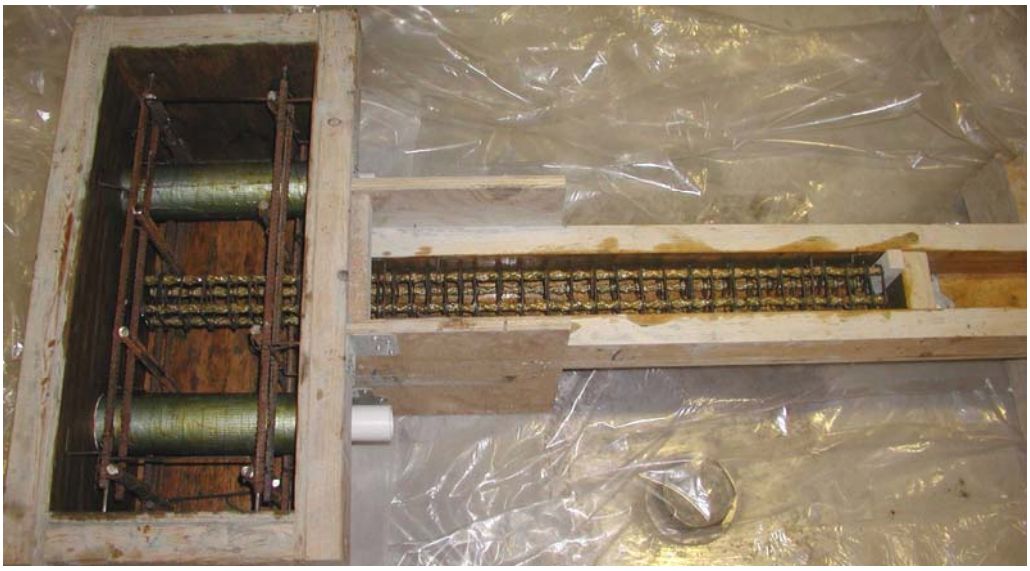

Figure 11.8: Reinforcing Cage in Form for Large-Scale Model DHFRP Columns.

Figure 11.9: Detail of Plastic Hinge Region for Large-Scale Model DHFRP Column Ready for Casting.

Figure 11.10:Footing Casting Insert for Anchor Bolts for Large-Scale Model DHFRP Columns.

The same mix used for the prototype beams was used for the large-scale model columns and is given in Table 11.1. The footing was filled first in three layers. After the second layer, the footing was vibrated using a pencil vibrator. Figure 11.11 shows the column footing being vibrated. Concrete from the footing flowed into the column and filled the plastic hinge region as shown in Figure 11.12. This ensured that there were no voids or entrapped air at the interface of the footing and the column base. Next, the column was filled in layers and vibrated. Finally, the footing was completely filled and the free-surface of the column and footing was finished. Plastic was placed over the column for curing. The finished columns and cylinders are shown in Figure 11.13.

Table 11.1: Concrete Mix Used for Large-Scale Model DHFRP R/C Beams.

Material	Ratio by weight	Weight for mix, lb (kg)
Coarse aggregate 3/8” dia.	3	351.76 (159.56)
Sand	2	234.51 (106.37)
Cement (Type III)	1	117.26 (53.19)
Water	0.45	52.77 (23.94)

Note: This is enough mix for 1 column and 6—4” x 8” cylinders

Figure 11.11:Vibrating of Wet Concrete in the Footing for Large-Scale Model DHFRP Columns.

Figure 11.12:Wet Concrete in the Plastic Hinge Region of Large-Scale Model DHFRP Columns.

Figure 11.13:Finished Large-Scale Model DHFRP Column After Casting.

11.2 Test Setup

The test setup for the large-scale model test was similar to the model tests. However, several things were modified due to increased load and displacement capacities and specimen size. The loading cap on top of the column and the LVDT mounting devices used at the column base were rebuilt and directly scaled from the small-scale columns to fit a 3.0" (76.2 mm) by 3.0" (76.2 mm) column. The same axial loading yoke used in the model column tests was also used in the large-scale model tests. The original axial loading system was designed to have sufficient capacity for both test groups. However, due to increased axial load levels, a hydraulic hand operated jack was used instead of a screw-driven jack. All other testing details were presented in Section 10.2.

Shown in Figure 11.14 is the overall setup for the large-scale model column tests. The column was bolted down to the existing frame using ¾" (19.1 mm) threaded bar and ½" (12.7 mm) thick plates. The axial load system was similar to the model tests; however, the axial load was jacked against the existing frame instead of a cantilevered beam added to the frame, as in the small-scale tests. The lateral loading system was modified since the overall lateral displacements of the column were greater than the model tests. The same type of jack was used as the model test, but two jacks were placed in series to provide a total combined stroke of 13 inches (330.2 mm). Also, since the column height was almost three times greater than the small-scale tests, a vertical strut made of steel channel and wood was used to support the lateral load system. The strut was articulated with a wheel at the base to provide translation as the loading cycles increased. Finally, preliminary testing of the large-scale specimens showed that for columns with axial load, as the lateral load cycles increased, out-of-plane P-Δ moments

resulted. Therefore, a lateral bracing system was designed to prevent any out-of-plane motion of the column. Square steel tubes (1/2" (12.7 mm) thick) were used to create a lateral bracing system.

Shown in Figures 11.15 through 11.21 are photographs showing key features of the large-scale column test setup. The overall setup is shown in Figure 11.15. Shown in Fig. 11.16 is the lateral load setup showing the two jacks in series. The articulated support strut used to support the lateral loading system is shown in Figure 11.17. A coaster wheel was screwed onto the bottom to allow for translation. The modified axial load setup is shown in Figure 11.18. A detail of the system is shown in Figure 11.19. The system is similar to the small-scale tests. A hydraulic jacked was used for the large-scale tests since the loading level was higher. Also, the jack head was welded to a 1/8" (3.18 mm) thick steel plate that was attached to the load cell. This prevented slipping between parts during testing. Figure 11.20 is the lateral bracing system used to prevent out-of-plane P-Δ moments (i.e., biaxial bending). Two sets of tubes were placed both in front of and behind the axial loading yoke, one at the bottom of the yoke and the other at the top. These tubes acted as braces so the axial loading device remained aligned with the longitudinal axis of the column. Shown in Figure 11.21 is the tensioning system used for the axial block and rail system in use during a test. Depending on the direction of the loading cycle, nuts on a piece of 5/8" (15.88 mm) threaded rod were either tightened or loosened. This allowed very controlled motion of the block and rail system enabling the axial loading yoke to always be directly over the column at all displacement levels.

Table 11.2 provides the axial load values used in the large-scale tests and Table 11.3 gives the displacement sequence for these tests.

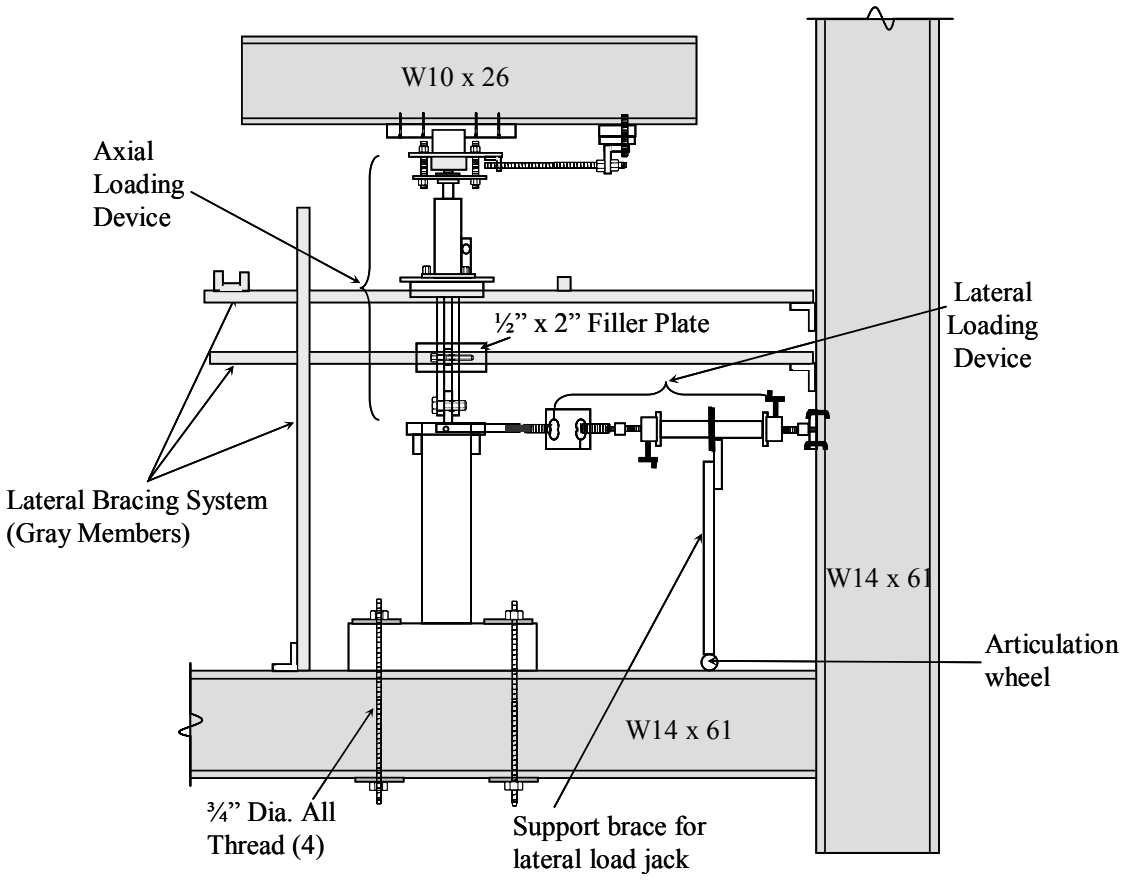

Figure 11.14:Test Setup for Large-Scale Model R/C Columns with 10-mm DHFRP Bars.

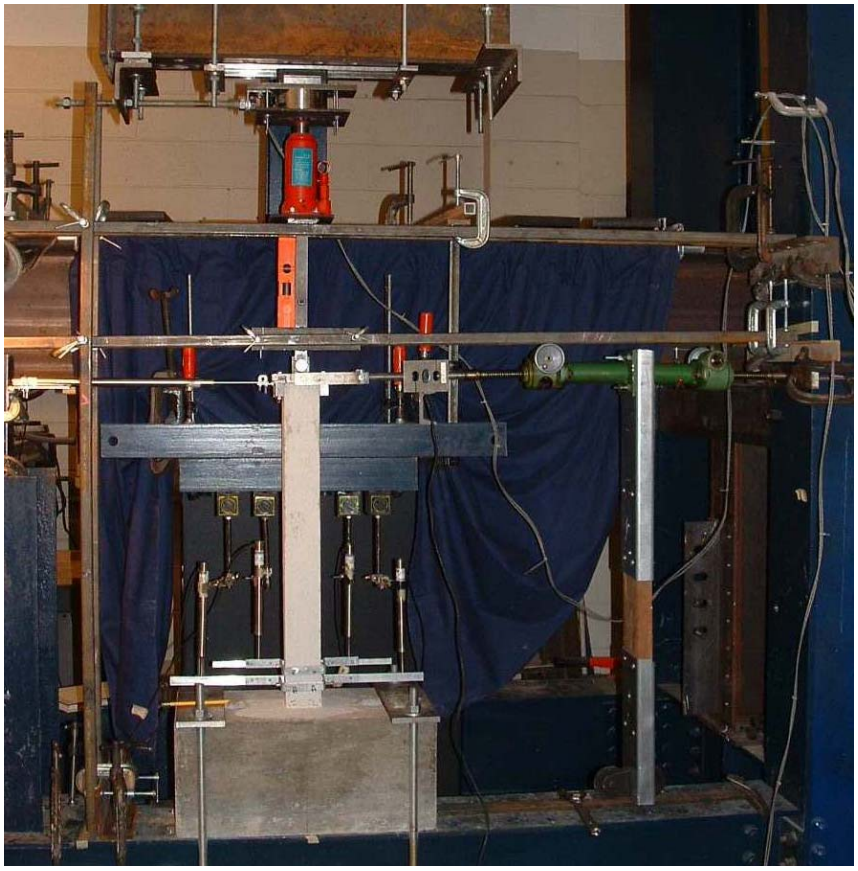

Figure 11.15:Overall Test Setup for Large-Scale Model R/C Columns with 10-mm DHFRP Bars.

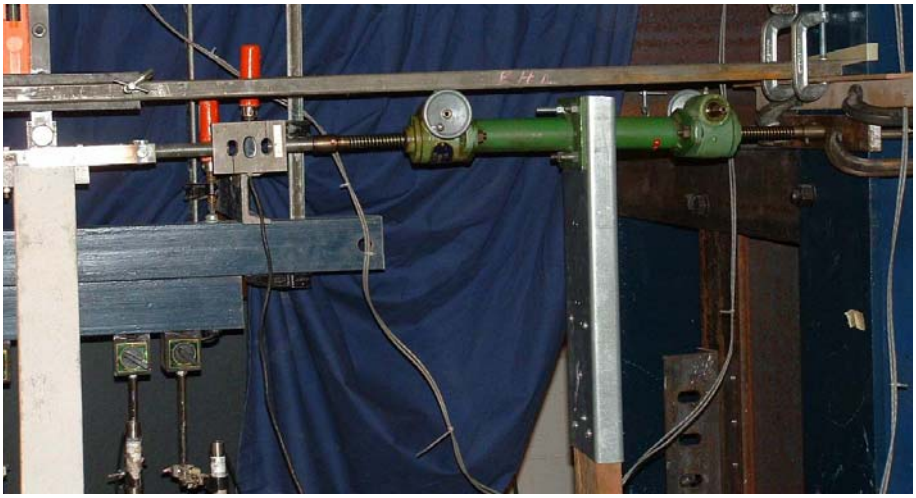

Figure 11.16:Lateral Loading Setup for Large-Scale Model 10-mm DHFRP R/C Columns.

Figure 11.17: Articulated Lateral Loading Support for Large-Scale Model 10-mm DHFRP R/C Columns.

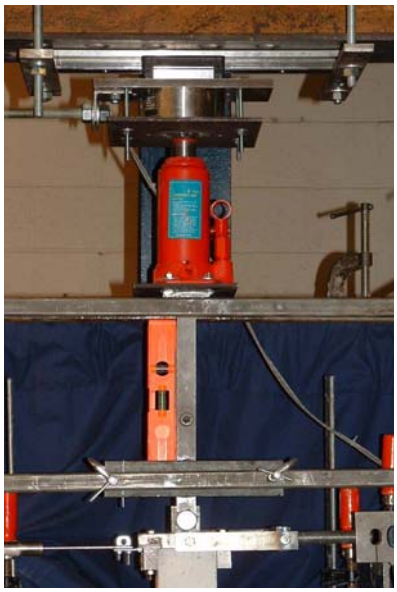

Figure 11.18: Modified Axial Loading Setup Used for Large-Scale Model 10-mm DHFRP R/C Columns.

Figure 11.19:Detail of Axial Loading Device for Large-Scale Model 10-mm DHFRP R/C Columns.

Figure 11.20:Lateral Bracing System Used for Large-Scale Model 10-mm DHFRP R/C Columns.

Figure 11.21: Axial Block and Rail Tensioning System for Large-Scale Model 10-mm DHFRP R/C Columns.

Table 11.2: Axial Load Values Used in Large-Scale DHFRP R/C Column Tests.

Axial Load Level	Load Value, lb (kN)
$0.1 f'_c A_g$	3600 (16.0)
$0.15 f'_c A_g$	5400 (24.0)
$0.2 f'_c A_g$	7200 (32.0)

Table 11.3: Lateral Loading Sequence Used for Large-Scale DHFRP Column Tests.

Displacement sequence	Displacement values, in (mm)
0.2 Δ_y	± 0.1219 (3.096)
0.4 Δ_y	± 0.2438 (6.193)
0.6 Δ_y	± 0.3656 (9.286)
0.8 Δ_y	± 0.4875 (12.38)
1 Δ_y	± 0.6094 (15.48)
2Δ_y	± 1.219 (30.96)
2.5 Δ_y	± 1.524 (38.71)
3 Δ_y	± 1.828 (46.43)
3.5 Δ_y	± 2.133 (54.18)
4 Δ_y	± 2.438 (61.93)
5 Δ_y	± 3.047 (77.39)
6 Δ_y	± 3.656 (92.86)

11.3 Results

The results from the large-scale column tests are presented in the form of documentation of the failure process and cracking patterns, load-deflection behavior, moment-rotation, and moment-curvature behavior. The same data reduction used for the small-scale tests was also used for the large-scale tests.

The results from the large-scale model column tests are presented in two forms. Qualitatively, the failure process was documented by observing the overall response of the columns including the cracking patterns, overall displacements at increasing cycles, and plastic hinge formation. The results were presented quantitatively by the load-deflection, moment-rotation, and moment-curvature behaviors.

The behavior of column P-1 is presented in Figures 11.22 through 11.25. Shown in Figure 11.22 is the cracking at displacement level 2.5 Δ_y. The overall displacement history at levels 1, 3, 3.5, and 4 are given in Figure 11.23. Shown in Figure 11.24 is the

column tip displacement at displacement level 4. A level was placed at the column base and a ruler was placed between the level and the column. Figure 11.25 shows the plastic hinge formation at both low and high displacement levels.

Figure 11.26 shows the development of cracking along the length of the column at displacement levels 1, 2, and 3 for column P-2. The failed column and a detail of the deterioration of the plastic hinge region for P-2 are shown in Figure 11.27.

The behavior of column P-3 is shown in Figures 11.28 through 11.30. The overall displacement history is shown in Figure 11.28 for displacement levels 1, 2, 3, and 4. Shown in Figure 11.29 is the formation of the plastic hinge region at displacement level 1 (low displacement) and level 4 (high displacement). The failed column and failed plastic hinge region is shown in Figure 11.30.

Three sets of data reduction were conducted for the large-scale column tests. The general cyclic load-displacements are shown in Figures 11.31 through 11.33. These demonstrate the overall hysteretic behavior of the model columns. The energy absorption was obtained by finding the area under each cycle of the load-displacement curve as explained in section 10.3. These results tests are presented in Table 11.4.

The moment-base rotation behavior is given in Figures 11.34 through 11.36. The moments include both the bending moment due to lateral load and the P-Δ moment due to axial load. The moment-curvature behavior at the column base is presented in Figures 11.37 through 11.39.

A comparison of experimental and theoretical moment-rotation and moment-curvature behaviors is presented in Figures 11.40 and 11.41, respectively.

Comparison of all test results is given in Table 11.5. Values of deflection, rotation, curvature, load, and moment at yield are listed. The drop in load at first yield is given. Also, the maximum values of the listed quantities are given for both compression and tension cycles. The ductility indices are listed in Table 11.6. These include definitions of ductility based on displacement, rotation, and curvature. Cylinders were tested to get the concrete compressive and tensile strengths. These results are tabulated in Table 11.7.

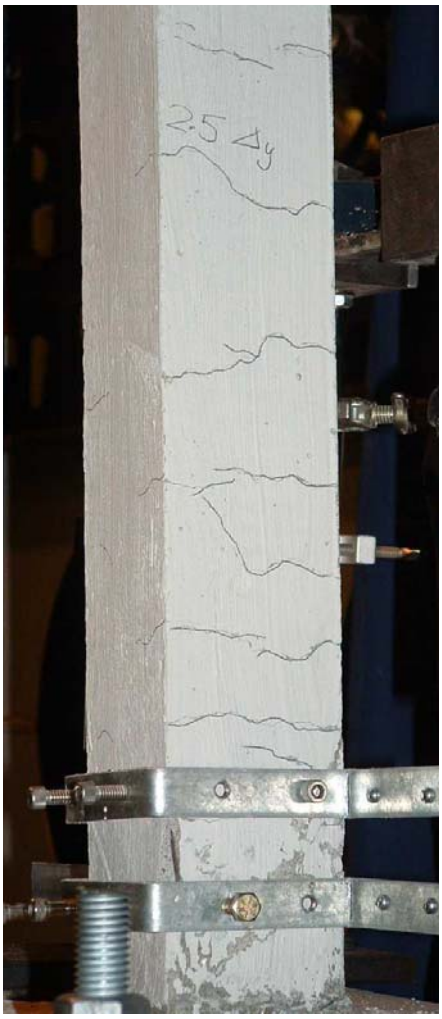

Figure 11.22: Cracking at Displacement Level 2.5 Δ_y for Large-Scale Model Column Test P-1, 10-mm DHFRP Reinforced R/C Column.

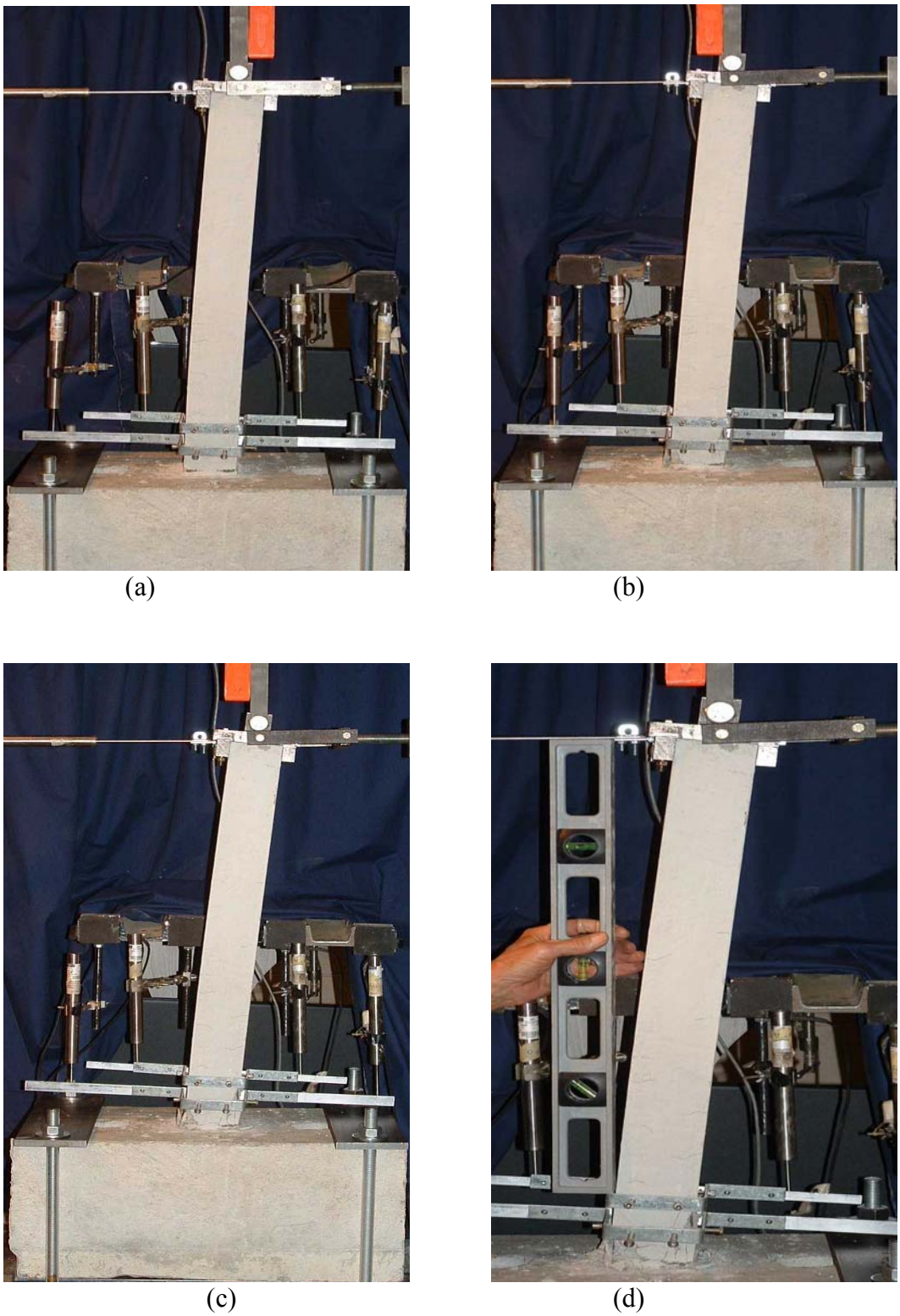

(a) (b)

(c) (d)

Figure 11.23:Displacement Levels (a) 1.0 Δ_y, (b) 3.0 Δ_y, (c) 3.5 Δ_y, and (d) 4.0 Δ_y, Large-Scale Cols. Test P-1, 10-mm DHFRP Reinforced R/C Column.

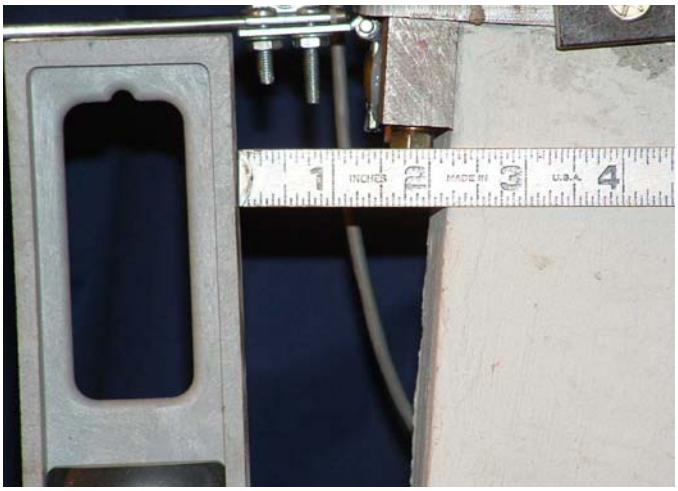

Figure 11.24:Column Tip Displacement at Displacement 4.0 Δ_y for Large-Scale Model Column Test P-1, 10-mm DHFRP Reinforced R/C Column.

(a) (b)

Figure 11.25:Plastic Hinge Formation for (a) Displacement 1.0 Δ_y and (b) Displacement 4.0 Δ_y for Large-Scale Model Column Test P-1, 10-mm DHFRP Reinforced R/C Column.

(a) (b)

Figure 11.26: Cracking Patterns for (a) Displacement 1.0 Δ_y, (b) Displacement 2.0 Δ_y, and (c) Displacement 3.0 Δ_y for Large-Scale Model Col. Test P-2, 10-mm DHFRP Reinforced R/C Column.

(c)

Figure 11.26 (continued)

(a)

(b)

(c)

Figure 11.27: Failed Column and Plastic Hinge Region for Large-Scale Model Column Test P-2, 10-mm DHFRP Reinforced R/C Column.

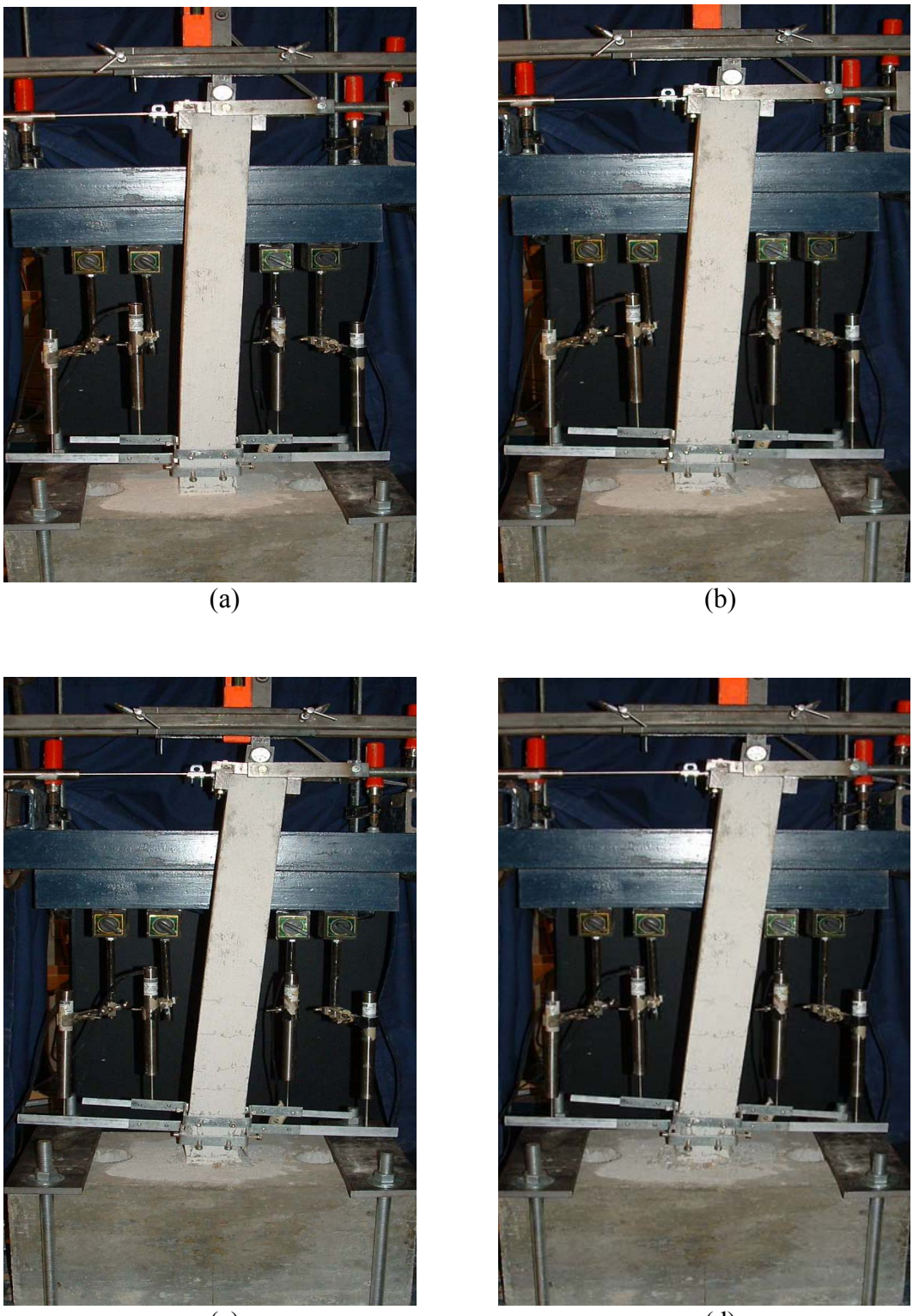

(a) (b)

(c) (d)

Figure 11.28:Displacement Levels (a) 1.0 Δ_y, (b) 2.0 Δ_y, (c) 3.0 Δ_y, and (d) 4.0 Δ_y Large-Scale Col. Test P-3, 10-mm DHFRP Reinforced R/C Column.

(a) (b)

Figure 11.29: Plastic Hinge Formation for (a) Displacement 1.0 Δ_y and (b) Displacement 4.0 Δ_y for Large-Scale Model Column Test P-3, 10-mm DHFRP Reinforced R/C Column.

(a)

(b)

(c)

Figure 11.30: Failed Column and Plastic Hinge Region for Large-Scale Model Column Test P-3, 10-mm DHFRP Reinforced R/C Column.

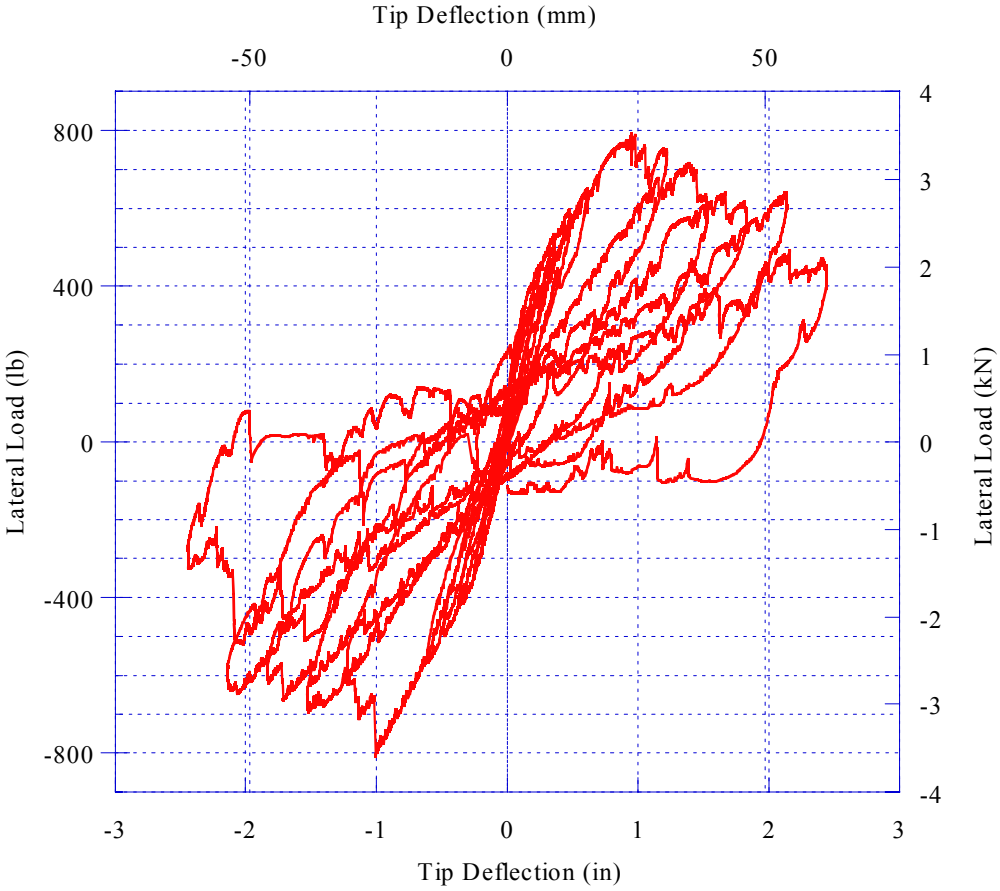

Figure 11.31: Hysteretic Load-Deflection Behavior of Test P-1, Large-Scale DHFRP R/C Column, $N = 0.1 f'_c A_g$.

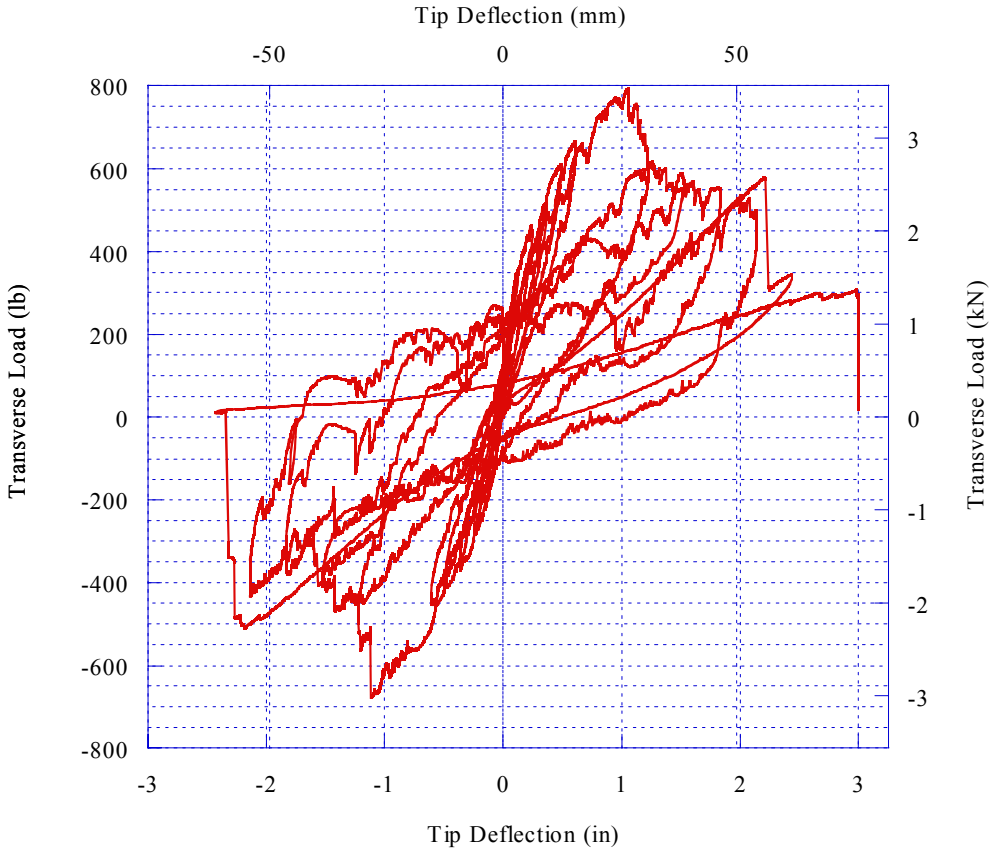

Figure 11.32: Hysteretic Load-Deflection Behavior of Test P-2, Large-Scale DHFRP R/C Column, $N = 0.15 f'_c A_g$.

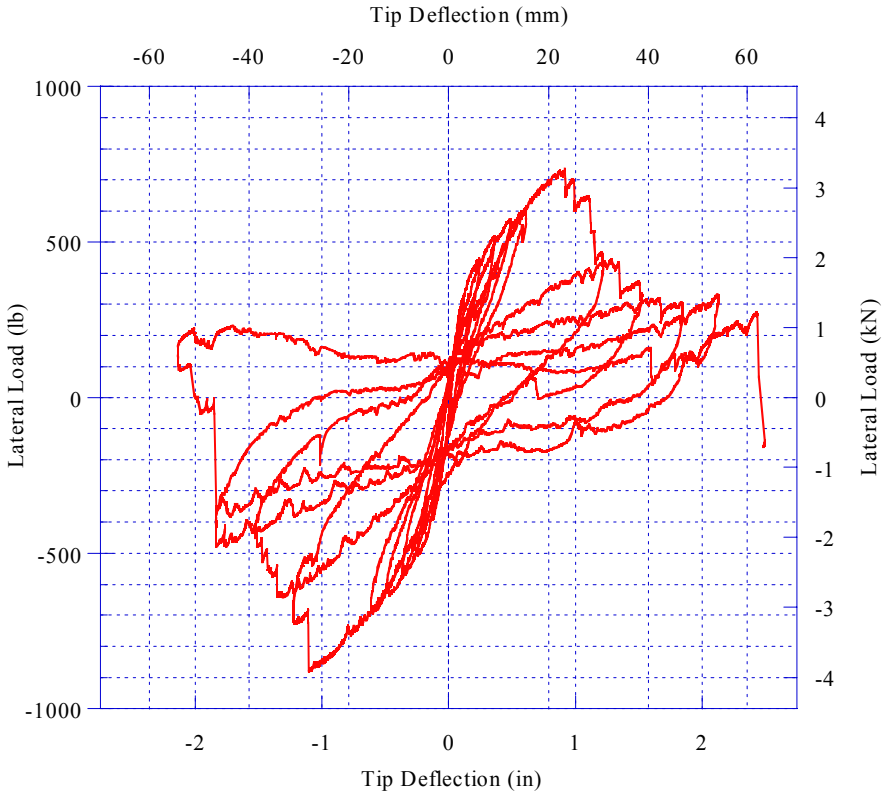

Figure 11.33: Hysteretic Load-Deflection Behavior of Test P-3, Large-Scale DHFRP R/C Column, $N = 0.2 f'_c A_g$.

Table 11.4: Energy Absorption Values for Large-Scale DHFRP Column Tests.

Specimen	Area, lb-in (N-m)	% of Max. Value
P-1	5345.85 (604.0)	88.9
P-2	6011.51 (679.2)	100
P-3	5426.33 (613.1)	90.3

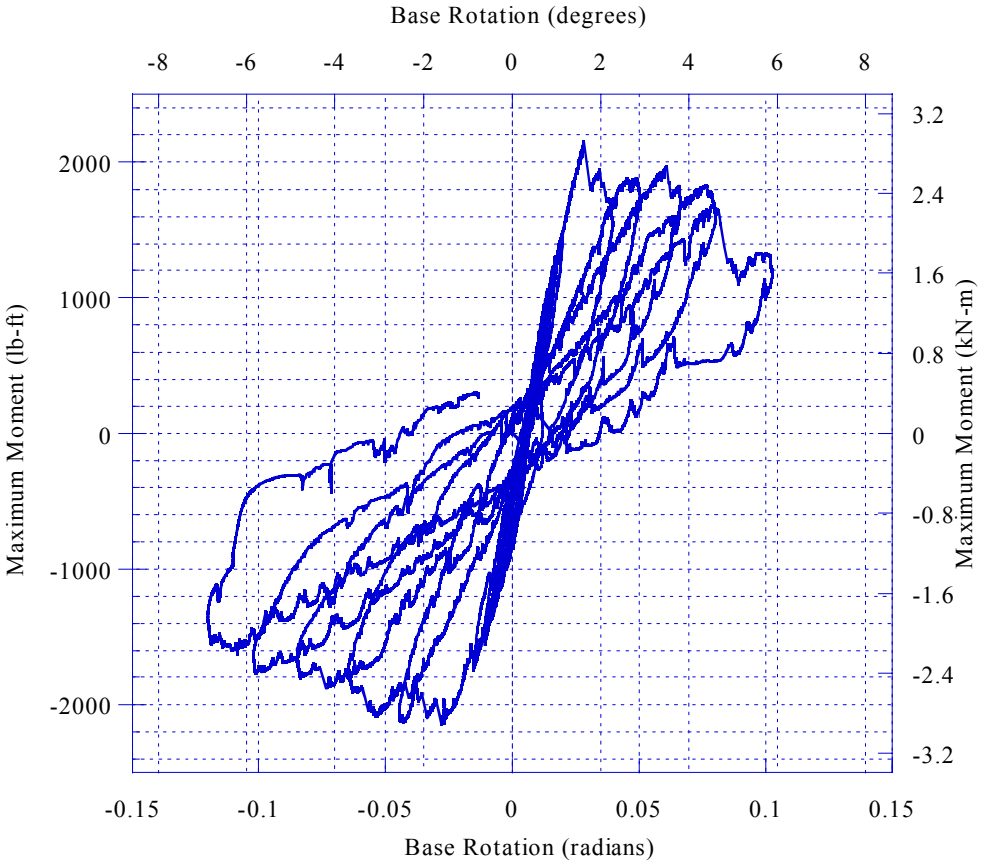

Figure 11.34: Moment-Base Rotation Behavior of Test P-1, Large-Scale DHFRP R/C Column, $N = 0.1 f'_c A_g$.

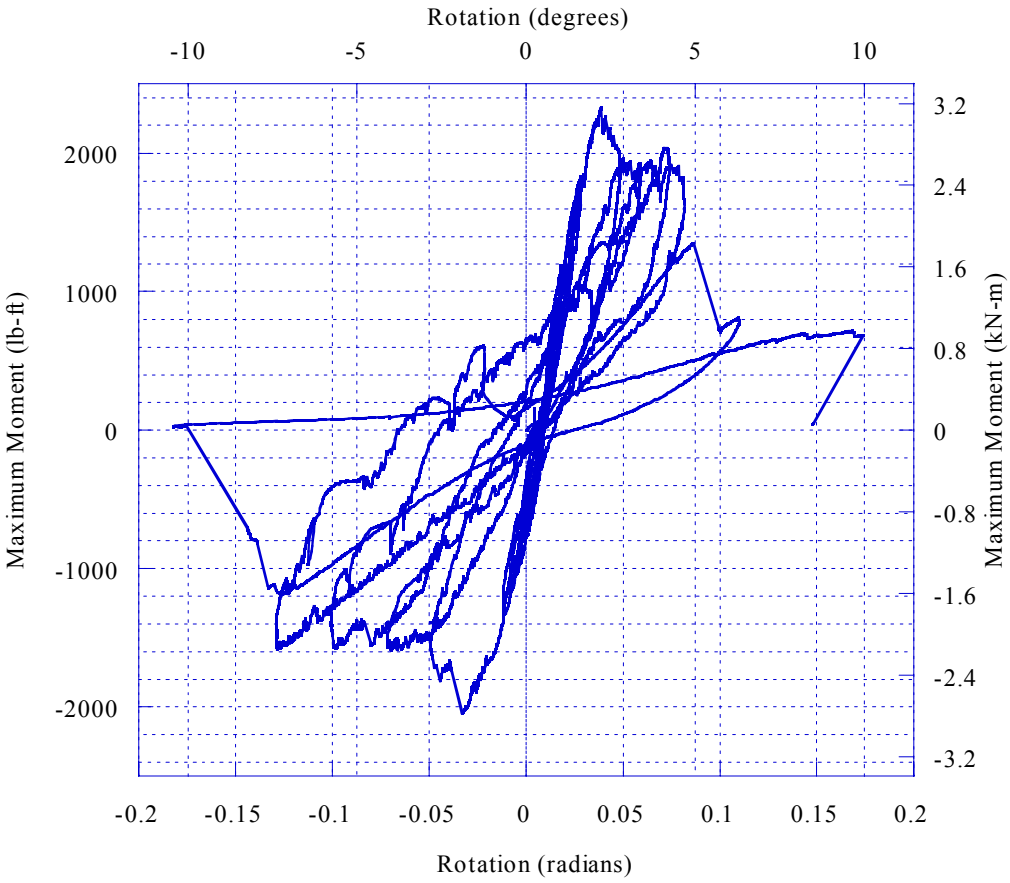

Figure 11.35: Moment-Base Rotation Behavior of Test P-2, Large-Scale DHFRP R/C Column, $N = 0.15 f'_c A_g$.

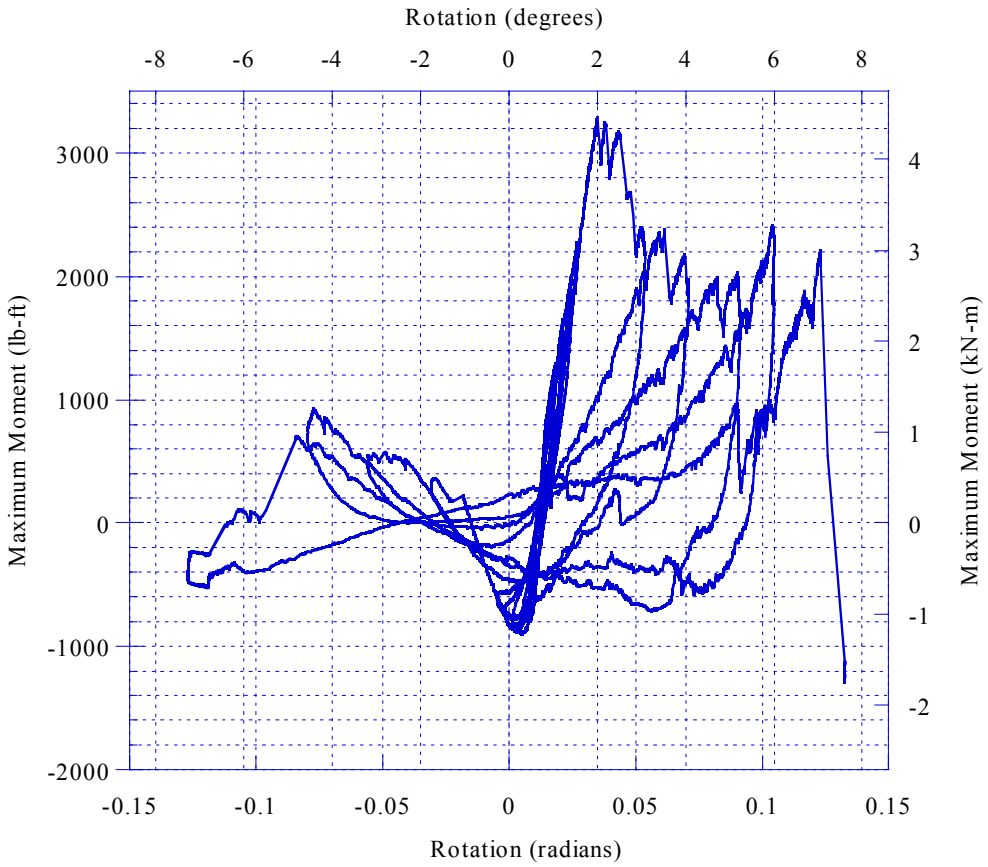

Figure 11.36: Moment-Base Rotation Behavior of Test P-3, Large-Scale DHFRP R/C Column, $N = 0.2 f'_c A_g$.

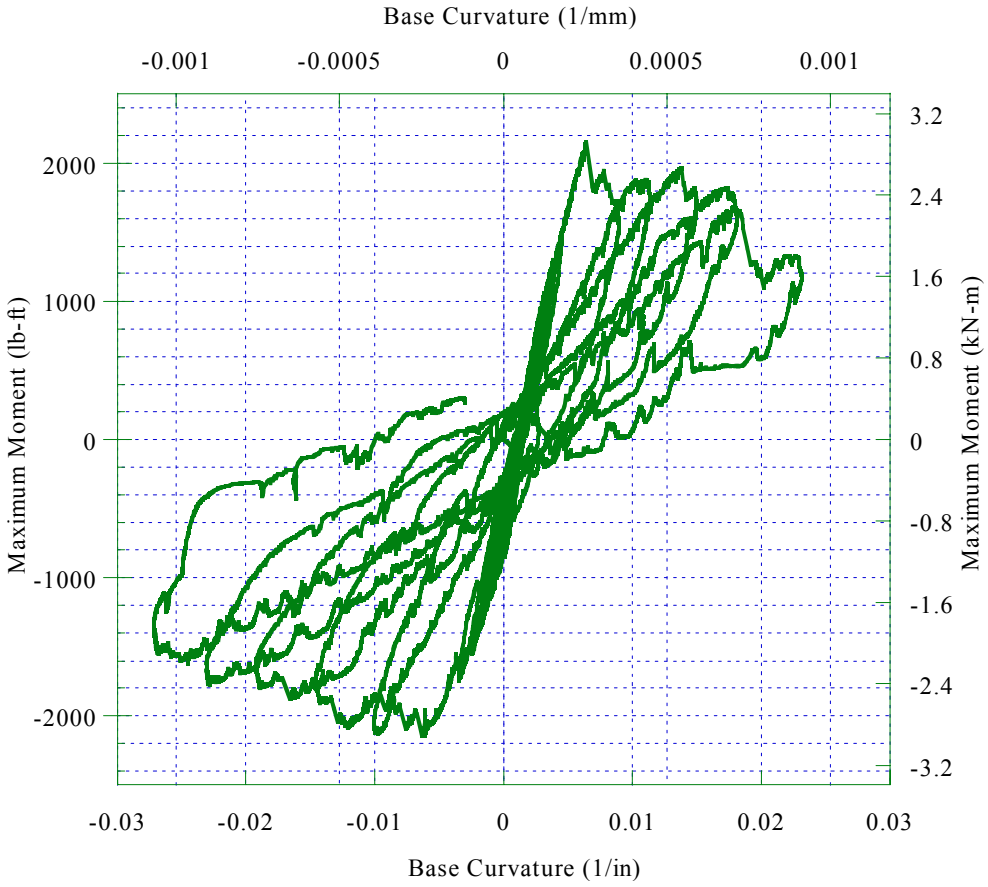

Figure 11.37: Moment-Curvature Behavior of Test P-1, Large-Scale DHFRP R/C Column, $N = 0.1\, f'_c\, A_g$.

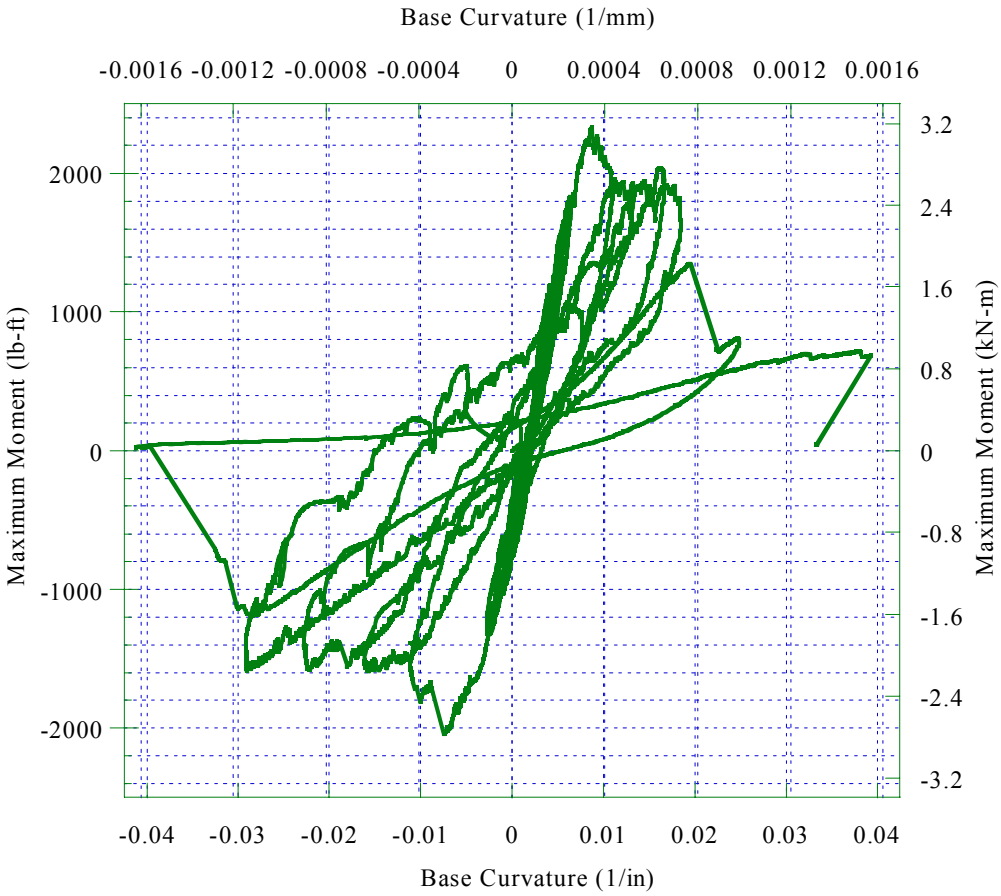

Figure 11.38: Moment-Curvature Behavior of Test P-2, Large-Scale DHFRP R/C Column, $N = 0.15 f'_c A_g$.

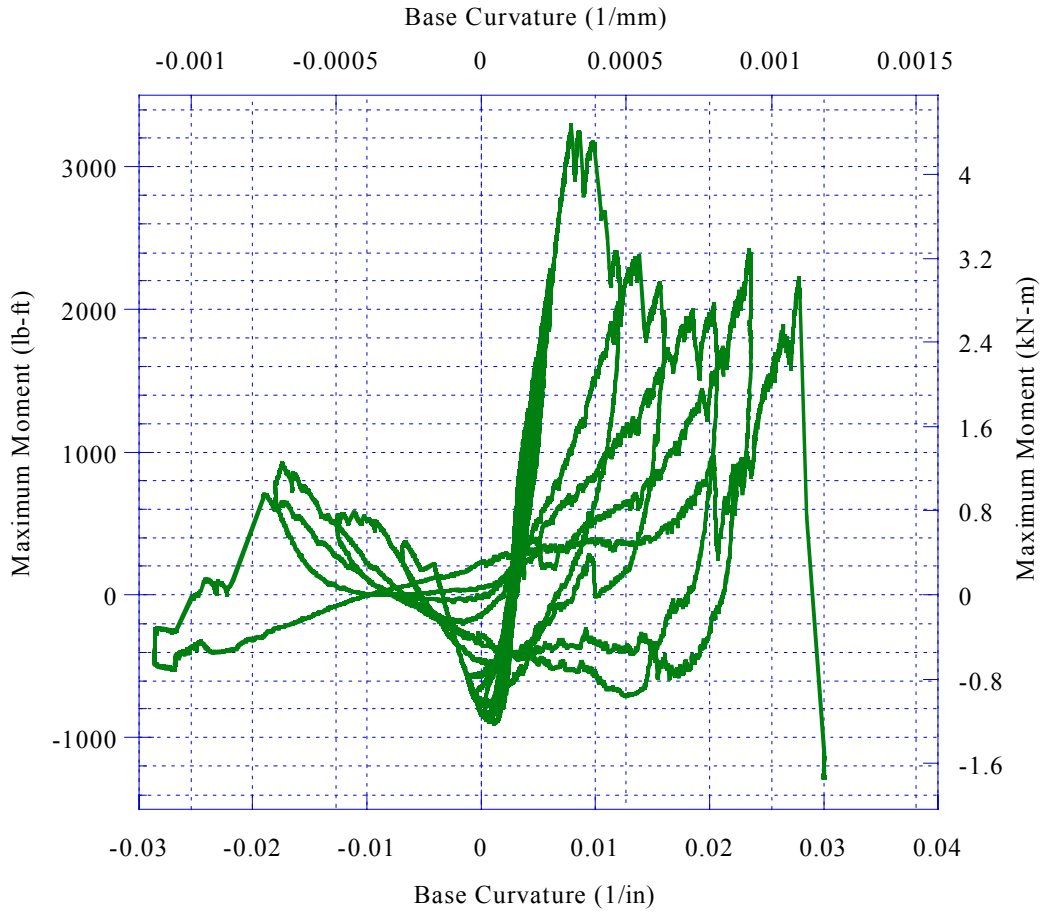

Figure 11.39: Moment-Curvature Behavior of Test P-3, Large-Scale DHFRP R/C Column, $N = 0.2\,f'_c\,A_g$.

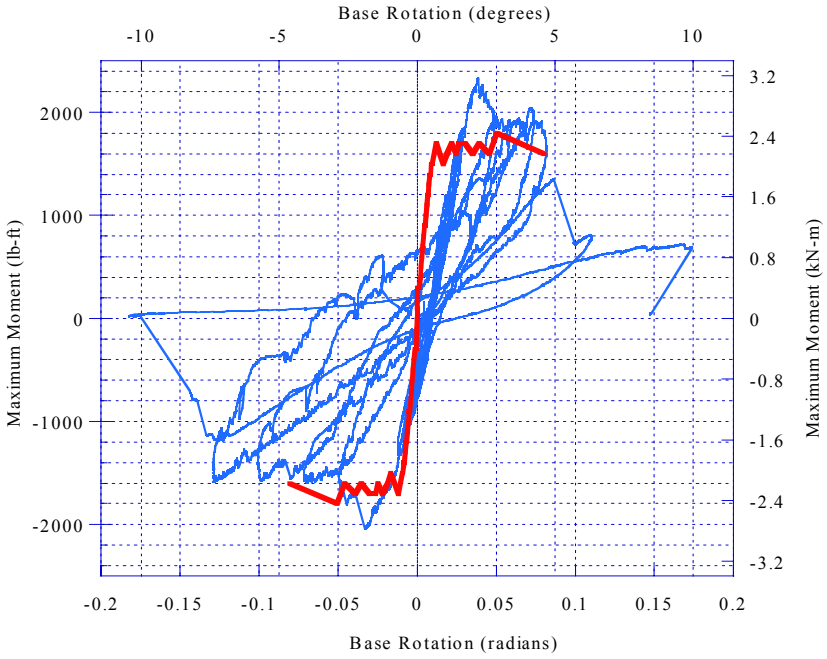

Figure 11.40: Comparison of Large-Scale Moment-Rotation and Theoretical Envelope Curves.

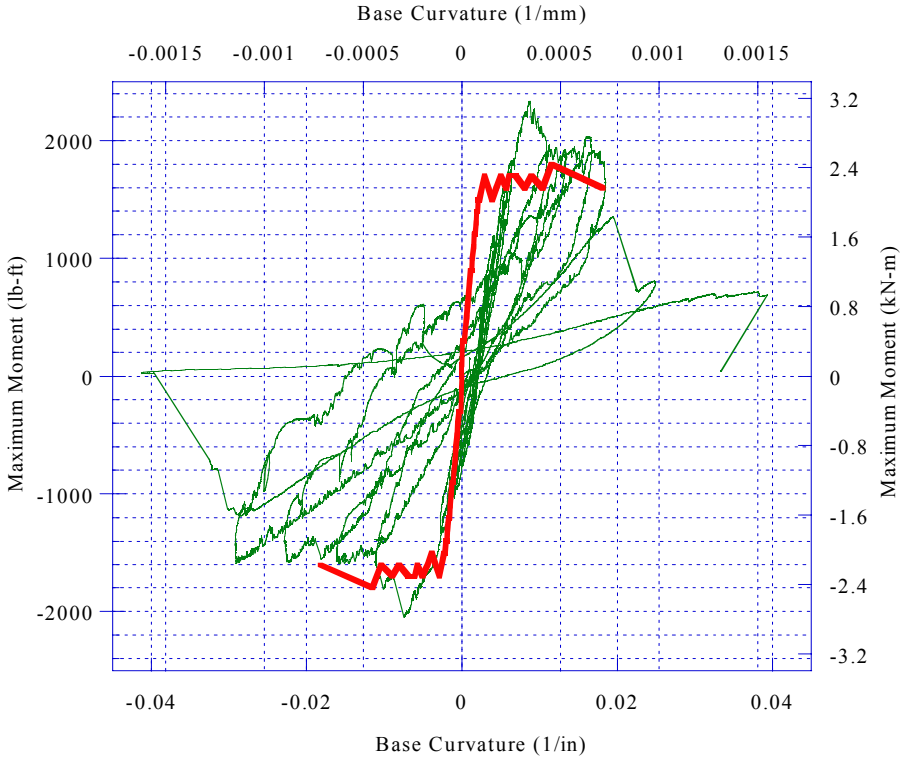

Figure 11.41: Comparison of Large-Scale Moment-Curvature and Theoretical Envelope Curves.

Table 11.5: Results of Cyclic Tests for 10-mm DHFRP Large-Scale Model R/C Columns.

Specimen	**Deflection (in)**	**Rotation (rad)**	**Curvature (1/in)**	**Lateral Load (lb)**	**Moment (lb-ft)**
P-1, yield	-1.01	0.028	0.006	808.18 → 665.72	2156.77
Maximums	2.44	0.102	0.023	808.18	2156.77
Minimums	-2.44	-0.120	-0.027	-791.56	-2147.81
P-2, yield	-1.06	0.039	0.009	793.16 → 735.31	2334.30
Maximums	2.43	0.174	0.039	793.16	2334.27
Minimums	-3.00	-0.182	-0.041	-679.47	-2048.57
P-3, yield	-0.92	0.035	0.008	735.3 → 677.2	3291.02
Maximums	2.14	0.133	0.030	735.34	3291.02
Minimums	-2.50	-0.127	-0.029	-880.08	-1286.34

Table 11.6: Ductility Indices for Large-Scale DHFRP Large-Scale Model R/C Columns.

Specimen	$\mu_\Delta = \Delta_u/\Delta_y$	$\mu_\theta = \theta_u/\theta_y$	$\mu_\phi = \phi_u/\phi_y$
P-1	2.43	3.61	4.24
P-2	2.84	4.50	4.71
P-3	2.72	3.65	3.82

Table 11.7: Concrete Compressive and Tensile Strengths for 10-mm DHFRP R/C Columns.

Specimen	Concrete Strength f'_c psi (MPa)	Concrete Tensile Strength f_t, psi (MPa)
P-1	7426.6 (51.2)	728.1 (5.0)
P-2	7815.9 (53.9)	738.0 (5.1)
P-3	7004.1 (48.3)	637.1 (4.4)

11.4 Discussion

The behavior of column P-1 was presented in Figures 11.22 through 11.25. Shown in Figure 11.22 was the cracking at displacement level 2.5 Δ_y. The cracking was limited to flexural cracking. Shear cracking did not occur for any column tested at either scale. The overall displacement history at levels 1, 3, 3.5, and 4 were given in Figure 11.23. Large inelastic deformation and base rotation with increasing deformation cycles is evident, especially in Fig. 11.23d. Shown in Figure 11.24 was the column tip displacement at displacement level 4. A level was placed at the column base and a ruler was placed between the level and the column. A tip displacement of approximately 2.25 in (57.15 mm) was recorded. Figure 11.25 showed the plastic hinge formation at both low and high displacement levels. At the high displacement level, spalling was evident at the base.

Figure 11.26 showed the development of cracking along the length of the columns at displacement levels 1, 2, and 3 for column P-2. Column P-2 had moderate axial load. The crack propagation is evident in Fig. 11.26c; however, the cracks were still flexural cracks with no sign of diagonal shear cracking. The failed column and a detail of the deterioration of the plastic hinge region for P-2 were shown in Figure 11.27. At moderate axial load, much greater hinge deterioration occurred than for low axial load. The cover concrete spalled off leaving on the core concrete in the hinge region. Also, the region of distress (plastic hinge region) was longer than for the case of low axial load.

The behavior of column P-3 (moderately-high axial load) was shown in Figures 11.28 through 11.30. The overall displacement history was shown in Figure 11.28 for displacement levels 1, 2, 3, and 4. Again, large inelastic base rotations and inelastic

deformations were evident in Fig. 11.28c and d. Shown in Figure 11.29 was the development of the plastic hinge region at displacement level 1 (low displacement) and level 4 (high displacement). At high displacements, significant spalling occurred. The failed column and failed plastic hinge region was shown in Figure 11.30. At high axial load, the plastic hinge region suffered the greatest distress. Most of the cover concrete spalled leaving only the core concrete. Fig. 11.30b shows the reduction in gross cross-section at column failure. Figure 11.30c shows the deteriorated hinge region. Two of the longitudinal DHFRP bars are visible.

Three sets of data reduction were conducted for the large-scale model column tests. The general cyclic load-displacements were shown in Figures 11.31 through 11.33. These demonstrated the overall hysteretic behavior of the model columns. The energy absorption was obtained by finding the area under each cycle of the load-displacement curve as explained in section 10.3. These results for the large-scale model column tests were presented in Table 11.4.

The hysteretic behavior of column P-1 was shown in Fig. 11.31. This column had low axial load. At higher displacement levels, much less pinching was evident than for low or no axial force levels. The axial load increased compression in the concrete, thereby suppressing the opening of tension cracks. The curves are jagged due to fiber breakage during the test, causing load drops. Also, it was difficult to maintain absolutely constant axial load, and therefore, small adjustments were made during the test. The energy absorbed by the column was 5345.85 lb-in (604.0 N-m). This was 88.9% of the maximum energy absorbed (test P-3). This is much greater than for no axial force. However, the stiffness degradation was slightly more severe than for columns with no

axial load. This was caused by the *P-Δ* moments due to the axial load and large inelastic displacements. As the load cycles increased, the *P-Δ* moments significantly influenced the overall column behavior. Therefore, the stiffness decreased at high displacement levels with large values of *P-Δ* moments. The displacement ductility index was 2.43. The maximum lateral load was 808.18 lb (3.6 kN) and the maximum lateral displacement was 2.44 in (62.0 mm). The test was terminated prematurely to prevent damage to the instrumentation.

The hysteretic behavior of column P-2 was shown in Fig. 11.32. This column had moderate axial load. At higher displacement levels, much less pinching was evident than for low or no axial force levels. The final loop had a low stiffness because the axial loading device was disconnected to prevent damage of the loading equipment. This final loop had only lateral load applied, and therefore, much reduced stiffness. The energy absorbed by the column was 6011.51 lb-in (679.2 N-m). This was the maximum energy absorbed. The stiffness degradation was more severe for moderate axial load. The displacement ductility index was 2.84. The maximum lateral load was 793.16 lb (3.5 kN) and the maximum lateral displacement was -3.00 in (76.2mm).

The hysteretic behavior of column P-3 was shown in Fig. 11.33. This column had high axial load. At high displacement levels, the column with high axial load had the least amount of pinching. The energy absorbed by the column was 5426.33 lb-in (613.1 N-m). This was 90.3% of the maximum energy absorbed. However, the stiffness degradation was the most severe with large axial load. This was caused by the *P-Δ* moments due to the axial load and large inelastic displacements. The displacement

ductility index was 2.72. The maximum lateral load was -880.08 lb (3.9 kN) and the maximum lateral displacement was -2.50 in (63.5mm).

The moment-base rotation behavior was given in Figures 11.34 through 11.36. The moments included both the bending moment due to lateral load and the *P-Δ* moment due to axial load. The overall trend of the moment-rotation was very similar to the load-deflection behavior. The same trends regarding pinching, stiffness degradation, and *P-Δ* behavior was similar for the moment-rotation behavior. At the maximum of large displacement cycles, the *P-Δ* moment dominated the value of the total moment because of the large magnitude of the axial load compared to the lateral load. The maximum moments ranged from 2156.77 lb-ft (2.9 kN-m) to 3291.02 lb-ft (4.5 kN-m). The maximum rotations ranged from 0.102 radians to 0.182 radians. The rotation ductility indices ranged from 3.61 to 4.50. The largest value of rotational ductility was column P-2 which had the largest energy absorption and the smallest value was column P-1, which had the lowest energy absorption due to ending the test prematurely. The compression cycle for specimen P-3 appears to have a reduced or pinched moment-rotation behavior. This is due to the lateral bending moment and the *P-Δ* moment being out of phase with each other. After reaching the maximum displacement for a given cycle, when the column is pulled back to center, the direction of the lateral bending moment is opposite to the *P-Δ* moment. Therefore, the *P-Δ* moment appears to have a negative effect on the energy absorption when observing moment-rotation and moment-curvature behaviors.

The moment-curvature behavior at the column base was presented in Figures 11.37 through 11.39. The moments included both the bending moment due to lateral load and the *P-Δ* moment due to axial load. The maximum moments ranged from -2156.77

lb-ft (2.9 kN-m) to 3291.02 lb-ft (4.5 kN-m). The maximum curvatures ranged from -0.027 1/in to -0.0411/in. The values of curvature represent the gradient of the strain profile at that section. The curvature ductility indices ranged from 3.82 (P-3, steel) to 4.71 (P-2).

A comparison of experimental and theoretical moment-rotation and moment-curvature behaviors was presented in Figures 11.40 and 11.41, respectively. Even though the theoretical curves were for monotonic loading, they provided the loading envelope for the experimental cyclic data. Good correlation between initial stiffness and rotation and curvature for both theoretical and experimental curves exist. The experimental ultimate rotation and curvature was greater than the theoretical. The theoretical curves had a limit on the concrete strain capacity which limited the ultimate rotation and curvature.

Based on the results of the large-scale model columns, the DHFRP provided sufficient column moment capacity well into the inelastic range, significant displacement ductility, and a stable hysteretic behavior. As the axial load increased, the energy absorption increased, but the hysteresis became more unstable due to increased P-Δ moments.

CHAPTER 12. SIMILITUDE COMPARISON OF MODEL AND PROTOTYPE DHFRP REINFORCED CONCRETE BEAM-COLUMNS, BEAMS, AND MATERIAL BEHAVIOR

Two sizes of DHFRP bars were developed and investigated: the 5-mm bar using the original preform and an improved 10-mm bar using the modified braidtrusion process. The geometry, material and mechanical properties, and behavior in concrete components were investigated at both scale levels. With respect to scaling or similitude, first the axial tensile strength for both scale bars was investigated (Chapter 6); then the bars were used to reinforce concrete elements. Beams reinforced with prototype bars and subjected to four-point monotonic loading were investigated (Chapter 8), and then R/C column behavior subjected to complete load reversals (Chapters 10-12) was investigated. The columns were investigated for both sized bars. Tension testing and beam testing on 5-mm bars was conducted by Somboonsong (1998).

The scaling effect or similitude between using model bars (5-mm dia.) and prototype-size bars (10-mm dia.) was investigated. The theory of similitude was presented in Chapter 3 and a design example is presented in Appendix A. The similitude of R/C behavior with DHFRP was investigated: first, the column behavior under reverse cyclic loading followed by beams subjected to monotonic loading. Finally, the DHFRP material behavior was investigated using similitude to compare the axial tensile behavior.

12.1 Applications and Similitude Terms

The primary application of dimensional analysis and similitude is to relate results from structural models to predict prototype-size structural behavior. Typically, the model response and behavior are obtained and are then ‘scaled-up’ using the similitude scale

factors developed in Chapter 3 and Appendix A to predict the prototype response and behavior. Using similitude only, a prediction of large-scale model R/C column behavior, R/C beam behavior, and tensile strength for 10-mm DHFRP bars can be made by using the 5-mm response only, without testing any 10-mm DHFRP elements.

For DHFRP R/C columns, beams, and the tensile behavior of DHFRP, the 5-mm model behavior was used to predict the prototype behavior. The prototype-size material and R/C components were then developed and tested as a verification of the similitude theory.

Strength models were used to compare tensile behavior and DHFRP R/C beam and column behavior. The strength model is a direct model that is made of similar materials to the prototype materials and predicts prototype behavior for all loads up to failure. The modeling of the complete inelastic behavior of reinforced concrete components was more difficult since they must include the failure mode, capacity, and bond behavior (Harris and Sabnis, 1999). Both the concrete compressive and tensile strength properties must be modeled correctly, and the surface conditions (i.e., bond) of the reinforcing bars must be carefully replicated at model scale. The requirement that the failure criteria for model concrete subjected to multi-axial stresses should be identical with that of the prototype concrete is usually relaxed. The two requirements are:

1. Stress-strain curves must be geometrically similar in model and prototype concrete for both uniaxial tension and compression
2. $\varepsilon_m = \varepsilon_p$ at failure under uniaxial tension and compression

The general similitude requirements for R/C models are presented in Table 12.1. These were used comparing model and prototype beam and column results. The

independent scale factors used were s_σ and s_l, the stress and the length; therefore, $s_\sigma = s_E = 1$.

Table 12.1: Scale Factors Used for Reinforced Concrete Models.

Quantities	Dimensions	Scale Factor
Material properties		
Concrete stress, σ_c	FL^{-2}	$S_\sigma = (1^*)$
Concrete strain, ε_c	—	*1*
Modulus of concrete, E_c	FL^{-2}	$S_\sigma = (1)$
Poisson's ratio	—	*1*
Reinforcing stress, σ_r	FL^{-2}	$S_\sigma = (1)$
Reinforcing strain, ε_r	—	*1*
Modulus of reinf., E_r	FL^{-2}	$S_\sigma = (1)$
Bond stress, u	FL^{-2}	$S_\sigma = (1)$
Geometry		
Linear dimension, l	L	S_l
Linear displacement, δ	L	S_l
Area of reinf., A_r	L^2	S_l^2
Loading		
Concentrated Load, Q or V	F	$S_\sigma S_l^2 = (S_l^2)$
Uniform load, w	FL^{-1}	$S_\sigma S_l = (S_l)$
Moment, M	FL	$S_\sigma S_l^3 = (S_l^3)$
* these values in parentheses are the values for practical true models		

12.2 Similitude Comparison of Small and Large-Scale Model Beam Columns

Using similitude, the small-scale model behavior was scaled up as a prediction of large-scale behavior. The small and large-scale behaviors were compared based on overall hysteresis response, column cracking patterns, and plastic hinge formation. For the beam-columns, both geometry and force must be 'scaled-up' using similitude. The geometric parameters are the specimen dimensions, reinforcing bar size, displacements,

strains, rotations, and curvatures. The force parameters include applied lateral and axial force and bending moments.

Table 12.2 provides the scale factors pertinent to the beam-column tests. The model values are given followed by the appropriate scale factors and the theoretical prototype values developed using the scaling factor only. These theoretical values are compared with the actual experimental values obtained and the percent difference is compared. The theoretical and experimental values for force and displacement are within 10% of each other. Since the large-scale model linear dimension L of the column was not exactly two times the model length, a distortion was introduced into the similitude. In particular, the required applied force and corresponding moment at the column base were distorted since the length and moment arm are not directly scaled from model to prototype. This distortion was corrected when computing the percent difference between theoretical and experimental values.

Shown in Figures 12.1 through 12.3 is the comparison of the scaled-up model behavior to the actual large-scale model response. The hysteretic load-displacement behavior (Fig. 12.1), moment-rotation (Fig. 12.2) and moment-curvature behaviors (Fig. 12.3) were compared. The load was scaled by a factor of four, the displacement by a factor of two, and the moment by a factor of eight. The strain must be the same in the model and prototype, and therefore, the rotations and curvatures should be the same for both model and prototype. Good correlation was observed between the predicted prototype behavior and experimental results for load-displacement, moment-rotation, and moment-curvature. Given in Table 12.3 are the results from the small and large-scale model cyclic column tests. The displacements, rotations, curvatures, loads, and moments

were compared at both yield and ultimate. An average value of each quantity for both small and large models was calculated. A comparison of the ductility indices based on displacement, rotation, and curvature for small and large-scale models is given in Table 12.4.

The comparison of final cracking patterns at various axial load levels is shown in Figures 12.4 through 12.6. Figure 12.4 compares the cracking pattern of the small to the large-scale columns at low levels of axial load ($0.1f'_cA_g$). The cracking of the large-scale model was much greater due to the lower tensile strength of the large-scale model concrete, and the corresponding crack spacing was much larger for the model columns. Shown in Figure 12.5 are the cracking patterns at $0.15\,f'_cA_g$ axial load. Again, the same behavior was observed as for lower axial loads, namely, the large-scale model column had much more extensive cracking than the model. At high axial loads ($0.2\,f'_cA_g$), the extent of cracking for the model and large-scale model was not as severe as for lower axial load levels. This was due to the axial compression force applied to the column, causing the concrete to be in a state of compression, making it more difficult for crack development and propagation to occur.

A comparison of the formation of plastic hinges at the column bases is illustrated in Figures 12.7 through 12.9 for various levels of axial loads. The deterioration of the plastic hinge was more severe at higher levels of axial compression. This was due to higher transverse stresses at the critical location of maximum stress (i.e., column base). The most severe case was at $0.2\,f'_cA_g$ axial force, Figure 12.8. For both the size models, the cover concrete spalled at the base, leaving only the core concrete inside the ties. The general plastic hinge formation and deterioration was consistent at both scale factors.

Table 12.2: Comparison of Theoretical Scale Factors and Experimental Results Used for DHFRP R/C Columns.

Quantities	small- Scale Values	Scale Factor	Prototype Similitude Values	Exper. Prototype Values	**% Difference**
Geometry					
Linear dimension, *L*	14	$S_l=2$	28	29.5	**5.4**
Linear displacement, Δ, in	1.06	$S_l=2$	2.12	2.65	**20**
Area of reinf., A_r, in^2	0.488	$S_l^2=4$	1.94	1.77	**8.8**
Loading					
Concentrated Load, *Q* (lb)	239.0	$S_\sigma S_l^2=1*2^2=4$	956	827.2	**13.4**
Moment, *M* (lb-ft)	227.3	$S_\sigma S_l^3=1*2^3=8$	1818.4	2594	**15**

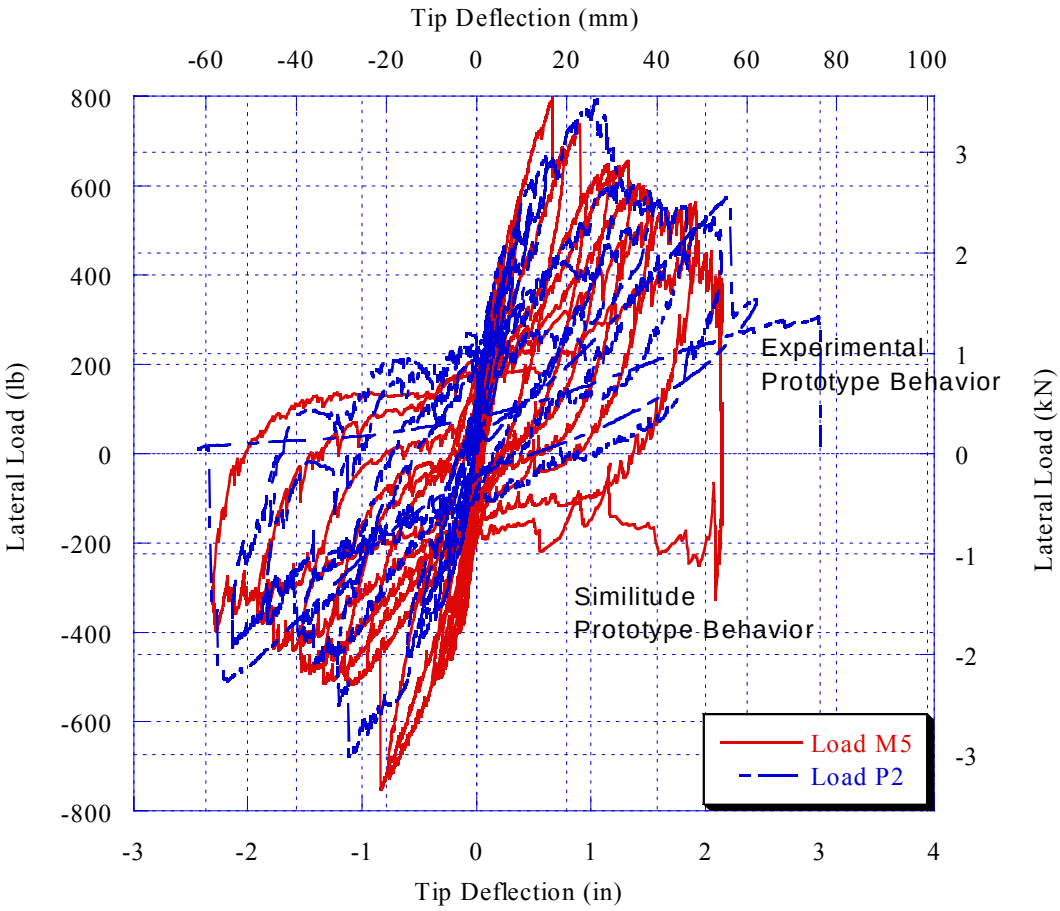

Figure 12.1: Comparison of Load-Displacement Behavior for Small and Large-Scale DHFRP Columns.

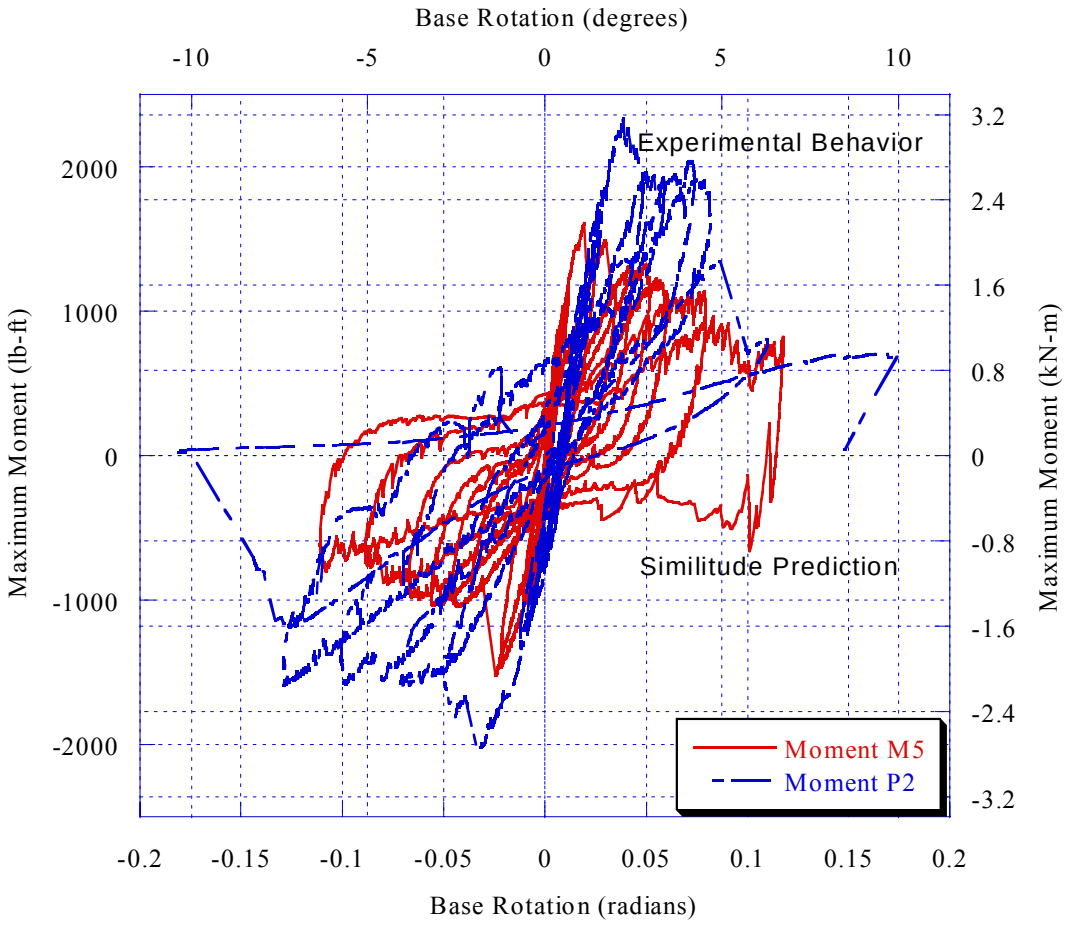

Figure 12.2: Comparison of Moment-Rotation Behavior for Small and Large-Scale DHFRP Columns.

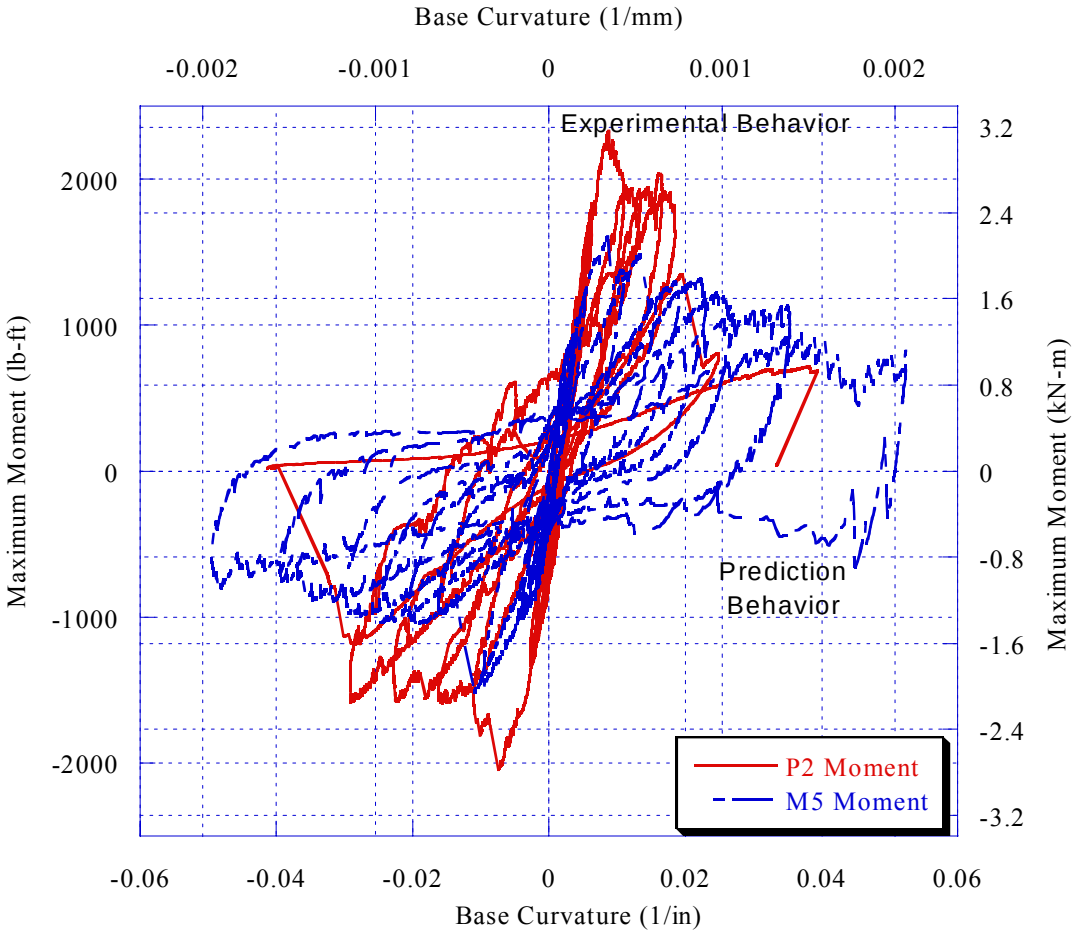

Figure 12.3: Comparison of Moment-Curvature Behavior for Small and Large-Scale DHFRP Columns.

Table 12.3: Experimental Results of Model and Large-Scale Model Beam-Column Tests.

		Specimens								
	M-2	M-3	M-4	M-5	M-6	**Avg**	P-1	P-2	P-3	**Avg**
Δ_y (in)	0.36	0.26	0.27	0.33	0.35	**0.31**	1.01	1.06	0.92	**0.99**
Δ_u (in)	1.11	0.79	1.13	1.15	1.13	**1.06**	2.44	3.00	2.50	**2.65**
θ_y (rad)	0.032	0.025	0.017	0.019	0.024	**0.023**	0.028	0.039	0.035	**0.034**
θ_u (rad)	0.164	0.092	0.098	0.118	0.117	**0.118**	0.102	0.182	0.133	**0.139**
ϕ_y (in^{-1})	0.014	0.011	0.008	0.009	0.011	**0.011**	0.006	0.009	0.008	**0.008**
ϕ_u (in^{-1})	0.073	0.041	0.044	0.052	0.052	**0.052**	0.027	0.041	0.030	**0.033**
P_y (lb)	204.8	145.0	133.6	199.3	241.7	**184.9**	808.2	793.2	735.3	**779.0**
P_y (lb) lower	160.6	125.9	107.1	171.2	194.6	**151.9**	665.7	735.3	677.2	**692.7**
Load drop	44.2	19.1	26.5	28.1	47.1	**33**	142.5	57.9	58.1	**86.2**
P_u (lb)	319.1	267.7	165.2	199.3	243.8	**239.0**	808.2	793.2	880.1	**827.2**
M_y (lb-ft)	192.0	123.1	131.5	201.4	244.3	**178.5**	2157	2334	3291	**2594**
M_u (lb-ft)	299.1	227.2	162.6	201.4	246.4	**227.3**	2157	2334	3291	**2594**

Table 12.4: Ductility Indices Comparison for Small and Large-Scale DHFRP R/C Columns.

Specimen	$\mu_\Delta=\Delta_u/\Delta_y$	$\mu_\theta=\theta_u/\theta_y$	$\mu_\phi=\phi_u/\phi_y$
M-2	3.13	5.19	5.18
M-3	3.04	3.65	3.69
M-4	4.12	5.23	5.79
M-5	3.47	5.85	6.08
M-6	3.23	4.50	4.79
Avg.	**3.40**	**4.89**	**5.11**
P-1	2.43	3.61	4.24
P-2	2.84	4.50	4.71
P-3	2.72	3.65	3.82
Avg.	**2.67**	**3.92**	**4.26**

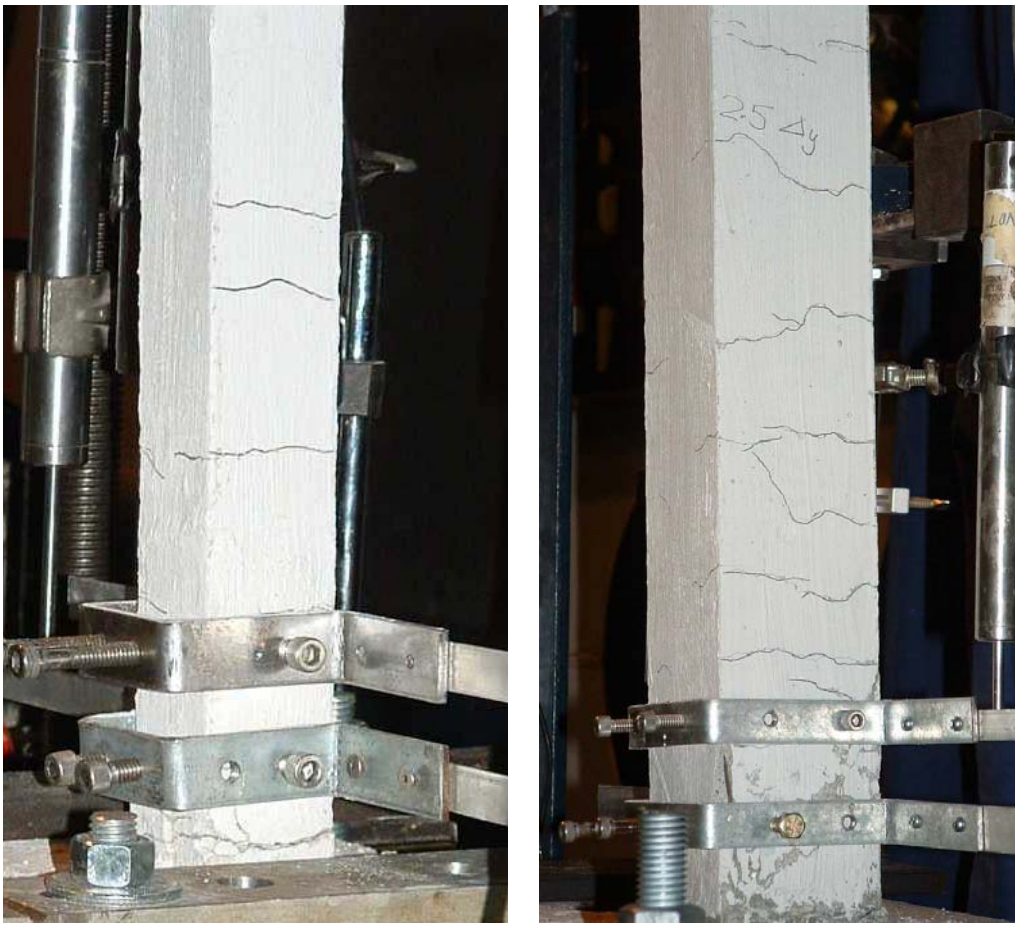

(a) (b)

Figure 12.4: Comparison of Cracking Patterns for Columns with $0.1 f'_c A_g$ Axial Force; (a) Model and (b) Large-Scale Model Columns.

(a) (b)

Figure 12.5: Comparison of Cracking Patterns for Columns with 0.15 $f'_c A_g$ Axial Force; (a) Model and (b) Large-Scale Model Columns.

(a) (b)

Figure 12.6: Comparison of Cracking Patterns for Columns with $0.2 f'_c A_g$ Axial Force; (a) Model and (b) Large-Scale Model Columns.

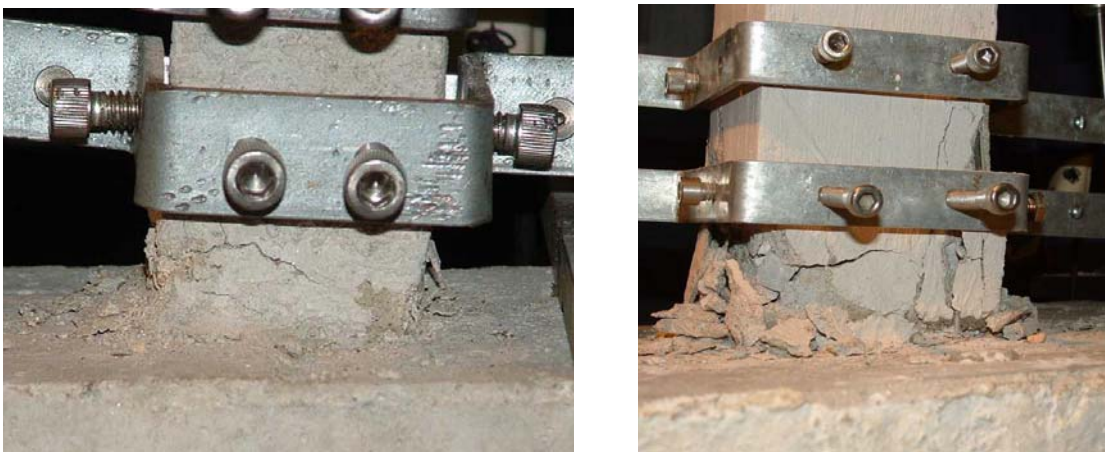

(a) (b)

Figure 12.7: Comparison of Plastic Hinge Formation for Columns with $0.1 f'_c A_g$ Axial Force; (a) Model and (b) Large-Scale Model Columns.

(a) (b)

Figure 12.8: Comparison of Plastic Hinge Formation for Columns with $0.15 f'_c A_g$ Axial Force; (a) Model and (b) Large-Scale Model Columns.

(a) (b)

Figure 12.9: Comparison of Plastic Hinge Formation for Columns with $0.2 f'_c A_g$ Axial Force; (a) Model and (b) Large-Scale Model Columns.

12.3 Similitude Comparison of Model and Prototype Beams

The similitude of R/C beams reinforced with four longitudinal DHFRP bars was investigated. Beams at both scales were tested under four point loading until failure. The model beams began to develop significant shear cracking, and therefore, external shear reinforcement in the form of steel plates was placed along the length to arrest the shear cracking and develop a ductile flexural failure.

Using similitude, the model behavior was scaled up as a prediction of prototype behavior. The model and prototype behaviors were compared based on overall load-displacement and moment-curvature response, beam cracking patterns, and failure mode. The geometric parameters scaled were the specimen dimensions, reinforcing bar size, displacements, strains, and curvatures. The force parameters include applied force and bending moments.

Table 12.5 provides the scale factors pertinent to the beam-column tests. The model values are given followed by the appropriate scale factors and the theoretical prototype values developed using the scaling factor only. These theoretical values are compared with the actual experimental values obtained and the percent difference is compared. The theoretical and experimental values for displacement and moments were within 10-15% of each other. The predicted and actual force values differ by almost 40%. This could be a distortion of the model; however, the ultimate tensile strength of the prototype DHFRP bars was not as high as the model predicted. Therefore, the applied force values were not directly scaleable due to the strength difference.

Shown in Figure 12.10 is the comparison between the predicted prototype load-deflection behavior using similitude and the actual 10-mm prototype DHFRP beam behavior. The moment-curvature is shown in Figure 12.11. There is a difference in the

curvature predicted by the model and the actual curvature obtained in the prototype beam tests. Since the strain of the model must equal the strain of the prototype, and the curvature of a section is the gradient of the strain profile, the curvatures at both scales should be identical. The 5-mm model beams had extensive shear cracking and failed prematurely, thereby limiting the ultimate curvatures. Given in Table 12.6 are the results of both the model and the prototype beam tests. Deflections, curvatures, loads, and moments are compared at both ultimate and yield values. Average values both scale were tabulated.

Given in Table 12.7 is a comparison of the ductility indices for both model and prototype behavior. The ductility indices were based on displacement and curvatures. The ductility indices were larger for the model beams.

Table 12.5: Comparison of Theoretical Scale Factors and Experimental Results Used for DHFRP R/C Beams.

Quantities	5-mm Model Values	Scale Factor	Prototype Similitude Values	Exper. Prototype Values	**% Difference**
Geometry					
Linear dimension, *L*	48	$S_l=2$	96	96	**0**
Linear displacement, Δ, in	1.69	$S_l=2$	3.38	3.5	**3.6**
Area of reinf., A_r, in^2	0.488	$S_l^2=4$	1.94	1.77	**8.8**
Loading					
Concentrated Load, *Q* (lb)	2552	$S_\sigma S_l^2=1*2^2=4$	10208	6849	**32.9**
Moment, *M* (lb-ft)	1624	$S_\sigma S_l^3=1*2^3=8$	12992	11130	**14.3**

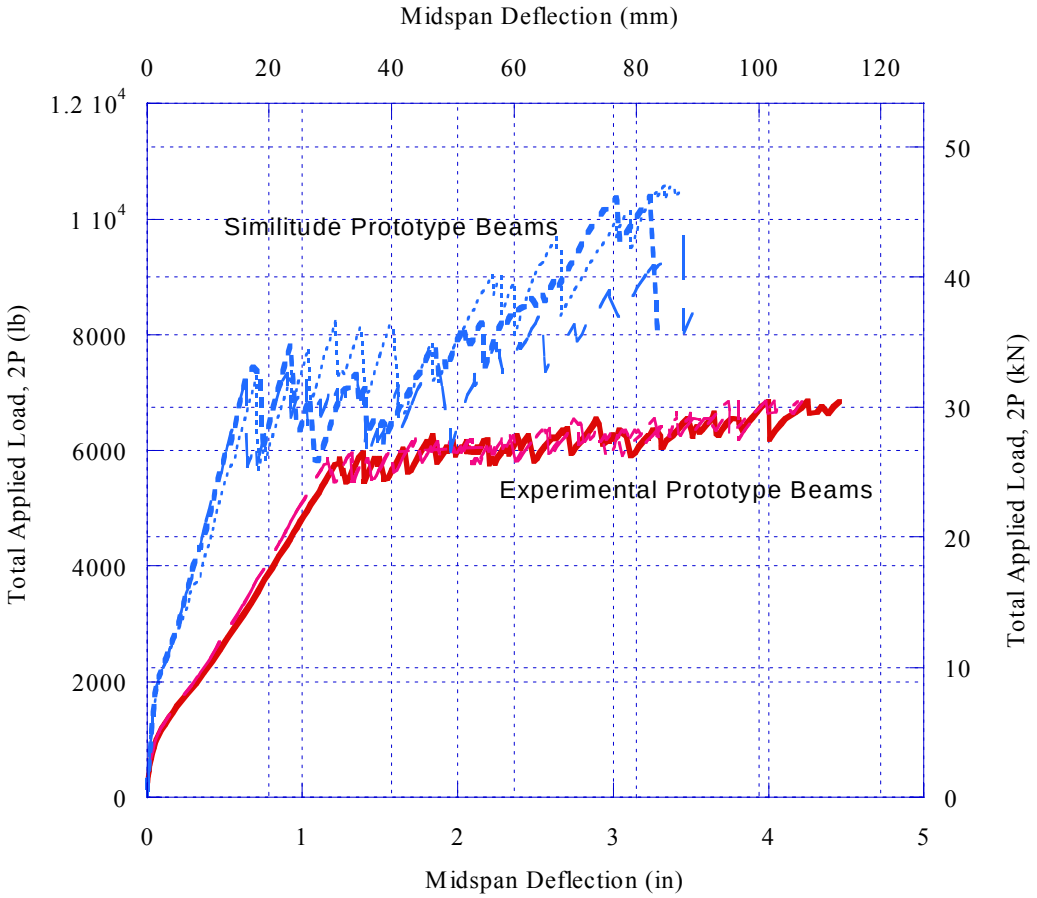

Figure 12.10: Similitude Comparison of Load-Deflection Behavior: Model and Large-Scale Model DHFRP R/C Beams.

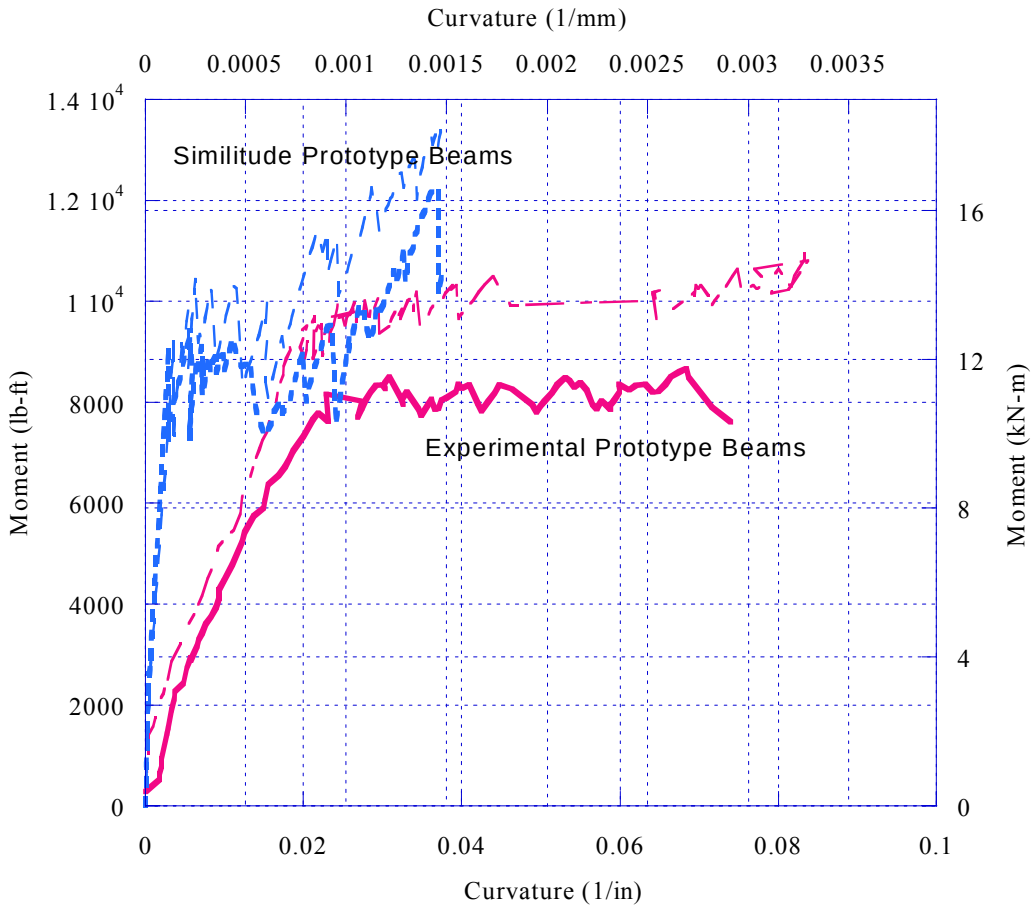

Figure 12.11: Similitude Comparison of Moment-Curvature Behavior: Model and Large-Scale Model DHFRP R/C Beams.

Table 12.6: Results of Beam Tests for 5-mm and 10-mm DHFRP R/C Beams.

	Specimens						
	M-1	M-2	M-3	**Avg**	P-1	P-2	**Avg**
Δ_y (in)	0.326	0.354	0.319	**0.33**	0.972	1.16	**1.07**
Δ_u (in)	1.62	1.72	1.73	**1.69**	1.81	4.19	**3.0**
ϕ_y (in^{-1})	0.0013	0.001	0.001	**0.0011**	0.0229	0.033	**0.028**
ϕ_u (in^{-1})	0.0087	0.0094	0.0093	**0.0091**	0.074	0.13	**0.10**
P_{cr} (lb)	520	480	480	**493.0**	1135.1	1370.5	**1252.8**
P_y (lb)	1947	1820	1800	**1856.0**	4940.2	5855.5	**5398**
P_u (lb)	2599	2630	2425	**2552**	5335.7	6849.3	**6093**
M_y (lb-ft)	938	1151	1138.2	**1076**	8155.3	8670.6	**8413**
M_u (lb-ft)	1667	1672	1533	**1624**	9515.2	11130.1	**10323**

Table 12.7: Ductility Indices Comparison for 5-mm and 10-mm DHFRP R/C Beams.

Specimen	$\mu_\Delta=\Delta_u/\Delta_y$	$\mu_\phi=\phi_u/\phi_y$
M-1	4.9	5.7
M-2	4.6	6.3
M-3	5.5	5.9
Avg.	**5.0**	**6.0**
P-1	1.86	3.23
P-2	3.61	3.94
Avg.	**2.74**	**3.59**

Shown in Figure 12.12 are the overall cracking and failure patterns of the 5-mm DHFRP beams. The cracking patterns had both vertical and diagonal cracks, indicative of flexural and shear cracking. Also, two beams failed by rupture of the DHFRP bars, thereby indicating a shear-governed failure. This is a brittle failure mode.

Given in Figures 12.13 and 12.14 are the overall cracking patterns of the prototype beams. Cracking was limited to the formation of vertical cracks only, thereby indicating a flexural or ductile failure. The crack spacing was closer than the model beams, thereby indicating good bond strength between the bar and concrete. Failure for both of these beams was by crushing of the concrete in compression before bar rupture, indicating a ductile failure mode.

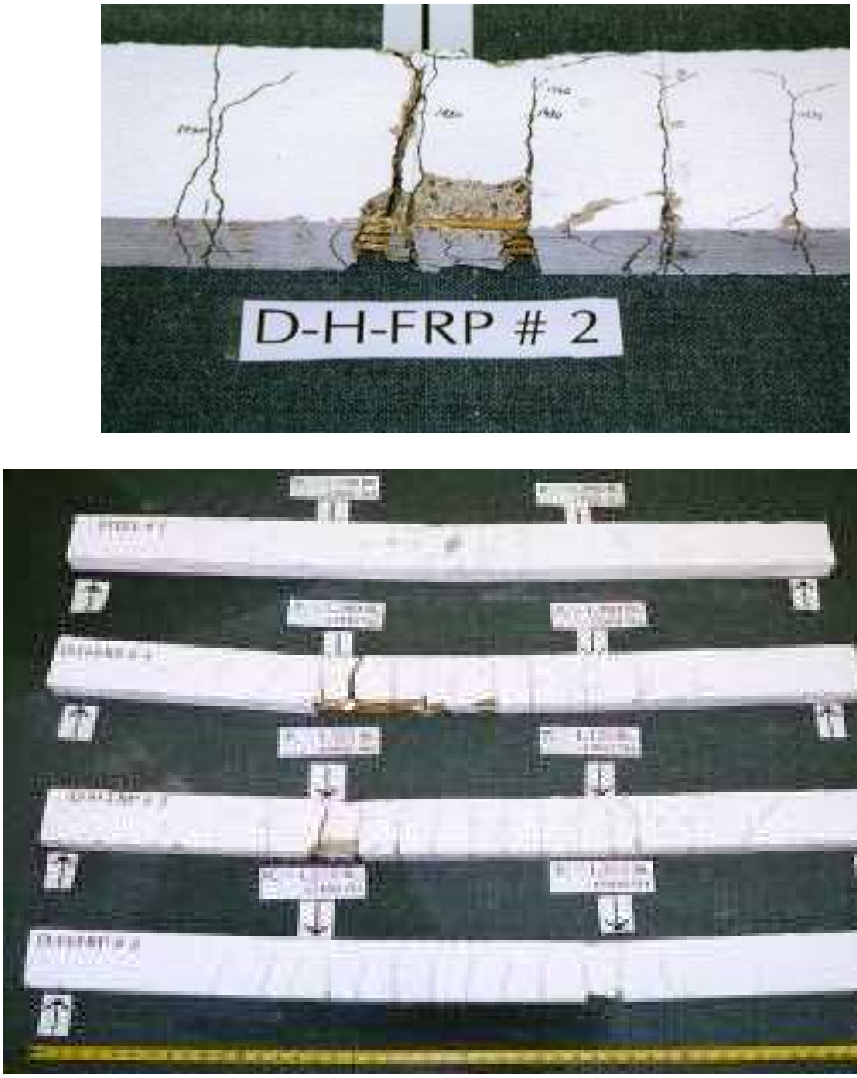

Figure 12.12: Cracking Patterns of 5-mm Diameter DHFRP R/C Beams.

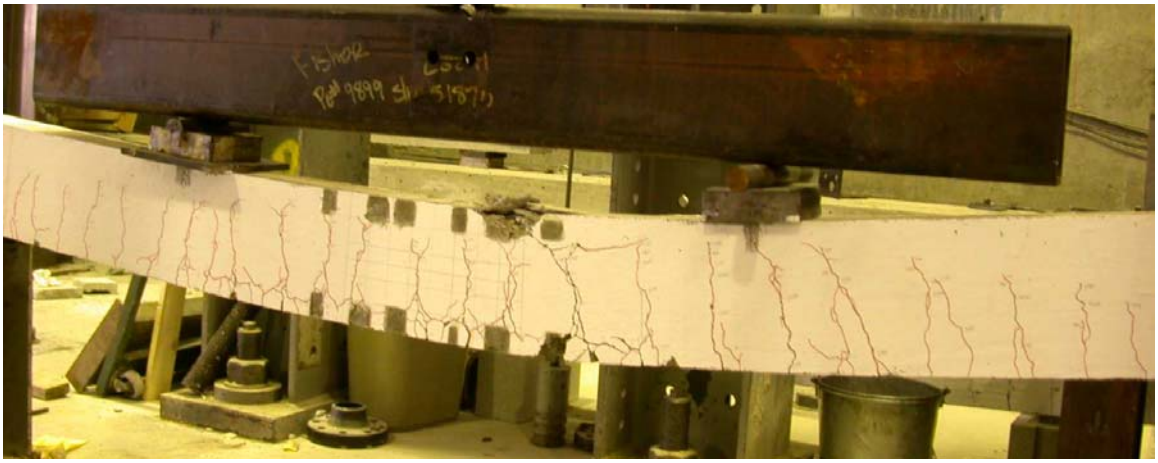

Figure 12.13: Cracking Pattern of 10-mm Diameter Large-Scale Model DHFRP R/C Beam P-2.

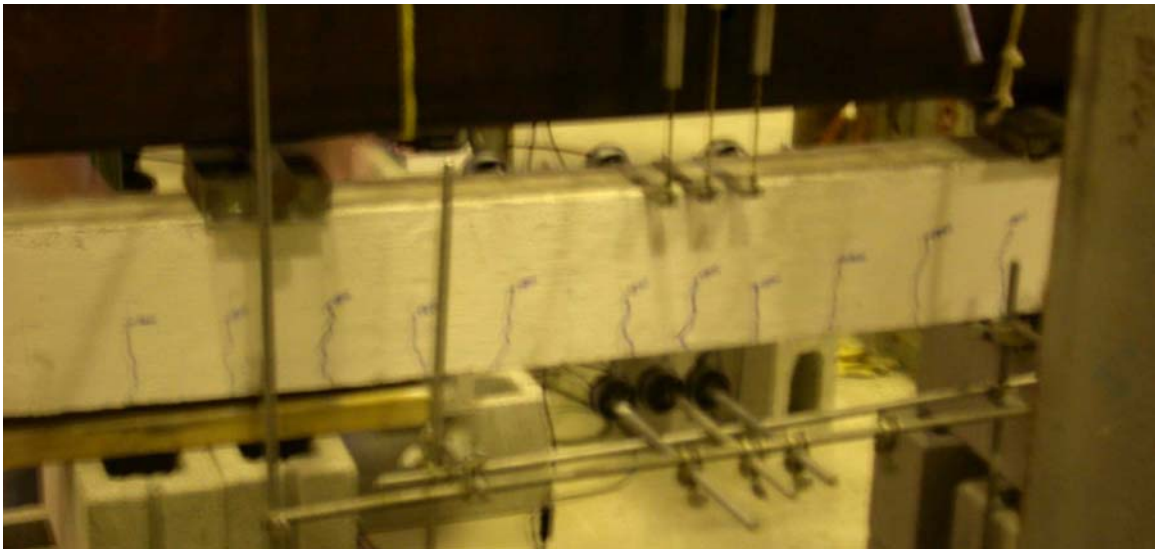

Figure 12.14: Cracking Pattern of 10-mm Diameter Large-Scale Model DHFRP R/C Beam P-1.

12.4 Similitude Comparison of 5-mm and 10-mm Diameter DHFRP Bars: Tensile Behavior

For the DHFRP tensile properties, both geometry and force must be 'scaled-up' using similitude. The geometric parameters were the number of yarns, the reinforcing bar cross sectional area, overall displacements, and strains. The force parameter is the applied axial force.

Table 12.8 provides the scale factors pertinent to the tensile tests. The model values are given followed by the appropriate scale factors and the theoretical prototype values developed using the scaling factor only. These theoretical values are compared with the actual experimental values obtained and the percent difference is compared. The theoretical and experimental values for force and displacement are within 10% of each other. There might be some distortion in the area since the 10-mm diameter prototype bar used the symmetric preform with four rib yarns, while the 5-mm model bar used the two rib yarn unsymmetrical preform.

Shown in Figure 12.15 is the experimental load-strain behavior for both the model and prototype-size bars. This was included to show the large difference in strength between the 5-mm and 10-mm diameter bars.

Figure 12.16 shows the predicted prototype tensile behavior using similitude and the actual experimental prototype behavior. There is very good correlation between the predicted and experimental behavior. The experimental load values are within 5-10% of the predicted behavior. A comparison of the model and prototype behavior is given in Table 12.9.

Table 12.8: Comparison of Theoretical Scale Factors and Experimental Results Used for DHFRP Tensile Properties.

Quantities	5-mm Model Values	Scale Factor	Prototype Similitude Values	Exper. Prototype Values	**% Difference**
Geometry					
Linear displacement, Δ, in	0.102	$S_l=2$	0.204	0.188	**7.8**
Area of reinf., A_r, in^2	0.488	$S_l^2=4$	1.94	1.77	**8.8**
Loading					
Concentrated Load, Q (lb)	1375	$S_\sigma S_l^2=1*2^2=4$	5500	6849	**24.5**

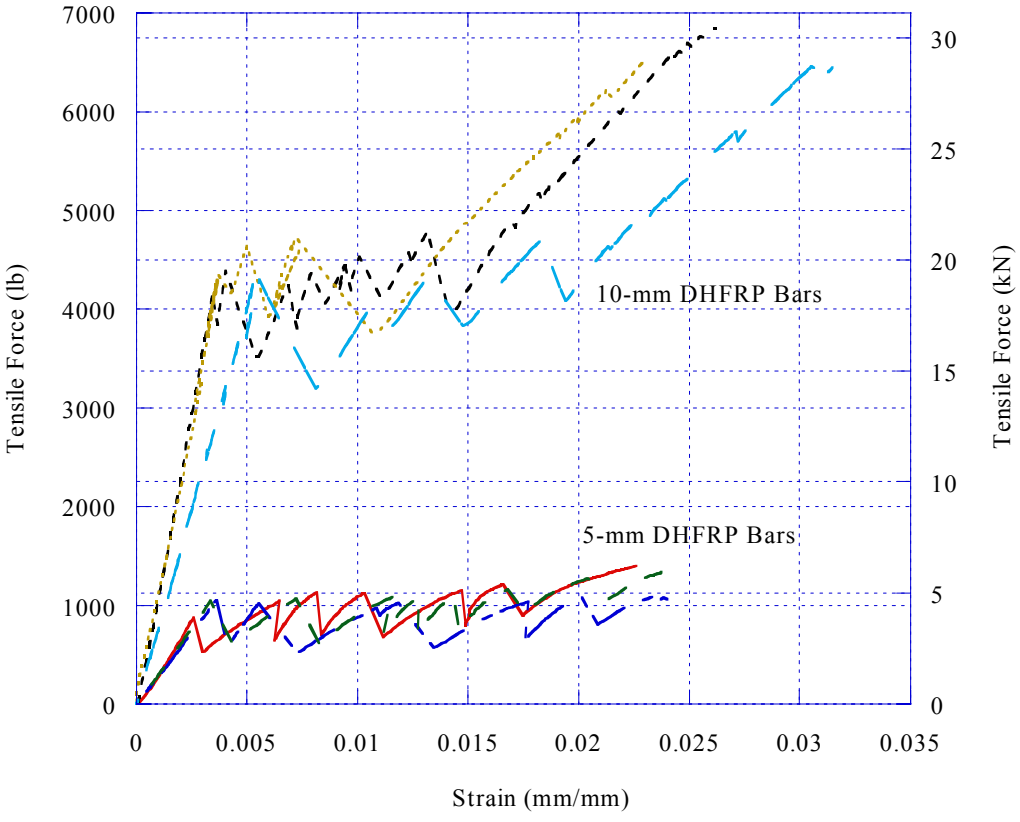

Figure 12.15: Tensile Behavior of 5-mm and 10-mm Diameter DHFRP Bars.

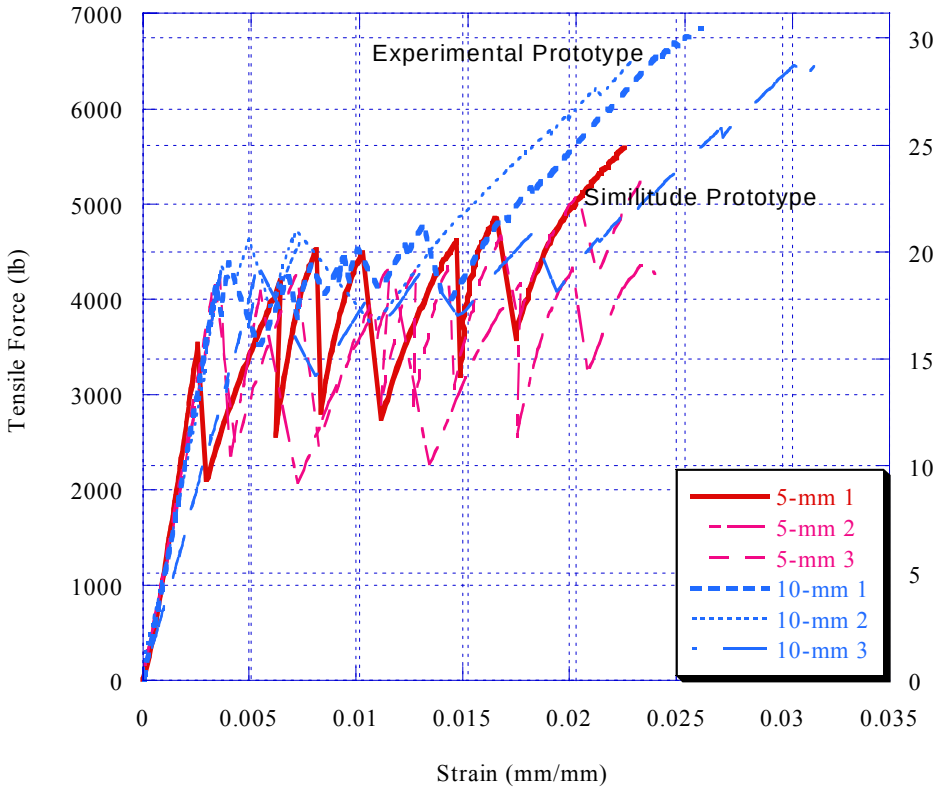

Figure 12.16: Similitude Comparison of Tensile Behavior of 5-mm and 10-mm Diameter DHFRP Bars.

Table 12.9: Values of Stress and Strain from 10-mm DHFRP Tension Tests.

	Model Behavior			Prototype Behavior		
	Yield stress, ksi (MPa)	Ultimate stress, ksi	Modulus, ksi (GPa)	Yield stress, ksi	Ultimate stress, ksi	Modulus, ksi
	58.01	53.57	10758.8	46.4	77.18	15499.4
	55.11	59.54	10647.5	56.75	85.78	15339.1
	50.76	62.58	10291.1	54.85	90.16	14825.6
	37.71	57.66	14725.3	61.77	83.06	11654.3
	31.91	59.03	16575.7	56.02	85.04	10569.0
	46.41	56.08	16244.2	60.03	80.79	12771.6
Average values	**46.65 (321.7)**	**68.65 (473.3)**	**14503.7 (100.0)**	**57.88 (399.1)**	**84.97 (585.8)**	**16131.8 (111.2)**

CHAPTER 13. CONCLUSIONS

The research conducted on 10-mm diameter DHFRP bars consisted of three sections: product development and processing, material and mechanical characterization, and behavior of 10-mm diameter DHFRP bars in concrete members. A parametric study of the processing of DHFRP was conducted, and the braidtrusion process was modified to produce an improved DHFRP bar. The mechanical characterization of 10-mm diameter DHFRP bars was performed by first quantifying the mechanical properties of the bar itself and then by studying the behavior of the bar in reinforced concrete (R/C) members. The short-term properties of DHFRP quantified included the microstructure of the bar, the uniaxial tensile strength, the bond strength with concrete, and the bending strength. Long-term properties explained included creep and stress-rupture behavior. These material and mechanical properties were needed before proper design and a sufficient level of design confidence of R/C members could be performed.

Testing of R/C members included prototype beam and slab sections in flexure reinforced with DHFRP bars. The final test series was to study the response of bridge piers reinforced with DHFRP longitudinal bars and subjected to increasing cycles of reverse cyclic loading. Both model size and prototype size DHFRP bars were used.

Computer code was written to verify many of the experimental results. The results are presented in Appendix E. Programs written included the Fiber Architecture Design Model (FADM) for the strength properties of DHFRP bars with various yarn types, resins, core and braid yarns, and yarn orientations. Programs were also written for the design and capacity analysis of rectangular R/C beams reinforced with DHFRP longitudinal bars. A program was also written to determine the load-deflection and

moment-curvature response of doubly-reinforced R/C beams subjected to four-point loading. A program was written to determine the interaction diagrams for R/C columns reinforced with either DHFRP or steel bars. A moment-curvature analysis, moment-rotation analysis, and axial load analysis was performed for DHFRP columns using the SEQMC program.

The key conclusions from each of the tests performed on DHFRP are presented.

- From tensile testing and SEM results it can be concluded that an appropriate process has been developed for manufacturing 10-mm diameter DHFRP rebar with fiber volume fraction in the order of 70% utilizing the braidtrusion technique. It is possible to produce a high-quality composite by braidtrusion without the need for a die.
- New rebar designed with 4-rib yarns and a higher braid angle (± 45°) showed significant increase in bond strength due to the increase in the number of criss-crosses per unit length. Since the criss-cross pattern is uniformly distributed around the circumference the stiffness is consistent regardless of bending direction. The symmetric rib pattern generates uniform pressure inside the die resulting in lower void content and less distortion in core shape.
- Lower modulus fiber materials (Kevlar 29/IM7 carbon) system can be used to lower the cost. With this materials system, the strength and strain of the rebar was significantly increased, while the modulus was approximately 20% lower than the results showed in the earliest study of 5-mm diameter rebar where Kevlar 49 and P55S carbon were used. As can be seen in Table 4, IM7 carbon content is only 11% by volume and Kevlar 29 is about 62%. If the

amount of Kevlar 29 is reduced and compensate by IM7 then the modulus of the rebar can be improved. If this is possible then the cost can be enormously reduced since IM7 carbon cost much less than P55S carbon.

- All DHFRP had a similar slip mechanism. For all embedment lengths, failure occurred by bar rupture, not by bar pullout. The DHFRP slip mechanism is extremely unique, and is directly dependent on the failure mechanism of the bar, as described in section 6.3. The load-slip curve for DHFRP is a stepped curve until bar rupture. When the load was increased, very little free-end slip was recorded. The DHFRP bars ruptured at embedment lengths as short as 2.5". This was because of the new symmetric preform design using more rib yarns. Also, keeping the braid angle at approximately 45 degrees increased the rib height and spacing, thereby improving the mechanical interlock. Also, the general surface of the DFRP bar away from the rib was rough since the bar was manufactured without a die. This greatly improved the bond strength of the DHFRP bars. From the bond pullout tests, the development length computed using the ACI 318-02 code results in very conservative values for the DHFRP bar.
- The bending test illustrated the flexural rigidity of 10-mm diameter DHFRP bars. Low flexural stiffness was evident; however, the bars when placed in concrete beams are subjected to axial tension. Therefore, the full axial strength of the composite in the 1-direction can still be realized. The creep rupture behavior First, failure at 50 years is shown. The load ratio value at this time is 0.69or 69 % of the ultimate load. These values are very promising

when compared to other results from creep tests. Other researchers had results in the range of 55- 65%, and therefore, the obtained results for DHFRP are either superior or comparable with other FRP materials.

- The performance of R/C beams with prototype DHFRP bars was measured in four ways: (1) the crack progression to failure, the (2) failure mode, (3) the load-deflection behavior and (4) moment-curvature behavior. These measures indicated the ductility, bond strength, and energy absorption of DHFRP. The crack pattern was very closely spaced and symmetric, similar to beam P-1 and to steel R/C beams. All of the cracks were vertical flexural cracks, and no signs of diagonal shear cracks were evident. The close spacing of the cracks indicated good bond strength. The failure mode of this beam was ductile, similar to beam P-1. Figure 8-54 showed the beam when the load was released. Large inelastic deformations resulted as indicated by the deformed shape of the beam. This behavior was verified by the load-deflection and moment-curvature behaviors. The displacement ductility factor was 3.61 and the curvature ductility factor was 3.94. This is very promising since most current FRPs have ratios closer to 2-3, whereas the DHFRP factors are closer to 4. This indicates significant ductility capacity which is essential to obtain the full plastic strength of the section (Paulay and Priestley, 1992). Also, since the bars did not rupture at failure, there was still residual strength in the DHFRP bars.
- The reverse cyclic loading behavior of bridge columns reinforced with DHFRP bars was promising. The hysteretic behavior showed significant

energy absorption capacity by the DHFRP, especially for large inelastic deformations. Ductility indices of 2.43-4.12 based on displacement, 3.61-5.85 based on rotation, and 3.69-6.08 based on curvature were obtained. This ability to absorb inelastic energy is critical during moderate to severe seismic events and is not typical for FRP materials.

13.1 Future Work with DHFRP

Future work to be conducted on DHFRP includes four main areas of research. These include failure mechanism characterization, processing, long-term behavior, and in-situ behavior and monitoring.

- The failure mechanism of DHFRP has been hypothesized, but is still relatively unknown. From the beam tests in Chapter 8, full length DHFRP bars were extracted from the beam after testing. The failure mechanism of the internal structure must be determined, especially the core yarn failure. The failure plane or planes of core yarns could be investigated using Time Domain Reflectometry (TDR). In this process, a signal or multiple signals would be recorded is there is a discontinuity in the carbon core (i.e., failure plane or multiple planes).
- The processing of DHFRP needs to be investigated using less-expensive reinforcing yarns. Work on Dialead coal tar pitch-based carbon fiber (Mitsubishi Chemical) will be performed. The modulus of Dialead is 63000 ksi to 92000 ksi (434.4 to 634.3 GPa) and the cost is $20/ lb and $ 30/ lb, respectively. Compared with P-55S 4K carbon at $60/ lb, the cost savings would be significant.

- Long-term behavior includes continued testing of creep and stress-rupture properties of DHFRP bars, especially 10-mm DHFRP bars. Also, the high-cycle fatigue strength needs to be characterized to determine the life-cycle behavior of DHFRP for bridge deck applications. This property is crucial for long-term monitoring projects.
- Long-term testing using in-situ loading and environmental conditions should be conducted. This will include the design, construction, and monitoring of a bridge deck subjected to long-term loading. The DHFRP bars developed for the long-term monitoring project would contain fiber optic filaments, placed during the manufacturing process. These new DHFRP would be smart-bars that could sense strains in the bar continuously for the duration of the test. Since the strains would be measured continuously along the length of each bar, the failure mechanism of DHRP could be closely monitored for both service loading and inelastic overloading. This is critical since the failure mechanism of DHFRP is still relatively undefined.

LIST OF REFERENCES

ACI Report 408.3-01 / 408.3R-01 (2001). "Splice and Development Length of High Relative Rib Area Reinforcing Bars in Tension (408.3-01) and Commentary (408.3R-01)." Reported by ACI Committee 408, Report Chair David Darwin, ACI, Box 9094, Farmington Hills, MI 48333-9094.

ACI Report 440.R1-01 (2001). "Guide for the Design and Construction of Concrete Reinforced with FRP Bars." Reported by ACI Committee 440, Report Chair Sami H. Rizkalla, ACI, Box 9094, Farmington Hills, MI 48333-9094.

Adimi, M.R., Rahman, A.H., and Benmokrane, B. (2000). "New Method for Testing Fiber-Reinforced Polymer Rods Under Fatigue." *Journal of Composites for Construction*, Vol. 4, No. 4, November, pp. 206-213.

Afaghi-Khatibi, A. and Mai, Y.-W. (2001). "On the Characterisation of Fibre/ Matrix interfacial Degradation Under Cyclic Loading—A New Method." *Proceedings of the 13th International Conference on Composite Materials*, 24-28 June, Beijing, China, ID-1669.

Agrawal, G.L., Tulin, L.G., and Gerstle, K.H. (1965). "Response of Doubly Reinforced Concrete Beams to Cyclic Loading." *Journal ACI*, Vol. 62, No. 7, July, pp. 823-836.

Aiello, M.A. and Ombres, L. (2000). "Load-Deflection Analysis of FRP Reinforced Concrete Flexural Members." *Journal of Composites for Construction*, Vol. 4, No. 4, November, pp. 164-171.

Al-Salloum, Y.A., Alsayed, S.H., and Almusallam, T.H. (2000). "Deflection Model for Concrete Beams Reinforced By GFRP Bar." *Composites in the Transportation Industry*, Edited by Bandyopadhyay, S., Gowripalan, N., Drayton, N., and Heslehurst, R., Proceedings of the ACUN-2, 14-18 February, Univ. of New South Wales, Sydney, Australia, pp. 78-83.

Assa, B., Nishiyama, M., and Watanabe, F. (2001). "New Approach for Modeling Confined Concrete. I: Circular Columns." *Journal of Structural Engineering*, Vol. 127, No. 7, July, pp. 743-750.

Assa, B., Nishiyama, M., and Watanabe, F. (2001). "New Approach for Modeling Confined Concrete. II: Rectangular Columns." *Journal of Structural Engineering*, Vol. 127, No. 7, July, pp. 751-757.

ASTM A615/A615M-95b (2002). "Standard Specification for Deformed and Plain Billet-Steel Bars fro Concrete Reinforcement." *Annual Book of ASTM Standards*, ASTM International, West Conshohocken, PA.

ASTM A775/A775M-01 (2002). "Standard Specification for Epoxy-Coated Reinforcing Steel Bars." *Annual Book of ASTM Standards*, ASTM International, West Conshohocken, PA.

ASTM A931-96(2002) (2002). "Standard Test Method for Tension Testing of Wire Ropes and Strand." *Annual Book of ASTM Standards*, ASTM International, West Conshohocken, PA.

ASTM C39/C39M-01 (2002). "Standard Test Method for Compressive Strength of Cylindrical Concrete Specimens." *Annual Book of ASTM Standards*, ASTM International, West Conshohocken, PA.

ASTM C900-01 (2002). "Standard Test Method for Pullout Strength of Hardened Concrete." *Annual Book of ASTM Standards*, ASTM International, West Conshohocken, PA.

ASTM D2990-01 (2002). "Standard Test Methods for Tensile, Compressive, and Flexural Creep and Creep-Rupture of Plastics." *Annual Book of ASTM Standards*, ASTM International, West Conshohocken, PA.

ASTM D4476-97 (2002). "Standard Test Method for Flexural Properties of Fiber Reinforced Pultruded Plastic Rods." *Annual Book of ASTM Standards*, ASTM International, West Conshohocken, PA.

ASTM D638-02 (2002). "Standard Test Method for Tensile Properties of Plastics." *Annual Book of ASTM Standards*, ASTM International, West Conshohocken, PA.

ASTM E1012-99 (2002). "Standard Practice for Verification of Specimen Alignment Under Tensile Loading." *Annual Book of ASTM Standards*, ASTM International, West Conshohocken, PA.

ASTM E1309-00 (2002). "Standard Guide for Identification of Fiber-Reinforced Polymer Matrix Composite Materials in Databases." *Annual Book of ASTM Standards*, ASTM International, West Conshohocken, PA.

ASTM E132-97 (2002). "Standard Test Method for Poisson's Ratio at Room Temperature." *Annual Book of ASTM Standards*, ASTM International, West Conshohocken, PA.

ASTM E290-97a (2002). "Standard Test Method for Bend Testing of Material for Ductility." *Annual Book of ASTM Standards*, ASTM International, West Conshohocken, PA.

ASTM E529-94 (2002). "Standard Guide for Conducting Flexural Tests on Beams and Girders for Building Construction." *Annual Book of ASTM Standards*, ASTM International, West Conshohocken, PA.

ASTM E606-92(1998) (2002). "Standard Practice for Strain-Controlled Fatigue Testing." *Annual Book of ASTM Standards*, ASTM International, West Conshohocken, PA.

Ayoub, A. and Fillippou, F.C. (1999). "Mixed Formulation of Bond-Slip Problems Under Cyclic Loads." *Journal of Structural Engineering*, Vol. 125, No. 6, June, pp. 661-671.

Bakis, C.E., Bank, V.L., Cosenza, E., Davalos, J.F., Lesko, J.J., Machida, A., Rizkalla, S.H., and Triantafillou, T.C. (2002). "Fiber-Reinforced Polymer Composites for Construction—State-of-the-Art Review." *Journal of Composites for Construction*, Vol. 6, No. 1, May, pp. 73-87.

Bayrak, O. and Sheikh, S.A. (2001). "Plastic Hinge Analysis." *Journal of Structural Engineering*, Vol. 127, No. 9, July, pp. 1092-1100.

Bedell, R. J. and Abrams, D. P. (1983). "Scale Relationships of Concrete Columns." *Report to the National Science Foundation,* Department of Civil, Environmental, and Architectural Engineering, University of Colorado, Boulder, 132 pp.

Bertero, V.V. and Bresler, B. (1969). "Seismic Behavior of Reinforced Concrete Framed Structures." *Proceedings of Fourth World Conference on Earthquake Engineering*, Vol. 1, Session B-2, pp. 109-124. Chile.

Bonacci, J.F. and Maalej, M. (2001). "Behavior Trends of RC Beams Strengthened with Externally Bonded FRP." *Journal of Composites for Construction*, Vol. 5, No. 2, May, pp. 102-113.

Bresler, B. and Bertero, B. (1968). "Behaviour of Reinforced Concrete Under Repeated Load." *Journal of the Structural Division, ASCE*, Vol. 94, ST6, June, pp. 1567-1589.

Burgueno, R., Davol, A, Zhao, L., Seible, F., and Karbhari, V.M. (2004). "Flexural Behavior of Hybrid Fiber-Reinforced Polymer/ Concrete Beam/Slab Bridge Component." *ACI Structural Journal*, Vol. 101, No. 2, March/April, pp. 228-236.

Butt, S.D., Limaye, V., Mufti, A.A., and Bakht, B. (2004). "Acoustic Transmission Technique for Evaluating Fatigue Damage in Concrete Bridge Deck Slabs." *ACI Structural Journal*, Vol. 101, No. 1, January/February, pp. 3-10.

Castro, P.F. and Carino, N.J. (1998). "Tensile and Nondestructive Testing of FRP Bars." *Journal of Composites for Construction*, Vol. 2, No. 1, February, pp. 17-27.

Cosenza, E., Manfredi, G., and Realfonzo, R. (1997). "Behavior of Modeling of Bond of FRP Rebars to Concrete." *Journal of Composites for Construction*, Vol. 1, No. 2, May, pp. 40-51.

Crookston, J.J., Souter, B.J., Long, A.C., and Jones, I.A. (2001). "The Application of a General Fibre Architecture Model for Composite Mechanical Property Prediction." *Proceedings of the 13th International Conference on Composite Materials*, 24-28 June, Beijing, China.

Davila Sanhdars, M.A. and Oehlers, D.J. (2000). "Ductility Design of RC Beams with FRP Bars." *Composites in the Transportation Industry*, Edited by Bandyopadhyay, S., Gowripalan, N., Drayton, N., and Heslehurst, R., Proceedings of the ACUN-2, 14-18 February, Univ. of New South Wales, Sydney, Australia, pp. 210-215.

DeLorenzis, L. and Nanni, A. (2001). "Characterization of FRP Rods as Near-Surface Mounted Reinforcement." *Journal of Composites for Construction*, Vol. 5, No. 2, May, pp. 114-121.

Dowling, N.E. (1999). *Mechanical Behavior of Materials: Engineering Methods for Deformation, Fracture, and Fatigue, Second Edition,* Prentice Hall, Inc., Upper Saddle River, NJ.

Eddie, D., Shalaby, A., and Rizkalla, S. (2001). "Glass Fiber-Reinforced Polymer Dowels for Concrete Pavements." *ACI Structural Journal*, Vol. 98, No. 2, March/April, pp. 201-206.

Ehlen, M.A. (1999). "Life-Cycle Cost of Fiber-Reinforced Polymer Bridge Decks." *Journal of Materials in Civil Engineering*, Vol. 11, No. 3, August, pp. 224-230.

Eligehausen, R., Popov, E.P., and Bertero, V.V. (1983). "Local Bond Stress-Slip Relationships of Deformed Bars Under General Excitations." *Report No. 83/23, EERC*, University of California, Berkeley.

Elmorsi, M., Kianoush, M. R., and Tso, W. K. (1998). "Nonlinear Analysis of Cyclically Loaded Reinforced Concrete Structures." *ACI Structural Journal,* Vol. 95, No. 6, November-December, pp. 725-739.

Esmaeily, A. and Xiao, Y. (2004). "Behavior of Reinforced Concrete Columns Under Variable Axial Loads." *ACI Structural Journal*, Vol. 101, No. 1, Jan./Feb., pp. 124-132.

Fanning, P.J. and Kelly, O. (2001). "Ultimate Response of RC Beams Strengthened with CRFP Plates." *Journal of Composites for Construction*, Vol. 5, No. 2, May, pp. 122-127.

Federal Highway Administration (2001). FHWA Bulletin, Highway Funding 1998-2001, March 6, 2001, Washington, D.C. http://www.fhwa.dot.gov/ohim/fhwa1.htm

Focacci, F., Nanni, A., and Bakis, C.E. (2000). "Local Bond-Slip Relationship for FRP Reinforcement in Concrete." *Journal of Composites for Construction*, Vol. 4, No. 1, February, pp. 24-31.

Freimanis, A.J., Bakis, C.E., Nanni, A. and Gremel, D. (1998). "A Comparison of Pull-Out and Tensile Behaviors of FRP Reinforcement for Concrete." Proceedings of the *2nd International Conference On Composites in Infrastructure*, Edited by Saadatmanesh, H. and Ehsani, M.R.., 15-17 Jan., Tucson, AZ, pp. 52-65.

Gergely, P. (1969). "Splitting Cracks Along the Main Reinforcement in Concrete Members." *Report to Bureau of Public Roads U.S. Department of Transportation,* Cornell University, Ithaca, NY, 90 pp.

Grace, N.F., Ragheb, W.F., and Abdel-Sayed, G. (2004). "Strengthening of Cantilever and Continuous Beams Using New Triaxially Braided Ductile Fabric." *ACI Structural Journal*, Vol. 101, No. 2, March/April, pp. 237-244.

Gerritse, A. and Taerwe, L. (2000). "Design Aspects for Concrete Members Pretensioned with AFRP." *Composites in the Transportation Industry*, Edited by Bandyopadhyay, S., Gowripalan, N., Drayton, N., and Heslehurst, R., Proceedings of the ACUN-2, 14-18 February, Univ. of New South Wales, Sydney, Australia, pp. 33-38.

Grace, N.F., Soliman, A.K., Abdel-Sayed, G., and Saleh, K.R. (1998). "Behavior and Ductility of Simple and Continuous FRP Reinforced Beams." *Journal of Composites for Construction*, Vol. 2, No. 4, November, pp. 186-194.

Green, M.F. (2000). "Canadian Perspective on Rehabilitation of Structures with FRP Materials." *Composites in the Transportation Industry*, Edited by Bandyopadhyay, S., Gowripalan, N., Drayton, N., and Heslehurst, R., Proceedings of the ACUN-2, 14-18 February, Univ. of New South Wales, Sydney, Australia, pp. 127-135.

Gould, N.C. and Harmon, T.G. (2002). "Confined Concrete Columns Subjected to Axial Load, Cyclic Shear, and Cyclic Flexure—Part II: Experimental Program." *ACI Structural Journal*, Vol. 99, No. 1, Jan./Feb., pp. 42-50.

Gowripalan, N. (2000). "Fiber Reinforced Polymer (FRP) Reinforcement for Concrete Bridges and Fibre Optic Monitoring Techniques." *Composites in the Transportation Industry*, Edited by Bandyopadhyay, S., Gowripalan, N., Drayton, N., and Heslehurst, R., Proceedings of the ACUN-2, 14-18 February, Univ. of New South Wales, Sydney, Australia, pp. 173-177.

Gutowski, T. G. (1997). *Advanced Composites Manufacturing,* John Wiley & Sons, Inc., New York, NY, pp. 259-296.

Hamidah, H.M., Gowripalan, N., and Fadhil, N.M. (2001). "Absorption of Aramid Prestressing Rods in Aggressive Solutions." *Journal of Composites for Construction*, Vol. 5, No. 4, November, pp. 254-257.

Hampton, F.P., Ko, F.K. and Harris, H.G. (1999). "Creep, Stress Rupture, and Behavior of a Ductile Hybrid Fiber Reinforced Polymer (D-H-FRP) For Concrete Structures", *Proceedings of the 12th International Conference on Composite Materials*, July 5-9, 1999, Paris, France, p. 731.

Hampton, F.P., Lam, H., Ko, F.K., and Harris, H.G. (2001). "Design Methodology of a Ductile Hybrid FRP For Concrete Structures By the Braidtrusion Process", *Proceedings of SAMPE 2001*, May 6-10, 2001, Long Beach, California.

Harajli, M.H. and Rteil, A.A. (2004). "Effect of Confinement Using Fiber-Reinforced Polymer or Fiber-Reinforced Concrete on Seismic Performance of Gravity Load-Designed Columns." *ACI Structural Journal*, Vol. 101, No. 1, Jan./Feb., pp. 47-56.

Harmon, T.G., Gould, N.C., Ramakrishnan, S., and Wang, E.H. (2002). "Confined Concrete Columns Subjected to Axial Load, Cyclic Shear, and Cyclic Flexure—Part I: Analytic Models." *ACI Structural Journal*, Vol. 99, No. 1, Jan./Feb., pp. 32-41.

Harris, H. G., Sabnis, G. M., and White, R. N. (1966)"Small Scale Direct Models of Reinforced and Prestressed Concrete Structures," *Report No. 326*, Department of Structural Engineering, Cornell Univ., Ithaca, NY, September, 362 pp.

Harris, H. G., Somboonsong, W. and Ko, F. K. (1997)"A New Ductile Hybrid Fiber Reinforced Polymer (FRP) Reinforcement for Concrete Structures," *International Conference on Engineering Materials*, Vol. 1, 8-11 June, CSCE, Ottawa, Canada, pp. 593-604.

Harris, H. G., Somboonsong, W. and Ko, F. K. (1998) "New Ductile Hybrid FRP Reinforced Bar For Concrete Structures," *Journal of Composites for Construction,* ASCE, Feb. pp. 1-10.

Harris, H. G., Somboonsong, W., Ko, F. K. and Huesgen, R. (1998) "A Second Generation Ductile Hybrid Fiber Reinforcement Polymer (FRP) For Concrete Structures," Proc. ICCI*, Second International Conference on Composites in Infrastructure*, Tucson, Arizona, Jan 5-7.

Harris H.G., Hampton, F. P., Martin, S., and Ko, F. K. (2000). "Cyclic Behavior of A Second Generation Ductile Hybrid Fiber Reinforced Polymer (D-H-FRP) for Earthquake Resistant Concrete Structures", *Proceedings of the 12th World Conference on Earthquake Engineering*, Jan. 3-Feb. 4, 2000, Aukland, New Zealand, pp. 1-8.

Harris, H.G. and Sabnis, G.M. (1999). *Structural Modeling and Experimental Techniques, Second Edition, CRC Press, Boca Raton, FL.*

Heffernan, P.J., Erki, M.A., and DuQuesnay, D.L. (2004). "Stress Redistribution in Cyclically Loaded Reinforced Concrete Beams." *ACI Structural Journal*, Vol. 101, No. 2, March/April, pp. 261-268.

Hoa, S.V. and Xie, M. (2001). "Interface Between Fiber Reinforced Plastic Rod and Concrete." *Proceedings of the 13th International Conference on Composite Materials*, 24-28 June, Beijing, China, ID-1246.

Huesgen, R. (1997), "Flexural Behavior of Ductile Hybrid FRP Rebars in Singly Reinforced Concrete Beams," MSc Thesis, Department of Civil and Architectural Engineering, Drexel University, Philadelphia, PA.

Ibell, T. and Burgoyne, C. (1999). "Use of Fiber-Reinforced Plastics Versus Steel for Shear Reinforcement of Concrete." *ACI Structural Journal*, Vol. 96, No. 6, Nov./Dec., pp. 997-1002.

Ismail, H.A.F. and Jirsa, J.O. (1972). "Behavior of Anchored Bars Under Low Cycle Over-loads Producing Inelastic Strains." *ACI Journal*, Vol. 69, No. 7, July., pp. 433-438.

Jaradat, O. A., McLean, D. I., and Marsh, M. L. (1998). "Performance of Existing Bridge Columns Under Cyclic Loading—Part 1: Experimental Results and Observed Behavior." *ACI Structural Journal*, Vol. 95, No. 6, Dec., pp.695-704.

Jaradat, O. A., McLean, D. I., and Marsh, M. L. (1999). "Performance of Existing Bridge Columns Under Cyclic Loading—Part 2: Analysis and Comparisons with Theory." *ACI Structural Journal*, Vol. 96, No. 1, Jan., pp.57-67.

Kalamkarov (2000). "Pultruded Smart Composite Reinforcements with Fiber Optic Sensors for Concrete Bridges and Structures." *Composites in the Transportation Industry*, Edited by Bandyopadhyay, S., Gowripalan, N., Drayton, N., and Heslehurst, R., Proceedings of the ACUN-2, 14-18 February, Univ. of New South Wales, Sydney, Australia, pp. 667-675.

Karbhari, V.M. (2000). "FRP Composites for Infrastructure Renewal—Status and Challenges for the 21st Century." *Composites in the Transportation Industry*, Edited by Bandyopadhyay, S., Gowripalan, N., Drayton, N., and Heslehurst, R., Proceedings of the ACUN-2, 14-18 February, Univ. of New South Wales, Sydney, Australia, pp. 51-60.

Karbhari, V.M. (2001). "Materials Considerations in FRP Rehabilitation of Concrete Structures." *Journal of Materials in Civil Engineering*, Vol. 3, No. 2, March/April, pp. 90-97.

Kato, B., Akiyama, H. and Yamanouchi, Y. (1973). "Predictable Properties of Material Under Incremental Cyclic Loading." Symposium on Resistance and Ultimate Deformability of Structures Acted on by Well-Defined Repeated Loads, *Reports of Working Commissions*, Vol. 13, International Association for Bridge and Structural Engineering, Lisbon, pp. 119-124.

Katz, A. (1998). "Effect of Helical Wrapping on Fatigue Resistance of GFRP." *Journal of Composites for Construction*, Vol. 2, No. 3, August, pp. 121-125.

Katz, A. (2000). "Bond to Concrete of FRP Rebars After Cyclic Loading." *Journal of Composites for Construction*, Vol. 4, No. 3, August, pp. 137-144.

Kent, D.C. and Park, R. (1971) "Flexural Members with Confined Concrete." *Journal of the Structural Division,* ASCE, Vol. 97, ST7, July pp. 1969-1990.

Kesner, K.E, Billington, S.L., and Douglas, K.S. (2003). "Cyclic Response of Highly Ductile Fiber-Reinforced Cement-Based Composites." *ACI Materials Journal*, Vol. 100, No. 5, Sept./Oct., pp. 381-390.

Khuntia, M., Stojadinovic, B., and Goel, S.C. (1999). "Shear Strength of Normal and High-Strength Fiber Reinforced Concrete Beams without Stirrups." *ACI Structural Journal*, Vol. 96, No.2, March/April, pp. 282-289.

Kim, W., El-Attar, A., and White, R. N. (1988). "Small-Scale Modeling Techniques for Reinforced Concrete Structures Subjected to Seismic Loads." *Technical Report, National Center for Earthquake Engineering Research*, Cornell University, Ithaca, New York, 58 pp.

Ko, F. K. (1987). "Braiding," *Engineered Materials Handbook, Vol. 1: Composites*, ASM International, pp. 519-528.

Ko, F. K. (1989). "Three Dimensional Fabrics for Composites," *Textile Structural Composites:* Series 3, Chou, T. W. and Ko, F.K., Editors, Elsevier, New York.

Ko, F. K., Pastore, C. M.. and Head, A. (1989), *Atkins and Pearce Handbook of Industrial Braids.*

Ko, F. K., Somboonsong, W. and Harris, H. G. (1997). "Fiber Architecture Based Design of Ductile Composite Rebar For Concrete Structures," Proc. ICCM*, Eleven International Conference on Composite Materials*, Australian Composite Structures Society, 14-18 July, Queenland, Australia, pp. VI723-VI730.

Kootsookos, A., Mouritz, A.P., and St. John, N.A. (2001). "Comparison of the Seawater Durability of Carbon- and Glass-Polymer Composites." *Proceedings of the 13th International Conference on Composite Materials*, 24-28 June, Beijing, China, ID-1200.

Kowalsky, M.J. (2000). "Deformation Limit States for Circular Reinforced Concrete Bridge Columns." *Journal of Structural Engineering*, Vol. 126, No. 8, August, pp. 869-878.

Lam, H., Hampton, F., Ko, F.K., and Harris, H.G. (2001). "Design Methodology of a Ductile Hybrid Kevlar-Carbon Reinforced Plastic For Concrete Structures By the Braidtrusion Process", *Proceedings of the 13th International Conference on Composite Materials*, June 24-28, 2001, Beijing, China.

Larralde, J., and Silva-Rodriguez, R. (1993). "Bond and Slip of FRP Rebars in Concrete." *Journal of Materials in Civil Engineering*, Vol. 5, No. 1, February, pp. 30-40.

Larralde, J., Mueller-Rochholz, J., Schneider, T., and Willmann, J. (1998). "Bond Strength of Steel, AFRP, and GFRP Bars in Concrete." Proceedings of the *2nd International Conference On Composites in Infrastructure*, Edited by Saadatmanesh, H. and Ehsani, M.R.., 15-17 Jan., Tucson, AZ, pp. 92-100.

La Tegola, A. (1998). "Actions for Verification of RC Structures with FRP Bars." *Journal of Composites for Construction*, Vol. 2, No. 3, August, pp. 145-148.

Letsch, R.. (2001). "Polymer Concrete with Metallic and Non-Metallic Reinforcement." *Proceedings of the 13th International Conference on Composite Materials*, 24-28 June, Beijing, China, ID-1090.

Leung, C.K.Y. (2001). "Modeling of Concrete Cracking Induced by Steel Expansion." *Journal of Materials in Civil Engineering*, Vol. 13, No. 3, May/June, pp. 169-175.

Li, J., Joshi, S.C., and Lam, Y.C. (2001). "Optimization of Die Heating for Pultrusion Processes." *Proceedings of the 13th International Conference on Composite Materials*, 24-28 June, Beijing, China, ID-1040.

Lim, K.Y. (1990), "Moment-Reducing Hinge Details for the Bases of Bridge Columns" Ph.D. Thesis, Department of Civil and Environmental Engineering, Washington State University, Pullman, WA.

Lim, K.Y. and McLean, D.I. (1991). "Scale Model Studies of Moment-Reducing Hinge Details in Bridge Columns." *ACI Structural Journal*, Vol. 88, No. 4, July/ August, pp. 465-474.

Liu, X.-L. and Paton, R. (2001). "Evolution of Temperature and Cure Profiles During Pultrusion of Composites." *Proceedings of the 13th International Conference on Composite Materials*, 24-28 June, Beijing, China, ID-1616.

Lomov, S.V., Belov, E., Parnas, R., Prodromou, A., and Verpoest, I. (2001). "Textile Composites Models: Integrating Strategies." *Proceedings of the 13th International Conference on Composite Materials*, 24-28 June, Beijing, China, ID-1532.

Lopez-Anido, R. and Naik, T.R. (2000). *Emerging Materials for Civil Infrastructure, State of the Art, American Society of Civil Engineers (ASCE),* Reston, VA.

Lutz, L.A. and Gergely, P. (1967). "Mechanics of Bond Slip of Deformed Bars in Concrete." *Journal ACI*, Vol. 64, No. 11, November, pp. 711-721.

MacGregor, G. J. (1997). *Reinforced Concrete: Mechanics and Design, Third Edition, Prentice -Hall,* Upper Saddle River, NJ.

Malvar, L.J. (1994). "Bond Stress-Slip Characteristics of FRP Rebars." *Report TR-2013-SHR*, Naval Facilities Engineering Service Center, Port Hueneme, CA.

Masmoudi, R., Theriault, M., and Benmokrane, B. (1998). "Flexural Behavior of Concrete Beams Reinforced with Deformed Fiber Reinforced Plastic Reinforcing Rods." *ACI Structural Journal,* Vol. 95, No. 6, November-December, pp. 654-664.

McCormac, J. C. (1991). *Reinforced Surveying Fundamentals, Second Edition, Prentice -Hall,* Englewood Cliffs, NJ.

Meyer, R.W. (1985). *Handbook of Pultrusion Technology*, Chapman and Hall, New York, NY.

Mirmiran, A., Samaan, M. Cabrera, S. and Shahawy, M. (1998). "Design, Manufacture and Testing of a New Hybrid Column." *Construction and Building Materials*, Vol. 12, No. 1, Elsevier Science Ltd., Great Britain, pp. 39-49.

Mo, Y.L. and Wang, S.J. (2000). "Seismic Behavior of RC Columns with Various Tie Configurations." *Journal of Structural Engineering*, Vol. 126, No. 10, October, pp. 1122-1130.

Monti, G. and Spacone, E. (1998). "Reinforced Concrete Fiber Beam Element with Bond-Slip." *Journal of Structural Engineering*, Vol. 126, No. 6, June, pp. 654-661.

Monti, G., Nistico, N., and Santini, S. (2001). "Design of FRP Jackets for Upgrade of Circular Bridge Piers." *Journal of Composites for Construction*, Vol. 5, No. 2, May, pp. 94-101.

Mosallam, A.S. (2000). "ASCE Prestandard for Pultruded Composite Structures." *Composites in the Transportation Industry*, Edited by Bandyopadhyay, S., Gowripalan, N., Drayton, N., and Heslehurst, R., Proceedings of the ACUN-2, 14-18 February, Univ. of New South Wales, Sydney, Australia, pp. 92-95.

Mosallam, A.S. and Elsanadedy, H.M. (2000). "Cyclic Performance of Reinforced Concrete Beam-Column Connections Repaired & Upgraded with Carbon/Epoxy Laminates." Proceedings of the *45th International SAMPE Symposium*, Edited by Loud, S., Karbhari, V., Adams, D., and Strong, B., 21-25 May, Long Beach Convention Center, Long Beach, CA, pp. 1823-1831.

Naito, C.J., Moehle, J.P., and Mosalam, K.M. (2002). "Evaluation of Bridge Beam-Column Joints Under Simulated Seismic Loading." *ACI Structural Journal*, Vol. 99, No. 1, Jan./Feb., pp. 62-71.

Navalurkar R. K., Hsu, C. T., Kim, S. K., and Wecharatana, M. (1999). "True Fracture Energy of Concrete." *ACI Materials Journal,* Vol. 96, No. 2, March-April, pp. 213-225.

Nguyen, D.M., Chan, T.K., and Cheong, H.K. (2001). "Brittle Failure and Bond Development Length of CFRP-Concrete Beams." *Journal of Composites for Construction*, Vol. 5, No. 1, Feb., pp. 12-17.

Ohnstad, T.S. and Kachlakev, D.I. (2001). "Hollow FRP Rebar- Its Unique Manufacturing Process and Applications." *Proceedings of the 46th International SAMPE Symposium*, 6-10, May, Long Beach, California, Repecka, L. and Saremi, F.F., editors, pp, 1749-1759.

Palermo, D. and Vecchio, F.J. (2004). "Compression Field Modeling of Reinforced Concrete Subjected to Reversed Loading: Verification." *ACI Structural Journal*, Vol. 101, No. 2, March/April, pp. 155-164.

Park, R., Kent, D.C., and Sampson, R.A. (1972). "Reinforced Concrete Members with Cyclic Loading." *Journal of the Structural Division*, ASCE, Vol. 98, ST7, July, pp. 1341-1360.

Paulay, T. and Priestley, M.J.N. (1992). *Seismic Design of Reinforced Concrete and Masonry Buildings, John Wiley and Sons, New York, NY.*

Pecce, M. and Fabbrocino, G. (1999). "Plastic Rotation Capacity of Beams in Normal and High-Performance Concrete." *ACI Structural Journal*, Vol. 96, No.2, March/April, pp. 290-296.

Pecce, M., Manfredi, G., Realfonzo, R., and Cosenza, E. (2001). "Experimental and Analytical Evaluation of Bond Properties of GFRP Bars." *Journal of Materials in Civil Engineering*, Vol. 13, No. 4, July/August, pp. 282-290.

Prentice, J.M. (2004). "The Evolution of the Reinforcing Bar." *Concrete International*, Vol. 26, No. 3, March, pp. 79-81.

Priestley, M.J.N., Seible, F., and Calvi, G.M. (1996). *Seismic Design and Retrofit of Bridges, John Wiley and Sons, New York, NY.*

Pujol, S. and Sozen, M. (2000). "Transverse Reinforcement for Columns of RC Frames to Resist Earthquakes." *Journal of Structural Engineering*, Vol. 126, No. 4, April, pp. 461-466.

Rao, P. S., Sarma, B. S., Lakshmanan, N., and Stangenberg, F. (1998). "Damage Model for Reinforced Concrete Elements under Cyclic Loading." *ACI Materials Journal,* Vol. 95, No. 6, November-December, pp. 682-690.

Rehm, G. (1968). "The Basic Principles of the Bond Between Steel and Concrete." *Translation No. 134*, Cement and Concrete Association, London, 66 pp.

Rodriguez, M.E., Botero, J.C., and Villa, J. (1999). "Cyclic Stress-Strain Behavior of Reinforcing Steel Including Effect of Buckling." *Journal of Structural Engineering*, Vol. 125, No. 6, June, pp. 605-612.

Ross, C.A., Jerome, D.M., Tedesco, J.W., and Hughes, M.L. (1999). "Strengthening of Reinforced Concrete Beams with Externally Bonded Composite Laminates." *ACI Structural Journal*, Vol. 96, No.2, March/April, pp. 212-220.

Saadatmanesh H. and Tannous F.E. (1999). "Relaxation, Creep, and Fatigue Behavior of Carbon Fiber Reinforced Plastic Tendons." *ACI Material Journal*, Vol. 96, No. 2, March/April, pp. 143-153.

Saadatmanesh H. and Tannous F.E. (1999). "Long-Term Behavior of Aramid Fiber Reinforced Plastic (AFRP) Tendons." *ACI Materials Journal*, Vol. 96, No. 3, May/June, pp. 299-305.

Saatcioglu, M. and Razvi, S.R. (2002). "Displacement-Based Design of Reinforced Concrete Columns for Confinement." *ACI Structural Journal*, Vol. 99, No. 1, Jan./Feb., pp. 3-11.

Sakino, K. and Sun, Y. (2000). "Steel Jacketing for Improvement of Column Strength and Ductility." *Proceedings of the 12th World Conference on Earthquake Engineering (12WCEE)*, 7-12 January, Auckland, New Zealand, ID-2525.

Sen, R., Shahawy, M., Rosas, J., and Sukumar, S. (1999). "Durability of Aramid Fiber Reinforced Plastic (AFRP) Pretensioned Elements under Tidal/Thermal Cycles." *ACI Structural Journal*, Vol. 96, No. 1, Jan./Feb., pp. 95-104.

Sheikh, S.A. and Yau, G. (2002). "Seismic Behavior of Concrete Columns Confined with Steel and Fiber-Reinforced Polymers." *ACI Structural Journal*, Vol. 99, No. 1, Jan./Feb., pp. 72-80.

Somboonsong, W. (1997). "Development of Ductile Hybrid Fiber Reinforced Polymer (D-H-FRP) Reinforcement for Concrete Structures" Ph.D. Thesis, Department of Civil and Architectural Engineering, Drexel University, Philadelphia, PA.

Somboonsong, W., Ko, F. K., and Harris, H. G. (1998). "Ductile Hybrid Fiber Reinforced Plastic (FRP) Rebar for Concrete Structures: Design Methodology," *ACI Materials Journal,* Vol. 95, No. 6, Nov./Dec.

Soong, W.H., Rizkalla, S., and Raghavan, J. (2001). "Bonding Between the Concrete and Polymer Composite Tendon." Proceedings of the *46th International SAMPE Symposium*, Edited by Repecka, L. and Saremi, F.F., 6-10 May, Long Beach Convention Center, Long Beach, CA, pp. 1723-1737.

Spadea, G. and Bencardino, F. (1997). "Behavior of Fiber-Reinforced Concrete Beams Under Cyclic Loading" *Journal of Structural Engineering*, Vol. 123, No. 5, May, pp. 660-668.

Taly, N. and GangaRao, H.V.S. (2001). "Bond Behavior of FRP Reinforcing Bars-The State of the Art." Proceedings of the *46th International SAMPE Symposium*, Edited by Repecka, L. and Saremi, F.F., 6-10 May, Long Beach Convention Center, Long Beach, CA, pp. 1784-1796.

Tamuzs, V., Apinis, R., Modniks, J., and Tepfers, R. (2001). "The Performance of Bond of FRP Reinforcement in Concrete." Proceedings of the *46th International SAMPE Symposium*, Edited by Repecka, L. and Saremi, F.F., 6-10 May, Long Beach Convention Center, Long Beach, CA, pp. 1738-1747.

Tang, H.C., Nguyen, T. Chuang, T. Chin, J., Lesko, J., and Wu, H.F. (2000). "Fatigue Model for Fiber-Reinforced Polymeric Composites." *Journal of Materials in Civil Engineering*, Vol. 12, No. 2, May, pp. 97-104.

Tepfers, R., Hedlung, G., and Rosinski, B. (1998). "Bond Strength of Steel, AFRP, and GFRP Bars in Concrete." Proceedings of the *2nd International Conference On Composites in Infrastructure*, Edited by Saadatmanesh, H. and Ehsani, M.R.., 15-17 Jan., Tucson, AZ, pp. 37-51.

Theriault, M. and Benmokrane, B. (1998). "Effects of FRP Reinforcement Ratio and Concrete Strength on Flexural Behavior of Concrete Beams." *Journal of Composites for Construction*, Vol. 2, No. 1, February, pp. 7-16.

Tighiouart, B., Benmokrane, B., and Gao, D. (1998a). "Investigation on the Bond of Fiber Reinforced Polymer (FRP) Rebars in Concrete." Proceedings of the *2nd International Conference On Composites in Infrastructure*, Edited by Saadatmanesh, H. and Ehsani, M.R.., 15-17 Jan., Tucson, AZ, pp. 102-111.

Tighiouart, B., Benmokrane, B., and Gao, D. (1998b). "Investigation of Bond in Concrete Member with Fibre Reinforced Polymer (FRP) Bars." *Construction and Building Materials*, Vol. 12, No. 1, Elsevier Science Ltd., Great Britain, pp. 453-462.

Uomoto, T., Mutsuyoshi, H., Katsuki, F., and Misra, S. (2002). "Use of Fiber Reinforced Polymer Composites as Reinforcing Material for Concrete." *Journal of Materials in Civil Engineering*, Vol. 14, No. 3, June, pp. 191-209.

Vaysburd, A.M., Emmon, P.H., Mailvaganam, N.P., McDonald, J.E., and Bissonnette, B. (2004). "Concrete Repair Technology-A Revised Approach is Needed." *Concrete International*, Vol. 26, No. 1, January, pp. 58-65.

Vecchio, F.J. (1999). "Towards Cyclic Load Modeling for Reinforced Concrete." *ACI Structural Journal*, Vol. 96, No.2, March/April, pp. 193-202.

Vermeeren, C.A.J.R. and Tsang, S.T.K.W. (2001). "An Efficient Resin-Wedge Anchorage System for Unidirectional CCFRP Rods." *Proceedings of the 13th International Conference on Composite Materials*, 24-28 June, Beijing, China, ID-1494.

Wehbe, N.I., Saiidi, M.S., and Sanders, D.H. (1999). "Seismic Performance of Rectangular Bridge Columns with Moderate Confinement." *ACI Structural Journal*, Vol. 96, No.2, March/April, pp. 248-258.

Yost, J.R., Goodspeed, C.H., and Schmeckpeper E.R. (2001). "Flexural Performance of Concrete Beams Reinforced with FRP Grids." *Journal of Composites for Construction*, Vol. 5, No. 1, Feb., pp. 18-25.

Yost, J.R., Gross, S.P., and Dinehart, D.W. (2001). "Shear Strength of Normal Strength Concrete Beams Reinforced with Deformed GFRP Bars." *Journal of Composites for Construction*, Vol. 5, No. 4, Nov., pp. 268-275.

Youssef, M.N., Haroun, M., Feng, M., and Mosallam, A. (2000). "Experimental Study on RC Bridge Columns Retrofitted Using Fiber Composite Materials." Proceedings of the *45th International SAMPE Symposium*, Edited by Loud, S., Karbhari, V., Adams, D., and Strong, B., 21-25 May, Long Beach Convention Center, Long Beach, CA, pp. 1803-1813.

Zhang, S. and Karbhari, V.M. (2000). "Irreversible Damage in Glass/ Vinylester Composites after Exposure to Aqueous and Alkaline Solutions." *Composites in the Transportation Industry*, Edited by Bandyopadhyay, S., Gowripalan, N., Drayton, N., and Heslehurst, R., Proceedings of the ACUN-2, 14-18 February, Univ. of New South Wales, Sydney, Australia, pp. 167-172.

Zheng, H. and Abel, A.A. (1999). "Fatigue Properties of Reinforcing Steel Produced by TEMPCORE Process." *Journal of Materials in Civil Engineering*, Vol. 11, No. 2, May, pp. 158-165.

Zhu, H. and Sankar, B.V. (2001). "Elasticity Analysis of Functionally Graded Beams." *Proceedings of the 13th International Conference on Composite Materials*, 24-28 June, Beijing, China, ID-1526.

Zou, X.W., Gowripalan, N., and Gilbert, R.I. (2000). "Ductility and Deformability of Prestressed Concrete Beams Containing Aramid Fibre Reinforced Polymer (AFRP)

Tendons." *Composites in the Transportation Industry*, Edited by Bandyopadhyay, S., Gowripalan, N., Drayton, N., and Heslehurst, R., Proceedings of the ACUN-2, 14-18 February, Univ. of New South Wales, Sydney, Australia, pp. 222-227.

APPENDIX A: SIMILITUDE CALCULATIONS

An example of the formation of π terms and corresponding scale factors is the case of a simply supported beam subjected to a transverse four-point loading as shown in Figure A.1. The beam is of length *l*, width *w* and height *h*. The model and prototype materials both have a modulus *E*, and a Poisson's ratio ν, which are not necessarily the same. In this example, the design conditions and the prediction equation for the deflection at any point are developed from the model to the prototype.

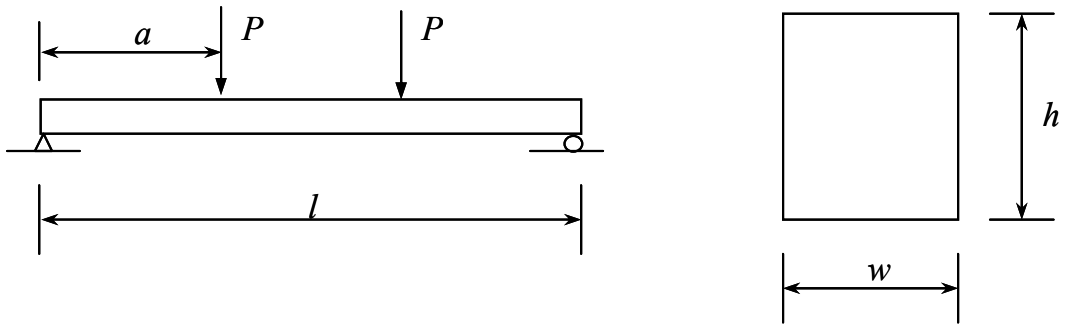

Figure A.1:Simple-Beam Used for Similitude Calculations.

Since the deflection δ is a function of the load, span length, shear span, material, and cross section (i.e., moment of inertia), define the independent quantities can be defined as

$$F(P, l, E, b, h, d, a) = 0 \qquad \text{A-1}$$

where all quantities were defined in Figure A.1. Table A.1 gives the dimensions of each quantity.

Table A.1: Dimensions of Physical Parameters from Beam Problem.

	P	l	E	b	h	δ	a
F	1	0	1	0	0	0	0
L	0	1	-2	1	1	1	1

The number of physical quantities is $n = 6$ and there are two independent quantities, force and length, so $r = 2$. Therefore, $m = 6\text{-}2 = 4$. There will be four π terms. E and l were chosen as independent terms, and all other π terms were made dimensionless using E and l. The dimensionless π terms are

$$\pi_1 = \frac{\delta}{l} \qquad \pi_2 = \frac{P}{El^2} \qquad \pi_3 = \frac{b}{l} \qquad \pi_4 = \frac{h}{l} \qquad \pi_5 = \frac{a}{l} \tag{A-2}$$

From the π terms, the prediction equation for deflection δ is

$$\pi_{1P} = \pi_{1m} \Rightarrow \frac{\delta_P}{l_P} = \frac{\delta_m}{l_m} \Rightarrow \delta_P = \frac{l_P}{l_m}\delta_m = s_l \delta_m \tag{A-3}$$

The design equation for applied load P is

$$\pi_{2P} = \pi_{2m} \Rightarrow \frac{P_P}{E_P l_P^2} = \frac{P_m}{E_m l_m^2} \Rightarrow P_P = \frac{E_P l_P^2}{E_m l_m^2} P_m = s_E s_l^2 P_m \tag{A-4}$$

The design equation for beam width b is

$$\pi_{3P} = \pi_{3m} \Rightarrow \frac{b_P}{l_P} = \frac{b_m}{l_m} \Rightarrow b_P = \frac{l_P}{l_m} b_m = s_l b_m \tag{A-5}$$

The design equation for beam height *h* is

$$\pi_{4P} = \pi_{4m} \Rightarrow \frac{h_P}{l_P} = \frac{h_m}{l_m} \Rightarrow h_P = \frac{l_P}{l_m} h_m = s_l h_m \qquad \text{A-6}$$

Finally, the design equation for the shear span *a* is

$$\pi_{5P} = \pi_{5m} \Rightarrow \frac{a_P}{l_P} = \frac{a_m}{l_m} \Rightarrow a_P = \frac{l_P}{l_m} a_m = s_l a_m \qquad \text{A-7}$$

APPENDIX B: YARN WINDING SPECIFICATIONS

A major deficiency in the manufacturing process of previously manufactured 10-mm bars was the winding of individual yarns onto bobbins to make a multi-ply yarn. As explained in Chapter 4, the yarn tension during the winding process was a critical parameter for ease of manufacturing and a resulting quality prototype-size product. For example, previously made 10-mm bars used 1140 denier Kevlar 49 yarn for the sleeve. This required the use of 12 yarns to make the braiding yarns and 60 yarns (i.e., ends) of Kevlar 49 to make the rib yarns. For example, to make the one tube of rib yarn using 1140 denier yarn, 20 three-ply yarns was made using the winding machine. Then five of the three-ply yarn tubes were wound to make a tube of 15 ends. This was repeated to make four 15-ply tubes. Then the four 15-ply tubes were wound by hand to make one 60-ply tube used for the rib yarn. Using so many levels of plying to make a thick enough yarn and by making the final ply by human winding instead of mechanical winding caused another level of great variability since additional unknown twist was put on the yarns. This difficulty and variability in winding became evident during the manufacturing of the 10-mm DHFRP bars primarily by yarn entanglement of the large-denier rib yarns.

Therefore, several things were done to correct the yarn tension during winding. First, different denier Kevlar 49 yarn was used to minimize the number of plies needed to make both braiding and rib yarns. 2840 denier yarn was used for the braiding yarns and 8520 denier yarn was used for the rib yarns. This gave a final yarn denier that was close to that using 1140 denier yarn. Using these deniers eliminated the need for excessive yarn plying. Two plies of the 2840 denier yarn were needed for the braiding yarns and

seven plies of the 8520 denier yarn were needed for the rib yarns (compared to 12 and 60 plies, respectively, using 1140 denier yarn). Using these yarns decreased the variability and also created a major time savings for yarn preparation for prototype bar. Second, the winder has only one traverse speed, which was too quick for winding large denier yarns. When the yarn denier became too large, entanglement occurred in the winder which caused difficulty. Therefore, to correct this problem, a variable autotransformer (STACO Energy Products Inc., 120V Input, 0-120/140V Output) was placed on the winder to control the speed as shown in Figure B.1. This allowed the yarns to be wound much slower and with more control allowing the winding of up to 60 yarns with no difficulty. The larger the yarn denier, a slower winding speed was required to ensure quality control. Also, slower winding speeds were necessary for brittle yarns such as some carbons such as P-55S.

Figure B.1: Leesona Tube Winder with Speed Control.

Figures B.2 through B.6 illustrate the procedure for winding yarns, especially larger denier yarns such as the rib yarns used for the prototype bar. Shown in Figure B.1 was the yarn being wound from the large spool which is a single-end yarn to a smaller paper tube. These smaller single-end tubes were used for plying the yarns. Figure B.2 shows a creel to dispense the multiple single-end tubes. This creel was capable of holding four 5 ¾" paper tubes and two additional 5 ⅜" paper tubes (the two standard sizes of paper tubes for braiding). Clips were placed on the ends of the dowels of the creel so the paper tubes would not roll off the dowel when winding commenced.

Figures B.3 and B.4 show the guides for the yarn which keep the yarn properly aligned during winding. There were three guides, two for yarn alignment and one for yarn tensioning. The first guide was an eyelet-type guide that provided yarn alignment (Fig. B.3 a). The second guide was a clip-type guide that was used for both yarn alignment and yarn tensioning (Fig. B.3 b). The tension was controlled by a small steel pin with has weight on the end. This kept this guide from opening up during winding. For small denier yarn, the tension provided by this pin was sufficient to keep the yarn properly aligned and tensioned. However, for larger denier yarns, additional weight must be added to the end of the pin to provide enough tension on the guide. The third guide is shown in Figure B.4. This was a short tubular guide on the traverse cam and provided yarn alignment while the yarn was placed onto the paper tube. For larger denier yarn, they yarn was taped to the paper tube before it was pull through the last guide. The yarn was then wound onto a paper tube and placed over the shaft of the winder which rotates. The yarn must be placed onto the tube and wound clockwise, the same direction as the shaft rotation direction.

Shown in Figures B.5 and B.6 is the yarn weight system to provide sufficient tension to the yarn. Shown is a small diameter steel pin that connects the tension guide to a lever arm. Sufficient yarn tension was critical especially for larger denier yarn. If sufficient tension was not provided, the yarn came out of the tension guide and the yarn had uneven tension. Also with insufficient tension, the yarn on the paper tube became bulky, even for smaller denier yarn. This uneven tension became evident when braiding the DHFRP bar because the rib yarns entangled often, which created numerous defects in the braided sleeve. However, if too much tension was provided by the added weight, the yarn would not move through the tension guide and winding became difficult. As shown in Figure B.6, a series of weights were used to hold the pin under higher tension. The weights were placed on a lever arm, which increased the tension in the pin. This provided sufficient yarn tension while winding. The number of weights was varied, depending on whether a braid yarn or a rib yarn was being plied, with higher tension (i.e., more weights) used for the larger denier yarns. The spring clip was placed on the end of the lever arm to prevent the weights from falling off and the arm from rotating during winding. The level arm had a tendency to rotate during winding when more weights were placed on. This caused the tension guide to be ineffective because once the weights rotated, no additional tension was provided by the weights. The spring clamp prevented this from occurring.

Figure B.5 b shows the traverse cam on the left with the paper tube wound around it and to the right of that is a spring-buttoned arm that moves clockwise. As this arm was moved clockwise, the traverse distance the yarn traveled decreased. This arm can only go so far before an automatic shutoff stops the machine. For the best uniformity of the

yarn, this spring-buttoned arm was moved outward or clockwise in increments. This gave the yarn a stepped appearance on the paper tubes as shown in Figure B.7. This became important when placing the tubes on the braider. This prevented the yarn from becoming too bulky and from falling off the end of the tube. The number of movements of the spring-buttoned arm was determined by the total number of strokes divided by the number of strokes per movement of the arm. These values were determined based on experience. It was difficult to make more than ten outward increments of the arm. Since the rib yarns were much thicker than the braiding yarns, the number of strokes was much less.

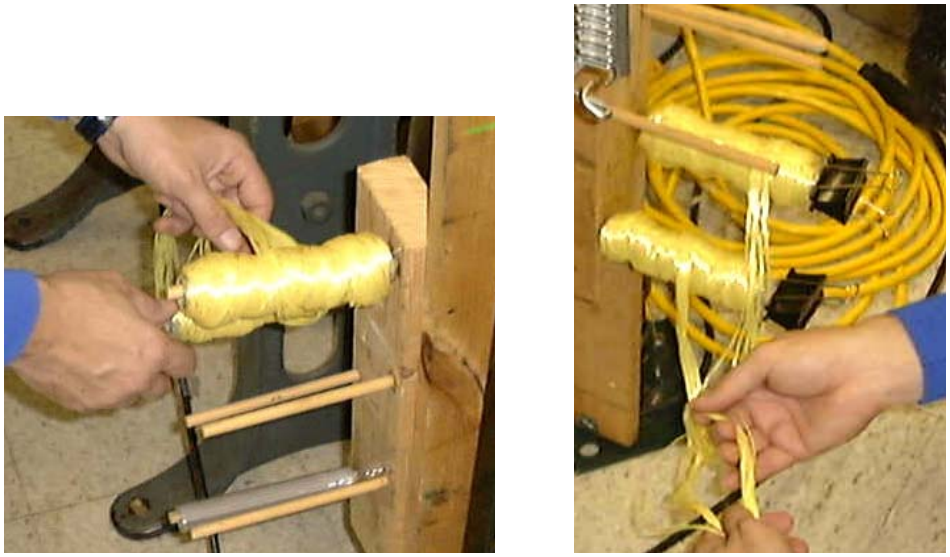

Figure B.2: Placement of Tubes on Yarn Creel for Yarn Plying (Kevlar 49 for Braid Yarns).

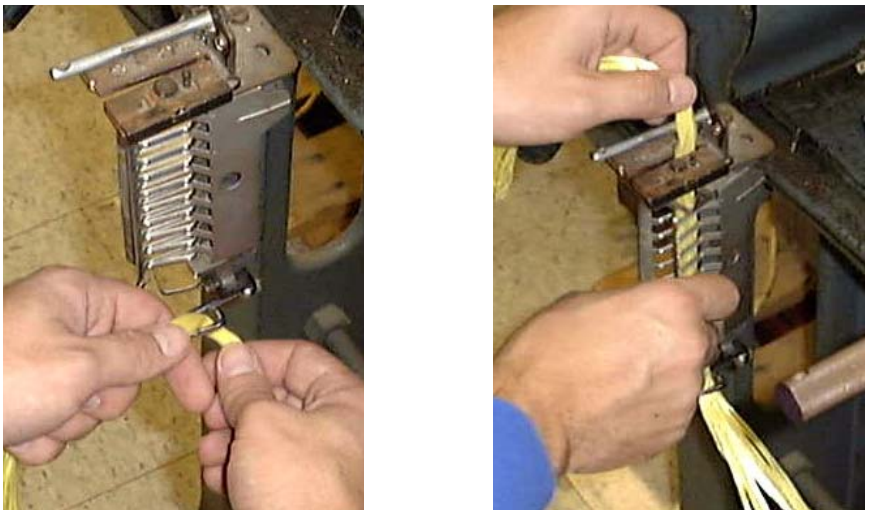

Figure B.3: Placement of Yarn Into Guides on the Leesona Winder, (a) Eyelet Guide and (b) Tension Guide.

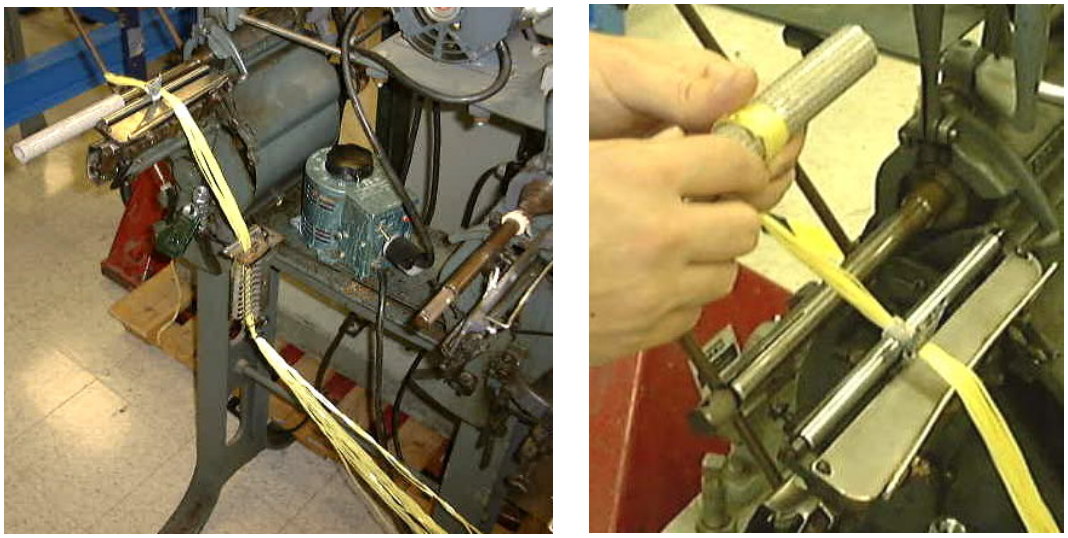

Figure B.4: Placement of Yarn on the Paper Tubes After Going Through the Final Guide (Right Figure).

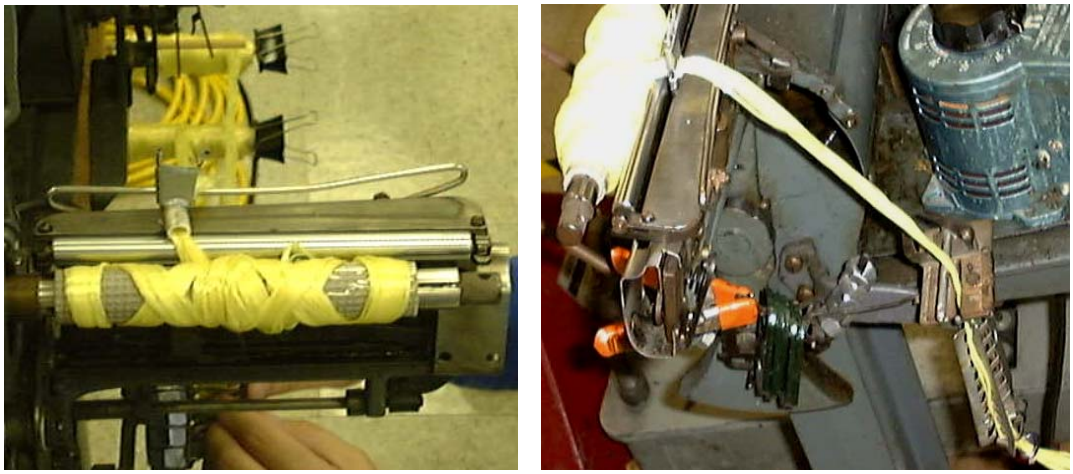

Figure B.5: (a) Plied Yarn During Winding Showing the Creel in the Background and (b) the Yarn During Winding with the Yarn Tensioning Device.

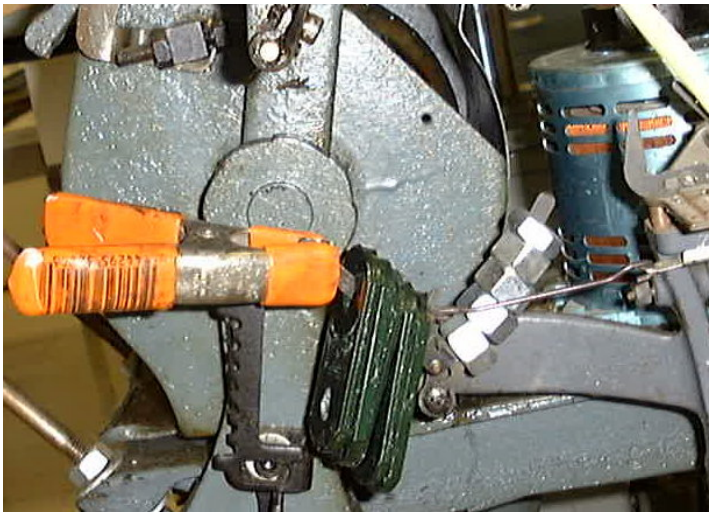

Figure B.6: Closeup of the Yarn Tensioning Device During Yarn Winding.

Figure B.7: Kevlar Yarn Wound on Paper Tubes with Yarn Stepped-Up on the Ends.

APPENDIX C: THREE POINT BENDING TEST OF BARS WITH VARIOUS CORES

Since the main application of DHFRP bars is for use in the field, the bending capacity of the bars is needed for in situ applications. The bar was designed to resist axial tension, but when the bars are being placed, they are subjected to transverse bending induced by workers walking on the bars. Therefore, the bending resistance of 10-mm DHFRP bars was quantified.

In addition to direct tensile properties, the flexural properties of DHFRP needed to be measured for serviceability conditions. The bending resistance of a material is a function of the amount of curvature a material undergoes and is shown by the moment-curvature relationship

$$\phi = \frac{1}{\rho} = \frac{M}{EI} \qquad \text{C-1}$$

where ϕ the curvature, ρ is the radius of curvature, M is the applied bending moment, E is the modulus of elasticity and I is the moment of inertia.

For a prismatic member subjected to transverse loading as shown in Figure C.1, the stress in the beam is given as

$$\sigma = \frac{My}{I} \qquad \text{C-2}$$

where y is defined as the distance from the neutral axis. For the beam shown in Fig. C.1, the maximum bending moment at mid-span is given as $M = PL/4$.

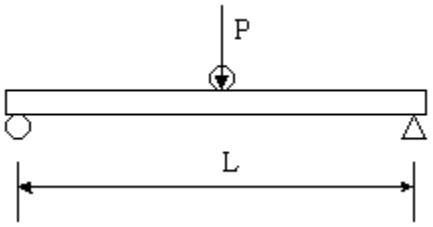

Figure C.1: Simple Beam Under Three Point Loading.

The DHFRP bar tested under three point loading was constructed with only two rib yarns (Figure C.2a) compared with the modified symmetrical design of using four rib yarns (Fig. C.2b). The use of two ribs, due to antisymmetry, had an effect on the moment of inertia similar to an I-beam being bent around its strong or weak axis. When the ribs are oriented vertically (Fig. C.3a), the moment of inertia of the cross section is

$$I_x = \frac{\pi d_1^4}{64} + 2I_2 + 2A_2 y_2^2 \qquad \text{C-3}$$

where A_2 is the area of the each rib and y_2 is the distance from the centroid of each rib to the bar centroidal axis. However, when the ribs are oriented in the horizontal direction (Fig. C.3b), the moment of inertia is given by

$$I_x = \frac{\pi d_1^4}{64} + 2I_2 \qquad \text{C-4}$$

where the parallel axis theorem does not apply. Therefore, for a bar with only two rib yarns used, the apparent stiffness of the bar in bending is dependent on the orientation of the bar along its strong or weak centroidal axis.

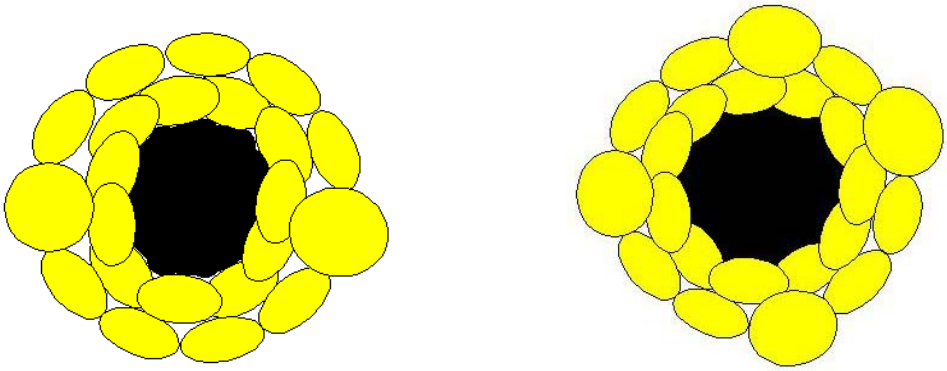

(a) (b)

Figure C.2: (a) Old and (b) New Design of Rib Pattern for 10-mm DHFRP Bars.

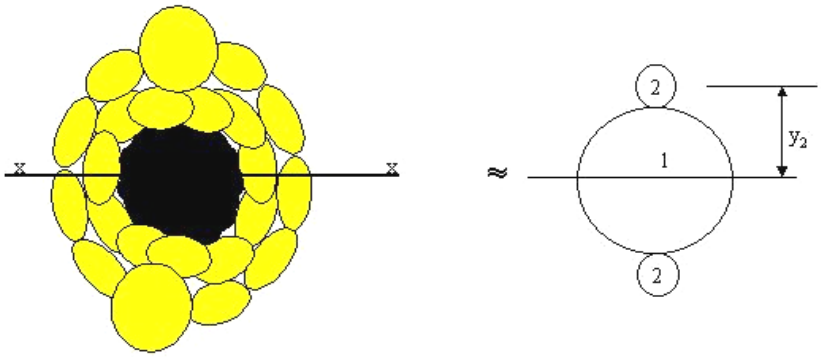

(a)

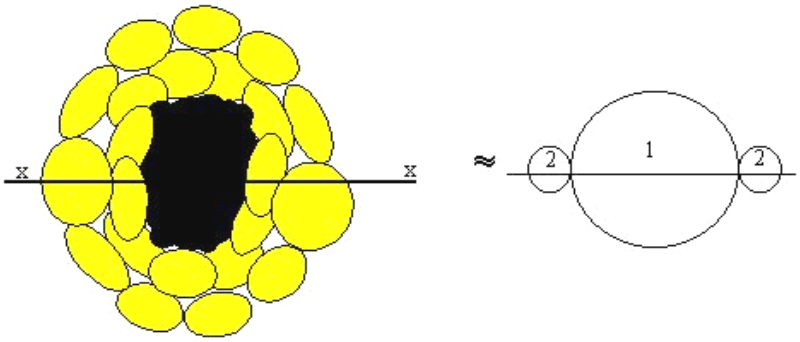

(b)

Figure C.3: (a) Strong and (b) Weak Axis Bending of 2-Rib 10-mm DHFRP Bars.

For a beam under three-point loading (Fig. C.1), the maximum elastic deflection is given as

$$\Delta = \frac{PL^3}{48EI} \qquad \text{C-5}$$

where Δ is the mid-span deflection, P is the applied load, and L is the span length. Rearranging this equation, the bending stiffness of a member can be obtained from experimental results as

$$E = \frac{PL^3}{48I\Delta} \qquad \text{C-6}$$

valid only in the elastic range and using small deflection theory.

Various processing parameters including the material selection for both the core and sleeve, braid angle and fiber volume fraction can influence the behavior of the DHFRP bars in both bending and axial tension applications. For example, the effect of using a high strength and stiffness core material such as carbon will give different results than using a low strength and stiffness material such as polypropylene. A material with very low stiffness will behave as a bar with essentially no core. The bending test used both carbon and polypropylene cores to study the sleeve behavior and the general DHFRP failure mechanism more fully.

The 3-point bend test was conducted at the Grundy Laboratory of Philadelphia University. The test setup was a conventional 3-point bending setup with a single load in the center of the span, as shown in Fig. C.1. The bars tested had only two rib yarns and the orientation of the bars was not recorded. At the time the test was conducted, the notion of the two-ribbed bar having a strong versus weak axis of bending was not realized. The test machine used was an Instron 500 kg bench-type machine (Figure C.4).

The data was recorded on a chart plotter. The scale of load and deflection used on the chart was 1:1 (i.e., a one to one relationship of chart deflection to actual deflection). The test was stopped when the deflection limit of the crosshead was exceeded. The test setup is shown in Figure C.5.

Figure C.4: Test Setup for Three-Point Bend Test.

Figure C.5: Test Setup of 10-mm DHFRP Bars.

The specimens did not fail in a brittle manner, but demonstrated some ability to stretch. The test was stopped when the deflection limit of the crosshead was exceeded (i.e., the crosshead 'bottomed out' on the specimen). Shown in Figure C.6 is a carbon core specimen during testing.

Figure C.6: Bending Specimen During Testing, Carbon Core.

Shown in Figure C.7 are the failed specimens. A total of four specimens with a polypropylene core were tested and three with a core of IM-7 carbon were tested. The stress-deflection curves for all specimens are shown in Figure C.8. The deflection, not the strain was measured in this test since the result is deflection critical for serviceability applications.

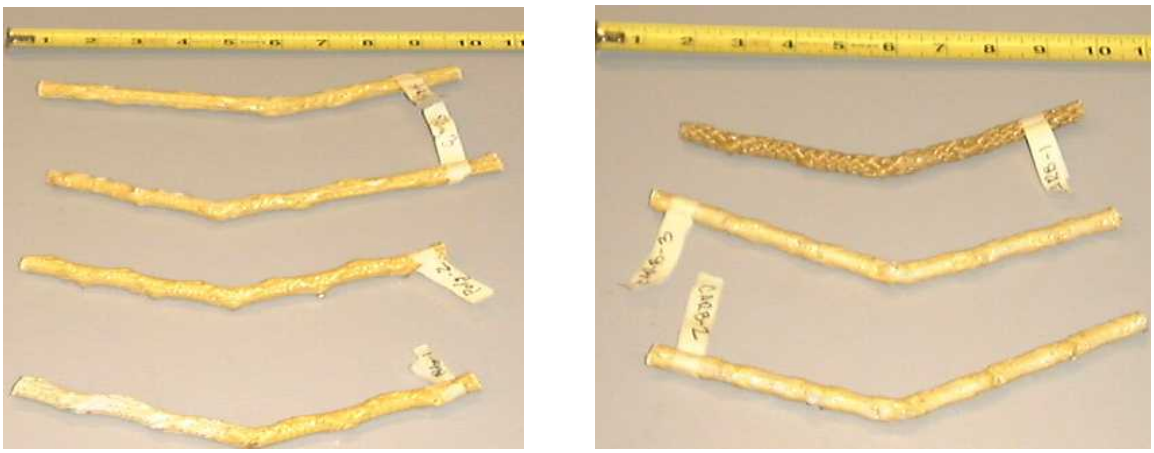

(a) (b)

Figure C.7: Failed Bending Specimens, (a) Polypropylene and (b) Carbon Core.

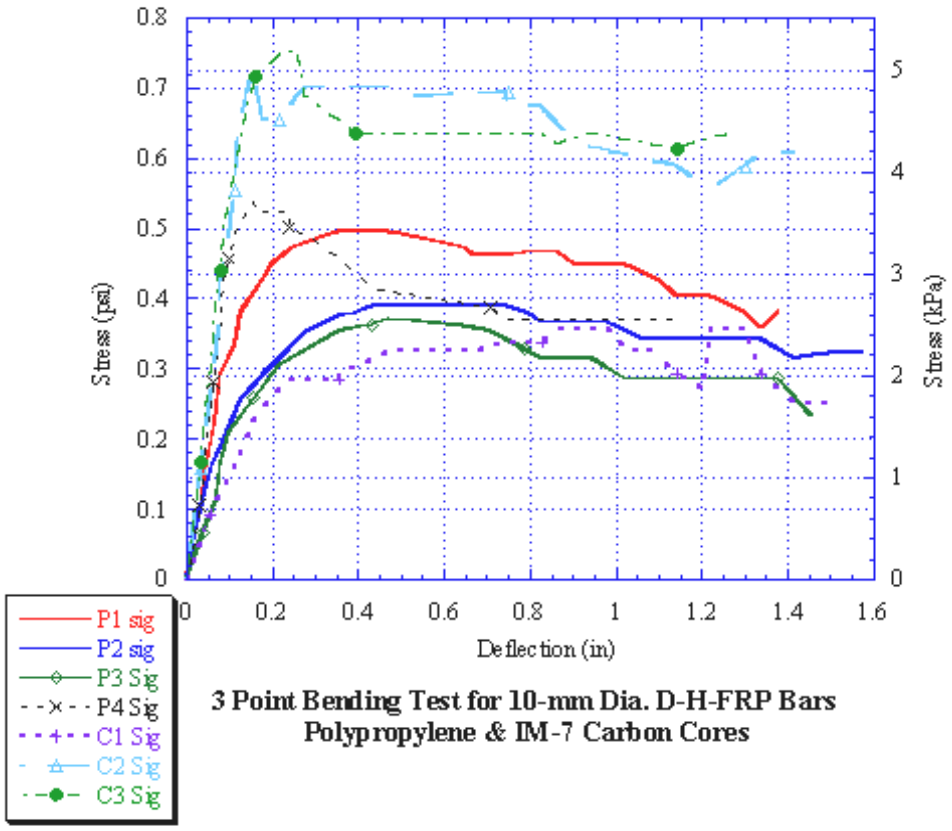

Figure C.8: Results of Three-Point Bending Test.

Since strain gages were not used, the bending stiffness of the specimens (linear portion of the curves in Fig. C.8) can be approximated using Eqn. C-6. These stiffness values are shown in Table C.1 for all specimens.

Table C.1: Average Bending Stiffness of 10-mm DHFRP Bars.

Specimen I.D.	Stiffness, *E* (psi)	Stiffness, *E* (kPa)
Poly 1	2.024	13.955
Poly 2	1.760	12.135
Poly 3	1.151	7.936
Poly 4	2.105	14.513
Carbon 1	0.957	6.598
Carbon 2	3.034	20.919
Carbon 3	3.442	23.732

As seen from the failed specimens, rupture did not occur due to the limitation of the crosshead movement. Specimens Poly 1 and Poly 2 had high braid angles (approaching ± 45°), Poly 3 had intermediate braid angles (around ± 30°), and Poly 4 had low braid angles (around ± 20°). This has a direct effect on the strength since as the braid angle approaches 0°, the composite will behave more like a unidirectional composites with higher strength and less ductility. The carbon specimens all had intermediate braid angles. As seen in Figure C.8, a bilinear load-deflection (or stress-deflection) behavior was evident. It should be noted that strains were not measured but instead, mid-span deflections. Strain gages would have had to be mounted on the extreme fibers of the cross section to measure strains. Also, the stress was plotted in Fig. C.8 instead of the

load. The reason for this was that the diameters of specimens were not identical. By using Equation C-2, the load-deflection values obtained during testing could be normalized by the moment of inertia of each specimen, and therefore, all specimens could be directly compared. Note that the specimens with the most stiffness were specimens Carbon 2 and 3. These specimens were made with the modified pultrusion system using a resin bath and die system. The polypropylene specimens (Poly 1-4) had intermediate bending rigidity, also produced using the modified pultrusion system. The stiffness of Poly 4 was higher since the braid angle was lower and the cross section was larger, giving a higher apparent stiffness. The bar with the lowest bending rigidity was the bar produced with P-55S carbon core and Kevlar 49. This bar was produced using the original manufacturing process, which had dry yarns (Chapter 5). Therefore, the core and sleeve debonded during testing, thereby resulting in poor stress transfer.

The stiffness of the carbon bars was larger than the polypropylene bars as was the strength at yield. The carbon bars showed a more definite yield region with a similar post-yield behavior. The core did not seem to have much effect other than on the bending strength of the material. Both core types had a similar mode of failure.

Shown in Table C.1 were the stiffness values for the linear portion of all specimens. Note that the bending or transverse stiffness values were extremely low for these bars. Note again that the bars made using the original process (Carbon 1) had very low stiffness values. This again was attributed to a poor interface between the carbon core and the Kevlar sleeve, thereby preventing a proper stress transfer.

The bending test illustrated the flexural rigidity of 10-mm diameter DHFRP bars. Low flexural stiffness was evident; however, the bars when placed in concrete beams are

subjected to axial tension. Therefore, the full axial strength of the composite in the 1-direction can still be realized.

APPENDIX D: FLEXURAL PROPERTIES OF DHFRP SLAB SECTIONS

To obtain the flexural properties of DHFRP R/C sections, slab sections reinforced with 10-mm DHFRP were tested. The bars used to reinforce these sections were 10-mm DHFRP bars made prior to the dieless braidtrusion. The sections failed in shear instead of flexure with bar rupture.

Four-point bending was used for this series of tests. The design of the specimens used for testing was based on the results obtained from preliminary tensile tests. The cross section of the member was optimized to have the maximum shear to moment ratio, indicating the shear capacity of the member is higher than the moment capacity, so that shear reinforcement would not be required. The cross section was 3 inches high by 6 inches wide (76.2 x 152.4 mm), and the span was 47 ¼ inches (1206.5 mm). Three members were reinforced longitudinally with two DHFRP bars, and one member was reinforced with steel bars. From design calculations using ACI 318-99, the ultimate moment of the member reinforced with DHFRP was higher due to its greater stiffness after yield. The steel reinforced member, however, should undergo much higher deflection before failure. The test setup is shown in Figure D.1

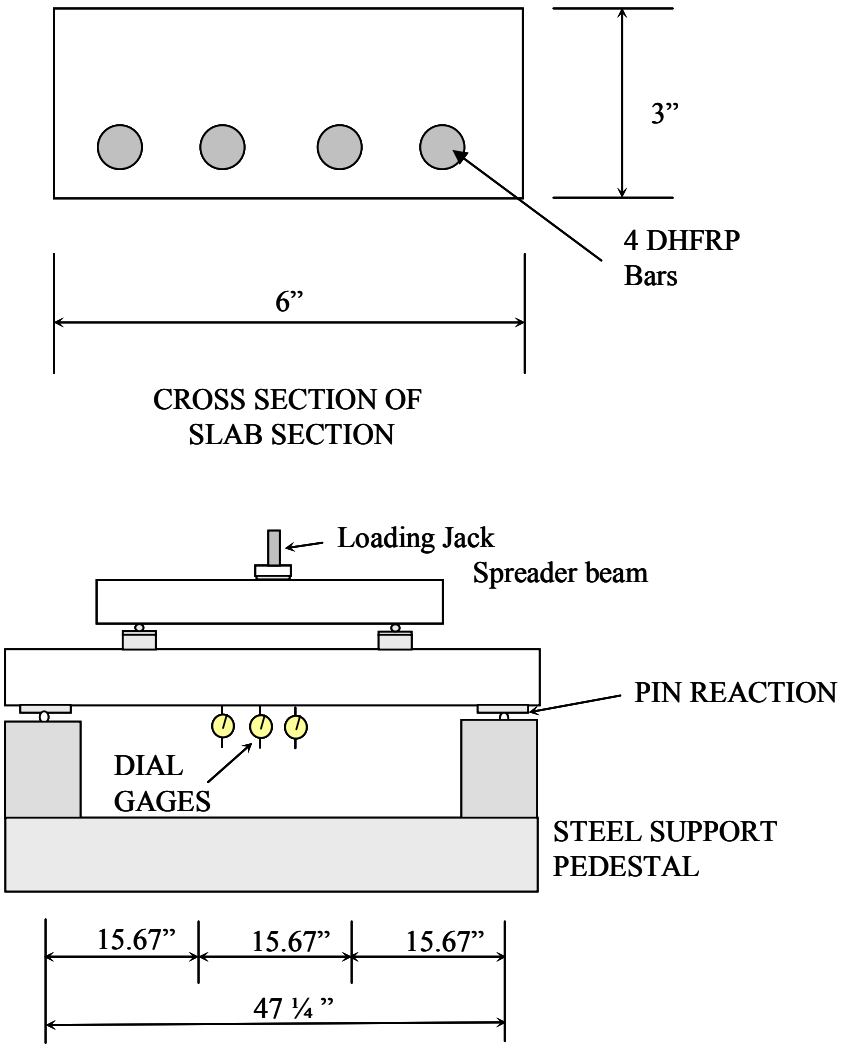

Figure D.1: Setup for Flexural Testing of DHFRP-Reinforced Slab Sections.

The slab sections were tested as simply-supported beams with equal concentrated loads applied at the third span to create four-point loading. The beams were also reinforced in the shear span to reduce the risk of a shear failure. Dial gauges were mounted on an independent support system below the member to measure deflections during testing. The tests were conducted at constant strain rates and the deflections of the beams were recorded as load increased. Shown in Figure D.2 is the failed beam.

Extensive shear cracking occurred, and therefore, external shear reinforcement was provided by clamping plates onto the beam. All beams failed by rupture of the reinforcement before crushing of the concrete, a brittle failure mode.

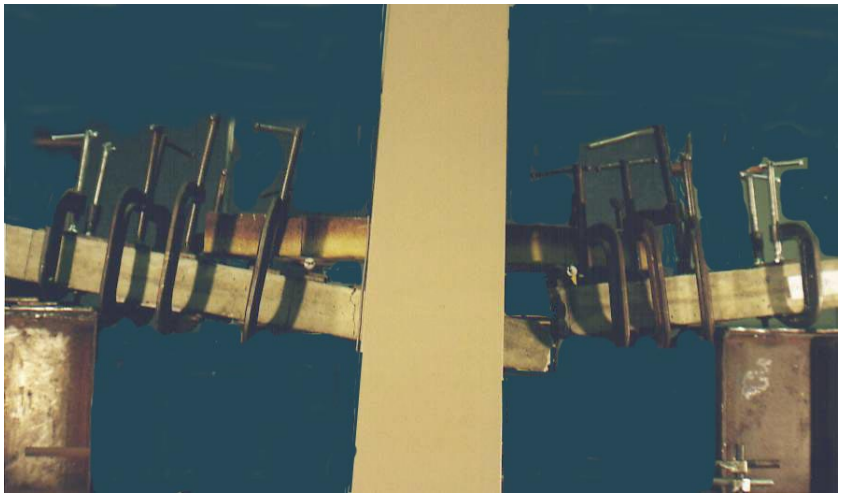

Figure D.2: Failed Beam Specimen Reinforced with 10-mm DHFRP Bars.

Each of the DHFRP reinforced beams failed by bar rupture due to their limited strain as observed in the tensile tests. These DHFRP bars were manufactured using the original preform and braidtrusion process. Load versus deflection plots were generated using the data that was recorded during the tests and is shown in Figure D.3. The behaviors of the members reinforced with DHFRP were reasonably ductile and had yield and ultimate moments rather close to the predicted values. With increased strains the

members would fail by crushing of the top fibers, much like that of a reinforced concrete beam.

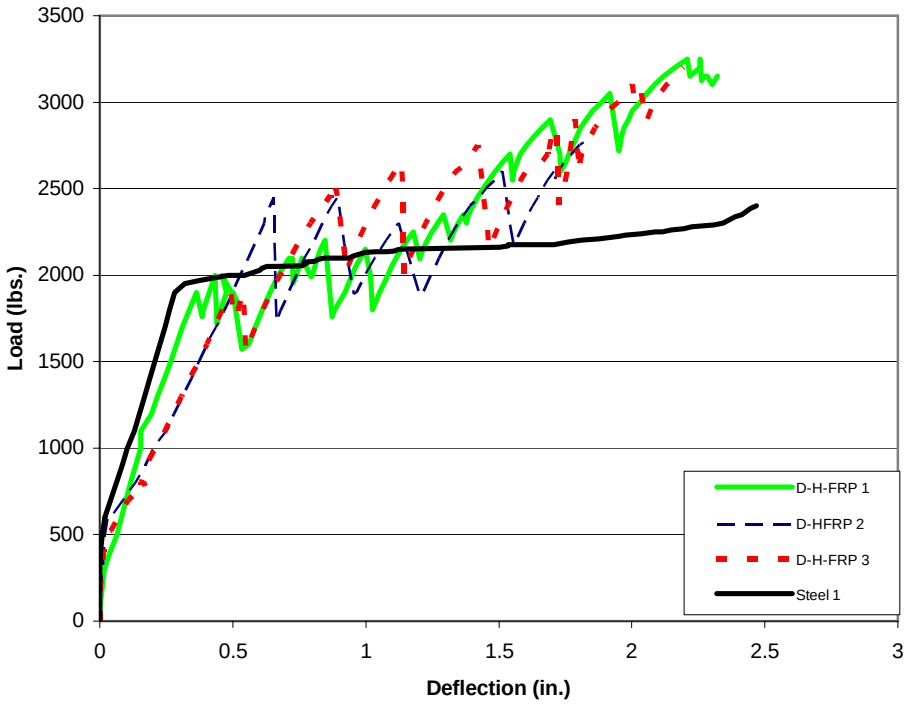

Figure D.3: Load-Deflection Behavior of Prototype R/C Beam-Slabs.

The crack patterns of the four failed beams indicated the bond characteristics of the DHFRP bar to the concrete and are shown in Figure D.4. The steel reinforced beam displayed a typical crack pattern for a well-bonded reinforcement. The cracks in the DHFRP beams were not quite as uniform as the steel beam, but the number of cracks on all specimens was very close.

Figure D.4: Cracking Patterns of Three DHFRP Beams and Companion Steel Beam.

The results of the test show that the behavior of the bar in a flexural application is very promising. The bars did not fail by the desired failure mechanism, but with some adjustments to the manufacturing process and braiding architecture the desired strain should be realized. The bond characteristics of the DHFRP was satisfactory, but further tests specifically design to test bond strength should be conducted to confirm this observation.

APPENDIX E. COMPUTER PROGRAMS

Several programs were coded using MATLAB to evaluate the behavior of DHFRP bars. This was necessary since DHFRP is a new material, and many programs are not coded for these unique material properties. Programs were written to predict the DHFRP tensile behavior (Chapter 5), the design and analysis of R/C beam members under flexure and the corresponding load-deflection and moment-curvature responses (Chapter 8), and the interaction behavior between bending moment and axial load for members subjected to reverse cyclic loading (Chapter 9). The codes are presented here as a guide for future theoretical work using pseudo-ductile FRP materials.

FADM Design Model

```
% ************* MODEL FOR P55-S CORE & KEVLAR 49 SLEEVE ***************
%
%  This program predicts the composite material properties of the DHFRP
%  10-mm diameter bars. The program calculates the mechanical
%  properties of the fiber using the various levels of material
%  architectural:  fiber level, yarn level, woven level, braiding
%  level, and composite level.  This program has been developed to be
%  used for a variety of material systems with different material
%  properties.
%
%  The input properties of various materials is contained in three
%  input files, one containing braid yarns, one containing core yarns,
%  and one containing pultrusion resin systems.
%
%  The computed yarn properties, including yarn denier and areas are
%  computed for braid, rib, and core yarns.
%  Therefore, different materials and yarn configurations can be used
%  for each of the three systems.
%
%*********************************************************************
%     VARIABLES DEFINED:
%
%  NOTE:  Any variable with the subscript _b or _c refers to braiding
yarns and core yarns, respectively.
%
%  VARIABLES DEFINED:    d_b,c   = denier of each yarn
%                        rho_b,c = density of fibers
%             N_b,c   = Total number of yarns used for the designed bar
```

```
%             D_b,c   = Total denier of each type of yarn used for the
%                       designed bar
%
%*****************************************************************
%
% INPUT INFORMATION
% Material properties:  Fibers + Resin
% NOTE:  MATERIAL PROPERTIES ARE DEFINED IN THE M-FILE STRUCTURE ARRAYS
braidyarns.m, coreyarns.m, & resins.m
%   BRAIDING YARNS
%  prop_b(1)   = Kevlar 49-1:New braid yarn denier material
%  prop_b(11) = Kevlar 49-1:New rib yarn denier material
%  prop_b(2)   = Kevlar 29-1:New denier material, both braid & yarns
%  prop_b(3)   = Kevlar 29-2:Old denier material, both b & r yarns
%  prop_b(4)   = Kevlar 49-2:Old denier material, both b& r yarns
%  prop_b(5)   = E-Glass
%  prop_b(6)   = S-Glass
%         CORE YARNS                      RESIN SYSTEMS
%      _c(1)   = IM-7-12K             _r(1) = EPON 9500/ EpiCure 9550
%      _c(2)   = P-55S-4K
%      _c(3)   = T-300
%      _c(4)   = Polypropylene
% BRAID YARN PROPERTIES
prop_b(1).sigma_u;
prop_b(1).modulus;
prop_b(1).epsilon_u;
prop_b(1).denier;
prop_b(1).rho;
prop_b(1).braid_ends;  % Ends/ carrier
% RIB YARN PROPERTIES
prop_b(11).sigma_u;
prop_b(11).modulus;
prop_b(11).epsilon_u;
prop_b(11).denier;
prop_b(11).rho;
prop_b(11).rib_ends;
% CORE YARN PROPERTIES
prop_c(1).sigma_u;
prop_c(1).modulus;
prop_c(1).epsilon_u;
prop_c(1).denier;
prop_c(1).rho;
prop_c(1).core_ends;
% RESINS
prop_r(1).sigma_y;
prop_r(1).modulus;
prop_r(1).epsilon_u;
prop_r(1).rho;
%
% BAR GEOMETRIC AND INPUT PARAMETERS
N_carrier_braid=20;   %define the total number of carriers used for
braiding yarns
N_carrier_rib=4;      %define the total number of carriers used for rib
yarns
Tot_ends_braid=prop_b(1).braid_ends*N_carrier_braid
Tot_ends_rib=prop_b(11).rib_ends*N_carrier_rib
% Now define the total number of yarns to be braided
```

```
N_b=Tot_ends_braid+Tot_ends_rib
%  Total number of core yarns defined in the input program coreyarns.m
%  Define the designed rebar size
Dia=.433;  % Diameter of bar in inches
theta_b=45;  % Braid angle in degrees
theta_c=0;   % All unidirectional yarns
%
*********************************************************************
%  OUTPUT INFORMATION
%
den_br_carrier=prop_b(1).denier*prop_b(1).braid_ends
den_rb_carrier=prop_b(11).denier*prop_b(11).rib_ends
D_braid=prop_b(1).denier*Tot_ends_braid % Total yarn denier based on
number of yarns used for the design
D_rib=prop_b(11).denier*Tot_ends_rib
D_c=prop_c(1).denier*prop_c(1).core_ends
%
%  Define area of yarn, first for each yarn
A_yarn_b=prop_b(1).denier/(5800000*prop_b(1).rho*cos(theta_b*pi/180));
A_yarn_r=prop_b(11).denier/(5800000*prop_b(11).rho*cos(theta_b*pi/180))
;
A_yarn_c=prop_c(1).denier/(5800000*prop_c(1).rho*cos(theta_c*pi/180));
%  Total yarn area for the designed bar
A_y_tot_b=A_yarn_b*Tot_ends_braid+A_yarn_r*Tot_ends_rib;
A_y_tot_c=A_yarn_c*prop_c(1).core_ends;
% Composite bar geometric calculations
A_comp=pi/4*Dia^2;  % Total bar area, based on average bar diameter
A_reinf=A_y_tot_b+A_y_tot_c
Vf_b=A_y_tot_b/(A_comp)
Vf_c=A_y_tot_c/(A_comp)
Vf_res=1-(Vf_b+Vf_c)
%
% ************COMPOSITE CALCULATIONS VIA RULE OF MIXTURES ********
% Calculate Composite bar properties
E_comp=Vf_b*prop_b(1).modulus*(cos(theta_b*pi/180))^4+Vf_c*prop_c(1).mo
dulus+Vf_res*prop_r(1).modulus  % [psi]
ep_y=prop_c(1).epsilon_u
ep_u=prop_b(1).epsilon_u/((cos(theta_b*pi/180))^2)
sigma_y_b=prop_b(1).modulus*ep_y *((cos(theta_b*pi/180))^2)
sigma_y_r=prop_r(1).modulus*ep_y
sigma_y=(Vf_b*sigma_y_b+Vf_c*prop_c(1).sigma_u+Vf_res*sigma_y_r)  %
[psi]
sigma_y_lower=Vf_b*sigma_y_b+Vf_res*sigma_y_r
sigma_u=Vf_b*prop_b(1).sigma_u*(cos(theta_b*pi/180))^2+Vf_res*prop_r(1)
.sigma_y  % [psi]
P_y=A_comp*sigma_y % [pounds]
P_u=A_comp*sigma_u  % [pounds]
%
% This subprogram plots the resulting stress-strain properties of a
DHFRP bar
%
% ************************** GRAPHICAL OUTPUT ***********************
%This plots TRI-LINEAR CURVE WITH DISCONTINUITIES
%
strain1=linspace(0,ep_y,200);
strain2=linspace(ep_y,ep_y,200);
strain3=linspace(ep_y,ep_u,200);
```

```
stress1=linspace(0,sigma_y,200);
stress2=linspace(sigma_y,sigma_y_lower,200);
stress3=linspace(sigma_y_lower,sigma_u,200);
plot(strain1,stress1,'b',strain2,stress2,'b',strain3,stress3,'b')
xlabel('Strain')
ylabel('Stress (psi)')
title('Design Stress-Strain Relation 4-Ribs, Kevlar 49 & P55S-4K')
```

DHFRP R/C BEAM DESIGN PROGRAM

```
%   This program is used to design R/C beams using either DHFRP or
%   steel longitudinal reinforcement. The design is based on 0.5 the
%   balanced ratio of steel.
%
%  GENERAL BAR INFORMATION
%     This gives both DHFRP and steel diameters and area per bar.
D_frp1=.433;   % 11-mm nominal diameter, inches
D_frp2=0.3937; % 10-mm nominal diameter, inches
D_s2=.25;      % Diameter of a number 2 steel rebar
D_s3=.375;     % Diameter of a number 2 steel rebar
D_s4=0.5;      % Diameter of a number 2 steel rebar
A_frp1=.1473;  % All areas in inches squared
A_frp2=.1217;
A_s2=.049;
A_s3=.11;
A_s4=.2;
%
%   MATERIAL & GEOMETRIC INPUT PARAMETERS
%
L=96;          % Span length in inches
a=L/3;         % The length of the shear span, inches
ep_cu=0.003;  % Ultimate strain of concrete in compression
E_s=29000;    % ksi
E_frp=8000;   % ksi
fy_s1=60000;  % psi
fy_frp1=40000
f_prime_c=4000 % concrete compressive strength, psi
B1=0.85;        % Beta factor
%*********************************************************************
%  DESIGN MODULE
%*********************************************************************
%  BEAM DESIGN FRP-1:  4" x 6" beam cross section
%
% PART 1:  FLEXURAL DESIGN
b1=4;  % beam width in inches
h1=6;  % beam height in inches
cc1=1; % clear cover
d1=h1-cc1;
rho_b1=0.85*B1*f_prime_c/fy_frp1*(87000/(87000+fy_frp1));
rho5_1=0.5*rho_b1;    % This computes 1/2 of rho balance
rho75_1=0.75*rho_b1;  % This computes 3/4 of rho balance
A_req1=rho5_1*b1*d1
```

```
Bar_num_frp1=A_req1/A_frp1
A_used_frp1=Bar_num_frp1*A_frp1;  % Actual area of bars used
%
a1=A_used_frp1*fy_frp1/(0.85*f_prime_c*b1);
% Check whether the section is a balanced section
ratio1=a1/d1
ratio_bal=B1*(87000/(87000+fy_frp1))
%
% Compute nominal moment capacity, neglecting dead weight of beam for
now.
Mn1=A_used_frp1*fy_frp1*(d1-a1/2)
Mu1=0.9*Mn1; % This gives the ultimate factored moment
Pu1=Mu1/a   % This gives the ultimate load for a tension controlled
failure
%
% PART 2:   SHEAR DESIGN
Phi=0.85;
Vu1=Pu1;
Vc1=2*sqrt(f_prime_c)*b1*d1;
%  Check -- Stirrups required if Vc/2 <= Vn
Vc_half1=Vc1/2
Vn1=Vu1/Phi     % Nominal shear capacity
% Design using double-leg stirrups
Av1=2*A_s2;
% ACI Sec. 12.13.2.1:  Stirrups anchored by a 90 deg. stirrup hook
around a bar
% Therefore, use 2 No. 2 bars in upper corners to anchor stirrups
%
% Determine maximum stirrup spacing
% (a) Based on beam depth
smax1=d1/2 %or 24 in... Probably smax1 will govern
%
% ACI 11.5.4.3 requires half this spacing if Vn> Vc + 4*sqrt(f'c)*bd
V_check1=6*sqrt(f_prime_c)*b1*d1
%
%
**********************************************************************
%  BEAM DESIGN FRP-2:  4" x 8" beam cross section
%
% PART 1:  FLEXURAL DESIGN
b2=4;  % beam width in inches
h2=8;  % beam height in inches
cc2=1.5; % clear cover
d2=h2-cc2;
A_req2=rho5_1*b2*d2
Bar_num_frp2=A_req2/A_frp1
A_used_frp2=Bar_num_frp2*A_frp1;
%
a2=A_used_frp2*fy_frp1/(0.85*f_prime_c*b2);
% To check whether the section is a balanced section
ratio2=a2/d2
ratio_bal=B1*(87000/(87000+fy_frp1))
%
% Compute nominal moment capacity, neglecting dead weight of beam for
now.
Mn2=A_used_frp2*fy_frp1*(d2-a2/2)
Mu2=0.9*Mn2; % This gives the ultimate factored moment
```

```
Pu2=Mu2/a   % This gives the ultimate load for a tension controlled
failure
%
% PART 2:   SHEAR DESIGN
Vu2=Pu2;
Vc2=2*sqrt(f_prime_c)*b2*d2;
%  Check -- Stirrups required if Vc/2 <= Vn
Vc_half2=Vc2/2
Vn2=Vu2/Phi     % Nominal shear capacity
% Design using double-leg stirrups, Av=2*A_s2
% ACI Sec. 12.13.2.1:  Stirrups anchored by a 90 deg. stirrup hook
around a bar
% Therefore, use 2 No. 2 bars in upper corners to anchor stirrups
%
% Determine maximum stirrup spacing
% (a) Based on beam depth
smax2=d2/2 %or 24 in... Probably smax1 will govern
%
% ACI 11.5.4.3 requires half this spacing if Vn> Vc + 4*sqrt(f'c)*bd
V_check2=6*sqrt(f_prime_c)*b2*d2%
%
%
**********************************************************************
%  BEAM DESIGN S-1:  4" x 6" beam cross section, STEEL
%  NOTE:  ASSUME THAT THE LONGITUDINAL STEEL ARE NUMBER 3 BARS.
% PART 1:  FLEXURAL DESIGN
rho_b2=0.85*B1*f_prime_c/fy_s1*(87000/(87000+fy_s1));
rho5_2=0.5*rho_b2;    % This computes 1/2 of rho balance
rho75_2=0.75*rho_b2;  % This computes 3/4 of rho balance
A_req3=rho5_2*b1*d1
Bar_num_s1=A_req3/A_s3
A_used_s1=Bar_num_s1*A_s3;
%
a3=A_used_s1*fy_s1/(0.85*f_prime_c*b1);
ratio3=a3/d1
ratio_bal3=B1*(87000/(87000+fy_s1))
% To check whether the section is a balanced section
%
% Compute nominal moment capacity, neglecting dead weight of beam for
now.
Mn3=A_used_s1*fy_s1*(d1-a3/2)
Mu3=0.9*Mn3; % This gives the ultimate factored moment
Pu3=Mu3/a   % This gives the ultimate load for a tension controlled
failure
%
% PART 2:   SHEAR DESIGN
Vu3=Pu3;
Vc3=2*sqrt(f_prime_c)*b1*d1;
%  Check -- Stirrups required if Vc/2 <= Vn
Vc_half3=Vc3/2
Vn3=Vu3/Phi     % Nominal shear capacity
% Design using double-leg stirrups
% ACI Sec. 12.13.2.1:  Stirrups anchored by a 90 deg. stirrup hook
around a bar
% Therefore, use 2 No. 2 bars in upper corners to anchor stirrups
%
% Determine maximum stirrup spacing
```

```
% (a) Based on beam depth
smax3=d1/2 %or 24 in... Probably smax1 will govern
%
% ACI 11.5.4.3 requires half this spacing if Vn> Vc + 4*sqrt(f'c)*bd
V_check3=6*sqrt(f_prime_c)*b1*d1
%
%
**********************************************************************
%  BEAM DESIGN S-2:  4" x 8" beam cross section, STEEL
%  Again, assume No. 3 bars are used for longitudinal steel
% PART 1:  FLEXURAL DESIGN
A_req4=rho5_2*b2*d2
Bar_num_s2=A_req4/A_s3
A_used_s2=Bar_num_s2*A_s3;
%
a4=A_used_s2*fy_s1/(0.85*f_prime_c*b2);
ratio4=a4/d2
ratio_bal4=B1*(87000/(87000+fy_s1))
% Check whether the section is a balanced section
%
% Compute nominal moment capacity, neglecting dead weight of beam for
now.
Mn4=A_used_s2*fy_s1*(d2-a4/2)
Mu4=0.9*Mn4; % This gives the ultimate factored moment
Pu4=Mu4/a   % This gives the ultimate load for a tension controlled
failure
%
% PART 2:   SHEAR DESIGN
Vu4=Pu4;
Vc4=2*sqrt(f_prime_c)*b2*d2;
%  Check -- Stirrups required if Vc/2 <= Vn
Vc_half4=Vc4/2
Vn4=Vu4/Phi     % Nominal shear capacity
% Design using double-leg stirrups
% ACI Sec. 12.13.2.1:  Stirrups anchored by a 90 deg. stirrup hook
around a bar
% Therefore, use 2 No. 2 bars in upper corners to anchor stirrups
%
% Determine maximum stirrup spacing
% (a) Based on beam depth
smax4=d2/2 %or 24 in... Probably smax1 will govern
%
% ACI 11.5.4.3 requires half this spacing if Vn> Vc + 4*sqrt(f'c)*bd
V_check4=6*sqrt(f_prime_c)*b2*d2
%
%
**********************************************************************
%    GRAPHICAL MODULE
%       This section plots the Ultimate Load and Moment Capacities and
the number of longitudinal bars
%    needed for each of the four beam designs.
%  Load Capacities
Load=[Pu1 Pu2 Pu3,Pu4];
Beam=[1 2 3,4];
figure(1)
bar(Beam,Load)
ylabel('Ultimate Load Capacity, (lb)')
```

```
title('Ultimate Load Capacity for Various Beam Designs')
gtext('4"x6" FRP Beam')
gtext('4"x8" FRP Beam')
gtext('4"x6" Steel Beam')
gtext('4"x8" Steel Beam')
%  Moment Capacities
Moment=[Mu1,Mu2,Mu3,Mu4];
figure(2)
bar(Beam,Moment)
ylabel('Ultimate Moment Capacity, (lb-in)')
title('Ultimate Moment Capacity for Various Beam Designs')
gtext('4"x6" FRP Beam')
gtext('4"x8" FRP Beam')
gtext('4"x6" Steel Beam')
gtext('4"x8" Steel Beam')
%  Number of bars needed for each design
Bar_Number=[Bar_num_frp1,Bar_num_frp2,Bar_num_s1,Bar_num_s2];
figure(3)
bar(Beam,Bar_Number)
ylabel('Number of Longitudinal Bars Needed')
title('Number of Bars Needed for Various Beam Designs')
gtext('4"x6" FRP Beam')
gtext('4"x8" FRP Beam')
gtext('4"x6" Steel Beam')
gtext('4"x8" Steel Beam')
```

DHFRP Interaction Diagram Program

```
%  This program produces an interaction diagram by a series of straight
%  lines joining the load and moment values corresponding to the
%  following five strain distributions:
%  1. A uniform compressive strain of 0.003
%  2. A strain diagram corresponding to incipient cracking, passing
%     through a compressive strain of of 0.003 on one face and zero
%     strain on the other
%  3. The balanced strain distribution and limiting compression-
%     controlled strain distribution having
%     a compressive strain of 0.003 on one face and a tensile strain of
%     -ep_y in the reinf. layer nearest to the tensile face
%  4. The limiting tension-controlled strain distribution having a
%     compressive strain of 0.003 on one face
%     and a tensile strain of -0.005 in the reinforcement layer nearest
%     to the tensile face
%  5. A uniform tensile strain of -ep_y in the steel with the concrete
%     cracked
%
%*********************************************************************
%     VARIABLES DEFINED
% Beam Geometric Input Parameters
%  b = beam width
%  h = beam height
%  d_i = depth from centroid of steel layer i to extreme compression
%        fiber of concrete
% Concrete Properties
%  f_prime_c = concrete compressive strength
%  Ec = modulus of elasticity of concrete
%  ep_c_ult = ultimate compressive strain of concrete
% Reinforcement Properties
%  fy, fy_frp = yield strength of longitudinal reinforcement
%  Es, E_frp = modulus of longitudinal reinforcement
%  d_bar = bar diameter of tensile steel
%  d_bar_prime = bar diameter of compression steel
%  Num_bar, Num_bar_prime, *_frp = total number of long. tension and
%  compression bars for both steel and frp
%  As, As_prime, *_frp = total area of steel for the section
%
%*********************************************************************
*
%
% Column and concrete input information
f_prime_c=4000; %psi
Ec=3200000;     %psi
ep_c_ult=0.003;
%
%
% ****** MODULE 1:  5-mm DHFRP-REINFORCED COLUMN ******
%
%  Reinforcement input information
fy_frp=40180; %psi
E_frp=11320000;
ep_y_frp=fy_frp/E_frp;
d_bar_frp=0.197;
```

```
Num_bar1_frp=2;
Num_bar2_frp=2;
Num_bar3_frp=0;
A1_frp=pi*d_bar_frp^2/4*Num_bar1_frp;
A2_frp=pi*d_bar_frp^2/4*Num_bar2_frp;
A3_frp=0;
%
% GEOMETRIC CALCULATIONS
b=1.5;  %width in inches
h=1.5;  %height in inches
Ag=b*h;  %Gross column area
d1=1.2;
d2=0.15;
d3=0;
d4=0;
A_tot_frp=A1_frp+A2_frp+A3_frp;
rho_t_frp=A_tot_frp/Ag;
%
% 1. Compute the concentric axial load capacity and maximum axial load
capacity
%
P_0_frp=.85*f_prime_c*(Ag-A_tot_frp)+fy_frp*A_tot_frp  % Nominal axial
load capacity
Phi_P0_frp=0.7*P_0_frp;     % for a tied column
Phi_Pn_max_frp=0.8*Phi_P0_frp;   % Maximum load allowed on column (ACI
Sec. 10.3.5.2)
%
%**************************************************************************
% 2. Point of Incipient Cracking, Z=0
%  (a) Determine c and the strains in the reinforcement
Z1_frp=0;
ep_frp1_1=Z1_frp*ep_y_frp;                    %strain in steel layer 1
c1_frp=(ep_c_ult/(ep_c_ult-ep_frp1_1))*d1;  %depth to neutral axis
ep_frp2_1=(c1_frp-d2)/c1_frp*ep_c_ult;      %strain in steel layer 2
%     (b) Compute the stresses in reinforcement layers
f_frp2_1=ep_frp2_1*E_frp; %positive in compression, negative in tension
f_frp1_1=ep_frp1_1*E_frp;
%     (c) Compute a
% the depth of the rectangular stress block, a, must be less than h
Beta1=1.05-.05*(f_prime_c/1000);   %f_prime_c in psi
a1_frp=Beta1*c1_frp;  %if a > h, then use a = h
%     (d) Compute the forces in the concrete and steel
Cc_1_frp=.85*f_prime_c*a1_frp*b;  % a*b= area of stress block
Ffrp1_1=f_frp1_1*A1_frp;
% Need to check if layer 2 lies in the compression zone; if so, then
must allow for the stress in the concrete displaced by the steel when
Fs2 is computed.
if a1_frp > d2
   Ffrp2_1=(f_frp2_1-.85*f_prime_c)*A2_frp;
else
   Ffrp2_1=f_frp2_1*A2_frp;
end
%     (e) Compute Pn
Pn1_frp=Cc_1_frp+Ffrp1_1+Ffrp2_1
%     (f) Compute Mn
Mn1_frp=(Cc_1_frp*(h/2-a1_frp/2)+Ffrp1_1*(h/2-d1)+Ffrp2_1*(h/2-d2))
%     (g) Compute Phi, Phi_Pn, and Phi_Mn
```

```
if ep_frp1_1 >= -ep_y_frp
   Phi1_frp=0.7;
elseif -ep_y_frp < ep_frp1_1 < -0.005
   Phi1_frp=0.56-68*ep_frp1_1;
elseif ep_frp1_1 < -0.005
   Phi1_frp=0.9;
end
Phi_Pn1_frp=Phi1_frp*Pn1_frp
Phi_Mn1_frp=Phi1_frp*Mn1_frp
%
%*********************************************************************
% 3. Compute Phi ad Phi_Mn for balanced failure
%  (a) Determine c and the strains in the reinforcement
Z2_frp=-1;
ep_frp1_2=Z2_frp*ep_y_frp;                  %strain in steel layer 1
c2_frp=(ep_c_ult/(ep_c_ult-ep_frp1_2))*d1;  %depth to neutral axis
ep_frp2_2=(c2_frp-d2)/c2_frp*ep_c_ult;      %strain in steel layer 2
%     (b) Compute the stresses in reinforcement layers
f_frp2_2=ep_frp2_2*E_frp; %positive in compression, negative in tension
if ep_frp1_2 < -ep_y_frp  % %Since -fy <= fsi <= fy is a condition
   f_frp1_2=-fy_frp;
else
   f_frp1_2=ep_frp1_2*E_frp;
end
%
%     (c) Compute a
% the depth of the rectangular stress block, a, must be less than h
a2_frp=Beta1*c2_frp;  %if a > h, then use a = h
%     (d) Compute the forces in the concrete and steel
Cc_2_frp=.85*f_prime_c*a2_frp*b;  % a*b= area of stress block
Ffrp1_2=f_frp1_2*A1_frp;
% Need to check if layer 2 lies in the compression zone; if so, then
must allow for the
% stress in the concrete displaced by the steel when Fs2 is computed
if a2_frp > d2
   Ffrp2_2=(f_frp2_2-.85*f_prime_c)*A2_frp;
else
   Ffrp2_2=f_frp2_2*A2_frp;
end
%     (e) Compute Pn
Pn2_frp=Cc_2_frp+Ffrp1_2+Ffrp2_2
%     (f) Compute Mn
Mn2_frp=(Cc_2_frp*(h/2-a2_frp/2)+Ffrp1_2*(h/2-d1)+Ffrp2_2*(h/2-d2))
%     (g) Compute Phi, Phi_Pn, and Phi_Mn
if ep_frp1_2 >= -ep_y_frp
   Phi2_frp=0.7;
elseif -ep_y_frp < ep_frp1_2 < -0.005
   Phi2_frp=0.56-68*ep_frp1_2;
elseif ep_frp1_2 < -0.005
   Phi2_frp=0.9;
end
Phi_Pn2_frp=Phi2_frp*Pn2_frp
Phi_Mn2_frp=Phi2_frp*Mn2_frp
%
%*********************************************************************
% 4. Compute Phi ad Phi_Mn for Z = -2
%  (a) Determine c and the strains in the reinforcement
```

```
Z3_frp=-2;
ep_frp1_3=Z3_frp*ep_y_frp;                  %strain in steel layer 1
c3_frp=(ep_c_ult/(ep_c_ult-ep_frp1_3))*d1;  %depth to neutral axis
ep_frp2_3=(c3_frp-d2)/c3_frp*ep_c_ult;      %strain in steel layer 2
%     (b) Compute the stresses in reinforcement layers
f_frp2_3=ep_frp2_3*E_frp; %positive in compression, negative in tension
if ep_frp1_3 < -ep_y_frp
   f_frp1_3=-fy_frp;
else
   f_frp1_3=ep_frp1_3*E_frp;
end
%     (c) Compute a
% the depth of the rectangular stress block, a, must be less than h
a3_frp=Beta1*c3_frp;  %if a > h, then use a = h
%     (d) Compute the forces in the concrete and steel
Cc_3_frp=.85*f_prime_c*a3_frp*b;  % a*b= area of stress block
Ffrp1_3=f_frp1_3*A1_frp;
% Need to check if layer 2 lies in the compression zone; if so, then
must allow for the
% stress in the concrete displaced by the steel when Fs2 is computed.
if a3_frp > d2
   Ffrp2_3=(f_frp2_3-.85*f_prime_c)*A2_frp;
else
   Ffrp2_3=f_frp2_3*A2_frp;
end
%     (e) Compute Pn
Pn3_frp=Cc_3_frp+Ffrp1_3+Ffrp2_3
%     (f) Compute Mn
Mn3_frp=(Cc_3_frp*(h/2-a3_frp/2)+Ffrp1_3*(h/2-d1)+Ffrp2_3*(h/2-d2))
%     (g) Compute Phi, Phi_Pn, and Phi_Mn
if ep_frp1_3 >= -ep_y_frp
   Phi3_frp=0.7;
elseif ep_frp1_3 < -0.005
   Phi3_frp=0.9;
   else
   Phi3_frp=0.56-68*ep_frp1_3;
end
Phi_Pn3_frp=Phi3_frp*Pn3_frp
Phi_Mn3_frp=Phi3_frp*Mn3_frp
%
%*********************************************************************
% 4. Compute Phi ad Phi_Mn for Z = -4
%  (a) Determine c and the strains in the reinforcement
Z4_frp=-4;
ep_frp1_4=Z4_frp*ep_y_frp;                  %strain in steel layer 1
c4_frp=(ep_c_ult/(ep_c_ult-ep_frp1_4))*d1;  %depth to neutral axis
ep_frp2_4=(c4_frp-d2)/c4_frp*ep_c_ult;      %strain in steel layer 2
%     (b) Compute the stresses in reinforcement layers
f_frp2_4=ep_frp2_4*E_frp; %positive in compression, negative in tension
if ep_frp1_4 < -ep_y_frp
   f_frp1_4=-fy_frp;
else
   f_frp1_4=ep_frp1_4*E_frp;
end
%
if f_frp1_4 > -fy_frp
   ffrp1_4=-fy_frp;
```

```
end
%     (c) Compute a
% the depth of the rectangular stress block, a, must be less than h
a4_frp=Beta1*c4_frp;  %if a > h, then use a = h
%     (d) Compute the forces in the concrete and steel
Cc_4_frp=.85*f_prime_c*a4_frp*b;  % a*b= area of stress block
Ffrp1_4=f_frp1_4*A1_frp;
% Need to check if layer 2 lies in the compression zone; if so, then
must allow for the
% stress in the concrete displaced by the steel when Fs2 is computed.
if a4_frp > d2
   Ffrp2_4=(f_frp2_4-.85*f_prime_c)*A2_frp;
else
   Ffrp2_4=f_frp2_4*A2_frp;
end
%     (e) Compute Pn
Pn4_frp=Cc_4_frp+Ffrp1_4+Ffrp2_4
%     (f) Compute Mn
Mn4_frp=(Cc_4_frp*(h/2-a4_frp/2)+Ffrp1_4*(h/2-d1)+Ffrp2_4*(h/2-d2))
%     (g) Compute Phi, Phi_Pn, and Phi_Mn
if ep_frp1_4 >= -ep_y_frp
   Phi4_frp=0.7;
elseif ep_frp1_4 < -0.005
   Phi4_frp=0.9;
   else
   Phi4_frp=0.56-68*ep_frp1_4;
end
Phi_Pn4_frp=Phi4_frp*Pn4_frp
Phi_Mn4_frp=Phi4_frp*Mn4_frp
%
%*********************************************************************
% 5. Compute the Capacity in Axial Tension
Mn5_frp=0;   %M= 0, since section is symmetrical
Phi_Mn5_frp=0;
Pn_t_frp=-fy_frp*(A1_frp+A2_frp)
Phi_Pn_t_frp=0.9*Pn_t_frp
%*********************************************************************
% COMPUTE AXIAL LOAD LEVEL ON DHFRP COLUMNS
%
Level1_frp=0.05*f_prime_c*Ag
Level2_frp=0.1*f_prime_c*Ag
Level3_frp=0.15*f_prime_c*Ag
Level4_frp=0.2*f_prime_c*Ag
Level5_frp=0.3*f_prime_c*Ag
%
% ****** MODULE 2:  STEEL-REINFORCED COLUMN ******
%  The steel module looks very similar to the DHFRP module, but with
%  the steel material properties.
%
% ****** MODULE 3:  PLOTTING OF RESULTS ******
% Plot moment-curvature results
% Actual results, DHFRP
moment11=linspace(0,Mn1_frp,200);
moment21=linspace(Mn1_frp,Mn2_frp,200);
moment31=linspace(Mn2_frp,Mn3_frp,200);
moment41=linspace(Mn3_frp,Mn4_frp,200);
moment51=linspace(Mn4_frp,Mn5_frp,200);
```

```
load11=linspace(P_0_frp,Pn1_frp,200);
load21=linspace(Pn1_frp,Pn2_frp,200);
load31=linspace(Pn2_frp,Pn3_frp,200);
load41=linspace(Pn3_frp,Pn4_frp,200);
load51=linspace(Pn4_frp,Pn_t_frp,200);
%
% Steel results
moment11s=linspace(0,Mn1,200);
moment21s=linspace(Mn1,Mn2,200);
moment31s=linspace(Mn2,Mn3,200);
moment41s=linspace(Mn3,Mn4,200);
moment51s=linspace(Mn4,Mn5,200);
load11s=linspace(P_0,Pn1,200);
load21s=linspace(Pn1,Pn2,200);
load31s=linspace(Pn2,Pn3,200);
load41s=linspace(Pn3,Pn4,200);
load51s=linspace(Pn4,Pn_t,200);
% Combine both results and plot
figure(1)
plot(moment11,load11,'b',moment21,load21,'b',moment31,load31,'b',moment
41,load41,'b',moment51,load51,'b',...
moment11s,load11s,'g',moment21s,load21s,'g',moment31s,load31s,'g',momen
t41s,load41s,'g',moment51s,load51s,'g')
xlabel('Moment, (in-lb)')
ylabel('Axial Load (lb)')
title('Theoretical Interaction Diagrams for DHFRP and Companion Steel
Rein. Beam-Columns')
gtext('DHFRP')
```

VITA

Francis Patrick Hampton was born on May 20, 1974 in Camden, New Jersey. He was awarded a Bachelor of Civil Engineering (BCE) and a Master of Civil Engineering (MCE) from the University of Delaware in 1996 and 1998, respectively. His area of research was the dynamic response of elevated water tanks using seismic isolation.

Mr. Hampton was admitted to the Ph.D. program in the Department of Civil and Architectural Engineering at Drexel University in June 1998. He was a two-time recipient of the Giegerich Memorial Fellowship (2000 and 2001), the Teaching Assistant Excellence Award (2001), and the first recipient in civil engineering of the Koerner Fellowship (2001).

Since 2002, he has been an adjunct faculty member at Villanova University in the Department of Civil and Environmental Engineering. He also has taught courses at Widener University and Drexel University in structural analysis and construction materials. He is a member of the American Society of Civil Engineers (ASCE), American Concrete Institute (ACI), and the Society for the Advancement of Material and Processing Engineering (SAMPE).

PUBLICATIONS:

Hampton, F.P., Ko, F.K., and Harris, H.G. (2004). "Low Cycle Fatigue Strength of a Ductile Hybrid Fiber Reinforced Polymer Bar for Earthquake Resistant Concrete Structures.", *Society of Manufacturing Engineers Technical Paper*, TP04PUB101.

Hampton, F.P., Ko, F.K., and Harris, H.G. (2003). "Low Cycle Fatigue Strength of a Ductile Hybrid Fiber Reinforced Polymer Bar for Earthquake Resistant Concrete Structures." *Proceedings of the 14th International Conference on Composite Materials*, July 18-22, San Diego, CA, USA.

Hampton, F.P., Harris, H.G., and Ko, F.K. (2003). "Cyclic Strength and Bond Performance of a Ductile Hybrid FRP for Concrete Structures." *Proceedings of SAMPE 2003*, May 6-10, Long Beach, California.

Lam, H.L., Hampton, F.P., Ko, F.K., and Harris, H.G. (2001). "Design Methodology of a Ductile Hybrid Kevlar-Carbon Reinforced Plastic For Concrete Structures By the Braidtrusion Process." *Proceedings of the 13th International Conference on Composite Materials*, June 24-28, Beijing, China.

Hampton, F.P, Lam, H.L., Ko, F.K., and Harris, H.G. (2001). "Design Methodology of a Ductile Hybrid FRP For Concrete Structures By the Braidtrusion Process." *Proceedings of SAMPE 2001*, May 6-10, Long Beach, California.